



## Description of the NCAR Community Atmosphere Model (CAM 5.0)

Richard B. Neale  
 Andrew Gettelman  
 Sungsu Park

Chih-Chieh Chen  
 Peter H. Lauritzen  
 David L. Williamson

Climate And Global Dynamics Division  
 National Center For Atmospheric Research  
 Boulder, Colorado, USA

Andrew J. Conley  
 Doug Kinnison  
 Dan Marsh  
 Anne K. Smith  
 Francis Vitt

Rolando Garcia  
 Jean-Francois Lamarque  
 Mike Mills  
 Simone Tilmes

Atmospheric Chemistry Division  
 National Center For Atmospheric Research  
 Boulder, Colorado, USA

<sup>2</sup> Hugh Morrison

Mesoscale and Microscale Meteorology  
 National Center For Atmospheric Research  
 Boulder, Colorado, USA

Philip Cameron-Smith

Lawrence Livermore National Lab  
 Livermore, California

William D. Collins

UC Berkeley/Lawrence Berkeley National Laboratory  
 Berkeley, California

Michael J. Iacono

Atmospheric and Environmental Research, Inc.  
 Lexington, Massachusetts

Richard C. Easter  
 Xiaohong Liu

Steven J. Ghan  
 Philip J. Rasch

Pacific Northwest National Laboratory  
 Richland, Washington

Mark A. Taylor

Sandia National Laboratories  
 Albuquerque, New Mexico

## NCAR TECHNICAL NOTES

4 The Technical Note series provides an outlet for a variety of NCAR manuscripts that contribute  
5 in specialized ways to the body of scientific knowledge but which are not suitable for journal,  
6 monograph, or book publication. Reports in this series are issued by the NCAR Scientific Di-  
7 visions; copies may be obtained on request from the Publications Office of NCAR. Designation  
8 symbols for the series include:

9

EDD: *Engineering, Design, or Development Reports*  
Equipment descriptions, test results, instrumentation,  
and operating and maintenance manuals.

IA: *Instructional Aids*  
Instruction manuals, bibliographies, film supplements,  
and other research or instructional aids.

PPR: *Program Progress Reports*  
Field program reports, interim and working reports,  
survey reports, and plans for experiments.

PROC: *Proceedings*  
Documentation of symposia, colloquia, conferences, workshops,  
and lectures. (Distribution may be limited to attendees.)

STR: *Scientific and Technical Reports*  
Data compilations, theoretical and numerical  
investigations, and experimental results.

10 *The National Center for Atmospheric Research (NCAR) is operated by the University Corpora-  
11 tion for Atmospheric Research (UCAR) and is sponsored by the National Science Foundation.  
12 Any opinions, findings, conclusions, or recommendations expressed in this publication are those  
13 of the author(s) and do not necessarily reflect the views of the National Science Foundation.*

# 14 Contents

15	<b>Acknowledgments</b>	xi
16	<b>1 Introduction</b>	1
17	1.1 Brief History . . . . .	1
18	1.1.1 CCM0 and CCM1 . . . . .	1
19	1.1.2 CCM2 . . . . .	2
20	1.1.3 CCM3 . . . . .	3
21	1.1.4 CAM3 . . . . .	4
22	1.1.5 CAM4 . . . . .	6
23	1.1.6 Overview of CAM 5.0 . . . . .	7
24	<b>2 Coupling of Dynamical Core and Parameterization Suite</b>	11
25	<b>3 Dynamics</b>	15
26	3.1 Finite Volume Dynamical Core . . . . .	15
27	3.1.1 Overview . . . . .	15
28	3.1.2 The governing equations for the hydrostatic atmosphere . . . . .	15
29	3.1.3 Horizontal discretization of the transport process on the sphere . . . . .	17
30	3.1.4 <i>A vertically Lagrangian and horizontally Eulerian control-volume discretization of the hy</i>	
31	3.1.5 Optional diffusion operators in CAM5 . . . . .	24
32	3.1.6 A mass, momentum, and total energy conserving mapping algorithm . . . . .	26
33	3.1.7 A geopotential conserving mapping algorithm . . . . .	28
34	3.1.8 Adjustment of pressure to include change in mass of water vapor . . . . .	29
35	3.1.9 Negative Tracer Fixer . . . . .	30
36	3.1.10 Global Energy Fixer . . . . .	30
37	3.1.11 Further discussion . . . . .	32
38	3.2 Spectral Element Dynamical Core . . . . .	33
39	3.2.1 Continuum Formulation of the Equations . . . . .	34
40	3.2.2 Conserved Quantities . . . . .	35
41	3.2.3 Horizontal Discretization: Functional Spaces . . . . .	36
42	3.2.4 Horizontal Discretization: Differential Operators . . . . .	38
43	3.2.5 Horizontal Discretization: Discrete Inner-Product . . . . .	39
44	3.2.6 Horizontal Discretization: The Projection Operators . . . . .	40
45	3.2.7 Horizontal Discretization: Galerkin Formulation . . . . .	40
46	3.2.8 Vertical Discretization . . . . .	41
47	3.2.9 Discrete formulation: Dynamics . . . . .	42

48	3.2.10	Consistency . . . . .	43
49	3.2.11	Time Stepping . . . . .	44
50	3.2.12	Dissipation . . . . .	44
51	3.2.13	Discrete formulation: Tracer Advection . . . . .	45
52	3.2.14	Conservation and Compatibility . . . . .	46
53	<b>3.3</b>	<b>Eulerian Dynamical Core . . . . .</b>	<b>47</b>
54	3.3.1	Generalized terrain-following vertical coordinates . . . . .	47
55	3.3.2	Conversion to final form . . . . .	49
56	3.3.3	Continuous equations using $\partial \ln(\pi)/\partial t$ . . . . .	50
57	3.3.4	Semi-implicit formulation . . . . .	51
58	3.3.5	Energy conservation . . . . .	53
59	3.3.6	Horizontal diffusion . . . . .	56
60	3.3.7	Finite difference equations . . . . .	58
61	3.3.8	Time filter . . . . .	60
62	3.3.9	Spectral transform . . . . .	61
63	3.3.10	Spectral algorithm overview . . . . .	61
64	3.3.11	Combination of terms . . . . .	64
65	3.3.12	Transformation to spectral space . . . . .	65
66	3.3.13	Solution of semi-implicit equations . . . . .	66
67	3.3.14	Horizontal diffusion . . . . .	67
68	3.3.15	Initial divergence damping . . . . .	68
69	3.3.16	Transformation from spectral to physical space . . . . .	69
70	3.3.17	Horizontal diffusion correction . . . . .	70
71	3.3.18	Semi-Lagrangian Tracer Transport . . . . .	71
72	3.3.19	Mass fixers . . . . .	75
73	3.3.20	Energy Fixer . . . . .	77
74	3.3.21	Statistics Calculations . . . . .	78
75	3.3.22	Reduced grid . . . . .	78
76	<b>3.4</b>	<b>Semi-Lagrangian Dynamical Core . . . . .</b>	<b>78</b>
77	3.4.1	Introduction . . . . .	78
78	3.4.2	Vertical coordinate and hydrostatic equation . . . . .	79
79	3.4.3	Semi-implicit reference state . . . . .	79
80	3.4.4	Perturbation surface pressure prognostic variable . . . . .	79
81	3.4.5	Extrapolated variables . . . . .	80
82	3.4.6	Interpolants . . . . .	80
83	3.4.7	Continuity Equation . . . . .	80
84	3.4.8	Thermodynamic Equation . . . . .	82
85	3.4.9	Momentum equations . . . . .	84
86	3.4.10	Development of semi-implicit system equations . . . . .	85
87	3.4.11	Trajectory Calculation . . . . .	91
88	3.4.12	Mass and energy fixers and statistics calculations . . . . .	91

89	<b>4 Model Physics</b>	<b>93</b>
90	4.1 Conversion to and from dry and wet mixing ratios for trace constituents in the model	95
91	4.2 Moist Turbulence Scheme	97
92	4.2.1 Bulk Moist Richardson Number	98
93	4.2.2 Identification of Convective, Stably Turbulent, and Stable Layers	100
94	4.2.3 Turbulent Length Scale	101
95	4.2.4 Steady-State Turbulent Kinetic Energy	101
96	4.2.5 Stability Functions	102
97	4.2.6 CL Extension-Merging Procedure	103
98	4.2.7 Entrainment Rates at the CL Top and Base Interfaces	104
99	4.2.8 Implicit Diffusion with Implicit Diffusivity	104
100	4.2.9 Implicit Surface Stress	106
101	4.3 Shallow Convection Scheme	108
102	4.3.1 Reconstruction of Mean Profiles and Cloud Condensate Partitioning	108
103	4.3.2 Source Air Properties of Convective Updraft	110
104	4.3.3 Closures at the Cloud Base	111
105	4.3.4 Vertical Evolution of A Single Updraft Plume	112
106	4.3.5 Penetrative Entrainment	113
107	4.3.6 Convective Fluxes at and below the PBL top interface	114
108	4.3.7 Grid-Mean Tendency of Conservative Scalars	115
109	4.3.8 Grid-Mean Tendency of Non-Conservative Scalars	116
110	4.4 Deep Convection	118
111	4.4.1 Updraft Ensemble	118
112	4.4.2 Downdraft Ensemble	121
113	4.4.3 Closure	122
114	4.4.4 Numerical Approximations	122
115	4.4.5 Deep Convective Momentum Transports	125
116	4.4.6 Deep Convective Tracer Transport	125
117	4.5 Evaporation of convective precipitation	127
118	4.6 Cloud Microphysics	128
119	4.6.1 Overview of the microphysics scheme	128
120	4.6.2 Radiative Treatment of Ice	133
121	4.6.3 Formulations for the microphysical processes	133
122	4.7 Cloud Macrophysics	141
123	4.7.1 Cloud Fractions	141
124	4.7.2 Cloud Overlaps	144
125	4.7.3 Condensation Processes	146
126	4.8 Aerosols	151
127	4.8.1 Emissions	152
128	4.8.2 Chemistry	153
129	4.8.3 Secondary Organic Aerosol	154
130	4.8.4 Nucleation	154
131	4.8.5 Condensation	154
132	4.8.6 Coagulation	155
133	4.8.7 Water Uptake	155

134	4.8.8	Subgrid Vertical Transport and Activation/Resuspension . . . . .	157
135	4.8.9	Wet Deposition . . . . .	157
136	4.8.10	Dry Deposition . . . . .	158
137	4.9	Condensed Phase Optics . . . . .	160
138	4.9.1	Tropospheric Aerosol Optics . . . . .	160
139	4.9.2	Stratospheric Volcanic Aerosol Optics . . . . .	160
140	4.9.3	Liquid Cloud Optics . . . . .	162
141	4.9.4	Ice Cloud Optics . . . . .	162
142	4.9.5	Snow Cloud Optics . . . . .	164
143	4.10	Radiative Transfer . . . . .	165
144	4.10.1	Combination of Aerosol Radiative Properties . . . . .	165
145	4.10.2	Combination of Cloud Optics . . . . .	165
146	4.10.3	Radiative Fluxes and Heating Rates . . . . .	166
147	4.10.4	Surface Radiative Properties . . . . .	169
148	4.10.5	Time Sampling . . . . .	169
149	4.10.6	Diurnal Cycle and Earth Orbit . . . . .	169
150	4.10.7	Solar Spectral Irradiance . . . . .	171
151	4.11	Surface Exchange Formulations . . . . .	176
152	4.11.1	Land . . . . .	176
153	4.11.2	Ocean . . . . .	180
154	4.11.3	Sea Ice . . . . .	181
155	4.12	Dry Adiabatic Adjustment . . . . .	182
156	4.13	Prognostic Greenhouse Gases . . . . .	183
157	<b>5</b>	<b>Extensions to CAM</b> . . . . .	<b>185</b>
158	5.1	Chemistry . . . . .	186
159	5.1.1	Introduction . . . . .	186
160	5.1.2	Emissions . . . . .	186
161	5.1.3	Lower boundary conditions . . . . .	186
162	5.1.4	Lightning . . . . .	187
163	5.1.5	Dry deposition . . . . .	187
164	5.1.6	Wet removal . . . . .	187
165	5.1.7	Photolytic Approach (Neutral Species) . . . . .	188
166	5.1.8	Numerical Solution Approach . . . . .	188
167	5.2	Superfast Chemistry . . . . .	190
168	5.2.1	Chemical mechanism . . . . .	190
169	5.2.2	LINOZ . . . . .	190
170	5.2.3	PSC ozone loss . . . . .	191
171	5.2.4	Upper boundary condition . . . . .	191
172	5.3	WACCM4.0 Physical Parameterizations . . . . .	192
173	5.3.1	WACCM4.0 Domain and Resolution . . . . .	192
174	5.3.2	Molecular Diffusion and Constituent Separation . . . . .	193
175	5.3.3	Gravity Wave Drag . . . . .	196
176	5.3.4	Turbulent Mountain Stress . . . . .	203
177	5.3.5	QBO Forcing . . . . .	204

178	5.3.6	Radiation	205
179	5.3.7	WACCM4.0 chemistry	207
180	5.3.8	Electric Field	222
181	5.3.9	Boundary Conditions	231
182	<b>6</b>	<b>Initial and Boundary Data</b>	<b>233</b>
183	6.1	Initial Data	233
184	6.2	Boundary Data	234

## Appendices

185	<b>A</b>	<b>Physical Constants</b>	<b>237</b>
186	<b>B</b>	<b>Acronyms</b>	<b>239</b>
187	<b>C</b>	<b>Resolution and dycore-dependent parameters</b>	<b>241</b>
188		<b>References</b>	<b>242</b>



# <sup>189</sup> List of Figures

190	3.1	A graphical illustration of the different levels of sub-cycling in CAM5. . . . .	24
191	3.2	Tiling the surface of the sphere with quadrilaterals. An inscribed cube is projected to the surface	
192	3.3	A $4 \times 4$ tensor product grid of GLL nodes used within each element, for a degree $d = 3$ discretiza	
193	3.4	Vertical level structure of CAM 5.0 . . . . .	53
194	3.5	Pentagonal truncation parameters . . . . .	62
195	4.1	Schematic structure of moist turbulence scheme . . . . .	99
196	4.2	Schematic structure of shallow cumulus scheme . . . . .	109
197	4.3	Predicted species for interstitial and cloud-borne component of each aerosol mode in MAM-7. St	
198	4.4	Predicted species for interstitial and cloud-borne component of each aerosol mode in MAM-3. St	
199	4.5	Kurucz spectrum. ssf in $\text{W}/\text{m}^2/\text{nm}$ . Source Data: AER. Range from [20, 20000] nm.173	
200	4.6	Lean spectrum. Average over 1 solar cycle, May 1, 1996 to Dec 31, 2006. Source Data: Marsh. s	
201	4.7	Relative difference, $\frac{\text{Lean} - \text{Kurucz}}{.5(\text{Lean} + \text{Kurucz})}$ between spectra. RRTMG band boundaries are marked with ve	
202	5.1	Global mean distribution of charged constituents during July solar minimum conditions.211	
203	5.2	a) Global distribution of ionization rates at $7.3 \times 10^{-5}$ hPa, July 1, UT0100 HRS. Contour interval	



<sup>204</sup> **List of Tables**

205	4.1	Size distributions of primary emissions. . . . .	156
206	4.2	Assumed SOA (gas) yields . . . . .	156
207	4.3	Hygroscopicity of aerosol components . . . . .	156
208	4.4	Density (kg/m <sup>3</sup> ) of aerosol material. . . . .	160
209	4.5	Hygroscopicity of aerosol components. . . . .	160
210	4.6	RRTMG_SW spectral band boundaries and the solar irradiance in each band. .	167
211	4.7	RRTMG_LW spectral band boundaries. . . . .	168
212	4.8	Band-level ratio of Solar Irradiances, based on average of one solar cycle . . . . .	172
213	5.1	Surface fluxes for CAM4 superfast chemistry. . . . .	186
214	5.2	WACCM4.0 Neutral Chemical Species (51 computed species + N <sub>2</sub> ) . . . . .	213
215	5.1	(continued) WACCM4.0 Neutral Chemical Species (51 computed species + N <sub>2</sub> ) .	214
216	5.2	WACCM4.0 Gas-phase Reactions. . . . .	215
217	5.2	(continued) WACCM4.0 Gas-phase Reactions. . . . .	216
218	5.2	(continued) WACCM4.0 Gas-phase Reactions. . . . .	217
219	5.2	(continued) WACCM4.0 Gas-phase Reactions. . . . .	218
220	5.2	(continued) WACCM4.0 Gas-phase Reactions. . . . .	219
221	5.3	WACCM4.0 Heterogeneous Reactions on liquid and solid aerosols. . . . .	219
222	5.4	WACCM4.0 Photolytic Reactions. . . . .	220
223	5.4	(continued) WACCM4.0 Photolytic Reactions. . . . .	221
224	5.5	Ion-neutral and recombination reactions and exothermicities. . . . .	222
225	5.6	Ionization reactions. . . . .	223
226	5.7	EUVAC model parameters. . . . .	223
227	C.1	Resolution-dependent parameters . . . . .	241



## <sup>228</sup> Acknowledgments

<sup>229</sup> The authors wish to acknowledge members of NCAR's Atmospheric Modeling and Predictability  
<sup>230</sup> Section (AMP), Computer Software and Engineering Group (CSEG), and Computation and  
<sup>231</sup> Information Systems Laboratory (CISL) for their contributions to the development of CAM 5.0.

<sup>232</sup> The new model would not exist without the significant input from members of the CESM  
<sup>233</sup> Atmospheric Model Working Group ([AMWG](#)) too numerous to mention. Leo Donner (GFDL),  
<sup>234</sup> Minghua Zhang (SUNY) and Phil Rasch (PNNL) were the co-chairs of the AMWG during the  
<sup>235</sup> development of CAM 5.0.

<sup>236</sup> We would like to acknowledge the substantial contributions to the CAM 5.0 effort from the  
<sup>237</sup> National Science Foundation, Department of Energy, the National Oceanic and Atmospheric  
<sup>238</sup> Administration, and the National Aeronautics and Space Administration.



<sup>239</sup> **Chapter 1**

<sup>240</sup> **Introduction**

<sup>241</sup> This report presents the details of the governing equations, physical parameterizations, and  
<sup>242</sup> numerical algorithms defining the version of the NCAR Community Atmosphere Model des-  
<sup>243</sup> ignated CAM 5.0. The material provides an overview of the major model components, and  
<sup>244</sup> the way in which they interact as the numerical integration proceeds. Details on the coding  
<sup>245</sup> implementation, along with in-depth information on running the CAM 5.0 code, are given in a  
<sup>246</sup> separate technical report entitled ‘‘User’s Guide to Community Atmosphere ModelCAM 5.0’’  
<sup>247</sup> [Eaton, 2010]. As before, it is our objective that this model provide NCAR and the university  
<sup>248</sup> research community with a reliable, well documented atmospheric general circulation model.  
<sup>249</sup> This version of the CAM 5.0 incorporates a number enhancements to the physics package (*e.g.*  
<sup>250</sup> adjustments to the deep convection algorithm including the addition of Convective Momentum  
<sup>251</sup> Transports (CMT), a transition to the finite volume dynamical core as default and the option  
<sup>252</sup> to run a computationally highly scaleable dynamical core). The ability to transition between  
<sup>253</sup> CAM-standalone and fully coupled experiment frameworks is much improved in CAM 5.0. We  
<sup>254</sup> believe that collectively these improvements provide the research community with a significantly  
<sup>255</sup> improved atmospheric modeling capability.

<sup>256</sup> **1.1 Brief History**

<sup>257</sup> **1.1.1 CCM0 and CCM1**

<sup>258</sup> Over the last twenty years, the NCAR Climate and Global Dynamics (CGD) Division has pro-  
<sup>259</sup> vided a comprehensive, three-dimensional global atmospheric model to university and NCAR  
<sup>260</sup> scientists for use in the analysis and understanding of global climate. Because of its widespread  
<sup>261</sup> use, the model was designated a community tool and given the name Community Climate  
<sup>262</sup> Model (CCM). The original versions of the NCAR Community Climate Model, CCM0A  
<sup>263</sup> [Washington, 1982] and CCM0B [Williamson, 1983], were based on the Australian spectral model  
<sup>264</sup> [Bourke et al., 1977; McAvaney et al., 1978] and an adiabatic, inviscid version of the ECMWF  
<sup>265</sup> spectral model [Baede et al., 1979]. The CCM0B implementation was constructed so that its  
<sup>266</sup> simulated climate would match the earlier CCM0A model to within natural variability (*e.g.* in-  
<sup>267</sup> corporated the same set of physical parameterizations and numerical approximations), but also  
<sup>268</sup> provided a more flexible infrastructure for conducting medium- and long-range global forecast  
<sup>269</sup> studies. The major strength of this latter effort was that all aspects of the model were described

270 in a series of technical notes, which included a Users' Guide [Sato et al., 1983], a subroutine guide  
271 which provided a detailed description of the code [Williamson et al., 1983] a detailed description  
272 of the algorithms [Williamson, 1983], and a compilation of the simulated circulation statistics  
273 [Williamson and Williamson, 1984]. This development activity firmly established NCAR's com-  
274 mitment to provide a versatile, modular, and well-documented atmospheric general circulation  
275 model that would be suitable for climate and forecast studies by NCAR and university scien-  
276 tists. A more detailed discussion of the early history and philosophy of the Community Climate  
277 Model can be found in Anthes [1986].

278 The second generation community model, CCM1, was introduced in July of 1987, and in-  
279 cluded a number of significant changes to the model formulation which were manifested in  
280 changes to the simulated climate. Principal changes to the model included major modifica-  
281 tions to the parameterization of radiation, a revised vertical finite-differencing technique for the  
282 dynamical core, modifications to vertical and horizontal diffusion processes, and modifications  
283 to the formulation of surface energy exchange. A number of new modeling capabilities were  
284 also introduced, including a seasonal mode in which the specified surface conditions vary with  
285 time, and an optional interactive surface hydrology that followed the formulation presented by  
286 Manabe [1969]. A detailed series of technical documentation was also made available for this ver-  
287 sion [Williamson et al., 1987; Bath et al., 1987; Williamson and Williamson, 1987; Hack et al.,  
288 1989] and more completely describe this version of the CCM.

### 289 1.1.2 CCM2

290 The most ambitious set of model improvements occurred with the introduction of the third  
291 generation of the Community Climate Model, CCM2, which was released in October of 1992.  
292 This version was the product of a major effort to improve the physical representation of a wide  
293 range of key climate processes, including clouds and radiation, moist convection, the planetary  
294 boundary layer, and transport. The introduction of this model also marked a new philosophy  
295 with respect to implementation. The CCM2 code was entirely restructured so as to satisfy three  
296 major objectives: much greater ease of use, which included portability across a wide range of  
297 computational platforms; conformance to a plug-compatible physics interface standard; and the  
298 incorporation of single-job multitasking capabilities.

299 The standard CCM2 model configuration was significantly different from its predecessor in  
300 almost every way, starting with resolution where the CCM2 employed a horizontal T42 spectral  
301 resolution (approximately  $2.8 \times 2.8$  degree transform grid), with 18 vertical levels and a rigid lid  
302 at 2.917 mb. Principal algorithmic approaches shared with CCM1 were the use of a semi-implicit,  
303 leap frog time integration scheme; the use of the spectral transform method for treating the dry  
304 dynamics; and the use of a bi-harmonic horizontal diffusion operator. Major changes to the  
305 dynamical formalism included the use of a terrain-following hybrid vertical coordinate, and the  
306 incorporation of a shape-preserving semi-Lagrangian transport scheme [Williamson and Olson,  
307 1994a] for advecting water vapor, as well as an arbitrary number of other scalar fields (e.g. cloud  
308 water variables, chemical constituents, etc.). Principal changes to the physics included the use  
309 of a  $\delta$ -Eddington approximation to calculate solar absorption [Briegleb, 1992]; the use of a Voigt  
310 line shape to more accurately treat infrared radiative cooling in the stratosphere; the inclusion  
311 of a diurnal cycle to properly account for the interactions between the radiative effects of the  
312 diurnal cycle and the surface fluxes of sensible and latent heat; the incorporation of a finite heat

capacity soil/sea ice model; a more sophisticated cloud fraction parameterization and treatment of cloud optical properties [Kiehl et al., 1994]; the incorporation of a sophisticated non-local treatment of boundary-layer processes [Holtslag and Boville, 1993a]; the use of a simple mass flux representation of moist convection [Hack, 1994a], and the optional incorporation of the Biosphere-Atmosphere Transfer Scheme (BATS) of Dickinson et al. [1987]. As with previous versions of the model, a User's Guide [Bath et al., 1992] and model description [Hack et al., 1993] were provided to completely document the model formalism and implementation. Control simulation data sets were documented in Williamson [1993].

### 1.1.3 CCM3

The CCM3 was the fourth generation in the series of NCAR's Community Climate Model. Many aspects of the model formulation and implementation were identical to the CCM2, although there were a number of important changes that were incorporated into the collection of parameterized physics, along with some modest changes to the dynamical formalism. Modifications to the physical representation of specific climate processes in the CCM3 were motivated by the need to address the more serious systematic errors apparent in CCM2 simulations, as well as to make the atmospheric model more suitable for coupling to land, ocean, and sea-ice component models. Thus, an important aspect of the changes to the model atmosphere was that they address well known systematic biases in the top-of-atmosphere and surface (to the extent that they were known) energy budgets. When compared to the CCM2, changes to the model formulation fell into five major categories: modifications to the representation of radiative transfer through both clear and cloudy atmospheric columns, modifications to hydrological processes (i.e., in the form of changes to the atmospheric boundary layer, moist convection, and surface energy exchange), the incorporation of a sophisticated land surface model, the incorporation of an optional slab mixed-layer ocean/thermodynamic sea-ice component, and a collection of other changes to the formalism which did not introduce significant changes to the model climate.

Changes to the clear-sky radiation formalism included the incorporation of minor CO<sub>2</sub> bands trace gases (*CH*<sub>4</sub>, *N*<sub>2</sub>*O*, *CFC*11, *CFC*12) in the longwave parameterization, and the incorporation of a background aerosol (0.14 optical depth) in the shortwave parameterization. All-sky changes included improvements to the way in which cloud optical properties (effective radius and liquid water path) were diagnosed, the incorporation of the radiative properties of ice clouds, and a number of minor modifications to the diagnosis of convective and layered cloud amount. Collectively these modifications substantially reduced systematic biases in the global annually averaged clear-sky and all-sky outgoing longwave radiation and absorbed solar radiation to well within observational uncertainty, while maintaining very good agreement with global observational estimates of cloud forcing. Additionally, the large warm bias in simulated July surface temperature over the Northern Hemisphere, the systematic over-prediction of precipitation over warm land areas, and a large component of the stationary-wave error in CCM2, were also reduced as a result of cloud-radiation improvements.

Modifications to hydrological processes included revisions to the major contributing parameterizations. The formulation of the atmospheric boundary layer parameterization was revised (in collaboration with Dr. A. A. M. Holtslag of KNMI), resulting in significantly improved estimates of boundary layer height, and a substantial reduction in the overall magnitude of the hydrological cycle. Parameterized convection was also modified where this process was repre-

356 sented using the deep moist convection formalism of [Zhang and McFarlane \[1995\]](#) in conjunction  
357 with the scheme developed by [Hack \[1994a\]](#) for CCM2. This change resulted in an additional  
358 reduction in the magnitude of the hydrological cycle and a smoother distribution of tropical pre-  
359 cipitation. Surface roughness over oceans was also diagnosed as a function of surface wind speed  
360 and stability, resulting in more realistic surface flux estimates for low wind speed conditions.  
361 The combination of these changes to hydrological components resulted in a 13% reduction in  
362 the annually averaged global latent heat flux and the associated precipitation rate. It should  
363 be pointed out that the improvements in the radiative and hydrological cycle characteristics of  
364 the model climate were achieved without compromising the quality of the simulated equilibrium  
365 thermodynamic structures (one of the major strengths of the CCM2) thanks in part to the  
366 incorporation of a [Sundqvist \[1988\]](#) style evaporation of stratiform precipitation.

367 The CCM3 incorporated version 1 of the Land Surface Model (LSM) developed by [Bonan](#)  
368 [[1996](#)] which provided for the comprehensive treatment of land surface processes. This was a  
369 one-dimensional model of energy, momentum, water, and CO<sub>2</sub> exchange between the atmosphere  
370 and land, accounting for ecological differences among vegetation types, hydraulic and thermal  
371 differences among soil types, and allowing for multiple surface types including lakes and wetlands  
372 within a grid cell. LSM replaced the prescribed surface wetness, prescribed snow cover, and  
373 prescribed surface albedos in CCM2. It also replaced the land surface fluxes in CCM2, using  
374 instead flux parameterizations that included hydrological and ecological processes (*e.g.* soil  
375 water, phenology, stomatal physiology, interception of water by plants).

376 The fourth class of changes to the CCM2 included the option to run CCM3 with a simple  
377 slab ocean-thermodynamic sea ice model. The model employs a spatially and temporally pre-  
378 scribed ocean heat flux and mixed layer depth, which ensures replication of realistic sea surface  
379 temperatures and ice distributions for the present climate. The model allowed for the simplest  
380 interactive surface for the ocean and sea ice components of the climate system.

381 The final class of model modifications included a change to the form of the hydrostatic matrix  
382 which ensures consistency between  $\omega$  and the discrete continuity equation, and a more general-  
383 ized form of the gravity wave drag parameterization. In the latter case, the parameterization  
384 was configured to behave in the same way as the CCM2 parameterization of wave drag, but  
385 included the capability to exploit more sophisticated descriptions of this process.

386 One of the more significant implementation differences with the earlier model was that CCM3  
387 included an optional message-passing configuration, allowing the model to be executed as a  
388 parallel task in distributed-memory environments. This was an example of how the Climate  
389 and Global Dynamics Division continued to invest in technical improvements to the CCM in  
390 the interest of making it easier to acquire and use in evolving computational environments. As  
391 was the case for CCM2, the code was internally documented, obviating the need for a separate  
392 technical note that describes each subroutine and common block in the model library. Thus,  
393 the Users' Guide, the land surface technical note, the CCM3 technical note [[Kiehl et al., 1996](#)],  
394 the actual code and a series of reviewed scientific publications (including a special issue of the  
395 *Journal of Climate*, Volume 11, Number 6) were designed to completely document CCM3.

### 396 1.1.4 CAM3

397 The CAM3 was the fifth generation of the NCAR atmospheric GCM. The name of the model  
398 series was changed from Community Climate Model to Community Atmosphere Model to reflect

399 the role of CAM3 in the fully coupled climate system. In contrast to previous generations of  
400 the atmospheric model, CAM3 had been designed through a collaborative process with users  
401 and developers in the Atmospheric Model Working Group (AMWG). The AMWG includes  
402 scientists from NCAR, the university community, and government laboratories. For CAM3,  
403 the consensus of the AMWG was to retain the spectral Eulerian dynamical core for the first  
404 official release although the code includes the option to run with semi-Lagrange dynamics or  
405 with finite-volume dynamics (FV). The addition of FV was a major extension to the model  
406 provided through a collaboration between NCAR and NASA Goddard's Data Assimilation Office  
407 (DAO). The major changes in the physics included treatment of cloud condensed water using a  
408 prognostic formulation with a bulk microphysical component following [Rasch and Kristjánsson \[1998a\]](#) and a macroscale component following [Zhang et al. \[2003b\]](#). The [Zhang and McFarlane \[1995\]](#) parameterization for deep convection was retained from CCM3.

411 A new treatment of geometrical cloud overlap in the radiation calculations computed the  
412 shortwave and longwave fluxes and heating rates for random overlap, maximum overlap, or  
413 an arbitrary combination of maximum and random overlap. The calculation was completely  
414 separated from the radiative parameterizations. The introduction of the generalized overlap  
415 assumptions permitted more realistic treatments of cloud-radiative interactions. The method-  
416 ology was designed and validated against calculations based upon the independent column ap-  
417 proximation (ICA). A new parameterization for the longwave absorptivity and emissivity of  
418 water vapor preserved the formulation of the radiative transfer equations using the absorptiv-  
419 ity/emissivity method. The components of the method related to water vapor were replaced with  
420 new terms calculated with the General Line-by-line Atmospheric Transmittance and Radiance  
421 Model (GENLN3). The mean absolute errors in the surface and top-of-atmosphere clear-sky  
422 longwave fluxes for standard atmospheres were reduced to less than 1 W/m<sup>2</sup>. The near-infrared  
423 absorption by water vapor was also updated to a parameterization based upon the HITRAN2k  
424 line database [[Rothman et al., 2003](#)] that incorporated the CKD 2.4 prescription for the con-  
425 tinuum. The magnitude of errors in flux divergences and heating rates relative to modern LBL  
426 calculations were reduced by approximately seven times compared to the previous CCM3 pa-  
427 rameterization. The uniform background aerosol was replaced with a present-day climatology  
428 of sulfate, sea-salt, carbonaceous, and soil-dust aerosols. The climatology was obtained from a  
429 chemical transport model forced with meteorological analysis and constrained by assimilation of  
430 satellite aerosol retrievals. These aerosols affect the shortwave energy budget of the atmosphere.  
431 CAM3 also included a mechanism for treating the shortwave and longwave effects of volcanic  
432 aerosols. Evaporation of convective precipitation following [Sundqvist \[1988\]](#) was implemented  
433 and enhancement of atmospheric moisture through this mechanism was offset by drying intro-  
434 duced by changes in the longwave absorptivity and emissivity. A careful formulation of vertical  
435 diffusion of dry static energy was also implemented.

436 Additional capabilities included a new thermodynamic package for sea ice in order to mimic  
437 the major non-dynamical aspects of CSIM; including snow depth, brine pockets, internal short-  
438 wave radiative transfer, surface albedo, ice-atmosphere drag, and surface exchange fluxes. CAM3  
439 also allowed for an explicit representation of fractional land and sea-ice coverage that gave a  
440 much more accurate representation of flux exchanges from coastal boundaries, island regions,  
441 and ice edges. This fractional specification provided a mechanism to account for flux differences  
442 due to sub-grid inhomogeneity of surface types. A new, extensible climatological and time-mean  
443 sea-surface temperature boundary data was made available from a blended product using the

444 global HadISST OI dataset prior to 1981 and the Smith/Reynolds EOF dataset post-1981. Cou-  
445 pling was upgraded in order to couple the dynamical core with the parameterization suite in a  
446 purely time split or process split manner. The distinction is that in the process split approx-  
447 imation the physics and dynamics are both calculated from the same past state, while in the  
448 time split approximations the dynamics and physics are calculated sequentially, each based on  
449 the state produced by the other.

#### 450 1.1.5 CAM4

451 The CAM4 was the sixth generation of the NCAR atmospheric GCM and had again been devel-  
452 oped through a collaborative process of users and developers in the Atmosphere Model Working  
453 Group (AMWG) with significant input from the Chemistry Climate Working Group (Chem-Clim  
454 WG) and the Whole Atmosphere Model Working Group (WAMWG). The model had science en-  
455 hancements from CAM3 and represented an intermediate release version as part of a staged and  
456 parallel process in atmospheric model development. In the CAM4 changes to the moist physi-  
457 cal representations centered on enhancements to the existing [Zhang and McFarlane \[1995\]](#) deep  
458 convection parameterization. The calculation of Convective Available Potential Energy (CAPE)  
459 assumed an entraining plume to provide the in-cloud temperature and humidity profiles used  
460 to determine buoyancy and related cloud closure properties (chapter 4.4). The modification is  
461 based on the conservation of moist entropy and mixing methods of [Raymond and Blyth \[1986,](#)  
462 [1992\]](#). It replaced the standard undilute non-entraining plume method used in CAM3 and was  
463 employed to increase convection sensitivity to tropospheric moisture and reduce the amplitude  
464 of the diurnal cycle of precipitation over land. Sub-grid scale Convective Momentum Trans-  
465 ports (CMT) were added to the deep convection scheme following [Richter and Rasch \[2008\]](#) and  
466 the methodology of [Gregory et al. \[1997b\]](#) (chapter 4.4.5). CMT affects tropospheric climate  
467 mainly through changes to the Coriolis torque. These changes resulted in improvement of the  
468 Hadley circulation during northern Winter and it reduced many of the model biases. In an  
469 annual mean, the tropical easterly bias, subtropical westerly bias, and the excessive southern  
470 hemisphere mid-latitude jet were improved.

471 In combination these modifications to the deep-convection lead to significant improvements  
472 in the phase, amplitude and spacial anomaly patterns of the modeled El Niño, as documented  
473 in [Neale et al. \[2008\]](#). The calculation of cloud fraction in polar climates was also modified for  
474 the CAM4.0. Due to the combination of a diagnostic cloud fraction and prognostic cloud water  
475 representation it was possible to model unphysical extensive cloud decks with near zero in-cloud  
476 water in the CAM3. This was particularly pervasive in polar climates in Winter. These calcula-  
477 tion inconsistencies and large cloud fractions are significantly reduced with modifications to the  
478 calculation of stratiform cloud following [Vavrus and Waliser \[2008\]](#). In the lower troposphere a  
479 'freeze-drying' process is performed whereby cloud fractions were systematically reduced for very  
480 low water vapor amounts. The low cloud reduction caused an Arctic-wide drop of  $15 \text{ W m}^{-2}$  in  
481 surface cloud radiative forcing (CRF) during winter and about a 50% decrease in mean annual  
482 Arctic CRF. Consequently, wintertime surface temperatures fell by up to 4 K on land and 2 K  
483 over the Arctic Ocean, thus significantly reducing the CAM3 pronounced warm bias. More gen-  
484 erally the radiation calculation was performed using inconsistent cloud fraction and condensate  
485 quantities in the CAM3. In CAM4 this was remedied with an updated cloud fraction calcula-  
486 tion prior to the radiation call at each physics timestep. The coupled climate performance with

487 the CAM4.0 physics changes was summarized in the horizontal resolution comparison study of  
488 Gent et al. [2009].

489 For the dynamical core component of CAM4 the finite volume (FV) scheme was made the  
490 default due to its superior transport properties [Lin and Rood, 1996]. Modifications were made  
491 that upgraded the code version to a more recent NASA Goddard supported version. Other  
492 changes provided new horizontal grid discretizations (e.g., 1.9x2.5 deg and 0.9x1.25 deg) for  
493 optimal computational processor decompostion and polar filtering changes for noise reductions  
494 and more continuous (in latitude) filtering. In addition to the existing finite volume and spectral-  
495 based dynamical core a new option was also made available that represents the first scheme  
496 released with CAM that removes the computational scalability restrictions associated with a  
497 pole convergent latitude-longitude grid and the associated polar filtering requirements.

498 Funded in part by the Department of Energy (DOE) Climate Change Prediction Program the  
499 scalable and efficient spectral-element-based atmospheric dynamical core uses the High Order  
500 Method Modeling Environment (HOMME) on a cubed sphere grid and was developed by mem-  
501 bers of the Computational Science Section and the Computational Numerics Group of NCAR's  
502 Computational and Information Systems Laboratory (CISL). The finite element dynamical core  
503 (commonly referred to as the HOMME core) is fully integrated into CCSM coupling architecture  
504 and is invaluable for high resolution climate integrations on existing and upcoming massively  
505 parallel computing platforms.

506 Model flexibility was increased significantly from the CAM3, both within CAM and the  
507 CCSM system as a whole. The method for running thermodynamic sea-ice in CAM-only mode  
508 was moved to be maintained entirely within the CICE model of the CCSM4. The single-column  
509 version of CAM was given the flexibility to be built and run using the same infrastructure as  
510 the CAM build and run mechanism. The SCAM GUI run method was no longer supported.  
511 The increased coupling flexibility also allowed the introduction of a more consistant method  
512 for performing slab-ocean model (SOM) experiments. SOM experiments were, by default, now  
513 performed using forcing data from an existing CCSM coupled run. This had the advantage of  
514 having a closed temperature budget for both the ice and the ocean mixed layer from a coupled  
515 run. The methodology was therefore configured to reproduce the fully coupled CCSM climate as  
516 opposed to a reproduction of a psuedo-observed climate available with the CAM3-specific SOM  
517 method. The CAM3-specific SOM method was no longer made available. For more information  
518 regarding updated run methods see the CAM4.0 users guide of Eaton [2010].

### 519 1.1.6 Overview of CAM 5.0

#### 520 *The Community Atmosphere Model*

521 CAM has been modified substantially with a range of enhancements and improvements in the  
522 representation of physical processes since version 4 (CAM4). In particular, the combination of  
523 physical parameterization enhancements makes it possible to simulate full aerosol cloud inter-  
524 actions including cloud droplet activation by aerosols, precipitation processes due to particle  
525 size dependant behavior and explicit radiative interaction of cloud particles. As such the CAM  
526 5.0represents the first version of CAM that is able to simulate the cloud-aerosol indirect radia-  
527 tive effects. More generally CAM 5.0forms the main atmopshere component of the CCommunity

528 Earth System Model, version 1 (CESM1). The extensive list of physical parameterization improvements are described below:

530 A new moist turbulence scheme (Section 4.2) is included that explicitly simulates stratus-radiation-turbulence interactions, making it possible to simulate full aerosol indirect effects within stratus. It is based on a diagnostic Turbulent Kinetic Energy (TKE) formulation and uses a 1<sup>st</sup> order K-diffusion scheme with entrainment [Bretherton and Park, 2009a] originally developed at the University of Washington.. The scheme operates in any layer of the atmosphere when the moist *Ri* ( Richardson number ) is larger than its critical value.

536 A new shallow convection scheme (Section 4.3) uses a realistic plume dilution equation and closure that accurately simulates the spatial distribution of shallow convective activity [Park and Bretherton, 2009]. A steady state convective updraft plume and small fractional area are assumed. An explicit computation of the convective updraft vertical velocity and updraft fraction is performed using an updraft vertical momentum equation, and thus provides a representation of convective momentum transports. The scheme is specifically designed to interact with the new moist turbulence scheme in order to prevent double counting seen in previous CAM parameterizations. The deep convection parameterization is retained from CAM4.0 (Section 4.4).

545 Stratiform microphysical processes (Section 4.6) are represented by a prognostic, two-moment formulation for cloud droplet and cloud ice with mass and number concentrations following the original parameterization of Morrison and Gettelman [2008]. The implementation in CAM 5.0 [Gettelman et al., 2008] determines liquid and ice particle sizes from gamma functions and their evolution in time is subject to grid-scale advection, convective detrainment, turbulent diffusion and several microphysical processes. Activation of cloud droplets occurs on an aerosol size distribution based on aerosol chemistry, temperature and vertical velocity. A sub-grid scale vertical velocity is provided through a turbulent kinetic energy approximation. A number of mechanisms are calculated for ice crystal nucleation [Liu et al., 2007] and combined with modifications to allow ice supersaturation [Gettelman et al., 2010b].

555 The revised cloud macrophysics scheme (Section 4.7, Park et al. [2010]) provides a more transparent treatment of cloud processes and imposes full consistency between cloud fraction and cloud condensate. Separate calculations are performed for liquid and ice stratiform cloud fractions which are assumed to be maximally overlapped. Liquid cloud fraction is based on an assumed triangular distribution of total relative humidity. Ice cloud fraction is based on Gettelman et al. [2010a] and allows supersaturation via a modified relative humidity over ice and the inclusion of ice condensate amount.

562 A new 3-mode modal aerosol scheme (MAM3, Section 4.8, Liu and Ghan [2010]) provides internally mixed representations of number concentrations and mass for Aitkin, accumulation and coarse aerosol modes which are merged characterizations of the more complex 7-mode version of the scheme. Anthropogenic emissions, defined as originating from industrial, domestic and agriculture activity sectors, are provided from the Lamarque et al. [2010a] IPCC AR5 emission data set. Emissions of black carbon and organic carbon represent an update of Bond et al. [2007] and Junker and Liousse [2008]. Emissions of sulfur dioxide are an update of Smith et al. [2001, 2004]. Injection heights, and size distribution of emissions data are not provided with the raw datasets so the protocols of [Dentener et al., 2006a] are followed for CAM 5.0. AEROCOM emission datasets are used for natural aerosol sources. All emission datasets required to run MAM for pre-industrial or 20th century scenarios are available for download. A full inventory of

573 observationally based aerosol emission mass and size is provided in standard available datasets.  
574 The 7-mode version of the scheme is also available.

575 Calculations and specifications for the condensed phase optics (aerosols, liquid cloud droplets,  
576 hydrometeors and ice crystals) are taken from the microphysics and aerosol parameteriza-  
577 tion quantities and provided as input to the radiation scheme (Section 4.9). The radiation  
578 scheme (Section 4.10) has been updated to the Rapid Radiative Transfer Method for GCMs  
579 (RRTMG, Iacono et al. [2008]; Mlawer et al. [1997]). It employs an efficient and accurate mod-  
580 ified correlated-k method for calculating radiative fluxes and heating rates in the clear sky and  
581 for the condensed phase species. For each short-wave band calculation extinction optical depth,  
582 single scattering albedo and asymmetry properties are specified. For each long-wave band mass-  
583 specific absorption is specified. The aerosol optical properties are defined for each mode of the  
584 MAM as described by [Ghan and Zaveri, 2007]. Hygroscopicity characteristics are specified for  
585 soluble species. For volcanic aerosols a geometric mean radius is used. Optical properties of  
586 aerosols are combined prior to the radiative calculation. Liquid-cloud optics are calculated fol-  
587 lowing Wiscombe [1996] and ice-cloud optics are calculated following Mitchell [2002]. Ice-cloud  
588 size optics are extended to allow for radiatively active falling snow. Optical properties of clouds  
589 (including separate fractions and in-cloud water contents) are combined prior to the radiative cal-  
590 culation. RRTM separates the short-wave spectrum into 14 bands extending from 0.2  $\mu\text{m}$  to 12.2  
591  $\mu\text{m}$ , and models sources of extinction for  $\text{H}_2\text{O}$ ,  $\text{O}_3$ ,  $\text{CO}_2$ ,  $\text{O}_2$ ,  $\text{CH}_4$ ,  $\text{N}_2$  and Rayleigh scattering.  
592 Solar irradiance is now specified for the short-wave bands from the Lean dataset [Wang et al.,  
593 2005]. The long-wave spectrum is separated into 16 bands extending from 3.1  $\mu\text{m}$  to 1000  $\mu\text{m}$   
594 with molecular sources of absorption for the same species, in addition to CFC-11 (containing  
595 multiple CFC species) and CFC-12. RRTMG has extensive modifications from the original  
596 RRTM in order to provide significant speed-up for long climate integrations. Chief amongst  
597 these is the Monte-Carlo Independent Column Approximation (McICA, Pincus and Morcrette  
598 [2003]) that represents sub-grid scale cloud variability. With these modifications RRTMG still  
599 retains superior offline agreement with line-by-line calculations when compared to the previous  
600 CAM radiation package (CAM-RT).

#### 601 *The CAM Chemistry Model (CAM-CHEM)*

602 Chemistry in CAM is now fully interactive and implemented in CESM (Section 5.1); in particu-  
603 lar, emissions of biogenic compounds and deposition of aerosols to snow, ice, ocean and vegeta-  
604 tion are handled through the coupler. The released version of CAM-chem in CESM is using the  
605 recently-developed superfast chemistry (Section 5.2), in collaboration with P. Cameron-Smith  
606 from LLNL and M. Prather from UCI) to perform centennial scale simulations at a minor cost  
607 increase over the base CAM4. These simulations use the recently developed 1850-2005 emissions  
608 created in support of CMIP5.

#### 609 *The Whole Atmosphere Community Climate Model (WACCM)*

610 WACCM4 (Section 5.3), incorporates several improvements and enhancements over the previous  
611 version (3.1.9). It can be run coupled to the POP2 and CICE CESM model components. The  
612 model's chemistry module (Section 5.1) has been updated according to the latest JPL-2006 rec-  
613 ommendations; a quasi-biennial oscillation may be imposed (as an option) by relaxing the winds

614 to observations in the Tropics; heating from stratospheric volcanic aerosols is now computed ex-  
615 plicitly; the effects of solar proton events are now included; the effect of unresolved orography is  
616 parameterized as a surface stress (turbulent mountain stress) leading to an improvement in the  
617 frequency of sudden stratospheric warmings; and gravity waves due to convective and frontal  
618 sources are parameterized based upon the occurrence of convection and the diagnosis of regions  
619 of frontogenesis in the model.

## 620 Chapter 2

# 621 Coupling of Dynamical Core and 622 Parameterization Suite

623 The CAM 5.0 cleanly separates the parameterization suite from the dynamical core, and makes  
624 it easier to replace or modify each in isolation. The dynamical core can be coupled to the  
625 parameterization suite in a purely time split manner or in a purely process split one, as described  
626 below.

Consider the general prediction equation for a generic variable  $\psi$ ,

$$\frac{\partial \psi}{\partial t} = D(\psi) + P(\psi) , \quad (2.1)$$

627 where  $\psi$  denotes a prognostic variable such as temperature or horizontal wind component. The  
628 dynamical core component is denoted  $D$  and the physical parameterization suite  $P$ .

629 A three-time-level notation is employed which is appropriate for the semi-implicit Eulerian  
630 spectral transform dynamical core. However, the numerical characteristics of the physical pa-  
631 rameterizations are more like those of diffusive processes rather than advective ones. They are  
632 therefore approximated with forward or backward differences, rather than centered three-time-  
633 level forms.

The *Process Split* coupling is approximated by

$$\psi^{n+1} = \psi^{n-1} + 2\Delta t D(\psi^{n+1}, \psi^n, \psi^{n-1}) + 2\Delta t P(\psi^*, \psi^{n-1}) , \quad (2.2)$$

where  $P(\psi^*, \psi^{n-1})$  is calculated first from

$$\psi^* = \psi^{n-1} + 2\Delta t P(\psi^*, \psi^{n-1}) . \quad (2.3)$$

The *Time Split* coupling is approximated by

$$\psi^* = \psi^{n-1} + 2\Delta t D(\psi^*, \psi^n, \psi^{n-1}) , \quad (2.4)$$

$$\psi^{n+1} = \psi^* + 2\Delta t P(\psi^{n+1}, \psi^*) . \quad (2.5)$$

634 The distinction is that in the *Process Split* approximation the calculations of  $D$  and  $P$  are  
635 both based on the same past state,  $\psi^{n-1}$ , while in the *Time Split* approximations  $D$  and  $P$  are  
636 calculated sequentially, each based on the state produced by the other.

637 As mentioned above, the Eulerian core employs the three-time-level notation in (2.2)-(2.5).  
 638 Eqns. (2.2)-(2.5) also apply to two-time-level finite volume, semi-Lagrangian and spectral ele-  
 639 ment (HOMME) cores by dropping centered  $n$  term dependencies, and replacing  $n-1$  by  $n$  and  
 640  $2\Delta t$  by  $\Delta t$ .

The parameterization package can be applied to produce an updated field as indicated in (2.3) and (2.5). Thus (2.5) can be written with an operator notation

$$\psi^{n+1} = \mathbf{P}(\psi^*) , \quad (2.6)$$

where only the past state is included in the operator dependency for notational convenience. The implicit predicted state dependency is understood. The *Process Split* equation (2.2) can also be written in operator notation as

$$\psi^{n+1} = \mathbf{D} \left( \psi^{n-1}, \frac{\mathbf{P}(\psi^{n-1}) - \psi^{n-1}}{2\Delta t} \right) , \quad (2.7)$$

where the first argument of  $\mathbf{D}$  denotes the prognostic variable input to the dynamical core and the second denotes the forcing rate from the parameterization package, e.g. the heating rate in the thermodynamic equation. Again only the past state is included in the operator dependency, with the implicit predicted state dependency left understood. With this notation the *Time Split* system (2.5) and (2.5) can be written

$$\psi^{n+1} = \mathbf{P}(\mathbf{D}(\psi^{n-1}, 0)) . \quad (2.8)$$

The total parameterization package in CAM 5.0 consists of a sequence of components, indicated by

$$P = \{M, R, S, T\} , \quad (2.9)$$

641 where  $M$  denotes (Moist) precipitation processes,  $R$  denotes clouds and Radiation,  $S$  denotes the  
 642 Surface model, and  $T$  denotes Turbulent mixing. Each of these in turn is subdivided into various  
 643 components:  $M$  includes an optional dry adiabatic adjustment (normally applied only in the  
 644 stratosphere), moist penetrative convection, shallow convection, and large-scale stable condens-  
 645 ation;  $R$  first calculates the cloud parameterization followed by the radiation parameterization;  
 646  $S$  provides the surface fluxes obtained from land, ocean and sea ice models, or calculates them  
 647 based on specified surface conditions such as sea surface temperatures and sea ice distribution.  
 648 These surface fluxes provide lower flux boundary conditions for the turbulent mixing  $T$  which  
 649 is comprised of the planetary boundary layer parameterization, vertical diffusion, and gravity  
 650 wave drag.

651 Defining operators following (2.6) for each of the parameterization components, the couplings  
 652 in CAM 5.0 are summarized as:

#### TIME SPLIT

$$\psi^{n+1} = \mathbf{T}(\mathbf{S}(\mathbf{R}(\mathbf{M}(\mathbf{D}(\psi^{n-1}, 0))))) \quad (2.10)$$

#### PROCESS SPLIT

$$\psi^{n+1} = \mathbf{D} \left( \psi^{n-1}, \frac{\mathbf{T}(\mathbf{S}(\mathbf{R}(\mathbf{M}(\psi^{n-1})))) - \psi^{n-1}}{2\Delta t} \right) \quad (2.11)$$

653 The labels *Time Split* and *Process Split* refer to the coupling of the dynamical core with the  
654 complete parameterization suite. The components within the parameterization suite are coupled  
655 via time splitting in both forms.

656 The *Process Split* form is convenient for spectral transform models. With *Time Split* approx-  
657 imations extra spectral transforms are required to convert the updated momentum variables  
658 provided by the parameterizations to vorticity and divergence for the Eulerian spectral core, or  
659 to recalculate the temperature gradient for the semi-Lagrangian spectral core. The *Time Split*  
660 form is convenient for the finite-volume core which adopts a Lagrangian vertical coordinate.  
661 Since the scheme is explicit and restricted to small time-steps by its non-advection component,  
662 it sub-steps the dynamics multiple times during a longer parameterization time step. With  
663 *Process Split* approximations the forcing terms must be interpolated to an evolving Lagrangian  
664 vertical coordinate every sub-step of the dynamical core. Besides the expense involved, it is not  
665 completely obvious how to interpolate the parameterized forcing, which can have a vertical grid  
666 scale component arising from vertical grid scale clouds, to a different vertical grid. [Williamson,  
667 2002] compares simulations with the Eulerian spectral transform dynamical core coupled to the  
668 CCM3 parameterization suite via *Process Split* and *Time Split* approximations.



669 **Chapter 3**

670 **Dynamics**

671 **3.1 Finite Volume Dynamical Core**

672 **3.1.1 Overview**

673 This document describes the Finite-Volume (FV) dynamical core that was initially developed  
674 and used at the NASA Data Assimilation Office (DAO) for data assimilation, numerical weather  
675 predictions, and climate simulations. The finite-volume discretization is local and entirely  
676 in physical space. The horizontal discretization is based on a conservative “*flux-form semi-*  
677 *Lagrangian*” scheme described by [Lin and Rood \[1996\]](#) (hereafter LR96) and [Lin and Rood](#)  
678 [\[1997\]](#) (hereafter LR97). The vertical discretization can be best described as *Lagrangian* with  
679 a conservative re-mapping, which essentially makes it *quasi-Lagrangian*. The *quasi-Lagrangian*  
680 aspect of the vertical coordinate is transparent to model users or physical parameterization de-  
681 velopers, and it functions exactly like the  $\eta$  – *coordinate* (a hybrid  $\sigma$  –  $p$  coordinate) used by  
682 other dynamical cores within CAM.

683 In the current implementation for use in CAM, the FV dynamics and physics are “time  
684 split” in the sense that all prognostic variables are updated sequentially by the “dynamics”  
685 and then the “physics”. The time integration within the FV dynamics is fully explicit, with  
686 sub-cycling within the 2D Lagrangian dynamics to stabilize the fastest wave (see section 3.1.4).  
687 The transport for tracers, however, can take a much larger time step (*e.g.*, 30 minutes as for the  
688 physics).

689 **3.1.2 The governing equations for the hydrostatic atmosphere**

690 For reference purposes, we present the continuous differential equations for the hydrostatic 3D  
691 atmospheric flow on the sphere for a general vertical coordinate  $\zeta$  (*e.g.*, [Kasahara \[1974\]](#)). Using  
692 standard notations, the hydrostatic balance equation is given as follows:

$$\frac{1}{\rho} \frac{\partial p}{\partial z} + g = 0, \quad (3.1)$$

693 where  $\rho$  is the density of the air,  $p$  the pressure, and  $g$  the gravitational constant. Introducing  
694 the “*pseudo-density*”  $\pi = \frac{\partial p}{\partial \zeta}$  (*i.e.*, the vertical pressure gradient in the general coordinate), from  
695 the hydrostatic balance equation the *pseudo-density* and the true density are related as follows:

$$\pi = -\frac{\partial \Phi}{\partial \zeta} \rho, \quad (3.2)$$

696 where  $\Phi = gz$  is the geopotential. Note that  $\pi$  reduces to the “true density” if  $\zeta = -gz$ , and  
 697 the “surface pressure”  $P_s$  if  $\zeta = \sigma$  ( $\sigma = \frac{p}{P_s}$ ). The conservation of total air mass using  $\pi$  as the  
 698 prognostic variable can be written as

$$\frac{\partial}{\partial t} \pi + \nabla \cdot (\vec{V} \pi) = 0, \quad (3.3)$$

699 where  $\vec{V} = (u, v, \frac{d\zeta}{dt})$ . Similarly, the mass conservation law for tracer species (or water vapor)  
 700 can be written as

$$\frac{\partial}{\partial t} (\pi q) + \nabla \cdot (\vec{V} \pi q) = 0, \quad (3.4)$$

701 where  $q$  is the mass mixing ratio (or specific humidity) of the tracers (or water vapor).

702 Choosing the (virtual) potential temperature  $\Theta$  as the thermodynamic variable, the first law  
 703 of thermodynamics is written as

$$\frac{\partial}{\partial t} (\pi \Theta) + \nabla \cdot (\vec{V} \pi \Theta) = 0. \quad (3.5)$$

704 Letting  $(\lambda, \theta)$  denote the (longitude, latitude) coordinate, the momentum equations can be  
 705 written in the “vector-invariant form” as follows:

$$\frac{\partial}{\partial t} u = \Omega v - \frac{1}{A \cos \theta} \left[ \frac{\partial}{\partial \lambda} (\kappa + \Phi - \nu D) + \frac{1}{\rho} \frac{\partial}{\partial \lambda} p \right] - \frac{d\zeta}{dt} \frac{\partial u}{\partial \zeta}, \quad (3.6)$$

$$\frac{\partial}{\partial t} v = -\Omega u - \frac{1}{A} \left[ \frac{\partial}{\partial \theta} (\kappa + \Phi - \nu D) + \frac{1}{\rho} \frac{\partial}{\partial \theta} p \right] - \frac{d\zeta}{dt} \frac{\partial v}{\partial \zeta}, \quad (3.7)$$

where  $A$  is the radius of the earth,  $\nu$  is the coefficient for the optional divergence damping,  $D$  is the horizontal divergence

$$D = \frac{1}{A \cos \theta} \left[ \frac{\partial}{\partial \lambda} (u) + \frac{\partial}{\partial \theta} (v \cos \theta) \right],$$

$$\kappa = \frac{1}{2} (u^2 + v^2),$$

706 and  $\Omega$ , the vertical component of the absolute vorticity, is defined as follows:

$$\Omega = 2\omega \sin \theta + \frac{1}{A \cos \theta} \left[ \frac{\partial}{\partial \lambda} v - \frac{\partial}{\partial \theta} (u \cos \theta) \right],$$

707 where  $\omega$  is the angular velocity of the earth. Note that the last term in (3.6) and (3.7) vanishes  
 708 if the vertical coordinate  $\zeta$  is a conservative quantity (e.g., entropy under adiabatic conditions  
 709 [Hsu and Arakawa, 1990] or an imaginary conservative tracer), and the 3D divergence opera-  
 710 tor becomes 2D along constant  $\zeta$  surfaces. The discretization of the 2D horizontal transport  
 711 process is described in section 3.1.3. The complete dynamical system using the Lagrangian  
 712 control-volume vertical discretization is described in section 3.1.4 and section 3.1.5 describes

713 the explicit diffusion operators available in CAM5. A mass, momentum, and total energy con-  
 714 servative mapping algorithm is described in section 3.1.6 and in section 3.1.7 an alternative  
 715 geopotential conserving vertical remapping method is described. Sections 3.1.8 and 3.1.9 are on  
 716 the adjustment of pressure to include the change in mass of water vapor and on the negative  
 717 tracer fixer in CAM, respectively. Last the global energy fixer is described (section 3.1.10).

### 718 3.1.3 Horizontal discretization of the transport process on the sphere

719 Since the vertical transport term would vanish after the introduction of the vertical Lagrangian  
 720 control-volume discretization (see section 3.1.4), we shall present here only the 2D (horizontal)  
 721 forms of the FFSL transport algorithm for the transport of density (3.3) and mixing ratio-like  
 722 quantities (3.4) on the sphere. The governing equation for the pseudo-density (3.3) becomes

$$\frac{\partial}{\partial t}\pi + \frac{1}{A\cos\theta} \left[ \frac{\partial}{\partial\lambda}(u\pi) + \frac{\partial}{\partial\theta}(v\pi\cos\theta) \right] = 0. \quad (3.8)$$

723 The finite-volume (*integral*) representation of the continuous  $\pi$  field is defined as follows:

$$\tilde{\pi}(t) \equiv \frac{1}{A^2\Delta\theta\Delta\lambda\cos\theta} \iint \pi(t; \lambda, \theta) A^2 \cos\theta d\theta d\lambda. \quad (3.9)$$

724 Given the *exact* 2D wind field  $\vec{V}(t; \lambda, \theta) = (U, V)$  the 2D integral representation of the conser-  
 725 vation law for  $\tilde{\pi}$  can be obtained by integrating (3.8) in time and in space

$$\tilde{\pi}^{n+1} = \tilde{\pi}^n - \frac{1}{A^2\Delta\theta\Delta\lambda\cos\theta} \int_t^{t+\Delta t} \left[ \oint \pi(t; \lambda, \theta) \vec{V} \cdot \vec{n} dl \right] dt. \quad (3.10)$$

726  
 727 The above 2D transport equation is still *exact for the finite-volume under consideration*. To  
 728 carry out the contour integral, certain approximations must be made. LR96 essentially decom-  
 729 posed the flux integral using two orthogonal 1D flux-form transport operators. Introducing the  
 730 following difference operator

$$\delta_x q = q(x + \frac{\Delta x}{2}) - q(x - \frac{\Delta x}{2}),$$

731 and assuming  $(u^*, v^*)$  is the time-averaged (from time  $t$  to time  $t + \Delta t$ )  $\vec{V}$  on the C-grid (e.g.,  
 732 Fig. 1 in LR96), the 1-D finite-volume flux-form transport operator  $F$  in the  $\lambda$ -direction is

$$F(u^*, \Delta t, \tilde{\pi}) = -\frac{1}{A\Delta\lambda\cos\theta} \delta_\lambda \left[ \int_t^{t+\Delta t} \pi U dt \right] = -\frac{\Delta t}{A\Delta\lambda\cos\theta} \delta_\lambda [\chi(u^*, \Delta t; \pi)], \quad (3.11)$$

733 where  $\chi$ , the time-accumulated (from  $t$  to  $t + \Delta t$ ) mass flux across the cell wall, is defined as  
 734 follows,

$$\chi(u^*, \Delta t; \pi) = \frac{1}{\Delta t} \int_t^{t+\Delta t} \pi U dt \equiv u^* \pi^*(u^*, \Delta t, \tilde{\pi}), \quad (3.12)$$

and

$$\pi^*(u^*, \Delta t; \tilde{\pi}) \approx \frac{1}{\Delta t} \int_t^{t+\Delta t} \pi dt \quad (3.13)$$

735 can be interpreted as a time mean (from time  $t$  to time  $t + \Delta t$ ) pseudo-density value of all  
 736 material that passed through the cell edge from the upwind direction.

737 Note that the above *time integration* is to be carried out along the *backward-in-time* trajectory  
 738 of the cell edge position from  $t = t + \Delta t$  (the arrival point; *e.g.*, point B in Fig. 3 of LR96)  
 739 back to time  $t$  (the departure point; *e.g.*, point B' in Fig. 3 of LR96). The very essence of the  
 740 1D finite-volume algorithm is to construct, based on the given initial cell-mean values of  $\tilde{\pi}$ , an  
 741 approximated subgrid distribution of the true  $\pi$  field, to enable an analytic integration of (3.13).  
 742 Assuming there is no error in obtaining the time-mean wind ( $u^*$ ), the only error produced by the  
 743 1D transport scheme would be solely due to the approximation to the continuous distribution  
 744 of  $\pi$  within the subgrid under consideration (this is not the case in 2D; [Lauritzen et al. \[2010\]](#)).  
 745 From this perspective, it can be said that the 1D finite-volume transport algorithm combines  
 746 the time-space discretization in the approximation of the time-mean cell-edge values  $\pi^*$ . The  
 747 physically correct way of approximating the integral (3.13) must be “upwind”, in the sense that  
 748 it is integrated along the backward trajectory of the cell edges. For example, a center difference  
 749 approximation to (3.13) would be physically incorrect, and consequently numerically unstable  
 750 unless artificial numerical diffusion is added.

751 Central to the accuracy and computational efficiency of the finite-volume algorithms is the  
 752 degrees of freedom that describe the subgrid distribution. The first order upwind scheme, for  
 753 example, has zero degrees of freedom within the volume as it is assumed that the subgrid distri-  
 754 bution is piecewise constant having the same value as the given volume-mean. The second order  
 755 finite-volume scheme (*e.g.*, [Lin et al. \[1994\]](#)) assumes a piece-wise linear subgrid distribution,  
 756 which allows one degree of freedom for the specification of the “slope” of the linear distribu-  
 757 tion to improve the accuracy of integrating (3.13). The Piecewise Parabolic Method (PPM,  
 758 [Colella and Woodward \[1984\]](#)) has two degrees of freedom in the construction of the second or-  
 759 der polynomial within the volume, and as a result, the accuracy is significantly enhanced. The  
 760 PPM appears to strike a good balance between computational efficiency and accuracy. There-  
 761 fore, the PPM is the basic 1D scheme we chose (see, *e.g.*, [Machenauer \[1998\]](#)). Note that the  
 762 subgrid PPM distributions are compact, and do not extend beyond the volume under consider-  
 763 ation. The accuracy is therefore significantly better than the order of the chosen polynomials  
 764 implies. While the PPM scheme possesses all the desirable attributes (mass conserving, mono-  
 765 tonicity preserving, and high-order accuracy) in 1D, it is important that a solution be found to  
 766 avoid the directional splitting in the multi-dimensional problem of modeling the dynamics and  
 767 transport processes of the Earth’s atmosphere.

768 The first step for reducing the splitting error is to apply the two orthogonal 1D flux-form  
 769 operators in a directionally symmetric way. After symmetry is achieved, the “inner operators”  
 770 are then replaced with corresponding advective-form operators (in CAM5 the “inner operators”  
 771 are based on constant cell-average values and not the PPM). A stability analysis of the conse-  
 772 quences of using different inner and outer operators in the LR96 scheme is given in [Lauritzen](#)  
 773 [\[2007\]](#). A consistent advective-form operator in the  $\lambda$ -direction can be derived from its flux-form  
 774 counterpart ( $F$ ) as follows:

$$f(u^*, \Delta t, \tilde{\pi}) = F(u^*, \Delta t, \tilde{\pi}) + \tilde{\rho} F(u^*, \Delta t, \tilde{\pi} \equiv 1) = F(u^*, \Delta t, \tilde{\pi}) + \tilde{\pi} C_{def}^\lambda, \quad (3.14)$$

$$C_{def}^\lambda = \frac{\Delta t \delta_\lambda u^*}{A \Delta \lambda \cos \theta}, \quad (3.15)$$

775 where  $C_{def}^\lambda$  is a dimensionless number indicating the degree of the flow deformation in the  $\lambda$ -  
776 direction. The above derivation of  $f$  is slightly different from LR96's approach, which adopted  
777 the traditional 1D advective-form semi-Lagrangian scheme. The advantage of using (3.14) is  
778 that computation of winds at cell centers (Eq. 2.25 in LR96) are avoided.

Analogously, the 1D flux-form transport operator  $G$  in the latitudinal ( $\theta$ ) direction is derived  
as follows:

$$G(v^*, \Delta t, \tilde{\pi}) = -\frac{1}{A \Delta \theta \cos \theta} \delta_\theta \left[ \int_t^{t+\Delta t} \pi V \cos \theta \, dt \right] = -\frac{\Delta t}{A \Delta \theta \cos \theta} \delta_\theta [v^* \cos \theta \pi^*], \quad (3.16)$$

and likewise the advective-form operator,

$$g(v^*, \Delta t, \tilde{\pi}) = G(v^*, \Delta t, \tilde{\pi}) + \tilde{\pi} C_{def}^\theta, \quad (3.17)$$

where

$$C_{def}^\theta = \frac{\Delta t \delta_\theta [v^* \cos \theta]}{A \Delta \theta \cos \theta}. \quad (3.18)$$

779 To complete the construction of the 2D algorithm on the sphere, we introduce the following  
780 short hand notations:

$$(\ )^\theta = (\ )^n + \frac{1}{2} g [v^*, \Delta t, (\ )^n], \quad (3.19)$$

$$(\ )^\lambda = (\ )^n + \frac{1}{2} f [u^*, \Delta t, (\ )^n]. \quad (3.20)$$

The 2D transport algorithm (*cf*, Eq. 2.24 in LR96) can then be written as

$$\tilde{\pi}^{n+1} = \tilde{\pi}^n + F [u^*, \Delta t, \tilde{\pi}^\theta] + G [v^*, \Delta t, \tilde{\pi}^\lambda]. \quad (3.21)$$

Using explicitly the mass fluxes ( $\chi, Y$ ), (3.21) is rewritten as

$$\tilde{\pi}^{n+1} = \tilde{\pi}^n - \frac{\Delta t}{A \cos \theta} \left\{ \frac{1}{\Delta \lambda} \delta_\lambda [\chi(u^*, \Delta t; \tilde{\pi}^\theta)] + \frac{1}{\Delta \theta} \delta_\theta [\cos \theta Y(v^*, \Delta t; \tilde{\pi}^\lambda)] \right\}, \quad (3.22)$$

781 where  $Y$ , the mass flux in the meridional direction, is defined in a similar fashion as  $\chi$  (3.12). The  
782 ability of the LR96 scheme to approximate the exact geometry of the fluxes for deformational  
783 flows is discussed in [Machenauer et al. \[2009\]](#) and [Lauritzen et al. \[2010\]](#).

It can be verified that in the special case of constant density flow ( $\tilde{\pi} = \text{constant}$ ) the above  
equation degenerates to the finite-difference representation of the *incompressibility condition* of  
the “time mean” wind field  $(u^*, v^*)$ , *i.e.*,

$$\frac{1}{\Delta \lambda} \delta_\lambda u^* + \frac{1}{\Delta \theta} \delta_\theta (v^* \cos \theta) = 0. \quad (3.23)$$

The fulfillment of the above *incompressibility condition* for constant density flows is crucial to the accuracy of the 2D flux-form formulation. For transport of volume mean mixing ratio-like quantities ( $\tilde{q}$ ) the mass fluxes ( $\chi, Y$ ) as defined previously should be used as follows

$$\tilde{q}^{n+1} = \frac{1}{\tilde{\pi}^{n+1}} [\tilde{\pi}^n \tilde{q}^n + F(\chi, \Delta t, \tilde{q}^\theta) + G(Y, \Delta t, \tilde{q}^\lambda)]. \quad (3.24)$$

784 Note that the above form of the tracer transport equation consistently degenerates to (3.21) if  
785  $\tilde{q} \equiv 1$  (*i.e.*, the tracer density equals to the background air density), which is another important  
786 condition for a flux-form transport algorithm to be able to avoid generation of noise (*e.g.*,  
787 creation of artificial gradients) and to maintain mass conservation.

### 788 3.1.4 A *vertically Lagrangian* and *horizontally Eulerian* control- 789 volume discretization of the hydrodynamics

790 The very idea of using Lagrangian vertical coordinate for formulating governing equations for  
791 the atmosphere is not entirely new. [Starr \[1945\]](#) is likely the first to have formulated, in the  
792 *continuous differential form*, the governing equations using a Lagrangian coordinate. Starr did  
793 not make use of the *discrete* Lagrangian control-volume concept for discretization nor did he  
794 present a solution to the problem of computing the pressure gradient forces. In the *finite-volume*  
795 *discretization* to be described here, the Lagrangian surfaces are treated as the bounding material  
796 surfaces of the Lagrangian control-volumes within which the finite-volume algorithms developed  
797 in LR96, LR97, and L97 will be directly applied.

798 To use a vertical Lagrangian coordinate system to reduce the 3D governing equations to the  
799 2D forms, one must first address the issue of whether it is an inertial coordinate or not. For  
800 hydrostatic flows, it is. This is because both the right-hand-side and the left-hand-side of the  
801 vertical momentum equation vanish for purely hydrostatic flows.

802 Realizing that the earth's surface, for all practical modeling purposes, can be regarded as  
803 a non-penetrable material surface, it becomes straightforward to construct a terrain-following  
804 Lagrangian control-volume coordinate system. In fact, any commonly used terrain-following  
805 coordinates can be used as the starting reference (*i.e.*, fixed, Eulerian coordinate) of the floating  
806 Lagrangian coordinate system. To close the coordinate system, the model top (at a prescribed  
807 constant pressure) is also assumed to be a Lagrangian surface, which is the same assumption  
808 being used by practically all global hydrostatic models.

809 The basic idea is to start the time marching from the chosen terrain-following Eulerian coor-  
810 dinate (*e.g.*, pure  $\sigma$  or hybrid  $\sigma$ - $p$ ), *treat the initial coordinate surfaces as material surfaces*,  
811 the finite-volumes bounded by two coordinate surfaces, *i.e.*, the Lagrangian control-volumes,  
812 are free vertically, to float, compress, or expand with the flow as dictated by the hydrostatic  
813 dynamics.

By choosing an imaginary conservative tracer  $\zeta$  that is a monotonic function of height and constant on the initial reference coordinate surfaces (*e.g.*, the value of “ $\eta$ ” in the hybrid  $\sigma - p$  coordinate used in CAM), the 3D governing equations written for the general vertical coordinate in section 1.2 can be reduced to 2D forms. After factoring out the constant  $\delta\zeta$ , (3.3), the conservation law for the pseudo-density ( $\pi = \frac{\delta p}{\delta \zeta}$ ), becomes

$$\frac{\partial}{\partial t} \delta p + \frac{1}{A \cos \theta} \left[ \frac{\partial}{\partial \lambda} (u \delta p) + \frac{\partial}{\partial \theta} (v \delta p \cos \theta) \right] = 0, \quad (3.25)$$

814 where the symbol  $\delta$  represents the vertical difference between the two neighboring Lagrangian  
 815 surfaces that bound the finite control-volume. From (3.1), the pressure thickness  $\delta p$  of that  
 816 control-volume is proportional to the total mass, *i.e.*,  $\delta p = -\rho g \delta z$ . Therefore, it can be said  
 817 that the Lagrangian control-volume vertical discretization has the hydrostatic balance built-in,  
 818 and  $\delta p$  can be regarded as the “pseudo-density” for the discretized Lagrangian vertical coordinate  
 819 system.

Similarly, (3.4), the mass conservation law for all tracer species, is

$$\frac{\partial}{\partial t}(q\delta p) + \frac{1}{A \cos \theta} \left[ \frac{\partial}{\partial \lambda}(uq\delta p) + \frac{\partial}{\partial \theta}(vq\delta p \cos \theta) \right] = 0, \quad (3.26)$$

820 the thermodynamic equation, (3.5), becomes

$$\frac{\partial}{\partial t}(\Theta \delta p) + \frac{1}{A \cos \theta} \left[ \frac{\partial}{\partial \lambda}(u\Theta \delta p) + \frac{\partial}{\partial \theta}(v\Theta \delta p \cos \theta) \right] = 0, \quad (3.27)$$

and (3.6) and (3.7), the momentum equations, are reduced to

$$\frac{\partial}{\partial t}u = \Omega v - \frac{1}{A \cos \theta} \left[ \frac{\partial}{\partial \lambda}(\kappa + \Phi - \nu D) + \frac{1}{\rho} \frac{\partial}{\partial \lambda}p \right], \quad (3.28)$$

$$\frac{\partial}{\partial t}v = -\Omega u - \frac{1}{A} \left[ \frac{\partial}{\partial \theta}(\kappa + \Phi - \nu D) + \frac{1}{\rho} \frac{\partial}{\partial \theta}p \right]. \quad (3.29)$$

Given the prescribed pressure at the model top  $P_\infty$ , the position of each Lagrangian surface  $P_l$  (horizontal subscripts omitted) is determined in terms of the hydrostatic pressure as follows:

$$P_l = P_\infty + \sum_{k=1}^l \delta P_k, \quad (\text{for } l = 1, 2, 3, \dots, N), \quad (3.30)$$

821 where the subscript  $l$  is the vertical index ranging from 1 at the lower bounding Lagrangian  
 822 surface of the first (the highest) layer to  $N$  at the Earth’s surface. There are  $N+1$  Lagrangian  
 823 surfaces to define a total number of  $N$  Lagrangian layers. The surface pressure, which is the  
 824 pressure at the lowest Lagrangian surface, is easily computed as  $P_N$  using (3.30). The sur-  
 825 face pressure is needed for the physical parameterizations and to define the reference Eulerian  
 826 coordinate for the mapping procedure (to be described in section 3.1.6).

827 With the exception of the pressure-gradient terms and the addition of a thermodynamic  
 828 equation, the above 2D Lagrangian dynamical system is the same as the shallow water system  
 829 described in LR97. The conservation law for the depth of fluid  $h$  in the shallow water system of  
 830 LR97 is replaced by (3.25) for the pressure thickness  $\delta p$ . The ideal gas law, the mass conservation  
 831 law for air mass, the conservation law for the potential temperature (3.27), together with the  
 832 modified momentum equations (3.28) and (3.29) close the 2D Lagrangian dynamical system,  
 833 which are vertically coupled only by the hydrostatic relation (see (3.54), section 3.1.6).

834 The time marching procedure for the 2D Lagrangian dynamics follows closely that of the  
 835 shallow water dynamics fully described in LR97. For computational efficiency, we shall take  
 836 advantage of the stability of the FFSL transport algorithm by using a much larger time step  
 837 ( $\Delta t$ ) for the transport of all tracer species (including water vapor). As in the shallow water

system, the Lagrangian dynamics uses a relatively small time step,  $\Delta\tau = \Delta t/m$ , where  $m$  is the number of the sub-cycling needed to stabilize the fastest wave in the system. We shall describe here this time-split procedure for the *prognostic variables*  $[\delta p, \Theta, u, v; q]$  on the D-grid. Discretization on the C-grid for obtaining the *diagnostic variables*, the time-averaged winds  $(u^*, v^*)$ , is analogous to that of the D-grid (see also LR97).

Introducing the following short hand notations (*cf*, (3.19) and (3.20)):

$$(\ )_i^\theta = (\ )^{n+\frac{i-1}{m}} + \frac{1}{2}g[v_i^*, \Delta\tau, (\ )^{n+\frac{i-1}{m}}],$$

$$(\ )_i^\lambda = (\ )^{n+\frac{i-1}{m}} + \frac{1}{2}f[u_i^*, \Delta\tau, (\ )^{n+\frac{i-1}{m}}],$$

and applying directly (3.22), the update of “pressure thickness”  $\delta p$ , using the fractional time step  $\Delta\tau = \Delta t/m$ , can be written as

$$\delta p^{n+\frac{i}{m}} = \delta p^{n+\frac{i-1}{m}} - \frac{\Delta\tau}{A\cos\theta} \left\{ \frac{1}{\Delta\lambda} \delta_\lambda [x_i^*(u_i^*, \Delta\tau; \delta p_i^\theta)] + \frac{1}{\Delta\theta} \delta_\theta [\cos\theta y_i^*(v_i^*, \Delta\tau; \delta p_i^\lambda)] \right\} \quad (3.31)$$

(for  $i = 1, \dots, m$ ),

where  $[x_i^*, y_i^*]$  are the background air mass fluxes, which are then used as input to Eq. 24 for transport of the potential temperature  $\Theta$ :

$$\Theta^{n+\frac{i}{m}} = \frac{1}{\delta p^{n+\frac{i}{m}}} \left[ \delta p^{n+\frac{i-1}{m}} \Theta^{n+\frac{i-1}{m}} + F(x_i^*, \Delta\tau; \Theta_i^\theta) + G(y_i^*, \Delta\tau, \Theta_i^\lambda) \right]. \quad (3.32)$$

The discretized momentum equations for the shallow water system (*cf*, Eq. 16 and Eq. 17 in LR97) are modified for the pressure gradient terms as follows:

$$u^{n+\frac{i}{m}} = u^{n+\frac{i-1}{m}} + \Delta\tau \left[ y_i^*(v_i^*, \Delta\tau; \Omega^\lambda) - \frac{1}{A\Delta\lambda\cos\theta} \delta_\lambda (\kappa^* - \nu D^*) + \widehat{P}_\lambda \right], \quad (3.33)$$

$$v^{n+\frac{i}{m}} = v^{n+\frac{i-1}{m}} - \Delta\tau \left[ x_i^*(u_i^*, \Delta\tau; \Omega^\theta) + \frac{1}{A\Delta\theta} \delta_\theta (\kappa^* - \nu D^*) - \widehat{P}_\theta \right], \quad (3.34)$$

where  $\kappa^*$  is the upwind-biased “kinetic energy” (as defined by Eq. 18 in LR97), and  $D^*$ , the horizontal divergence on the D-grid, is discretized as follows:

$$D^* = \frac{1}{A\cos\theta} \left[ \frac{1}{\Delta\lambda} \delta_\lambda u^{n+\frac{i-1}{m}} + \frac{1}{\Delta\theta} \delta_\theta (v^{n+\frac{i-1}{m}} \cos\theta) \right].$$

The finite-volume mean pressure-gradient terms in (3.33) and (3.34) are computed as follows:

$$\widehat{P}_\lambda = \frac{\oint_{\Pi=\lambda} \phi d\Pi}{A\cos\theta \oint_{\Pi=\lambda} \Pi d\lambda}, \quad (3.35)$$

$$\widehat{P}_\theta = \frac{\oint_{\Pi=\theta} \phi d\Pi}{A \oint_{\Pi=\theta} \Pi d\theta}, \quad (3.36)$$

843 where  $\Pi = p^\kappa$  ( $\kappa = R/C_p$ ), and the symbols “ $\Pi \rightleftharpoons \lambda$ ” and “ $\Pi \rightleftharpoons \theta$ ” indicate that the contour  
 844 integrations are to be carried out, using the finite-volume algorithm described in L97, in the  
 845  $(\Pi, \lambda)$  and  $(\Pi, \theta)$  space, respectively.

846 To complete one time step, equations (3.31-3.34), together with their counterparts on the  
 847 C-grid are cycled  $m$  times using the fractional time step  $\Delta\tau$ , which are followed by the tracer  
 848 transport using (3.26) with the large-time-step  $\Delta t$ .

Mass fluxes  $(x^*, y^*)$  and the winds  $(u^*, v^*)$  on the C-grid are accumulated for the large-time-step transport of tracer species (including water vapor)  $q$  as

$$q^{n+1} = \frac{1}{\delta p^{n+1}} [q^n \delta p^n + F(X^*, \Delta t, q^\theta) + G(Y^*, \Delta t, q^\lambda)], \quad (3.37)$$

where the time-accumulated mass fluxes  $(X^*, Y^*)$  are computed as

$$X^* = \sum_{i=1}^m x_i^*(u_i^*, \Delta\tau, \delta p_i^\theta), \quad (3.38)$$

$$Y^* = \sum_{i=1}^m y_i^*(v_i^*, \Delta\tau, \delta p_i^\lambda). \quad (3.39)$$

849 The time-averaged winds  $(U^*, V^*)$ , defined as follows, are to be used as input for the com-  
 850 putations of  $q^\lambda$  and  $q^\theta$ :

$$U^* = \frac{1}{m} \sum_{i=1}^m u_i^*, \quad (3.40)$$

$$V^* = \frac{1}{m} \sum_{i=1}^m v_i^*. \quad (3.41)$$

851 The use of the time accumulated mass fluxes and the time-averaged winds for the large-  
 852 time-step tracer transport in the manner described above ensures the conservation of the tracer  
 853 mass and maintains the highest degree of consistency possible given the time split integration  
 854 procedure. A graphical illustration of the different levels of sub-cycling in CAM5 is given on  
 855 Figure 3.1.

856 The algorithm described here can be readily applied to a regional model if appropriate bound-  
 857 ary conditions are supplied. There is formally no Courant number related time step restriction  
 858 associated with the transport processes. There is, however, a stability condition imposed by the  
 859 gravity-wave processes. For application on the whole sphere, it is computationally advantageous  
 860 to apply a polar filter to allow a dramatic increase of the size of the small time step  $\Delta\tau$ . The  
 861 effect of the polar filter is to stabilize the short-in-wavelength (and high-in-frequency) gravity  
 862 waves that are being unnecessarily and unidirectionally resolved at very high latitudes in the  
 863 zonal direction. To minimize the impact to meteorologically significant larger scale waves, the  
 864 polar filter is highly scale selective and is applied only to the diagnostic variables on the auxiliary  
 865 C-grid and the tendency terms in the D-grid momentum equations. No polar filter is applied  
 866 directly to any of the prognostic variables.

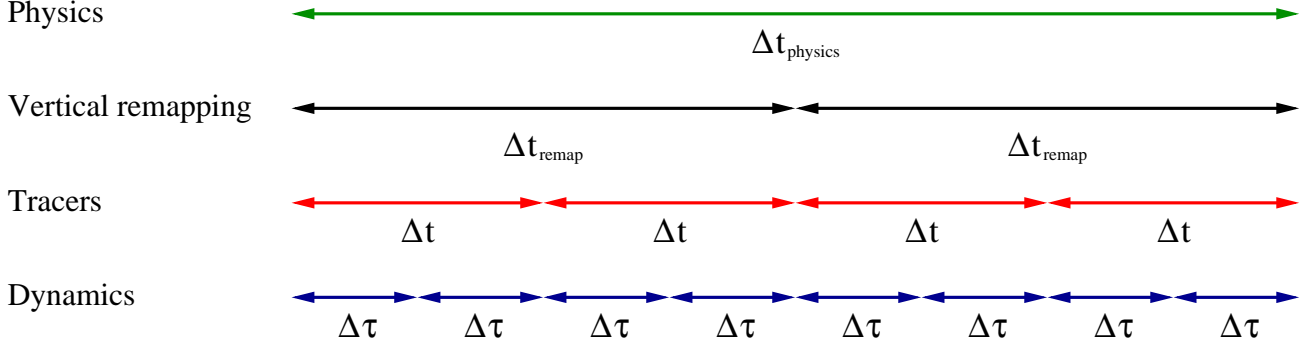


Figure 3.1: A graphical illustration of the different levels of sub-cycling in CAM5.

867 The design of the polar filter follows closely that of [Suarez and Takacs \[1995\]](#) for the C-grid  
 868 Arakawa type dynamical core (e.g., [Arakawa and Lamb \[1981\]](#)). For the CAM 5.0 the fast-  
 869 fourier transform component of the polar filtering has replaced the algebraic form at all filtering  
 870 latitudes. Because our prognostic variables are computed on the D-grid and the fact that the  
 871 FFSL transport scheme is stable for Courant number greater than one, in realistic test cases  
 872 the maximum size of the time step is about two to three times larger than a model based on  
 873 Arakawa and Lamb's C-grid differencing scheme. It is possible to avoid the use of the polar  
 874 filter if, for example, the "Cubed grid" is chosen, instead of the current latitude-longitude grid.  
 875 rewrite of the rest of the model codes including physics parameterizations, the land model, and  
 876 most of the post processing packages.

877 The size of the small time step for the Lagrangian dynamics is only a function of the horizontal  
 878 resolution. Applying the polar filter, for the 2-degree horizontal resolution, a small-time-step size  
 879 of 450 seconds can be used for the Lagrangian dynamics. From the large-time-step transport  
 880 perspective, the small-time-step integration of the 2D Lagrangian dynamics can be regarded  
 881 as a very accurate iterative solver, with  $m$  iterations, for computing the time mean winds  
 882 and the mass fluxes, analogous in functionality to a semi-implicit algorithm's elliptic solver  
 883 (e.g., [Ringler et al. \[2000\]](#)). Besides accuracy, the merit of an "explicit" versus "semi-implicit"  
 884 algorithm ultimately depends on the computational efficiency of each approach. In light of the  
 885 advantage of the explicit algorithm in parallelization, we do not regard the explicit algorithm for  
 886 the Lagrangian dynamics as an impedance to computational efficiency, particularly on modern  
 887 parallel computing platforms.

### 888 3.1.5 Optional diffusion operators in CAM5

The 'CD'-grid discretization method used in the CAM finite-volume dynamical core provides explicit control over the rotational modes at the grid scale, due to monotonicity constraint in the PPM-based advection, but there is no explicit control over the divergent modes at the grid scale [see, e.g., [Skamarock, 2010](#)]. Therefore divergence damping terms appear on the right-hand side of the momentum equations ((3.28) and (3.29)):

$$- \frac{1}{A \cos \theta} \left[ \frac{\partial}{\partial \lambda} (-\nu D) \right] \quad (3.42)$$

and

$$-\frac{1}{A} \left[ \frac{\partial}{\partial \theta} (-\nu D) \right], \quad (3.43)$$

respectively, where the strength of the divergence damping is controlled by the coefficient  $\nu$  given by

$$\nu = \frac{\nu_2 (A^2 \Delta \lambda \Delta \theta)}{\Delta t}, \quad (3.44)$$

where  $\nu_2 = 1/128$  throughout the atmosphere except in the top model levels where it monotonically increases to approximately  $4/128$  at the top of the atmosphere. The divergence damping described above is referred to as ‘second-order’ divergence damping as it effectively damps divergence with a  $\nabla^2$  operator.

In CAM5 optional ‘fourth-order’ divergence damping has been implemented where the divergence is effectively damped with a  $\nabla^4$ -operator which is usually more scale selective than ‘second-order’ damping operators. For ‘fourth-order’ divergence damping the terms

$$-\frac{1}{A \cos \theta} \left[ \frac{\partial}{\partial \lambda} (-\nu_4 \nabla^2 D) \right] \quad (3.45)$$

and

$$-\frac{1}{A} \left[ \frac{\partial}{\partial \theta} (-\nu_4 \nabla^2 D) \right], \quad (3.46)$$

are added to the right-hand side of (3.28) and (3.29), respectively. The horizontal Laplacian  $\nabla^2$ -operator in spherical coordinates for a scalar  $\psi$  is given by

$$\nabla^2 \psi = \frac{1}{A^2 \cos^2 \theta} \frac{\partial^2 \psi}{\partial^2 \lambda} + \frac{1}{A^2 \cos \theta} \frac{\partial}{\partial \theta} \left( \cos \theta \frac{\partial \psi}{\partial \theta} \right). \quad (3.47)$$

The fourth-order divergence damping coefficient is given by

$$\nu_4 = 0.01 (A^2 \cos(\theta) \Delta \lambda \Delta \theta)^2 / \Delta t. \quad (3.48)$$

Since divergence damping is added explicitly to the equations of motion it is unstable if the time-step is too large or the damping coefficients ( $\nu$  or  $\nu_4$ ) are too large. To stabilize the fourth-order divergence damping the winds used to compute the divergence are filtered using the same FFT filtering which is applied to stabilize the gravity waves.

To control potentially excessive polar night jets in high-resolution configurations of CAM, Laplacian damping of the wind components has been added as an option in CAM5. That is, the terms

$$\nu_{del2} \nabla^2 u \quad (3.49)$$

and

$$\nu_{del2} \nabla^2 v \quad (3.50)$$

are added to the right-hand side of the momentum equations (3.28) and (3.29), respectively. The damping coefficient  $\nu_{del2}$  is zero throughout the atmosphere except in the top layers where it increases monotonically and smoothly from zero to approximately four times a user-specified damping coefficient at the top of the atmosphere (the user-specified damping coefficient is typically on the order of  $2.5 \times 10^5 \text{ m}^2 \text{sec}^{-1}$ ).

902 **3.1.6 A mass, momentum, and total energy conserving mapping al-  
903 gorithm**

904 The Lagrangian surfaces that bound the finite-volume will eventually deform, particularly in  
905 the presence of persistent diabatic heating/cooling, in a time scale of a few hours to a day  
906 depending on the strength of the heating and cooling, to a degree that it will negatively impact  
907 the accuracy of the horizontal-to-Lagrangian-coordinate transport and the computation of the  
908 pressure gradient forces. Therefore, a key to the success of the Lagrangian control-volume  
909 discretization is an accurate and conservative algorithm for mapping the deformed Lagrangian  
910 coordinate back to a fixed reference Eulerian coordinate.

911 There are some degrees of freedom in the design of the vertical mapping algorithm. To ensure  
912 conservation, our current (and recommended) mapping algorithm is based on the reconstruction  
913 of the “mass” (pressure thickness  $\delta p$ ), zonal and meridional “winds”, “tracer mixing ratios”, and  
914 “total energy” (volume integrated sum of the internal, potential, and kinetic energy), using the  
915 monotonic Piecewise Parabolic sub-grid distributions with the hydrostatic pressure (as defined  
916 by (3.30)) as the mapping coordinate. We outline the mapping procedure as follows.

917 **Step 1:** Define a suitable Eulerian reference coordinate as a target coordinate. The  
918 mass in each layer ( $\delta p$ ) is then distributed vertically according to the chosen  
919 Eulerian coordinate. The surface pressure typically plays an “anchoring” role  
920 in defining the terrain following Eulerian vertical coordinate. The hybrid  $\eta$  –  
921 *coordinate* used in the NCAR CCM3 [Kiehl et al., 1996] is adopted in the current  
922 model setup.

923 **Step 2:** Construct the piece-wise continuous vertical subgrid profiles of tracer mixing  
924 ratios ( $q$ ), zonal and meridional winds ( $u$  and  $v$ ), and total energy ( $\Gamma$ ) in the  
925 Lagrangian control-volume coordinate, or the source coordinate. The total energy  
926  $\Gamma$  is computed as the sum of the finite-volume integrated geopotential  $\phi$ , internal  
927 energy ( $C_v T_v$ ), and the kinetic energy ( $K$ ) as follows:

$$\Gamma = \frac{1}{\delta p} \int \left[ C_v T_v + \phi + \frac{1}{2} (u^2 + v^2) \right] dp. \quad (3.51)$$

928 Applying integration by parts and the ideal gas law, the above integral can be  
929 rewritten as

$$\begin{aligned} \Gamma &= \frac{1}{\delta p} \left\{ \int \left[ C_p T_v + \frac{1}{2} (u^2 + v^2) \right] dp + \int d(p\phi) \right\} \\ &= C_p \overline{T_v} + \frac{1}{\delta p} \delta(p\phi) + K, \end{aligned} \quad (3.52)$$

930 where  $\overline{T_v}$  is the layer mean virtual temperature,  $K$  is the layer mean kinetic  
931 energy,  $p$  is the pressure at layer edges, and  $C_v$  and  $C_p$  are the specific heat of the  
932 air at constant volume and at constant pressure, respectively. The total energy

in each grid cell is calculated as

$$\begin{aligned}\Gamma_{i,j,k} = & C_p T_{v_{i,j,k}} + \frac{1}{\delta p_{i,j,k}} \left( p_{i,j,k+\frac{1}{2}} \phi_{i,j,k+\frac{1}{2}} - p_{i,j,k-\frac{1}{2}} \phi_{i,j,k-\frac{1}{2}} \right) + \\ & \frac{1}{2} \left( \frac{u_{i,j-\frac{1}{2},k}^2 + u_{i,j+\frac{1}{2},k}^2}{2} + \frac{v_{i-\frac{1}{2},j,k}^2 + v_{i+\frac{1}{2},j,k}^2}{2} \right)\end{aligned}$$

The method employed to create subgrid profiles is set by the flag *te\_method*. For *te\_method* = 0 (default), the Piece-wise Parabolic Method (PPM, Colella and Woodward [1984]) over a pressure coordinate is used and for *te\_method* = 1 a cubic spline over a logarithmic pressure coordinate is used.

**Step 3:** Layer mean values of  $q$ ,  $(u, v)$ , and  $\Gamma$  in the Eulerian coordinate system are obtained by integrating analytically the sub-grid distributions, in the vertical direction, from model top to the surface, layer by layer. Since the hydrostatic pressure is chosen as the mapping coordinate, tracer mass, momentum, and total energy are locally and globally conserved. In mapping a variable from the source coordinate to the target coordinate, different limiter constraints may be used and they are controlled by two flags, *iv* and *kord*. For winds on D-grid, *iv* should be set to -1. For tracers, *iv* should be set to 0. For all others, *iv* = 1. *kord* directly controls which limiter constraint is used. For *kord*  $\geq 7$ , Huynh's 2nd constraint is used. If *kord* = 7, the original quasi-monotonic constraint is used. If *kord*  $> 7$ , a full monotonic constraint is used. If *kord* is less than 7, the variable, *lmt*, is determined by the following:

$$\begin{aligned}lmt &= kord - 3, \\ lmt &= \max(0, lmt), \\ \text{if}(iv = 0) \quad lmt &= \min(2, lmt).\end{aligned}$$

If *lmt* = 0, a standard PPM constraint is used. If *lmt* = 1, an improved full monotonicity constraint is used. If *lmt* = 2, a positive definite constraint is used. If *lmt* = 3, the algorithm will do nothing.

**Step 4:** Retrieve virtual temperature in the Eulerian (target) coordinate. Start by computing kinetic energy in the Eulerian coordinate system for each layer. Then substitute kinetic energy and the hydrostatic relationship into (3.52). The layer mean temperature  $\bar{T}_{vk}$  for layer  $k$  in the Eulerian coordinate is then retrieved from the reconstructed total energy (done in Step 3) by a fully explicit integration procedure starting from the surface up to the model top as follows:

$$\bar{T}_{vk} = \frac{\Gamma_k - K_k - \phi_{k+\frac{1}{2}}}{C_p \left[ 1 - \kappa p_{k-\frac{1}{2}} \frac{\ln p_{k+\frac{1}{2}} - \ln p_{k-\frac{1}{2}}}{p_{k+\frac{1}{2}} - p_{k-\frac{1}{2}}} \right]}, \quad (3.53)$$

where  $\kappa = R_d/C_p$  and  $R_d$  is the gas constant for dry air.

To convert the potential virtual temperature  $\Theta_v$  to the layer mean temperature the conversion factor is obtained by equating the following two equivalent forms of the hydrostatic relation for  $\Theta$  and  $\overline{T}_v$ :

$$\delta\phi = -C_p\Theta_v\delta\Pi, \quad (3.54)$$

$$\delta\phi = -R_d\overline{T}_v\delta\ln p, \quad (3.55)$$

where  $\Pi = p^\kappa$ . The conversion formula between layer mean temperature and layer mean potential temperature is obtained as follows:

$$\Theta_v = \kappa \frac{\delta\ln p}{\delta\Pi} \overline{T}_v. \quad (3.56)$$

The physical implication of retrieving the layer mean temperature from the total energy as described in Step 3 is that the dissipated kinetic energy, if any, is locally converted into internal energy via the vertically sub-grid mixing (dissipation) processes. Due to the monotonicity preserving nature of the sub-grid reconstruction the column-integrated kinetic energy inevitably decreases (dissipates), which leads to local frictional heating. The frictional heating is a physical process that maintains the conservation of the total energy in a closed system.

As viewed by an observer riding on the Lagrangian surfaces, the mapping procedure essentially performs the physical function of the relative-to-the-Eulerian-coordinate vertical transport, by vertically redistributing (air and tracer) mass, momentum, and total energy from the Lagrangian control-volume back to the Eulerian framework.

As described in section 3.1.4, the model time integration cycle consists of  $m$  small time steps for the 2D Lagrangian dynamics and one large time step for tracer transport. The mapping time step can be much larger than that used for the large-time-step tracer transport. In tests using the Held-Suarez forcing [Held and Suarez, 1994], a three-hour mapping time interval is found to be adequate. In the full model integration, one may choose the same time step used for the physical parameterizations so as to ensure the input state variables to physical parameterizations are in the usual “Eulerian” vertical coordinate. In CAM5, vertical remapping takes place at each physics time step.

### 3.1.7 A geopotential conserving mapping algorithm

An alternative vertical mapping approach is available in CAM5. Instead of retrieving temperature by remapped total energy in the Eulerian coordinate, the alternative approach maps temperature directly from the Lagrangian coordinate to the Eulerian coordinate. Since geopotential is defined as

$$\delta\phi = -C_p\Theta_v\delta\Pi = -R_dT_v\delta\ln p,$$

mapping  $\Theta_v$  over  $\Pi$  or  $T_v$  over  $\ln p$  preserves the geopotential at the model lid. This approach prevents the mapping procedure from generating spurious pressure gradient forces at the model lid. Unlike the energy-conserving algorithm which could produce substantial temperature fluctuations at the model lid, the geopotential conserving approach guarantees a smooth (potential) temperature profile. However, the geopotential conserving does not conserve total energy in the remapping procedure. This may be resolved by a global energy fixer already implemented in the model (see section 3.1.10).

963 **3.1.8 Adjustment of pressure to include change in mass of water  
964 vapor**

965 The physics parameterizations operate on a model state provided by the dynamics, and are  
966 allowed to update specific humidity. However, the surface pressure remains fixed throughout  
967 the physics updates, and since there is an explicit relationship between the surface pressure and  
968 the air mass within each layer, the total air mass must remain fixed as well throughout the  
969 physics updates. If no further correction were made, this would imply that the dry air mass  
970 changed if the water vapor mass changed in the physics updates. Therefore the pressure field is  
971 changed to include the change in water vapor mass due to the physics updates. We impose the  
972 restrictions that dry air mass and water mass are conserved as follows:

The total pressure  $p$  is

$$p = d + e. \quad (3.57)$$

with dry pressure  $d$ , water vapor pressure  $e$ . The specific humidity is

$$q = \frac{e}{p} = \frac{e}{d + e}, \quad d = (1 - q)p. \quad (3.58)$$

We define a layer thickness as  $\delta^k p \equiv p^{k+1/2} - p^{k-1/2}$ , so

$$\delta^k d = (1 - q^k) \delta^k p. \quad (3.59)$$

973 We are concerned about 3 time levels:  $q_n$  is input to physics,  $q_{n*}$  is output from physics,  $q_{n+1}$  is  
974 the adjusted value for dynamics.

Dry mass is the same at  $n$  and  $n + 1$  but not at  $n*$ . To conserve dry mass, we require that

$$\delta^k d_n = \delta^k d_{n+1} \quad (3.60)$$

or

$$(1 - q_n^k) \delta^k p_n = (1 - q_{n+1}^k) \delta^k p_{n+1}. \quad (3.61)$$

Water mass is the same at  $n*$  and  $n + 1$ , but not at  $n$ . To conserve water mass, we require  
that

$$q_{n*}^k \delta^k p_n = q_{n+1}^k \delta^k p_{n+1}. \quad (3.62)$$

Substituting (3.62) into (3.61),

$$(1 - q_n^k) \delta^k p_n = \delta^k p_{n+1} - q_{n*}^k \delta^k p_n \quad (3.63)$$

$$\delta^k p_{n+1} = (1 - q_n^k + q_{n*}^k) \delta^k p_n \quad (3.64)$$

which yields a modified specific humidity for the dynamics:

$$q_{n+1}^k = q_n^k \frac{\delta^k p_n}{\delta^k p_{n+1}} = \frac{q_{n*}^k}{1 - q_n^k + q_{n*}^k}. \quad (3.65)$$

975 We note that this correction as implemented makes a small change to the water vapor as well.  
976 The pressure correction could be formulated to leave the water vapor unchanged.

### 977 3.1.9 Negative Tracer Fixer

978 In the Finite Volume dynamical core, neither the monotonic transport nor the conservative vertical  
979 remapping guarantee that tracers will remain positive definite. Thus the Finite Volume  
980 dynamical core includes a negative tracer fixer applied before the parameterizations are calcu-  
981 lated. For negative mixing ratios produced by horizontal transport, the model will attempt to  
982 borrow mass from the east and west neighboring cells. In practice, most negative values are  
983 introduced by the vertical remapping which does not guarantee positive definiteness in the first  
984 and last layer of the vertical column.

985 A minimum value  $q_{min}$  is defined for each tracer. If the tracer falls below that minimum value,  
986 it is set to that minimum value. If there is enough mass of the tracer in the layer immediately  
987 above, tracer mass is removed from that layer to conserve the total mass in the column. If  
988 there is not enough mass in the layer immediately above, no compensation is applied, violating  
989 conservation. Usually such computational sources are very small.

The amount of tracer needed from the layer above to bring  $q_k$  up to  $q_{min}$  is

$$q_{fill} = (q_{min} - q_k) \frac{\Delta p_k}{\Delta p_{k-1}} \quad (3.66)$$

where  $k$  is the vertical index, increasing downward. After the filling

$$q_{k_{FILLED}} = q_{min} \quad (3.67)$$

$$q_{k-1_{FILLED}} = q_{k-1} - q_{fill} \quad (3.68)$$

990 Currently  $q_{min} = 1.0 \times 10^{-12}$  for water vapor,  $q_{min} = 0.0$  for CLDLIQ, CLDICE, NUMLIQ and  
991 NUMICE, and  $q_{min} = 1.0 \times 10^{-36}$  for the remaining constituents.

### 992 3.1.10 Global Energy Fixer

993 The finite-volume dynamical core as implemented in CAM and described here conserves the dry  
994 air and all other tracer mass exactly without a “mass fixer”. The vertical Lagrangian discretiza-  
995 tion and the associated remapping conserves the total energy exactly. The only remaining issue  
996 regarding conservation of the total energy is the horizontal discretization and the use of the  
997 “diffusive” transport scheme with monotonicity constraint. To compensate for the loss of total  
998 energy due to horizontal discretization, we apply a global fixer to add the loss in kinetic energy  
999 due to “diffusion” back to the thermodynamic equation so that the total energy is conserved.  
1000 The loss in total energy (in flux unit) is found to be around 2 ( $W/m^2$ ) with the 2 degrees  
1001 resolution.

1002 The energy fixer is applied following the negative tracer fixer. The fixer is applied on the  
1003 unstaggered physics grid rather than on the staggered dynamics grid. The energies on these  
1004 two grids are difficult to relate because of the nonlinear terms in the energy definition and  
1005 the interpolation of the state variables between the grids. The energy is calculated in the  
1006 parameterization suite before the state is passed to the finite volume core as described in the  
1007 beginning of Chapter 4. The fixer is applied just before the parameterizations are calculated.  
1008 The fixer is a simplification of the fixer in the Eulerian dynamical core described in section  
1009 3.3.20.

Let minus sign superscript  $(\ )^-$  denote the values at the beginning of the dynamics time step, i.e. after the parameterizations are applied, let a plus sign superscript  $(\ )^+$  denote the values after fixer is applied, and let a hat  $(\hat{\ })^+$  denote the provisional value before adjustment. The total energy over the entire computational domain after the fixer is

$$E^+ = \int_{p_t}^{p_s} \int_0^{2\pi} \int_{-\frac{\pi}{2}}^{\frac{\pi}{2}} \frac{1}{g} \left[ C_p T^+ + \Phi + \frac{1}{2} (u^{+2} + v^{+2}) + (L_v + L_i) q_v^+ + L_i q_\ell^+ \right] A^2 \cos \theta d\theta d\lambda dp, \quad (3.69)$$

where  $L_v$  is the latent heat of vaporation,  $L_i$  is the latent heat of fusion,  $q_v$  is water vapor mixing ratio, and  $q_\ell$  is cloud water mixing ratio.  $E^+$  should equal the energy at the beginning of the dynamics time step

$$E^- = \int_{p_t}^{p_s} \int_0^{2\pi} \int_{-\frac{\pi}{2}}^{\frac{\pi}{2}} \frac{1}{g} \left[ c_p T^- + \Phi + \frac{1}{2} (u^{-2} + v^{-2}) + (L_v + L_i) q_v^- + L_i q_\ell^- \right] A^2 \cos \theta d\theta d\lambda dp. \quad (3.70)$$

Let  $\hat{E}^+$  denote the energy of the provisional state provided by the dynamical core before the adjustment.

$$\hat{E}^+ = \int_{p_t}^{p_s} \int_0^{2\pi} \int_{-\frac{\pi}{2}}^{\frac{\pi}{2}} \frac{1}{g} \left[ c_p \hat{T}^+ + \hat{\Phi}^+ + \frac{1}{2} (\hat{u}^{+2} + \hat{v}^{+2}) + (L_v + L_i) \hat{q}_v^+ + L_i \hat{q}_\ell^+ \right] A^2 \cos \theta d\theta d\lambda dp. \quad (3.71)$$

Thus, the total energy added into the system by the dynamical core is  $\hat{E}^+ - E^-$ . The energy fixer then changes dry static energy ( $s = C_p T + \Phi$ ) by a constant amount over each grid cell to conserve total energy in the entire computational domain. The dry static energy added to each grid cell may be expressed as

$$\Delta s = \frac{E^- - \hat{E}^+}{\int_{p_t}^{p_s} \int_0^{2\pi} \int_{-\frac{\pi}{2}}^{\frac{\pi}{2}} A^2 \cos \theta d\theta d\lambda \frac{dp}{g}}. \quad (3.72)$$

Therefore,

$$s^+ = \hat{s}^+ + \Delta s, \quad (3.73)$$

or

$$C_p T^+ + \Phi^+ = \hat{s}^+ + \Delta s. \quad (3.74)$$

1010 This will ensure  $E^+ = E^-$ .

By hydrostatic approximation, the geopotential equation is

$$d\Phi = -R_d T_v d \ln p, \quad (3.75)$$

and for any arbitrary point between  $p_{k+\frac{1}{2}}$  and  $p_{k-\frac{1}{2}}$  the geopotential may be written as

$$\int_{\Phi_{k+\frac{1}{2}}}^{\Phi} d\Phi' = -R_d T_v \int_{p_{k+\frac{1}{2}}}^p d \ln p', \quad (3.76)$$

$$\Phi = \Phi_{k+\frac{1}{2}} + R_d T_v \left( \ln p_{k+\frac{1}{2}} - \ln p \right). \quad (3.77)$$

The geopotential at the mid point of a model layer between  $p_{k+\frac{1}{2}}$  and  $p_{k-\frac{1}{2}}$ , or the layer mean, is

$$\begin{aligned}
\Phi_k &= \frac{\int_{p_{k-\frac{1}{2}}}^{p_{k+\frac{1}{2}}} \Phi \, dp}{\int_{p_{k-\frac{1}{2}}}^{p_{k+\frac{1}{2}}} dp} \\
&= \frac{\int_{p_{k-\frac{1}{2}}}^{p_{k+\frac{1}{2}}} \left[ \Phi_{k+\frac{1}{2}} + R_d T_v \left( \ln p_{k+\frac{1}{2}} - \ln p \right) \right] \, dp}{\int_{p_{k-\frac{1}{2}}}^{p_{k+\frac{1}{2}}} dp} \\
&= \Phi_{k+\frac{1}{2}} + R_d T_v \ln p_{k+\frac{1}{2}} - \frac{\int_{p_{k-\frac{1}{2}}}^{p_{k+\frac{1}{2}}} \ln p \, dp}{p_{k+\frac{1}{2}} - p_{k-\frac{1}{2}}} \\
&= \Phi_{k+\frac{1}{2}} + R_d T_v \left( 1 - p_{k-\frac{1}{2}} \frac{\ln p_{k+\frac{1}{2}} - \ln p_{k-\frac{1}{2}}}{p_{k+\frac{1}{2}} - p_{k-\frac{1}{2}}} \right)
\end{aligned} \tag{3.78}$$

For layer  $k$ , the energy fixer will solve the following equation based on (3.74),

$$C_p T_k^+ + \Phi_{k+\frac{1}{2}}^+ + R_d T_k^+ (1 + \epsilon q_{v_k}^+) \left( 1 - p_{k-\frac{1}{2}}^+ \frac{\ln p_{k+\frac{1}{2}}^+ - \ln p_{k-\frac{1}{2}}^+}{p_{k+\frac{1}{2}}^+ - p_{k-\frac{1}{2}}^+} \right) = \hat{s}^+ + \Delta s. \tag{3.79}$$

Since the energy fixer will not alter the water vapor mixing ratio and the pressure field,

$$q_v^+ = \hat{q}_v^+, \tag{3.80}$$

$$p^+ = \hat{p}^+. \tag{3.81}$$

Therefore,

$$T_k^+ = \frac{(\hat{s}^+ + \Delta s) - \Phi_{k+\frac{1}{2}}^+}{C_p + R_d (1 + \epsilon \hat{q}_{v_k}^+) \left( 1 - \hat{p}_{k-\frac{1}{2}}^+ \frac{\ln \hat{p}_{k+\frac{1}{2}}^+ - \ln \hat{p}_{k-\frac{1}{2}}^+}{\hat{p}_{k+\frac{1}{2}}^+ - \hat{p}_{k-\frac{1}{2}}^+} \right)}. \tag{3.82}$$

1011 The energy fixer starts from the Earth's surface and works its way up to the model top in  
1012 adjusting the temperature field. At the surface layer,  $\Phi_{k+\frac{1}{2}}^+ = \Phi_s$ . After the temperature is  
1013 adjusted in a grid cell, the geopotential at the upper interface of the cell is updated which is  
1014 needed for the temperature adjustment in the grid cell above.

### 1015 3.1.11 Further discussion

1016 There are still aspects of the numerical formulation in the finite volume dynamical core that can  
1017 be further improved. For example, the choice of the horizontal grid, the computational efficiency  
1018 of the split-explicit time marching scheme, the choice of the various monotonicity constraints,  
1019 and how the conservation of total energy is achieved.

1020 The impact of the non-linear diffusion associated with the monotonicity constraint is dif-  
1021 ficult to assess. All discrete schemes must address the problem of subgrid-scale mixing. The  
1022 finite-volume algorithm contains a non-linear diffusion that mixes strongly when monotonicity

1023 principles are locally violated. However, the effect of nonlinear diffusion due to the imposed  
1024 monotonicity constraint diminishes quickly as the resolution matches better to the spatial struc-  
1025 ture of the flow. In other numerical schemes, however, an explicit (and tunable) linear diffusion  
1026 is often added to the equations to provide the subgrid-scale mixing as well as to smooth and/or  
1027 stabilize the time marching.

## 1028 3.2 Spectral Element Dynamical Core

1029 The CAM includes an optional dynamical core from HOMME, NCAR’s High-Order Method  
1030 Modeling Environment [Dennis et al., 2005]. The stand-alone HOMME is used for re-  
1031 search in several different types of dynamical cores. The dynamical core incorporated into  
1032 CAM4 uses HOMME’s continuous Galerkin spectral finite element method [Taylor et al., 1997;  
1033 Fournier et al., 2004; Thomas and Loft, 2005; Wang et al., 2007; Taylor and Fournier, 2010],  
1034 here abbreviated to the spectral element method (SEM). This method is designed for fully  
1035 unstructured quadrilateral meshes. The current configurations in the CAM are based on the  
1036 cubed-sphere grid. The main motivation for the inclusion of HOMME is to improve the scalabil-  
1037 ity of the CAM by introducing quasi-uniform grids which require no polar filters [Taylor et al.,  
1038 2008]. HOMME is also the first dynamical core in the CAM which locally conserves energy in  
1039 addition to mass and two-dimensional potential vorticity [Taylor, 2010].

1040 HOMME represents a large change in the horizontal grid as compared to the other dynamical  
1041 cores in CAM. Almost all other aspects of HOMME are based on a combination of well-tested ap-  
1042 proaches from the Eulerian and FV dynamical cores. For tracer advection, HOMME is modeled  
1043 as closely as possible on the FV core. It uses the same conservation form of the transport equa-  
1044 tion and the same vertically Lagrangian discretization [Lin, 2004]. The HOMME dynamics are  
1045 modeled as closely as possible on Eulerian core. They share the same vertical coordinate, vertical  
1046 discretization, hyper-viscosity based horizontal diffusion, top-of-model dissipation, and solve the  
1047 same moist hydrostatic equations. The main differences are that HOMME advects the surface  
1048 pressure instead of its logarithm (in order to conserve mass and energy), and HOMME uses the  
1049 vector-invariant form of the momentum equation instead of the vorticity-divergence formulation.  
1050 Several dry dynamical cores including HOMME are evaluated in Lauritzen et al. [2010] using a  
1051 grid-rotated version of the baroclinic instability test case [Jablonowski and Williamson, 2006].

1052 The timestepping in HOMME is a form of dynamics/tracer/physics subcycling, achieved  
1053 through the use of multi-stage 2nd order accurate Runge-Kutta methods. The tracers and  
1054 dynamics use the same timestep which is controlled by the maximum anticipated wind speed,  
1055 but the dynamics uses more stages than the tracers in order to maintain stability in the presence  
1056 of gravity waves. The forcing is applied using a time-split approach. The optimal forcing  
1057 strategy in HOMME has not yet been determined, so HOMME supports several options. The  
1058 first option is modeled after the FV dynamical core and the forcing is applied as an adjustment  
1059 at each physics timestep. The second option is to convert all forcings into tendencies which are  
1060 applied at the end of each dynamics/tracer timestep. If the physics timestep is larger than the  
1061 tracer timestep, then the tendencies are held fixed and only updated at each physics timestep.  
1062 Finally, a hybrid approach can be used where the tracer tendencies are applied as in the first  
1063 option and the dynamics tendencies are applied as in the second option.

### 3.2.1 Continuum Formulation of the Equations

HOMME uses a conventional vector-invariant form of the moist primitive equations. For the vertical discretization it uses the hybrid  $\eta$  pressure vertical coordinate system modeled after 3.3.1. The formulation here differs only in that surface pressure is used as a prognostic variable as opposed to its logarithm.

In the  $\eta$ -coordinate system, the pressure is given by

$$p(\eta) = A(\eta)p_0 + B(\eta)p_s.$$

The hydrostatic approximation  $\partial p/\partial z = -g\rho$  is used to replace the mass density  $\rho$  by an  $\eta$ -coordinate pseudo-density  $\partial p/\partial\eta$ . The material derivative in  $\eta$ -coordinates can be written (e.g. Satoh [2004], Sec.3.3),

$$\frac{DX}{Dt} = \frac{\partial X}{\partial t} + \vec{u} \cdot \nabla X + \dot{\eta} \frac{\partial X}{\partial \eta}$$

where the  $\nabla()$  operator (as well as  $\nabla \cdot()$  and  $\nabla \times()$  below) is the two-dimensional gradient on constant  $\eta$ -surfaces,  $\partial/\partial\eta$  is the vertical derivative,  $\dot{\eta} = D\eta/Dt$  is a vertical flow velocity and  $\vec{u}$  is the horizontal velocity component (tangent to constant  $z$ -surfaces, not  $\eta$ -surfaces).

The  $\eta$ -coordinate atmospheric primitive equations, neglecting dissipation and forcing terms can then be written as

$$\frac{\partial \vec{u}}{\partial t} + (\zeta + f) \hat{k} \times \vec{u} + \nabla \left( \frac{1}{2} \vec{u}^2 + \Phi \right) + \dot{\eta} \frac{\partial \vec{u}}{\partial \eta} + \frac{RT_v}{p} \nabla p = 0 \quad (3.83)$$

$$\frac{\partial T}{\partial t} + \vec{u} \cdot \nabla T + \dot{\eta} \frac{\partial T}{\partial \eta} - \frac{RT_v}{c_p^* p} \omega = 0 \quad (3.84)$$

$$\frac{\partial}{\partial t} \left( \frac{\partial p}{\partial \eta} \right) + \nabla \cdot \left( \frac{\partial p}{\partial \eta} \vec{u} \right) + \frac{\partial}{\partial \eta} \left( \dot{\eta} \frac{\partial p}{\partial \eta} \right) = 0 \quad (3.85)$$

$$\frac{\partial}{\partial t} \left( \frac{\partial p}{\partial \eta} q \right) + \nabla \cdot \left( \frac{\partial p}{\partial \eta} q \vec{u} \right) + \frac{\partial}{\partial \eta} \left( \dot{\eta} \frac{\partial p}{\partial \eta} q \right) = 0. \quad (3.86)$$

These are prognostic equations for  $\vec{u}$ , the temperature  $T$ , density  $\frac{\partial p}{\partial \eta}$ , and  $\frac{\partial p}{\partial \eta} q$  where  $q$  is the specific humidity. The prognostic variables are functions of time  $t$ , vertical coordinate  $\eta$  and two coordinates describing the surface of the sphere. The unit vector normal to the surface of the sphere is denoted by  $\hat{k}$ . This formulation has already incorporated the hydrostatic equation and the ideal gas law,  $p = \rho RT_v$ . There is a no-flux ( $\dot{\eta} = 0$ ) boundary condition at  $\eta = 1$  and  $\eta = \eta_{\text{top}}$ . The vorticity is denoted by  $\zeta = \hat{k} \cdot \nabla \times \vec{u}$ ,  $f$  is a Coriolis term and  $\omega = Dp/Dt$  is the pressure vertical velocity. The virtual temperature  $T_v$  and variable-of-convenience  $c_p^*$  are defined as in 3.3.1.

The diagnostic equations for the geopotential height field  $\Phi$  is

$$\Phi = \Phi_s + \int_{\eta}^1 \frac{RT_v}{p} \frac{\partial p}{\partial \eta} d\eta \quad (3.87)$$

where  $\Phi_s$  is the prescribed surface geopotential height (given at  $\eta = 1$ ). To complete the system, we need diagnostic equations for  $\dot{\eta}$  and  $\omega$ , which come from integrating (3.85) with respect to

$\eta$ . In fact, (3.85) can be replaced by a diagnostic equation for  $\dot{\eta} \frac{\partial p}{\partial \eta}$  and a prognostic equation for surface pressure  $p_s$

$$\frac{\partial}{\partial t} p_s + \int_{\eta_{\text{top}}}^1 \nabla \cdot \left( \frac{\partial p}{\partial \eta} \vec{u} \right) d\eta = 0 \quad (3.88)$$

$$\dot{\eta} \frac{\partial p}{\partial \eta} = -\frac{\partial p}{\partial t} - \int_{\eta_{\text{top}}}^{\eta} \nabla \cdot \left( \frac{\partial p}{\partial \eta'} \vec{u} \right) d\eta', \quad (3.89)$$

where (3.88) is (3.89) evaluated at the model bottom ( $\eta = 1$ ) after using that  $\partial p / \partial t = B(\eta) \partial p_s / \partial t$  and  $\dot{\eta}(1) = 0, B(1) = 1$ . Using Eq 3.89, we can derive a diagnostic equation for the pressure vertical velocity  $\omega = Dp/Dt$ ,

$$\omega = \frac{\partial p}{\partial t} + \vec{u} \cdot \nabla p + \dot{\eta} \frac{\partial p}{\partial \eta} = \vec{u} \cdot \nabla p - \int_{\eta_{\text{top}}}^{\eta} \nabla \cdot \left( \frac{\partial p}{\partial \eta} \vec{u} \right) d\eta'$$

Finally, we rewrite (3.89) as

$$\dot{\eta} \frac{\partial p}{\partial \eta} = B(\eta) \int_{\eta_{\text{top}}}^1 \nabla \cdot \left( \frac{\partial p}{\partial \eta} \vec{u} \right) d\eta - \int_{\eta_{\text{top}}}^{\eta} \nabla \cdot \left( \frac{\partial p}{\partial \eta'} \vec{u} \right) d\eta', \quad (3.90)$$

### 1080 3.2.2 Conserved Quantities

The equations have infinitely many conserved quantities, including mass, tracer mass, potential temperature defined by

$$M_X = \iint \frac{\partial p}{\partial \eta} X d\eta d\mathcal{A}$$

with ( $X = 1, q$  or  $(p/p_0)^{-\kappa} T$ ) and the total moist energy  $E$  defined by

$$E = \iint \frac{\partial p}{\partial \eta} \left( \frac{1}{2} \vec{u}^2 + c_p^* T \right) d\eta d\mathcal{A} + \int p_s \Phi_s d\mathcal{A} \quad (3.91)$$

1081 where  $d\mathcal{A}$  is the spherical area measure. To compute these quantities in their traditional units  
1082 they should be divided by the constant of gravity  $g$ . We have omitted this scaling since  $g$   
1083 has also been scaled out from (3.83)–(3.86). We note that in this formulation of the primitive  
1084 equations, the pressure  $p$  is a moist pressure, representing the effects of both dry air and water  
1085 vapor. The unforced equations conserve both the moist air mass ( $X = 1$  above) and the dry air  
1086 mass ( $X = 1 - q$ ). However, in the presence of a forcing term in (3.86) (representing sources  
1087 and sinks of water vapor as would be present in a full model) a corresponding forcing term must  
1088 be added to (3.85) to ensure that dry air mass is conserved.

The energy (3.91) is specific to the hydrostatic equations. We have omitted terms from the physical total energy which are constant under the evolution of the unforced hydrostatic equations [Staniforth et al., 2003]. It can be converted into a more universal form involving  $\frac{1}{2} \vec{u}^2 + c_v^* T + \Phi$ , with  $c_v^*$  defined similarly to  $c_p^*$ , so that  $c_v^* = c_v + (c_{vv} - c_v)q$  where  $c_v$  and  $c_{vv}$  are the specific heats of dry air and water vapor defined at constant volume. We note that  $c_p = R + c_v$  and  $c_{pv} = R_v + c_{vv}$  so that  $c_p^* T = c_v^* T + RT_v$ . Expanding  $c_p^* T$  with this expression,

integrating by parts with respect to  $\eta$  and making use of the fact that the model top is at a constant pressure

$$\int \frac{\partial p}{\partial \eta} R T_v d\eta = - \int p \frac{\partial \Phi}{\partial \eta} d\eta = \int \frac{\partial p}{\partial \eta} \Phi d\eta - (p\Phi) \Big|_{\eta=\eta_{\text{top}}}^{\eta=1}$$

and thus

$$E = \iint \frac{\partial p}{\partial \eta} \left( \frac{1}{2} \vec{u}^2 + c_v^* T + \Phi \right) d\eta dA + \int p_{\text{top}} \Phi(\eta_{\text{top}}) dA. \quad (3.92)$$

1089 The model top boundary term in (3.92) vanishes if  $p_{\text{top}} = 0$ . Otherwise it must be included to  
 1090 be consistent with the hydrostatic equations. It is present due to the fact that the hydrostatic  
 1091 momentum equation (3.83) neglects the vertical pressure gradient.

### 1092 3.2.3 Horizontal Discretization: Functional Spaces

1093 In the finite element method, instead of constructing discrete approximations to derivative  
 1094 operators, one constructs a discrete functional space, and then finds the function in this space  
 1095 which solves the equations of interest in a minimum residual sense. As compared to finite  
 1096 volume methods, there is less choice in how one constructs the discrete derivative operators  
 1097 in this setting, since functions in the discrete space are represented in terms of known basis  
 1098 functions whose derivatives are known, often analytically.

Let  $x^\alpha$  and  $\vec{x} = x^1 \vec{e}_1 + x^2 \vec{e}_2$  be the Cartesian coordinates and position vector of a point in the reference square  $[-1, 1]^2$  and let  $r^\alpha$  and  $\vec{r}$  be the coordinates and position vector of a point on the surface of the sphere, denoted by  $\Omega$ . We mesh  $\Omega$  using the cubed-sphere grid (Fig. 3.2) first used in [Sadourny \[1972\]](#). Each cube face is mapped to the surface of the sphere with the equal-angle gnomonic projection [\[Rančić et al., 1996\]](#). The map from the reference element  $[-1, 1]^2$  to the cube face is a translation and scaling. The composition of these two maps defines a  $\mathcal{C}^1$  map from the spherical elements to the reference element  $[-1, 1]^2$ . We denote this map and its inverse by

$$\vec{r} = \vec{r}(\vec{x}; m), \quad \vec{x} = \vec{x}(\vec{r}; m). \quad (3.93)$$



Figure 3.2: Tiling the surface of the sphere with quadrilaterals. An inscribed cube is projected to the surface of the sphere. The faces of the cubed sphere are further subdivided to form a quadrilateral grid of the desired resolution. Coordinate lines from the gnomonic equal-angle projection are shown.

We now define the discrete space used by the SEM. First we denote the space of polynomials up to degree  $d$  in  $[-1, 1]^2$  by

$$\mathcal{P}_d = \underset{i,j=0}{\overset{d}{\text{span}}}(x^1)^i(x^2)^j = \underset{\vec{r} \in \mathbb{I}}{\text{span}} \phi_{\vec{r}}(\vec{x}),$$

where  $\mathbb{I} = \{0, \dots, d\}^2$  contains all the degrees and  $\phi_{\vec{r}}(\vec{x}) = \varphi_{i^1}(x^1)\varphi_{i^2}(x^2)$ ,  $i^\alpha = 0, \dots, d$ , are the cardinal functions, namely polynomials that interpolate the tensor-product of degree- $d$  Gauss-Lobatto-Legendre (GLL) nodes  $\vec{\xi}_{\vec{r}} = \xi_{i^1}\vec{e}_1 + \xi_{i^2}\vec{e}_2$ . The GLL nodes used within an element for  $d = 3$  are shown in Fig. 3.3. The cardinal-function expansion coefficients of a function  $g$  are its GLL nodal values, so we have

$$g(\vec{x}) = \underset{\vec{r} \in \mathbb{I}}{\sum} g(\vec{\xi}_{\vec{r}}) \phi_{\vec{r}}(\vec{x}). \quad (3.94)$$

We can now define the piecewise-polynomial SEM spaces  $\mathcal{V}^0$  and  $\mathcal{V}^1$  as

$$\mathcal{V}^0 = \{f \in \mathcal{L}^2(\Omega) : f(\vec{r}(\cdot; m)) \in \mathcal{P}_d, \forall m\} = \underset{m=1}{\overset{M}{\text{span}}} \{\phi_{\vec{r}}(\vec{x}(\cdot; m))\}_{\vec{r} \in \mathbb{I}} \quad (3.95)$$

$$\text{and} \quad \mathcal{V}^1 = \mathcal{C}^0(\Omega) \cap \mathcal{V}^0.$$

Functions in  $\mathcal{V}^0$  are polynomial within each element but may be discontinuous at element boundaries and  $\mathcal{V}^1$  is the subspace of continuous function in  $\mathcal{V}^0$ . We take  $M_d = \dim \mathcal{V}^0 = (d+1)^3 M$ , and  $L = \dim \mathcal{V}^1 < M_d$ . We then construct a set of  $L$  unique points by

$$\{\vec{r}_\ell\}_{\ell=1}^L = \underset{m=1}{\overset{M}{\bigcup}} \vec{r}(\{\vec{\xi}_{\vec{r}}\}_{\vec{r} \in \mathbb{I}}; m), \quad (3.96)$$

- 1100 For every point  $\vec{r}_\ell$ , there exists at least one element  $\Omega_m$  and at least one GLL node  $\vec{\xi}_{\vec{r}} = \vec{x}(\vec{r}_\ell; m)$ .  
 1101 In 2D, if  $\vec{r}_\ell$  belongs to exactly one  $\Omega_m$  it is an element-interior node. If it belongs to exactly two  $\Omega_m$ s, it is an element-edge interior node. Otherwise it is a vertex node.

Figure 3.3: A  $4 \times 4$  tensor product grid of GLL nodes used within each element, for a degree  $d = 3$  discretization. Nodes on the boundary are shared by neighboring elements.

1102

We also define similar spaces for 2D vectors. We introduce two families of spaces, with a subscript of either *con* or *cov*, denoting if the contravariant or covariant components of the vectors are piecewise polynomial, respectively.

$$\begin{aligned} \mathcal{V}_{\text{con}}^0 &= \{\vec{u} \in \mathcal{L}^2(\Omega)^2 : u^\alpha \in \mathcal{V}^0, \alpha = 1, 2\} \\ \text{and} \quad \mathcal{V}_{\text{con}}^1 &= \mathcal{C}^0(\Omega)^2 \cap \mathcal{V}_{\text{con}}^0, \end{aligned}$$

where  $u^1, u^2$  are the contravariant components of  $\vec{u}$  defined below. Vectors in  $\mathcal{V}_{\text{con}}^1$  are globally continuous and their contravariant components are polynomials in each element. Similarly,

$$\begin{aligned} \mathcal{V}_{\text{cov}}^0 &= \{\vec{u} \in \mathcal{L}^2(\Omega)^2 : u_\beta \in \mathcal{V}^0, \beta = 1, 2\} \\ \text{and} \quad \mathcal{V}_{\text{cov}}^1 &= \mathcal{C}^0(\Omega)^2 \cap \mathcal{V}_{\text{cov}}^0. \end{aligned}$$

The SEM is a Galerkin method with respect to the  $\mathcal{V}^1$  subspace and it can be formulated solely in terms of functions in  $\mathcal{V}^1$ . In CAM-HOMME, the typical configuration is to run with  $d = 3$  which achieves a 4th order accurate horizontal discretization [Taylor and Fournier, 2010]. All variables in the CAM-HOMME initial condition and history files as well as variables passed to the physics routines are represented by their grid point values at the points  $\{\vec{r}_\ell\}_{\ell=1}^L$ . However, for some intermediate quantities and internally in the dynamical core it is useful to consider the larger  $\mathcal{V}^0$  space, where variables are represented by their grid point values at the  $M_d$  mapped GLL nodes. This later representation can also be considered as the cardinal-function (3.94) expansion of a function  $f$  local to each element,

$$f(\vec{r}) = \sum_{\vec{i} \in \mathbb{I}} f(\vec{r}(\vec{\xi}_{\vec{i}}; m)) \phi_{\vec{i}}(\vec{x}(\vec{r}; m)) \quad (3.97)$$

since the expansion coefficients are the function values at the mapped GLL nodes. Functions  $f$  in  $\mathcal{V}^0$  can be multiple-valued at GLL nodes that are *redundant* (i.e., shared by more than one element), while for  $f \in \mathcal{V}^1$ , the values at any redundant points must all be the same.

### 3.2.4 Horizontal Discretization: Differential Operators

We use the standard curvilinear coordinate formulas for vector operators following Heinbockel [2001]. Given the  $2 \times 2$  Jacobian of the the mapping (3.93) from  $[-1, 1]^2$  to  $\Omega_m$ , we denote its determinant-magnitude by

$$J = \left| \frac{\partial \vec{r}}{\partial \vec{x}} \right|. \quad (3.98)$$

A vector  $\vec{v}$  may be written in terms of physical or covariant or contravariant components,  $v[\gamma]$  or  $v_\beta$  or  $v^\alpha$ ,

$$\vec{v} = \sum_{\gamma=1}^3 v[\gamma] \frac{\partial \vec{r}}{\partial r^\gamma} = \sum_{\beta=1}^3 v_\beta \vec{g}^\beta = \sum_{\alpha=1}^3 v^\alpha \vec{g}_\alpha, \quad (3.99)$$

that are related by  $v_\beta = \vec{v} \cdot \vec{g}_\beta$  and  $v^\alpha = \vec{v} \cdot \vec{g}^\alpha$ , where  $\vec{g}^\alpha = \nabla x^\alpha$  is a contravariant basis vector and  $\vec{g}_\beta = \frac{\partial \vec{r}}{\partial x^\beta}$  is a covariant basis vector.

The dot product and contravariant components of the cross product are Heinbockel [2001, Table 1]

$$\vec{u} \cdot \vec{v} = \sum_{\alpha=1}^3 u_\alpha v^\alpha \quad \text{and} \quad (\vec{u} \times \vec{v})^\alpha = \frac{1}{J} \sum_{\beta, \gamma=1}^3 \epsilon^{\alpha\beta\gamma} u_\beta v_\gamma \quad (3.100)$$

where  $\epsilon^{\alpha\beta\gamma} \in \{0, \pm 1\}$  is the Levi-Civita symbol. The divergence, covariant coordinates of the gradient and contravariant coordinates of the curl are Heinbockel [2001, eqs. 2.1.1, 2.1.4 & 2.1.6]

$$\nabla \cdot \vec{v} = \frac{1}{J} \sum_{\alpha} \frac{\partial}{\partial x^\alpha} (J v^\alpha), \quad (\nabla f)_\alpha = \frac{\partial f}{\partial x^\alpha} \quad \text{and} \quad (\nabla \times \vec{v})^\alpha = \frac{1}{J} \sum_{\beta, \gamma} \epsilon^{\alpha\beta\gamma} \frac{\partial v_\gamma}{\partial x^\beta}. \quad (3.101)$$

In the SEM, these operators are all computed in terms of the derivatives with respect to  $\vec{x}$  in the reference element, computed exactly (to machine precision) by differentiating the local element expansion (3.97). For the gradient, the covariant coordinates of  $\nabla f$ ,  $f \in \mathcal{V}^0$  are thus computed

1112 exactly within each element. Note that  $\nabla f \in \mathcal{V}_{\text{cov}}^0$ , but may not be in  $\mathcal{V}_{\text{cov}}^1$  even for  $f \in \mathcal{V}^1$   
 1113 due to the fact that its components will be multi-valued at element boundaries because  $\nabla f$   
 1114 computed in adjacent elements will not necessarily agree along their shared boundary. In the  
 1115 case where  $J$  is constant within each element, the SEM curl of  $\vec{v} \in \mathcal{V}_{\text{cov}}^0$  and the divergence of  
 1116  $\vec{u} \in \mathcal{V}_{\text{con}}^0$  will also be exact, but as with the gradient, multiple-valued at element boundaries.

For non-constant  $J$ , these operators may not be computed exactly by the SEM due to the Jacobian factors in the operators and the Jacobian factors that appear when converting between covariant and contravariant coordinates. We follow [Thomas and Loft \[2000\]](#) and evaluate these operators in the form shown in (3.101). The quadratic terms that appear are first projected into  $\mathcal{V}^0$  via interpolation at the GLL nodes and then this interpolant is differentiated exactly using (3.97). For example, to compute the divergence of  $\vec{v} \in \mathcal{V}_{\text{con}}^0$ , we first compute the interpolant  $\mathcal{I}(Jv^\alpha) \in \mathcal{V}^0$  of  $Jv^\alpha$ , where the GLL interpolant of a product  $fg$  derives simply from the product of the GLL nodal values of  $f$  and  $g$ . This operation is just a reinterpretation of the nodal values and is essentially free in the SEM. The derivatives of this interpolant are then computed exactly from (3.97). The sum of partial derivatives are then divided by  $J$  at the GLL nodal values and thus the SEM divergence operator  $\nabla_h \cdot (\cdot)$  is given by

$$\nabla \cdot \vec{v} \approx \nabla_h \cdot \vec{v} = \mathcal{I} \left( \frac{1}{J} \sum_{\alpha} \frac{\partial \mathcal{I}(Jv^\alpha)}{\partial x^\alpha} \right) \in \mathcal{V}^0. \quad (3.102)$$

Similarly, the gradient and curl are approximated by

$$(\nabla f)_{\alpha} \approx (\nabla_h f)_{\alpha} = \frac{\partial f}{\partial x^{\alpha}} \quad (3.103)$$

$$\text{and} \quad (\nabla \times \vec{v})^{\alpha} \approx (\nabla_h \times \vec{v})^{\alpha} = \sum_{\beta, \gamma} \epsilon^{\alpha \beta \gamma} \mathcal{I} \left( \frac{1}{J} \frac{\partial v_{\gamma}}{\partial x^{\beta}} \right) \quad (3.104)$$

1117 with  $\nabla_h f \in \mathcal{V}_{\text{cov}}^0$  and  $\nabla_h \times \vec{v} \in \mathcal{V}_{\text{con}}^0$ . The SEM is well known for being quite efficient in computing  
 1118 these types of operations. The SEM divergence, gradient and curl can all be evaluated at the  
 1119  $(d+1)^3$  GLL nodes within each element in  $\mathcal{O}(d)$  operations per node using the tensor-product  
 1120 property of these points [[Deville et al., 2002](#); [Karniadakis and Sherwin, 2005](#)].

### 1121 3.2.5 Horizontal Discretization: Discrete Inner-Product

Instead of using exact integration of the basis functions as in a traditional finite-element method, the SEM uses a GLL quadrature approximation for the integral over  $\Omega$ , that we denote by  $\langle \cdot \rangle$ . We can write this integral as a sum of area-weighted integrals over the set of elements  $\{\Omega_m\}_{m=1}^M$  used to decompose the domain,

$$\int f g d\mathcal{A} = \sum_{m=1}^M \int_{\Omega_m} f g d\mathcal{A}.$$

The integral over a single element  $\Omega_m$  is written as an integral over  $[-1, 1]^2$  by

$$\int_{\Omega_m} f g d\mathcal{A} = \iint_{[-1,1]^2} f(\vec{r}(\cdot; m)) g(\vec{r}(\cdot; m)) J_m dx^1 dx^2 \approx \langle f g \rangle_{\Omega_m},$$

where we approximate the integral over  $[-1, 1]^2$  by GLL quadrature,

$$\langle fg \rangle_{\Omega_m} = \sum_{\vec{i} \in \mathbb{I}} w_{i^1} w_{i^2} J_m(\vec{\xi}_{\vec{i}}) f(\vec{r}(\vec{\xi}_{\vec{i}}; m)) g(\vec{r}(\vec{\xi}_{\vec{i}}; m)) \quad (3.105)$$

The SEM approximation to the global integral is then naturally defined as

$$\int f g d\mathcal{A} \approx \sum_{m=1}^M \langle fg \rangle_{\Omega_m} = \langle fg \rangle \quad (3.106)$$

When applied to the product of functions  $f, g \in \mathcal{V}^0$ , the quadrature approximation  $\langle fg \rangle$  defines a discrete inner-product in the usual manner.

### 3.2.6 Horizontal Discretization: The Projection Operators

Let  $P : \mathcal{V}^0 \rightarrow \mathcal{V}^1$  be the unique orthogonal (self-adjoint) projection operator from  $\mathcal{V}^0$  onto  $\mathcal{V}^1$  w.r.t. the SEM discrete inner product (3.106). The operation  $P$  is essentially the same as the common procedure in the SEM described as *assembly* [Karniadakis and Sherwin, 2005, p. 7], or *direct stiffness summation* [Deville et al., 2002, eq. 4.5.8]. Thus the SEM assembly procedure is not an ad-hoc way to remove the redundant degrees of freedom in  $\mathcal{V}^0$ , but is in fact the natural projection operator  $P$ . Applying the projection operator in a finite element method requires inverting the finite element mass matrix. A remarkable fact about the SEM is that with the GLL based discrete inner product and the careful choice of global basis functions, the mass matrix is diagonal [Maday and Patera, 1987]. The resulting projection operator then has a very simple form: at element interior points, it leaves the nodal values unchanged, while at element boundary points shared by multiple elements it is a Jacobian-weighted average over all redundant values [Taylor and Fournier, 2010].

To apply the projection  $P : \mathcal{V}_{\text{cov}}^0 \rightarrow \mathcal{V}_{\text{cov}}^1$  to vectors  $\vec{u}$ , one cannot project the covariant components since the corresponding basis vectors  $\vec{g}_\beta$  and  $\vec{g}^\alpha$  do not necessarily agree along element faces. Instead we must define the projection as acting on the components using a globally continuous basis such as the latitude-longitude unit vectors  $\hat{\theta}$  and  $\hat{\lambda}$ ,

$$P(\vec{u}) = P(\vec{u} \cdot \hat{\lambda}) \hat{\lambda} + P(\vec{u} \cdot \hat{\theta}) \hat{\theta}.$$

### 3.2.7 Horizontal Discretization: Galerkin Formulation

The SEM solves a Galerkin formulation of the equations of interest. Given the discrete differential operators described above, the primitive equations can be written as an ODE for a generic prognostic variable  $U$  and right-hand-side (RHS) terms

$$\frac{\partial U}{\partial t} = \text{RHS}.$$

The SEM solves this equation in integral form with respect to the SEM inner product. That is, for a RHS  $\in \mathcal{V}^0$ , the SEM finds the unique  $\frac{\partial U}{\partial t} \in \mathcal{V}^1$  such that

$$\left\langle \phi \frac{\partial U}{\partial t} \right\rangle = \langle \phi \text{ RHS} \rangle \quad \forall \phi \in \mathcal{V}^1.$$

As the prognostic variable is assumed to belong to  $\mathcal{V}^1$ , the RHS will in general belong to  $\mathcal{V}^0$  since it contains derivatives of the prognostic variables, resulting in the loss of continuity at the element boundaries. If one picks a suitable basis for  $\mathcal{V}^1$ , this discrete integral equation results in a system of  $L$  equations for the  $L$  expansion coefficients of  $\frac{\partial U}{\partial t}$ . The SEM solves these equations exactly, and the solution can be written in terms of the SEM projection operator as

$$\frac{\partial U}{\partial t} = P(\text{RHS}).$$

1138 The projection operator commutes with any time-stepping scheme, so the equations can be  
1139 solved in a two step process, illustrated here for simplicity with the forward Euler method

- Step 1:

$$U^* = U^t + \Delta t \text{RHS} \quad U^* \in \mathcal{V}^0$$

- Step 2:

$$U^{t+1} = P(U^*) \quad U^{t+1} \in \mathcal{V}^1$$

For compactness of notation, we will denote this two step procedure in what follows by

$$P^{-1} \frac{\partial U}{\partial t} = \text{RHS}.$$

1140 Note that  $P$  maps a  $M_d$  dimensional space  $\mathcal{V}^0$  into a  $L$  dimensional space  $\mathcal{V}^1$ , so here  $P^{-1}$  denotes  
1141 the left inverse of  $P$ . This inverse will never be computed, it is only applied as in step 2 above.

1142 This two step Galerkin solution process represents a natural separation between computation  
1143 and communication for the implementation of the SEM on a parallel computer. The computa-  
1144 tions in step 1 are all local to the data contained in a single element. Assuming an element-based  
1145 decomposition so that each processor contains at least one element, no inter-processor commu-  
1146 nication is required in step 1. All inter-processor communication in HOMME is isolated to the  
1147 projection operator step, in which element boundary data must be exchanged between adjacent  
1148 elements.

### 1149 3.2.8 Vertical Discretization

The vertical coordinate system uses a Lorenz staggering of the variables as shown in [3.4](#). Let  $K$  be the total number of layers, with variables  $\vec{u}, T, q, \omega, \Phi$  at layer mid points denoted by  $k = 1, 2, \dots, K$ . We denote layer interfaces by  $k + \frac{1}{2}, k = 0, 1, \dots, K$ , so that  $\eta_{1/2} = \eta_{\text{top}}$  and  $\eta_{K+1/2} = 1$ . The  $\eta$ -integrals will be replaced by sums. We will use  $\delta_\eta$  to denote the discrete  $\partial/\partial\eta$  operator. The  $\delta_\eta$  operator uses centered differences to compute derivatives with respect to  $\eta$  at layer mid point from layer interface values,  $\delta_\eta(X)_k = (X_{k+1/2} - X_{k-1/2})/(\eta_{k+1/2} - \eta_{k-1/2})$ . We will use the over-bar notation for vertical averaging,  $\bar{q}_{k+1/2} = (q_{k+1} + q_k)/2$ . We also introduce the symbol  $\pi$  to denote the discrete pseudo-density  $\frac{\partial p}{\partial \eta}$  given by

$$\pi_k = \delta_\eta(p)_k$$

1150 .

We will use  $\overline{\dot{\eta}\delta_\eta}$  to denote the discrete form of the  $\dot{\eta}\partial/\partial\eta$  operator. We use the discretization given in 3.3.5. This operator acts on quantities defined at layer mid-points and returns a result also at layer mid-points,

$$\overline{\dot{\eta}\delta_\eta}(X)_k = \frac{1}{2\pi_k\Delta\eta_k} [(\dot{\eta}\pi)_{k+1/2}(X_{k+1} - X_k) + (\dot{\eta}\pi)_{k-1/2}(X_k - X_{k-1})] \quad (3.107)$$

where  $\Delta\eta_k = \eta_{k+1/2} - \eta_{k-1/2}$ . We use the over-bar notation since the formula can be seen as a  $\pi$ -weighted average of a layer interface centered difference approximation to  $\dot{\eta}\partial/\partial\eta$ . This formulation was constructed in [Simmons and Burridge \[1981\]](#) in order to ensure mass and energy conservation. Here we will use an equivalent expression that can be written in terms of  $\delta_\eta$ ,

$$\overline{\dot{\eta}\delta_\eta}(X)_k = \frac{1}{\pi_k} \left[ \delta_\eta (\dot{\eta}\pi \overline{X})_k - X \delta_\eta (\dot{\eta}\pi)_k \right]. \quad (3.108)$$

### 1151 3.2.9 Discrete formulation: Dynamics

We discretize the equations exactly in the form shown in (3.83), (3.84), (3.88) and (3.90), obtaining

$$P^{-1} \frac{\partial \vec{u}}{\partial t} = -(\zeta + f) \hat{k} \times \vec{u} + \nabla_h \left( \frac{1}{2} \vec{u}^2 + \Phi \right) - \overline{\dot{\eta}\delta_\eta}(\vec{u}) - \frac{RT_v}{p} \nabla_h(p) \quad (3.109)$$

$$P^{-1} \frac{\partial T}{\partial t} = -\vec{u} \cdot \nabla_h(T) - \overline{\dot{\eta}\delta_\eta}(T) + \frac{RT_v}{c_p^* p} \omega \quad (3.110)$$

$$P^{-1} \frac{\partial p_s}{\partial t} = - \sum_{j=1}^K \nabla_h \cdot (\pi \vec{u})_j \Delta\eta_j \quad (3.111)$$

$$(\dot{\eta}\pi)_{i+1/2} = B(\eta_{i+1/2}) \sum_{j=1}^K \nabla_h \cdot (\pi \vec{u})_j \Delta\eta_j - \sum_{j=1}^i \nabla_h \cdot (\pi \vec{u})_j \Delta\eta_j. \quad (3.112)$$

1152 We consider  $(\dot{\eta}\pi)$  a single quantity given at layer interfaces and defined by (3.112). The no-flux  
 1153 boundary condition is  $(\dot{\eta}\pi)_{1/2} = (\dot{\eta}\pi)_{K+1/2} = 0$ . In (3.112), we used a midpoint quadrature  
 1154 rule to evaluate the indefinite integral from (3.90). In practice  $\Delta\eta$  can be eliminated from the  
 1155 discrete equations by scaling  $\pi$ , but here we retain them so as to have a direct correspondence  
 1156 with the continuum form of the equations written in terms of  $\frac{\partial p}{\partial \eta}$ .

Finally we give the approximations for the diagnostic equations. We first integrate to layer interface  $i - \frac{1}{2}$  using the same mid-point rule as used to derive (3.112), and then add an additional term representing the integral from  $i - \frac{1}{2}$  to  $i$ :

$$\omega_i = (\vec{u} \cdot \nabla_h p)_i - \sum_{j=1}^{i-1} \nabla_h \cdot (\pi \vec{u})_j \Delta\eta_j + \nabla_h \cdot (\pi \vec{u})_i \frac{\Delta\eta_i}{2} \quad (3.113)$$

$$= (\vec{u} \cdot \nabla_h p)_i - \sum_{j=1}^K C_{ij} \nabla_h \cdot (\pi \vec{u})_j \quad (3.114)$$

where

$$C_{ij} = \begin{cases} \Delta\eta_j & i > j \\ \Delta\eta_j/2 & i = j \\ 0 & i < j \end{cases}$$

and similar for  $\Phi$ ,

$$(\Phi - \Phi_s)_i = \left( \frac{RT_v}{p} \pi \right)_i \frac{\Delta\eta_i}{2} + \sum_{j=i+1}^K \left( \frac{RT_v}{p} \pi \right)_j \Delta\eta_j \quad (3.115)$$

$$= \sum_{j=1}^K H_{ij} \left( \frac{RT_v}{p} \pi \right)_j \quad (3.116)$$

where

$$H_{ij} = \begin{cases} \Delta\eta_j & i < j \\ \Delta\eta_j/2 & i = j \\ 0 & i > j \end{cases}$$

Similar to 3.3.5, we note that

$$\Delta\eta_i C_{ij} = \Delta\eta_j H_{ji} \quad (3.117)$$

<sup>1157</sup> which ensures energy conservation [Taylor, 2010].

### <sup>1158</sup> 3.2.10 Consistency

It is important that the discrete equations be as consistent as possible. In particular, we need a discrete version of (3.85), the non-vertically averaged continuity equation. Equation (3.112) implicitly implies such an equation. To see this, apply  $\delta_\eta$  to (3.112) and using that  $\partial p / \partial t = B(\eta) \partial p_s / \partial t$  then we can derive, at layer mid-points,

$$P^{-1} \frac{\partial \pi}{\partial t} = -\nabla_h \cdot (\pi \vec{u}) - \delta_\eta (\dot{\eta} \pi). \quad (3.118)$$

A second type of consistency that has been identified as important is that (3.113), the discrete equation for  $\omega$ , be consistent with (3.112), the discrete continuity equation [Williamson and Olson, 1994b]. The two discrete equations should imply a reasonable discretization of  $\omega = Dp/Dt$ . To show this, we take the average of (3.112) at layers  $i-1/2$  and  $i+1/2$  and combine this with (3.113) (at layer mid-points  $i$ ) and assuming that  $B(\eta_i) = B(\eta_{i-1/2}) + B(\eta_{i+1/2})$  we obtain

$$P^{-1} \frac{\partial p}{\partial t} = \omega_i - (\vec{u} \cdot \nabla_h p)_i - \frac{1}{2} ((\dot{\eta} \delta_\eta)_{i-1/2} + (\dot{\eta} \delta_\eta)_{i+1/2}).$$

<sup>1159</sup> which, since  $\vec{u} \cdot \nabla_h p$  is given at layer mid-points and  $\dot{\eta} \pi$  at layer interfaces, is the SEM discretization of  $w = \partial p / \partial t + \vec{u} \cdot \nabla_h p + \dot{\eta} \pi$ .<sup>1160</sup>

### 1161 3.2.11 Time Stepping

Applying the SEM discretization to (3.109)-(3.112) results in a system of ODEs. These are solved with an  $N$ -stage Runge-Kutta method. This method allows for a gravity-wave based CFL number close to  $N - 1$ , (normalized so that the largest stable timestep of the Robert filtered Leapfrog method has a CFL number of 1.0). The value of  $N$  is chosen large enough so that the dynamics will be stable at the same timestep used by the tracer advection scheme. To determine  $N$ , we first note that the tracer advection scheme uses a less efficient (in terms of maximum CFL) strong stability preserving Runge-Kutta method described below. It is stable at an advective CFL number of 1.4. Let  $u_0$  be a maximum wind speed and  $c_0$  be the maximum gravity wave speed. The gravity wave and advective CFL conditions are

$$\Delta t \leq (N - 1)\Delta x/c_0, \quad \Delta t \leq 1.4\Delta x/u_0.$$

1162 In the case where  $\Delta t$  is chosen as the largest stable timestep for advection, then we require  
 1163  $N \geq 1 + 1.4c_0/u_0$  for a stable dynamics timestep. Using a typical values  $u_0 = 120$  m/s and  
 1164  $c_0 = 340$  m/s gives  $N = 5$ . CAM places additional restrictions on the timestep (such as that the  
 1165 physics timestep must be an integer multiple of  $\Delta t$ ) which also influence the choice of  $\Delta t$  and  
 1166  $N$ .

### 1167 3.2.12 Dissipation

A horizontal hyper-viscosity operator, modeled after 3.3.6 is applied to the momentum and temperature equations. It is applied in a time-split manner after each dynamics timestep. The hyper-viscosity step for vectors can be written as

$$\frac{\partial \vec{u}}{\partial t} = -\nu \Delta^2 \vec{u}.$$

An integral form of this equation suitable for the SEM is obtained using a mixed finite element formulation (following Giraldo [1999]) which writes the equation as a system of equations involving only first derivatives. We start by introduced an auxiliary vector  $\vec{f}$  and using the identity  $\Delta \vec{u} = \nabla(\nabla \cdot \vec{u}) - \nabla \times (\nabla \times \vec{u})$ ,

$$\frac{\partial \vec{u}}{\partial t} = -\nu \left( \nabla(\nabla \cdot \vec{f}) - \nabla \times \hat{k}(\nabla \times \vec{f}) \right) \quad (3.119)$$

$$\vec{f} = \nabla(\nabla \cdot \vec{u}) - \nabla \times (\nabla \times \vec{u}) \hat{k}. \quad (3.120)$$

Integrating the gradient and curl operators by parts gives

$$\iint \vec{\phi} \cdot \frac{\partial \vec{u}}{\partial t} d\mathcal{A} = \nu \iint \left[ (\nabla \cdot \vec{\phi})(\nabla \cdot \vec{f}) + (\nabla \times \vec{\phi}) \cdot \hat{k}(\nabla \times \vec{f}) \right] d\mathcal{A} \quad (3.121)$$

$$\iint \vec{\phi} \cdot \vec{f} d\mathcal{A} = - \iint \left[ (\nabla \cdot \vec{\phi})(\nabla \cdot \vec{u}) + (\nabla \times \vec{\phi}) \cdot \hat{k}(\nabla \times \vec{u}) \right] d\mathcal{A}. \quad (3.122)$$

$$(3.123)$$

The SEM Galerkin solution of this integral equation is most naturally written in terms of an inverse mass matrix instead of the projection operator. It can be written in terms of the SEM

projection operator by first testing with the product of the element cardinal functions and the contravariant basis vector  $\vec{\phi} = \phi_{\vec{i}} \vec{g}_\alpha$ . With this type of test function, the RHS of (3.122) can be defined as a weak Laplacian operator  $\vec{f} = D(\vec{u}) \in \mathcal{V}_{\text{cov}}^0$ . The covariant components of  $\vec{f}$  given by  $f_\alpha = \vec{f} \cdot \vec{g}_\alpha$  are then

$$f_\alpha(\vec{r}(\vec{\xi}_{\vec{i}}; m)) = \frac{-1}{w_{i^1} w_{i^2} J_m(\vec{\xi}_{\vec{i}})} \left\langle (\nabla_h \cdot \phi_{\vec{i}} \vec{g}_\alpha) (\nabla_h \cdot \vec{u}) + (\nabla_h \times \phi_{\vec{i}} \vec{g}_\alpha) \cdot \hat{k} (\nabla_h \times \vec{u}) \right\rangle$$

Then the SEM solution to (3.121) and (3.122) is given by

$$\vec{u}(t + \Delta t) = \vec{u}(t) - \nu \Delta t P \left( D \left( P(D(\vec{u})) \right) \right).$$

Because of the SEM tensor product decomposition, the expression for  $D$  can be evaluated in only  $O(d)$  operations per grid point, and in CAM-HOMME typically  $d = 3$ .

Following 3.3.6, a correction term is added so the hyper-viscosity does not damp rigid rotation. The hyper-viscosity formulation used for scalars such as  $T$  is much simpler, since instead of the vector Laplacian identity we use  $\Delta T = \nabla \cdot \nabla T$ . Otherwise the approach is identical to that used above so we omit the details. The correction for terrain following coordinates given in 3.3.6 is not yet implemented in CAM-HOMME.

### 3.2.13 Discrete formulation: Tracer Advection

All tracers, including specific humidity, are advected with a discretized version of (3.86). HOMME uses the vertically Lagrangian approach (see 3.1.4) from Lin [2004]. At the beginning of each timestep, the tracers are assumed to be given on the  $\eta$ -coordinate layer mid points. The tracers are advanced in time on a moving vertical coordinate system  $\eta'$  defined so that  $\dot{\eta}' = 0$ . At the end of the timestep, the tracers are remapped back to the  $\eta$ -coordinate layer mid points using the monotone remap algorithm from Zerroukat et al. [2005].

The horizontal advection step consists of using the SEM to solve

$$\frac{\partial}{\partial t} (\pi q) = -\nabla_h \cdot \left( \overline{(\pi \vec{u}) q} \right) \quad (3.124)$$

on the surfaces defined by the  $\eta'$  layer mid points. The quantity  $\overline{(\pi \vec{u})}$  is the mean flux computed during the dynamics update. The mean flux used in (3.124), combined with a suitable mean vertical flux used in the remap stage allows HOMME to preserve mass/tracer-mass consistency: The tracer advection of  $\pi q$  with  $q = 1$  will be identical to the advection of  $\pi$  implied from (3.118). The mass/tracer-mass consistency capability is not in the version of HOMME included in CAM 4.0, but should be in all later versions.

The equation is discretized in time using the optimal 3 stage strong stability preserving (SSP) second order Runge-Kutta method from Spiteri and Ruuth [2002]. The RK-SSP method is chosen because it will preserve the monotonicity properties of the horizontal discretization. RK-SSP methods are convex combinations of forward-Euler timesteps, so each stage  $s$  of the RK-SSP timestep looks like

$$(\pi q)^{s+1} = (\pi q)^s - \Delta t \nabla_h \cdot \left( \overline{(\pi \vec{u}) q^s} \right) \quad (3.125)$$

1188 Simply discretizing this equation with the SEM will result in locally conservative, high-order  
 1189 accurate but oscillatory transport scheme. A limiter is added to reduce or eliminate these oscillations [Taylor et al., 2009]. HOMME supports both monotone and sign-preserving limiters, but  
 1190 the most effective limiter for HOMME has not yet been determined. The default configuration  
 1191 in CAM4 is to use the sign-preserving limiter to prevent negative values of  $q$  coupled with a  
 1192 sign-preserving hyper-viscosity operator which dissipates  $q^2$ .  
 1193

### 1194 3.2.14 Conservation and Compatibility

The SEM is compatible, meaning it has a discrete version of the divergence theorem, Stokes theorem and curl/gradient annihilator properties Taylor and Fournier [2010]. The divergence theorem is the key property of the horizontal discretization that is needed to show conservation. For an arbitrary scalar  $h$  and vector  $\vec{u}$  at layer mid-points, the divergence theorem (or the divergence/gradient adjoint relation) can be written

$$\int h \nabla \cdot \vec{u} dA + \int \vec{u} \nabla h dA = 0.$$

The discrete version obeyed by the SEM discretization, using (3.106), is given by

$$\langle h \nabla_h \cdot \vec{u} \rangle + \langle \vec{u} \cdot \nabla_h h \rangle = 0. \quad (3.126)$$

1195 The discrete divergence and Stokes theorem apply locally at the element with the addition of  
 1196 an element boundary integral. The local form is used to show local conservation of mass and  
 1197 that the horizontal advection operator locally conserves the two-dimensional potential vorticity  
 1198 [Taylor and Fournier, 2010].

In the vertical, Simmons and Burridge [1981] showed that the  $\delta_\eta$  and  $\overline{\dot{\eta}\delta_\eta}$  operators needed to satisfy two integral identities to ensure conservation. For any  $\dot{\eta}$  layer interface velocity which satisfies  $\dot{\eta}_{1/2} = \dot{\eta}_{K+1/2} = 0$  and  $f, g$  arbitrary functions of layer mid points. The first identity is the adjoint property (compatibility) for  $\delta_\eta$  and  $\pi$ ,

$$\sum_{i=1}^K \Delta\eta_i \pi_i \overline{\dot{\eta}\delta_\eta}(f) + \sum_{i=1}^K \Delta\eta_i f_i \delta_\eta(\dot{\eta}\pi) = 0 \quad (3.127)$$

which follows directly from the definition of the  $\overline{\dot{\eta}\delta_\eta}$  difference operator given in (3.108). The second identity we write in terms of  $\delta_\eta$ ,

$$\sum_{i=1}^K \Delta\eta_i f g \delta_\eta(\dot{\eta}\pi) = \sum_{i=1}^K \Delta\eta_i f \delta_\eta(\dot{\eta}\pi \overline{g}) + \sum_{i=1}^K \Delta\eta_i g \delta_\eta(\dot{\eta}\pi \overline{f}) \quad (3.128)$$

1199 which is a discrete integrated-by-parts analog of  $\partial(fg) = f\partial g + g\partial f$ . Construction of methods  
 1200 with both properties on a staggered unequally spaced grid is the reason behind the complex  
 1201 definition for  $\overline{\dot{\eta}\delta_\eta}$  in (3.108).

The energy conservation properties of CAM-HOMME were studied in Taylor [2010] using the aqua planet test case [Neale and Hoskins, 2001a,b]. CAM-HOMME uses

$$E = \left\langle \sum_{i=1}^K \Delta\eta_i \pi_i \left( \frac{1}{2} \vec{u}^2 + c_p^* T \right)_i \right\rangle + \langle p_s \Phi_s \rangle$$

1202 as the discretization of the total moist energy (3.91). The conservation of  $E$  is *semi-discrete*,  
 1203 meaning that the only error in conservation is the time truncation error. In the adiabatic case  
 1204 (with no hyper-viscosity and no limiters), running from a fully spun up initial condition, the error  
 1205 in conservation decreases to machine precision at a second-order rate with decreasing timestep.  
 1206 In the full non-adiabatic case with a realistic timestep,  $dE/dt \sim 0.013\text{W/m}^2$ .

1207 The CAM physics conserve a dry energy  $E_{\text{dry}}$  from [Boville and Bretherton \[2003a\]](#) which is  
 1208 not conserved by the moist primitive equations. Although  $E - E_{\text{dry}}$  is small, adiabatic processes  
 1209 in the primitive equations result in a net heating  $dE_{\text{dry}}/dt \sim 0.5\text{W/m}^2$  [\[Taylor, 2010\]](#). If it is  
 1210 desired that the dynamical core conserve  $E_{\text{dry}}$  instead of  $E$ , HOMME uses the energy fixer from  
 1211 [3.3.20](#).

### 1212 3.3 Eulerian Dynamical Core

1213 The hybrid vertical coordinate that has been implemented in CAM 5.0 is described in this  
 1214 section. The hybrid coordinate was developed by [Simmons and Strüfing \[1981\]](#) in order to  
 1215 provide a general framework for a vertical coordinate which is terrain following at the Earth's  
 1216 surface, but reduces to a pressure coordinate at some point above the surface. The hybrid  
 1217 coordinate is more general in concept than the modified  $\sigma$  scheme of [Sangster \[1960\]](#), which is  
 1218 used in the GFDL SKYHI model. However, the hybrid coordinate is normally specified in such  
 1219 a way that the two coordinates are identical.

1220 The following description uses the same general development as [Simmons and Strüfing \[1981\]](#),  
 1221 who based their development on the generalized vertical coordinate of [Kasahara \[1974\]](#). A  
 1222 specific form of the coordinate (the hybrid coordinate) is introduced at the latest possible point.  
 1223 The description here differs from [Simmons and Strüfing \[1981\]](#) in allowing for an upper boundary  
 1224 at finite height (nonzero pressure), as in the original development by Kasahara. Such an upper  
 1225 boundary may be required when the equations are solved using vertical finite differences.

#### 1226 3.3.1 Generalized terrain-following vertical coordinates

1227 Deriving the primitive equations in a generalized terrain-following vertical coordinate requires  
 1228 only that certain basic properties of the coordinate be specified. If the surface pressure is  $\pi$ ,  
 1229 then we require the generalized coordinate  $\eta(p, \pi)$  to satisfy:

- 1230 1.  $\eta(p, \pi)$  is a monotonic function of  $p$ .
- 1231 2.  $\eta(\pi, \pi) = 1$
- 1232 3.  $\eta(0, \pi) = 0$
- 1233 4.  $\eta(p_t, \pi) = \eta_t$  where  $p_t$  is the top of the model.

The latter requirement provides that the top of the model will be a pressure surface, simplifying  
 the specification of boundary conditions. In the case that  $p_t = 0$ , the last two requirements  
 are identical and the system reduces to that described in [Simmons and Strüfing \[1981\]](#). The  
 boundary conditions that are required to close the system are:

$$\dot{\eta}(\pi, \pi) = 0, \quad (3.129)$$

$$\dot{\eta}(p_t, \pi) = \omega(p_t) = 0. \quad (3.130)$$

Given the above description of the coordinate, the continuous system of equations can be written following [Kasahara \[1974\]](#) and [Simmons and Strüfing \[1981\]](#). The prognostic equations are:

$$\frac{\partial \zeta}{\partial t} = \mathbf{k} \cdot \nabla \times (\mathbf{n} / \cos \phi) + F_{\zeta_H}, \quad (3.131)$$

$$\frac{\partial \delta}{\partial t} = \nabla \cdot (\mathbf{n} / \cos \phi) - \nabla^2 (E + \Phi) + F_{\delta_H}, \quad (3.132)$$

$$\begin{aligned} \frac{\partial T}{\partial t} = & \frac{-1}{a \cos^2 \phi} \left[ \frac{\partial}{\partial \lambda} (UT) + \cos \phi \frac{\partial}{\partial \phi} (VT) \right] + T\delta - \dot{\eta} \frac{\partial T}{\partial \eta} + \frac{R}{c_p^*} T_v \frac{\omega}{p} \\ & + Q + F_{T_H} + F_{F_H}, \end{aligned} \quad (3.133)$$

$$\frac{\partial q}{\partial t} = \frac{-1}{a \cos^2 \phi} \left[ \frac{\partial}{\partial \lambda} (Uq) + \cos \phi \frac{\partial}{\partial \phi} (Vq) \right] + q\delta - \dot{\eta} \frac{\partial q}{\partial \eta} + S, \quad (3.134)$$

$$\frac{\partial \pi}{\partial t} = \int_1^{\eta_t} \nabla \cdot \left( \frac{\partial \mathbf{p}}{\partial \eta} \mathbf{V} \right) d\eta. \quad (3.135)$$

The notation follows standard conventions, and the following terms have been introduced with  $\mathbf{n} = (n_U, n_V)$ :

$$n_U = +(\zeta + f)V - \dot{\eta} \frac{\partial U}{\partial \eta} R \frac{T_v}{p} \frac{1}{a} - \frac{\partial p}{\partial \lambda} + F_U, \quad (3.136)$$

$$n_V = -(\zeta + f)U - \dot{\eta} \frac{\partial V}{\partial \eta} - R \frac{T_v}{p} \frac{\cos \phi}{a} \frac{\partial p}{\partial \phi} + F_V, \quad (3.137)$$

$$E = \frac{U^2 + V^2}{2 \cos^2 \phi}, \quad (3.138)$$

$$(U, V) = (u, v) \cos \phi, \quad (3.139)$$

$$T_v = \left[ 1 + \left( \frac{R_v}{R} - 1 \right) q \right] T, \quad (3.140)$$

$$c_p^* = \left[ 1 + \left( \frac{c_{p_v}}{c_p} - 1 \right) q \right] c_p. \quad (3.141)$$

1234 The terms  $F_U, F_V, Q$ , and  $S$  represent the sources and sinks from the parameterizations for  
1235 momentum (in terms of  $U$  and  $V$ ), temperature, and moisture, respectively. The terms  $F_{\zeta_H}$  and  
1236  $F_{\delta_H}$  represent sources due to horizontal diffusion of momentum, while  $F_{T_H}$  and  $F_{F_H}$  represent  
1237 sources attributable to horizontal diffusion of temperature and a contribution from frictional  
1238 heating (see sections on horizontal diffusion and horizontal diffusion correction).

In addition to the prognostic equations, three diagnostic equations are required:

$$\Phi = \Phi_s + R \int_{p(\eta)}^{p(1)} T_v d \ln p, \quad (3.142)$$

$$\dot{\eta} \frac{\partial p}{\partial \eta} = - \frac{\partial p}{\partial t} - \int_{\eta_t}^{\eta} \nabla \cdot \left( \frac{\partial \mathbf{p}}{\partial \eta} \mathbf{V} \right) d\eta, \quad (3.143)$$

$$\omega = \mathbf{V} \cdot \nabla p - \int_{\eta_t}^{\eta} \nabla \cdot \left( \frac{\partial \mathbf{p}}{\partial \eta} \mathbf{V} \right) d\eta. \quad (3.144)$$

1239 Note that the bounds on the vertical integrals are specified as values of  $\eta$  (e.g.  $\eta_t, 1$ ) or as  
1240 functions of  $p$  (e.g.  $p(1)$ , which is the pressure at  $\eta = 1$ ).

### 1241 3.3.2 Conversion to final form

1242 Equations (3.129)-(3.144) are the complete set which must be solved by a GCM. However, in  
 1243 order to solve them, the function  $\eta(p, \pi)$  must be specified. In advance of actually specifying  
 1244  $\eta(p, \pi)$ , the equations will be cast in a more convenient form. Most of the changes to the  
 1245 equations involve simple applications of the chain rule for derivatives, in order to obtain terms  
 1246 that will be easy to evaluate using the predicted variables in the model. For example, terms  
 1247 involving horizontal derivatives of  $p$  must be converted to terms involving only  $\partial p / \partial \pi$  and  
 1248 horizontal derivatives of  $\pi$ . The former can be evaluated once the function  $\eta(p, \pi)$  is specified.

The vertical advection terms in (3.133), (3.134), (3.136), and (3.137) may be rewritten as:

$$1249 \quad \dot{\eta} \frac{\partial \psi}{\partial \eta} = \dot{\eta} \frac{\partial p}{\partial \eta} \frac{\partial \psi}{\partial p}, \quad (3.145)$$

since  $\dot{\eta} \partial p / \partial \eta$  is given by (3.143). Similarly, the first term on the right-hand side of (3.143) can be expanded as

$$1250 \quad \frac{\partial p}{\partial t} = \frac{\partial p}{\partial \pi} \frac{\partial \pi}{\partial t}, \quad (3.146)$$

1249 and (3.135) invoked to specify  $\partial \pi / \partial t$ .

The integrals which appear in (3.135), (3.143), and (3.144) can be written more conveniently by expanding the kernel as

$$1251 \quad \nabla \cdot \left( \frac{\partial p}{\partial \eta} \mathbf{V} \right) = \mathbf{V} \cdot \nabla \left( \frac{\partial p}{\partial \eta} \right) + \frac{\partial p}{\partial \eta} \nabla \cdot \mathbf{V}. \quad (3.147)$$

The second term in (3.147) is easily treated in vertical integrals, since it reduces to an integral in pressure. The first term is expanded to:

$$1252 \quad \begin{aligned} \mathbf{V} \cdot \nabla \left( \frac{\partial p}{\partial \eta} \right) &= \mathbf{V} \cdot \frac{\partial}{\partial \eta} (\nabla p) \\ &= \mathbf{V} \cdot \frac{\partial}{\partial \eta} \left( \frac{\partial p}{\partial \pi} \nabla \pi \right) \\ &= \mathbf{V} \cdot \frac{\partial}{\partial \eta} \left( \frac{\partial p}{\partial \pi} \right) \nabla \pi + \mathbf{V} \cdot \frac{\partial p}{\partial \pi} \nabla \left( \frac{\partial \pi}{\partial \eta} \right). \end{aligned} \quad (3.148)$$

1250 The second term in (3.148) vanishes because  $\partial \pi / \partial \eta = 0$ , while the first term is easily treated  
 1251 once  $\eta(p, \pi)$  is specified. Substituting (3.148) into (3.147), one obtains:

$$1252 \quad \nabla \cdot \left( \frac{\partial p}{\partial \eta} \mathbf{V} \right) = \frac{\partial}{\partial \eta} \left( \frac{\partial p}{\partial \pi} \right) \mathbf{V} \cdot \nabla \pi + \frac{\partial p}{\partial \eta} \nabla \cdot \mathbf{V}. \quad (3.149)$$

1252 Using (3.149) as the kernel of the integral in (3.135), (3.143), and (3.144), one obtains integrals  
 1253 of the form

$$1253 \quad \begin{aligned} \int \nabla \cdot \left( \frac{\partial p}{\partial \eta} \mathbf{V} \right) d\eta &= \int \left[ \frac{\partial}{\partial \eta} \left( \frac{\partial p}{\partial \pi} \right) \mathbf{V} \cdot \nabla \pi + \frac{\partial p}{\partial \eta} \nabla \cdot \mathbf{V} \right] d\eta \\ &= \int \mathbf{V} \cdot \nabla \pi d \left( \frac{\partial p}{\partial \pi} \right) + \int \delta dp. \end{aligned} \quad (3.150)$$

The original primitive equations (3.131)-(3.135), together with (3.136), (3.137), and (3.142)-(3.144) can now be rewritten with the aid of (3.145), (3.146), and (3.150).

$$\frac{\partial \zeta}{\partial t} = \mathbf{k} \cdot \nabla \times (\mathbf{n} / \cos \phi) + F_{\zeta_H}, \quad (3.151)$$

$$\frac{\partial \delta}{\partial t} = \nabla \cdot (\mathbf{n} / \cos \phi) - \nabla^2 (E + \Phi) + F_{\delta_H}, \quad (3.152)$$

$$\begin{aligned} \frac{\partial T}{\partial t} = & \frac{-1}{a \cos^2 \phi} \left[ \frac{\partial}{\partial \lambda} (UT) + \cos \phi \frac{\partial}{\partial \phi} (VT) \right] + T\delta - \dot{\eta} \frac{\partial p}{\partial \eta} \frac{\partial T}{\partial p} + \frac{R}{c_p^*} T_v \frac{\omega}{p} \\ & + Q + F_{T_H} + F_{F_H} \end{aligned} \quad (3.153)$$

$$\frac{\partial q}{\partial t} = \frac{-1}{a \cos^2 \phi} \left[ \frac{\partial}{\partial \lambda} (Uq) + \cos \phi \frac{\partial}{\partial \phi} (Vq) \right] + q\delta - \dot{\eta} \frac{\partial p}{\partial \eta} \frac{\partial q}{\partial p} + S, \quad (3.154)$$

$$\frac{\partial \pi}{\partial t} = - \int_{(\eta_t)}^{(1)} \mathbf{V} \cdot \nabla \pi d \left( \frac{\partial p}{\partial \pi} \right) - \int_{p(\eta_t)}^{p(1)} \delta dp, \quad (3.155)$$

$$n_U = +(\zeta + f)V - \dot{\eta} \frac{\partial p}{\partial \eta} \frac{\partial - U}{\partial p} - R \frac{T_v}{a} \frac{1}{p} \frac{\partial p}{\partial \pi} \frac{\partial \pi}{\partial \lambda} + F_U, \quad (3.156)$$

$$n_V = -(\zeta + f)U - \dot{\eta} \frac{\partial p}{\partial \eta} \frac{\partial - V}{\partial p} R \frac{T_v \cos \phi}{a} \frac{1}{p} \frac{\partial p}{\partial \pi} \frac{\partial \pi}{\partial \phi} + F_V, \quad (3.157)$$

$$\Phi = \Phi_s + R \int_{p(\eta)}^{p(1)} T_v d \ln p, \quad (3.158)$$

$$\begin{aligned} \dot{\eta} \frac{\partial p}{\partial \eta} = & \frac{\partial p}{\partial \pi} \left[ \int_{(\eta_t)}^{(1)} \mathbf{V} \cdot \nabla \pi d \left( \frac{\partial p}{\partial \pi} \right) + \int_{p(\eta_t)}^{p(1)} \delta dp \right] \\ & - \int_{(\eta_t)}^{(\eta)} \mathbf{V} \cdot \nabla \pi d \left( \frac{\partial p}{\partial \pi} \right) - \int_{p(\eta_t)}^{p(\eta)} \delta dp, \end{aligned} \quad (3.159)$$

$$\omega = \frac{\partial p}{\partial \pi} \mathbf{V} \cdot \nabla \pi - \int_{(\eta_t)}^{(\eta)} \mathbf{V} \cdot \nabla \pi d \left( \frac{\partial p}{\partial \pi} \right) - \int_{p(\eta_t)}^{p(\eta)} \delta dp. \quad (3.160)$$

1254 Once  $\eta(p, \pi)$  is specified, then  $\partial p / \partial \pi$  can be determined and (3.151)-(3.160) can be solved in a  
1255 GCM.

1256 In the actual definition of the hybrid coordinate, it is not necessary to specify  $\eta(p, \pi)$  ex-  
1257 plicitly, since (3.151)-(3.160) only requires that  $p$  and  $\partial p / \partial \pi$  be determined. It is sufficient to  
1258 specify  $p(\eta, \pi)$  and to let  $\eta$  be defined implicitly. This will be done in section 3.3.7. In the case  
1259 that  $p(\eta, \pi) = \sigma \pi$  and  $\eta_t = 0$ , (3.151)-(3.160) can be reduced to the set of equations solved by  
1260 CCM1.

### 1261 3.3.3 Continuous equations using $\partial \ln(\pi) / \partial t$

1262 In practice, the solutions generated by solving the above equations are excessively noisy. This  
1263 problem appears to arise from aliasing problems in the hydrostatic equation (3.158). The  $\ln p$   
1264 integral introduces a high order nonlinearity which enters directly into the divergence equation  
1265 (3.152). Large gravity waves are generated in the vicinity of steep orography, such as in the  
1266 Pacific Ocean west of the Andes.

1267 The noise problem is solved by converting the equations given above, which use  $\pi$  as a  
 1268 prognostic variable, to equations using  $\Pi = \ln(\pi)$ . This results in the hydrostatic equation  
 1269 becoming only quadratically nonlinear except for moisture contributions to virtual temperature.  
 1270 Since the spectral transform method will be used to solve the equations, gradients will be  
 1271 obtained during the transform from wave to grid space. Outside of the prognostic equation for  
 1272  $\Pi$ , all terms involving  $\nabla\pi$  will then appear as  $\pi\nabla\Pi$ .

Equations (3.151)-(3.160) become:

$$\frac{\partial\zeta}{\partial t} = \mathbf{k} \cdot \nabla \times (\mathbf{n}/\cos\phi) + F_{\zeta_H}, \quad (3.161)$$

$$\frac{\partial\delta}{\partial t} = \nabla \cdot (\mathbf{n}/\cos\phi) - \nabla^2(E + \Phi) + F_{\delta_H}, \quad (3.162)$$

$$\frac{\partial T}{\partial t} = \frac{-1}{a\cos^2\phi} \left[ \frac{\partial}{\partial\lambda}(UT) + \cos\phi \frac{\partial}{\partial\phi}(VT) \right] + T\delta - \dot{\eta} \frac{\partial p}{\partial\eta} \frac{\partial T}{\partial p} + \frac{R}{c_p^*} T_v \frac{\omega}{p} \quad (3.163)$$

$$+ Q + F_{T_H} + F_{F_H},$$

$$\frac{\partial q}{\partial t} = \frac{-1}{a\cos^2\phi} \left[ \frac{\partial}{\partial\lambda}(Uq) + \cos\phi \frac{\partial}{\partial\phi}(Vq) \right] + q\delta - \dot{\eta} \frac{\partial p}{\partial\eta} \frac{\partial q}{\partial p} + S, \quad (3.164)$$

$$\frac{\partial\Pi}{\partial t} = - \int_{(\eta_t)}^{(1)} \mathbf{V} \cdot \nabla\Pi d\left(\frac{\partial p}{\partial\pi}\right) - \frac{1}{\pi} \int_{p(\eta_t)}^{p(1)} \delta dp, \quad (3.165)$$

$$n_U = +(\zeta + f)V - \dot{\eta} \frac{\partial p}{\partial\eta} \frac{\partial - U}{\partial p} R \frac{T_v}{a} \frac{\pi}{p} \frac{\partial p}{\partial\pi} \frac{\partial\Pi}{\partial\lambda} + F_U, \quad (3.166)$$

$$n_V = -(\zeta + f)U - \dot{\eta} \frac{\partial p}{\partial\eta} \frac{\partial - V}{\partial p} R \frac{T_v}{a} \frac{\cos\phi}{p} \frac{\pi}{\partial\pi} \frac{\partial p}{\partial\phi} \frac{\partial\Pi}{\partial\lambda} + F_V, \quad (3.167)$$

$$\Phi = \Phi_s + R \int_{p(\eta)}^{p(1)} T_v d\ln p, \quad (3.168)$$

$$\dot{\eta} \frac{\partial p}{\partial\eta} = \frac{\partial p}{\partial\pi} \left[ \int_{(\eta_t)}^{(1)} \pi \mathbf{V} \cdot \nabla\Pi d\left(\frac{\partial p}{\partial\pi}\right) + \int_{p(\eta_t)}^{p(1)} \delta dp \right] - \int_{(\eta_t)}^{(\eta)} \pi \mathbf{V} \cdot \nabla\Pi d\left(\frac{\partial p}{\partial\pi}\right) - \int_{p(\eta_t)}^{p(\eta)} \delta dp, \quad (3.169)$$

$$\omega = \frac{\partial p}{\partial\pi} \pi \mathbf{V} \cdot \nabla\Pi - \int_{(\eta_t)}^{(\eta)} \pi \mathbf{V} \cdot \nabla\Pi d\left(\frac{\partial p}{\partial\pi}\right) - \int_{p(\eta_t)}^{p(\eta)} \delta dp. \quad (3.170)$$

1273 The above equations reduce to the standard  $\sigma$  equations used in CCM1 if  $\eta = \sigma$  and  $\eta_t = 0$ .  
 1274 (Note that in this case  $\partial p/\partial\pi = p/\pi = \sigma$ .)

### 1275 3.3.4 Semi-implicit formulation

The model described by (3.161)-(3.170), without the horizontal diffusion terms, together with boundary conditions (3.129) and (3.130), is integrated in time using the semi-implicit leapfrog scheme described below. The semi-implicit form of the time differencing will be applied to (3.162) and (3.164) without the horizontal diffusion sources, and to (3.165). In order to derive the semi-implicit form, one must linearize these equations about a reference state. Isolating

the terms that will have their linear parts treated implicitly, the prognostic equations (3.161), (3.162), and (3.165) may be rewritten as:

$$\frac{\partial \delta}{\partial t} = -RT_v \nabla^2 \ln p - \nabla^2 \Phi + X_1, \quad (3.171)$$

$$\frac{\partial T}{\partial t} = +\frac{R}{c_p^*} T_v \frac{\omega}{p} - \dot{\eta} \frac{\partial p}{\partial \eta} \frac{\partial T}{\partial p} + Y_1, \quad (3.172)$$

$$\frac{\partial \Pi}{\partial t} = -\frac{1}{\pi} \int_{p(\eta_t)}^{p(1)} \delta dp + Z_1, \quad (3.173)$$

where  $X_1, Y_1, Z_1$  are the remaining nonlinear terms not explicitly written in (3.171)-(3.173). The terms involving  $\Phi$  and  $\omega$  may be expanded into vertical integrals using (3.168) and (3.170), while the  $\nabla^2 \ln p$  term can be converted to  $\nabla^2 \Pi$ , giving:

$$\frac{\partial \delta}{\partial t} = -RT \frac{\pi}{p} \frac{\partial p}{\partial \pi} \nabla^2 \Pi - R \nabla^2 \int_{p(\eta)}^{p(1)} T d \ln p + X_2, \quad (3.174)$$

$$\frac{\partial T}{\partial t} = -\frac{R}{c_p} \frac{T}{p} \int_{p(\eta_t)}^{p(\eta)} \delta dp - \left[ \frac{\partial p}{\partial \pi} \int_{p(\eta_t)}^{p(1)} \delta dp - \int_{p(\eta_t)}^{p(\eta)} \delta dp \right] \frac{\partial T}{\partial p} + Y_2, \quad (3.175)$$

$$\frac{\partial \Pi}{\partial t} = -\frac{1}{\pi} \int_{p(\eta_t)}^{p(1)} \delta dp + Z_2. \quad (3.176)$$

1276 Once again, only terms that will be linearized have been explicitly represented in (3.174)-(3.176),  
1277 and the remaining terms are included in  $X_2, Y_2$ , and  $Z_2$ . Anticipating the linearization,  $T_v$  and  
1278  $c_p^*$  have been replaced by  $T$  and  $c_p$  in (3.174) and (3.175). Furthermore, the virtual temperature  
1279 corrections are included with the other nonlinear terms.

In order to linearize (3.174)-(3.176), one specifies a reference state for temperature and pressure, then expands the equations about the reference state:

$$T = T^r + T', \quad (3.177)$$

$$\pi = \pi^r + \pi', \quad (3.178)$$

$$p = p^r(\eta, \pi^r) + p'. \quad (3.179)$$

1280 In the special case that  $p(\eta, \pi) = \sigma \pi$ , (3.174)-(3.176) can be converted into equations involving  
1281 only  $\Pi = \ln \pi$  instead of  $p$ , and (3.178) and (3.179) are not required. This is a major difference  
1282 between the hybrid coordinate scheme being developed here and the  $\sigma$  coordinate scheme in  
1283 CCM1.

Expanding (3.174)-(3.176) about the reference state (3.177)-(3.179) and retaining only the linear terms explicitly, one obtains:

$$\frac{\partial \delta}{\partial t} = -R \nabla^2 \left[ T^r \frac{\pi^r}{p^r} \left( \frac{\partial p}{\partial \pi} \right)^r \Pi + \int_{p^r(\eta)}^{p^r(1)} T' d \ln p^r + \int_{p^r(\eta)}^{p^r(1)} \frac{T^r}{p^r} dp' \right] + X_3, \quad (3.180)$$

$$\frac{\partial T}{\partial t} = -\frac{R}{c_p} \frac{T^r}{p^r} \int_{p^r(\eta_t)}^{p^r(\eta)} \delta dp^r - \left[ \left( \frac{\partial p}{\partial \pi} \right)^r \int_{p^r(\eta_t)}^{p^r(1)} \delta dp^r - \int_{p^r(\eta_t)}^{p^r(\eta)} \delta dp^r \right] \frac{\partial T^r}{\partial p^r} + Y_3, \quad (3.181)$$

$$\frac{\partial \Pi}{\partial t} = -\frac{1}{\pi^r} \int_{p^r(\eta_t)}^{p^r(1)} \delta dp^r + Z_3. \quad (3.182)$$

Figure 3.4: Vertical level structure of CAM 5.0

The semi-implicit time differencing scheme treats the linear terms in (3.180)-(3.182) by averaging in time. The last integral in (3.180) is reduced to purely linear form by the relation

$$dp' = \pi' d \left( \frac{\partial p}{\partial \pi} \right)^r + x. \quad (3.183)$$

1284 In the hybrid coordinate described below,  $p$  is a linear function of  $\pi$ , so  $x$  above is zero.

We will assume that centered differences are to be used for the nonlinear terms, and the linear terms are to be treated implicitly by averaging the previous and next time steps. Finite differences are used in the vertical, and are described in the following sections. At this stage only some very general properties of the finite difference representation must be specified. A layering structure is assumed in which field values are predicted on  $K$  layer midpoints denoted by an integer index,  $\eta_k$  (see Figure 3.4). The interface between  $\eta_k$  and  $\eta_{k+1}$  is denoted by a half-integer index,  $\eta_{k+1/2}$ . The model top is at  $\eta_{1/2} = \eta_t$ , and the Earth's surface is at  $\eta_{K+1/2} = 1$ . It is further assumed that vertical integrals may be written as a matrix (of order  $K$ ) times a column vector representing the values of a field at the  $\eta_k$  grid points in the vertical. The column vectors representing a vertical column of grid points will be denoted by underbars, the matrices will be denoted by bold-faced capital letters, and superscript  $T$  will denote the vector transpose. The finite difference forms of (3.180)-(3.182) may then be written down as:

$$\begin{aligned} \underline{\delta}^{n+1} &= \underline{\delta}^{n-1} + 2\Delta t \underline{X}^n \\ &\quad - 2\Delta t R \underline{b}^r \nabla^2 \left( \frac{\Pi^{n-1} + \Pi^{n+1}}{2} - \Pi^n \right) \\ &\quad - 2\Delta t R \mathbf{H}^r \nabla^2 \left( \frac{(\underline{T}')^{n-1} + (\underline{T}')^{n+1}}{2} - (\underline{T}')^n \right) \\ &\quad - 2\Delta t R \underline{h}^r \nabla^2 \left( \frac{\Pi^{n-1} + \Pi^{n+1}}{2} - \Pi^n \right), \end{aligned} \quad (3.184)$$

$$\underline{T}^{n+1} = \underline{T}^{n-1} + 2\Delta t \underline{Y}^n - 2\Delta t \mathbf{D}^r \left( \frac{\underline{\delta}^{n-1} + \underline{\delta}^{n+1}}{2} - \underline{\delta}^n \right), \quad (3.185)$$

$$\Pi^{n+1} = \Pi^{n-1} + 2\Delta t Z^n - 2\Delta t \left( \frac{\underline{\delta}^{n-1} + \underline{\delta}^{n+1}}{2} - \underline{\delta}^n \right)^T \frac{1}{\Pi^r} \underline{\Delta p}^r, \quad (3.186)$$

1285 where  $(\cdot)^n$  denotes a time varying value at time step  $n$ . The quantities  $\underline{X}^n$ ,  $\underline{Y}^n$ , and  $Z^n$  are 1286 defined so as to complete the right-hand sides of (3.171)-(3.173). The components of  $\underline{\Delta p}^r$  are 1287 given by  $\Delta p_k^r = p_{k+\frac{1}{2}}^r - p_{k-\frac{1}{2}}^r$ . This definition of the vertical difference operator  $\Delta$  will be used in 1288 subsequent equations. The reference matrices  $\mathbf{H}^r$  and  $\mathbf{D}^r$ , and the reference column vectors  $\underline{b}^r$  1289 and  $\underline{h}^r$ , depend on the precise specification of the vertical coordinate and will be defined later.

1290 **3.3.5 Energy conservation**

We shall impose a requirement on the vertical finite differences of the model that they conserve the global integral of total energy *in the absence of sources and sinks*. We need to derive

equations for kinetic and internal energy in order to impose this constraint. The momentum equations (more painfully, the vorticity and divergence equations) without the  $F_U, F_V, F_{\zeta_H}$  and  $F_{\delta_H}$  contributions, can be combined with the continuity equation

$$\frac{\partial}{\partial t} \left( \frac{\partial p}{\partial \eta} \right) + \nabla \cdot \left( \frac{\partial p}{\partial \eta} \mathbf{V} \right) + \frac{\partial}{\partial \eta} \left( \frac{\partial p}{\partial \eta} \dot{\eta} \right) = 0 \quad (3.187)$$

to give an equation for the rate of change of kinetic energy:

$$\begin{aligned} \frac{\partial}{\partial t} \left( \frac{\partial p}{\partial \eta} E \right) &= -\nabla \cdot \left( \frac{\partial p}{\partial \eta} E \mathbf{V} \right) - \frac{\partial}{\partial \eta} \left( \frac{\partial p}{\partial \eta} E \dot{\eta} \right) \\ &\quad - \frac{RT_v}{p} \frac{\partial p}{\partial \eta} \mathbf{V} \cdot \nabla p - \frac{\partial p}{\partial \eta} \mathbf{V} \cdot \nabla \Phi - . \end{aligned} \quad (3.188)$$

1291 The first two terms on the right-hand side of (3.188) are transport terms. The horizontal integral  
1292 of the first (horizontal) transport term should be zero, and it is relatively straightforward to  
1293 construct horizontal finite difference schemes that ensure this. For spectral models, the integral  
1294 of the horizontal transport term will not vanish in general, but we shall ignore this problem.

1295 The vertical integral of the second (vertical) transport term on the right-hand side of (3.188)  
1296 should vanish. Since this term is obtained from the vertical advection terms for momentum,  
1297 which will be finite differenced, we can construct a finite difference operator that will ensure  
1298 that the vertical integral vanishes.

The vertical advection terms are the product of a vertical velocity ( $\dot{\eta} \partial p / \partial \eta$ ) and the vertical derivative of a field ( $\partial \psi / \partial p$ ). The vertical velocity is defined in terms of vertical integrals of fields (3.170), which are naturally taken to interfaces. The vertical derivatives are also naturally taken to interfaces, so the product is formed there, and then adjacent interface values of the products are averaged to give a midpoint value. It is the definition of the average that must be correct in order to conserve kinetic energy under vertical advection in (3.188). The derivation will be omitted here, the resulting vertical advection terms are of the form:

$$\left( \dot{\eta} \frac{\partial p}{\partial \eta} \frac{\partial \psi}{\partial p} \right)_k = \frac{1}{2\Delta p_k} \left[ \left( \dot{\eta} \frac{\partial p}{\partial \eta} \right)_{k+1/2} (\psi_{k+1} - \psi_k) + \left( \dot{\eta} \frac{\partial p}{\partial \eta} \right)_{k-1/2} (\psi_k - \psi_{k-1}) \right], \quad (3.189)$$

$$\Delta p_k = p_{k+1/2} - p_{k-1/2}. \quad (3.190)$$

1299 The choice of definitions for the vertical velocity at interfaces is not crucial to the energy con-  
1300 servation (although not completely arbitrary), and we shall defer its definition until later. The  
1301 vertical advection of temperature is not required to use (3.189) in order to conserve mass or en-  
1302 ergy. Other constraints can be imposed that result in different forms for temperature advection,  
1303 but we will simply use (3.189) in the system described below.

The last two terms in (3.188) contain the conversion between kinetic and internal (potential) energy and the form drag. Neglecting the transport terms, under assumption that global integrals will be taken, noting that  $\nabla p / p = \frac{\pi}{p} \frac{\partial p}{\partial \pi} \nabla \Pi$ , and substituting for the geopotential using (3.168), (3.188) can be written as:

$$\begin{aligned} \frac{\partial}{\partial t} \left( \frac{\partial p}{\partial \eta} E \right) &= -RT_v \frac{\partial p}{\partial \eta} \mathbf{V} \cdot \left( \frac{\pi}{p} \frac{\partial p}{\partial \pi} \nabla \Pi \right) \\ &\quad - \frac{\partial p}{\partial \eta} \mathbf{V} \cdot \nabla \Phi_s - \frac{\partial p}{\partial \eta} \mathbf{V} \cdot \nabla \int_{p(\eta)}^{p(1)} RT_v d \ln p + \dots \end{aligned} \quad (3.191)$$

The second term on the right-hand side of (3.192) is a source (form drag) term that can be neglected as we are only interested in internal conservation properties. The last term on the right-hand side of (3.192) can be rewritten as

$$\frac{\partial p}{\partial \eta} \mathbf{V} \cdot \nabla \int_{p(\eta)}^{p(1)} RT_v d \ln p = \nabla \cdot \left\{ \frac{\partial p}{\partial \eta} \mathbf{V} \int_{p(\eta)}^{p(1)} RT_v d \ln p \right\} - \nabla \cdot \left( \frac{\partial p}{\partial \eta} \mathbf{V} \right) \int_{p(\eta)}^{p(1)} RT_v d \ln p. \quad (3.192)$$

The global integral of the first term on the right-hand side of (3.192) is obviously zero, so that (3.192) can now be written as:

$$\frac{\partial}{\partial t} \left( \frac{\partial p}{\partial \eta} E \right) = -RT_v \frac{\partial p}{\partial \eta} \mathbf{V} \cdot \left( \frac{\pi}{p} \frac{\partial p}{\partial \pi} \nabla \Pi \right) + \nabla \cdot \left( \frac{\partial p}{\partial \eta} \mathbf{V} \right) \int_{p(\eta)}^{p(1)} RT_v d \ln p + \dots \quad (3.193)$$

We now turn to the internal energy equation, obtained by combining the thermodynamic equation (3.164), without the  $Q$ ,  $F_{T_H}$ , and  $F_{F_H}$  terms, and the continuity equation (3.187):

$$\frac{\partial}{\partial t} \left( \frac{\partial p}{\partial \eta} c_p^* T \right) = -\nabla \cdot \left( \frac{\partial p}{\partial \eta} c_p^* T \mathbf{V} \right) - \frac{\partial}{\partial \eta} \left( \frac{\partial p}{\partial \eta} c_p^* T \dot{\eta} \right) + RT_v \frac{\partial p}{\partial \eta} \frac{\omega}{p}. \quad (3.194)$$

As in (3.188), the first two terms on the right-hand side are advection terms that can be neglected under global integrals. Using (3.144), (3.194) can be written as:

$$\frac{\partial}{\partial t} \left( \frac{\partial p}{\partial \eta} c_p^* T \right) = RT_v \frac{\partial p}{\partial \eta} \mathbf{V} \cdot \left( \frac{\pi}{p} \frac{\partial p}{\partial \pi} \nabla \Pi \right) - RT_v \frac{\partial p}{\partial \eta} \frac{1}{p} \int_{\eta_t}^{\eta} \nabla \cdot \left( \frac{\partial p}{\partial \eta} \mathbf{V} \right) d\eta + \dots \quad (3.195)$$

1304 The rate of change of total energy due to internal processes is obtained by adding (3.193) and  
1305 (3.195) and must vanish. The first terms on the right-hand side of (3.193) and (3.195) obviously  
1306 cancel in the continuous form. When the equations are discretized in the vertical, the terms will  
1307 still cancel, providing that the same definition is used for  $(1/p \partial p / \partial \pi)_k$  in the nonlinear terms  
1308 of the vorticity and divergence equations (3.166) and (3.167), and in the  $\omega$  term of (3.164) and  
1309 (3.170).

The second terms on the right-hand side of (3.193) and (3.195) must also cancel in the global mean. This cancellation is enforced locally in the horizontal on the column integrals of (3.193) and (3.195), so that we require:

$$\int_{\eta_t}^1 \left\{ \nabla \cdot \left( \frac{\partial p}{\partial \eta} \mathbf{V} \right) \int_{p(\eta)}^{p(1)} RT_v d \ln p \right\} d\eta = \int_{\eta_t}^1 \left\{ RT_v \frac{\partial p}{\partial \eta} \frac{1}{p} \int_{\eta_t}^{\eta} \nabla \cdot \left( \frac{\partial p}{\partial \eta'} \mathbf{V} \right) d\eta' \right\} d\eta. \quad (3.196)$$

The inner integral on the left-hand side of (3.196) is derived from the hydrostatic equation (3.168), which we shall approximate as

$$\begin{aligned} \Phi_k &= \Phi_s + R \sum_{\ell=k}^K H_{k\ell} T_{v\ell}, \\ &= \Phi_s + R \sum_{\ell=1}^K H_{k\ell} T_{v\ell}, \end{aligned} \quad (3.197)$$

$$\underline{\Phi} = \underline{\Phi_s} + R \underline{\mathbf{H} T_v}, \quad (3.198)$$

where  $H_{k\ell} = 0$  for  $\ell < k$ . The quantity  $\underline{1}$  is defined to be the unit vector. The inner integral on the right-hand side of (3.196) is derived from the vertical velocity equation (3.170), which we shall approximate as

$$\left(\frac{\omega}{p}\right)_k = \left(\frac{\pi}{p} \frac{\partial p}{\partial \pi}\right)_k \mathbf{V}_k \cdot \nabla \Pi - \sum_{\ell=1}^K C_{k\ell} \left[ \delta_\ell \Delta p_\ell + \pi (\mathbf{V}_\ell \cdot \nabla \Pi) \Delta \left(\frac{\partial p}{\partial \pi}\right)_\ell \right], \quad (3.199)$$

where  $C_{k\ell} = 0$  for  $\ell > k$ , and  $C_{k\ell}$  is included as an approximation to  $1/p_k$  for  $\ell \leq k$  and the symbol  $\Delta$  is similarly defined as in (3.190).  $C_{k\ell}$  will be determined so that  $\omega$  is consistent with the discrete continuity equation following Williamson and Olson [1994a]. Using (3.197) and (3.199), the finite difference analog of (3.196) is

$$\begin{aligned} & \sum_{k=1}^K \left\{ \frac{1}{\Delta \eta_k} \left[ \delta_k \Delta p_k + \pi (\mathbf{V}_k \cdot \nabla \Pi) \Delta \left(\frac{\partial p}{\partial \pi}\right)_k \right] R \sum_{\ell=1}^K H_{k\ell} T_{v\ell} \right\} \Delta \eta_k \\ &= \sum_{k=1}^K \left\{ R T_{vk} \frac{\Delta p_k}{\Delta \eta_k} \sum_{\ell=1}^K C_{k\ell} \left[ \delta_\ell \Delta p_\ell + \pi (\mathbf{V}_\ell \cdot \nabla \Pi) \Delta \left(\frac{\partial p}{\partial \pi}\right)_\ell \right] \right\} \Delta \eta_k, \end{aligned} \quad (3.200)$$

where we have used the relation

$$\nabla \cdot \mathbf{V} (\partial p / \partial \eta)_k = [\delta_k \Delta p_k + \pi (\mathbf{V}_k \cdot \nabla \Pi) \Delta (\partial p / \partial \pi)_k] / \Delta \eta_k \quad (3.201)$$

(see 3.150). We can now combine the sums in (3.200) and simplify to give

$$\begin{aligned} & \sum_{k=1}^K \sum_{\ell=1}^K \left\{ \left[ \delta_k \Delta p_k + \pi (\mathbf{V}_k \cdot \nabla \Pi) \Delta \left(\frac{\partial p}{\partial \pi}\right)_k \right] H_{k\ell} T_{v\ell} \right\} \\ &= \sum_{k=1}^K \sum_{\ell=1}^K \left\{ \left[ \delta_\ell \Delta p_\ell + \pi (\mathbf{V}_\ell \cdot \nabla \Pi) \Delta \left(\frac{\partial p}{\partial \pi}\right)_\ell \right] \Delta p_k C_{k\ell} T_{vk} \right\}. \end{aligned} \quad (3.202)$$

Interchanging the indexes on the left-hand side of (3.202) will obviously result in identical expressions if we require that

$$H_{k\ell} = C_{\ell k} \Delta p_\ell. \quad (3.203)$$

Given the definitions of vertical integrals in (3.198) and (3.199) and of vertical advection in (3.189) and (3.190) the model will conserve energy as long as we require that  $\mathbf{C}$  and  $\mathbf{H}$  satisfy (3.203). We are, of course, still neglecting lack of conservation due to the truncation of the horizontal spherical harmonic expansions.

### 3.3.6 Horizontal diffusion

CAM 5.0 contains a horizontal diffusion term for  $T, \zeta$ , and  $\delta$  to prevent spectral blocking and to provide reasonable kinetic energy spectra. The horizontal diffusion operator in CAM 5.0 is also used to ensure that the CFL condition is not violated in the upper layers of the model. The horizontal diffusion is a linear  $\nabla^2$  form on  $\eta$  surfaces in the top three levels of the model and a linear  $\nabla^4$  form with a partial correction to pressure surfaces for temperature elsewhere.

1320 The  $\nabla^2$  diffusion near the model top is used as a simple sponge to absorb vertically propagating  
 1321 planetary wave energy and also to control the strength of the stratospheric winter jets. The  $\nabla^2$   
 1322 diffusion coefficient has a vertical variation which has been tuned to give reasonable Northern  
 1323 and Southern Hemisphere polar night jets.

In the top three model levels, the  $\nabla^2$  form of the horizontal diffusion is given by

$$F_{\zeta_H} = K^{(2)} [\nabla^2 (\zeta + f) + 2(\zeta + f)/a^2], \quad (3.204)$$

$$F_{\delta_H} = K^{(2)} [\nabla^2 \delta + 2(\delta/a^2)], \quad (3.205)$$

$$F_{T_H} = K^{(2)} \nabla^2 T. \quad (3.206)$$

1324 Since these terms are linear, they are easily calculated in spectral space. The undifferentiated  
 1325 correction term is added to the vorticity and divergence diffusion operators to prevent damping  
 1326 of uniform ( $n = 1$ ) rotations [Orszag, 1974; Bourke et al., 1977]. The  $\nabla^2$  form of the horizontal  
 1327 diffusion is applied *only* to pressure surfaces in the standard model configuration.

The horizontal diffusion operator is better applied to pressure surfaces than to terrain-following surfaces (applying the operator on isentropic surfaces would be still better). Although the governing system of equations derived above is designed to reduce to pressure surfaces above some level, problems can still occur from diffusion along the lower surfaces. Partial correction to pressure surfaces of harmonic horizontal diffusion ( $\partial\xi/\partial t = K\nabla^2\xi$ ) can be included using the relations:

$$\begin{aligned} \nabla_p \xi &= \nabla_\eta \xi - p \frac{\partial \xi}{\partial p} \nabla_\eta \ln p \\ \nabla_p^2 \xi &= \nabla_\eta^2 \xi - p \frac{\partial \xi}{\partial p} \nabla_\eta^2 \ln p - 2 \nabla_\eta \left( \frac{\partial \xi}{\partial p} \right) \cdot \nabla_\eta p + \frac{\partial^2 \xi}{\partial^2 p} \nabla_\eta^2 p. \end{aligned} \quad (3.207)$$

Retaining only the first two terms above gives a correction to the  $\eta$  surface diffusion which involves only a vertical derivative and the Laplacian of log surface pressure,

$$\nabla_p^2 \xi = \nabla_\eta^2 \xi - \pi \frac{\partial \xi}{\partial p} \frac{\partial p}{\partial \pi} \nabla^2 \Pi + \dots \quad (3.208)$$

Similarly, biharmonic diffusion can be partially corrected to pressure surfaces as:

$$\nabla_p^4 \xi = \nabla_\eta^4 \xi - \pi \frac{\partial \xi}{\partial p} \frac{\partial p}{\partial \pi} \nabla^4 \Pi + \dots \quad (3.209)$$

The bi-harmonic  $\nabla^4$  form of the diffusion operator is applied at all other levels (generally throughout the troposphere) as

$$F_{\zeta_H} = -K^{(4)} [\nabla^4 (\zeta + f) - (\zeta + f) (2/a^2)^2], \quad (3.210)$$

$$F_{\delta_H} = -K^{(4)} [\nabla^4 \delta - \delta (2/a^2)^2], \quad (3.211)$$

$$F_{T_H} = -K^{(4)} [\nabla^4 T - \pi \frac{\partial T}{\partial p} \frac{\partial p}{\partial \pi} \nabla^4 \Pi]. \quad (3.212)$$

1328 The second term in  $F_{T_H}$  consists of the leading term in the transformation of the  $\nabla^4$  operator  
 1329 to pressure surfaces. It is included to offset partially a spurious diffusion of  $T$  over mountains.

1330 As with the  $\nabla^2$  form, the  $\nabla^4$  operator can be conveniently calculated in spectral space. The  
 1331 correction term is then completed after transformation of  $T$  and  $\nabla^4\Pi$  back to grid-point space.  
 1332 As with the  $\nabla^2$  form, an undifferentiated term is added to the vorticity and divergence diffusion  
 1333 operators to prevent damping of uniform rotations.

1334 **3.3.7 Finite difference equations**

1335 The governing equations are solved using the spectral method in the horizontal, so that only the  
 1336 vertical and time differences are presented here. The dynamics includes horizontal diffusion of  
 1337  $T$ ,  $(\zeta + f)$ , and  $\delta$ . Only  $T$  has the leading term correction to pressure surfaces. Thus, equations  
 1338 that include the terms in this time split sub-step are of the form

$$\frac{\partial \psi}{\partial t} = \text{Dyn}(\psi) - (-1)^i K^{(2i)} \nabla_\eta^{2i} \psi, \quad (3.213)$$

for  $(\zeta + f)$  and  $\delta$ , and

$$\frac{\partial T}{\partial t} = \text{Dyn}(T) - (-1)^i K^{(2i)} \left\{ \nabla_\eta^{2i} T - \pi \frac{\partial T}{\partial p} \frac{\partial p}{\partial \pi} \nabla^{2i} \Pi \right\}, \quad (3.214)$$

where  $i = 1$  in the top few model levels and  $i = 2$  elsewhere (generally within the troposphere). These equations are further subdivided into time split components:

$$\psi^{n+1} = \psi^{n-1} + 2\Delta t \text{Dyn}(\psi^{n+1}, \psi^n, \psi^{n-1}), \quad (3.215)$$

$$\psi^* = \psi^{n+1} - 2\Delta t (-1)^i K^{(2i)} \nabla_\eta^{2i} (\psi^{n+1}), \quad (3.216)$$

$$\hat{\psi}^{n+1} = \psi^*, \quad (3.217)$$

for  $(\zeta + f)$  and  $\delta$ , and

$$T^{n+1} = T^{n-1} + 2\Delta t \text{Dyn}(T^{n+1}, T^n, T^{n-1}) \quad (3.218)$$

$$T^* = T^{n+1} - 2\Delta t (-1)^i K^{(2i)} \nabla^{2i} \eta(T^*), \quad (3.219)$$

$$\hat{T}^{n+1} = T^* + 2\Delta t (-1)^i K^{(2i)} \pi \frac{\partial T^*}{\partial p} \frac{\partial p}{\partial \pi} \nabla^{2i} \Pi, \quad (3.220)$$

1339 for  $T$ , where in the standard model  $i$  only takes the value 2 in (3.220). The first step from  $(\ )^{n-1}$   
 1340 to  $(\ )^{n+1}$  includes the transformation to spectral coefficients. The second step from  $(\ )^{n+1}$  to  
 1341  $(\ )^{n+1}$  for  $\delta$  and  $\zeta$ , or  $(\ )^{n+1}$  to  $(\ )^*$  for  $T$ , is done on the spectral coefficients, and the final step  
 1342 from  $(\ )^*$  to  $(\ )^{n+1}$  for  $T$  is done after the inverse transform to the grid point representation.

The following finite-difference description details only the forecast given by (3.215) and (3.218). The finite-difference form of the forecast equation for water vapor will be presented later in Section 3c. The general structure of the complete finite difference equations is determined by the semi-implicit time differencing and the energy conservation properties described above. In order to complete the specification of the finite differencing, we require a definition of the vertical coordinate. The actual specification of the generalized vertical coordinate takes advantage of the structure of the equations (3.161)-(3.170). The equations can be finite-differenced in the vertical and, in time, without having to know the value of  $\eta$  anywhere. The quantities that must

be known are  $p$  and  $\partial p/\partial\pi$  at the grid points. Therefore the coordinate is defined implicitly through the relation:

$$p(\eta, \pi) = A(\eta)p_0 + B(\eta)\pi, \quad (3.221)$$

which gives

$$\frac{\partial p}{\partial\pi} = B(\eta). \quad (3.222)$$

<sup>1343</sup> A set of levels  $\eta_k$  may be specified by specifying  $A_k$  and  $B_k$ , such that  $\eta_k \equiv A_k + B_k$ , and  
<sup>1344</sup> difference forms of (3.161)-(3.170) may be derived.

The finite difference forms of the Dyn operator (3.161)-(3.170), including semi-implicit time integration are:

$$\underline{\zeta}^{n+1} = \underline{\zeta}^{n-1} + 2\Delta t \mathbf{k} \cdot \nabla \times (\underline{\mathbf{n}}^n / \cos \phi), \quad (3.223)$$

$$\begin{aligned} \underline{\delta}^{n+1} = & \underline{\delta}^{n-1} + 2\Delta t \left[ \nabla \cdot (\underline{\mathbf{n}}^n / \cos \phi) - \nabla^2 \left( \underline{\mathbf{E}}^n + \Phi_s \underline{1} + R \mathbf{H}^n (\underline{\mathbf{T}}_v')^n \right) \right] \\ & - 2\Delta t R \mathbf{H}^r \nabla^2 \left( \frac{(\underline{\mathbf{T}}')^{n-1} + (\underline{\mathbf{T}}')^{n+1}}{2} - (\underline{\mathbf{T}}')^n \right) \\ & - 2\Delta t R (\underline{b}^r + \underline{h}^r) \nabla^2 \left( \frac{\Pi^{n-1} + \Pi^{n+1}}{2} - \Pi^n \right), \end{aligned} \quad (3.224)$$

$$\begin{aligned} (\underline{\mathbf{T}}')^{n+1} = & (\underline{\mathbf{T}}')^{n-1} - 2\Delta t \left[ \frac{1}{a \cos^2 \phi} \frac{\partial}{\partial \lambda} (\underline{\mathbf{U}} \underline{\mathbf{T}}')^n + \frac{1}{a \cos \phi} \frac{\partial}{\partial \phi} (\underline{\mathbf{V}} \underline{\mathbf{T}}')^n - \underline{\Gamma}^n \right] \\ & - 2\Delta t \mathbf{D}^r \left( \frac{\underline{\delta}^{n-1} + \underline{\delta}^{n+1}}{2} - \underline{\delta}^n \right) \end{aligned} \quad (3.225)$$

$$\begin{aligned} \Pi^{n+1} = & \Pi^{n-1} - 2\Delta t \frac{1}{\pi^n} \left( (\underline{\delta}^n)^T \underline{\Delta p}^n + (\underline{\mathbf{V}}^n)^T \cdot \nabla \Pi^n \pi^n \underline{\Delta B} \right) \\ & - 2\Delta t \left( \frac{\underline{\delta}^{n-1} + \underline{\delta}^{n+1}}{2} - \underline{\delta}^n \right)^T \frac{1}{\pi^r} \underline{\Delta p}^r, \end{aligned} \quad (3.226)$$

$$\begin{aligned} (n_U)_k = & (\zeta_k + f) V_k - R T_{vk} \left( \frac{1}{p} \frac{\partial p}{\partial \pi} \right)_k \pi \frac{1}{a} \frac{\partial \Pi}{\partial \lambda} \\ & - \frac{1}{2\Delta p_k} \left[ \left( \dot{\eta} \frac{\partial p}{\partial \eta} \right)_{k+1/2} (U_{k+1} - U_k) + \left( \dot{\eta} \frac{\partial p}{\partial \eta} \right)_{k-1/2} (U_k - U_{k-1}) \right] \\ & + (F_U)_k, \end{aligned} \quad (3.227)$$

$$\begin{aligned} (n_V)_k = & -(\zeta_k + f) U_k - R T_{vk} \left( \frac{1}{p} \frac{\partial p}{\partial \pi} \right)_k \pi \frac{\cos \phi}{a} \frac{\partial \Pi}{\partial \phi} \\ & - \frac{1}{2\Delta p_k} \left[ \left( \dot{\eta} \frac{\partial p}{\partial \eta} \right)_{k+1/2} (V_{k+1} - V_k) + \left( \dot{\eta} \frac{\partial p}{\partial \eta} \right)_{k-1/2} (V_k - V_{k-1}) \right] \\ & + (F_V)_k, \end{aligned} \quad (3.228)$$

$$\begin{aligned} \Gamma_k = & T'_k \delta_k + \frac{R T_{vk}}{(\underline{C}_p^*)_k} \left( \frac{\omega}{p} \right)_k - Q \\ & - \frac{1}{2\Delta p_k} \left[ \left( \dot{\eta} \frac{\partial p}{\partial \eta} \right)_{k+1/2} (T_{k+1} - T_k) + \left( \dot{\eta} \frac{\partial p}{\partial \eta} \right)_{k-1/2} (T_k - T_{k-1}) \right], \end{aligned} \quad (3.229)$$

$$E_k = (u_k)^2 + (v_k)^2, \quad (3.230)$$

$$\frac{RT_{vk}}{(c_p^*)_k} = \frac{R}{c_p} \left( \frac{T_k^r + T_{vk}'}{1 + \left( \frac{c_{pv}}{c_p} - 1 \right) q_k} \right), \quad (3.231)$$

$$\begin{aligned} \left( \dot{\eta} \frac{\partial p}{\partial \eta} \right)_{k+1/2} &= B_{k+1/2} \sum_{\ell=1}^K [\delta_\ell \Delta p_\ell + \mathbf{V}_\ell \cdot \pi \nabla \Pi \Delta B_\ell] \\ &\quad - \sum_{\ell=1}^k [\delta_\ell \Delta p_\ell + \mathbf{V}_\ell \cdot \pi \nabla \Pi \Delta B_\ell], \end{aligned} \quad (3.232)$$

$$\left( \frac{\omega}{p} \right)_k = \left( \frac{1}{p} \frac{\partial p}{\partial \pi} \right)_k \mathbf{V}_k \cdot \pi \nabla \Pi - \sum_{\ell=1}^k C_{k\ell} [\delta_\ell \Delta p_\ell + \mathbf{V}_\ell \cdot \pi \nabla \Pi \Delta B_\ell], \quad (3.233)$$

$$C_{k\ell} = \begin{cases} \frac{1}{p_k}, & \ell < k \\ \frac{1}{2p_k}, & \ell = k, \end{cases} \quad (3.234)$$

$$H_{k\ell} = C_{\ell k} \Delta p_\ell, \quad (3.235)$$

$$\begin{aligned} D_{k\ell}^r &= \Delta p_\ell^r \frac{R}{c_p} T_k^r C_{\ell k}^r + \frac{\Delta p_\ell^r}{2\Delta p_k^r} (T_k^r - T_{k-1}^r) (\epsilon_{k\ell+1} - B_{k-1/2}) \\ &\quad + \frac{\Delta p_\ell^r}{2\Delta p_k^r} (T_{k+1}^r - T_k^r) (\epsilon_{k\ell} - B_{k+1/2}), \end{aligned} \quad (3.236)$$

$$\frac{\epsilon_{k\ell}}{R} = \begin{cases} 1, & \ell \leq k \\ 0, & \ell > k, \end{cases} \quad (3.237)$$

where notation such as  $(\underline{U}\underline{T}')^n$  denotes a column vector with components  $(U_k T_k')^n$ . In order to complete the system, it remains to specify the reference vector  $\underline{h}^r$ , together with the term  $(1/p \partial p / \partial \pi)$ , which results from the pressure gradient terms and also appears in the semi-implicit reference vector  $\underline{b}^r$ :

$$\left( \frac{1}{p} \frac{\partial p}{\partial \pi} \right)_k = \left( \frac{1}{p} \right)_k \left( \frac{\partial p}{\partial \pi} \right)_k = \frac{B_k}{p_k}, \quad (3.238)$$

$$\underline{b}^r = \underline{T}^r, \quad (3.239)$$

$$\underline{h}^r = 0. \quad (3.240)$$

1345 The matrices  $\mathbf{C}^n$  and  $\mathbf{H}^n$  (*i.e.* with components  $C_{k\ell}$  and  $H_{k\ell}$ ) must be evaluated at each time  
 1346 step and each point in the horizontal. It is more efficient computationally to substitute the  
 1347 definitions of these matrices into (3.224) and (3.233) at the cost of some loss of generality in  
 1348 the code. The finite difference equations have been written in the form (3.223)-(3.240) because  
 1349 this form is quite general. For example, the equations solved by [Simmons and Strüfing \[1981\]](#)  
 1350 at ECMWF can be obtained by changing only the vectors and hydrostatic matrix defined by  
 1351 (3.237)-(3.240).

### 3.3.8 Time filter

1352 The time step is completed by applying a recursive time filter originally designed by [\[Robert, 1966\]](#) and later studied by [\[Asselin, 1972\]](#).

$$\bar{\psi}^n = \psi^n + \alpha \left( \bar{\psi}^{n-1} - 2\psi^n + \psi^{n+1} \right) \quad (3.241)$$

### 1355 3.3.9 Spectral transform

1356 The spectral transform method is used in the horizontal exactly as in CCM1. As shown earlier,  
 1357 the vertical and temporal aspects of the model are represented by finite-difference approxima-  
 1358 tions. The horizontal aspects are treated by the spectral-transform method, which is described  
 1359 in this section. Thus, at certain points in the integration, the prognostic variables  $(\zeta + f), \delta, T,$   
 1360 and  $\Pi$  are represented in terms of coefficients of a truncated series of spherical harmonic func-  
 1361 tions, while at other points they are given by grid-point values on a corresponding Gaussian  
 1362 grid. In general, physical parameterizations and nonlinear operations are carried out in grid-  
 1363 point space. Horizontal derivatives and linear operations are performed in spectral space. Ex-  
 1364 ternally, the model appears to the user to be a grid-point model, as far as data required and  
 1365 produced by it. Similarly, since all nonlinear parameterizations are developed and carried out in  
 1366 grid-point space, the model also appears as a grid-point model for the incorporation of physical  
 1367 parameterizations, and the user need not be too concerned with the spectral aspects. For users  
 1368 interested in diagnosing the balance of terms in the evolution equations, however, the details are  
 1369 important and care must be taken to understand which terms have been spectrally truncated  
 1370 and which have not. The algebra involved in the spectral transformations has been presented in  
 1371 several publications [Daley et al., 1976; Bourke et al., 1977; Machenhauer, 1979]. In this report,  
 1372 we present only the details relevant to the model code; for more details and general philosophy,  
 1373 the reader is referred to these earlier papers.

### 1374 3.3.10 Spectral algorithm overview

The horizontal representation of an arbitrary variable  $\psi$  consists of a truncated series of spherical harmonic functions,

$$\psi(\lambda, \mu) = \sum_{m=-M}^M \sum_{n=|m|}^{\mathcal{N}(m)} \psi_n^m P_n^m(\mu) e^{im\lambda}, \quad (3.242)$$

where  $\mu = \sin \phi$ ,  $M$  is the highest Fourier wavenumber included in the east-west representation, and  $\mathcal{N}(m)$  is the highest degree of the associated Legendre polynomials for longitudinal wavenumber  $m$ . The properties of the spherical harmonic functions used in the representation can be found in the review by Machenhauer [1979]. The model is coded for a general pentagonal truncation, illustrated in Figure 3.5, defined by three parameters:  $M, K$ , and  $N$ , where  $M$  is defined above,  $K$  is the highest degree of the associated Legendre polynomials, and  $N$  is the highest degree of the Legendre polynomials for  $m = 0$ . The common truncations are subsets of this pentagonal case:

$$\begin{aligned} \text{Triangular : } & M = N = K, \\ \text{Rhomboidal : } & K = N + M, \\ \text{Trapezoidal : } & N = K > M. \end{aligned} \quad (3.243)$$

Figure 3.5: Pentagonal truncation parameters

<sup>1375</sup> The quantity  $\mathcal{N}(m)$  in (3.242) represents an arbitrary limit on the two-dimensional wavenumber  
<sup>1376</sup>  $n$ , and for the pentagonal truncation described above is simply given by  
<sup>1377</sup>  $\mathcal{N}(m) = \min(N + |m|, K)$ .

The associated Legendre polynomials used in the model are normalized such that

$$\int_{-1}^1 [P_n^m(\mu)]^2 d\mu = 1. \quad (3.244)$$

With this normalization, the Coriolis parameter  $f$  is

$$f = \frac{\Omega}{\sqrt{0.375}} P_1^o, \quad (3.245)$$

<sup>1378</sup> which is required for the absolute vorticity.

The coefficients of the spectral representation (3.242) are given by

$$\psi_n^m = \int_{-1}^1 \frac{1}{2\pi} \int_0^{2\pi} \psi(\lambda, \mu) e^{-im\lambda} d\lambda P_n^m(\mu) d\mu. \quad (3.246)$$

The inner integral represents a Fourier transform,

$$\psi^m(\mu) = \frac{1}{2\pi} \int_0^{2\pi} \psi(\lambda, \mu) e^{-im\lambda} d\lambda, \quad (3.247)$$

which is performed by a Fast Fourier Transform (FFT) subroutine. The outer integral is performed via Gaussian quadrature,

$$\psi_n^m = \sum_{j=1}^J \psi^m(\mu_j) P_n^m(\mu_j) w_j, \quad (3.248)$$

where  $\mu_j$  denotes the Gaussian grid points in the meridional direction,  $w_j$  the Gaussian weight at point  $\mu_j$ , and  $J$  the number of Gaussian grid points from pole to pole. The Gaussian grid points ( $\mu_j$ ) are given by the roots of the Legendre polynomial  $P_J(\mu)$ , and the corresponding weights are given by

$$w_j = \frac{2(1 - \mu_j^2)}{[J P_{J-1}(\mu_j)]^2}. \quad (3.249)$$

The weights themselves satisfy

$$\sum_{j=1}^J w_j = 2.0. \quad (3.250)$$

The Gaussian grid used for the north–south transformation is generally chosen to allow unaliased computations of quadratic terms only. In this case, the number of Gaussian latitudes  $J$  must satisfy

$$J \geq (2N + K + M + 1)/2 \quad \text{for } M \leq 2(K - N), \quad (3.251)$$

$$J \geq (3K + 1)/2 \quad \text{for } M \geq 2(K - N). \quad (3.252)$$

For the common truncations, these become

$$J \geq (3K + 1)/2 \quad \text{for triangular and trapezoidal,} \quad (3.253)$$

$$J \geq (3N + 2M + 1)/2 \quad \text{for rhomboidal.} \quad (3.254)$$

In order to allow exact Fourier transform of quadratic terms, the number of points  $P$  in the east–west direction must satisfy

$$P \geq 3M + 1. \quad (3.255)$$

- <sup>1379</sup> The actual values of  $J$  and  $P$  are often not set equal to the lower limit in order to allow use of  
<sup>1380</sup> more efficient transform programs.

Although in the next section of this model description, we continue to indicate the Gaussian quadrature as a sum from pole to pole, the code actually deals with the symmetric and antisymmetric components of variables and accumulates the sums from equator to pole only. The model requires an even number of latitudes to easily use the symmetry conditions. This may be slightly inefficient for some spectral resolutions. We define a new index, which goes from  $-I$  at the point next to the south pole to  $+I$  at the point next to the north pole and not including 0 (there are no points at the equator or pole in the Gaussian grid), *i.e.*, let  $I = J/2$  and  $i = j - J/2$  for  $j \geq J/2 + 1$  and  $i = j - J/2 - 1$  for  $j \leq J/2$ ; then the summation in (3.248) can be rewritten as

$$\psi_n^m = \sum_{i=-I, i \neq 0}^I \psi^m(\mu_i) P_n^m(\mu_i) w_i. \quad (3.256)$$

The symmetric (even) and antisymmetric (odd) components of  $\psi^m$  are defined by

$$\begin{aligned} (\psi_E)_i^m &= \frac{1}{2} (\psi_i^m + \psi_{-i}^m), \\ (\psi_O)_i^m &= \frac{1}{2} (\psi_i^m - \psi_{-i}^m). \end{aligned} \quad (3.257)$$

Since  $w_i$  is symmetric about the equator, (3.256) can be rewritten to give formulas for the coefficients of even and odd spherical harmonics:

$$\psi_n^m = \begin{cases} \sum_{i=1}^I (\psi_E)_i^m (\mu_i) P_n^m(\mu_i) 2w_i & \text{for } n - m \text{ even,} \\ \sum_{i=1}^I (\psi_O)_i^m (\mu_i) P_n^m(\mu_i) 2w_i & \text{for } n - m \text{ odd.} \end{cases} \quad (3.258)$$

- <sup>1381</sup> The model uses the spectral transform method [Machenhauer, 1979] for all nonlinear terms.  
<sup>1382</sup> However, the model can be thought of as starting from grid–point values at time  $t$  (consistent  
<sup>1383</sup> with the spectral representation) and producing a forecast of the grid–point values at time  $t + \Delta t$   
<sup>1384</sup> (again, consistent with the spectral resolution). The forecast procedure involves computation  
<sup>1385</sup> of the nonlinear terms including physical parameterizations at grid points; transformation via  
<sup>1386</sup> Gaussian quadrature of the nonlinear terms from grid–point space to spectral space; computation  
<sup>1387</sup> of the spectral coefficients of the prognostic variables at time  $t + \Delta t$  (with the implied spectral  
<sup>1388</sup> truncation to the model resolution); and transformation back to grid–point space. The details  
<sup>1389</sup> of the equations involved in the various transformations are given in the next section.

### 1390 3.3.11 Combination of terms

In order to describe the transformation to spectral space, for each equation we first group together all undifferentiated explicit terms, all explicit terms with longitudinal derivatives, and all explicit terms with meridional derivatives appearing in the Dyn operator. Thus, the vorticity equation (3.223) is rewritten

$$\underline{(\zeta + f)}^{n+1} = \underline{V} + \frac{1}{a(1 - \mu^2)} \left[ \frac{\partial}{\partial \lambda} (\underline{V}_\lambda) - (1 - \mu^2) \frac{\partial}{\partial \mu} (\underline{V}_\mu) \right], \quad (3.259)$$

where the explicit forms of the vectors  $\underline{V}$ ,  $\underline{V}_\lambda$ , and  $\underline{V}_\mu$  are given as

$$\underline{V} = \underline{(\zeta + f)}^{n-1}, \quad (3.260)$$

$$\underline{V}_\lambda = 2\Delta t \underline{n}_V^n, \quad (3.261)$$

$$\underline{V}_\mu = 2\Delta t \underline{n}_U^n. \quad (3.262)$$

The divergence equation (3.224) is

$$\begin{aligned} \underline{\delta}^{n+1} = & \underline{D} + \frac{1}{a(1 - \mu^2)} \left[ \frac{\partial}{\partial \lambda} (\underline{D}_\lambda) + (1 - \mu^2) \frac{\partial}{\partial \mu} (\underline{D}_\mu) \right] - \nabla^2 \underline{D}_\nabla \\ & - \Delta t \nabla^2 (R \mathbf{H}^r \underline{\mathcal{T}}'^{n+1} + R (\underline{b}^r + \underline{h}^r) \Pi^{n+1}). \end{aligned} \quad (3.263)$$

The mean component of the temperature is not included in the next-to-last term since the Laplacian of it is zero. The thermodynamic equation (3.226) is

$$\underline{\mathcal{T}}'^{n+1} = \underline{\mathcal{T}} - \frac{1}{a(1 - \mu^2)} \left[ \frac{\partial}{\partial \lambda} (\underline{\mathcal{T}}_\lambda) + (1 - \mu^2) \frac{\partial}{\partial \mu} (\underline{\mathcal{T}}_\mu) \right] - \Delta t \mathbf{D}^r \underline{\delta}^{n+1}. \quad (3.264)$$

The surface-pressure tendency (3.226) is

$$\Pi^{n+1} = PS - \frac{\Delta t}{\pi^r} (\underline{\Delta p}^r)^T \underline{\delta}^{n+1}. \quad (3.265)$$

The grouped explicit terms in (3.263)–(3.265) are given as follows. The terms of (3.263) are

$$\underline{D} = \underline{\delta}^{n-1}, \quad (3.266)$$

$$\underline{D}_\lambda = 2\Delta t \underline{n}_U^n, \quad (3.267)$$

$$\underline{D}_\mu = 2\Delta t \underline{n}_V^n, \quad (3.268)$$

$$\begin{aligned} \underline{D}_\nabla = & 2\Delta t \left[ \underline{E}^n + \Phi_s \underline{1} + R \mathbf{H}^r \underline{\mathcal{T}}'^n \right] \\ & + \Delta t \left[ R \mathbf{H}^r \left( (\underline{\mathcal{T}}')^{n-1} - 2(\underline{\mathcal{T}}')^n \right) + R (\underline{b}^r + \underline{h}^r) (\Pi^{n-1} - 2\Pi^n) \right]. \end{aligned} \quad (3.269)$$

The terms of (3.264) are

$$\underline{\mathcal{T}} = (\underline{\mathcal{T}}')^{n-1} + 2\Delta t \underline{\Gamma}^n - \Delta t \mathbf{D}^r [\underline{\delta}^{n-1} - 2\underline{\delta}^n], \quad (3.270)$$

$$\underline{\mathcal{T}}_\lambda = 2\Delta t (\underline{U \mathcal{T}'})^n, \quad (3.271)$$

$$\underline{\mathcal{T}}_\mu = 2\Delta t (\underline{V \mathcal{T}'})^n. \quad (3.272)$$

The nonlinear term in (3.265) is

$$PS = \Pi^{n-1} - 2\Delta t \frac{1}{\pi^n} \left[ (\underline{\delta}^n)^T (\underline{\Delta p}^n) + (\underline{V}^n)^T \nabla \Pi^n \pi^n \underline{\Delta B} \right] - \Delta t \left[ (\underline{\Delta p}^r)^T \frac{1}{\pi^r} \right] [\underline{\delta}^{n-1} - 2\underline{\delta}^n]. \quad (3.273)$$

### 1391 3.3.12 Transformation to spectral space

1392 Formally, Equations (3.259)-(3.265) are transformed to spectral space by performing the opera-  
 1393 tions indicated in (3.274) to each term. We see that the equations basically contain three types  
 1394 of terms, for example, in the vorticity equation the undifferentiated term  $\underline{V}$ , the longitudinally  
 1395 differentiated term  $\underline{V}_\lambda$ , and the meridionally differentiated term  $\underline{V}_\mu$ . All terms in the original  
 1396 equations were grouped into one of these terms on the Gaussian grid so that they could be  
 1397 transformed at once.

Transformation of the undifferentiated term is obtained by straightforward application of (3.246)-(3.248),

$$\{\underline{V}\}_n^m = \sum_{j=1}^J \underline{V}^m(\mu_j) P_n^m(\mu_j) w_j, \quad (3.274)$$

where  $\underline{V}^m(\mu_j)$  is the Fourier coefficient of  $\underline{V}$  with wavenumber  $m$  at the Gaussian grid line  $\mu_j$ . The longitudinally differentiated term is handled by integration by parts, using the cyclic boundary conditions,

$$\left\{ \frac{\partial}{\partial \lambda} (\underline{V}_\lambda) \right\}^m = \frac{1}{2\pi} \int_0^{2\pi} \frac{\partial \underline{V}_\lambda}{\partial \lambda} e^{-im\lambda} d\lambda, \quad (3.275)$$

$$= im \frac{1}{2\pi} \int_0^{2\pi} \underline{V}_\lambda e^{-im\lambda} d\lambda, \quad (3.276)$$

$$(3.277)$$

so that the Fourier transform is performed first, then the differentiation is carried out in spectral space. The transformation to spherical harmonic space then follows (3.280):

$$\left\{ \frac{1}{a(1-\mu^2)} \frac{\partial}{\partial \lambda} (\underline{V}_\lambda) \right\}_n^m = im \sum_{j=1}^J \underline{V}_\lambda^m(\mu_j) \frac{P_n^m(\mu_j)}{a(1-\mu_j^2)} w_j, \quad (3.278)$$

1398 where  $\underline{V}_\lambda^m(\mu_j)$  is the Fourier coefficient of  $\underline{V}_\lambda$  with wavenumber  $m$  at the Gaussian grid line  $\mu_j$ .

The latitudinally differentiated term is handled by integration by parts using zero boundary conditions at the poles:

$$\left\{ \frac{1}{a(1-\mu^2)} (1-\mu^2) \frac{\partial}{\partial \mu} (\underline{V}_\mu) \right\}_n^m = \int_{-1}^1 \frac{1}{a(1-\mu^2)} (1-\mu^2) \frac{\partial}{\partial \mu} (\underline{V}_\mu)^m P_n^m d\mu, \quad (3.279)$$

$$= - \int_{-1}^1 \frac{1}{a(1-\mu^2)} (\underline{V}_\mu)^m (1-\mu^2) \frac{dP_n^m}{d\mu} d\mu. \quad (3.280)$$

Defining the derivative of the associated Legendre polynomial by

$$H_n^m = (1 - \mu^2) \frac{dP_n^m}{d\mu}, \quad (3.281)$$

(3.283) can be written

$$\left\{ \frac{1}{a(1 - \mu^2)} (1 - \mu^2) \frac{\partial}{\partial \mu} (\underline{V}_\mu) \right\}_n^m = - \sum_{j=1}^J (\underline{V}_\mu)_j^m \frac{H_n^m(\mu_j)}{a(1 - \mu_j^2)} w_j. \quad (3.282)$$

Similarly, the  $\nabla^2$  operator in the divergence equation can be converted to spectral space by sequential integration by parts and then application of the relationship

$$\nabla^2 P_n^m(\mu) e^{im\lambda} = \frac{-n(n+1)}{a^2} P_n^m(\mu) e^{im\lambda}, \quad (3.283)$$

to each spherical harmonic function individually so that

$$\left\{ \nabla^2 \underline{D}_\nabla \right\}_n^m = \frac{-n(n+1)}{a^2} \sum_{j=1}^J \underline{D}_\nabla^m(\mu_j) P_n^m(\mu_j) w_j, \quad (3.284)$$

1399 where  $\underline{D}_\nabla^m(\mu)$  is the Fourier coefficient of the original grid variable  $\underline{D}_\nabla$ .

### 1400 3.3.13 Solution of semi-implicit equations

The prognostic equations can be converted to spectral form by summation over the Gaussian grid using (3.274), (3.278), and (3.282). The resulting equation for absolute vorticity is

$$(\underline{\zeta} + f)_n^m = \underline{VS}_n^m, \quad (3.285)$$

where  $(\underline{\zeta} + f)_n^m$  denotes a spherical harmonic coefficient of  $(\underline{\zeta} + f)^{n+1}$ , and the form of  $\underline{VS}_n^m$ , as a summation over the Gaussian grid, is given as

$$\underline{VS}_n^m = \sum_{j=1}^J \left[ \underline{V}^m(\mu_j) P_n^m(\mu_j) + im \underline{V}_\lambda^m(\mu_j) \frac{P_n^m(\mu_j)}{a(1 - \mu_j^2)} + \underline{V}_\mu^m(\mu_j) \frac{H_n^m(\mu_j)}{a(1 - \mu_j^2)} \right] w_j. \quad (3.286)$$

The spectral form of the divergence equation (3.263) becomes

$$\underline{\delta}_n^m = \underline{DS}_n^m + \Delta t \frac{n(n+1)}{a^2} [R \underline{H}^r \underline{T}_n'^m + R (\underline{b}^r + \underline{h}^r) \Pi_n^m], \quad (3.287)$$

where  $\underline{\delta}_n^m$ ,  $\underline{T}_n'^m$ , and  $\Pi_n^m$  are spectral coefficients of  $\underline{\delta}^{n+1}$ ,  $\underline{T}'^{n+1}$ , and  $\Pi^{n+1}$ . The Laplacian of the total temperature in (3.263) is replaced by the equivalent Laplacian of the perturbation temperature in (3.287).  $\underline{DS}_n^m$  is given by

$$\begin{aligned} \underline{DS}_n^m = & \sum_{j=1}^J \left\{ \left[ \underline{D}^m(\mu_j) + \frac{n(n+1)}{a^2} \underline{D}_\nabla^m(\mu_j) \right] P_n^m(\mu_j) \right. \\ & \left. + im \underline{D}_\lambda^m(\mu_j) \frac{P_n^m(\mu_j)}{a(1 - \mu_j^2)} - \underline{D}_\mu^m(\mu_j) \frac{H_n^m(\mu_j)}{a(1 - \mu_j^2)} \right\} w_j. \end{aligned} \quad (3.288)$$

The spectral thermodynamic equation is

$$\underline{T}'_n^m = \underline{TS}_n^m - \Delta t \mathbf{D}^r \underline{\delta}_n^m, \quad (3.289)$$

with  $\underline{TS}_n^m$  defined as

$$\underline{TS}_n^m = \sum_{j=1}^J \left[ \underline{I}^m(\mu_j) P_n^m(\mu_j) - im \underline{I}_\lambda^m(\mu_j) \frac{P_n^m(\mu_j)}{a(1-\mu_j^2)} + \underline{I}_\mu^m(\mu_j) \frac{H_n^m(\mu_j)}{a(1-\mu_j^2)} \right] w_j, \quad (3.290)$$

while the surface pressure equation is

$$\Pi_n^m = PS_n^m - \underline{\delta}_n^m (\underline{\Delta p}^r)^T \frac{\Delta t}{\pi^r}, \quad (3.291)$$

where  $PS_n^m$  is given by

$$PS_n^m = \sum_{j=1}^J PS^m(\mu_j) P_n^m(\mu_j) w_j. \quad (3.292)$$

Equation (3.285) for vorticity is explicit and complete at this point. However, the remaining equations (3.287)–(3.291) are coupled. They are solved by eliminating all variables except  $\underline{\delta}_n^m$ :

$$\mathbf{A}_n \underline{\delta}_n^m = \underline{DS}_n^m + \Delta t \frac{n(n+1)}{a^2} [R \mathbf{H}^r (\underline{TS})_n^m + R (\underline{b}^r + \underline{h}^r) (PS)_n^m], \quad (3.293)$$

where

$$\mathbf{A}_n = \mathbf{I} + \Delta t^2 \frac{n(n+1)}{a^2} \left[ R \mathbf{H}^r \mathbf{D}^r + R (\underline{b}^r + \underline{h}^r) \left( (\underline{\Delta p}^r)^T \frac{1}{\pi^r} \right) \right], \quad (3.294)$$

which is simply a set of  $K$  simultaneous equations for the coefficients with given wavenumbers  $(m, n)$  at each level and is solved by inverting  $\mathbf{A}_n$ . In order to prevent the accumulation of round-off error in the global mean divergence (which if exactly zero initially, should remain exactly zero)  $(\mathbf{A}_o)^{-1}$  is set to the null matrix rather than the identity, and the formal application of (3.293) then always guarantees  $\underline{\delta}_o^m = 0$ . Once  $\underline{\delta}_n^m$  is known,  $\underline{T}'_n^m$  and  $\Pi_n^m$  can be computed from (3.289) and (3.291), respectively, and all prognostic variables are known at time  $n+1$  as spherical harmonic coefficients. Note that the mean component  $\underline{T}'_o^m$  is not necessarily zero since the perturbations are taken with respect to a specified  $\underline{T}^r$ .

### 3.3.14 Horizontal diffusion

As mentioned earlier, the horizontal diffusion in (3.216) and (3.219) is computed implicitly via time splitting after the transformations into spectral space and solution of the semi-implicit equations. In the following, the  $\zeta$  and  $\delta$  equations have a similar form, so we write only the  $\delta$  equation:

$$(\delta^*)_n^m = (\delta^{n+1})_n^m - (-1)^i 2\Delta t K^{(2i)} \left[ \nabla^{2i} (\delta^*)_n^m - (-1)^i (\delta^*)_n^m (2/a^2)^i \right], \quad (3.295)$$

$$(T^*)_n^m = (T^{n+1})_n^m - (-1)^i 2\Delta t K^{(2i)} \left[ \nabla^{2i} (T^*)_n^m \right]. \quad (3.296)$$

The extra term is present in (3.295), (3.299) and (3.301) to prevent damping of uniform rotations. The solutions are just

$$(\delta^*)_n^m = K_n^{(2i)}(\delta) (\delta^{n+1})_n^m, \quad (3.297)$$

$$(T^*)_n^m = K_n^{(2i)}(T) (T^{n+1})_n^m, \quad (3.298)$$

$$K_n^{(2)}(\delta) = \left\{ 1 + 2\Delta t D_n K^{(2)} \left[ \left( \frac{n(n+1)}{a^2} \right) - \frac{2}{a^2} \right] \right\}^{-1}, \quad (3.299)$$

$$K_n^{(2)}(T) = \left\{ 1 + 2\Delta t D_n K^{(2)} \left( \frac{n(n+1)}{a^2} \right) \right\}^{-1}, \quad (3.300)$$

$$K_n^{(4)}(\delta) = \left\{ 1 + 2\Delta t D_n K^{(4)} \left[ \left( \frac{n(n+1)}{a^2} \right)^2 - \frac{4}{a^4} \right] \right\}^{-1}, \quad (3.301)$$

$$K_n^{(4)}(T) = \left\{ 1 + 2\Delta t D_n K^{(4)} \left( \frac{n(n+1)}{a^2} \right)^2 \right\}^{-1}. \quad (3.302)$$

1410  $K_n^{(2)}(\delta)$  and  $K_n^{(4)}(\delta)$  are both set to 1 for  $n = 0$ . The quantity  $D_n$  represents the “Courant  
1411 number limiter”, normally set to 1. However,  $D_n$  is modified to ensure that the CFL criterion  
1412 is not violated in selected upper levels of the model. If the maximum wind speed in any of  
1413 these upper levels is sufficiently large, then  $D_n = 1000$  in that level for all  $n > n_c$ , where  
1414  $n_c = a\Delta t / \max |\mathbf{V}|$ . This condition is applied whenever the wind speed is large enough that  
1415  $n_c < K$ , the truncation parameter in (3.243), and temporarily reduces the effective resolution of  
1416 the model in the affected levels. The number of levels at which this “Courant number limiter”  
1417 may be applied is user-selectable, but it is only used in the top level of the 26 level CAM 5.0  
1418 control runs.

1419 The diffusion of  $T$  is not complete at this stage. In order to make the partial correction from  
1420  $\eta$  to  $p$  in (3.210) local, it is not included until grid-point values are available. This requires  
1421 that  $\nabla^4 \Pi$  also be transformed from spectral to grid-point space. The values of the coefficients  
1422  $K^{(2)}$  and  $K^{(4)}$  for the standard T42 resolution are  $2.5 \times 10^5 \text{m}^2 \text{sec}^{-1}$  and  $1.0 \times 10^{16} \text{m}^4 \text{sec}^{-1}$ ,  
1423 respectively.

### 1424 3.3.15 Initial divergence damping

1425 Occasionally, with poorly balanced initial conditions, the model exhibits numerical instability  
1426 during the beginning of an integration because of excessive noise in the solution. Therefore, an  
1427 optional divergence damping is included in the model to be applied over the first few days. The  
1428 damping has an initial e-folding time of  $\Delta t$  and linearly decreases to 0 over a specified number  
1429 of days,  $t_D$ , usually set to be 2. The damping is computed implicitly via time splitting after the  
1430 horizontal diffusion.

$$r = \max \left[ \frac{1}{\Delta t} (t_D - t) / t_D, 0 \right] \quad (3.303)$$

$$(\delta^*)_n^m = \frac{1}{1 + 2\Delta t r} (\delta^*)_n^m \quad (3.304)$$

### 1431 3.3.16 Transformation from spectral to physical space

After the prognostic variables are completed at time  $n+1$  in spectral space  $\left(\underline{(\zeta+f)^*}\right)_n^m, \underline{(\delta^*)}_n^m, \underline{(T^*)}_n^m, \underline{(\Pi^{n+1})}_n^m$  they are transformed to grid space. For a variable  $\psi$ , the transformation is given by

$$\psi(\lambda, \mu) = \sum_{m=-M}^M \left[ \sum_{n=|m|}^{\mathcal{N}(m)} \psi_n^m P_n^m(\mu) \right] e^{im\lambda}. \quad (3.305)$$

The inner sum is done essentially as a vector product over  $n$ , and the outer is again performed by an FFT subroutine. The term needed for the remainder of the diffusion terms,  $\nabla^4 \Pi$ , is calculated from

$$\nabla^4 \Pi^{n+1} = \sum_{m=-M}^M \left[ \sum_{n=|m|}^{\mathcal{N}(m)} \left( \frac{n(n+1)}{a^2} \right)^2 \underline{(\Pi^{n+1})}_n^m P_n^m(\mu) \right] e^{im\lambda}. \quad (3.306)$$

In addition, the derivatives of  $\Pi$  are needed on the grid for the terms involving  $\nabla \Pi$  and  $\mathbf{V} \cdot \nabla \Pi$ ,

$$\mathbf{V} \cdot \nabla \Pi = \frac{U}{a(1-\mu^2)} \frac{\partial \Pi}{\partial \lambda} + \frac{V}{a(1-\mu^2)} (1-\mu^2) \frac{\partial \Pi}{\partial \mu}. \quad (3.307)$$

These required derivatives are given by

$$\frac{\partial \Pi}{\partial \lambda} = \sum_{m=-M}^M im \left[ \sum_{n=|m|}^{\mathcal{N}(m)} \Pi_n^m P_n^m(\mu) \right] e^{im\lambda}, \quad (3.308)$$

and using (3.281),

$$(1-\mu^2) \frac{\partial \Pi}{\partial \mu} = \sum_{m=-M}^M \left[ \sum_{n=|m|}^{\mathcal{N}(m)} \Pi_n^m H_n^m(\mu) \right] e^{im\lambda}, \quad (3.309)$$

which involve basically the same operations as (3.306). The other variables needed on the grid are  $U$  and  $V$ . These can be computed directly from the absolute vorticity and divergence coefficients using the relations

$$(\zeta + f)_n^m = -\frac{n(n+1)}{a^2} \psi_n^m + f_n^m, \quad (3.310)$$

$$\delta_n^m = -\frac{n(n+1)}{a^2} \chi_n^m, \quad (3.311)$$

in which the only nonzero  $f_n^m$  is  $f_1^o = \Omega/\sqrt{.375}$ , and

$$U = \frac{1}{a} \frac{\partial \chi}{\partial \lambda} - \frac{(1-\mu^2)}{a} \frac{\partial \psi}{\partial \mu}, \quad (3.312)$$

$$V = \frac{1}{a} \frac{\partial \psi}{\partial \lambda} + \frac{(1-\mu^2)}{a} \frac{\partial \chi}{\partial \mu}. \quad (3.313)$$

Thus, the direct transformation is

$$\begin{aligned} U &= - \sum_{m=-M}^M a \sum_{n=|m|}^{\mathcal{N}(m)} \left[ \frac{im}{n(n+1)} \delta_n^m P_n^m(\mu) - \frac{1}{n(n+1)} (\zeta + f)_n^m H_n^m(\mu) \right] e^{im\lambda} \\ &\quad - \frac{a}{2} \frac{\Omega}{\sqrt{0.375}} H_1^o, \end{aligned} \quad (3.314)$$

$$V = - \sum_{m=-M}^M a \sum_{n=|m|}^{\mathcal{N}(m)} \left[ \frac{im}{n(n+1)} (\zeta + f)_n^m P_n^m(\mu) + \frac{1}{n(n+1)} \delta_n^m H_n^m(\mu) \right] e^{im\lambda}. \quad (3.315)$$

The horizontal diffusion tendencies are also transformed back to grid space. The spectral coefficients for the horizontal diffusion tendencies follow from (3.295) and (3.296):

$$F_{T_H}(T^*)_n^m = (-1)^{i+1} K^{2i} [\nabla^{2i}(T^*)]_n^m, \quad (3.316)$$

$$F_{\zeta_H}((\zeta + f)^*)_n^m = (-1)^{i+1} K^{2i} \left\{ \nabla^{2i}(\zeta + f)^* - (-1)^i (\zeta + f)^* (2/a^2)^i \right\}, \quad (3.317)$$

$$F_{\delta_H}(\delta^*)_n^m = (-1) K^{2i} \left\{ \nabla^{2i}(\delta^*) - (-1)^i \delta^* (2/a^2)^i \right\}, \quad (3.318)$$

1432 using  $i = 1$  or  $2$  as appropriate for the  $\nabla^2$  or  $\nabla^4$  forms. These coefficients are transformed to  
1433 grid space following (3.242) for the  $T$  term and (3.314) and (3.315) for vorticity and divergence.  
1434 Thus, the vorticity and divergence diffusion tendencies are converted to equivalent  $U$  and  $V$   
1435 diffusion tendencies.

### 1436 3.3.17 Horizontal diffusion correction

After grid-point values are calculated, frictional heating rates are determined from the momentum diffusion tendencies and are added to the temperature, and the partial correction of the  $\nabla^4$  diffusion from  $\eta$  to  $p$  surfaces is applied to  $T$ . The frictional heating rate is calculated from the kinetic energy tendency produced by the momentum diffusion

$$F_{F_H} = -u^{n-1} F_{u_H}(u^*)/c_p^* - v^{n-1} F_{v_H}(v^*)/c_p^*, \quad (3.319)$$

where  $F_{u_H}$ , and  $F_{v_H}$  are the momentum equivalent diffusion tendencies, determined from  $F_{\zeta_H}$  and  $F_{\delta_H}$  just as  $U$  and  $V$  are determined from  $\zeta$  and  $\delta$ , and

$$c_p^* = c_p \left[ 1 + \left( \frac{c_{p_v}}{c_p} - 1 \right) q^{n+1} \right]. \quad (3.320)$$

These heating rates are then combined with the correction,

$$\hat{T}_k^{n+1} = T_k^* + (2\Delta t F_{F_H})_k + 2\Delta t \left( \pi B \frac{\partial T^*}{\partial p} \right)_k K^{(4)} \nabla^4 \Pi^{n+1}. \quad (3.321)$$

The vertical derivatives of  $T^*$  (where the  $*$  notation is dropped for convenience) are defined by

$$\left( \pi B \frac{\partial T}{\partial p} \right)_1 = \frac{\pi}{2\Delta p_1} \left[ B_{1+\frac{1}{2}} (T_2 - T_1) \right] , \quad (3.322)$$

$$\left( \pi B \frac{\partial T}{\partial p} \right)_k = \frac{\pi}{2\Delta p_k} \left[ B_{k+\frac{1}{2}} (T_{k+1} - T_k) + B_{k-\frac{1}{2}} (T_k - T_{k-1}) \right] , \quad (3.323)$$

$$\left( \pi B \frac{\partial T}{\partial p} \right)_K = \frac{\pi}{2\Delta p_K} \left[ B_{K-\frac{1}{2}} (T_K - T_{K-1}) \right] . \quad (3.324)$$

The corrections are added to the diffusion tendencies calculated earlier (3.316) to give the total temperature tendency for diagnostic purposes:

$$\hat{F}_{T_H}(T^*)_k = F_{T_H}(T^*)_k + (2\Delta t F_{F_H})_k + 2\Delta t B_k \left( \pi \frac{\partial T^*}{\partial p} \right)_k K^{(4)} \nabla^4 \Pi^{n+1} . \quad (3.325)$$

### 1437 3.3.18 Semi-Lagrangian Tracer Transport

The forecast equation for water vapor specific humidity and constituent mixing ratio in the  $\eta$  system is from (3.164) excluding sources and sinks.

$$\frac{dq}{dt} = \frac{\partial q}{\partial t} + \mathbf{V} \cdot \nabla q + \dot{\eta} \frac{\partial p}{\partial \eta} \frac{\partial q}{\partial p} = 0 \quad (3.326)$$

or

$$\frac{dq}{dt} = \frac{\partial q}{\partial t} + \mathbf{V} \cdot \nabla q + \dot{\eta} \frac{\partial q}{\partial \eta} = 0 . \quad (3.327)$$

1438 Equation (3.327) is more economical for the semi-Lagrangian vertical advection, as  $\Delta\eta$  does not  
 1439 vary in the horizontal, while  $\Delta p$  does. Written in this form, the  $\eta$  advection equations look  
 1440 exactly like the  $\sigma$  equations.

The parameterizations are time-split in the moisture equation. The tendency sources have already been added to the time level  $(n - 1)$ . The semi-Lagrangian advection step is subdivided into horizontal and vertical advection sub-steps, which, in an Eulerian form, would be written

$$q^* = q^{n-1} + 2\Delta t (\mathbf{V} \cdot \nabla q)^n \quad (3.328)$$

and

$$q^{n+1} = q^* + 2\Delta t \left( \dot{\eta} \frac{\partial q}{\partial n} \right)^n . \quad (3.329)$$

In the semi-Lagrangian form used here, the general form is

$$q^* = L_{\lambda\varphi} (q^{n-1}) , \quad (3.330)$$

$$q^{n+1} = L_\eta (q^*) . \quad (3.331)$$

1441 Equation (3.330) represents the horizontal interpolation of  $q^{n-1}$  at the departure point calculated  
 1442 assuming  $\dot{\eta} = 0$ . Equation (3.331) represents the vertical interpolation of  $q^*$  at the departure  
 1443 point, assuming  $\mathbf{V} = 0$ .

The horizontal departure points are found by first iterating for the mid-point of the trajectory, using winds at time  $n$ , and a first guess as the location of the mid-point of the previous time step

$$\lambda_M^{k+1} = \lambda_A - \Delta t u^n(\lambda_M^k, \varphi_M^k) / a \cos \varphi_M^k, \quad (3.332)$$

$$\varphi_M^{k+1} = \varphi_A - \Delta t v^n(\lambda_M^k, \varphi_M^k) / a, \quad (3.333)$$

where subscript  $A$  denotes the arrival (Gaussian grid) point and subscript  $M$  the midpoint of the trajectory. The velocity components at  $(\lambda_M^k, \varphi_M^k)$  are determined by Lagrange cubic interpolation. For economic reasons, the equivalent Hermite cubic interpolant with cubic derivative estimates is used at some places in this code. The equations will be presented later.

Once the iteration of (3.332) and (3.333) is complete, the departure point is given by

$$\lambda_D = \lambda_A - 2\Delta t u^n(\lambda_M, \varphi_M) / a \cos \varphi_M, \quad (3.334)$$

$$\varphi_D = \varphi_A - 2\Delta t v^n(\lambda_M, \varphi_M) / a, \quad (3.335)$$

where the subscript  $D$  denotes the departure point.

The form given by (3.332)-(3.335) is inaccurate near the poles and thus is only used for arrival points equatorward of  $70^\circ$  latitude. Poleward of  $70^\circ$  we transform to a local geodesic coordinate for the calculation at each arrival point. The local geodesic coordinate is essentially a rotated spherical coordinate system whose equator goes through the arrival point. Details are provided in [Williamson and Rasch \[1989\]](#). The transformed system is rotated about the axis through  $(\lambda_A - \frac{\pi}{2}, 0)$  and  $(\lambda_A + \frac{\pi}{2}, 0)$ , by an angle  $\varphi_A$  so the equator goes through  $(\lambda_A, \varphi_A)$ . The longitude of the transformed system is chosen to be zero at the arrival point. If the local geodesic system is denoted by  $(\lambda', \varphi')$ , with velocities  $(u', v')$ , the two systems are related by

$$\sin \phi' = \sin \phi \cos \phi_A - \cos \phi \sin \phi_A \cos(\lambda_A - \lambda), \quad (3.336)$$

$$\sin \phi = \sin \phi' \cos \phi_A + \cos \phi' \sin \phi_A \cos \lambda', \quad (3.337)$$

$$\sin \lambda' \cos \phi' = -\sin(\lambda_A - \lambda) \cos \phi, \quad (3.338)$$

$$\begin{aligned} v' \cos \phi' &= v [\cos \phi \cos \phi_A + \sin \phi \sin \phi_A \cos(\lambda_A - \lambda)] \\ &\quad - u \sin \phi_A \sin(\lambda_A - \lambda), \end{aligned} \quad (3.339)$$

$$u' \cos \lambda' - v' \sin \lambda' \sin \phi' = u \cos(\lambda_A - \lambda) + v \sin \phi \sin(\lambda_A - \lambda). \quad (3.340)$$

The calculation of the departure point in the local geodesic system is identical to (3.332)-(3.335) with all variables carrying a prime. The equations can be simplified by noting that  $(\lambda'_A, \varphi'_A) = (0, 0)$  by design and  $u'(\lambda'_A, \varphi'_A) = u(\lambda_A, \varphi_A)$  and  $v'(\lambda'_A, \varphi'_A) = v(\lambda_A, \varphi_A)$ . The interpolations are always done in global spherical coordinates.

The interpolants are most easily defined on the interval  $0 \leq \theta \leq 1$ . Define

$$\theta = (x_D - x_i) / (x_{i+1} - x_i), \quad (3.341)$$

where  $x$  is either  $\lambda$  or  $\varphi$  and the departure point  $x_D$  falls within the interval  $(x_i, x_{i+1})$ . Following (23) of [\[Rasch and Williamson, 1990\]](#) with  $r_i = 3$  the Hermite cubic interpolant is given by

$$\begin{aligned} q_D &= q_{i+1} [3 - 2\theta] \theta^2 - d_{i+1} [h_i \theta^2 (1 - \theta)] \\ &\quad + q_i [3 - 2(1 - \theta)] (1 - \theta)^2 + d_i [h_i \theta (1 - \theta)^2] \end{aligned} \quad (3.342)$$

1453 where  $q_i$  is the value at the grid point  $x_i$ ,  $d_i$  is the derivative estimate given below, and  $h_i =$   
 1454  $x_{i+1} - x_i$ .

Following (3.2.12) and (3.2.13) of [Hildebrand \[1956\]](#), the Lagrangian cubic polynomial interpolant used for the velocity interpolation, is given by

$$f_D = \sum_{j=-1}^2 \ell_j(x_D) f_{i+j} \quad (3.343)$$

where

$$\ell_j(x_D) = \frac{(x_D - x_{i-1}) \dots (x_D - x_{i+j-1}) (x_D - x_{i+j+1}) \dots (x_D - x_{i+2})}{(x_{i+j} - x_{i-1}) \dots (x_{i+j} - x_{i+j-1}) (x_{i+j} - x_{i+j+1}) \dots (x_{i+j} - x_{i+2})} \quad (3.344)$$

1455 where  $f$  can represent either  $u$  or  $v$ , or their counterparts in the geodesic coordinate system.

The derivative approximations used in (3.342) for  $q$  are obtained by differentiating (3.343) with respect to  $x_D$ , replacing  $f$  by  $q$  and evaluating the result at  $x_D$  equal  $x_i$  and  $x_{i+1}$ . With these derivative estimates, the Hermite cubic interpolant (3.342) is equivalent to the Lagrangian (3.343). If we denote the four point stencil  $(x_{i-1}, x_i, x_{i+1}, x_{i+2})$  by  $(x_1, x_2, x_3, x_4)$ , the cubic derivative estimates are

$$d_2 = \left[ \frac{(x_2 - x_3)(x_2 - x_4)}{(x_1 - x_2)(x_1 - x_3)(x_1 - x_4)} \right] q_1 \quad (3.345)$$

$$- \left[ \frac{1}{(x_1 - x_2)} - \frac{1}{(x_2 - x_3)} - \frac{1}{(x_2 - x_4)} \right] q_2 \quad (3.346)$$

$$+ \left[ \frac{(x_2 - x_1)(x_2 - x_4)}{(x_1 - x_3)(x_2 - x_3)(x_3 - x_4)} \right] q_3 \quad (3.347)$$

$$- \left[ \frac{(x_2 - x_1)(x_2 - x_3)}{(x_1 - x_4)(x_2 - x_4)(x_3 - x_4)} \right] q_4 \quad (3.348)$$

and

$$d_3 = \left[ \frac{(x_3 - x_2)(x_3 - x_4)}{(x_1 - x_2)(x_1 - x_3)(x_1 - x_4)} \right] q_1 \quad (3.349)$$

$$- \left[ \frac{(x_3 - x_1)(x_3 - x_4)}{(x_1 - x_2)(x_2 - x_3)(x_2 - x_4)} \right] q_2 \quad (3.350)$$

$$- \left[ \frac{1}{(x_1 - x_3)} + \frac{1}{(x_2 - x_3)} - \frac{1}{(x_3 - x_4)} \right] q_3 \quad (3.351)$$

$$- \left[ \frac{(x_3 - x_1)(x_3 - x_2)}{(x_1 - x_4)(x_2 - x_4)(x_3 - x_4)} \right] q_4 \quad (3.352)$$

1456 The two dimensional  $(\lambda, \varphi)$  interpolant is obtained as a tensor product application of the  
 1457 one-dimensional interpolants, with  $\lambda$  interpolations done first. Assume the departure point falls  
 1458 in the grid box  $(\lambda_i, \lambda_{i+1})$  and  $(\varphi_i, \varphi_{i+1})$ . Four  $\lambda$  interpolations are performed to find  $q$  values  
 1459 at  $(\lambda_D, \varphi_{j-1})$ ,  $(\lambda_D, \varphi_j)$ ,  $(\lambda_D, \varphi_{j+1})$ , and  $(\lambda_D, \varphi_{j+2})$ . This is followed by one interpolation in  $\varphi$   
 1460 using these four values to obtain the value at  $(\lambda_D, \varphi_D)$ . Cyclic continuity is used in longitude.  
 1461 In latitude, the grid is extended to include a pole point (row) and one row across the pole. The

<sup>1462</sup> pole row is set equal to the average of the row next to the pole for  $q$  and to wavenumber 1  
<sup>1463</sup> components for  $u$  and  $v$ . The row across the pole is filled with the values from the first row  
<sup>1464</sup> below the pole shifted  $\pi$  in longitude for  $q$  and minus the value shifted by  $\pi$  in longitude for  $u$   
<sup>1465</sup> and  $v$ .

Once the departure point is known, the constituent value of  $q^* = q_D^{n-1}$  is obtained as indicated in (3.330) by Hermite cubic interpolation (3.342), with cubic derivative estimates (3.343) and (3.344) modified to satisfy the Sufficient Condition for Monotonicity with  $C^\circ$  continuity (SCMO) described below. Define  $\Delta_i q$  by

$$\Delta_i q = \frac{q_{i+1} - q_i}{x_{i+1} - x_i} . \quad (3.353)$$

First, if  $\Delta_i q = 0$  then

$$d_i = d_{i+1} = 0 . \quad (3.354)$$

Then, if either

$$0 \leq \frac{d_i}{\Delta_i q} \leq 3 \quad (3.355)$$

or

$$0 \leq \frac{d_{i+1}}{\Delta_i q} \leq 3 \quad (3.356)$$

<sup>1466</sup> is violated,  $d_i$  or  $d_{i+1}$  is brought to the appropriate bound of the relationship. These conditions  
<sup>1467</sup> ensure that the Hermite cubic interpolant is monotonic in the interval  $[x_i, x_{i+1}]$ .

The horizontal semi-Lagrangian sub-step (3.330) is followed by the vertical step (3.331). The vertical velocity  $\dot{\eta}$  is obtained from that diagnosed in the dynamical calculations (3.222) by

$$(\dot{\eta})_{k+\frac{1}{2}} = \left( \dot{\eta} \frac{\partial p}{\partial \eta} \right)_{k+\frac{1}{2}} \Bigg/ \left( \frac{p_{k+1} - p_k}{\eta_{k+1} - \eta_k} \right) , \quad (3.357)$$

with  $\eta_k = A_k + B_k$ . Note, this is the only place that the model actually requires an explicit specification of  $\eta$ . The mid-point of the vertical trajectory is found by iteration

$$\eta_M^{k+1} = \eta_A - \Delta t \dot{\eta}^n (\eta_M^k) . \quad (3.358)$$

Note, the arrival point  $\eta_A$  is a mid-level point where  $q$  is carried, while the  $\dot{\eta}$  used for the interpolation to mid-points is at interfaces. We restrict  $\eta_M$  by

$$\eta_1 \leq \eta_M \leq \eta_K , \quad (3.359)$$

which is equivalent to assuming that  $q$  is constant from the surface to the first model level and above the top  $q$  level. Once the mid-point is determined, the departure point is calculated from

$$\eta_D = \eta_A - 2 \Delta t \dot{\eta}^n (\eta_M) , \quad (3.360)$$

with the restriction

$$\eta_1 \leq \eta_D \leq \eta_K . \quad (3.361)$$

<sup>1468</sup> The appropriate values of  $\dot{\eta}$  and  $q$  are determined by interpolation (3.342), with the derivative  
<sup>1469</sup> estimates given by (3.343) and (3.344) for  $i = 2$  to  $K - 1$ . At the top and bottom we assume  
<sup>1470</sup> a zero derivative (which is consistent with (3.359) and (3.361)),  $d_i = 0$  for the interval  $k = 1$ ,

1471 and  $\delta_{i+1} = 0$  for the interval  $k = K - 1$ . The estimate at the interior end of the first and last  
1472 grid intervals is determined from an uncentered cubic approximation; that is  $d_{i+1}$  at the  $k = 1$   
1473 interval is equal to  $d_i$  from the  $k = 2$  interval, and  $d_i$  at the  $k = K - 1$  interval is equal to  $d_{i+1}$   
1474 at the  $k = K - 2$  interval. The monotonic conditions (3.355) to (3.356) are applied to the  $q$   
1475 derivative estimates.

### 1476 3.3.19 Mass fixers

1477 This section describes original and modified fixers used for the Eulerian and semi-Lagrangian  
1478 dynamical cores.

1479 Let  $\pi^0$ ,  $\Delta p^0$  and  $q^0$  denote the values of air mass, pressure intervals, and water vapor specific  
1480 humidity at the beginning of the time step (which are the same as the values at the end of the  
1481 previous time step.)

1482  $\pi^+$ ,  $\Delta p^+$  and  $q^+$  are the values after fixers are applied at the end of the time step.

1483  $\pi^-$ ,  $\Delta p^-$  and  $q^-$  are the values after the parameterizations have updated the moisture field  
1484 and tracers.

1485 Since the physics parameterizations do not change the surface pressure,  $\pi^-$  and  $\Delta p^-$  are also  
1486 the values at the beginning of the time step.

The fixers which ensure conservation are applied to the dry atmospheric mass, water vapor specific humidity and constituent mixing ratios. For water vapor and atmospheric mass the desired discrete relations, following [Williamson and Olson \[1994a\]](#) are

$$\int_2 \pi^+ - \int_3 q^+ \Delta p^+ = \mathbf{P}, \quad (3.362)$$

$$\int_3 q^+ \Delta p^+ = \int_3 q^- \Delta p^-, \quad (3.363)$$

where  $\mathbf{P}$  is the dry mass of the atmosphere. From the definition of the vertical coordinate,

$$\Delta p = p_0 \Delta A + \pi \Delta B, \quad (3.364)$$

and the integral  $\int_2$  denotes the normal Gaussian quadrature while  $\int_3$  includes a vertical sum followed by Gaussian quadrature. The actual fixers are chosen to have the form

$$\pi^+ (\lambda, \varphi) = \mathbf{M} \hat{\pi}^+ (\lambda, \varphi), \quad (3.365)$$

preserving the horizontal gradient of  $\Pi$ , which was calculated earlier during the inverse spectral transform, and

$$q^+ (\lambda, \varphi, \eta) = \hat{q}^+ + \alpha \eta \hat{q}^+ |\hat{q}^+ - q^-|. \quad (3.366)$$

In (3.365) and (3.366) the  $(\hat{\phantom{a}})$  denotes the provisional value before adjustment. The form (3.366) forces the arbitrary corrections to be small when the mixing ratio is small and when the change made to the mixing ratio by the advection is small. In addition, the  $\eta$  factor is included to make the changes approximately proportional to mass per unit volume [[Rasch et al., 1995](#)]. Satisfying

(3.362) and (3.363) gives

$$\alpha = \frac{\int_3 q^- \Delta p^- - \int_3 \hat{q}^+ p_0 \Delta A - M \int_3 \hat{q}^+ \hat{\pi}^+ \Delta B}{\int_3 \eta \hat{q}^+ |\hat{q}^+ - q^-| p_0 \Delta A + M \int_3 \eta \hat{q}^+ |\hat{q}^+ - q^-| \hat{\pi}^+ \Delta B} \quad (3.367)$$

and

$$\mathbf{M} = \left( \mathbf{P} + \int_3 q^- \Delta p^- \right) \bigg/ \int_2 \hat{\pi}^+ . \quad (3.368)$$

Note that water vapor and dry mass are corrected simultaneously. Additional advected constituents are treated as mixing ratios normalized by the mass of dry air. This choice was made so that as the water vapor of a parcel changed, the constituent mixing ratios would not change. Thus the fixers which ensure conservation involve the dry mass of the atmosphere rather than the moist mass as in the case of the specific humidity above. Let  $\chi$  denote the mixing ratio of constituents. Historically we have used the following relationship for conservation:

$$\int_3 \chi^+ (1 - q^+) \Delta p^+ = \int_3 \chi^- (1 - q^-) \Delta p^- . \quad (3.369)$$

The term  $(1 - q) \Delta p$  defines the dry air mass in a layer. Following [Rasch et al. \[1995\]](#) the change made by the fixer has the same form as (3.366)

$$\chi^+ (\lambda, \varphi, \eta) = \hat{\chi}^+ + \alpha_\chi \eta \hat{\chi}^+ |\hat{\chi}^+ - \chi^-| . \quad (3.370)$$

Substituting (3.370) into (3.369) and using (3.365) through (3.368) gives

$$\alpha_\chi = \frac{\int_3 \chi^- (1 - q^-) \Delta p^- - \int_{A,B} \hat{\chi}^+ (1 - \hat{q}^+) \Delta \hat{p}^+ + \alpha \int_{A,B} \hat{\chi}^+ \eta \hat{q}^+ |\hat{q}^+ - q^-| \Delta p}{\int_{A,B} \eta \hat{\chi}^+ |\hat{\chi}^+ - \chi^-| (1 - \hat{q}^+) \Delta p - \alpha \int_{A,B} \eta \hat{\chi}^+ |\hat{\chi}^+ - \chi^-| \eta \hat{q}^+ |\hat{q}^+ - q^-| \Delta p} , \quad (3.371)$$

where the following shorthand notation is adopted:

$$\int_{A,B} (\ ) \Delta p = \int_3 (\ ) p_0 \Delta A + M \int_3 (\ ) p_s \Delta B . \quad (3.372)$$

We note that there is a small error in (3.369). Consider a situation in which moisture is transported by a physical parameterization, but there is no source or sink of moisture. Under this circumstance  $q^- \neq q^0$ , but the surface pressure is not allowed to change. Since  $(1 - q^-) \Delta p^- \neq (1 - q^0) \Delta p^0$ , there is an implied change of dry mass of dry air in the layer, and even in circumstances where there is no change of dry mixing ratio  $\chi$  there would be an implied change in mass of the tracer. The solution to this inconsistency is to define a dry air mass *only once* within the model time step, and use it consistently throughout the model. In this revision, we have chosen to fix the dry air mass in the model time step where the surface pressure is updated, e.g. at the end of the model time step. Therefore, we now replace (3.369) with

$$\int_3 \chi^+ (1 - q^+) \Delta p^+ = \int_3 \chi^- (1 - q^0) \Delta p^0 . \quad (3.373)$$

1487 There is a corresponding change in the first term of the numerator of (3.371) in which  
 1488  $q^-$  is replaced by  $q^0$ . CAM 5.0 uses (3.371) for water substances and constituents affecting the  
 1489 temperature field to prevent changes to the IPCC simulations. In the future, constituent fields  
 1490 may use a *corrected* version of (3.371).

### 1491 3.3.20 Energy Fixer

Following notation in section 3.3.19, the total energy integrals are

$$\int_3 \frac{1}{g} \left[ c_p T^+ + \Phi_s + \frac{1}{2} (u^{+2} + v^{+2}) \right] \Delta p^+ = \mathbf{E} \quad (3.374)$$

$$\mathbf{E} = \int_3 \frac{1}{g} \left[ c_p T^- + \Phi_s + \frac{1}{2} (u^{-2} + v^{-2}) \right] \Delta p^- + \mathbf{S} \quad (3.375)$$

$$\mathbf{S} = \int_2 [(FSNT - FLNT) - (FSNS - FLNS - SHFLX - \rho_{H_2O} L_v PRECT) -] \Delta t \quad (3.376)$$

$$\mathbf{S} = \int_2 [(FSNT - FLNT) - (FSNS - FLNS - SHFLX)] \Delta t \quad (3.377)$$

$$+ \int_2 [\rho_{H_2O} L_v (PRECL + PRECC) + \rho_{H_2O} L_i (PRESL + PRES) ] \Delta t \quad (3.378)$$

where  $\mathbf{S}$  is the net source of energy from the parameterizations.  $FSNT$  is the net downward solar flux at the model top,  $FLNT$  is the net upward longwave flux at the model top,  $FSNS$  is the net downward solar flux at the surface,  $FLNS$  is the net upward longwave flux at the surface,  $SHFLX$  is the surface sensible heat flux, and  $PRECT$  is the total precipitation during the time step. From equation (3.365)

$$\pi^+ (\lambda, \varphi) = \mathbf{M} \hat{\pi}^+ (\lambda, \varphi) \quad (3.379)$$

and from (3.364)

$$\Delta p = p_0 \Delta A + \pi \Delta B \quad (3.380)$$

The energy fixer is chosen to have the form

$$T^+ (\lambda, \varphi, \eta) = \hat{T}^+ + \beta \quad (3.381)$$

$$u^+ (\lambda, \varphi, \eta) = \hat{u}^+ \quad (3.382)$$

$$v^+ (\lambda, \varphi, \eta) = \hat{v}^+ \quad (3.383)$$

Then

$$\beta = \frac{g \mathbf{E} - \int_3 \left[ c_p \hat{T}^+ + \Phi_s + \frac{1}{2} (\hat{u}^{+2} + \hat{v}^{+2}) \right] p_0 \Delta A - \mathbf{M} \int_3 \left[ c_p \hat{T}^+ + \Phi_s + \frac{1}{2} (\hat{u}^{+2} + \hat{v}^{+2}) \right] \hat{\pi}^+ \Delta B}{\int_3 c_p p_0 \Delta A + \mathbf{M} \int_3 c_p \hat{\pi}^+ \Delta B} \quad (3.384)$$

### 1492 3.3.21 Statistics Calculations

At each time step, selected global average statistics are computed for diagnostic purposes when the model is integrated with the Eulerian and semi-Lagrangian dynamical cores. Let  $\int_3$  denote a global and vertical average and  $\int_2$  a horizontal global average. For an arbitrary variable  $\psi$ , these are defined by

$$\int_3 \psi dV = \sum_{k=1}^K \sum_{j=1}^J \sum_{i=1}^I \psi_{ijk} w_j \left( \frac{\Delta p_k}{\pi} \right) / 2I, \quad (3.385)$$

and

$$\int_2 \psi dA = \sum_{j=1}^J \sum_{i=1}^I \psi_{ijk} w_j / 2I, \quad (3.386)$$

where recall that

$$\sum_{j=1}^J w_j = 2. \quad (3.387)$$

The quantities monitored are:

$$\text{global rms } (\zeta + f)(\text{s}^{-1}) = \left[ \int_3 (\zeta^n + f)^2 dV \right]^{1/2}, \quad (3.388)$$

$$\text{global rms } \delta(\text{s}^{-1}) = \left[ \int_3 (\delta^n)^2 dV \right]^{1/2}, \quad (3.389)$$

$$\text{global rms } T (\text{K}) = \left[ \int_3 (T^r + T'^n)^2 dV \right]^{1/2}, \quad (3.390)$$

$$\text{global average mass times } g (\text{Pa}) = \int_2 \pi^n dA, \quad (3.391)$$

$$\text{global average mass of moisture } (\text{kg m}^{-2}) = \int_3 \pi^n q^n / gdV. \quad (3.392)$$

### 1493 3.3.22 Reduced grid

1494 The Eulerian core and semi-Lagrangian tracer transport can be run on reduced grids. The term  
 1495 reduced grid generally refers to a grid based on latitude and longitude circles in which the longitu-  
 1496 dinal grid increment increases at latitudes approaching the poles so that the longitudinal distance  
 1497 between grid points is reasonably constant. Details are provided in [Williamson and Rosinski,  
 1498 2000]. This option provides a saving of computer time of up to 25%.

## 1499 3.4 Semi-Lagrangian Dynamical Core

### 1500 3.4.1 Introduction

1501 The two-time-level semi-implicit semi-Lagrangian spectral transform dynamical core in  
 1502 CAM 5.0 evolved from the three-time-level CCM2 semi-Lagrangian version detailed in

1503 Williamson and Olson [1994a] hereafter referred to as W&O94. As a first approximation,  
 1504 to convert from a three-time-level scheme to a two-time-level scheme, the time level index  $n-1$   
 1505 becomes  $n$ , the time level index  $n$  becomes  $n+\frac{1}{2}$ , and  $2\Delta t$  becomes  $\Delta t$ . Terms needed at  $n+\frac{1}{2}$   
 1506 are extrapolated in time using time  $n$  and  $n-1$  terms, except the Coriolis term which is implicit  
 1507 as the average of time  $n$  and  $n+1$ . This leads to a more complex semi-implicit equation to solve.  
 1508 Additional changes have been made in the scheme to incorporate advances in semi-Lagrangian  
 1509 methods developed since W&O94. In the following, reference is made to changes from the  
 1510 scheme developed in W&O94. The reader is referred to that paper for additional details of  
 1511 the derivation of basic aspects of the semi-Lagrangian approximations. Only the details of the  
 1512 two-time-level approximations are provided here.

### 1513 3.4.2 Vertical coordinate and hydrostatic equation

The semi-Lagrangian dynamical core adopts the same hybrid vertical coordinate ( $\eta$ ) as the Eulerian core defined by

$$p(\eta, p_s) = A(\eta)p_o + B(\eta)p_s, \quad (3.393)$$

1514 where  $p$  is pressure,  $p_s$  is surface pressure, and  $p_o$  is a specified constant reference pressure. The  
 1515 coefficients  $A$  and  $B$  specify the actual coordinate used. As mentioned by Simmons and Burridge  
 1516 [1981] and implemented by Simmons and Strüfing [1981] and Simmons and Strüfing [1983], the  
 1517 coefficients  $A$  and  $B$  are defined only at the discrete model levels. This has implications in the  
 1518 continuity equation development which follows.

In the  $\eta$  system the hydrostatic equation is approximated in a general way by

$$\Phi_k = \Phi_s + R \sum_{l=k}^K H_{kl}(p) T_{vl} \quad (3.394)$$

1519 where  $k$  is the vertical grid index running from 1 at the top of the model to  $K$  at the first model  
 1520 level above the surface,  $\Phi_k$  is the geopotential at level  $k$ ,  $\Phi_s$  is the surface geopotential,  $T_v$  is the  
 1521 virtual temperature, and  $R$  is the gas constant. The matrix  $H$ , referred to as the hydrostatic  
 1522 matrix, represents the discrete approximation to the hydrostatic integral and is left unspecified  
 1523 for now. It depends on pressure, which varies from horizontal point to point.

### 1524 3.4.3 Semi-implicit reference state

The semi-implicit equations are linearized about a reference state with constant  $T^r$  and  $p_s^r$ . We choose

$$T^r = 350\text{K}, \quad p_s^r = 10^5\text{Pa} \quad (3.395)$$

### 1525 3.4.4 Perturbation surface pressure prognostic variable

To ameliorate the mountain resonance problem, Ritchie and Tanguay [1996] introduce a perturbation  $\ln p_s$  surface pressure prognostic variable

$$\ln p'_s = \ln p_s - \ln p_s^* \quad (3.396)$$

$$\ln p_s^* = -\frac{\Phi_s}{RT^r} \quad (3.397)$$

1526 The perturbation surface pressure,  $\ln p'_s$ , is never actually used as a grid point variable in the  
 1527 CAM 5.0 code. It is only used for the semi-implicit development and solution. The total  $\ln p_s$   
 1528 is reclaimed in spectral space from the spectral coefficients of  $\Phi_s$  immediately after the semi-  
 1529 implicit equations are solved, and transformed back to spectral space along with its derivatives.  
 1530 This is in part because  $\nabla^4 \ln p_s$  is needed for the horizontal diffusion correction to pressure  
 1531 surfaces. However the semi-Lagrangian CAM 5.0 default is to run with no horizontal diffusion.

### 1532 3.4.5 Extrapolated variables

Variables needed at time  $(n + \frac{1}{2})$  are obtained by extrapolation

$$( \ )^{n+\frac{1}{2}} = \frac{3}{2} ( \ )^n - \frac{1}{2} ( \ )^{n-1} \quad (3.398)$$

### 1533 3.4.6 Interpolants

1534 Lagrangian polynomial quasi-cubic interpolation is used in the prognostic equations for the  
 1535 dynamical core. Monotonic Hermite quasi-cubic interpolation is used for tracers. Details are  
 1536 provided in the Eulerian Dynamical Core description. The trajectory calculation uses tri-linear  
 1537 interpolation of the wind field.

### 1538 3.4.7 Continuity Equation

The discrete semi-Lagrangian, semi-implicit continuity equation is obtained from (16) of W&O94 modified to be spatially uncentered by a fraction  $\epsilon$ , and to predict  $\ln p'_s$

$$\begin{aligned} \Delta B_l \left\{ \left( \ln p'_{s_l} \right)_A^{n+1} - \left[ \left( \ln p_{s_l} \right)^n + \frac{\Phi_s}{RT^r} \right]_{D_2} \right\} / \Delta t = \\ - \frac{1}{2} \left\{ \left[ (1 + \epsilon) \Delta \left( \frac{1}{p_s} \dot{\eta} \frac{\partial p}{\partial \eta} \right)_l \right]_A^{n+1} + \left[ (1 - \epsilon) \Delta \left( \frac{1}{p_s} \dot{\eta} \frac{\partial p}{\partial \eta} \right)_l \right]_{D_2}^n \right\} \\ - \left( \frac{1}{p_s} \delta_l \Delta p_l \right)_{M_2}^{n+\frac{1}{2}} + \frac{\Delta B_l}{RT^r} (\mathbf{V}_l \cdot \nabla \Phi_s)_{M_2}^{n+\frac{1}{2}} \\ - \left\{ \frac{1}{2} \left[ (1 + \epsilon) \left( \frac{1}{p_s^r} \delta_l \Delta p_l^r \right)_A^{n+1} + (1 - \epsilon) \left( \frac{1}{p_s^r} \delta_l \Delta p_l^r \right)_{D_2}^n \right] - \left( \frac{1}{p_s^r} \delta_l \Delta p_l^r \right)_{M_2}^{n+\frac{1}{2}} \right\} \end{aligned} \quad (3.399)$$

where

$$\Delta( \ )_l = ( \ )_{l+\frac{1}{2}} - ( \ )_{l-\frac{1}{2}} \quad (3.400)$$

and

$$( \ )_{M_2}^{n+\frac{1}{2}} = \frac{1}{2} \left[ (1 + \epsilon) ( \ )_A^{n+\frac{1}{2}} + (1 - \epsilon) ( \ )_{D_2}^{n+\frac{1}{2}} \right] \quad (3.401)$$

1539  $\Delta( \ )_l$  denotes a vertical difference,  $l$  denotes the vertical level,  $A$  denotes the arrival point,  $D_2$   
 1540 the departure point from horizontal (two-dimensional) advection, and  $M_2$  the midpoint of that  
 1541 trajectory.

The surface pressure forecast equation is obtained by summing over all levels and is related to (18) of W&O94 but is spatially uncentered and uses  $\ln p'_s$

$$\begin{aligned}
 (\ln p'_s)_A^{n+1} = & \sum_{l=1}^K \Delta B_l \left[ (\ln p_{s_l})^n + \frac{\Phi_s}{RT^r} \right]_{D_2} - \frac{1}{2} \Delta t \sum_{l=1}^K \left[ (1 - \epsilon) \Delta \left( \frac{1}{p_s} \dot{\eta} \frac{\partial p}{\partial \eta} \right)_l \right]_{D_2} \\
 & - \Delta t \sum_{l=1}^K \left( \frac{1}{p_s} \delta_l \Delta p_l \right)_{M_2}^{n+\frac{1}{2}} + \Delta t \sum_{l=1}^K \frac{\Delta B_l}{RT^r} (\mathbf{V}_l \cdot \nabla \Phi_s)_{M_2}^{n+\frac{1}{2}} \\
 & - \Delta t \sum_{l=1}^K \frac{1}{p_s^r} \left\{ \frac{1}{2} \left[ (1 + \epsilon) (\delta_l)_A^{n+1} + (1 - \epsilon) (\delta_l)_{D_2}^n \right] - (\delta_l)_{M_2}^{n+\frac{1}{2}} \right\} \Delta p_l^r
 \end{aligned} \tag{3.402}$$

1542 The corresponding  $\left( \frac{1}{p_s} \dot{\eta} \frac{\partial p}{\partial \eta} \right)$  equation for the semi-implicit development follows and is related  
1543 to (19) of W&O94, again spatially uncentered and using  $\ln p'_s$ .

$$\begin{aligned}
 (1 + \epsilon) \left( \frac{1}{p_s} \dot{\eta} \frac{\partial p}{\partial \eta} \right)_{k+\frac{1}{2}}^{n+1} = & - \frac{2}{\Delta t} \left\{ B_{k+\frac{1}{2}} (\ln p'_s)_A^{n+1} - \sum_{l=1}^k \Delta B_l \left[ (\ln p_{s_l})^n + \frac{\Phi_s}{RT^r} \right]_{D_2} \right\} \\
 & - \sum_{l=1}^k \left[ (1 - \epsilon) \Delta \left( \frac{1}{p_s} \dot{\eta} \frac{\partial p}{\partial \eta} \right)_l \right]_{D_2}^n \\
 & - 2 \sum_{l=1}^k \left( \frac{1}{p_s} \delta_l \Delta p_l \right)_{M_2}^{n+\frac{1}{2}} + 2 \sum_{l=1}^k \frac{\Delta B_l}{RT^r} (\mathbf{V}_l \cdot \nabla \Phi_s)_{M_2}^{n+\frac{1}{2}} \\
 & - 2 \sum_{l=1}^k \frac{1}{p_s^r} \left\{ \frac{1}{2} \left[ (1 + \epsilon) (\delta_l)_A^{n+1} + (1 - \epsilon) (\delta_l)_{D_2}^n \right] - (\delta_l)_{M_2}^{n+\frac{1}{2}} \right\} \Delta p_l^r
 \end{aligned} \tag{3.403}$$

1544 This is not the actual equation used to determine  $\left( \frac{1}{p_s} \dot{\eta} \frac{\partial p}{\partial \eta} \right)$  in the code. The equation actually  
1545 used in the code to calculate  $\left( \frac{1}{p_s} \dot{\eta} \frac{\partial p}{\partial \eta} \right)$  involves only the divergence at time  $(n+1)$  with  $(\ln p'_s)^{n+1}$   
1546 eliminated.

$$\begin{aligned}
(1 + \epsilon) \left( \frac{1}{p_s} \dot{\eta} \frac{\partial p}{\partial \eta} \right)_{k+\frac{1}{2}}^{n+1} = & \\
\frac{2}{\Delta t} \left[ \sum_{l=1}^k - B_{k+\frac{1}{2}} \sum_{l=1}^K \right] \Delta B_l \left[ (\ln p_{s_l})^n + \frac{\Phi_s}{RT^r} \right]_{D_2} & \\
- \left[ \sum_{l=1}^k - B_{k+\frac{1}{2}} \sum_{l=1}^K \right] \left[ (1 - \epsilon) \Delta \left( \frac{1}{p_s} \dot{\eta} \frac{\partial p}{\partial \eta} \right)_l \right]_D^n & \\
- 2 \left[ \sum_{l=1}^k - B_{k+\frac{1}{2}} \sum_{l=1}^K \right] \left( \frac{1}{p_s} \delta_l \Delta p_l \right)_{M_2}^{n+\frac{1}{2}} & \\
+ 2 \left[ \sum_{l=1}^k - B_{k+\frac{1}{2}} \sum_{l=1}^K \right] \frac{\Delta B_l}{RT^r} (\mathbf{V}_l \cdot \nabla \Phi_s)_{M_2}^{n+\frac{1}{2}} & \\
- 2 \left[ \sum_{l=1}^k - B_{k+\frac{1}{2}} \sum_{l=1}^K \right] \frac{1}{p_s^r} \left\{ \frac{1}{2} \left[ (1 + \epsilon) (\delta_l)_A^{n+1} + (1 - \epsilon) (\delta_l)_{D_2}^n \right] - (\delta_l)_{M_2}^{n+\frac{1}{2}} \right\} \Delta p_l^r & \\
\end{aligned} \tag{3.404}$$

1547 The combination  $\left[ (\ln p_{s_l})^n + \frac{\Phi_s}{RT^r} + \frac{1}{2} \frac{\Delta t}{RT^r} (\mathbf{V} \cdot \nabla \Phi_s)^{n+\frac{1}{2}} \right]_{D_2}$  is treated as a unit, and follows from  
1548 (3.401).

### 1549 3.4.8 Thermodynamic Equation

The thermodynamic equation is obtained from (25) of W&O94 modified to be spatially uncentered and to use  $\ln p_s'$ . In addition Hortal's modification [Temperton et al., 2001] is included, in which

$$\frac{d}{dt} \left[ - \left( p_s B \frac{\partial T}{\partial p} \right)_{ref} \frac{\Phi_s}{RT^r} \right] \tag{3.405}$$

1550 is subtracted from both sides of the temperature equation. This is akin to horizontal diffusion  
1551 which includes the first order term converting horizontal derivatives from eta to pressure co-  
1552 ordinates, with  $(\ln p_s)$  replaced by  $-\frac{\Phi_s}{RT^r}$ , and  $\left( p_s B \frac{\partial T}{\partial p} \right)_{ref}$  taken as a global average so it is  
1553 invariant with time and can commute with the differential operators.

$$\begin{aligned}
\frac{T_A^{n+1} - T_D^n}{\Delta t} &= \left\{ \left\{ \left[ - \left( p_s B(\eta) \frac{\partial T}{\partial p} \right)_{ref} \frac{\Phi_s}{RT^r} \right]_A^{n+1} - \left[ - \left( p_s B(\eta) \frac{\partial T}{\partial p} \right)_{ref} \frac{\Phi_s}{RT^r} \right]_D^n \right\} \right\} \Big/ \Delta t \\
&+ \frac{1}{RT^r} \left[ \left( p_s B(\eta) \frac{\partial T}{\partial p} \right)_{ref} \mathbf{V} \cdot \nabla \Phi_s + \Phi_s \dot{\eta} \frac{\partial}{\partial \eta} \left( p_s B(\eta) \frac{\partial T}{\partial p} \right)_{ref} \right]_M^{n+\frac{1}{2}} \\
&+ \left( \frac{RT_v \omega}{c_p^* p} \right)_M^{n+\frac{1}{2}} + Q_M^n \\
&+ \frac{RT^r p_s^r}{c_p p^r} \left[ B(\eta) \frac{d_2 \ln p_s'}{dt} + \overline{\left( \frac{1}{p_s} \dot{\eta} \frac{\partial p}{\partial \eta} \right)}^t \right] \\
&- \frac{RT^r p_s^r}{c_p p^r} \left[ \left( \frac{p}{p_s} \right) \left( \frac{\omega}{p} \right) \right]_M^{n+\frac{1}{2}} \\
&- \frac{RT^r p_s^r}{c_p p^r} B(\eta) \left[ \frac{1}{RT^r} \mathbf{V} \cdot \nabla \Phi_s \right]_{M_2}^{n+\frac{1}{2}}
\end{aligned} \tag{3.406}$$

1554 Note that  $Q^n$  represents the heating calculated to advance from time  $n$  to time  $n + 1$  and is  
1555 valid over the interval.

1556 The calculation of  $\left( p_s B \frac{\partial T}{\partial p} \right)_{ref}$  follows that of the ECMWF (Research Manual 3, ECMWF  
1557 Forecast Model, Adiabatic Part, ECMWF Research Department, 2nd edition, 1/88, pp 2.25-  
1558 2.26) Consider a constant lapse rate atmosphere

$$T = T_0 \left( \frac{p}{p_0} \right)^{R\gamma/g} \quad (3.407)$$

$$\frac{\partial T}{\partial p} = \frac{1}{p} \frac{R\gamma}{g} T_0 \left( \frac{p}{p_0} \right)^{R\gamma/g} \quad (3.408)$$

$$p_s B \frac{\partial T}{\partial p} = B \frac{p_s}{p} \frac{R\gamma}{g} T \quad (3.409)$$

$$\left( p_s B \frac{\partial T}{\partial p} \right)_{ref} = B_k \frac{(p_s)_{ref}}{(p_k)_{ref}} \frac{R\gamma}{g} (T_k)_{ref} \quad \text{for } (T_k)_{ref} > T_C \quad (3.410)$$

$$\left( p_s B \frac{\partial T}{\partial p} \right)_{ref} = 0 \quad \text{for } (T_k)_{ref} \leq T_C \quad (3.411)$$

$$(p_k)_{ref} = A_k p_0 + B_k (p_s)_{ref} \quad (3.412)$$

$$(T_k)_{ref} = T_0 \left( \frac{(p_k)_{ref}}{(p_s)_{ref}} \right)^{R\gamma/g} \quad (3.413)$$

$$(p_s)_{ref} = 1013.25 \text{mb} \quad (3.414)$$

$$T_0 = 288 \text{K} \quad (3.415)$$

$$p_0 = 1000 \text{mb} \quad (3.416)$$

$$\gamma = 6.5 \text{K/km} \quad (3.417)$$

$$T_C = 216.5 \text{K} \quad (3.418)$$

### 1559 3.4.9 Momentum equations

1560 The momentum equations follow from (3) of W&O94 modified to be spatially uncentered, to use  
 1561  $\ln p'_s$ , and with the Coriolis term implicit following Côté and Staniforth [1988] and Temperton  
 1562 [1997]. The semi-implicit, semi-Lagrangian momentum equation at level  $k$  (but with the level  
 1563 subscript  $k$  suppressed) is

$$\begin{aligned}
\frac{\mathbf{V}_A^{n+1} - \mathbf{V}_D^n}{\Delta t} = & -\frac{1}{2} \left\{ (1+\epsilon) \left[ f\hat{\mathbf{k}} \times \mathbf{V} \right]_A^{n+1} + (1-\epsilon) \left[ f\hat{\mathbf{k}} \times \mathbf{V} \right]_D^n \right\} + \mathbf{F}_M^n \\
& -\frac{1}{2} \left\{ (1+\epsilon) \left[ \nabla (\Phi_s + R\mathbf{H}_k \cdot \mathbf{T}_v) + RT_v \frac{B}{p} p_s \nabla \ln p_s \right]_A^{n+\frac{1}{2}} \right. \\
& \quad \left. + (1-\epsilon) \left[ \nabla (\Phi_s + R\mathbf{H}_k \cdot \mathbf{T}_v) + RT_v \frac{B}{p} p_s \nabla \ln p_s \right]_D^{n+\frac{1}{2}} \right\} \\
& -\frac{1}{2} \left\{ (1+\epsilon) \nabla [R\mathbf{H}_k^r \cdot \mathbf{T} + RT^r \ln p_s']_A^{n+1} \right. \\
& \quad \left. - (1+\epsilon) \nabla [\Phi_s + R\mathbf{H}_k^r \cdot \mathbf{T} + RT^r \ln p_s]_A^{n+\frac{1}{2}} \right. \\
& \quad \left. + (1-\epsilon) \nabla [\Phi_s + R\mathbf{H}_k^r \cdot \mathbf{T} + RT^r \ln p_s]_D^n \right. \\
& \quad \left. - (1-\epsilon) \nabla [\Phi_s + R\mathbf{H}_k^r \cdot \mathbf{T} + RT^r \ln p_s]_D^{n+\frac{1}{2}} \right\} \tag{3.419}
\end{aligned}$$

1564 The gradient of the geopotential is more complex than in the  $\sigma$  system because the hydro-  
1565 static matrix  $\mathbf{H}$  depends on the local pressure:

$$\nabla (\mathbf{H}_k \cdot \mathbf{T}_v) = \mathbf{H}_k \cdot [(1+\epsilon_v \mathbf{q}) \nabla \mathbf{T} + \epsilon_v \mathbf{T} \nabla \mathbf{q}] + \mathbf{T}_v \cdot \nabla \mathbf{H}_k \tag{3.420}$$

where  $\epsilon_v$  is  $(R_v/R - 1)$  and  $R_v$  is the gas constant for water vapor. The gradient of  $T$  is calculated from the spectral representation and that of  $q$  from a discrete cubic approximation that is consistent with the interpolation used in the semi-Lagrangian water vapor advection. In general, the elements of  $\mathbf{H}$  are functions of pressure at adjacent discrete model levels

$$H_{kl} = f_{kl}(p_{l+1/2}, p_l, p_{l-1/2}) \tag{3.421}$$

The gradient is then a function of pressure and the pressure gradient

$$\nabla H_{kl} = g_{kl}(p_{l+1/2}, p_l, p_{l-1/2}, \nabla p_{l+1/2}, \nabla p_l, \nabla p_{l-1/2}) \tag{3.422}$$

The pressure gradient is available from (3.393) and the surface pressure gradient calculated from the spectral representation

$$\nabla p_l = B_l \nabla p_s = B_l p_s \nabla \ln p_s \tag{3.423}$$

### 1566 3.4.10 Development of semi-implicit system equations

The momentum equation can be written as

$$\begin{aligned}
\frac{\mathbf{V}_A^{n+1} - \mathbf{V}_D^n}{\Delta t} = & -\frac{1}{2} \left\{ (1+\epsilon) \left[ f\hat{\mathbf{k}} \times \mathbf{V} \right]_A^{n+1} + (1-\epsilon) \left[ f\hat{\mathbf{k}} \times \mathbf{V} \right]_D^n \right\} \\
& -\frac{1}{2} \left\{ (1+\epsilon) \nabla [R\mathbf{H}_k^r \cdot \mathbf{T} + RT^r \ln p_s']_A^{n+1} \right\} + RHS_V, \tag{3.424}
\end{aligned}$$

1567 where  $RHS_{\mathbf{V}}$  contains known terms at times  $(n + \frac{1}{2})$  and  $(n)$ .

By combining terms, 3.424 can be written in general as

$$\mathcal{U}_A^{n+1} \hat{\mathbf{i}}_A + \mathcal{V}_A^{n+1} \hat{\mathbf{j}}_A = \mathcal{U}_A \hat{\mathbf{i}}_A + \mathcal{V}_A \hat{\mathbf{j}}_A + \mathcal{U}_D \hat{\mathbf{i}}_D + \mathcal{V}_D \hat{\mathbf{j}}_D , \quad (3.425)$$

where  $\hat{\mathbf{i}}$  and  $\hat{\mathbf{j}}$  denote the spherical unit vectors in the longitudinal and latitudinal directions, respectively, at the points indicated by the subscripts, and  $\mathcal{U}$  and  $\mathcal{V}$  denote the appropriate combinations of terms in 3.424. Note that  $\mathcal{U}_A^{n+1}$  is distinct from the  $\mathcal{U}_A$ . Following Bates et al. [1990], equations for the individual components are obtained by relating the unit vectors at the departure points  $(\hat{\mathbf{i}}_D, \hat{\mathbf{j}}_D)$  to those at the arrival points  $(\hat{\mathbf{i}}_A, \hat{\mathbf{j}}_A)$ :

$$\hat{\mathbf{i}}_D = \alpha_A^u \hat{\mathbf{i}}_A + \beta_A^u \hat{\mathbf{j}}_A \quad (3.426)$$

$$\hat{\mathbf{j}}_D = \alpha_A^v \hat{\mathbf{i}}_A + \beta_A^v \hat{\mathbf{j}}_A , \quad (3.427)$$

1568 in which the vertical components ( $\hat{\mathbf{k}}$ ) are ignored. The dependence of  $\alpha$ 's and  $\beta$ 's on the latitudes  
1569 and longitudes of the arrival and departure points is given in the Appendix of Bates et al. [1990].

W&O94 followed Bates et al. [1990] which ignored rotating the vector to remain parallel to the earth's surface during translation. We include that factor by keeping the length of the vector written in terms of  $(\hat{\mathbf{i}}_A, \hat{\mathbf{j}}_A)$  the same as the length of the vector written in terms of  $(\hat{\mathbf{i}}_D, \hat{\mathbf{j}}_D)$ . Thus, (10) of W&O94 becomes

$$\begin{aligned} \mathcal{U}_A^{n+1} &= \mathcal{U}_A + \gamma \alpha_A^u \mathcal{U}_D + \gamma \alpha_A^v \mathcal{V}_D \\ \mathcal{V}_A^{n+1} &= \mathcal{V}_A + \gamma \beta_A^u \mathcal{U}_D + \gamma \beta_A^v \mathcal{V}_D \end{aligned} \quad (3.428)$$

where

$$\gamma = \left[ \frac{\mathcal{U}_D^2 + \mathcal{V}_D^2}{(\mathcal{U}_D \alpha_A^u + \mathcal{V}_D \alpha_A^v)^2 + (\mathcal{U}_D \beta_A^u + \mathcal{V}_D \beta_A^v)^2} \right]^{\frac{1}{2}} \quad (3.429)$$

After the momentum equation is written in a common set of unit vectors

$$\mathbf{V}_A^{n+1} + \left( \frac{1+\epsilon}{2} \right) \Delta t \left[ f \hat{\mathbf{k}} \times \mathbf{V} \right]_A^{n+1} + \left( \frac{1+\epsilon}{2} \right) \Delta t \nabla [R \mathbf{H}_k^r \cdot \mathbf{T} + RT^r \ln p_s']_A^{n+1} = \mathcal{R}_{\mathbf{V}}^* \quad (3.430)$$

Drop the  $(\quad)_A^{n+1}$  from the notation, define

$$\alpha = (1 + \epsilon) \Delta t \Omega \quad (3.431)$$

and transform to vorticity and divergence

$$\zeta + \alpha \sin \varphi \delta + \frac{\alpha}{a} v \cos \varphi = \frac{1}{a \cos \varphi} \left[ \frac{\partial \mathcal{R}_v^*}{\partial \lambda} - \frac{\partial}{\partial \varphi} (\mathcal{R}_v^* \cos \varphi) \right] \quad (3.432)$$

$$\begin{aligned} \delta - \alpha \sin \varphi \zeta + \frac{\alpha}{a} u \cos \varphi &+ \left( \frac{1+\epsilon}{2} \right) \Delta t \nabla^2 [R \mathbf{H}_k^r \cdot \mathbf{T} + RT^r \ln p_s']_A^{n+1} \\ &= \frac{1}{a \cos \varphi} \left[ \frac{\partial \mathcal{R}_u^*}{\partial \lambda} + \frac{\partial}{\partial \varphi} (\mathcal{R}_u^* \cos \varphi) \right] \end{aligned} \quad (3.433)$$

Note that

$$u \cos \varphi = \frac{1}{a} \frac{\partial}{\partial \lambda} (\nabla^{-2} \delta) - \frac{\cos \varphi}{a} \frac{\partial}{\partial \varphi} (\nabla^{-2} \zeta) \quad (3.434)$$

$$v \cos \varphi = \frac{1}{a} \frac{\partial}{\partial \lambda} (\nabla^{-2} \zeta) + \frac{\cos \varphi}{a} \frac{\partial}{\partial \varphi} (\nabla^{-2} \delta) \quad (3.435)$$

Then the vorticity and divergence equations become

$$\begin{aligned} \zeta + \alpha \sin \varphi \delta + \frac{\alpha}{a^2} \frac{\partial}{\partial \lambda} (\nabla^{-2} \zeta) + \frac{\alpha \cos \varphi}{a^2} \frac{\partial}{\partial \varphi} (\nabla^{-2} \delta) \\ = \frac{1}{a \cos \varphi} \left[ \frac{\partial \mathcal{R}_v^*}{\partial \lambda} - \frac{\partial}{\partial \varphi} (\mathcal{R}_u^* \cos \varphi) \right] = \mathcal{L} \end{aligned} \quad (3.436)$$

$$\begin{aligned} \delta - \alpha \sin \varphi \zeta + \frac{\alpha}{a^2} \frac{\partial}{\partial \lambda} (\nabla^{-2} \delta) - \frac{\alpha \cos \varphi}{a^2} \frac{\partial}{\partial \varphi} (\nabla^{-2} \zeta) + \left( \frac{1+\epsilon}{2} \right) \Delta t \nabla^2 [R \mathbf{H}_k^r \cdot \mathbf{T} + RT^r \ln p_s']_A^{n+1} \\ = \frac{1}{a \cos \varphi} \left[ \frac{\partial \mathcal{R}_u^*}{\partial \lambda} + \frac{\partial}{\partial \varphi} (\mathcal{R}_v^* \cos \varphi) \right] = \mathcal{M} \end{aligned} \quad (3.437)$$

Transform to spectral space as described in the description of the Eulerian spectral transform dynamical core. Note, from (4.5b) and (4.6) on page 177 of [Machenauer \[1979\]](#)

$$\mu P_n^m = D_{n+1}^m P_{n+1}^m + D_n^m P_{n-1}^m \quad (3.438)$$

$$D_n^m = \left( \frac{n^2 - m^2}{4n^2 - 1} \right)^{\frac{1}{2}} \quad (3.439)$$

and from (4.5a) on page 177 of [Machenauer \[1979\]](#)

$$(1 - \mu^2) \frac{\partial}{\partial \mu} P_n^m = -n D_{n+1}^m P_{n+1}^m + (n+1) D_n^m P_{n-1}^m \quad (3.440)$$

Then the equations for the spectral coefficients at time  $n+1$  at each vertical level are

$$\zeta_n^m \left( 1 - \frac{im\alpha}{n(n+1)} \right) + \delta_{n+1}^m \alpha \left( \frac{n}{n+1} \right) D_{n+1}^m + \delta_{n-1}^m \alpha \left( \frac{n+1}{n} \right) D_n^m = \mathcal{L}_n^m \quad (3.441)$$

$$\delta_n^m \left( 1 - \frac{im\alpha}{n(n+1)} \right) - \zeta_{n+1}^m \alpha \left( \frac{n}{n+1} \right) D_{n+1}^m - \zeta_{n-1}^m \alpha \left( \frac{n+1}{n} \right) D_n^m \quad (3.442)$$

$$- \left( \frac{1+\epsilon}{2} \right) \Delta t \frac{n(n+1)}{a^2} [R \mathbf{H}_k^r \cdot \mathbf{T}_n^m + RT^r \ln p_{sn}'] = \mathcal{M}_n^m$$

$$\ln p_{sn}^m = \text{PS}_n^m - \left( \frac{1+\epsilon}{2} \right) \frac{\Delta t}{p_s^r} (\underline{\Delta p}^r)^T \underline{\delta}_n^m \quad (3.443)$$

$$\underline{T}_n^m = \text{TS}_n^m - \left( \frac{1+\epsilon}{2} \right) \Delta t \mathbf{D}^r \underline{\delta}_n^m \quad (3.444)$$

The underbar denotes a vector over vertical levels. Rewrite the vorticity and divergence equations in terms of vectors over vertical levels.

$$\begin{aligned} \underline{\delta}_n^m \left( 1 - \frac{im\alpha}{n(n+1)} \right) - \underline{\zeta}_{n+1}^m \alpha \left( \frac{n}{n+1} \right) - D_{n+1}^m \underline{\zeta}_{n-1}^m \alpha \left( \frac{n+1}{-n} \right) D_n^m \\ - \left( \frac{1+\epsilon}{2} \right) \Delta t \frac{n(n+1)}{a^2} [R\mathbf{H}^r \underline{T}_n^m + R\underline{T}^r \ln p_{sn}'^m] = \underline{DS}_n^m \end{aligned} \quad (3.445)$$

$$\underline{\zeta}_n^m \left( 1 - \frac{im\alpha}{n(n+1)} \right) + \underline{\delta}_{n+1}^m \alpha \left( \frac{n}{n+1} \right) D_{n+1}^m + \underline{\delta}_{n-1}^m \alpha \left( \frac{n+1}{n} \right) D_n^m = \underline{VS}_n^m \quad (3.446)$$

Define  $\underline{h}_n^m$  by

$$g\underline{h}_n^m = R\mathbf{H}^r T_n^m + R\underline{T}^r \ln p_{sn}'^m \quad (3.447)$$

and

$$\mathcal{A}_n^m = 1 - \frac{im\alpha}{n(n+1)} \quad (3.448)$$

$$\mathcal{B}_{n+1}^m = \alpha \left( \frac{n}{n+1} \right) D_{n+1}^m \quad (3.449)$$

$$\mathcal{B}_n^m = \alpha \left( \frac{n+1}{n} \right) D_n^m \quad (3.450)$$

Then the vorticity and divergence equations are

$$\mathcal{A}_n^m \underline{\zeta}_n^m + \mathcal{B}_{n+1}^m \underline{\delta}_{n+1}^m + \mathcal{B}_n^m \underline{\delta}_{n-1}^m = \underline{VS}_n^m \quad (3.451)$$

$$\mathcal{A}_n^m \underline{\delta}_n^m - \mathcal{B}_{n+1}^m \underline{\zeta}_{n+1}^m \mathcal{B}_n^m - \underline{\zeta}_{n-1}^m - \left( \frac{1+\epsilon}{2} \right) \Delta t \frac{n(n+1)}{a^2} g\underline{h}_n^m = \underline{DS}_n^m \quad (3.452)$$

1570 Note that these equations are uncoupled in the vertical, i.e. each vertical level involves variables  
1571 at that level only. The equation for  $\underline{h}_n^m$  however couples all levels.

$$g\underline{h}_n^m = - \left( \frac{1+\epsilon}{2} \right) \Delta t \left[ R\mathbf{H}^r \mathbf{D}^r + R\underline{T}^r \frac{(\Delta p^r)^T}{p_s^r} \right] \underline{\delta}_n^m + R\mathbf{H}^r \underline{TS}_n^m + R\underline{T}^r \underline{PS}_n^m \quad (3.453)$$

Define  $\mathbf{C}^r$  and  $\underline{HS}_n^m$  so that

$$g\underline{h}_n^m = - \left( \frac{1+\epsilon}{2} \right) \Delta t \mathbf{C}^r \underline{\delta}_n^m + \underline{HS}_n^m \quad (3.454)$$

1572 Let  $g\mathbf{D}_\ell$  denote the eigenvalues of  $\mathbf{C}^r$  with corresponding eigenvectors  $\underline{\Phi}_\ell$  and  $\Phi$  is the matrix  
1573 with columns  $\underline{\Phi}_\ell$

$$\Phi = ( \underline{\Phi}_1 \underline{\Phi}_2 \dots \underline{\Phi}_L ) \quad (3.455)$$

1574 and  $g\mathbf{D}$  the diagonal matrix of corresponding eigenvalues

$$g\mathbf{D} = g \begin{pmatrix} D_1 & 0 & \cdots & 0 \\ 0 & D_2 & \cdots & 0 \\ \vdots & \vdots & \ddots & \vdots \\ 0 & 0 & \cdots & D_L \end{pmatrix} \quad (3.456)$$

$$\mathbf{C}^r \Phi = \Phi g\mathbf{D} \quad (3.457)$$

$$\Phi^{-1} \mathbf{C}^r \Phi = g\mathbf{D} \quad (3.458)$$

Then transform

$$\underline{\zeta}_n^m = \Phi^{-1} \underline{\zeta}_n^m, \quad \underline{\mathcal{V}\mathcal{S}}_n^m = \Phi^{-1} \underline{\mathcal{V}\mathcal{S}}_n^m \quad (3.459)$$

$$\underline{\delta}_n^m = \Phi^{-1} \underline{\delta}_n^m, \quad \underline{\mathcal{D}\mathcal{S}}_n^m = \Phi^{-1} \underline{\mathcal{D}\mathcal{S}}_n^m \quad (3.460)$$

$$\underline{h}_n^m = \Phi^{-1} \underline{h}_n^m, \quad \underline{\mathcal{H}\mathcal{S}}_n^m = \Phi^{-1} \underline{\mathcal{H}\mathcal{S}}_n^m \quad (3.461)$$

$$\mathcal{A}_n^m \underline{\zeta}_n^m + \mathcal{B}_n^m \underline{\delta}_{n+1}^m + \mathcal{B}_{-n}^m \underline{\delta}_{n-1}^m = \underline{\mathcal{V}\mathcal{S}}_n^m \quad (3.462)$$

$$\mathcal{A}_n^m \underline{\delta}_n^m - \mathcal{B}_n^m \underline{\zeta}_{n+1}^m \mathcal{B}_{-n}^m - \underline{\zeta}_{n-1}^m - \left( \frac{1+\epsilon}{2} \right) \Delta t \frac{n(n+1)}{a^2} g \underline{h}_n^m = \underline{\mathcal{D}\mathcal{S}}_n^m \quad (3.463)$$

$$g \underline{h}_n^m + \left( \frac{1+\epsilon}{2} \right) \Delta t \Phi^{-1} \mathbf{C}^r \Phi \Phi^{-1} \underline{\delta}_n^m = \underline{\mathcal{H}\mathcal{S}}_n^m \quad (3.464)$$

$$\underline{h}_n^m + \left( \frac{1+\epsilon}{2} \right) \Delta t \mathbf{D} \underline{\delta}_n^m = \frac{1}{g} \underline{\mathcal{H}\mathcal{S}}_n^m \quad (3.465)$$

1575 Since  $\mathbf{D}$  is diagonal, all equations are now uncoupled in the vertical.

1576 For each vertical mode, i.e. element of  $(\underline{\zeta})_n^m$ , and for each Fourier wavenumber  $m$  we have  
1577 a system of equations in  $n$  to solve. In following we drop the Fourier index  $m$  and the modal  
1578 element index  $(\ )_\ell$  from the notation.

$$\mathcal{A}_n \underline{\zeta}_n + \mathcal{B}_n^+ \underline{\delta}_{n+1} + \mathcal{B}_{-n}^- \underline{\delta}_{n-1} = \underline{\mathcal{V}\mathcal{S}}_n \quad (3.466)$$

$$\mathcal{A}_n \underline{\delta}_n - \mathcal{B}_n^+ \underline{\zeta}_{n+1} \mathcal{B}_{-n}^- \underline{\zeta}_{n-1} - \left( \frac{1+\epsilon}{2} \right) \Delta t \frac{n(n+1)}{a^2} g \underline{h}_n = \underline{\mathcal{D}\mathcal{S}}_n \quad (3.467)$$

$$\underline{h}_n + \left( \frac{1+\epsilon}{2} \right) \Delta t \mathbf{D}_\ell \underline{\delta}_n = \frac{1}{g} \underline{\mathcal{H}\mathcal{S}}_n \quad (3.468)$$

1579 The modal index  $(\ )_\ell$  was included in the above equation on  $\mathbf{D}$  only as a reminder, but will also  
1580 be dropped in the following.

1581 Substitute  $\tilde{\zeta}$  and  $\tilde{h}$  into the  $\tilde{\delta}$  equation.

$$\begin{aligned} & \left[ \mathcal{A}_n + \left( \frac{1+\epsilon}{2} \right)^2 (\Delta t)^2 \frac{n(n+1)}{a^2} g \mathbf{D} + \mathcal{B}_n^+ \mathcal{A}_{n+1}^{-1} \mathcal{B}_{-n+1}^- + \mathcal{B}_{-n}^- \mathcal{A}_{n-1}^{-1} \mathcal{B}_{-n-1}^+ \right] \tilde{\delta}_n \\ & + (\mathcal{B}_n^+ \mathcal{A}_{n+1}^{-1} \mathcal{B}_{-n+1}^-) \tilde{\delta}_{n+2} + (\mathcal{B}_{-n}^- \mathcal{A}_{n-1}^{-1} \mathcal{B}_{-n-1}^+) \tilde{\delta}_{n-2} \\ & = \underline{\mathcal{D}\mathcal{S}}_n + \left( \frac{1+\epsilon}{2} \right) \Delta t \frac{n(n+1)}{a^2} \underline{\mathcal{H}\mathcal{S}}_n + \mathcal{B}_n^+ \mathcal{A}_{n+1}^{-1} \underline{\mathcal{V}\mathcal{S}}_{n+1} + \mathcal{B}_{-n}^- \mathcal{A}_{n-1}^{-1} \underline{\mathcal{V}\mathcal{S}}_{n-1} \end{aligned} \quad (3.469)$$

1582 which is just two tri-diagonal systems of equations, one for the even and one for the odd  $n$ 's,  
1583 and  $m \leq n \leq N$

At the end of the system, the boundary conditions are

$$\begin{aligned} n = m, \quad \mathcal{B}^-_n = \mathcal{B}^-_m &= 0 \\ n = m + 1, \quad \mathcal{B}^-_{n-1} = \mathcal{B}^-_m &= \mathcal{B}^-_{(m+1)-1} = 0 \end{aligned} \quad (3.470)$$

the  $\tilde{\delta}_{n-2}$  term is not present, and from the underlying truncation

$$\tilde{\delta}_{N+1}^m = \tilde{\delta}_{N+2}^m = 0 \quad (3.471)$$

For each  $m$  and  $\ell$  we have the general systems of equations

$$-A_n \tilde{\delta}_{n+2} + B_n \tilde{\delta}_n - C_n - \tilde{\delta}_{n-2} = D_n, \quad \begin{cases} n = m, m+2, \dots, \begin{cases} N+1 \\ \text{or} \\ N+2 \end{cases} \\ n = m+1, m+3, \dots, \begin{cases} N+1 \\ \text{or} \\ N+2 \end{cases} \end{cases} \quad (3.472)$$

$$C_m = C_{m+1} = 0 \quad (3.473)$$

$$\tilde{\delta}_{N+1} = \tilde{\delta}_{N+2} = 0 \quad (3.474)$$

Assume solutions of the form

$$\tilde{\delta}_n = E_n \tilde{\delta}_{n+2} + F_n \quad (3.475)$$

then

$$E_m = \frac{A_m}{B_m} \quad (3.476)$$

$$F_M = \frac{D_m}{B_m} \quad (3.477)$$

$$E_n = \frac{A_n}{B_n - C_n E_{n-2}}, \quad n = m+2, m+4, \dots, \begin{cases} N-2 \\ \text{or} \\ N-3 \end{cases} \quad (3.478)$$

$$F_n = \frac{D_n + C_n F_{n-2}}{B_n - C_n E_{n-2}}, \quad n = m+2, m+4, \dots, \begin{cases} N \\ \text{or} \\ N-1 \end{cases} \quad (3.479)$$

$$\tilde{\delta}_N = F_N \quad \text{or} \quad \tilde{\delta}_{N-1} = F_{N-1}, \quad (3.480)$$

$$\tilde{\delta}_n = E_n \tilde{\delta}_{n+2} + F_n, \quad \begin{cases} n = N-2, N-4, \dots, \begin{cases} m \\ \text{or} \\ m+1 \end{cases} \\ n = N-3, N-5, \dots, \begin{cases} m+1 \\ \text{or} \\ m \end{cases} \end{cases} \quad (3.481)$$

<sup>1584</sup> Divergence in physical space is obtained from the vertical mode coefficients by

$$\underline{\delta}_n^m = \Phi \tilde{\underline{\delta}}_n^m \quad (3.482)$$

<sup>1585</sup> The remaining variables are obtained in physical space by

$$\zeta_n^m \left( 1 - \frac{im\alpha}{n(n+1)} \right) = \mathcal{L}_n^m - \delta_{n+1}^m \alpha \left( \frac{n}{n+1} \right) D_{n+1}^m - \delta_{n-1}^m \alpha \left( \frac{n+1}{n} \right) D_n^m \quad (3.483)$$

$$\underline{T}_n^m = \underline{\text{TS}}_n^m - \left( \frac{1+\epsilon}{2} \right) \Delta t \mathbf{D}^r \underline{\delta}_n^m \quad (3.484)$$

$$\ln p_{sn}^m = \text{PS}_n^m - \left( \frac{1+\epsilon}{2} \right) \frac{\Delta t}{p_s^r} (\underline{\Delta p}^r)^T \underline{\delta}_n^m \quad (3.485)$$

### <sup>1586</sup> 3.4.11 Trajectory Calculation

The trajectory calculation follows [Hortal \[1999\]](#) Let  $\mathbf{R}$  denote the position vector of the parcel,

$$\frac{d\mathbf{R}}{dt} = \mathbf{V} \quad (3.486)$$

which can be approximated in general by

$$\mathbf{R}_D^n = \mathbf{R}_A^{n+1} - \Delta t \mathbf{V}_M^{n+\frac{1}{2}} \quad (3.487)$$

Hortal's method is based on a Taylor's series expansion

$$\mathbf{R}_A^{n+1} = \mathbf{R}_D^n + \Delta t \left( \frac{d\mathbf{R}}{dt} \right)_D^n + \frac{\Delta t^2}{2} \left( \frac{d^2\mathbf{R}}{dt^2} \right)_D^n + \dots \quad (3.488)$$

or substituting for  $d\mathbf{R}/dt$

$$\mathbf{R}_A^{n+1} = \mathbf{R}_D^n + \Delta t \mathbf{V}_D^n + \frac{\Delta t^2}{2} \left( \frac{d\mathbf{V}}{dt} \right)_D^n + \dots \quad (3.489)$$

Approximate

$$\left( \frac{d\mathbf{V}}{dt} \right)_D^n \approx \frac{\mathbf{V}_A^n - \mathbf{V}_D^{n-1}}{\Delta t} \quad (3.490)$$

giving

$$\mathbf{V}_M^{n+\frac{1}{2}} = \frac{1}{2} [(2\mathbf{V}^n - \mathbf{V}^{n-1})_D + \mathbf{V}_A^n] \quad (3.491)$$

<sup>1587</sup> for the trajectory equation.

### <sup>1588</sup> 3.4.12 Mass and energy fixers and statistics calculations

<sup>1589</sup> The semi-Lagrangian dynamical core applies the same mass and energy fixers and statistical  
<sup>1590</sup> calculations as the Eulerian dynamical core. These are described in sections [3.3.19](#), [3.3.20](#), and  
<sup>1591</sup> [3.3.21](#).



1592 

# Chapter 4

1593 

## Model Physics

As stated in chapter 2, the total parameterization package in CAM 5.0 consists of a sequence of components, indicated by

$$P = \{M, R, S, T\} , \quad (4.1)$$

1594 where  $M$  denotes (Moist) precipitation processes,  $R$  denotes clouds and Radiation,  $S$  denotes the  
1595 Surface model, and  $T$  denotes Turbulent mixing. Each of these in turn is subdivided into vari-  
1596 ous components:  $M$  includes an optional dry adiabatic adjustment normally applied only in the  
1597 stratosphere, moist penetrative convection, shallow convection, and large-scale stable condensa-  
1598 tion;  $R$  first calculates the cloud parameterization followed by the radiation parameterization;  
1599  $S$  provides the surface fluxes obtained from land, ocean and sea ice models, or calculates them  
1600 based on specified surface conditions such as sea surface temperatures and sea ice distribution.  
1601 These surface fluxes provide lower flux boundary conditions for the turbulent mixing  $T$  which  
1602 is comprised of the planetary boundary layer parameterization, vertical diffusion, and gravity  
1603 wave drag.

The updating described in the preceding paragraph of all variable except temperature is straightforward. Temperature, however, is a little more complicated and follows the general procedure described by [Boville and Bretherton \[2003a\]](#) involving dry static energy. The state variable updated after each time-split parameterization component is the dry static energy  $s_i$ . Let  $i$  be the index in a sequence of  $I$  time-split processes. The dry static energy at the end of the  $i$ th process is  $s_i$ . The dry static energy is updated using the heating rate  $Q$  calculated by the  $i$ th process:

$$s_i = s_{i-1} + (\Delta t) Q_i(s_{i-1}, T_{i-1}, \Phi_{i-1}, q_{i-1}, \dots) \quad (4.2)$$

1604 In processes not formulated in terms of dry static energy but rather in terms of a temperature  
1605 tendency, the heating rate is given by  $Q_i = (T_i - T_{i-1}) / (C_p \Delta t)$ .

The temperature,  $T_i$ , and geopotential,  $\Phi_i$ , are calculated from  $s_i$  by inverting the equation for  $s$

$$s = C_p T + g z = C_p T + \Phi \quad (4.3)$$

with the hydrostatic equation

$$\Phi_k = \Phi_s + R \sum_{l=k}^K H_{kl} T_{vl} \quad (4.4)$$

1606 substituted for  $\Phi$ .

The temperature tendencies for each process are also accumulated over the processes. For processes formulated in terms of dry static energy the temperature tendencies are calculated from the dry static energy tendency. Let  $\Delta T_i/\Delta t$  denote the total accumulation at the end of the  $i$ th process. Then

$$\frac{\Delta T_i}{\Delta t} = \frac{\Delta T_{i-1}}{\Delta t} + \frac{\Delta s_i}{\Delta t}/C_p \quad (4.5)$$

$$\frac{\Delta s_i}{\Delta t}/C_p = \frac{(s_i - s_{i-1})}{\Delta t}/C_p \quad (4.6)$$

which assumes  $\Phi$  is unchanged. Note that the inversion of  $s$  for  $T$  and  $\Phi$  changes  $T$  and  $\Phi$ . This is not included in the  $\Delta T_i/\Delta t$  above for processes formulated to give dry static energy tendencies.. In processes not formulated in terms of dry static energy but rather in terms of a temperature tendency, that tendency is simply accumulated.

After the last parameterization is completed, the dry static energy of the last update is saved. This final column energy is saved and used at the beginning of the next physics calculation following the Finite Volume dynamical update to calculate the global energy fixer associated with the dynamical core. The implication is that the energy inconsistency introduced by sending the  $T$  described above to the FV rather than the  $T$  returned by inverting the dry static energy is included in the fixer attributed to the dynamics. The accumulated physics temperature tendency is also available after the last parameterization is completed,  $\Delta T_I/\Delta t$ . An updated temperature is calculated from it by adding it to the temperature at the beginning of the physics.

$$T_I = T_0 + \frac{\Delta T_I}{\Delta t} * \Delta t \quad (4.7)$$

This temperature is converted to virtual potential temperature and passed to the Finite Volume dynamical core. The temperature tendency itself is passed to the spectral transform Eulerian and semi-Lagrangian dynamical cores. The inconsistency in the use of temperature and dry static energy apparent in the description above should be eliminated in future versions of the model.

1616 **4.1 Conversion to and from dry and wet mixing ratios**  
1617 **for trace constituents in the model**

1618 There are trade offs in the various options for the representation of trace constituents  $\chi$  in any  
1619 general circulation model:

- 1620 1. When the air mass in a model layer is defined to include the water vapor, it is frequently  
1621 convenient to represent the quantity of trace constituent as a “moist” mixing ratio  $\chi^m$ ,  
1622 that is, the mass of tracer per mass of moist air in the layer. The advantage of the  
1623 representation is that one need only multiply the moist mixing ratio by the moist air mass  
1624 to determine the tracer air mass. It has the disadvantage of implicitly requiring a change  
1625 in  $\chi^m$  whenever the water vapor  $q$  changes within the layer, even if the mass of the trace  
1626 constituent does not.
- 1627 2. One can also utilize a “dry” mixing ratio  $\chi^d$  to define the amount of constituent in a  
1628 volume of air. This variable does not have the implicit dependence on water vapor, but  
1629 does require that the mass of water vapor be factored out of the air mass itself in order to  
1630 calculate the mass of tracer in a cell.

1631 NCAR atmospheric models have historically used a combination of dry and moist mixing ratios.  
1632 Physical parameterizations (including convective transport) have utilized moist mixing ratios.  
1633 The resolved scale transport performed in the Eulerian (spectral), and semi-Lagrangian dynam-  
1634 ics use dry mixing ratios, specifically to prevent oscillations associated with variations in water  
1635 vapor requiring changes in tracer mixing ratios. The finite volume dynamics module utilizes  
1636 moist mixing ratios, with an attempt to maintain internal consistency between transport of  
1637 water vapor and other constituents.

1638 There is no “right” way to resolve the requirements associated with the simultaneous treat-  
1639 ment of water vapor, air mass in a layer and tracer mixing ratios. But the historical treatment  
1640 significantly complicates the interpretation of model simulations, and in the latest version of  
1641 CAM we have also provided an “alternate” representation. That is, we allow the user to specify  
1642 whether any given trace constituent is interpreted as a “dry” or “wet” mixing ratio through the  
1643 specification of an “attribute” to the constituent in the physics state structure. The details of  
1644 the specification are described in the users manual, but we do identify the interaction between  
1645 state quantities here.

At the end of the dynamics update to the model state, the surface pressure, specific humidity, and tracer mixing ratios are returned to the model. The physics update then is allowed to update specific humidity and tracer mixing ratios through a sequence of operator splitting updates *but the surface pressure is not allowed to evolve*. Because there is an explicit relationship between the surface pressure and the air mass within each layer we assume that water mass can change within the layer by physical parameterizations *but dry air mass cannot*. We have chosen to define the dry air mass in each layer at the beginning of the physics update as

$$\delta p_{i,k}^d = (1 - q_{i,k}^0) \delta p_{i,k}^m$$

for column  $i$ , level  $k$ . Note that the specific humidity used is the value defined at the beginning of the physics update. We define the transformation between dry and wet mixing ratios to be

$$\chi_{i,k}^d = (\delta p_{i,k}^d / \delta p_{i,k}^m) \chi_{i,k}^m$$

1646 We note that the various physical parameterizations that operate on tracers on the model  
 1647 (convection, turbulent transport, scavenging, chemistry) will require a specification of the air  
 1648 mass within each cell as well as the value of the mixing ratio in the cell. We have modified the  
 1649 model so that it will use the correct value of  $\delta p$  depending on the attribute of the tracer, that  
 1650 is, we use couplets of  $(\chi^m, \delta p^m)$  or  $(\chi^d, \delta p^d)$  in order to assure that the process conserves mass  
 1651 appropriately.

We note further that there are a number of parameterizations (*e.g.* convection, vertical diffusion) that transport species using a continuity equation in a flux form that can be written generically as

$$\frac{\partial \chi}{\partial t} = \frac{\partial F(\chi)}{\partial p} \quad (4.8)$$

1652 where  $F$  indicates a flux of  $\chi$ . For example, in convective transports  $F(\chi)$  might correspond  
 1653 to  $M_u \chi$  where  $M_u$  is an updraft mass flux. In principle one should adjust  $M_u$  to reflect the fact  
 1654 that it may be moving a mass of dry air or a mass of moist air. We assume these differences are  
 1655 small, and well below the errors required to produce equation 4.8 in the first place. The same is  
 1656 true for the diffusion coefficients involved in turbulent transport. All processes using equations  
 1657 of such a form still satisfy a conservation relationship

$$\frac{\partial}{\partial t} \sum_k \chi_k \delta p_k = F_{kbot} - F_{ktop}$$

1658 provided the appropriate  $\delta p$  is used in the summation.

1659 **4.2 Moist Turbulence Scheme**

1660

1661 Moist turbulence scheme in CAM5 is from [Bretherton and Park \[2009a\]](#) that is a replacement  
 1662 of dry turbulence scheme of [Holtslag and Boville \[1993b\]](#) in CAM3 and CAM4. The role of moist  
 1663 turbulence scheme is to vertically transport heat ( dry static energy  $s \equiv C_p \cdot T + g \cdot z$  ), moistures  
 1664 (  $q_v, q_l, q_i, n_l, n_i$  where  $n_l, n_i$  are number concentrations of cloud liquid droplets and ice crystals  
 1665 ), horizontal momentum (  $u, v$  ), and tracers ( mass and number concentrations of aerosol  
 1666 and chemical species ) by symmetric turbulences. In the symmetric turbulence, updraft and  
 1667 downdraft have similar vertical velocities, fractional areas, and degrees of saturation.

1668

1669 Compared to the dry PBL ( Planetary Boundary Layer ) scheme in CAM3 and CAM4, moist  
 1670 turbulence scheme in CAM5 has the following unique characteristics: (1) it is a diagnostic TKE-  
 1671 based ( Turbulent Kinetic Energy,  $e$  ) 1<sup>st</sup> order K-diffusion scheme with entrainment parameter-  
 1672 ization but without counter-gradient transport, (2) it simulates *cloud – radiation – turbulence*  
 1673 interactions in an explicit way, which makes it possible to simulate full aerosol indirect effects  
 1674 with direct interactions with cloud macro-microphysics and radiation schemes, (3) using a single  
 1675 set of consistent physical formula, it is operating in any layers above as well as within PBL as  
 1676 long as moist  $Ri$  ( Richardson number ) is larger than a critical value  $Ri_c=0.19$ . Thanks to  
 1677 explicit simulation of moist turbulences driven by LW ( Longwave ) radiative cooling at the  
 1678 cloud top, CAM5 does not need a separate formula for stability-based stratus fraction - stratus  
 1679 fraction is computed only using mean relative humidity. It performs much better in the cloud-  
 1680 topped PBL than CAM3/4's dry PBL scheme with similar or superior performance in dry stable  
 and convective PBLs.

1681

In order to illucidate conceptual background behind the CAM5's moist turbulence scheme, let's imagine a single symmetric turbulence being perturbed by a static vertical distance  $l$  from its equilibrium height. This symmetric turbulence is assumed to be imbedded in the environment without vertical discontinuity such as sharp inversion. If  $l$  is sufficiently smaller than the vertical length scale over which vertical gradient of environmental scalar (  $\gamma_{\bar{\phi}} \equiv \partial \bar{\phi} / \partial z$  ) changes and if turbulent vertical velocity (  $w'$  ) is approximated to  $\sqrt{e}$ , we can easily derive that turbulent flux of any conservative scalar (  $\phi$  ) becomes  $w' \phi' = -l \cdot \sqrt{e} \cdot \gamma_{\bar{\phi}}$ . In reality, however, atmospheric stability controls turbulent vertical velocity ( i.e.,  $w'$  will be a product of  $\sqrt{e}$  and an anisotropic factor of TKE, which is a function of atmospheric stability ) and actual vertical perturbation distance of turbulent updraft and downdraft ( i.e., turbulent *mixing* length will be a product of a *static* perturbation distance  $l$  and a certain atmospheric stability parameter ). In addition, during vertical displacement, turbulent properties may be changed due to diabatic forcings or mixing with environment. All of these anomalous effects associated with atmospheric stability, diabatic forcings, and mixing are incorporated into a single stability function,  $S$ . As a result, turbulent flux of conservative scalar by symmetric turbulences embedded in the vertically-smooth-transitioning environment becomes

$$\overline{w' \phi'} = -l \cdot \sqrt{e} \cdot S \cdot \gamma_{\bar{\phi}} = -K \cdot \gamma_{\bar{\phi}} \quad (4.9)$$

1682

1683 Thus, computation of turbulent fluxes by symmetric turbulence is reduced to the computations of static turbulence length scale (  $l$  ), turbulent kinetic energy (  $e$  ), and stability function (  $S$  ). The product of these 3 terms is so called eddy diffusivity,  $K = l \cdot \sqrt{e} \cdot S$ . Due to diabatic  
 1684 adjustment of turbulent horizontal momentum to the environment during vertical displacement,

1685  $S$  for horizontal momentum (  $S_m$  ) is likely to be smaller than the  $S$  for heat and moisture (  $S_h$  ). This means that  $K_\phi$  is a function of scalar,  $\phi$ .

1686 If turbulence is embedded in the environment with a sharp vertical transition of stability such as inversion layer at the top of convective PBL, Eqn.(4.9) is inappropriate since turbulent motion will be suppressed in the stable portion of the discontinuous interface. In this case, we use the following entrainment parameterization.

$$\overline{w'\phi'} = -w_e \cdot \Delta \bar{\phi} = -\Delta z_e \cdot w_e \cdot \gamma_{\bar{\phi}} = -K_e \cdot \gamma_{\bar{\phi}} \quad (4.10)$$

1687 where  $w_e$  is entrainment rate and  $\Delta z_e$  is the thickness of the entrainment interfacial layer. Above 1688 entrainment parameterization is applied at the top and base interfaces of Convective Layer ( 1689 CL. See Fig.1 ) after finishing CL extension-merging procedures that will be explained later. In 1690 this case, eddy diffusivity is simply a product of  $\Delta z_e$  and  $w_e$ , identical for all scalars.

1691 CAM5's moist turbulence scheme consists of 9 main processes: (1) Bulk Moist Richardson 1692 number, (2) Initial identification of Convective ( CL ), Stably Turbulent ( STL ), and Stable ( SL 1693 ) Layers, (3) Turbulence Length Scale (  $l$  ), (4) Steady-State TKE (  $e$  ), (5) Stability Functions 1694 (  $S_\phi$  ), (6) CL Extension-Merging Procedures, (7) Entrainment Rates at the CL Top and Base 1695 Interfaces (  $w_e$  ), (8) Implicit Diffusion with Implicit Eddy Diffusivity, and (9) Implicit Surface 1696 Stress. Since many symmetric turbulences exist with different vertical length and velocity scales 1697 at any interface, the quantities we are trying to parameterize (  $l, e, S_\phi, w_e$  ) should be understood 1698 as the ensemble of all symmetric turbulences.

#### 1699 4.2.1 Bulk Moist Richardson Number

1700 Richardson number (  $Ri$  ) is used to diagnose the existence of turbulences. It is defined 1701 as the ratio of buoyancy production (  $P_b \equiv \overline{w'b'} = (g/\theta_v) \cdot \overline{w'\theta'_v}$  ) to shear production (  $P_s \equiv$  1702  $-\overline{w'u'} \cdot \partial \bar{u} / \partial z - \overline{w'v'} \cdot \partial \bar{v} / \partial z$  ) at the model interface.  $P_b$  represents energy conversion from mean 1703 available potential energy ( APE ) to TKE, while  $P_s$  is converison from mean kinetic energy to 1704 TKE. If  $Ri$  is negative, turbulence is absolutely generated but if it is positive, turbulence can 1705 be either generated or dissipated depending on the relative magnitude of  $|P_b|$  and  $|P_s|$ .

1706 Special treatment is necessary for saturated turbulences. If turbulence keeps its unsaturated state during vertical diplacement,  $\theta_v$  is a conserved quantity and Eqn.(4.9) can be directly used for computing  $\overline{w'\theta'_v}$ . However, if it is saturated,  $\theta_v$  decreases within downdraft due to evaporative cooling of cloud droplet, while increases within updraft due to condensation heating of water vapor. The resulting  $\overline{w'b'}$  including the effects of condensation and evaporation can be represented by the linear combinations of  $\overline{w's'_c}$  and  $\overline{w'q'_t}$  where  $s_c \equiv C_p \cdot T + g \cdot z - L_v \cdot q_l - L_s \cdot q_i$  is *condensate static energy* and  $q_t \equiv q_v + q_l + q_i$  is *total specific humidity*. Both  $s_c$  and  $q_t$  are conserved during vertical displacement and phase change. If we know saturated fractional area at the model interface ( e.g., stratus fraction ), we can write

$$\overline{w'b'} = c_h \cdot \overline{w's'_c} + c_q \cdot \overline{w'q'_t} \quad (4.11)$$

$$c_h = c_{h,s} \cdot a + c_{h,u} \cdot (1 - a), \quad c_q = c_{q,s} \cdot a + c_{q,u} \cdot (1 - a) \quad (4.12)$$

1707 where  $c_h, c_m$  are buoyancy coefficients for heat (  $s_c$  ) and moisture (  $q_t$  ) which are complex 1708 functions of temperature and pressure ( Schubert et al. [1979], Bretherton and Park [2009a] ),

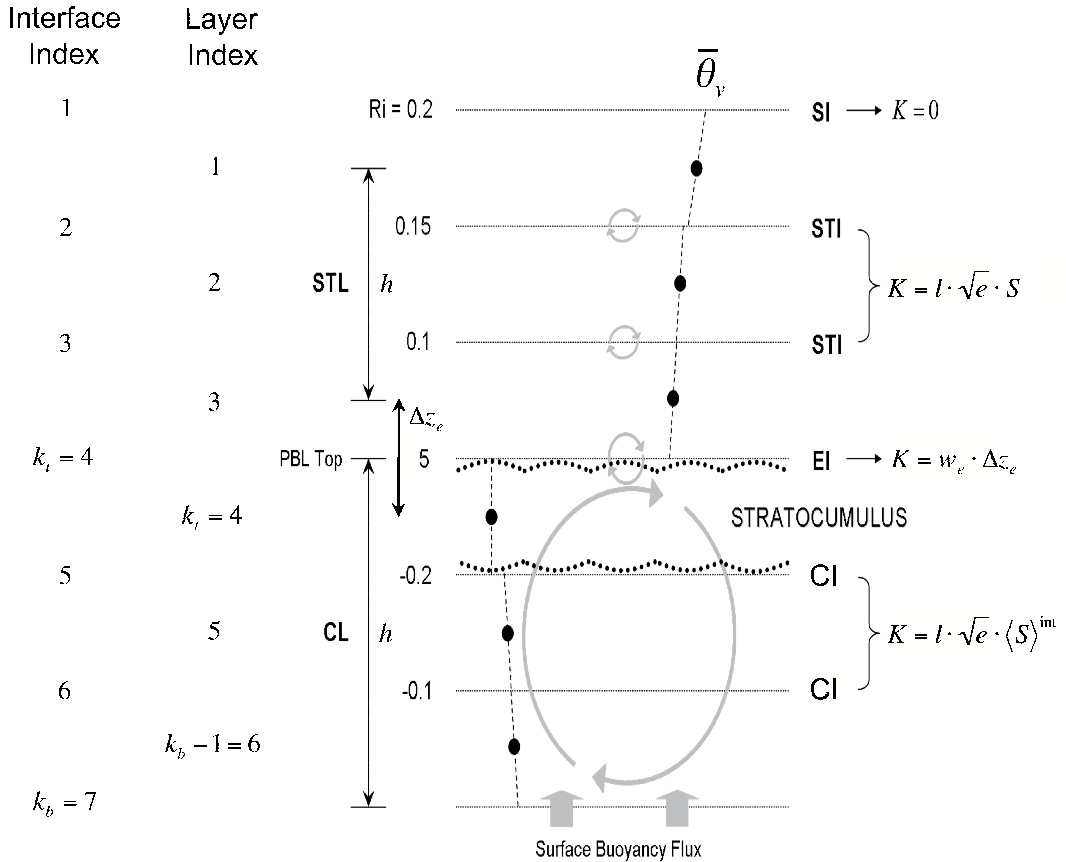


Figure 4.1: The indexing and example of turbulent layer structure in the bottom part of a typical column in the CAM5's moist turbulence scheme. Layer indexing used in CAM5 is shown at left. The bulk Richardson number  $Ri$  is used to locate a stable interface ( SI ) with  $Ri > Ri_c$ , stably turbulent interfaces ( STI ) with  $0 < Ri < Ri_c$  comprising an STL, and unstable convective interfaces ( CI ) with  $Ri < 0$  comprising a CL core. The CL is extended up to an entrainment interfaces ( EI ), at which the turbulent eddy diffusivity is computed from an explicitly predicted entrainment rate  $w_e$ . In the interior interfaces of the turbulent layers, the turbulent diffusivity  $K$  is conventionally using a length scale, diagnosed TKE, and stability function computed from local  $Ri$  in an STL and from layer-mean RI in a CL. Thickness of STL and CL are denoted by  $h$ , and the thickness of entrainment interface is denoted by  $\Delta z_e$ . See text for further details.

subscripts  $s, u$  denotes saturated and unsaturated turbulences, and  $a$  is stratus fraction. Applying Eqn.(4.9) to each term on the R.H.S. of Eqn.(4.11) and assuming  $K_h \approx K_m$ ,  $Ri$  can be written solely in terms of grid mean variables as follows.

$$Ri \equiv -\mathcal{C}P_bP_s = \mathcal{C}K_h \cdot N^2 K_m \cdot S^2 \approx \mathcal{C}N^2 S^2 \quad (4.13)$$

$$N^2 \equiv c_h \cdot \mathcal{C}\partial\bar{s}_c\partial z + c_q \cdot \mathcal{C}\partial\bar{q}_t\partial z, \quad S^2 \equiv (\mathcal{C}\partial\bar{u}\partial z)^2 + (\mathcal{C}\partial\bar{v}\partial z)^2 \quad (4.14)$$

1707 In the code,  $c_{h,s}, c_{h,u}, c_{q,s}, c_{q,u}$  and  $a$  are given at the layer mid-points. By averaging two  
 1708 adjacent layers' mid-point values, these are converted into model interface values. However, if  $a$   
 1709 in the adjacent upper layer is smaller than the average value, we took the smaller value, which is  
 1710 a necessary procedure to identify stably stratified interface at the top of stratocumulus-capped  
 1711 PBL.

## 1712 4.2.2 Identification of Convective, Stably Turbulent, and Stable Lay- 1713 ers

1714  
 1715 Using  $Ri$  defined at the interfaces, all model interfaces are grouped into *Convective Interface*  
 1716 ( CI with  $Ri \leq 0$  ), *Stably Turbulent Interface* ( STI with  $0 \leq Ri \leq Ri_c$  ), and *Stable Interface*  
 1717 ( SI with  $Ri > Ri_c$  ). Here,  $Ri_c = 0.19$  is a critical Richardson number and turbulence can exist  
 1718 only when  $Ri < Ri_c$  ( see Fig.4.1 ). If several CIs are adjacent ( or even when one CI exists ),  
 1719 they form a single *Convective Layer*, CL. If several STIs are adjacent ( or even when one STI  
 1720 exists ), they form a single *Stably Turbulent Layer*, STL. The remaining SIs form *Stable Layer*,  
 1721 SL where no turbulence exists. After finishing CL extension-merging which will be explained  
 1722 later, the external interfaces surrounding CL will be named as *Entrainment Interface* ( EI with  
 1723  $Ri > 0$  ) and the remaining CL interfaces as CL internal interfaces.

1724 In CL and STL, we neglect TKE storage. In STL, we further neglect TKE transport. In CL,  
 1725 turbulence can exist from the base to the top interfaces of CL, but in the STL, turbulence can  
 1726 exist from the layer mid-point just below the lowest STI to the layer mid-point just above the  
 1727 highest STI. This defines turbulent layer thickness,  $h$  in a slightly different way between CL and  
 1728 STL ( see Fig.4.1 ). After CL extension-merging, a single stability function  $\langle S \rangle^{int}$  is assigned to  
 1729 all CL internal interfaces.

1730 We use Eqn.(4.9) to compute eddy diffusivity at all interfaces except the top entrainment  
 1731 interface of CL where Eqn.(4.10) is used. If CL is elevated from the surface, Eqn.(4.10) is also  
 1732 applied to the CL base entrainment interface. If any interface is a double entraining interface  
 1733 from above and below, final eddy diffusivity is a simple sum of the two eddy diffusivities obtained  
 1734 from above CL and below CL. If surface buoyancy flux is positive ( negative ), surface is  
 1735 considered as a CL internal ( external ) interface and contributes ( does not contribute ) to  
 1736 the computation of internal energetics of CL.

1737 Several CLs and STLs can exist in a single grid column. The same physical equation set is  
 1738 used for all CLs and STLs regardless of whether they are based at the surface or elevated. Our  
 1739 moist turbulence scheme, thus, is not a PBL scheme - it is operating in all layers above as well  
 1740 as within the PBL. The conventional PBL is simply a surface-based CL or surface-based STL  
 1741 in our scheme. PBL top height is defined as the top external interface of surface-based CL. If

1742 STL is based at the surface instead, PBL top height is defined as the layer mid-point height just  
 1743 above the STL top interface. We don't impose any minimum value on the PBL height.

1744 We also define additional *Single Radiatively Driven Convective Layer* ( SRCL ) if any single  
 1745 layer satisfies the following 5 conditions: it has (1) grid-mean LWC larger than  $10^{-2} [g \cdot kg^{-1}]$  but  
 1746 no LWC in the layer just above it, (2) LW radiative cooling, (3)  $Ri > Ri_c$  at the top interface,  
 1747 (4) positive buoyancy production in the upper half-layer, and (5) it is not within the previously  
 1748 identified CLs. Similar to other CLs, entrainment parameterization is applied at the top and  
 1749 base interfaces of SRCL. Several SRCLs can exist in a single column.

### 1750 4.2.3 Turbulent Length Scale

1751 Following [Blackadar \[1962\]](#) and [Grenier and Bretherton \[2001\]](#), turbulent length scale is com-  
 puted as

$$(C1l)^\alpha = (C1k \cdot z)^\alpha + (C1l_\infty)^\alpha \quad (4.15)$$

$$l_\infty = \eta \cdot h \quad (4.16)$$

$$\eta = \begin{cases} 0.085 & \text{at STI} \\ 0.085 \cdot [2 - \exp(\min(0, \langle Ri \rangle^{int}))] & \text{at CI} \end{cases} \quad (4.17)$$

1752 where  $k = 0.4$  is a von Karman constant,  $l_\infty$  is asymptotic length scale,  $h$  is turbulent layer  
 1753 thickness, and  $\langle Ri \rangle^{int} = \langle l^2 \cdot N^2 \rangle^{int} / \langle l^2 \cdot S^2 \rangle^{int}$  is the mean Ri averaged over CL internal interfaces  
 1754 (  $\langle \rangle^{int}$  denotes vertical average over the CL internal interfaces ). We chose  $\alpha = 3$ .

1755 As explained in the previous section and [Fig.4.1](#),  $h$  for CL is defined as the depth between  
 1756 two external interfaces, while  $h$  for STL is defined as the distance between the two outmost  
 1757 layers' mid-points. When CL is based at surface but surface buoyancy flux is negative,  $h$  is  
 1758 defined down to the mid-point of the lowest model layer instead of down to the surface.

1759 Our formulation approximates  $l$  to  $l_\infty$  except near the ground, where it asymptotes  $k \cdot z$  to  
 1760 match surface layer similarity theory. As explained before, the actual turbulent *mixing* length  
 1761 should be understood as the product of  $l$  and stability function  $S$ .

### 1762 4.2.4 Steady-State Turbulent Kinetic Energy

1763 We assume steady-state TKE, that is, at each model interface,  $P_b + P_s + T_e - D = 0$  where  
 dissipation (  $D$  ) and TKE transport (  $T_e$  ) are parameterized as

$$D = [C e^{3/2} b_1 \cdot l] \quad (4.18)$$

$$T_e = [a_e \cdot C \sqrt{e} \cdot (\langle e \rangle - e) l] \quad (4.19)$$

where  $b_1 = 5.8$  and  $\langle e \rangle$  denotes TKE averaged over the whole CL. In case of STL,  $a_e = 0$  ( no TKE transport ) while in CL,  $a_e = 1$ . Ideally,  $\langle T_e \rangle$  should be zero but [Eqn.\(4.19\)](#) only satisfies this condition approximately. Combining with  $P_b$  and  $P_s$ , steady-state TKE at any model interface becomes

$$e = b_1 \cdot [C l \sqrt{e} \cdot (P_b + P_s) + a_e \cdot (\langle e \rangle - e)] \quad (4.20)$$

1764 At the internal interfaces of CL,  $P_b = -K_h \cdot N^2$  and  $P_s = K_m \cdot S^2$  with  $K_h = l \cdot \sqrt{e} \cdot \langle S_h \rangle^{int}$   
 1765 and  $K_m = l \cdot \sqrt{e} \cdot \langle S_m \rangle^{int}$  where  $\langle S_h \rangle^{int}$  and  $\langle S_m \rangle^{int}$  are mean stability functions averaged over  
 1766 internal interfaces of CL computed by using  $\langle Ri \rangle^{int}$  and Eqn.(4.23) and (4.24).

At entrainment interfaces,  $P_b = -K_e \cdot N^2 + f_R \cdot c_{h,s} \cdot \Delta \bar{F}_R / \rho$  and  $P_s = K_e \cdot S^2$  with  $K_e = w_e \cdot \Delta z_e$  where  $\Delta z_e$  is the thickness of entrainment interface. In computing  $P_b$  at the entrainment interfaces,  $N^2$  is redefined using the cloud fraction in the half-layer just below ( above ) the CL top ( base ) entrainment interface. This redefinition of  $N^2$  is necessary in order to correctly take into account of buoyancy production associated with the evaporative cooling of entrained airs.  $\Delta \bar{F}_R$  is grid-mean radiative flux divergence across the CL top layer in unit of  $[W \cdot m^{-2}]$  given from the radiation scheme and  $0 \leq f_R \leq 1$  is the fraction of radiative flux divergence confined in the thin transition zone near the top entrainment interface of CL among  $\Delta \bar{F}_R$ . Following Bretherton and Park [2009a],  $f_R$  is parameterized as

$$f_R = [\mathcal{C} \tau \cdot (4 + \tau) 24 + \tau \cdot (6 + \tau)] \quad (4.21)$$

$$\tau = 156 \cdot \bar{q}_l^{top} \cdot \Delta p^{top} / g \quad (4.22)$$

1767 where  $\tau$  is the grid-mean cloud optical depth of CL top layer that has grid-mean LWC of  $\bar{q}_l^{top}$   
 1768 and a thickness of  $\Delta p^{top}$ . As PBL deepens, cloud can be formed in the layer just above the PBL  
 1769 top ( i.e., *ambiguous layer* ). In this case, most of radiative flux divergence will be confined  
 1770 at the top of the ambiguous layer. In order to take into account of this case, we simply added  
 1771  $f_R \cdot \Delta \bar{F}_R / \rho$  both in the CL top and ambiguous layers.

1772 At the surface interface,  $P_{b,sfc} = c_h \cdot (F_h^* / \rho) + c_m \cdot (F_q^* / \rho)$  where  $F_h^*$  is sensible heat flux  
 1773  $[J \cdot s^{-1} \cdot m^{-2}]$  and  $F_q^*$  is water vapor flux  $[kg \cdot s^{-1} \cdot m^{-2}]$  at surface given from the surface flux  
 1774 computation scheme to the moist turbulence scheme, and  $P_{s,sfc} = u_*^3 / (k \cdot z_0)$  where  $z_0$  is the  
 1775 mid-point height of the lowest model layer and  $u_*$  is frictional velocity at surface defined as  
 1776  $u_*^2 = \sqrt{\tau_x^2 + \tau_y^2} / \rho$  where  $\tau_x, \tau_y$  is surface momentum flux  $[kg \cdot m \cdot s^{-1} \cdot s^{-1} \cdot m^{-2}]$ . Assuming no  
 1777 TKE transport and turbulent length scale  $l = k \cdot z_0$ , we compute TKE at surface half-layer,  $e_{sfc}$   
 1778 using Eqn.(4.20). In order to prevent negative  $e_s$ , we impose a minimum positive value on  $e_{sfc}$ .

1779 By integrating Eqn.(4.20) over the whole CL with an approximation of  $e \approx \langle e \rangle$  at the  
 1780 entrainment interfaces, we can compute  $\langle e \rangle$  by solving a cubic equation of  $\langle e \rangle^{1/2}$ . Once  $\langle e \rangle$  is  
 1781 computed, we can compute  $e$  at each internal interfaces of CL using Eqn.(4.20) again.

1782 Our moist turbulence scheme computes characteristic excesses ( or standard deviations ) of  
 1783 turbulent updraft vertical velocity (  $\sigma_w$  ), temperature (  $\sigma_T$  ), and water vapor (  $\sigma_q$  ) within  
 1784 PBL or near surface. If PBL is CL ( STL ), we estimate  $\sigma_w = \sqrt{\langle e \rangle}$  (  $\sigma_w = u_* / 8.5$  ) and then  
 1785  $\sigma_T = (F_h^* / \rho / C_p) / \sigma_w$  and  $\sigma_q = (F_q^* / \rho) / \sigma_w$ . These characteristic convective excesses when PBL  
 1786 is CL are used to define cumulus source air properties within deep convection scheme.

## 1787 4.2.5 Stability Functions

1788 Following Galperin et al. [1988], stability functions are parameterized as

$$S_h = [\mathcal{C} \alpha_5 1 + \alpha_3 \cdot G_h] \quad (4.23)$$

$$S_m = [\mathcal{C} \alpha_1 + \alpha_2 \cdot G_h (1 + \alpha_3 \cdot G_h) \cdot (1 + \alpha_4 \cdot G_h)] \quad (4.24)$$

where  $\alpha_1 = 0.5562$ ,  $\alpha_2 = -4.3643$ ,  $\alpha_3 = -34.6764$ ,  $\alpha_4 = -6.1272$ ,  $\alpha_5 = 0.6986$  and  $G_h \equiv -N^2 \cdot l^2 / (2 \cdot e)$  is a nondimensional stability ratio restricted by  $-3.5334 < G_h < 0.0233$ . In case of STL,  $G_h$  is obtained by combining Eqn.(4.20),(4.23),(4.24) as follows.

$$Ri \cdot (1 + \alpha_3 \cdot G_h) \cdot (1 + \alpha_4 \cdot G_h) = 2 \cdot b_1 \cdot G_h \cdot [Ri \cdot \alpha_5 \cdot (1 + \alpha_4 \cdot G_h) - (\alpha_1 + \alpha_2 \cdot G_h)] \quad (4.25)$$

For  $Ri > Ri_c = 0.19$ , there is no physically realizable solution  $G_h$  and the interface is assumed to be non-turbulent. For  $Ri < Ri_c$ , this polynomial has two real roots, but only the larger one is realizable. In case of internal CL, we use the same Eqn.(4.25) but with  $\langle Ri \rangle^{int} = \langle l^2 \cdot N^2 \rangle^{int} / \langle l^2 \cdot S^2 \rangle^{int}$  to compute  $\langle G_h \rangle^{int}$ ,  $\langle S_h \rangle^{int}$  and  $\langle S_m \rangle^{int}$ . For  $\langle Ri \rangle^{int} < -44.5$ , the allowable upper bound  $\langle G_h \rangle^{int} = 0.0233$  is exceeded and stability functions assume their maximum values  $S_h^{max} = 3.64$  and  $S_m^{max} = 2.76$ .

## 4.2.6 CL Extension-Merging Procedure

Several CLs can be identified in a single grid column. A contiguous set of interfaces with negative  $Ri$  is initially identified as a CL core. Starting from the lowest CL, each CL is extended first upward as far as possible, then downward as far as possible from the CL core into any adjacent layers of sufficiently weak stable stratification. Any external interface of CL is incorporated into the CL if the following criterion is satisfied.

$$(\Delta z \cdot l^2 \cdot N^2)^E < \left[ \mathcal{C}r_{inc} 1 - r_{inc} \right] \cdot \int_{CL_{int}} l^2 \cdot N^2 \cdot dz \quad (4.26)$$

where superscript  $E$  denotes CL external interface being tested for incorporation into CL,  $\Delta z$  is the thickness of external interface, and the R.H.S. denotes vertical integration over the CL internal interfaces. We chose  $r_{inc} = -0.04$  to be consistent with a dry convective boundary layer in which the entrainment buoyancy flux is -0.2 of the surface buoyancy flux. Strictly speaking, Eqn.(4.26) compares buoyancy production during TKE dissipation time scale by assuming that  $S_h$  of the external interface being tested for merging is the same as the  $\langle S_h \rangle^{int}$ . The first interface above ( below ) CL that fails this criterion will be the top ( bottom ) entrainment interface for that CL. No extension-merging is performed for SRCL since SRCL does not have internal interfaces.

Above criteria ensures that as long as the initial CL internal core (  $CL_{int}$  ) has net positive buoyancy production, the internal CL after incorporating external interface will also have positive buoyancy production. Our incorporation test also guarantees that if any external interface is unstably stratified, it will be incorporated. Thus, if we incorporate any of the interior of a CL, we will incorporate or merge all of it.

If CL is based at surface and surface buoyancy flux is positive, the contribution of surface half-layer is also incorporated into the above integration of  $CL_{int}$ . In the surface half-layer, we use  $G_h = (k \cdot z_0 \cdot P_{b,sfc}) / (2 \cdot S_h \cdot e_{sfc}^{3/2})$  and by combining with Eqn.(4.23),  $S_h$  can be computed. Finally,  $(l^2 \cdot N^2)_{sfc} = -k \cdot z_0 \cdot P_{b,sfc} / (S_h \cdot \sqrt{e_{sfc}})$ .

In computing turbulent length scale from Eqns.(4.15)-(4.17) during CL extension-merging procedure, we simply assume  $\eta = 0.5 \cdot (0.085 + 0.170) = 0.1275$  for all merging and merged

1817 interfaces and turbulent layer thickness  $h$  is fixed by the initial value before CL extension-  
 1818 merging. After finishing all the extension-merging procedure,  $\langle S_h \rangle^{int}$  and  $\langle S_m \rangle^{int}$  are computed  
 1819 using  $\langle Ri \rangle^{int} = \langle l^2 \cdot N^2 \rangle^{int} / \langle l^2 \cdot S^2 \rangle^{int}$  and the updated  $h$ .

## 1820 4.2.7 Entrainment Rates at the CL Top and Base Interfaces

1821 At entrainment interfaces, eddy diffusivity is computed using Eqn.(4.10). Entrainment rate  
 $w_e$  is computed as

$$w_e = A \cdot (\mathcal{C} \bar{s}_{vl} g) \cdot [\mathcal{C} w_*^3 \Delta^E \bar{s}_{vl} \cdot h] \quad (4.27)$$

where  $h = z_t - z_b$  is the thickness of CL,  $\Delta^E \bar{s}_{vl}$  is the jump of mean liquid virtual static energy  
 $s_{vl} \equiv s_l \cdot (1 + 0.61 \cdot q_t)$  across the entrainment interfaces at the top (  $\Delta^E \bar{s}_{vl} = \bar{s}_{vl}(k_t - 1) - \bar{s}_{vl}(k_t)$  ) and base (  $\Delta^E \bar{s}_{vl} = \bar{s}_{vl}(k_b - 1) - \bar{s}_{vl}(k_b)$  ) of the CL.  $w_*$  is convective velocity defined as

$$w_* = \left[ 2.5 \cdot \int_{z_b}^{z_t} P_b \cdot dz \right]^{1/3} \quad (4.28)$$

and  $A$  is an entrainment coefficient defined as

$$A = \begin{cases} 0.2 \cdot [1 + a_2 \cdot 0.8 \cdot (\mathcal{C} L_v \cdot \bar{q}_l^{top} \Delta^E \bar{s}_{vl})] & \text{at CL top} \\ 0.2 & \text{at CL base} \end{cases} \quad (4.29)$$

1822 where  $a_2$  is a tuning parameter being allowed to be changed between 10 and 60, and we chose  
 1823  $a_2 = 30$ . As PBL deepens, cloud can be formed in the ambiguous layer. In order to fully take  
 1824 into account of all possible mixtures between PBL air and free air above inversion,  $\Delta^E \bar{s}_{vl}$  in  
 1825 *computing A* in Eqn.(4.29) is obtained by using the layer-value just above the ambiguous layer,  
 1826 not the value in the ambiguous layer ( i.e.,  $\Delta^E \bar{s}_{vl} = \bar{s}_{vl}(k_t - 2) - \bar{s}_{vl}(k_t)$  in Eqn.(4.29) ). In the  
 1827 similar context, we take  $\bar{q}_l^{top} = \max[\bar{q}_l(k_t), \bar{q}_l(k_t - 1)]$ .

1828 Due to the way how the model is structured, we don't have information on  $K_h$  when en-  
 1829 trainment rate is computed. Thus, in computing  $P_b = -K_h \cdot N^2$  at CL internal interfaces for  
 1830 entrainment parameterization, we use  $K_h$  of previous iteration or previous time step. Since  
 1831 we are using a predictor-corrector iteration method,  $K_h$  is likely to converge as iteration is  
 1832 proceeded.

1833 If eddy diffusivity at the entrainment interface is smaller than the value obtained by assuming  
 1834 entrainment interface is STI, the final eddy diffusivity is set to be that of STI.

## 1835 4.2.8 Implicit Diffusion with Implicit Diffusivity

1836  
 1837 CAM5 is using process splitting. At each time step, successive parameterizations oper-  
 1838 ate on the updated state resulting from the previous parameterizations. The parameter-  
 1839 izations in CAM5 are called in the following order at each time step: **deep convection**  
 1840 → **shallow convection** ( computes (1) cumulus fraction and condensate, (2) vertical  
 1841 transport of heat, moisture, momentum, and tracers by asymmetric turbulences ) →  
 1842 **stratiform macrophysics** ( stratus fractions and stratiform net condensation-deposition rates  
 1843 ) → **stratiform microphysics** ( (1) activation of cloud liquid droplets and ice crystals, (2)

1844 conversions among cloud liquid droplets, ice crystals, rain, and snow, (3) evaporation of pre-  
 1845 precipitation and sedimented cloud condensates ) → **wet deposition of aerosols** → **radiation**  
 1846 → **surface fluxes** ( upward fluxes of heat, water vapor, momentum, and tracers at surface ) →  
 1847 **aerosol and chemical conversion processes** ( conversions among various aerosol and chem-  
 1848 ical species ) → **turbulent diffusion** ( vertical transport of heat, moisture, momentum, and  
 1849 tracers by symmetric turbulences ) → **gravity wave drag** → **dry deposition of aerosols** →  
 1850 **dynamics** ( large scale advection of grid mean heat, moisture, momentum, and tracers ).

Given a diffusivity profile  $K(z)$  and an input state  $\bar{\phi}^*(z)$  updated to include all physical and dynamic processes ( including explicit deposition of surface fluxes into the lowest model layer except horizontal momentum ), our moist turbulence scheme diffuses  $\bar{\phi}^*$  using the following implicit backward Euler scheme.

$$[\mathcal{C}\bar{\phi}(t + \Delta t) - \bar{\phi}^* \Delta t] = \mathcal{C}\partial\partial z [K(z) \cdot \mathcal{C}\partial\partial z \bar{\phi}(t + \Delta t)] \quad (4.30)$$

1851 subject to specified upward surface fluxes of horizontal momentums (  $\tau_{x,tot} = \tau_x^* - k_{tms} \cdot \bar{u}_{s,i}$ ,  
 1852  $\tau_{y,tot} = \tau_y^* - k_{tms} \cdot \bar{v}_{s,i}$  in unit of  $[kg \cdot m \cdot s^{-1} \cdot s^{-1} \cdot m^{-2}]$  where the second term on the R.H.S.  
 1853 is turbulent mountain stress obtained by using updated surface wind  $\bar{u}_{s,i}, \bar{v}_{s,i}$  after  $i^{th}$  iteration  
 1854 ), sensible heat (  $F_h^*$  in unit of  $[J \cdot s^{-1} \cdot m^{-2}]$  ), and water vapor (  $F_q^*$  in unit of  $[kg \cdot s^{-1} \cdot m^{-2}]$   
 1855 ) where superscript \* denotes the input value given to the moist turbulence scheme. The eddy  
 1856 diffusivity profile  $K(z)$  may be computed using the input state variable  $\bar{\phi}^*$ . However, when a  
 1857 long time step  $\Delta t = 1800$  [s] is used as in CAM5, this is not a desirable approach since the  
 1858 physical processes proceeding turbulent diffusion scheme ( e.g., radiation ) can dramatically  
 1859 destabilize the input profile  $\bar{\phi}^*(z)$ , resulting in unreasonable  $K(z)$ . To address this problem, we  
 1860 use an iterative predictor-corrector approach to recalculate eddy diffusivities based on an better  
 1861 approximation to the post-diffusion state.

Let's assume that  $K_i$  is diffusivity profile obtained from  $\bar{\phi}_i$ . When  $i = 0$ ,  $\bar{\phi}_0 \equiv \bar{\phi}^*$  and  $K_0 \equiv K^*$ . Using  $\bar{\phi}_0$ , we compute  $K_0$  and obtain the first diffused profile  $\bar{\phi}_1$  by solving Eqn.(4.30) applied to the initial state  $\bar{\phi}^*$ . Using  $\bar{\phi}_1$ , we compute  $K_1$  and the predictor-corrector averaged  $K_{0:1} \equiv \lambda \cdot K_1 + (1 - \lambda) \cdot K_0$ . Using this  $K_{0:1}$ , we diffuse the *input state*  $\bar{\phi}^*$  again and obtain the second diffused profile  $\bar{\phi}_2$  from which  $K_2$  and  $K_{0:2} \equiv \lambda \cdot K_2 + (1 - \lambda) \cdot K_{0:1}$  are computed. By repeating this process, the predictor-corrector averaged  $K$  profile after  $N$  iteration becomes

$$K_{0:N} \equiv \lambda \cdot K_N + (1 - \lambda) \cdot K_{0:N-1} \quad (4.31)$$

$$K_{0:0} \equiv K^* \quad (4.32)$$

1862 We chose  $N = 4$  and  $\lambda = 0.5$  to compute the final eddy diffusivity  $K = K_{0:N}$  from the  
 1863 eddy diffusion scheme. During individual iterative diffusion processes of  $\bar{\phi}^*$  by  $K = K_{0:n}$  ( $1 \leq$   
 1864  $n \leq N$ ), we diffused conservative scalars  $\bar{\phi}^* = \bar{s}_l^*, \bar{q}_t^*, \bar{u}^*, \bar{v}^*$  and reconstructed the diffused non-  
 1865 conservative scalars  $\bar{T}, \bar{q}_v, \bar{q}_l, \bar{q}_i$  profiles by assuming that (1)  $\bar{q}_i$  is not diffused and (2) the layer  
 1866 has homogeneous distribution of cloud condensate across the grid at saturation equilibrium  
 1867 state.

1868 Since the initial profiles  $\bar{\phi}^*$  are continuously updated within each iteration, we should also  
 1869 update surface fluxes (  $\tau_x^*, \tau_y^*, F_h^*, F_q^*$  ) and the profiles of stratus fraction and radiative heating  
 1870 rate within each iteration. However, this will hugely increase computation time and make the  
 1871 CAM5 structure much more complex. Thus, we simply ignore the variations of surface fluxes,  
 1872 stratus fraction and radiative heating rate during iteration. This simplification can inevitably

cause  $K_i$  ( $i \geq 1$ ) to be computed on the  $\bar{\phi}_i$  that has inconsistency among various state variables. Finally, because of the flipping of layer structures and corresponding eddy diffusivities between the iterations, our predictor-corrector method may not produce fully convergent  $K$  regardless of the iteration number. By choosing  $\lambda = 0.5$ , however, we address this issue to our best. Once the final  $K$  is obtained from Eqn.(4.31), we diffuse the input grid mean scalars ( $\bar{s}, \bar{q}_v, \bar{q}_l, \bar{q}_i, \bar{n}_i, \bar{u}, \bar{v}$ ).

Vertical transport of horizontal momentum by symmetric turbulence conserves column-mean horizontal momentum. However, it will change column-mean kinetic energy ( KE ) of the mean wind. In reality, this KE change will be converted into TKE and eventually internal heat energy ( or potential energy, PE ). In CAM5, however, we don't store TKE between time steps because of steady-state TKE assumption and yet require conservation of column-mean total energy, PE+KE. In order to conserve total energy in each column, we computed KE dissipation heating rate in each layer following [Boville and Bretherton \[2003b\]](#) after diffusing horizontal momentum, and explicitly added KE dissipation heating into  $\bar{s}$  before diffusing  $\bar{s}$ .

Since air parcel temperature changes during vertical displacement due to adiabatic compression-expansion, moist turbulence scheme should also handle associated condensation-evaporation of cloud droplets during vertical transport. The same should be true for convection and large-scale advection schemes. However, this evaporation-condensation associated with vertical diplacement of air parcels will be treated in the following stratiform cloud macrophysics. Thus, diffusing non-conservative scalars with a phase change ( $\bar{s}, \bar{q}_v, \bar{q}_l, \bar{q}_i, \bar{n}_l, \bar{n}_i$ ) is not a problem if we admit that reasonable profiles of cloud condensates can be restored only after stratiform macro-microphysics.

When turbulence transports non-saturated airs into the overlying saturated airs, new cloud droplets can be formed without the change of cloud condensate mass ( so called, cloud droplet activation ). In order to handle adiabatic turbulent vertical transport and concurrent diabatic sources of cloud droplet number in a consistent way, turbulent diffusions of  $\bar{n}_l$ , aerosol mass and numbers are separately treated by the cloud droplet activation routine within the stratiform microphysics.

#### 4.2.9 Implicit Surface Stress

In CAM5, surface fluxes of various scalars ( $s, q_v, q_l, q_i, n_l, n_i$  and tracers) are explicitly deposited into the lowest model layer ( this forms the input  $\bar{\phi}^*$  to Eqn.(4.30) ) and then implicit vertical diffusion is performed using Eqn.(4.30). In case of surface momentum fluxes ( $\tau_x^*, \tau_y^*$ ), however, such explicit adding can flip the direction of the lowest model layer wind ( $\bar{u}_s^*, \bar{v}_s^*$ ). This is not a physically realizable situation since as wind speed decreases by surface drag, surface drag itself decreases too, preventing flipping of wind in nature. This flipping of the wind in the model can be a source of numerical instability especially when the lowest model layer is thin. Thus,  $\tau_x^*, \tau_y^*$  should be added into the lowest model layer in an implicit way. This implicit adding, however, will cause discrepancy between the horizontal momentum that the Earth surface lost ( which are explicit surface momentum flux  $\tau_x^*, \tau_y^*$  given to the turbulent diffusion scheme ) and the momentum that the atmosphere receives ( which are implicit surface momentum flux ). To conserve horizontal momentum of the whole coupled system, they should be identical. In order to address both the numerical stability and momentum conservation

1916 issues, we partitioned the residual surface momentum flux ( = explicit surface momentum flux  
 1917 - implicit surface momentum flux ) over a certain time interval, e.g., 2 hr. This process is called  
 1918 implicit surface stress being detailed below.

First, in order to compute implicit surface stress, we compute total surface drag coefficient (  $k_{tot}$  ) by summing the *normal* drag coefficient (  $k_{nor}$  ) obtained from the lowest model layer wind and the *turbulent mountain stress* drag coefficient (  $k_{tms}$  ) triggered by sub-grid distribution of surface topography. This  $k_{tms}$  is computed by separate turbulent mountain stress module.

$$k_{nor} = \max \left[ \mathcal{C} \sqrt{(\tau_x^*)^2 + (\tau_y^*)^2} \max(\sqrt{(\bar{u}_s^*)^2 + (\bar{v}_s^*)^2}, 1), 10^{-4} \right] \quad (4.33)$$

$$k_{tot} = k_{nor} + k_{tms} \quad (4.34)$$

Second, a certain fraction of residual stress accumulated upto the current time step from the first time step is added into the lowest model layer. This changes the wind in the lowest model layer.

$$\bar{u}_s^+(t) = \bar{u}_s^*(t) + \tau_{x,res}(t) \cdot \Lambda (\mathcal{C}g\Delta p) \cdot \Delta t, \quad \bar{v}_s^+(t) = \bar{v}_s^*(t) + \tau_{y,res}(t) \cdot \Lambda (\mathcal{C}g\Delta p) \cdot \Delta t, \quad (4.35)$$

$$\Lambda = [\mathcal{C}\Delta t \Delta t_{res}], \quad \Delta t \leq \Delta t_{res} = 7200 \text{ [sec]} \quad (4.36)$$

1919 where  $\tau_{x,res}(t), \tau_{y,res}(t)$  are residual stress accumulated upto the current time step from the first  
 1920 time step, and  $\Delta t_{res}$  is a time interval over which residual stress is deposited into the atmosphere.  
 1921 With  $K(z)$ ,  $k_{tot}$ , and given input wind profiles of  $\bar{u}^*(t)$  and  $\bar{v}^*(t)$  but with the lowest model layer  
 1922 winds of  $\bar{u}_s^+(t)$  and  $\bar{v}_s^+(t)$  instead of  $\bar{u}_s^*(t)$  and  $\bar{v}_s^*(t)$ , we can solve Eqn.(4.30) to obtain implicitly  
 1923 time-marched wind profiles,  $\bar{u}(t + \Delta t)$  and  $\bar{v}(t + \Delta t)$ .

Finally, the net residual stress accumulated upto the end of current time step which will be used at the next time step becomes

$$\tau_{x,res}(t + \Delta t) = \tau_{x,res}(t) \cdot (1 - \Lambda) + \tau_x^* + k_{nor} \cdot \bar{u}_s(t + \Delta t) \quad (4.37)$$

$$\tau_{y,res}(t + \Delta t) = \tau_{y,res}(t) \cdot (1 - \Lambda) + \tau_y^* + k_{nor} \cdot \bar{v}_s(t + \Delta t) \quad (4.38)$$

1924 where  $\bar{u}_s(t + \Delta t)$  and  $\bar{v}_s(t + \Delta t)$  are implicitly marched winds of the lowest model layer at  
 1925 the end of turbulent diffusion scheme at the current time step. At the first time step, it is  
 1926  $\tau_{x,res}(t) = \tau_{y,res}(t) = 0$ . Our formulation assumes that turbulent mountain stress is fully implicitly  
 1927 added into the atmosphere without generating any residual stress. This assumption causes  
 1928 no conservation problem since turbulent mountain stress is used only within the atmospheric  
 1929 model not in the ocean, sea ice, and land models.

1930 One complexity arises because  $K(z)$  is iteratively computed at each time step. We assume  
 1931 that all of  $\tau_{x,res}(t)$ ,  $k_{tms}$  and  $k_{nor}$  are not changed within the iteration loop :  $k_{tms}$  and  $k_{nor}$   
 1932 are obtained from the initial wind profile  $\bar{u}_s^*(t), \bar{v}_s^*(t)$  given to the moist turbulence scheme. In  
 1933 computing eddy diffusivity  $K_i$  within each iteration loop, however, we used  $\tau_{x,tot} = \tau_x^* - k_{tms} \cdot$   
 1934  $\bar{u}_{s,i}(t)$ ,  $\tau_{y,tot} = \tau_y^* - k_{tms} \cdot \bar{v}_{s,i}(t)$  where  $\bar{u}_{s,i}(t), \bar{v}_{s,i}(t)$  are iteratively updated wind in the lowest  
 1935 model layer after  $i^{th}$  iteration at the current time step. Here, we included turbulent mountain  
 1936 stress in computing eddy diffusivity since it is a source of shear production and TKE in the  
 1937 lowest model layer, too.

## 1938 4.3 Shallow Convection Scheme

1939 Shallow convection scheme in CAM5 is from [Park and Bretherton \[2009\]](#) that is a replacement  
1940 of [Hack \[1994b\]](#) shallow convection scheme in CAM3 and CAM4. Similar to its precedents,  
1941 CAM5 performs shallow convection scheme just after deep convection scheme. In general, dis-  
1942 tinctions between deep and shallow convective processes are made by the differences in cloud top height,  
1943 the existence of convective precipitation and convective downdraft. While named as shallow  
1944 convection, CAM5's shallow convection scheme does not have any limitation on its cloud top  
1945 height and convective precipitation. However, because the proceeding deep convection scheme  
1946 consumes most of Convective Available Potential Energy ( CAPE ) and stabilizes the atmo-  
1947 sphere, cloud top height simulated by shallow convection scheme is naturally limited in the  
1948 tropical regions. In contrast to deep convection scheme, shallow convection scheme does not  
1949 have a separate formulation for convective downdraft, but have an explicit parameterization of  
1950 penetrative entrainment in the overshooting zone near cumulus top. Future implementation of  
1951 convective downdraft as well as refinements of other aspects ( e.g., updraft mixing rate and  
1952 cloud microphysics ) can make shallow convection scheme work for deep convective case, too.

1953 The role of shallow convection scheme is to vertically transport heat, moisture, momentum,  
1954 and tracers by asymmetric turbulences. On the other hands, vertical transport by symmetric  
1955 turbulences are performed by separate moist turbulence scheme. CAM5's shallow convection  
1956 scheme is carefully designed to optimally operate with CAM5's moist turbulence scheme without  
1957 missing or double-counting processes. Similar to the other convection schemes, CAM5 shallow  
1958 convection scheme assumes (1) steady state convective updraft plume, and (2) small updraft  
1959 fractional area, so that compensating subsidence entirely exists within the same grid box as  
1960 convective updraft. One of the unique aspects of CAM5 shallow convection scheme is its ability  
1961 to compute convective updraft vertical velocity and updraft fractional area by using updraft  
1962 vertical momentum equation. Computation of updraft vertical velocity enables to compute more  
1963 refined fractional entrainment-detrainment rates, cloud top height, and penetrative entrainment.  
1964 While not implemented in the current CAM5's shallow convection scheme, updraft vertical  
1965 velocity will make it possible to compute activated fraction of aerosol masses and numbers at  
1966 the cumulus base, more elegant cumulus microphysics, and aerosol-cumulus interactions.

1967 CAM5's shallow convection scheme consists of 8 main processes: (1) Reconstruction of mean  
1968 profiles and cloud condensate partitioning, (2) Computation of source air properties of a sin-  
1969 gle ensemble-mean updraft plume at the PBL ( Planetary Boundary Layer ) top, (3) Cloud  
1970 base mass flux and updraft vertical velocity closures using Convective Inhibition ( CIN ) and  
1971 TKE ( Turbulent Kinetic Energy ), (4) Vertical evolution of a single entraining-detraining buoy-  
1972 ancy sorting plume from the PBL top to the cumulus top, (5) Penetrative entrainment in the  
1973 overshooting zone near cumulus top, (6) Computation of convective fluxes within the PBL, (7)  
1974 Computation of grid-mean tendencies of conservative scalars, and (8) Computation of grid-mean  
1975 tendencies of non-conservative scalars. The following sections describe each of these processes  
1976 in detail.

### 1977 4.3.1 Reconstruction of Mean Profiles and Cloud Condensate Par- 1978 titioning

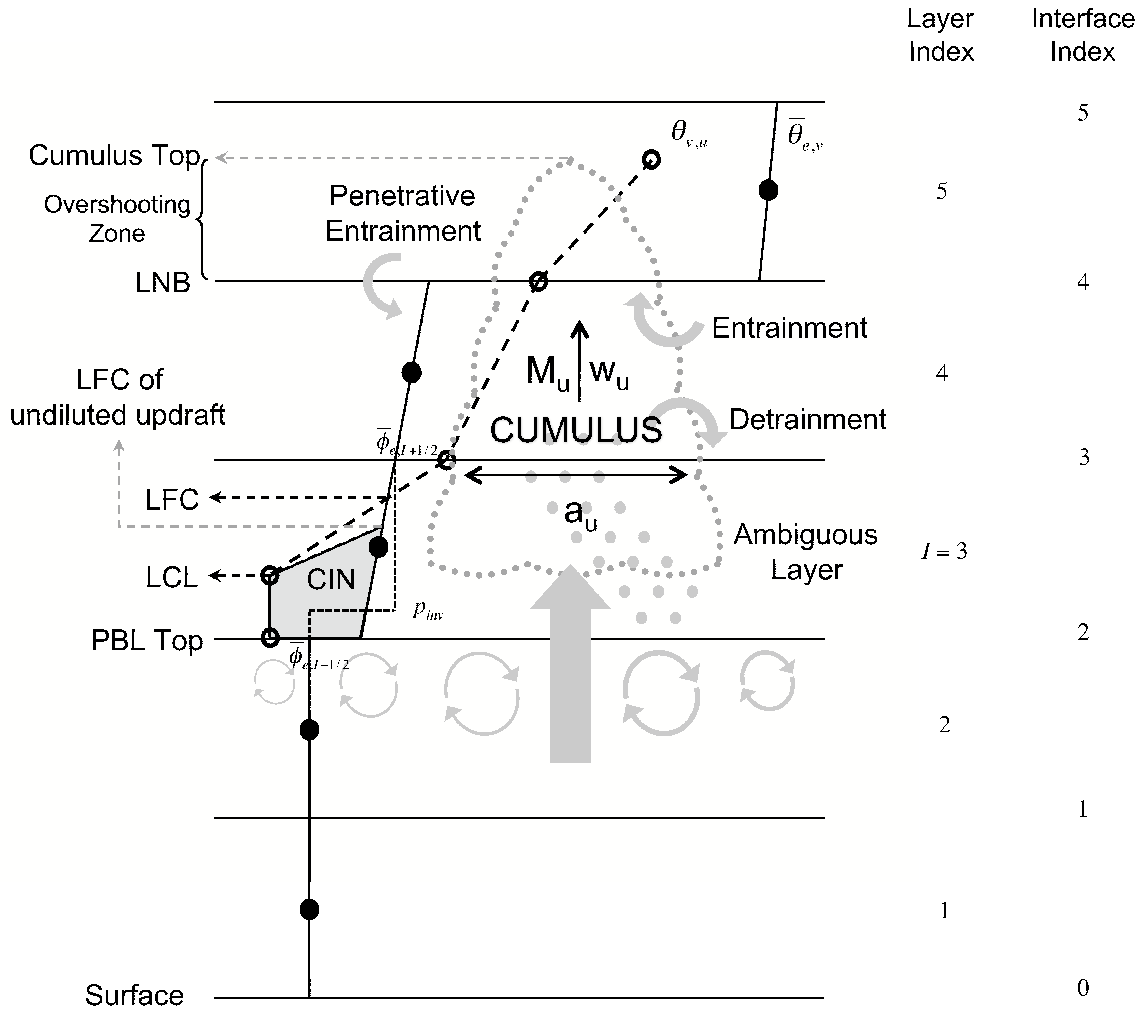


Figure 4.2: Schematic structure of shallow cumulus scheme describing vertical evolution of a bulk cumulus updraft and its interaction with environment and the subcloud layer. Black dots denote environmental mean virtual potential temperature  $\bar{\theta}_{e,v}$ , from which a  $\bar{\theta}_{e,v}$  profile ( solid line ) is reconstructed. The horizontal solid lines are flux interfaces, where the updraft virtual potential temperature  $\theta_{v,u}$  ( open circles ) is computed, from which a cumulus updraft  $\theta_{v,u}$  profile ( dashed ) is reconstructed. The model layer and interface indices used in CAM5 are denoted on the right axis. The layer index  $I$  indicates the ambiguous layer, and  $p_{inv}$  is the reconstructed PBL capping inversion within this layer. Environmental conservative variables reconstructed just above and below the ambiguous layer are denoted by  $\bar{\phi}_{e,I+1/2}$  and  $\bar{\phi}_{e,I-1/2}$ , respectively. See the text for details.

1980 The input state variables to shallow convection scheme are environmental mean  
 1981  $\bar{q}_v, \bar{q}_l, \bar{q}_i, \bar{T}, \bar{u}, \bar{v}$ , and mass and number of aerosols,  $\bar{\zeta}$ . While stratus condensate should reside  
 1982 only within cloudy portion, shallow convection scheme assumes uniform distribution of stratus  
 1983 condensate across the grid except when evaporation of precipitation is computed. From the  
 1984 given inputs, we compute *condensate potential temperature*  $\bar{\theta}_c = \bar{\theta} - (L_v/C_p/\pi) \cdot \bar{q}_l - (L_s/C_p/\pi) \cdot \bar{q}_i$   
 1985 and *total specific humidity*  $\bar{q}_t = \bar{q}_v + \bar{q}_l + \bar{q}_i$ . With respect to vertical displacement involving  
 1986 phase change but without precipitation formation and evaporation of precipitation,  $\theta_c$  is nearly  
 1987 conserved and  $q_t$  is completely conserved.

1988 Instead of assuming zero slope, we assign a certain slope of  $\bar{\theta}_c$  and  $\bar{q}_t$  within each layer. In  
 1989 each layer, upward  $[(\bar{\theta}_c(k+1) - \bar{\theta}_c(k))/(p(k+1) - p(k))]$  and downward  $[(\bar{\theta}_c(k) - \bar{\theta}_c(k-1))/(p(k) - p(k-1))]$  slopes are computed. If they have different signs or either of two has zero  
 1990 slope, internal slope is set to zero. If they have the same sign, we take the one with minimum  
 1991 absolute slope. In the lowest model layer, internal slope is set to the upward slope, and in the  
 1992 top model layer, it is set to the slope of the layer below. This profile reconstruction is performed  
 1993 independently to each of  $\bar{\theta}_c, \bar{q}_t, \bar{u}, \bar{v}$  and  $\bar{\zeta}$ . The reconstructed profiles conserve mean quantity in  
 1994 each layer but have discontinuity across the model interfaces. Similar profile reconstruction is  
 1995 performed in the moist turbulence scheme.

1996 From the reconstructed  $\bar{\theta}_c$  and  $\bar{q}_t$ , we compute *virtual potential temperature*  $\bar{\theta}_v = \bar{\theta} \cdot (1 +$   
 1997  $0.61 \cdot \bar{q}_v - \bar{q}_l - \bar{q}_i)$  at just below and above each model interface by assuming that ice fraction  
 1998 among cloud condensate is a ramping function of temperature between 248 K and 268 K, and  
 1999 saturation specific humidity is a weighting average of two values defined over water and ice.  
 2000 The same temperature partitioning is applied to cloud condensate within convective updraft.  
 2001 In case of detrained convective condensate, we use 238.15 K and 268.15 K as the two end  
 2002 points of temperature in the cloud condensate ramping function. For computation of radiative  
 2003 properties of cumulus updraft, we repartition in-cumulus condensate into liquid and ice following  
 2004 the partitioning of pre-existing of stratus clouds.

### 2006 4.3.2 Source Air Properties of Convective Updraft

2007

At the PBL top, we define source air properties of a single updraft plume. In CAM5, PBL top is located at the top most interface of convective boundary layer, which is diagnosed by the separate moist turbulence scheme. Here, we define  $\hat{q}_{t,src}, \hat{\theta}_{c,src}, \hat{u}_{src}, \hat{v}_{src}, \hat{\zeta}_{src}$  where the *hat* denotes convective updraft properties and the subscript *src* denotes the values of convective updraft source air at the PBL top interface.  $\hat{q}_{t,src}$  is defined as the environmental-mean value in the lowest model layer ( In the below equations, (1) denotes the lowest model layer value ).  $\hat{\zeta}_{src}$  is defined in the same way as  $\hat{q}_{t,src}$ . We first define condensate virtual potential temperature of source air (  $\theta_{vc} = \theta_c \cdot (1 + 0.61 \cdot q_t)$  ) using the profile-reconstructed minimum value within the PBL (  $\bar{\theta}_{vc,min}$  ), and from  $\hat{q}_{t,src}$  and  $\hat{\theta}_{vc,min}$ ,  $\hat{\theta}_{c,src}$  is computed.  $\hat{u}_{src}$  and  $\hat{v}_{src}$  are defined as the profile-reconstructed values just below the PBL top interface.

$$\hat{q}_{t,src} = \bar{q}_t(1) \quad (4.39)$$

$$\hat{\theta}_{c,src} = \left[ C \bar{\theta}_{vc,min} (1 + 0.61 \cdot \hat{q}_{t,src}) \right] \quad (4.40)$$

$$\hat{u}_{src} = \bar{u}_{top} \quad (4.41)$$

$$\hat{v}_{src} = \bar{v}_{top} \quad (4.42)$$

$$\hat{\zeta}_{src} = \bar{\zeta}(1) \quad (4.43)$$

2008       $\zeta$  includes the mass of individual aerosol species and aerosol numbers in each mode ( Aitken,  
2009      Accumulation, Coarse ).  $\zeta$  also contains the numbers of cloud liquid droplets and ice crystals.  
2010      Since CAM5's cumulus microphysics is the first moment scheme and the size of in-cumulus  
2011      and detrained shallow convective condensate are independently specified, vertical convective  
2012      transport of cloud droplet numbers do not influence climate simulation in the current CAM5.  
2013      But we retain this functionality to transport cloud droplet number for future development of  
2014      higher order cumulus microphysics and aerosol-cumulus interactions.

2015      The only unknown source air properties at this stage are updraft mass flux (  $\hat{M}_{src}$  ) and  
2016      updraft vertical velocity (  $\hat{w}_{src}$  ) which are computed in the next section.  $\hat{M}_{src}$  and  $\hat{w}_{src}$  allows  
2017      us to compute updraft fractional area,  $A_{src}$ .

### 2018      4.3.3 Closures at the Cloud Base

2019      We assume that turbulent updraft vertical velocity  $w$  at the PBL top follows a symmetric  
2020      Gaussian distribution. The width of the distribution  $\sigma_w$  is determined by the mean TKE within  
2021      the PBL (  $\bar{e}_{PBL}$  ) given from the moist turbulence scheme,  $\sigma_w = \sqrt{k \cdot \bar{e}_{PBL} + e_m}$  where  $k = 1$   
2022      and  $e_m = 5 \cdot 10^{-4}$  [  $m^2 \cdot s^{-2}$  ] is a background minimum TKE.  $P(w)$ , PDF of  $w$  at the PBL top  
2023      is given as

$$P(w) = \mathcal{C}1\sigma_w \cdot \sqrt{2 \cdot \pi} \cdot \exp\left[-\mathcal{C}w^2 2 \cdot \sigma_w^2\right] \quad (4.44)$$

2024      Among these, only strong updrafts enough to reach to their undiluted Level of Free Convec-  
2025      tion ( LFC ) are assumed to form a *single ensemble mean convective updraft* being simulated  
2026      by shallow convection scheme. The effects of remaining weak updrafts that eventually sink back  
2027      to the PBL by negative buoyancy are implicitly simulated by the separate moist turbulence  
2028      scheme through entrainment parameterization. We define CIN as the strength of potential en-  
2029      ergy barrier of the undiluted ensemble-mean plume from the PBL top to the undiluted LFC  
2030      ( see Fig.4.2 ). Then, the minimum vertical velocity of the deflatable convective updrafts, or  
2031      critical vertical velocity becomes  $w_c = \sqrt{2 \cdot a \cdot CIN}$  where buoyancy coefficient  $a = 1$ . In order  
2032      to reduce the on-and-off behavior of convection between the long model time step  $\Delta t = 1800$  [s],  
2033      CIN is computed using thermodynamic profiles at the end of convection time step ( so called,  
2034      implicit CIN ) as described in [Park and Bretherton \[2009\]](#).

Then, mass flux (  $\hat{M}_{src}$  ), updraft fractional area (  $\hat{A}_{src}$  ), and area-weighted updraft vertical  
velocity (  $\hat{w}_{src}$  ) of a single ensemble-mean convective updraft at the PBL top can be computed  
as follows by integrating all deflatable plumes with  $w > w_c$ .

$$\hat{M}_{src} = \rho \cdot \int_{w_c}^{\infty} w \cdot P(w) \cdot dw = \rho \cdot \mathcal{C}\sigma_w \sqrt{2 \cdot \pi} \cdot \exp\left[-\mathcal{C}a \cdot CIN\sigma_w^2\right] \quad (4.45)$$

$$\hat{A}_{src} = \int_{w_c}^{\infty} P(w) \cdot dw = \mathcal{C}12 \cdot \text{erf}\left[\mathcal{C}\sqrt{a \cdot CIN}\sigma_w\right] \quad (4.46)$$

$$\hat{w}_{src} = \left[ \mathcal{C} \int_{w_c}^{\infty} w \cdot P(w) \cdot dw \int_{w_c}^{\infty} P(w) \cdot dw \right] = \left[ \mathcal{C} \hat{M}_{src} \rho \cdot \hat{A}_{src} \right] \quad (4.47)$$

2031 Here, we impose additional constraints that (1)  $\hat{M}_{src}$  should be smaller than 0.9 of the mass  
 2032 in the layer just below the PBL top, that is,  $\hat{M}_{src} < 0.9 \cdot \Delta p(I-1)/g/\Delta t$  where  $\Delta p(I-1)$  is the  
 2033 pressure thickness of the layer just below the PBL top, and (2)  $\hat{A}_{src}$  and  $\hat{A}_{LCL}$  ( updraft core  
 2034 fractional area at the LCL ) are smaller than 0.1, assuming no lateral mixing from the PBL top  
 2035 to the LCL. From the constrained  $\hat{M}_{src}$  and  $\hat{A}_{src}$ , we compute the constrained  $\hat{w}_{src}$ . As of this,  
 2036 we finished the convective closure at the PBL top.

### 2037 4.3.4 Vertical Evolution of A Single Updraft Plume

2038 Assuming steady-state updraft plume ( or updraft plume with very small fractional area ),  
 2039 vertical variations of updraft mass flux and conservative scalars can be written as

$$\mathcal{C}1\hat{M} \cdot \mathcal{C}\partial\hat{M}\partial p = \epsilon - \delta \quad (4.48)$$

$$\mathcal{C}\partial\hat{\phi}\partial p = -\epsilon \cdot (\hat{\phi} - \bar{\phi}_e) + \hat{S}_{\phi} + \hat{C}_{\phi} \quad (4.49)$$

2039 where pressure coordinate  $p$  is defined increasing upward,  $(\epsilon, \delta)$  are fractional entrainment and  
 2040 detrainment rates, respectively,  $\phi = q_t, \theta_c, u, v, \zeta$  is scalar being transported,  $\hat{\phi}$  is updraft value,  
 2041  $\bar{\phi}_e$  is environmental mean value ( note that this is different from the grid-mean  $\bar{\phi} = \hat{A} \cdot \hat{\phi} + (1 -$   
 2042  $\hat{A}) \cdot \bar{\phi}_e$  unless  $\hat{A} = 0$  ),  $\hat{S}_{\phi}$  is net diabatic source within cumulus updraft, and  $\hat{C}_{\phi}$  is a direct  
 2043 conversion term from environmental to updraft without lateral mass exchange. In case of steady  
 2044 state updraft plume,  $\hat{S}_{\phi}$  changes the column mean total energy, while  $\hat{C}_{\phi}$  conserves the column  
 2045 mean total energy.  $\hat{S}_{\phi}$  and  $\hat{C}_{\phi}$  for each component are parameterized as follows. Otherwise,  
 2046 they are set to zero.

$$\hat{S}_{q_t} \cdot \Delta p = -\max(\hat{q}_l + \hat{q}_i - \hat{q}_{c,crit}, 0) \quad (4.50)$$

$$\hat{S}_{\theta_c} \cdot \Delta p = \max \left[ (\mathcal{C}L_v \cdot \hat{q}_l + L_s \cdot \hat{q}_i C_p \cdot \pi \cdot (\hat{q}_l + \hat{q}_i)) \cdot (\hat{q}_l + \hat{q}_i - \hat{q}_{c,crit}), 0 \right] \quad (4.51)$$

$$\hat{C}_u = PGFc \cdot (\mathcal{C}\partial\bar{u}_e\partial p), \quad \hat{C}_v = PGFc \cdot (\mathcal{C}\partial\bar{v}_e\partial p) \quad (4.52)$$

2047 where  $\hat{q}_{c,crit} = 0.7 [g \cdot kg^{-1}]$  is maximum cloud condensate amount that cumulus updraft can hold,  
 2048 and  $PGFc = 0.7$  measures the degree to which cumulus updraft adjusts to environment by large-  
 2049 scale horizontal pressure gradient force during vertical motion. Above  $\hat{S}_{q_t}$  and  $\hat{S}_{\theta_c}$  assume that if  
 2050 in-cumulus cloud condensate is larger than  $\hat{q}_{c,crit}$ , the excessive condensate is simply precipitated  
 2051 out. This simple cumulus microphysics can be refined using updraft vertical velocity and cloud  
 2052 drop size distribution in future. Following [Gregory et al. \[1997a\]](#),  $\hat{C}_u$  and  $\hat{C}_v$  assume that when  
 2053 cumulus updraft rises across the layer with vertical shear of environmental horizontal wind,  
 2054 updraft gains horizontal momentum increment directly from the environment without lateral  
 2055 mass exchange. We neglect radiative effect and evaporation of convective precipitation within  
 2056 convective updraft.

One unique aspect of our shallow convection scheme is to compute updraft vertical velocity  
 for computing (1) updraft fractional area, (2) lateral entrainment and detrainment rates, and

(3) cumulus top height and penetrative entrainment rates. Steady state vertical momentum equation is

$$\mathcal{C}12 \cdot \mathcal{C} \partial \hat{w}^2 \partial p = a \cdot B - b \cdot \epsilon \cdot \hat{w}^2 \quad (4.53)$$

2057 where  $B$  is updraft buoyancy ( $B = (g/\bar{\theta}_v) \cdot (\hat{\theta}_v - \bar{\theta}_v)$ ), and non-dimentional coefficients  $a, b$   
 2058 include the partition of perturbation vertical PGF into buoyancy and entrainment drag forces.  
 2059 Without perturbation vertical PGF,  $a = b = 1$  but we use  $a = 1, b = 2$  assuming that  
 2060 perturbation vertical PGF is entirely incorporated into entrainment drag force.

Instead of directly parameterizing  $(\epsilon, \delta)$ , we assume that a certain amount of updraft airs ( $\epsilon_o \cdot \hat{M} \cdot \delta p$ ) is mixed with the same amount of environmental airs during incremental vertical displacement  $\delta p$ , producing a spectrum of mixtures with the same mixing probability  $P(\chi) = 1$  where  $0 \leq \chi \leq 1$  ( $\chi = 0$  is cumulus updraft,  $\chi = 1$  is environmental air). Among these mixtures, we entrain (1) positively buoyant mixtures and (2) negatively buoyant mixtures with vertical velocity strong enough to reach 0.1 of cumulus top height. This process is so called *inertial buoyancy sorting* ([Kain and Fritsch \[1990\]](#), [Bretherton et al. \[2004\]](#)). This allows us to compute a single critical mixing fraction  $\chi_c$ : mixtures with  $\chi \leq \chi_c$  are entrained while the others are detrained. Then, we can derive  $(\epsilon, \delta)$  as follows.

$$\epsilon = \epsilon_o \cdot \chi_c^2 \quad (4.54)$$

$$\delta = \epsilon_o \cdot (1 - \chi_c)^2 \quad (4.55)$$

where fractional mixing rate  $\epsilon_o$  is parameterized as an inverse function of geometric height,

$$\epsilon_o = \left[ \mathcal{C} c \rho \cdot g \cdot z \right] \quad (4.56)$$

2061 where non-dimensional coefficient  $c = 8$  and  $z$  is geometric height above the surface. In order to  
 2062 simulate deep convection, we can use a smaller value, e.g.,  $c = 4$ . Cumulus top height necessary  
 2063 to compute  $\chi_c$  is initially set to the previous time step's value and then recomputed using an  
 2064 iteration loop.

2065 Now, we can compute vertical evolution of  $\hat{M}, \hat{\phi}, \hat{w}$ . Instead of solving discrete numerical  
 2066 equation, we used the explicit analytical solution by solving the first order differential equation  
 2067 to obtain the cumulus updraft properties at the top interface of each layer from the value at  
 2068 the base interface. In solving Eqn.(4.53), we assume a linear profile of  $B$  in each layer. At  
 2069 the top interface, we computed updraft fractional area  $\hat{A}$  from  $\hat{M}$  and  $\hat{w}$ , and if  $\hat{A} > 0.1$ ,  
 2070 detrainment rate  $\delta$  is enhanced such that  $\hat{A}$  is always less than 0.1. Note that this enhancement  
 2071 of detrainment only changes  $\hat{M}$  not  $\hat{w}$  at the top interface.

### 2072 4.3.5 Penetrative Entrainment

2073 When convective updraft rises into the stably stratified layers ( i.e., Overshooting Zone. See  
 Fig.4.2 ) above the Level of Neutral Buoyancy ( LNB ), some air masses within the overshooting  
 zone are entrained into the layers below. This process is so called *penetrative entrainment*.  
 We assume that the amount of penetratively entrained airs ( $M_{pen}$ ) is proportional to the  
 mass involved in the lateral mixing in the overshooting zone and the properties of penetratively

entrained airs (  $\phi_{pen}$  ) are identical to the mean environmental values from LNB to LNB +  $\Delta p_{pen}$ :

$$M_{pen} = r_{pen} \cdot \hat{M} \cdot \epsilon_o \cdot \Delta p_{pen} \quad (4.57)$$

$$\phi_{pen} = \bar{\phi}_e \quad (4.58)$$

2074 where  $\Delta p_{pen}$  is vertical overshooting distance of cumulus updraft above LNB and  $1 \leq r_{pen} \leq 10$   
2075 is a tunable non-dimensional penetrative entrainment coefficient. In CAM5, we chose  $r_{pen} = 10$ .  
2076 The thickness of overshooting zone above LNB, or the cumulus top height is diagnosed as the  
2077 level where convective updraft vertical velocity  $\hat{w}$  becomes zero.

2078 When convective updraft penetrates into several layers above LNB, Eqn.(4.57) and (4.58)  
2079 are computed for each layers within penetrative overshooting zone, and all the penetratively  
2080 entrained mass is deposited into a single layer just below LNB. We neglect convective updraft  
2081 fluxes at the interfaces at and above LNB since most of updraft mass fluxes crossing over the  
2082 LNB are likely to sink down below LNB due to negative updraft buoyancy in the overshooting  
2083 zone. The thickness of overshooting zone above LNB, or the cumulus top height is diagnosed as  
2084 the level where convective updraft vertical velocity  $\hat{w}$  becomes zero.

#### 2085 4.3.6 Convective Fluxes at and below the PBL top interface

2086

We view the layer just above the PBL top ( *ambiguous layer*,  $I$ . See Fig.4.2 ) as the accumulation of partial grid layer of PBL air and another partial grid layer of above-PBL air. The interface between these two partial layers, the reconstructed PBL top height  $p_{inv}$ , is computed using a simple conservation principle for individual scalar component  $\phi = q_t, \theta_c, u, v, \zeta$  as follows.

$$p_{inv} = p_{I-1} - r \cdot |\Delta p_I|, \quad r = \left[ \mathcal{C} \bar{\phi}_{e,I} - \bar{\phi}_{e,I+1/2} \bar{\phi}_{e,I-1/2} - \bar{\phi}_{e,I+1/2} \right] \quad (4.59)$$

2087 where  $|\Delta p_I|$  is the pressure thickness of the ambiguous layer,  $p_I$  is the pressure at the model  
2088 interface,  $\bar{\phi}_{e,I-1/2}$  and  $\bar{\phi}_{e,I+1/2}$  are the profile-reconstructed environmental values just below the  
2089 PBL top interface and just above the ambiguous layer, respectively ( See Fig.4.2 ).

Convective updraft mass flux  $\hat{M}_{src}$  is assumed to be deflated from the  $p_{inv}$  with  $\hat{\phi}_{src}$ , which  
enables us to compute convective flux at the  $p_{inv}$ . To avoid over stabilizing or destabilizing  
the ambiguous layer and PBL through cumulus ventilation, this flux is uniformly extracted  
throughout the whole PBL, which results in the following linear profile of convective flux at  
model interfaces below  $p_{inv}$ .

$$(\overline{\omega' \phi})(k) = g \cdot \hat{M}_{src} \cdot (\hat{\phi}_{src} - \bar{\phi}_{e,I-1/2}) \cdot \left[ \mathcal{C} p_{I-1} - p_{I-1} p_{I-1} - p_{inv} \right], \quad for \quad 0 \leq k \leq I-1 \quad (4.60)$$

2090 where  $\omega$  is pressure vertical velocity,  $k = 0$  is surface,  $k = I - 1$  is PBL top interface index.

It is possible for compensating subsidence associated with cumulus updraft mass flux to  
lower the  $p_{inv}$  below the bottom of the ambiguous layer, in which case compensating subsidence  
will also warm and dry the grid layer below. To diagnose whether compensating subsidence  
would lower  $p_{inv}$  below  $p_{I-1}$  during  $\Delta t$ , we compare the normalized cumulus updraft mass flux,  
 $r_c = (g \cdot \hat{M}_{src} \cdot \Delta t) / |\Delta p_I|$  to  $r$ . If  $r_c \geq r$ ,  $p_{inv}$  will be lowered down into the layer  $I - 1$ , replacing

PBL-top air with  $\phi = \bar{\phi}_{e,I-1/2}$  with above-PBL air with  $\phi = \bar{\phi}_{e,I+1/2}$ . This effect is included by adding the below compensating subsidence flux

$$(\overline{\omega' \phi})(k = I - 1) = -g \cdot \hat{M}_{src} \cdot (\bar{\phi}_{e,I+1/2} - \bar{\phi}_{e,I-1/2}) \cdot \left[ 1 - \mathcal{C}rr_c \right], \quad \text{for } r_c > r \quad (4.61)$$

where we assumed that cumulus mass flux is not strong enough to lower down  $p_{inv}$  below  $p_{I-2}$ , that is,  $g \cdot \hat{M}_{src} \cdot \Delta t < r \cdot |\Delta p_I| + |\Delta p_{I-1}|$ . In order to ensure this condition, we impose an upper bound on the convective base mass flux of  $g \cdot \hat{M}_{src} \cdot \Delta t < 0.9 \cdot |\Delta p_{I-1}|$ .

### 4.3.7 Grid-Mean Tendency of Conservative Scalars

In case of steady state updraft plume approximation with a finite updraft fractional area but compensating subsidence entirely within the same grid box as convective updraft, the budget equation of grid mean conservative scalar represented in flux convergence form becomes

$$\mathcal{C} \partial \bar{\phi} / \partial t = \mathcal{C} \partial \partial t (A_e \cdot \bar{\phi}_e) = -g \cdot \mathcal{C} \partial \partial p \left[ \hat{M} \cdot (\hat{\phi} - \bar{\phi}_e) + M_{pen} \cdot (\phi_{pen} - \bar{\phi}_e) \right] + g \cdot \hat{M} \cdot \hat{S}_\phi + \mathcal{C} \partial \partial t (A_e \cdot \bar{\phi}_e)_S \quad (4.62)$$

where  $A_e = 1 - \hat{A}$  is environmental fractional area and on the R.H.S. the first and second terms are convergence of convective updraft and penetrative entrainment fluxes, respectively, and the third and fourth terms are diabatic sources within convective updraft and environment, respectively. We use the above flux convergence form to compute tendencies of conservative scalars in order to ensure conservation of column-integrated energy during vertical redistribution of air masses by convective updraft.  $\hat{M}$  in the third term of the R.H.S. is obtained by averaging updraft mass fluxes at the top and base interfaces of each layer. In contrast to  $\hat{\phi}$ ,  $\bar{\phi}_e$  is discontinuous across the model interface due to profile reconstruction. In order to take into account of the effects of compensating subsidence ( upwelling ) in this flux form,  $\bar{\phi}_e$  in the first ( second ) term on the R.H.S is taken as the reconstructed environmental value just above the top interface ( below the base interface ) of each layer. If downdraft is also considered in future, we should add  $-g \cdot \partial / \partial p [\hat{M}_d \cdot (\hat{\phi}_d - \bar{\phi}_e)] + g \cdot \hat{M}_d \cdot \hat{S}_{d,\phi}$  on the R.H.S.

If  $\phi = u, v$ , diabatic sources both within convective updraft ( $\hat{S}_\phi$ ) and environment are zero. Note that a direct conversion term from environment to updraft without lateral mass exchange ( $\hat{C}_\phi$ ) should not be included in this tendency equation in order to conserve column-integrated horizontal momentum. If  $\phi = q_t, \theta_c$ , these diabatic sources are precipitation production within convective updraft ( Eqn.(4.50),(4.51) ) and evaporation of precipitation within environment. Following the formulation in CAM3 and CAM4, we assume that whenever convective precipitation flux exists, it is spread all over the grid. The resulting formulation of evaporation of convective precipitation within environment is

$$\mathcal{C} \partial \partial t (A_e \cdot \bar{q}_{t,e})_S = A_e \cdot k_e \cdot (1 - \bar{U}_e) \cdot (\sqrt{\bar{F}_R} + \sqrt{\bar{F}_S}) \quad (4.63)$$

where  $\bar{F}_R$  and  $\bar{F}_S$  are grid-mean rain and snow fluxes respectively in unit of  $[kg \cdot m^{-2} \cdot s^{-1}]$  falling into the model layer from the top interface, and  $\bar{U}_e$  is mean relative humidity within environment obtained using a mean saturation specific humidity that is a weighting average over water and ice,  $k_e = 2 \cdot 10^{-6} [(kg \cdot m^{-2} \cdot s^{-1})^{-1/2} \cdot s^{-1}]$  is evaporation efficiency. We also consider snow

melting during fall and corresponding changes of  $\theta_c$ . This is a very simple formula bypassing the detailed vertical overlap structure of cumulus and stratus clouds. More refined treatment considering vertical cloud overlap will be done in future.

Vertical transport of horizontal momentum by convective updraft does not change column-mean horizontal momentum. However, it will change column-mean kinetic energy ( KE ) of the mean wind. In reality, this KE change will be eventually converted into internal heat energy ( or potential energy, PE ). In CAM5, we require conservation of column-mean total energy, PE+KE. In order to satisfy this constraint, we add kinetic energy dissipation heating into  $\bar{\theta}_c$  following [Boville and Bretherton \[2003b\]](#). Similar treatment was made in the moist turbulence scheme.

In CAM5, input state variables passed into individual physical schemes is *not* the grid-mean value including cumulus updraft contribution (  $\bar{\phi} = \hat{A} \cdot \hat{\phi} + (1 - \hat{A}) \cdot \bar{\phi}_e$  ) *but* the environmental mean value without cumulus portion (  $\bar{\phi}_e$  ). In order to conserve column-integrated grid-mean energy, we print out  $\partial(A_e \cdot \bar{\phi}_e)/\partial t$  instead of  $\partial(\bar{\phi}_e)/\partial t$  from our shallow convection scheme. Under the approximation of very small updraft fractional area (  $\hat{A} \approx 0$  and  $A_e \approx 1$  ), it is  $\partial(A_e \cdot \bar{\phi}_e)/\partial t \approx \partial(\bar{\phi}_e)/\partial t$ . In Eqn.(4.63), we also approximate  $A_e \approx 1$ .

### 4.3.8 Grid-Mean Tendency of Non-Conservative Scalars

In contrast to the conservative scalars, we use the following explicit *detrainment* and *compensating subsidence* tendency form to compute the tendency of non-conservative scalars. We first compute the tendencies of cloud condensates, and then the tendencies of water vapor (  $\bar{q}_v$  ) and dry static energy (  $\bar{s}$  ) are extracted from them.

$$\mathcal{C}\partial\partial t(A_e \cdot \bar{q}_{l,e}) = -g \cdot (\hat{M} - M_{pen}) \cdot \mathcal{C}\partial\bar{q}_{l,e}\partial p + g \cdot \hat{M} \cdot \delta \cdot (\hat{q}_l - \bar{q}_{l,e}) + g \cdot M_{pen} \cdot (q_{l,pen} - \bar{q}_{l,e}) \quad (4.64)$$

$$\mathcal{C}\partial\partial t(A_e \cdot \bar{q}_{i,e}) = -g \cdot (\hat{M} - M_{pen}) \cdot \mathcal{C}\partial\bar{q}_{i,e}\partial p + g \cdot \hat{M} \cdot \delta \cdot (\hat{q}_i - \bar{q}_{i,e}) + g \cdot M_{pen} \cdot (q_{i,pen} - \bar{q}_{i,e}) \quad (4.65)$$

$$\mathcal{C}\partial\partial t(A_e \cdot \bar{q}_{v,e}) = \mathcal{C}\partial\partial t(A_e \cdot \bar{q}_{t,e}) - \mathcal{C}\partial\partial t(A_e \cdot \bar{q}_{l,e}) - \mathcal{C}\partial\partial t(A_e \cdot \bar{q}_{i,e}) \quad (4.66)$$

$$\mathcal{C}\partial\partial t(A_e \cdot \bar{s}_e) = \mathcal{C}\partial\partial t(A_e \cdot \bar{s}_{c,e}) + L_v \cdot \mathcal{C}\partial\partial t(A_e \cdot \bar{q}_{l,e}) + L_s \cdot \mathcal{C}\partial\partial t(A_e \cdot \bar{q}_{i,e}) \quad (4.67)$$

where *condensate static energy*  $s_c = C_p \cdot \pi \cdot \theta_c + g \cdot z$  and the first term on the R.H.S in Eqn.(4.64) and (4.65) is tendency associated with compensating subsidence and upwelling of environmental condensate, and the second and third terms are tendencies due to condensate detrainment from convective updraft and penetrative entrainment masses. If  $\hat{M} - M_{pen} > 0$  (  $\hat{M} - M_{pen} < 0$  ), downward ( upward ) diffencing between upper ( lower ) and current layers is used in computing compensating subsidence ( upwelling ) tendency. Any convective updraft condensate detrained into the layers above the LNB are assumed to move down into the layer just below LNB by negative buoyancy and be detrained there. That is, the second term on the R.H.S. in Eqn.(4.64) and (4.65) is zero in the overshooting zone. Similarly, all the penetratively entrained condensate are detrained into the layer just below LNB. That is, the third term on the R.H.S. in Eqn.(4.64) and (4.65) is non-zero only in the layer just below LNB.

If environmental condensate is displaced vertically by compensating subsidence/upwelling, phase change should occur due to compression heating/expansion cooling. Ideally, this phase

2147 change should be treated within convection scheme but our current scheme does not. How-  
2148 ever, this phase change of displaced condensate will be treated by separate stratiform macro-  
2149 microphysics schemes later.

2150 The tendencies of cloud droplet number concentration (  $\bar{n}_{l,e}, \bar{n}_{i,e}$  ) by compensationg sub-  
2151 sidence/upwelling are treated in a similar way as the tendencies of cloud condensate mass.  
2152 However, because CAM5's cumulus microphysics is the 1<sup>st</sup> moment scheme, we don't have any  
2153 information on the droplet number concentration within cumulus updraft (  $\hat{n}_l, \hat{n}_i$  ). We assume  
2154 that the effective droplet radius of detrained shallow ( deep ) convective condensate is 8 ( 10 )  
2155 and 25 ( 50 ) [  $\mu m$  ] for liquid and ice respectively.

## 2156 4.4 Deep Convection

2157 The process of deep convection is treated with a parameterization scheme developed by  
 2158 [Zhang and McFarlane \[1995\]](#) and modified with the addition of convective momentum  
 2159 transports by [Richter and Rasch \[2008\]](#) and a modified dilute plume calculation following  
 2160 [Raymond and Blyth \[1986, 1992\]](#). The scheme is based on a plume ensemble approach where it  
 2161 is assumed that an ensemble of convective scale updrafts (and the associated saturated down-  
 2162 drafts) may exist whenever the atmosphere is conditionally unstable in the lower troposphere.  
 2163 The updraft ensemble is comprised of plumes sufficiently buoyant so as to penetrate the unstable  
 2164 layer, where all plumes have the same upward mass flux at the bottom of the convective layer.  
 2165 Moist convection occurs only when there is convective available potential energy (CAPE) for  
 2166 which parcel ascent from the sub-cloud layer acts to destroy the CAPE at an exponential rate  
 2167 using a specified adjustment time scale. For the convenience of the reader we will review some  
 2168 aspects of the formulation, but refer the interested reader to [Zhang and McFarlane \[1995\]](#) for  
 2169 additional detail, including behavioral characteristics of the parameterization scheme. Evap-  
 2170 oration of convective precipitation is computed following the procedure described in section  
 2171 [4.5](#).

The large-scale budget equations distinguish between a cloud and sub-cloud layer where temperature and moisture response to convection in the cloud layer is written in terms of bulk convective fluxes as

$$c_p \left( \frac{\partial T}{\partial t} \right)_{cu} = -\frac{1}{\rho} \frac{\partial}{\partial z} (M_u S_u + M_d S_d - M_c S) + L(C - E) \quad (4.68)$$

$$\left( \frac{\partial q}{\partial t} \right)_{cu} = -\frac{1}{\rho} \frac{\partial}{\partial z} (M_u q_u + M_d q_d - M_c q) + E - C , \quad (4.69)$$

for  $z \geq z_b$ , where  $z_b$  is the height of the cloud base. For  $z_s < z < z_b$ , where  $z_s$  is the surface height, the sub-cloud layer response is written as

$$c_p \left( \rho \frac{\partial T}{\partial t} \right)_m = -\frac{1}{z_b - z_s} (M_b [S(z_b) - S_u(z_b)] + M_d [S(z_b) - S_d(z_b)]) \quad (4.70)$$

$$\left( \rho \frac{\partial q}{\partial t} \right)_m = -\frac{1}{z_b - z_s} (M_b [q(z_b) - q_u(z_b)] + M_d [q(z_b) - q_d(z_b)]) , \quad (4.71)$$

2172 where the net vertical mass flux in the convective region,  $M_c$ , is comprised of upward,  $M_u$ , and  
 2173 downward,  $M_d$ , components,  $C$  and  $E$  are the large-scale condensation and evaporation rates,  
 2174  $S, S_u, S_d, q, q_u, q_d$ , are the corresponding values of the dry static energy and specific humidity,  
 2175 and  $M_b$  is the cloud base mass flux.

### 2176 4.4.1 Updraft Ensemble

The updraft ensemble is represented as a collection of entraining plumes, each with a characteristic fractional entrainment rate  $\lambda$ . The moist static energy in each plume  $h_c$  is given by

$$\frac{\partial h_c}{\partial z} = \lambda(h - h_c), \quad z_b < z < z_D . \quad (4.72)$$

Mass carried upward by the plumes is detrained into the environment in a thin layer at the top of the plume,  $z_D$ , where the detrained air is assumed to have the same thermal properties as in the environment ( $S_c = S$ ). Plumes with smaller  $\lambda$  penetrate to larger  $z_D$ . The entrainment rate  $\lambda_D$  for the plume which detrains at height  $z$  is then determined by solving (4.72), with lower boundary condition  $h_c(z_b) = h_b$ :

$$\frac{\partial h_c}{\partial(z - z_b)} = \lambda_D(h - h_b) - \lambda_D(h_c - h_b) \quad (4.73)$$

$$\frac{\partial(h_c - h_b)}{\partial(z - z_b)} - \lambda_D(h_c - h_b) = \lambda_D(h - h_b) \quad (4.74)$$

$$\frac{\partial(h_c - h_b)e^{\lambda_D(z - z_b)}}{\partial(z - z_b)} = \lambda_D(h - h_b)e^{\lambda_D(z - z_b)} \quad (4.75)$$

$$(h_c - h_b)e^{\lambda_D(z - z_b)} = \int_{z_b}^z \lambda_D(h - h_b)e^{\lambda_D(z' - z_b)} dz' \quad (4.76)$$

$$(h_c - h_b) = \lambda_D \int_{z_b}^z (h - h_b)e^{\lambda_D(z' - z)} dz' . \quad (4.77)$$

Since the plume is saturated, the detraining air must have  $h_c = h^*$ , so that

$$(h_b - h^*) = \lambda_D \int_{z_b}^z (h_b - h)e^{\lambda_D(z' - z)} dz' . \quad (4.78)$$

2177 Then,  $\lambda_D$  is determined by solving (4.78) iteratively at each  $z$ .

The top of the shallowest of the convective plumes,  $z_0$  is assumed to be no lower than the mid-tropospheric minimum in saturated moist static energy,  $h^*$ , ensuring that the cloud top detrainment is confined to the conditionally stable portion of the atmospheric column. All condensation is assumed to occur within the updraft plumes, so that  $C = C_u$ . Each plume is assumed to have the same value for the cloud base mass flux  $M_b$ , which is specified below. The vertical distribution of the cloud updraft mass flux is given by

$$M_u = M_b \int_0^{\lambda_D} \frac{1}{\lambda_0} e^{\lambda(z - z_b)} d\lambda = M_b \frac{e^{\lambda_D(z - z_b)} - 1}{\lambda_0(z - z_b)} , \quad (4.79)$$

where  $\lambda_0$  is the maximum detrainment rate, which occurs for the plume detraining at height  $z_0$ , and  $\lambda_D$  is the entrainment rate for the updraft that detrains at height  $z$ . Detrainment is confined to regions where  $\lambda_D$  decreases with height, so that the total detrainment  $D_u = 0$  for  $z < z_0$ . Above  $z_0$ ,

$$D_u = -\frac{M_b}{\lambda_0} \frac{\partial \lambda_D}{\partial z} . \quad (4.80)$$

The total entrainment rate is then just given by the change in mass flux and the total detrainment,

$$E_u = \frac{\partial M_u}{\partial z} - D_u . \quad (4.81)$$

The updraft budget equations for dry static energy, water vapor mixing ratio, moist static energy, and cloud liquid water,  $\ell$ , are:

$$\frac{\partial}{\partial z} (M_u S_u) = (E_u - D_u) S + \rho L C_u \quad (4.82)$$

$$\frac{\partial}{\partial z} (M_u q_u) = E_u q - D_u q^* + \rho C_u \quad (4.83)$$

$$\frac{\partial}{\partial z} (M_u h_u) = E_u h - D_u h^* \quad (4.84)$$

$$\frac{\partial}{\partial z} (M_u \ell) = -D_u \ell_d + \rho C_u - \rho R_u, \quad (4.85)$$

where (4.84) is formed from (4.82) and (4.83) and detraining air has been assumed to be saturated ( $q = q^*$  and  $h = h^*$ ). It is also assumed that the liquid content of the detrained air is the same as the ensemble mean cloud water ( $\ell_d = \ell$ ). The conversion from cloud water to rain water is given by

$$\rho R_u = c_0 M_u \ell, \quad (4.86)$$

following Lord et al. [1982], with  $c_0 = 2 \times 10^{-3} \text{ m}^{-1}$ .

Since  $M_u$ ,  $E_u$  and  $D_u$  are given by (4.79-4.81), and  $h$  and  $h^*$  are environmental profiles, (4.84) can be solved for  $h_u$ , given a lower boundary condition. The lower boundary condition is obtained by adding a 0.5 K temperature perturbation to the dry (and moist) static energy at cloud base, or  $h_u = h + c_p \times 0.5$  at  $z = z_b$ . Below the lifting condensation level (LCL),  $S_u$  and  $q_u$  are given by (4.82) and (4.83). Above the LCL,  $q_u$  is reduced by condensation and  $S_u$  is increased by the latent heat of vaporization. In order to obtain to obtain a saturated updraft at the temperature implied by  $S_u$ , we define  $\Delta T$  as the temperature perturbation in the updraft, then:

$$h_u = S_u + L q_u \quad (4.87)$$

$$S_u = S + c_p \Delta T \quad (4.88)$$

$$q_u = q^* + \frac{dq^*}{dT} \Delta T. \quad (4.89)$$

Substituting (4.88) and (4.89) into (4.87),

$$h_u = S + L q^* + c_p \left( 1 + \frac{L}{c_p} \frac{dq^*}{dT} \right) \Delta T \quad (4.90)$$

$$= h^* + c_p (1 + \gamma) \Delta T \quad (4.91)$$

$$\gamma \equiv \frac{L}{c_p} \frac{dq^*}{dT} \quad (4.92)$$

$$\Delta T = \frac{1}{c_p} \frac{h_u - h^*}{1 + \gamma}. \quad (4.93)$$

The required updraft quantities are then

$$S_u = S + \frac{h_u - h^*}{1 + \gamma} \quad (4.94)$$

$$q_u = q^* + \frac{\gamma}{L} \frac{h_u - h^*}{1 + \gamma}. \quad (4.95)$$

2179 With  $S_u$  given by (4.94), (4.82) can be solved for  $C_u$ , then (4.85) and (4.86) can be solved for  $\ell$   
2180 and  $R_u$ .

The expressions above require both the saturation specific humidity to be

$$q^* = \frac{\epsilon e^*}{p - e^*}, \quad e^* < p, \quad (4.96)$$

where  $e^*$  is the saturation vapor pressure, and its dependence on temperature (in order to maintain saturation as the temperature varies) to be

$$\frac{dq^*}{dT} = \frac{\epsilon}{p - e^*} \frac{de^*}{dT} - \frac{\epsilon e^*}{(p - e^*)^2} \frac{d(p - e^*)}{dT} \quad (4.97)$$

$$= \frac{\epsilon}{p - e^*} \left( 1 + \frac{1}{p - e^*} \right) \frac{de^*}{dT} \quad (4.98)$$

$$= \frac{\epsilon}{p - e^*} \left( 1 + \frac{q^*}{\epsilon e^*} \right) \frac{de^*}{dT}. \quad (4.99)$$

The deep convection scheme does not use the same approximation for the saturation vapor pressure  $e^*$  as is used in the rest of the model. Instead,

$$e^* = c_1 \exp \left[ \frac{c_2(T - T_f)}{(T - T_f + c_3)} \right], \quad (4.100)$$

where  $c_1 = 6.112$ ,  $c_2 = 17.67$ ,  $c_3 = 243.5$  K and  $T_f = 273.16$  K is the freezing point. For this approximation,

$$\frac{de^*}{dT} = e^* \frac{d}{dT} \left[ \frac{c_2(T - T_f)}{(T - T_f + c_3)} \right] \quad (4.101)$$

$$= e^* \left[ \frac{c_2}{(T - T_f + c_3)} - \frac{c_2(T - T_f)}{(T - T_f + c_3)^2} \right] \quad (4.102)$$

$$= e^* \frac{c_2 c_3}{(T - T_f + c_3)^2} \quad (4.103)$$

$$\frac{dq^*}{dT} = q^* \left( 1 + \frac{q^*}{\epsilon e^*} \right) \frac{c_2 c_3}{(T - T_f + c_3)^2}. \quad (4.104)$$

We note that the expression for  $\gamma$  in the code gives

$$\frac{dq^*}{dT} = \frac{c_p}{L} \gamma = q^* \left( 1 + \frac{q^*}{\epsilon} \right) \frac{\epsilon L}{RT^2}. \quad (4.105)$$

2181 The expressions for  $dq^*/dT$  in (4.104) and (4.105) are not identical. Also,  $T - T_f + c_3 \neq T$  and  
2182  $c_2 c_3 \neq \epsilon L/R$ .

## 2183 4.4.2 Downdraft Ensemble

Downdrafts are assumed to exist whenever there is precipitation production in the updraft ensemble where the downdrafts start at or below the bottom of the updraft detrainment layer.

Detrainment from the downdrafts is confined to the sub-cloud layer, where all downdrafts have the same mass flux at the top of the downdraft region. Accordingly, the ensemble downdraft mass flux takes a similar form to (4.79) but includes a “proportionality factor” to ensure that the downdraft strength is physically consistent with precipitation availability. This coefficient takes the form

$$\alpha = \mu \left[ \frac{P}{P + E_d} \right] , \quad (4.106)$$

where  $P$  is the total precipitation in the convective layer and  $E_d$  is the rain water evaporation required to maintain the downdraft in a saturated state. This formalism ensures that the downdraft mass flux vanishes in the absence of precipitation, and that evaporation cannot exceed some fraction,  $\mu$ , of the precipitation, where  $\mu = 0.2$ .

### 4.4.3 Closure

The parameterization is closed, i.e., the cloud base mass fluxes are determined, as a function of the rate at which the cumulus consume convective available potential energy (CAPE). Since the large-scale temperature and moisture changes in both the cloud and sub-cloud layer are linearly proportional to the cloud base updraft mass flux (e.g. see eq. 4.68 – 4.71), the CAPE change due to convective activity can be written as

$$\left( \frac{\partial A}{\partial t} \right)_{eu} = -M_b F , \quad (4.107)$$

where  $F$  is the CAPE consumption rate per unit cloud base mass flux. The closure condition is that the CAPE is consumed at an exponential rate by cumulus convection with characteristic adjustment time scale  $\tau = 7200$  s:

$$M_b = \frac{A}{\tau F} . \quad (4.108)$$

### 4.4.4 Numerical Approximations

The quantities  $M_{u,d}$ ,  $\ell$ ,  $S_{u,d}$ ,  $q_{u,d}$ ,  $h_{u,d}$  are defined on layer interfaces, while  $D_u$ ,  $C_u$ ,  $R_u$  are defined on layer midpoints.  $S$ ,  $q$ ,  $h$ ,  $\gamma$  are required on both midpoints and interfaces and the interface values  $\psi^{k\pm}$  are determined from the midpoint values  $\psi^k$  as

$$\psi^{k-} = \log \left( \frac{\psi^{k-1}}{\psi^k} \right) \frac{\psi^{k-1}\psi^k}{\psi^{k-1} - \psi^k} . \quad (4.109)$$

All of the differencing within the deep convection is in height coordinates. The differences are naturally taken as

$$\frac{\partial \psi}{\partial z} = \frac{\psi^{k-} - \psi^{k+}}{z^{k-} - z^{k+}} , \quad (4.110)$$

where  $\psi^{k-}$  and  $\psi^{k+}$  represent values on the upper and lower interfaces, respectively for layer  $k$ . The convention elsewhere in this note (and elsewhere in the code) is  $\delta^k \psi = \psi^{k+} - \psi^{k-}$ . Therefore, we avoid using the compact  $\delta^k$  notation, except for height, and define

$$d^k z \equiv z^{k-} - z^{k+} = -\delta^k z , \quad (4.111)$$

so that  $d^k z$  corresponds to the variable  $dz(k)$  in the deep convection code.

Although differences are in height coordinates, the equations are cast in flux form and the tendencies are computed in units  $\text{kg m}^{-3} \text{ s}^{-1}$ . The expected units are recovered at the end by multiplying by  $g\delta z/\delta p$ .

The environmental profiles at midpoints are

$$S^k = c_p T^k + g z^k \quad (4.112)$$

$$h^k = S^k + L q^k \quad (4.113)$$

$$h^{*k} = S^k + L q^{*k} \quad (4.114)$$

$$q^{*k} = \epsilon e^{*k} / (p^k - e^{*k}) \quad (4.115)$$

$$e^{*k} = c_1 \exp \left[ \frac{c_2 (T^k - T_f)}{(T^k - T_f + c_3)} \right] \quad (4.116)$$

$$\gamma^k = q^{*k} \left( 1 + \frac{q^{*k}}{\epsilon} \right) \frac{\epsilon L^2}{c_p R T^{k^2}} . \quad (4.117)$$

The environmental profiles at interfaces of  $S$ ,  $q$ ,  $q^*$ , and  $\gamma$  are determined using (4.109) if  $|\psi^{k-1} - \psi^k|$  is large enough. **However, there are inconsistencies in what happens if  $|\psi^{k-1} - \psi^k|$  is not large enough.** For  $S$  and  $q$  the condition is

$$\psi^{k-} = (\psi^{k-1} + \psi^k)/2, \quad \frac{|\psi^{k-1} - \psi^k|}{\max(\psi^{k-1} - \psi^k)} \leq 10^{-6} . \quad (4.118)$$

For  $q^*$  and  $\gamma$  the condition is

$$\psi^{k-} = \psi^k, \quad |\psi^{k-1} - \psi^k| \leq 10^{-6} . \quad (4.119)$$

Interface values of  $h$  are not needed and interface values of  $h^*$  are given by

$$h^{*k-} = S^{k-} + L q^{*k-} . \quad (4.120)$$

The unitless updraft mass flux (scaled by the inverse of the cloud base mass flux) is given by differencing (4.79) as

$$M_u^{k-} = \frac{1}{\lambda_0(z^{k-} - z_b)} \left( e^{\lambda_D^k(z^{k-} - z_b)} - 1 \right) , \quad (4.121)$$

with the boundary condition that  $M_u^{M+} = 1$ . The entrainment and detrainment are calculated using

$$m_u^{k-} = \frac{1}{\lambda_0(z^{k-} - z_b)} \left( e^{\lambda_D^{k+1}(z^{k-} - z_b)} - 1 \right) \quad (4.122)$$

$$E_u^k = \frac{m_u^{k-} - M_u^{k+}}{d^k z} \quad (4.123)$$

$$D_u^k = \frac{m_u^{k-} - M_u^{k-}}{d^k z} . \quad (4.124)$$

Note that  $M_u^{k-}$  and  $m_u^{k-}$  differ only by the value of  $\lambda_D$ .

The updraft moist static energy is determined by differencing (4.84)

$$\frac{M_u^{k-}h_u^{k-} - M_u^{k+}h_u^{k+}}{d^k z} = E_u^k h^k - D_u^k h^{*k} \quad (4.125)$$

$$h_u^{k-} = \frac{1}{M_u^{k-}} [M_u^{k+}h_u^{k+} + d^k z (E_u^k h^k - D_u^k h^{*k})] , \quad (4.126)$$

2195 with  $h_u^{M-} = h^M + c_p/2$ , where  $M$  is the layer of maximum  $h$ .

Once  $h_u$  is determined, the lifting condensation level is found by differencing (4.82) and (4.83) similarly to (4.84):

$$S_u^{k-} = \frac{1}{M_u^{k-}} [M_u^{k+}S_u^{k+} + d^k z (E_u^k S^k - D_u^k S^k)] \quad (4.127)$$

$$q_u^{k-} = \frac{1}{M_u^{k-}} [M_u^{k+}q_u^{k+} + d^k z (E_u^k q^k - D_u^k q^{*k})] . \quad (4.128)$$

2196 The detrainment of  $S_u$  is given by  $D_u^k S^k$  not by  $D_u^k S_u^k$ , since detrainment occurs at the environmental value of  $S$ . The detrainment of  $q_u$  is given by  $D_u^k q^{*k}$ , even though the updraft is not yet 2197 saturated. The LCL will usually occur below  $z_0$ , the level at which detrainment begins, but this 2198 is not guaranteed. 2199

The lower boundary conditions,  $S_u^{M-} = S^M + c_p/2$  and  $q_u^{M-} = q^M$ , are determined from the first midpoint values in the plume, rather than from the interface values of  $S$  and  $q$ . The solution of (4.127) and (4.128) continues upward until the updraft is saturated according to the condition

$$q_u^{k-} > q^*(T_u^{k-}), \quad (4.129)$$

$$T_u^{k-} = \frac{1}{c_p} (S_u^{k-} - g z^{k-}) . \quad (4.130)$$

The condensation (in units of  $\text{m}^{-1}$ ) is determined by a centered differencing of (4.82):

$$\frac{M_u^{k-}S_u^{k-} - M_u^{k+}S_u^{k+}}{d^k z} = (E_u^k - D_u^k)S^k + L C_u^k \quad (4.131)$$

$$C_u^k = \frac{1}{L} \left[ \frac{M_u^{k-}S_u^{k-} - M_u^{k+}S_u^{k+}}{d^k z} - (E_u^k - D_u^k)S^k \right] . \quad (4.132)$$

The rain production (in units of  $\text{m}^{-1}$ ) and condensed liquid are then determined by differencing (4.85) as

$$\frac{M_u^{k-}\ell^{k-} - M_u^{k+}\ell^{k+}}{d^k z} = -D_u^k \ell^{k+} + C_u^k - R_u^k , \quad (4.133)$$

and (4.86) as

$$R_u^k = c_0 M_u^{k-} \ell^{k-} . \quad (4.134)$$

Then

$$M_u^{k-}\ell^{k-} = M_u^{k+}\ell^{k+} - d^k z (D_u^k \ell^{k+} - C_u^k + c_0 M_u^{k-} \ell^{k-}) \quad (4.135)$$

$$M_u^{k-}\ell^{k-} (1 + c_0 d^k z) = M_u^{k+}\ell^{k+} + d^k z (D_u^k \ell^{k+} - C_u^k) \quad (4.136)$$

$$\ell^{k-} = \frac{1}{M_u^{k-} (1 + c_0 d^k z)} [M_u^{k+}\ell^{k+} - d^k z (D_u^k \ell^{k+} - C_u^k)] . \quad (4.137)$$

## 2200 4.4.5 Deep Convective Momentum Transports

Sub-grid scale Convective Momentum Transports (CMT) have been added to the existing deep convection parameterization following [Richter and Rasch \[2008\]](#) and the methodology of [Gregory et al. \[1997b\]](#). The sub-grid scale transport of momentum can be cast in the same manner as (4.69). Expressing the grid mean horizontal velocity vector,  $\mathbf{V}$ , tendency due to deep convection transport following [Kershaw and Gregory \[1997\]](#) gives

$$\left( \frac{\partial \mathbf{V}}{\partial t} \right)_{cu} = -\frac{1}{\rho} \frac{\partial}{\partial z} (M_u \mathbf{V}_u + M_d \mathbf{V}_d - M_c \mathbf{V}) , \quad (4.138)$$

and neglecting the contribution from the environment the updraft and downdraft budget equation can similarly be written as

$$-\frac{\partial}{\partial z} (M_u \mathbf{V}_u) = E_u \mathbf{V} - D_u \mathbf{V}_u + \mathbf{P}_G^u \quad (4.139)$$

$$-\frac{\partial}{\partial z} (M_d \mathbf{V}_d) = E_d \mathbf{V} + \mathbf{P}_G^d , \quad (4.140)$$

where  $\mathbf{P}_G^u$  and  $\mathbf{P}_G^d$  the updraft and downdraft pressure gradient sink terms parameterized from [Gregory et al. \[1997b\]](#) as

$$\mathbf{P}_G^u = -C_u M_u \frac{\partial \mathbf{V}}{\partial z} \quad (4.141)$$

$$\mathbf{P}_G^d = -C_d M_d \frac{\partial \mathbf{V}}{\partial z} . \quad (4.142)$$

2201  $C_u$  and  $C_d$  are tunable parameters. In the CAM 5.0 implementation we use  $C_u = C_d = 0.4$ . The  
 2202 value of  $C_u$  and  $C_d$  control the strength of convective momentum transport. As these coefficients  
 2203 increase so do the pressure gradient terms, and convective momentum transport decreases.

## 2204 4.4.6 Deep Convective Tracer Transport

2205 The CAM 5.0 provides the ability to transport constituents via convection. The method used  
 2206 for constituent transport by deep convection is a modification of the formulation described in  
 2207 [Zhang and McFarlane \[1995\]](#).

2208 We assume the updrafts and downdrafts are described by a steady state mass continuity  
 2209 equation for a “bulk” updraft or downdraft

$$\frac{\partial (M_x q_x)}{\partial p} = E_x q_e - D_x q_x . \quad (4.143)$$

2210 The subscript  $x$  is used to denote the updraft ( $u$ ) or downdraft ( $d$ ) quantity.  $M_x$  here is the  
 2211 mass flux in units of Pa/s defined at the layer interfaces,  $q_x$  is the mixing ratio of the updraft or  
 2212 downdraft.  $q_e$  is the mixing ratio of the quantity in the environment (that part of the grid volume  
 2213 not occupied by the up and downdrafts).  $E_x$  and  $D_x$  are the entrainment and detrainment rates  
 2214 (units of  $s^{-1}$ ) for the up- and down-drafts. Updrafts are allowed to entrain or detrain in any  
 2215 layer. Downdrafts are assumed to entrain only, and all of the mass is assumed to be deposited  
 2216 into the surface layer.

2217     Equation 4.143 is first solved for up and downdraft mixing ratios  $q_u$  and  $q_d$ , assuming the  
2218     environmental mixing ratio  $q_e$  is the same as the gridbox averaged mixing ratio  $\bar{q}$ .

Given the up- and down-draft mixing ratios, the mass continuity equation used to solve for the gridbox averaged mixing ratio  $\bar{q}$  is

$$\frac{\partial \bar{q}}{\partial t} = \frac{\partial}{\partial p} (M_u(q_u - \bar{q}) + M_d(q_d - \bar{q})) . \quad (4.144)$$

2219     These equations are solved for in subroutine CONVTRAN. There are a few numerical details  
2220     employed in CONVTRAN that are worth mentioning here as well.

- 2221     • mixing quantities needed at interfaces are calculated using the geometric mean of the layer  
2222       mean values.
- 2223     • simple first order upstream biased finite differences are used to solve 4.143 and 4.144.
- 2224     • fluxes calculated at the interfaces are constrained so that the resulting mixing ratios are  
2225       positive definite. *This means that this parameterization is not suitable for moving mixing*  
2226       *ratios of quantities meant to represent perturbations of a trace constituent about a mean*  
2227       *value (in which case the quantity can meaningfully take on positive and negative mix-*  
2228       *ing ratios). The algorithm can be modified in a straightforward fashion to remove this*  
2229       *constraint, and provide meaningful transport of perturbation quantities if necessary. the*  
2230       *reader is warned however that there are other places in the model code where similar mod-*  
2231       *ifications are required because the model assumes that all mixing ratios should be positive*  
2232       *definite quantities.*

2233 **4.5 Evaporation of convective precipitation**

The CAM 5.0 employs a Sundqvist [1988] style evaporation of the convective precipitation as it makes its way to the surface. This scheme relates the rate at which raindrops evaporate to the local large-scale subsaturation, and the rate at which convective rainwater is made available to the subsaturated model layer

$$E_{r_k} = K_E (1 - \text{RH}_k) (\hat{R}_{r_k})^{1/2} . \quad (4.145)$$

where  $\text{RH}_k$  is the relative humidity at level  $k$ ,  $\hat{R}_{r_k}$  denotes the total rainwater flux at level  $k$  (which can be different from the locally diagnosed rainwater flux from the convective parameterization, as will be shown below), the coefficient  $K_E$  takes the value  $0.2 \cdot 10^{-5} (\text{kg m}^{-2} \text{s}^{-1})^{-1/2} \text{s}^{-1}$ , and the variable  $E_{r_k}$  has units of  $\text{s}^{-1}$ . The evaporation rate  $E_{r_k}$  is used to determine a local change in  $q_k$  and  $T_k$ , associated with an evaporative reduction of  $\hat{R}_{r_k}$ . Conceptually, the evaporation process is invoked after a vertical profile of  $R_{r_k}$  has been evaluated. An evaporation rate is then computed for the uppermost level of the model for which  $R_{r_k} \neq 0$  using (4.145), where in this case  $R_{r_k} \equiv \hat{R}_{r_k}$ . This rate is used to evaluate an evaporative reduction in  $R_{r_k}$  which is then accumulated with the previously diagnosed rainwater flux in the layer below,

$$\hat{R}_{r_{k+1}} = \hat{R}_{r_k} - \left( \frac{\Delta p_k}{g} \right) E_{r_k} + R_{r_{k+1}} . \quad (4.146)$$

A local increase in the specific humidity  $q_k$  and a local reduction of  $T_k$  are also calculated in accordance with the net evaporation

$$q_k = q_k + E_{r_k} 2\Delta t , \quad (4.147)$$

and

$$T_k = T_k - \left( \frac{L}{c_p} \right) E_{r_k} 2\Delta t . \quad (4.148)$$

The procedure, (4.145)-(4.148), is then successively repeated for each model level in a downward direction where the final convective precipitation rate is that portion of the condensed rainwater in the column to survive the evaporation process

$$P_s = \left( \hat{R}_{r_K} - \left( \frac{\Delta p_K}{g} \right) E_{r_K} \right) / \rho_{H_20} . \quad (4.149)$$

2234 In global annually averaged terms, this evaporation procedure produces a very small reduction  
 2235 in the convective precipitation rate where the evaporated condensate acts to moisten the middle  
 2236 and lower troposphere.

## 2237 4.6 Cloud Microphysics

2238 The base parameterization of stratiform cloud microphysics is described by [Morrison and Gettelman](#)  
2239 [\[2008\]](#). Details of the CAM implementation are described by [Gettelman et al. \[2008\]](#). Mod-  
2240 ifications to handle ice nucleation and ice supersaturation are described by [Gettelman et al.](#)  
2241 [\[2010b\]](#).

2242 The scheme seeks the following:

- 2243 • A more flexible, self-consistent, physically-based treatment of cloud physics.
- 2244 • A reasonable level of simplicity and computational efficiency.
- 2245 • Treatment of both number concentration and mixing ratio of cloud particles to address  
2246 indirect aerosol effects and cloud-aerosol interaction.
- 2247 • Representation of precipitation number concentration, mass, and phase to better treat wet  
2248 deposition and scavenging of aerosol and chemical species.
- 2249 • The achievement of equivalent or better results relative to the CAM3 microphysics pa-  
2250 rameterization when compared to observations.

2251 The novel aspects of the scheme are an explicit representation of sub-grid cloud water distri-  
2252 bution for calculation of the various microphysical process rates, and the diagnostic two-moment  
2253 treatment of rain and snow.

### 2254 4.6.1 Overview of the microphysics scheme

2255 The two-moment scheme is based loosely on the approach of [Morrison et al. \[2005\]](#). This scheme  
2256 predicts the number concentrations ( $N_c$ ,  $N_i$ ) and mixing ratios ( $q_c$ ,  $q_i$ ) of cloud droplets (sub-  
2257 script  $c$ ) and cloud ice (subscript  $i$ ). Hereafter, unless stated otherwise, the cloud variables  $N_c$ ,  
2258  $N_i$ ,  $q_c$ , and  $q_i$  represent grid-averaged values; prime variables represent mean in-cloud quantities  
2259 (e.g., such that  $N_c = F_{\text{cld}} N_c$ , where  $F_{\text{cld}}$  is cloud fraction); and double prime variables re-  
2260 present local in-cloud quantities. The treatment of sub-grid cloud variability is detailed in section  
2261 2.1.

2262 The cloud droplet and ice size distributions  $\phi$  are represented by gamma functions:

$$\phi(D) = N_0 D^\mu \exp^{-\lambda D} \quad (4.150)$$

2263 where  $D$  is diameter,  $N_0$  is the intercept parameter,  $\lambda$  is the slope parameter, and  $\mu = 1/\eta^2 - 1$  is the spectra shape parameter;  $\eta$  is the relative radius dispersion of the size distribution.  
2264 The parameter  $\eta$  for droplets is specified following [Martin et al. \[1994\]](#). Their observations of  
2265 maritime versus continental warm stratocumulus have been approximated by the following  $\eta - N_c''$   
2266 relationship:

$$\eta = 0.0005714 N_c'' + 0.2714 \quad (4.151)$$

2267 where  $N_c''$  has units of  $\text{cm}^{-3}$ . The upper limit for  $\eta$  is 0.577, corresponding with a  $N_c''$  of 535  
2268  $\text{cm}^{-3}$ . Note that this expression is uncertain, especially when applied to cloud types other than  
2269 those observed by [Martin et al. \[1994\]](#). In the current version of the scheme,  $\mu = 0$  for cloud ice.

The spectral parameters  $N_0$  and  $\lambda$  are derived from the predicted  $N''$  and  $q''$  and specified  $\mu$ :

$$\lambda = \left[ \frac{\pi \rho N'' \Gamma(\mu + 4)}{6 q'' \Gamma(\mu + 1)} \right]^{(1/3)} \quad (4.152)$$

$$N_0 = \frac{N'' \lambda^{\mu+1}}{\Gamma(\mu + 1)} \quad (4.153)$$

where  $\Gamma$  is the Euler gamma function. Note that 4.152 and 4.153 assume spherical cloud particles with bulk density  $\rho = 1000 \text{ kg m}^{-3}$  for droplets and  $\rho = 500 \text{ kg m}^{-3}$  for cloud ice following Reisner et al. [1998].

The effective size for cloud ice needed by the radiative transfer scheme is obtained directly by dividing the third and second moments of the size distribution given by 4.150 and accounting for differences in cloud ice density and that of pure ice. After rearranging terms, this yields

$$d_{ei} = \frac{3\rho}{\lambda \rho_i} \quad (4.154)$$

where  $\rho_i = 917 \text{ kg m}^{-3}$  is the bulk density of pure ice. Note that optical properties for cloud droplets are calculated using a lookup table from the  $N_0$  and  $\lambda$  parameters. The droplet effective radius, which is used for output purposes only, is given by

$$r_{ec} = \frac{\Gamma(\mu + 4)}{2\lambda \Gamma(\mu + 3)} \quad (4.155)$$

The time evolution of  $q$  and  $N$  is determined by grid-scale advection, convective detrainment, turbulent diffusion, and several microphysical processes:

$$\frac{\partial N}{\partial t} + \frac{1}{\rho} \nabla \cdot [\rho \mathbf{u} N] = \left( \frac{\partial N}{\partial t} \right)_{nuc} + \left( \frac{\partial N}{\partial t} \right)_{evap} + \left( \frac{\partial N}{\partial t} \right)_{auto} + \left( \frac{\partial N}{\partial t} \right)_{acer} + \left( \frac{\partial N}{\partial t} \right)_{accs} + \left( \frac{\partial N}{\partial t} \right)_{het} + \left( \frac{\partial N}{\partial t} \right)_{hom} + \left( \frac{\partial N}{\partial t} \right)_{mult} \quad (4.156)$$

$$\frac{\partial q}{\partial t} + \frac{1}{\rho} \nabla \cdot [\rho \mathbf{u} q] = \left( \frac{\partial q}{\partial t} \right)_{cond} + \left( \frac{\partial q}{\partial t} \right)_{evap} + \left( \frac{\partial q}{\partial t} \right)_{auto} + \left( \frac{\partial q}{\partial t} \right)_{acer} + \left( \frac{\partial q}{\partial t} \right)_{accs} + \left( \frac{\partial q}{\partial t} \right)_{het} + \left( \frac{\partial q}{\partial t} \right)_{hom} + \left( \frac{\partial q}{\partial t} \right)_{mult} \quad (4.157)$$

where  $t$  is time,  $\mathbf{u}$  is the 3D wind vector,  $\rho$  is the air density, and  $D$  is the turbulent diffusion operator. The symbolic terms on the right hand side of 4.156 and 4.157 represent the grid-average microphysical source/sink terms for  $N$  and  $q$ . Note that the source/sink terms for  $q$  and  $N$  are considered separately for cloud water and ice (giving a total of four rate equations), but are generalized here using 4.156 and 4.157 for conciseness. These terms include activation of cloud condensation nuclei or deposition/condensation-freezing nucleation on ice nuclei to form droplets or cloud ice (subscript  $nuc$ ;  $N$  only); ice multiplication via rime-splintering on snow (subscript  $mult$ ); condensation/deposition (subscript  $cond$ ;  $q$  only), evaporation/sublimation (subscript  $evap$ ), autoconversion of cloud droplets and ice to form rain and snow (subscript  $auto$ ), accretion of cloud droplets and ice by rain (subscript  $accr$ ), accretion of cloud droplets and ice by snow (subscript  $accs$ ), heterogeneous freezing of droplets to form ice (subscript  $het$ ),

homogeneous freezing of cloud droplets (subscript hom), melting (subscript mlt), ice multiplication (subscript mult), sedimentation (subscript sed), and convective detrainment (subscript det). The formulations for these processes are detailed in section 3. Numerical aspects in solving 4.156 and 4.157 are detailed in section 4.

## Sub-grid cloud variability

Sub-grid variability is considered for cloud water but neglected for cloud ice and precipitation at present; furthermore, we neglect sub-grid variability of droplet number concentration for simplicity. We assume that the PDF of in-cloud cloud water,  $P(q''_c)$ , follows a gamma distribution function based on observations of optical depth in marine boundary layer clouds [Barker, 1996; Barker et al., 1996; McFarlane and Klein, 1999]:

$$P(q''_c) = \frac{q''_c^{\nu-1} \alpha^\nu}{\Gamma(\nu)} \exp^{-\alpha q''_c} \quad (4.158)$$

where  $\nu = 1/\sigma^2$ ;  $\sigma^2$  is the relative variance (i.e., variance divided by  $q'_c$ ); and  $\alpha = \nu/q'_c$  ( $q'_c$  is the mean in-cloud cloud water mixing ratio). Note that this PDF is applied to all cloud types treated by the stratiform cloud scheme; the appropriateness of such a PDF for stratiform cloud types other than marine boundary layer clouds (e.g., deep frontal clouds) is uncertain given a lack of observations.

Satellite retrievals described by Barker et al. [1996] suggest that  $\nu > 1$  in overcast conditions and  $\nu \sim 1$  (corresponding to an exponential distribution) in broken stratocumulus. The model assumes a constant  $\nu = 1$  for simplicity.

A major advantage of using gamma functions to represent sub-grid variability of cloud water is that the grid-average microphysical process rates can be derived in a straightforward manner as follows. For any generic local microphysical process rate  $M_p = x q''_c^y$ , replacing  $q''_c$  with  $P(q''_c)$  from 4.158 and integrating over the PDF yields a mean in-cloud process rate

$$M'_p = x \frac{\Gamma(\nu + y)}{\Gamma(\nu) \nu^y} q'_c^y \quad (4.159)$$

Thus, each cloud water microphysical process rate in 4.156 and 4.157 is multiplied by a factor

$$E = \frac{\Gamma(\nu + y)}{\Gamma(\nu) \nu^y} \quad (4.160)$$

## Diagnostic treatment of precipitation

As described by Ghan and Easter [1992], diagnostic treatment of precipitation allows for a longer time step, since prognostic precipitation is constrained by the Courant criterion for sedimentation. Furthermore, the neglect of horizontal advection of precipitation in the diagnostic approach is reasonable given the large grid spacing ( $\sim 100$  km) and long time step ( $\sim 15\text{-}40$  min) of GCMs. A unique aspect of this scheme is the diagnostic treatment of both precipitation mixing ratio  $q_p$  and number concentration  $N_p$ . Considering only the vertical dimension, the grid-scale time rates of change of  $q_p$  and  $N_p$  are:

$$\frac{\partial q_p}{\partial t} = \frac{1}{\rho} \frac{\partial (V_q \rho q_p)}{\partial z} + S_q \quad (4.161)$$

$$\frac{\partial N_p}{\partial t} = \frac{1}{\rho} \frac{\partial (V_N \rho N_p)}{\partial z} + S_N \quad (4.162)$$

2323 where  $z$  is height,  $V_q$  and  $V_N$  are the mass- and number-weighted terminal fallspeeds, respec-  
 2324 tively, and  $S_q$  and  $S_N$  are the grid-mean source/sink terms for  $q_p$  and  $N_p$ , respectively:

$$S_q = \left( \frac{\partial q_p}{\partial t} \right)_{auto} + \left( \frac{\partial q_p}{\partial t} \right)_{accw} + \left( \frac{\partial q_p}{\partial t} \right)_{acci} + \left( \frac{\partial q_p}{\partial t} \right)_{het} + \left( \frac{\partial q_p}{\partial t} \right)_{hom} + \left( \frac{\partial q_p}{\partial t} \right)_{mlt} + \left( \frac{\partial q_p}{\partial t} \right)_{mult} + \left( \frac{\partial q_p}{\partial t} \right)_{evap} + \left( \frac{\partial q_p}{\partial t} \right)_{coll} \quad (4.163)$$

$$S_N = \left( \frac{\partial N_p}{\partial t} \right)_{auto} + \left( \frac{\partial N_p}{\partial t} \right)_{het} + \left( \frac{\partial N_p}{\partial t} \right)_{hom} + \left( \frac{\partial N_p}{\partial t} \right)_{mlt} + \left( \frac{\partial N_p}{\partial t} \right)_{evap} + \left( \frac{\partial N_p}{\partial t} \right)_{self} + \left( \frac{\partial N_p}{\partial t} \right)_{coll} \quad (4.164)$$

2325 The symbolic terms on the right-hand sides of 4.163 and 4.164 are autoconversion (subscript  
 2326 auto), accretion of cloud water (subscript accw), accretion of cloud ice (subscript acci), heterogeneous  
 2327 freezing (subscript het), homogeneous freezing (subscript hom), melting (subscript mlt),  
 2328 ice multiplication via rime splintering (subscript mult; qp only), evaporation (subscript evap),  
 2329 and self-collection (subscript self; collection of rain drops by other rain drops, or snow crystals  
 2330 by other snow crystals; Np only), and collection of rain by snow (subscript coll). Formulations  
 2331 for these processes are described in section 3.

2332 In the diagnostic treatment,  $(\partial q_p / \partial t) = 0$  and  $(\partial N_p / \partial t) = 0$ . This allows 4.161 and 4.162  
 2333 to be expressed as a function of  $z$  only. The  $q_p$  and  $N_p$  are therefore determined by discretizing  
 2334 and numerically integrating 4.161 and 4.162 downward from the top of the model atmosphere  
 2335 following [Ghan and Easter \[1992\]](#):

$$\rho_{a,k} V_{q,k} q_{p,k} = \rho_{a,k+1} V_{q,k+1} q_{p,k+1} + \frac{1}{2} [\rho_{a,k} S_{q,k} \delta Z_k + \rho_{a,k+1} S_{q,k+1} \delta Z_{k+1}] \quad (4.165)$$

$$\rho_{a,k} V_{N,k} N_{p,k} = \rho_{a,k+1} V_{N,k+1} N_{p,k+1} + \frac{1}{2} [\rho_{a,k} S_{N,k} \delta Z_k + \rho_{a,k+1} S_{N,k+1} \delta Z_{k+1}] \quad (4.166)$$

2336 where  $k$  is the vertical level (increasing with height, i.e.,  $k+1$  is the next vertical level above  
 2337  $k$ ). Since  $V_{q,k}$ ,  $S_{q,k}$ ,  $V_{N,k}$ , and  $S_{N,k}$  depend on  $q_{p,k}$  and  $N_{p,k}$ , 4.165 and 4.166 must be solved by  
 2338 iteration or some other method. The approach of [Ghan and Easter \[1992\]](#) uses values of  $q_{p,k}$  and  
 2339  $N_{p,k}$  from the previous time step as provisional estimates in order to calculate  $V_{q,k}$ ,  $V_{N,k}$ ,  $S_{p,k}$ ,  
 2340 and  $S_{N,k}$ . “Final” values of  $q_{p,k}$  and  $N_{p,k}$  are calculated from these values of  $V_{q,k}$ ,  $V_{N,k}$ ,  $S_{q,k}$  and  
 2341  $S_{N,k}$  using 4.165 and 4.166. Here we employ another method that obtains provisional values of  
 2342  $q_{p,k}$  and  $N_{p,k}$  from 4.165 and 4.166 assuming  $V_{q,k} \sim V_{q,k+1}$  and  $V_{N,k} \sim V_{N,k+1}$ . It is also assumed  
 2343 that all source/sink terms in  $S_{q,k}$  and  $S_{N,k}$  can be approximated by the values at  $k+1$ , except  
 2344 for the autoconversion, which can be obtained directly at the  $k$  level since it does not depend  
 2345 on  $q_{p,k}$  or  $N_{p,k}$ . If there is no precipitation flux from the level above, then the provisional  $q_{p,k}$   
 2346 and  $N_{p,k}$  are calculated using autoconversion at the  $k$  level in  $S_{q,k}$  and  $S_{N,k}$ ;  $V_{q,k}$  and  $V_{N,k}$  are

estimated assuming newly-formed rain and snow particles have fallspeeds of 0.45 m/s for rain and 0.36 m/s for snow.

Rain and snow are considered separately, and both may occur simultaneously in supercooled conditions (hereafter subscript p for precipitation is replaced by subscripts r for rain and s for snow). The rain/snow particle size distributions are given by 4.150, with the shape parameter  $\mu = 0$ , resulting in Marshall-Palmer (exponential) size distributions. The size distribution parameters  $\lambda$  and  $N_0$  are similarly given by 4.152 and 4.153 with  $\mu = 0$ . The bulk particle density (parameter  $\rho$  in 4.152) is  $\rho = 1000 \text{ kg m}^{-3}$  for rain and  $\rho = 100 \text{ kg m}^{-3}$  for snow following Reisner et al. [1998].

## Cloud and precipitation particle terminal fallspeeds

The mass- and number-weighted terminal fallspeeds for all cloud and precipitation species are obtained by integration over the particle size distributions with appropriate weighting by number concentration or mixing ratio:

$$V_N = \frac{\int_0^\infty \left(\frac{\rho_a}{\rho_{a0}}\right)^{0.54} a D^b \phi(D) dD}{\int_0^\infty \phi(D) dD} = \frac{\left(\frac{\rho_a}{\rho_{a0}}\right)^{0.54} a \Gamma(1 + b + \mu)}{\lambda^b \Gamma(\mu + 1)} \quad (4.167)$$

$$V_q = \frac{\int_0^\infty \frac{\pi \rho}{6} \left(\frac{\rho_a}{\rho_{a0}}\right)^{0.54} a D^{b+3} \phi(D) dD}{\int_0^\infty \frac{\pi \rho}{6} D^3 \phi(D) dD} = \frac{\left(\frac{\rho_a}{\rho_{a0}}\right)^{0.54} a \Gamma(4 + b + \mu)}{\lambda^b \Gamma(\mu + 4)} \quad (4.168)$$

where  $\rho^{a0}$  is the reference air density at 850 mb and 0 C,  $a$  and  $b$  are empirical coefficients in the diameter-fallspeed relationship  $V = a D^b$ , where  $V$  is terminal fallspeed for an individual particle with diameter  $D$ . The air density correction factor is from Heymsfield and Bansemer (2007).  $V_N$  and  $V_q$  are limited to maximum values of 9.1 m/s for rain and 1.2 m/s for snow. The  $a$  and  $b$  coefficients for each hydrometeor species are given in Table 2. Note that for cloud water fallspeeds, sub-grid variability of  $q$  is considered by appropriately multiplying the  $V_N$  and  $V_q$  by the factor  $E$  given by 4.160.

## Ice Cloud Fraction

Several modifications have been made to the determination of diagnostic fractional cloudiness in the simulations. The ice and liquid cloud fractions are now calculated separately. Ice and liquid cloud can exist in the same grid box. Total cloud fraction, used for radiative transfer, is determined assuming maximum overlap between the two.

The diagnostic ice cloud fraction closure is constructed using a total water formulation of the Slingo [1987a] scheme. There is an indirect dependence of prognostic cloud ice on the ice cloud fraction since the in-cloud ice content is used for all microphysical processes involving ice. The new formulation of ice cloud fraction ( $CF_i$ ) is calculated using relative humidity (RH) based on total ice water mixing ratio, including the ice mass mixing ratio ( $q_i$ ) and the vapor mixing ratio ( $q_v$ ). The RH based on total ice water ( $RH_{ti}$ ) is then  $RH_{ti} = (q_v + q_i)/q_{sat}$  where  $q_{sat}$  is the saturation vapor mixing ratio over ice. Because this is for ice clouds only, we do not include  $q_l$  (liquid mixing ratio). We have tested that the inclusion of  $q_l$  does not substantially impact the scheme (since there is little liquid present in this regime).

2381 Ice cloud fraction is then given by  $CF_i = \min(1, RH_d^2)$  where

$$RH_d = \max \left( 0, \frac{RH_{ti} - RH_{i_{min}}}{RH_{i_{max}} - RH_{i_{min}}} \right) \quad (4.169)$$

2382  $RH_{i_{max}}$  and  $RH_{i_{min}}$  are prescribed maximum and minimum threshold humidities with re-  
2383 spect to ice, set at  $RH_{i_{max}}=1.1$  and  $RH_{i_{min}}=0.8$ . These are adjustable parameters that reflect  
2384 assumptions about the variance of humidity in a grid box. The scheme is not very sensitive to  
2385  $RH_{i_{min}}$ .  $RH_{i_{max}}$  affects the total ice supersaturation and ice cloud fraction.

2386 With  $RH_{i_{max}} = 1$  and  $q_i = 0$  the scheme reduces to the [Slingo \[1987a\]](#) scheme.  $RH_{ti}$  is  
2387 preferred over  $RH$  in  $RH_d$  because when  $q_i$  increases due to vapor deposition, it reduces  $q_v$ , and  
2388 without any precipitation or sedimentation the decrease in  $RH$  would change diagnostic cloud  
2389 fraction, whereas  $RH_{ti}$  is constant.

## 2390 4.6.2 Radiative Treatment of Ice

2391 The simulations use a self consistent treatment of ice in the radiation code. The radiation code  
2392 uses as input the prognostic effective diameter of ice from the cloud microphysics (give eq. #  
2393 from above). Ice cloud optical properties are calculated based on the modified anomalous diffrac-  
2394 tion approximation (MADA), described in [Mitchell \[2000, 2002\]](#) and [Mitchell et al. \[2006a\]](#). The  
2395 mass-weighted extinction (volume extinction coefficient/ice water content) and the single scat-  
2396 tering albedo,  $\omega_0$ , are evaluated using a look-up table. For solar wavelengths, the asymmetry  
2397 parameter  $g$  is determined as a function of wavelength and ice particle size and shape as de-  
2398 scribed in [Mitchell et al. \[1996a\]](#) and [Nousiainen and McFarquhar \[2004\]](#) for quasi-spherical ice  
2399 crystals. For terrestrial wavelengths,  $g$  was determined following [Yang et al. \[2005\]](#). An ice par-  
2400 ticle shape recipe was assumed when calculating these optical properties. The recipe is described  
2401 in [Mitchell et al. \[2006b\]](#) based on mid-latitude cirrus cloud data from [Lawson et al. \[2006\]](#) and  
2402 consists of 50% quasi-spherical and 30% irregular ice particles, and 20% bullet rosettes for the  
2403 cloud ice (i.e. small crystal) component of the ice particle size distribution (PSD). Snow is also  
2404 included in the radiation code, using the diagnosed mass and effective diameter of falling snow  
2405 crystals (MG2008). For the snow component, the ice particle shape recipe was based on the  
2406 crystal shape observations reported in [Lawson et al. \[2006\]](#) at -45°C: 7% hexagonal columns,  
2407 50% bullet rosettes and 43% irregular ice particles.

## 2408 4.6.3 Formulations for the microphysical processes

### 2409 Activation of cloud droplets

2410 Activation of cloud droplets, occurs on a multi-modal lognormal aerosol size distribution  
2411 based on the scheme of [Abdul-Razzak and Ghan \[2000a\]](#). Activation of cloud droplets oc-  
2412 curs if  $N_c$  decreases below the number of active cloud condensation nuclei diagnosed as a  
2413 function of aerosol chemical and physical parameters, temperature, and vertical velocity (see  
2414 [Abdul-Razzak and Ghan \[2000a\]](#)), and if liquid condensate is present. We use the existing  $N_c$   
2415 as a proxy for the number of aerosols previously activated as droplets since the actual number  
2416 of activated aerosols is not tracked as a prognostic variable from time step to time step (for

coupling with prescribed aerosol scheme). This approach is similar to that of Lohmann et al. [1999].

Since local rather than grid-scale vertical velocity is needed for calculating droplet activation, a sub-grid vertical velocity  $w_{sub}$  is derived from the square root of the Turbulent Kinetic Energy (TKE) following Morrison and Pinto [2005]:

$$w_{sub} = \sqrt{\frac{2}{3} TKE} \quad (4.170)$$

where TKE is defined using a steady state energy balance (eqn [17] and [28] in Bretherton and Park [2009b])

In regions with weak turbulent diffusion, a minimum sub-grid vertical velocity of 10 cm/s is assumed. Some models use the value of  $w$  at cloud base to determine droplet activation in the cloud layer (e.g., Lohmann et al. [1999]); however, because of coarse vertical and horizontal resolution and difficulty in defining the cloud base height in GCMs, we apply the  $w_{sub}$  calculated for a given layer to the droplet activation for that layer. Note that the droplet number may locally exceed the number activated for a given level due to advection of  $N_c$ . Some models implicitly assume that the timescale for droplet activation over a cloud layer is equal to the model time step (e.g., Lohmann et al. [1999]), which could enhance sensitivity to the time step. This timescale can be thought of as the timescale for recirculation of air parcels to regions of droplet activation (i.e., cloud base), similar to the timescale for large eddy turnover; here, we assume an activation timescale of 20 min.

## Primary ice nucleation

Ice crystal nucleation is based on Liu et al. [2007], which includes homogeneous freezing of sulfate competing with heterogeneous immersion freezing on mineral dust in ice clouds (with temperatures below -37°C) [Liu and Penner, 2005]. Because mineral dust at cirrus levels is very likely coated [Wiacek and Peter, 2009], deposition nucleation is not explicitly included in this work for pure ice clouds. Immersion freezing is treated for cirrus (pure ice), but not for mixed phase clouds. The relative efficiency of immersion versus deposition nucleation in mixed phase clouds is an unsettled problem, and the omission of immersion freezing in mixed phase clouds may not be appropriate (but is implicitly included in the deposition/condensation nucleation: see below). Deposition nucleation may act at temperatures lower than immersion nucleation (i.e.  $T < -25^\circ\text{C}$ ) [Field et al., 2006], and immersion nucleation has been inferred to dominate in mixed phase clouds [Ansmann et al., 2008, 2009; Hoose and Kristjansson, 2010]. We have not treated immersion freezing on soot because while Liu and Penner [2005] assumed it was an efficient mechanism for ice nucleation, more recent studies [Kärcher et al., 2007] indicate it is still highly uncertain.

In the mixed phase cloud regime ( $-37 < T < 0^\circ\text{C}$ ), deposition/condensation nucleation is considered based on Meyers et al. [1992], with a constant nucleation rate for  $T < -20^\circ\text{C}$ . The Meyers et al. [1992] parameterization is assumed to treat deposition/condensation on dust in the mixed phase. Since it is based on observations taken at water saturation, it should include all important ice nucleation mechanisms (such as the immersion and deposition nucleation discussed above) except contact nucleation, though we cannot distinguish all the specific processes. Meyers et al. [1992] has been shown to produce too many ice nuclei during the Mixed Phase

2457 Arctic Clouds Experiment (MPACE) by [Prenni et al. \[2007\]](#). Contact nucleation by mineral  
 2458 dust is included based on [Young \[1974\]](#) and related to the coarse mode dust number. It acts in  
 2459 the mixed phase where liquid droplets are present and includes Brownian diffusion as well  
 2460 as phoretic forces. Hallet-Mossop secondary ice production due to accretion of drops by snow  
 2461 is included following [Cotton et al. \[1986\]](#).

2462 In the [Liu and Penner \[2005\]](#) scheme, the number of ice crystals nucleated is a function of  
 2463 temperature, humidity, sulfate, dust and updraft velocity, derived from fitting the results from  
 2464 cloud parcel model experiments. A threshold  $RH_w$  for homogeneous nucleation was fitted as  
 2465 a function of temperature and updraft velocity (see [Liu et al. \[2007\]](#), equation 6). For driving  
 2466 the parameterization, the sub-grid velocity for ice ( $w_{sub}$ ) is derived following [ewuation 4.170](#). A  
 2467 minimum of  $0.2 \text{ m s}^{-1}$  is set for ice nucleation.

2468 It is also implicitly assumed that there is some variation in humidity over the grid box. For  
 2469 purposes of ice nucleation, nucleation rates for a grid box are estimated based on the ‘most  
 2470 humid portion’ of the grid-box. This is assumed to be the grid box average humidity plus a  
 2471 fixed value (20% RH). This implies that the ‘local’ threshold supersaturation for ice nucleation  
 2472 will be reached at a grid box mean value 20% lower than the RH process threshold value. This  
 2473 represents another gross assumption about the RH variability in a model grid box and is an  
 2474 adjustable parameter in the scheme. In the baseline case, sulfate for homogeneous freezing is  
 2475 taken as the portion of the Aitken mode particles with radii greater than 0.1 microns, and  
 2476 was chosen to better reproduce observations (this too can be adjusted to alter the balance of  
 2477 homogeneous freezing). The size represents the large tail of the Aitken mode. In the upper  
 2478 troposphere there is little sulfate in the accumulation mode (it falls out), and almost all sulfate  
 2479 is in the Aitken mode.

## 2480 **Deposition/sublimation of ice**

2481 Several cases are treated below that involve ice deposition in ice-only clouds or mixed-phase  
 2482 clouds in which all liquid water is depleted within the time step. Case [1] Ice only clouds in  
 2483 which  $q_v > q_{vi}^*$  where  $q_v$  is the grid mean water vapor mixing ratio and  $q_{vi}^*$  is the local vapor  
 2484 mixing ratio at ice saturation ( $q_{sat}$ ). Case [2] is the same as case [1] ( $q_v > q_{vi}^*$ ) but there is  
 2485 existing liquid water depleted by the Bergeron-Findeisen process (*ber*). Case [3], liquid water is  
 2486 depleted by the Bergeron-Findeisen process and the local liquid is less than local ice saturation  
 2487 ( $q_v^* \leq q_{vi}^*$ ). In Case [4]  $q_v < q_{vi}^*$  so sublimation of ice occurs.

2488 Case [1]: If the ice cloud fraction is larger than the liquid cloud fraction (including grid  
 2489 cells with ice but no liquid water), or if all new and existing liquid water in mixed-phase clouds  
 2490 is depleted via the Bergeron-Findeisen process within the time step, then vapor depositional  
 2491 ice growth occurs at the expense of water vapor. In the case of a grid cell where ice cloud  
 2492 fraction exceeds liquid cloud fraction, vapor deposition in the pure ice cloud portion of the cell  
 2493 is calculated similarly to eq. [21] in MG08:

$$\left( \frac{\partial q_i}{\partial t} \right)_{dep} = \frac{(q_v - q_{vi}^*)}{\Gamma_p \tau}, q_v > q_{vi}^* \quad (4.171)$$

2494 where  $\Gamma_p = 1 + \frac{L_s}{c_p} \frac{dq_{vi}}{dT}$  is the psychrometric correction to account for the release of latent  
 2495 heat,  $L_s$  is the latent heat of sublimation,  $c_p$  is the specific heat at constant pressure,  $\frac{dq_{vi}}{dT}$  is the  
 2496 change of ice saturation vapor pressure with temperature, and  $\tau$  is the supersaturation relaxation

timescale associated with ice deposition given by eq. [22] in MG08 (a function of ice crystal surface area and the diffusivity of water vapor in air). The assumption for pure ice clouds is that the in-cloud vapor mixing ratio for deposition is equal to the grid-mean value. The same assumption is used in Liu et al. [2007], and while it is uncertain, it is the most straightforward. Thus we do not consider sub-grid variability of water vapor for calculating vapor deposition in pure ice-clouds.

The form of the deposition rate in equation 4.171 differs from that used by Rotstayn et al. [2000] and Liu et al. [2007] because they considered the increase in ice mixing ratio  $q_i$  due to vapor deposition during the time step, and formulated an implicit solution based on this consideration (see eq. [6] in Rotstayn et al. [2000]). However, these studies did not consider sinks for the ice due to processes such as sedimentation and conversion to precipitation when formulating their implicit solution; these sink terms may partially (or completely) balance the source for the ice due to vapor deposition. Thus, we use a simple explicit forward-in-time solution that does not consider changes of  $q_i$  within the microphysics time step.

Case [2]: When all new and existing liquid water is depleted via the Bergeron-Findeisen process (*ber*) within the time step, the vapor deposition rate is given by a weighted average of the values for growth in mixed phase conditions prior to the depletion of liquid water (first term on the right hand side) and in pure ice clouds after depletion (second term on the right hand side):

$$\left( \frac{\partial q_i}{\partial t} \right)_{dep} = \frac{q_c^*}{\Delta t} + \left( 1 - \frac{q_c^*}{\Delta t} \left( \frac{\partial q_i}{\partial t} \right)_{ber}^{-1} \right) \left( \frac{(q_v^* - q_{vi}^*)}{\Gamma_p \tau} \right), q_v > q_{vi}^* \quad (4.172)$$

where  $q_c^*$  is the sum of existing and new liquid condensate mixing ratio,  $\Delta t$  is the model time step,  $\left( \frac{\partial q_i}{\partial t} \right)_{ber}$  is the ice deposition rate in the presence of liquid water (i.e., assuming vapor mixing ratio is equal to the value at liquid saturation) as described above, and  $q_v^*$  is an average of the grid-mean vapor mixing ratio and the value at liquid saturation.

Case [3]: If  $q_v^* \leq q_{vi}^*$  then it is assumed that no additional ice deposition occurs after depletion of the liquid water. The deposition rate in this instance is given by:

$$\left( \frac{\partial q_i}{\partial t} \right)_{dep} = \left( \frac{q_c^*}{\Delta t} \right), q_v^* \leq q_{vi}^* \quad (4.173)$$

Case [4]: Sublimation of pure ice cloud occurs when the grid-mean water vapor mixing ratio is less than value at ice saturation. In this case the sublimation rate of ice is given by:

$$\left( \frac{\partial q_i}{\partial t} \right)_{sub} = \frac{(q_v - q_{vi}^*)}{\Gamma_p \tau}, q_v < q_{vi}^* \quad (4.174)$$

Again, the use of grid-mean vapor mixing ratio in equation 4.174 follows the assumption of Liu et al. [2007] that the in-cloud  $q_v$  is equal to the grid box mean in pure ice clouds. Grid-mean deposition and sublimation rates are given by the in-cloud values for pure ice or mixed-phase clouds described above, multiplied by the appropriate ice or mixed-phase cloud fraction. Finally, ice deposition and sublimation are limited to prevent the grid-mean mixing ratio from falling below the value for ice saturation in the case of deposition and above this value in the case of sublimation.

Cloud water condensation and evaporation are given by the bulk closure scheme within the cloud macrophysics scheme, and therefore not described here.

2528 **Conversion of cloud water to rain**

2529 Autoconversion of cloud droplets and accretion of cloud droplets by rain is given by a version  
 2530 of the [Khairoutdinov and Kogan \[2000\]](#) scheme that is modified here to account for sub-grid  
 2531 variability of cloud water within the cloudy part of the grid cell as described previously in section  
 2532 2.1. Note that the Khairoutdinov and Kogan scheme was originally developed for boundary layer  
 2533 stratocumulus, but is applied here to all stratiform cloud types.

2534 The grid-mean autoconversion and accretion rates are found by replacing the  $qc$  in Eqs.  
 2535 (29) and (33) of [Khairoutdinov and Kogan \[2000\]](#) with  $P(q_c'')$  given by equation 4.158 here,  
 2536 integrating the resulting expressions over the cloud water PDF, and multiplying by the cloud  
 2537 fraction. This yields

$$\left( \frac{\partial q_c}{\partial t} \right)_{auto} = -F_{cld} \frac{\Gamma(\nu + 2.47)}{\Gamma(\nu)\nu^{2.47}} 1350 q_c'^{2.47} N_c'^{-1.79} \quad (4.175)$$

$$\left( \frac{\partial q_c}{\partial t} \right)_{accr} = -F_{cld} \frac{\Gamma(\nu + 1.15)}{\Gamma(\nu)\nu^{1.15}} 67 (q_c' q_r')^{1.15} \quad (4.176)$$

2538 The changes in  $qr$  due to autoconversion and accretion are given by  $(\partial q_r / \partial t)_{auto} =$   
 2539  $-(\partial q_c / \partial t)_{auto}$  and  $(\partial q_r / \partial t)_{accr} = -(\partial q_c / \partial t)_{accr}$ . The changes in  $N_c$  and  $N_r$  due to autocon-  
 2540 version and accretion  $(\partial N_c / \partial t)_{auto}$ ,  $(\partial N_r / \partial t)_{auto}$ ,  $(\partial N_c / \partial t)_{accr}$ , are derived from Eqs. (32) and  
 2541 (35) in [Khairoutdinov and Kogan \[2000\]](#). Since accretion is nearly linear with respect to  $q_c$ , sub-  
 2542 grid variability of cloud water is much less important for accretion than it is for autoconversion.

2543 Note that in the presence of a precipitation flux into the layer from above, new drizzle drops  
 2544 formed by cloud droplet autoconversion would be accreted rapidly by existing precipitation  
 2545 particles (rain or snow) given collection efficiencies near unity for collision of drizzle with rain  
 2546 or snow (e.g., [Pruppacher and Klett \[1997\]](#)). This may be especially important in models with  
 2547 low vertical resolution, since they cannot resolve the rapid growth of precipitation that occurs  
 2548 over distances much less than the vertical grid spacing. Thus, if the rain or snow mixing ratio  
 2549 in the next level above is greater than 10-6 g kg<sup>-1</sup>, we assume that autoconversion produces an  
 2550 increase in rain mixing ratio but not number concentration (since the newly-formed drops are  
 2551 assumed to be rapidly accreted by the existing precipitation). Otherwise, autoconversion results  
 2552 in a source of both rain mixing ratio and number concentration.

2553 **Conversion of cloud ice to snow**

2554 The autoconversion of cloud ice to form snow is calculated by integration of the cloud ice  
 2555 mass- and number-weighted size distributions greater than some specified threshold size, and  
 2556 transferring the resulting mixing ratio and number into the snow category over some specified  
 2557 timescale, similar to [Ferrier \[1994\]](#). The grid-scale changes in  $qi$  and  $Ni$  due to autoconversion  
 2558 are

$$\left( \frac{\partial q_i}{\partial t} \right)_{auto} = -F \frac{\pi \rho_i N_{0i}}{6\tau_{auto}} \left[ \frac{D_{cs}^3}{\lambda_i} + \frac{3D_{cs}^2}{\lambda_i^2} + \frac{6D_{cs}}{\lambda_i^3} + \frac{6D}{\lambda_i^4} \right] \exp^{-\lambda_i D_{cs}} \quad (4.177)$$

$$\left( \frac{\partial N_i}{\partial t} \right)_{auto} = -F \frac{N_{0i}}{\lambda_i \tau_{auto}} \exp^{-\lambda_i D_{cs}} \quad (4.178)$$

2559 where  $D_{cs} = 200 \mu\text{m}$  is the threshold size separating cloud ice from snow,  $\rho_i$  is the bulk  
2560 density of cloud ice, and  $\tau_{auto} = 3 \text{ min}$  is the assumed autoconversion timescale. Note that this  
2561 formulation assumes the shape parameter  $\mu = 0$  for the cloud ice size distribution; different  
2562 formulation must be used for other values of  $\mu$ . The changes in  $q_s$  and  $N_s$  due to autoconversion  
2563 are given by  $(\partial q_s / \partial t)_{auto} = -(\partial q_i / \partial t)_{auto}$  and  $(\partial N_s / \partial t)_{auto} = -(\partial N_i / \partial t)_{auto}$ .

2564 Accretion of  $q_i$  and  $N_i$  by snow  $(\partial q_i / \partial t)_{accs}$ ,  $(\partial N_i / \partial t)_{accs}$ ,  $(\partial q_s / \partial t)_{acci}$ , and  $(\partial q_s / \partial t)_{acci} =$   
2565  $-(\partial q_i / \partial t)_{accs}$ , are given by the continuous collection equation following [Lin et al. \[1983\]](#), which  
2566 assumes that the fallspeed of snow  $\gg$  cloud ice fallspeed. The collection efficiency for collisions  
2567 between cloud ice and snow is 0.1 following [Reisner et al. \[1998\]](#). Newly- formed snow particles  
2568 formed by cloud ice autoconversion are not assumed to be rapidly accreted by existing snowflakes,  
2569 given aggregation efficiencies typically much less than unity (e.g., [Field et al. \[2007\]](#)).

## 2570 Other collection processes

2571 The accretion of  $q_c$  and  $N_c$  by snow  $(\partial q_c / \partial t)_{accs}$ ,  $(\partial N_c / \partial t)_{accs}$ , and  $(\partial q_s / \partial t)_{accw} = -(\partial q_c / \partial t)_{accs}$   
2572 are given by the continuous collection equation. The collection efficiency for droplet-snow col-  
2573 lisions is a function of the Stokes number following [Thompson et al. \[2004\]](#) and thus depends  
2574 on droplet size. Self-collection of snow,  $(\partial N_s / \partial t)_{self}$  follows [Reisner et al. \[1998\]](#) using an as-  
2575 sumed collection efficiency of 0.1. Self-collection of rain  $(\partial N_r / \partial t)_{self}$  follows [Beheng \[1994\]](#).  
2576 Collisions between rain and cloud ice, cloud droplets and cloud ice, and self-collection of cloud  
2577 ice are neglected for simplicity. Collection of  $q_r$  and  $N_r$  by snow in subfreezing conditions,  
2578  $(\partial q_r / \partial t)_{coll} = -(\partial q_s / \partial t)_{coll}$  and  $(\partial N_r / \partial t)_{coll}$ , is given by [Ikawa and Saito \[1990\]](#) assuming col-  
2579 lection efficiency of unity.

## 2580 Freezing of cloud droplets and rain and ice multiplication

2581 Heterogeneous freezing of cloud droplets and rain to form cloud ice and snow, respectively,  
2582 occurs by immersion freezing following [Bigg \[1953\]](#), which has been utilized in previous micro-  
2583 physics schemes (e.g., [Reisner et al. \[1998\]](#), see Eq. A.22, A.55, A.56; [Morrison et al. \[2005\]](#);  
2584 [Thompson et al. \[2008\]](#)). Here the freezing rates are integrated over the mass- and number-  
2585 weighted cloud droplet and rain size distributions and the impact of sub-grid cloud water vari-  
2586 ability is included as described previously. Homogeneous freezing of cloud droplets to form cloud  
2587 ice occurs instantaneously at  $-40^\circ\text{C}$ . All rain is assumed to freeze instantaneously at  $-5^\circ\text{C}$ .

2588 Contact freezing of cloud droplets by mineral dust is included based on [Young \[1974\]](#) and  
2589 related to the coarse mode dust number. It acts in the mixed phase where liquid droplets are  
2590 present and includes Brownian diffusion as well as phoretic forces. Hallet-Mossop ice multi-  
2591 plication (secondary ice production) due to accretion of drops by snow is included following  
2592 [Cotton et al. \[1986\]](#). This represents a sink term for snow mixing ratio and source term for  
2593 cloud ice mixing ratio and number concentration.

## 2594 Melting of cloud ice and snow

2595 For simplicity, detailed formulations for heat transfer during melting of ice and snow are not  
2596 included. Melting of cloud ice occurs instantaneously at  $0^\circ\text{C}$ . Melting of snow occurs instan-  
2597 taneously at  $+2^\circ\text{C}$ . We have tested the sensitivity of both single- column and global results

2598 to changing the specified snow melting temperature from +2° to 0°C and found no significant  
2599 changes.

## 2600 Evaporation/sublimation of precipitation

2601 Evaporation of rain and sublimation of snow,  $(\partial q_s / \partial t)_{evap}$  and  $(\partial q_r / \partial t)_{evap}$ , are given by dif-  
2602 fusional mass balance in subsaturated conditions [Lin et al. \[1983\]](#), including ventilation effects.  
2603 Evaporation of precipitation occurs within the region of the grid cell containing precipitation  
2604 but outside of the cloudy region. The fraction of the grid cell with evaporation of precipitation  
2605 is therefore  $F_{pre}$ , where  $F_{pre}$  is the precipitation fraction.  $F_{pre}$  is calculated assuming maximum  
2606 cloud overlap between vertical levels, and neglecting tilting of precipitation shafts due to wind  
2607 shear ( $F_{pre} = F_{cld}$  at cloud top). The out-of-cloud water vapor mixing ratio is given by

$$q_{clr} = \frac{q_v - F_{cld}q_s(T)}{1 - F_{cld}}, F_{cld} < 1 \quad (4.179)$$

2608 where  $q_s(T)$  is the in-cloud water vapor mixing ratio after bulk condensation/evaporation of  
2609 cloud water and ice as described previously. As in the older CAM3 microphysics parameteri-  
2610 zation, condensation/deposition onto rain/snow is neglected. Following [Morrison et al. \[2005\]](#),  
2611 the evaporation/sublimation of  $N_r$  and  $N_s$ ,  $(\partial N_r / \partial t)_{evap}$  and  $(\partial N_s / \partial t)_{evap}$ , is proportional to  
2612 the reduction of  $q_r$  and  $q_s$  during evaporation/sublimation.

## 2613 Sedimentation of cloud water and ice

2614 The time rates of change of  $q$  and  $N$  for cloud water and cloud ice due to sedimentation,  
2615  $(\partial q_c / \partial t)_{sed}$ ,  $(\partial q_i / \partial t)_{sed}$ ,  $(\partial N_c / \partial t)_{sed}$ , and  $(\partial N_i / \partial t)_{sed}$ , are calculated with a first-order forward-  
2616 in-time-backward-in-space scheme. Numerical stability for cloud water and ice sedimentation is  
2617 ensured by sub-stepping the time step, although these numerical stability issues are insignificant  
2618 for cloud water and ice because of the low terminal fallspeeds ( $\ll 1$  m/s). We assume that the  
2619 sedimentation of cloud water and ice results in evaporation/sublimation when the cloud fraction  
2620 at the level above is larger than the cloud fraction at the given level (i.e., a sedimentation  
2621 flux from cloudy into clear regions), with the evaporation/condensate rate proportional to the  
2622 difference in cloud fraction between the levels.

## 2623 Convective detrainment of cloud water and ice

2624 The ratio of ice to total cloud condensate detrained from the convective parameterizations,  $F_{det}$ ,  
2625 is a linear function of temperature between -40° C and -10° C;  $F_{det} = 1$  at  $T < -40^\circ$  C, and  $F_{det}$   
2626 = 0 at  $T > -10^\circ$  C. Detrainment of number concentration is calculated by assuming a mean  
2627 volume radius of 8 and 32 micron for droplets and cloud ice, respectively.

## 2628 Numerical considerations

2629 To ensure conservation of both  $q$  and  $N$  for each species, the magnitudes of the various sink terms  
2630 are reduced if the provisional  $q$  and  $N$  are negative after stepping forward in time. This approach  
2631 ensures critical water and energy balances in the model, and is similar to the approach employed  
2632 in other bulk microphysics schemes (e.g., [Reisner et al. \[1998\]](#)). Inconsistencies are possible

2633 because of the separate treatments for N and q, potentially leading to unrealistic mean cloud and  
2634 precipitation particle sizes. For consistency, N is adjusted if necessary so that mean (number-  
2635 weighted) particle diameter ( ) remains within a specified range of values for each species.  
2636 Limiting to a maximum mean diameter can be thought of as an implicit parameterization of  
2637 particle breakup.

2638 For the diagnostic precipitation, the source terms for q and N at a given vertical level are  
2639 adjusted if necessary to ensure that the vertical integrals of the source terms (from that level to  
2640 the model top) are positive. In other words, we ensure that at any given level, there isn't more  
2641 precipitation removed (both in terms of mixing ratio and number concentration) than is available  
2642 falling from above (this is also the case in the absence of any sources/sinks at that level). This  
2643 check and possible adjustment of the precipitation and cloud water also ensures conservation  
2644 of the total water and energy. Our simple adjustment procedure to ensure conservation could  
2645 potentially result in sensitivity to time step, although as described in section 3, time truncation  
2646 errors are minimized with appropriate sub-stepping.

2647 Melting rates of cloud ice and snow are limited so that the temperature of the layer does not  
2648 decrease below the melting point (i.e., in this instance an amount of cloud ice or snow is melted  
2649 so that the temperature after melting is equal to the melting point). A similar approach is  
2650 applied to ensure that homogeneous freezing does increase the temperature above homogeneous  
2651 freezing threshold.

2652 **4.7 Cloud Macrophysics**

2653 Cloud macrophysics is a suite of physical processes that computes (1) cloud fractions in each  
2654 layer, (2) horizontal and vertical overlapping structures of clouds, (3) net conversion rates of  
2655 water vapor into cloud condensates. Cloud macrophysics is a process unique for GCM that  
2656 handles partial cloud fraction. In case of cloud resolving model, for example, cloud fraction in  
2657 each layer is either 0 or 1, and so there is no need to use special treatment for cloud overlap  
2658 and partial condensation. Along with convection scheme, correct setting of cloud macrophysics  
2659 is essential for developing a seamless GCM across the various sizes of horizontal GCM grid.

2660 Cloud macrophysics sets a stage for cloud droplet activation and nucleation, cloud micro-  
2661 physics ( i.e., processes controlling conversion from sustained to falling hydrometeors ), wet  
2662 scavenging of aerosols, radiative transfer, and moist turbulent processes. Cloud macrophysics in  
2663 CAM3/CAM4 ( cloud macrophysics in CAM3 is nearly identical to the cloud macrophysics in  
2664 CAM4 ) was constructed to be compatible with and to some degrees to compensate for the in-  
2665 complete CAM3/CAM4 physics package. For example, (1) without a need to do explicit droplet  
2666 nucleation and activation processes due to the prescribed cloud droplet radius, CAM3/CAM4  
2667 simply assume zero supersaturation within ice stratus, (2) without the information of realistic  
2668 in-cumulus condensate from shallow and deep convection schemes, CAM3/CAM4 assumes that  
2669 in-cumulus condensate is identical to in-stratus condensate, and (3) without cloud-radiation-  
2670 turbulence interaction in the dry PBL scheme, CAM3/CAM4 uses additional stability-based  
2671 stratus fraction as well as RH-based stratus fraction to simulate marine stratocumulus over the  
2672 subtropical, mid-latitude and Arctic oceans. With the new CAM5 physics addressing these lim-  
2673 itations in the CAM3/CAM4 physics, cloud macrophysics should also be revised for consistency  
2674 among various model physics. Here, we document the revised cloud macrophysics in CAM5.  
2675 Additional details on CAM5's cloud macrophysics are discussed in [Park et al. \[2010\]](#).

2676 In the following sections, we will document how CAM5 computes (1) cloud fractions - deep  
2677 cumulus fraction, shallow cumulus fraction, and stratus ( liquid and ice separately ) fractions,  
2678 (2) horizontal and vertical overlapping structures of clouds, and (3) net condensation rates of  
2679 water vapor into cloud liquid and ice.

2680 **4.7.1 Cloud Fractions**

2681  
2682 Cloud fraction is a volume containing hydrometeors sustained in the atmosphere. In CAM5,  
2683 two types of clouds exist: *stratus* and *cumulus*. In nature, these two clouds can be identified  
2684 by their shapes and turbulent properties. Stratus is horizontally extended with symmetric  
2685 turbulence properties: fractional area, strength of vertical velocity, vertical extent, and degree  
2686 of saturation within updraft are similar to those within downdraft. On the other hand, cumulus  
2687 is vertically stretched with asymmetric turbulence properties: updraft is narrow, strong, and  
2688 usually saturated while compensating subsidence is broad, weak, and unsaturated. In CAM5,  
2689 moist turbulence scheme is designed to simulate symmetric turbulences while convection schemes  
2690 are for simulating asymmetric turbulences. While there is an attempt to treat these two distinct  
2691 turbulences in a unified way, we stick to the more convectional approach.

2692 **Deep Cumulus Fraction**

2693

Similar to CAM3/CAM4, CAM5 computes deep cumulus fraction  $a_{dp,cu}$  using the following empirical formula.

$$a_{dp,cu} = k_{1,dp} \cdot \log_e(1 + \cdot k_2 M_{dp,cu}), \quad a_{dp,cu} = \max(0, \min(a_{dp,cu}, 0.6)) \quad (4.180)$$

2694 where  $k_{1,dp}$  is an adjustable parameter given in Appendix C,  $k_2 = 675$  and  $M_{dp,cu}$  is convective  
2695 updraft mass flux [ $kg \cdot m^{-2} \cdot s^{-1}$ ] from deep convection scheme. When identified to be active,  
2696  $M_{dp,cu}$  is non-zero from the lowest model layer to the cumulus top. With no further attempt to  
2697 separate dry and moist deep convection, Eqn.(4.180) can generate *empty* ( without in-cumulus  
2698 condensate ) deep convective cloud fraction in the layers below the Lifting Condensation Level  
2699 ( LCL ). In contrast to stratus fraction that will be discussed later, we compute a single deep  
2700 cumulus fraction not the separate liquid and ice deep cumulus fractions. We impose a constraint  
2701 that  $a_{dp,cu}$  is always smaller than 0.6.

2702 Originally, this empirical formula was obtained by including not only cumulus but also  
2703 stratus generated by detrained cumulus condensate, which by construction results in overestimated  
2704 cumulus fraction. Thus, we are using a freedom to change the two coefficients 0.04 and  
2705 675 to simulate convective updraft fractional area only. Currently these coefficients are also  
2706 used as tuning parameters to obtain reasonable regional/global radiation budget and grid-mean  
2707 LWC/IWC.

2708 **Shallow Cumulus Fraction**

2709

In contrast to CAM3/CAM4, CAM5's new shallow convection scheme ( Park and Bretherton, 2009 ) computes vertical velocity as well as mass flux within cumulus updraft. Thus, shallow cumulus fraction  $a_{sh,cu}$  in CAM5 is directly computed using the definition of convective updraft mass flux:

$$a_{sh,cu} = 2 \cdot \left[ \mathcal{C} M_{sh,cu} \rho \cdot w_{u,cu} \right], \quad a_{sh,cu} = \max(0, \min(a_{sh,cu}, 0.2)) \quad (4.181)$$

2710 where  $M_{sh,cu}$  is shallow convective mass flux within cumulus updraft [ $kg \cdot m^{-2} \cdot s^{-1}$ ],  $\rho$  is density  
2711 [ $kg \cdot m^{-3}$ ] and  $w_{u,cu}$  is vertical velocity within cumulus updraft [ $m \cdot s^{-1}$ ]. Note that a factor  
2712 2 is multiplied by considering the difference between *core* ( e.g., positively buoyant saturated  
2713 portions ) updraft fractional area and saturated updraft fractional area estimated from the LES.  
2714 The details on how to compute  $M_{sh,cu}$  and  $w_{u,cu}$  are described in [Park and Bretherton \[2009\]](#).  
2715 This  $a_{sh,cu}$  is computed from the LCL of cumulus updraft ( or PBL top if LCL is within the  
2716 PBL ) to the cumulus top where updraft vertical velocity is zero. So,  $a_{sh,cu}$  always contains  
2717 positive cumulus condensate, that is, there is no empty shallow cumulus clouds. Similar to deep  
2718 cumulus fraction, we compute a single shallow cumulus fraction not the separate liquid and ice  
2719 shallow cumulus fractions. We impose a constraint that  $a_{sh,cu}$  is always smaller than 0.2.

2720 **Liquid Stratus Fraction**

2721

2722 In CAM3/CAM4, stratus fraction was parameterized as a sum of *RH-based* and  
 2723 *Stability-based* cloud fractions. The latter was necessary because the dry PBL scheme in  
 2724 CAM3/CAM4 cannot moisten upper portion of stratocumulus-topped PBL due to its inability  
 2725 to simulate cloud-radiation-turbulence interactions.

The RH-based stratus fraction in CAM3/CAM4 is a quadratic function of grid-mean RH ( Slingo [1987b], Rasch and Kristjansson [1998b] ).

$$a_{st} = \left[ \mathcal{C}U - U_c 1 - U_c \right]^2 \quad (4.182)$$

where  $U$  is grid-mean RH defined using saturation specific humidity over a mixture of cloud water and ice where mixing fraction is a function of temperature, and  $U_c$  is a critical RH. Stratus is formed only when  $U$  is larger than  $U_c$ . Note that CAM3/CAM4 diagnoses a single stratus fraction not the separate liquid and ice stratus fractions in contrast to CAM5. While simple to use, above Eqn.(4.182) has two shortcomings. First, at the limit of  $a_{st} \rightarrow 1$ , we expect that RH in the clear portion ( $U_r$ ) approaches to 1 in nature. However, Eqn.(4.182) does not satisfy this condition unless  $U_c \rightarrow 1$  as shown below:

$$\lim_{a_{st} \rightarrow 1} U_r = \lim_{a_{st} \rightarrow 1} \left[ \mathcal{C}(1 - U_c) \sqrt{a_{st}} + U_c - a_{st} 1 - a_{st} \right] = 0.5 \cdot (1 + U_c) \quad (4.183)$$

Second, Eqn.(4.182) is not derived from the explicit subgrid scale distributions of total specific humidity, making it hard to impose internal consistency between stratus fraction and in-stratus condensate. Following Smith [1990], liquid stratus fraction in CAM5 is derived from the assumed triangular distribution of total relative humidity,  $v = q_{t,l}/q_{s,w}$  where  $q_{t,l}$  is total liquid specific humidity ( $=q_v + q_l$ ) and  $q_{s,w}$  is saturation specific humidity over water. Then liquid stratus fraction  $a_{l,st}$  becomes a function of grid-mean RH over water,  $U_l$  ( Park et al. [2010] ).

$$a_{l,st} = \begin{cases} 1 & \text{if } U_l \geq \hat{U}_l, \\ 1 - \left[ \mathcal{C}3\sqrt{2} \cdot \left( \mathcal{C}\hat{U}_l - U_l \hat{U}_l - U_{cl} \right) \right]^{2/3} & \text{if } \mathcal{C}16 \cdot (5 + U_{cl}) \leq U_l \leq \hat{U}_l, \\ 4 \cdot \cos \left[ \mathcal{C}13 \cdot \left\{ \text{acos} \left( \mathcal{C}32 \cdot \sqrt{2} \cdot \left( \mathcal{C}U_l - U_{cl} \hat{U}_l - U_{cl} \right) \right) - 2 \cdot \pi \right\} \right] & \text{if } U_{cl} \leq U_l \leq \mathcal{C}16 \cdot (5 + U_{cl}), \\ 0 & \text{if } U_l \leq U_{cl}, \end{cases} \quad (4.184)$$

2726 where  $\hat{U}_l$  is RH within liquid stratus ( $=1$ ) and  $U_{cl}$  is critical RH that liquid stratus is formed  
 2727 when  $U_l$  is larger than  $U_{cl}$ . We can easily check  $\lim_{a_{l,st} \rightarrow 1} RH_r = 1$ . For a given  $U_l \geq U_{cl}$ , CAM5  
 2728 ( Eqn.(4.184) ) produces less stratus fraction than CAM3/CAM4 ( Eqn.(4.182) ). In addition,  
 2729 the sensitivity of liquid stratus fraction to the changes of grid-mean RH differs between the two  
 2730 models.

2731 Note that  $U_{cl} = 1 - \Delta v$  where  $\Delta v$  is the half-width of the triangular distribution. Ideally,  
 2732 subgrid-scale variability  $\Delta v$  should be internally computed by considering all sources of subgrid-  
 2733 scale motions from individual physical processes - moist turbulence, detrainment of convective  
 2734 condensate, meso-scale organizations, gravity waves induced by convection or surface inhomoge-  
 2735 neity, and etc. In CAM5, however,  $U_{cl}$  is externally specified as a function of height and  
 2736 surface properties and being used as a tuning parameter. We chose  $U_{cl} = 0.89$  in the layers

2737 below 700 hPa ( Low-Level Stratus ) but  $U_{cl} = 0.79$  over lands when a water-equivalent snow  
 2738 depth is less than  $10^{-6}$  [m],  $U_{cl} = 0.80$  in the layers above 400 hPa ( High-Level Stratus ), and  
 2739 a linearly-interpolated  $U_{cl}$  between 700 hPa and 400 hPa ( Mid-Level Stratus ).

2740 In principle, LWC within the liquid stratus can be diagnosed from the assumed triangular  
 2741 PDF ( [Smith \[1990\]](#), [Park et al. \[2010\]](#) ). However, CAM5 uses a separate prognostic con-  
 2742 densation scheme for liquid stratus condensation similar to CAM3/CAM4. This ( diagnostic  
 2743 cloud fraction but separate prognostic condensation for liquid stratus ) can cause inconsis-  
 2744 tency between stratus fraction and in-stratus cloud condensate. We perform additional pseudo  
 2745 condensation-evaporation process to remove this inconsistency as will be discussed later.

## 2746 Ice Stratus Fraction

2747 In CAM3/CAM4, a single stratus fraction  $a_{st}$  was diagnosed using a mean saturation specific  
 2748 humidity  $q_s = \alpha \cdot q_{s,w} + (1 - \alpha) \cdot q_{s,i}$  where  $q_{s,w}$  and  $q_{s,i}$  are saturation specific humidities over  
 2749 water and ice, respectively, and  $0 \leq \alpha \leq 1$  is a function of temperature. In CAM5, however,  
 2750 we separately diagnose ice stratus fraction  $a_{i,st}$  using a modified Slingo's formula as below ( [Gettelman et al. \[2010a\]](#) ).

$$2751 a_{i,st} = \left[ \mathcal{C}U_i - U_{ci}\hat{U}_i - U_{ci} \right]^2 \quad (4.185)$$

$$2752 U_i = \left[ \mathcal{C}q_v + q_i q_{s,i} \right]$$

2753 where  $U_i$  is grid-mean total RH *including ice condensate* defined over ice, and  $\hat{U}_i$  is RH within ice  
 2754 stratus. In contrast to liquid condensation that always occurs whenever  $q_v > q_{s,w}$ , ice nucleation  
 2755 and ice growth processes are not spontaneous and very slow. Thus, the linkage between ice  
 2756 saturation excess  $s = q_v - q_{s,i}$  and the amount of ice condensate is weak. Eqn.(4.185) is an  
 2757 attempt to address these properties of ice processes: supersaturation within ice stratus is taken  
 2758 into account by using  $\hat{U}_i > 1$ , and by including ice condensate in the definition of  $U_i$ , ice  
 2759 condensate as well as ice saturation excess contributes to ice stratus fraction. In CAM5, we  
 2760 chose  $\hat{U}_i = 1.1$  and  $U_{ci} = 0.80$  regardless of heights and the properties of the Earth surface.

### 2761 4.7.2 Cloud Overlaps

2762 We have computed 4 independent cloud fractions (  $0 \leq a_{l,st}, a_{i,st} \leq 1$ ,  $0 \leq a_{sh,cu} \leq 0.2$ ,  $0 \leq$   
 2763  $a_{dp,cu} \leq 0.6$  ) in each layer. The performance of individual physical processes is sensitive how  
 2764 these clouds are distributed in the horizontal plane and vertical column. For example, if  $a_{l,st}$   
 2765 and  $a_{i,st}$  are maximally-overlapped ( non-overlapped ) in the horizontal, Bergeron-Findeisen  
 2766 conversion process from cloud liquid droplet to ice crystal will be active ( inactive ). If cumulus  
 2767 preferentially grows into the pre-existing stratus ( clear portions ), cumulus will detrain convective  
 2768 condensate into the pre-existing stratus ( clear portions ) without ( with ) evaporation. We can  
 2769 also easily expect that the vertical profiles of grid-mean radiative flux, evaporation of precipita-  
 2770 tion, activation and wet deposition of aerosols are sensitive to the vertical overlapping structures  
 2771 of various clouds. Given the 2-moment stratiform microphysics in CAM5, correct simulations

2768 of activation and wet deposition of aerosols become even more important. So, parameterization  
 2769 of cloud overlapping structures is as important as the parameterization of individual cloud frac-  
 2770 tions. Ideally, all physics schemes should use a single consistent cloud overlapping structure. In  
 2771 this section, we describe the horizontal and vertical overlapping structures of clouds in CAM5.

## 2772 Horizontal Overlap

2773

In CAM5, we assume that (1) shallow and deep cumulus fractions are non-overlapped with each other, (2) liquid and ice stratus fractions are maximally overlapped, i.e.,  $a_{st} = \max(a_{l,st}, a_{i,st})$ , and (3) stratus only fills the non-cumulus areas, i.e., a higher occupancy priority is given to the cumulus over stratus in each layer. Stratiform microphysics in CAM5 assumes that stratus LWC/IWC is uniformly distributed over the single stratus fraction  $a_{st}$  even though further elaboration is possible. The third assumption above comes from distinct turbulent properties in each clouds: cumulus updraft is strong and grows vertically, and so, if there are any pre-existing stratus on its path, cumulus updraft will push out the pre-existing stratus and occupy the original portion. The assumed horizontal overlapping structure between cumulus and stratus determines the *physical* stratus fractions. If  $a$  is each of 4 cloud fractions computed in the previous section, the physical cloud fraction  $A$  of each cloud fraction  $a$  becomes

$$A_{sh,cu} = a_{sh,cu} \leq 0.2 \quad (4.186)$$

$$A_{dp,cu} = a_{dp,cu} \leq 0.6$$

$$A_{cu} = A_{sh,cu} + A_{dp,cu} \leq 0.8$$

$$A_{l,st} = (1 - A_{cu}) \cdot a_{l,st} \leq 1$$

$$A_{i,st} = (1 - A_{cu}) \cdot a_{i,st} \leq 1$$

$$A_{st} = \max(A_{l,st}, A_{i,st}) \leq 1$$

$$A_{net} = A_{st} + A_{cu} \leq 1$$

2774 where  $U_l$  and  $U_i$  in Eqs.(4.184) and (4.185) are now changed to the mean RH averaged over the  
 2775 non-cumulus areas in each layer. In CAM5, state variables saved into the standard physical state  
 2776 arrays are the mean values averaged over the non-cumulus areas, that is, environmental mean  
 2777 not the grid mean. These physical cloud fractions  $A$  are passed into various physics schemes  
 2778 following the cloud macrophysics.

## 2779 Vertical Overlap

2780

In CAM5, the following physical processes make use of vertical overlap assumption of clouds:  
 2781 (a) deep and shallow convection schemes to compute evaporation of convective precipitations,  
 2782 (b) stratiform microphysics to compute production and evaporation of stratiform precipitation,  
 2783 (c) activation and wet scavenging of aerosols by convective and stratiform precipitations, and  
 2784 (d) radiation scheme. While computations of cloud fractions and horizontal cloud overlaps  
 2785 are substantially revised, CAM5's vertical cloud overlap is similar to CAM3/CAM4, which is  
 2786 summarized below.

2788 (a) CAM5's deep and shallow convection schemes assume that convective precipitation area  
2789 is always 1 if convective precipitation flux is positive. In reality, however, if vertical shear  
2790 of horizontal winds is neglected, most of the convective precipitation is likely to fall into the  
2791 saturated cumulus updraft not into clear portions. Thus, CAM5's vertical cumulus overlap may  
2792 overestimate evaporation of convective precipitation, leading to excessive water vapor in the  
2793 atmosphere.

2794 (b) CAM5's stratiform microphysics assumes that stratus fraction  $a_{st}$  is maximally over-  
2795 lapped in vertical regardless of vertical separation distance, and stratiform precipitation area is  
2796 the same as maximum stratus fraction in the layers above the current layer as long as precipita-  
2797 tion flux is positive. In reality, however, precipitation falling into clear portion can be completely  
2798 evaporated, so that precipitation area can be smaller than the maximum stratus fraction in the  
2799 layers above.

2800 (c) CAM5's cloud droplet activation routine assumes maximum overlap of stratus fraction  
2801 between any adjacent layers. CAM5 computes wet scavenging of aerosols by two processes. The  
2802 first is the scavenging of activated aerosols within cloud droplets by the production of precipita-  
2803 tion. The second is the scavenging of the remaining non-activated aerosols by the precipitation  
2804 flux. These two processes are separately applied for each convective and stratiform precipi-  
2805 tations. For the purpose of wet scavenging of aerosols, CAM5 assumes that (1) convective ( strati-  
2806 form ) precipitation area at any height is a sum of cumulus ( stratus ) fractions in the layers  
2807 above weighted by the ratio of net production rate of convective ( stratiform ) precipitation in  
2808 each layer to the vertically integrated net production rate of convective ( stratiform ) precipi-  
2809 tation from the top layer to the layer just above the current layer, and (2) in computing wet  
2810 scavenging of non-activated aerosols, precipitation flux area at the top interface of each layer is  
2811 randomly overlapped with the cloud fraction. The second assumption allows CAM5 to bypass  
2812 the computation of complex overlapping areas between precipitation flux and cloud fractions.

2813 (d) CAM5's radiation scheme computes one single cloud fraction and in-cloud LWC/IWC  
2814 in each layer by combining deep and shallow cumulus and stratus cloud properties through a  
2815 simple cloud area weighting. Then, it assumes a maximum vertical overlap in each of the 3  
2816 regimes representing lower (  $p > 700$  hPa ), middle (  $400$  hPa  $< p < 700$  hPa ), and upper (  $p <$   
2817  $400$  hPa ) atmospheres, and a random vertical overlap between these 3 regimes. This generates  
2818 a set of sub-columns in which cloud fraction is either 1 or 0 in each layer. By averaging each  
2819 sub-column's radiative heating rate, it computes grid-mean radiative heating rate.

2820 In principle, all the above 4 processes should use the identical vertical cloud overlapping  
2821 structure. Due to the contrasting natures of turbulences, cumulus and stratus are likely to  
2822 have different vertical cloud overlap. If vertical shear of horizontal winds is neglected, cumulus  
2823 fractions are likely to be maximally overlapped over the entire depth of convective updrafts. On  
2824 the other hand, vertical distance over which stratus is maximally overlapped is likely to be much  
2825 smaller than the cumulus. Simultaneous treatment of different vertical overlapping structures  
2826 of cumulus and stratus and implementation of the single unified vertical cloud overlap into the  
2827 CAM is one of the future development plans.

#### 2828 4.7.3 Condensation Processes

2829  
2830 This section describes how much water vapor is converted into cloud condensates. This

2831 process differs from the conversion of cloud droplet into precipitation, which is treated by the  
 2832 cloud microphysics.

2833 **Stratus Liquid**

2834

2835 Similar to CAM3/4 ( [Zhang et al. \[2003a\]](#) ), CAM5 uses prognostic condensation scheme  
 2836 for liquid stratus condensate. The fundamental assumption used for computing grid-mean net  
 2837 condensation rate of water vapor into liquid stratus droplet (  $Q$  ) is that (1) RH over the water  
 2838 within the liquid stratus is always 1, and (2) no liquid stratus droplet exists in the clear portion  
 2839 outside of the liquid stratus fraction. These two conditions will be called *saturation equilibrium*  
 2840 of liquid stratus. Whenever any GCM grid is perturbed by external forcings, the system always  
 2841 tries to restore the saturation equilibrium state. This allows us to compute the grid-mean  
 2842 net condensation rate of water vapor into liquid stratus condensate for a given set of external  
 2843 forcings. The details of liquid stratus condensation is described in [Park et al. \[2010\]](#).

Let's assume that one GCM grid layer is in saturation equilibrium state at a certain moment. During the model time step  $\Delta t$ , the layer is perturbed by external forcings ( e.g., stratiform microphysics, radiation, moist turbulence, large-scale advection, and convections ). In order to restore saturation equilibrium,  $Q$  should be initiated within the layer. The changes of grid-mean liquid stratus condensate  $\bar{q}_{l,st} = A_{l,st} \cdot \hat{q}_{l,st}$  during  $\Delta t$  is the sum of grid-mean net condensate rate  $Q$  and the grid-mean external forcings of liquid condensates  $\bar{F}_l$ :

$$Q = \dot{\bar{q}}_{l,st} - \bar{F}_l = A_{l,st} \cdot \dot{\hat{q}}_{l,st} + c \cdot \hat{q}_{l,st} \cdot \dot{A}_{l,st} - \bar{F}_l \quad (4.187)$$

2844 where  $0 \leq c \leq 1$  is the ratio of in-cloud condensate of newly formed or dissipated stratus to the  
 2845 in-cloud condensate of pre-existing stratus. The  $\dot{\phi}$  denotes time-tendency of  $\phi$ . If liquid stratus  
 2846 has homogeneous condensate, it will be  $c = 1$ , but it is likely that  $c < 1$  in nature since stratus  
 2847 has non-homogeneous condensate in general. In CAM5, we use  $c = 0.1$ .

From the two assumptions for saturation equilibrium of liquid stratus, we can derive the following simultaneous linear equations ( [Park et al. \[2010\]](#) ).

$$a_{11} \cdot \dot{\bar{q}}_{l,st} + a_{12} \cdot \dot{A}_{l,st} = b_1 \quad (4.188)$$

$$a_{21} \cdot \dot{\bar{q}}_{l,st} + a_{22} \cdot \dot{A}_{l,st} = b_2$$

where individual coefficients  $a_{ij}$  and  $b_i$  are

$$a_{11} = \gamma \cdot A_{l,st} \quad (4.189)$$

$$a_{12} = G + \gamma \cdot c \cdot \hat{q}_{l,st}$$

$$a_{21} = \alpha + (\mathcal{C}L_v C_p) \cdot \hat{\beta} \cdot A_{l,st}$$

$$a_{22} = (\mathcal{C}L_v C_p) \cdot \hat{\beta} \cdot c \cdot \hat{q}_{l,st}$$

$$b_1 = \alpha \cdot \dot{\bar{q}}_{t,all} - \beta \cdot \dot{\bar{T}}_{l,all} - G \cdot a_{l,st} \cdot \dot{a}_{cu}$$

$$b_2 = \alpha \cdot \dot{\bar{q}}_{t,all} - \beta \cdot \dot{\bar{T}}_{l,all}$$

with

$$\begin{aligned}
\alpha &= [\mathcal{C}1q_{s,w}] & (4.190) \\
\beta &= \mathcal{C}\bar{q}_v q_{s,w}^2 \cdot (\mathcal{C}\partial q_{s,w} \partial T) \\
\hat{\beta} &= \alpha \cdot (\mathcal{C}\partial q_{s,w} \partial T) \\
\gamma &= \alpha + \mathcal{C}L_v C_p \cdot \beta \\
G &= \mathcal{C}11 - a_{cu} \cdot (\mathcal{C}\partial a_{l,st} \partial \bar{U}_e)^{-1}
\end{aligned}$$

and

$$\dot{\bar{q}}_{t,all} = \dot{\bar{q}}_{v,adv} + \dot{\bar{q}}_{l,adv} + \dot{\bar{q}}_{v,mic} + \dot{\bar{q}}_{l,mic} \quad (4.191)$$

$$\dot{\bar{T}}_{l,all} = \dot{\bar{T}}_{adv} + \dot{\bar{T}}_{mic} - \mathcal{C}L_v C_p \cdot (\dot{\bar{q}}_{l,adv} + \dot{\bar{q}}_{l,mic}) \quad (4.192)$$

$$\dot{\hat{q}}_{t,all} = \dot{\bar{q}}_{v,adv} + \dot{\bar{q}}_{l,adv} + \dot{\hat{q}}_{l,mic} \quad (4.193)$$

$$\dot{\hat{q}}_{l,mic} = [\mathcal{C}\dot{\bar{q}}_{l,mic} \max(A_{l,st}, A_{i,st})] \quad (4.194)$$

where  $\dot{\bar{\phi}}$  denotes local time-tendency, subscript *all* denotes all the processes except cloud macro-physics, which is the sum of cloud microphysics ( subscript *mic* ) and the other processes denoted by subscript *adv*. In Eqn.(4.194), we used  $\max(A_{l,st}, A_{i,st})$  instead of  $A_{l,st}$  since stratiform microphysics is formulated based on a single stratus fraction,  $\max(A_{l,st}, A_{i,st})$ . Above formulation was derived assuming that temperature is uniform within the grid, and stratiform microphysics does not change water vapor within the liquid stratus, and all forcings except stratiform microphysics are uniformly applied into the grid. Using  $A_{l,st}$  from Eqn.(4.184) and (4.186), we can compute  $Q$  if  $\bar{F}_l$  is given.

Although the computation of  $Q$  explicitly makes use of  $A_{l,st}$ , the updated  $\bar{q}_{l,st}(t + \Delta t)$  is not necessarily consistent with the updated  $A_{l,st}(t + \Delta t)$ . For example, it can be  $\bar{q}_{l,st}(t + \Delta t) = 0$  but  $A_{l,st}(t + \Delta t) > 0$  ( so called *empty cloud* ) or  $\bar{q}_{l,st}(t + \Delta t) > 0$  but  $A_{l,st}(t + \Delta t) = 0$  ( so called *infinitely dense cloud* ). This inconsistency between stratus fraction and in-stratus condensate comes from the combined use of prognostic stratiform condensation and diagnostic stratus fraction schemes with a finite model intergation time step  $\Delta t$ . In order to prevent these unreasonable situations, we additionally condensate water vapor or evaporate stratus liquid droplets until the *in-stratus LWC*,  $\hat{q}_{l,st}(t + \Delta t)$  falls within the externally specified ranges,  $0.02 \leq \hat{q}_{l,st}(t + \Delta t) [g \cdot kg^{-1}] \leq 3$ . Note that this *pseudo condensation – evaporation* process does not change the grid-mean liquid stratus condensate and is not performed if  $\bar{q}_{l,st}(t + \Delta t) = 0$  and  $A_{l,st}(t + \Delta t) = 0$  at the beginning.

CAM5 is using two moment stratiform microphysics and so prognoses not only the mass but also the number concentration of cloud droplets. When net condensation occurs (  $Q > 0$  ), cloud macrophysics does not change droplet number concentration, but when net evaporation occurs (  $Q < 0$  ), droplet number concentration is reduced in proportion to the decrease of the mass of stratus liquid droplets. Regardless of the sign of  $Q$ , however, droplet activation process within stratus is additionally performed at the beginning of cloud microphysics at each time step. Thus, cloud droplet number is consistently generated when  $Q > 0$  in the initially clear layer.

2875 **Stratus Ice**

2876

2877 In contrast to liquid stratus, we cannot assume a certain equilibrium state for ice stratus  
2878 because ice process is much slower than the liquid process. Thus, deposition-sublimation rate  
2879 between water vapor and ice crystals are computed using an explicit process algorithm.

2880 In CAM5, deposition of water vapor into ice crystals ( this is a separate process from the  
2881 Bergeron-Findeisen conversion of cloud liquid droplets into ice crystals ) only occurs when ice  
2882 stratus exists at temperature lower than 273.15K. In case of pure ice stratus, in-cloud water vapor  
2883 is set to the grid-mean water vapor. If in-cloud water vapor is larger than the saturation water  
2884 vapor over ice, water vapor is deposited into ice crystals. In case of mixed-phase stratus, in-  
2885 cloud water vapor is set to the equal weighting average of grid-mean water vapor and saturation  
2886 water vapor over water. In this case, however, direct deposition of water vapor into ice crystals  
2887 occurs only after pre-existing cloud liquid droplets are completely depleted into ice crystals by  
2888 Bergeron-Findeisen process. That is, if Bergeron-Findeisen process is not strong enough to  
2889 deplete pre-existing cloud liquid droplets, no direct deposition occurs from the water vapor into  
2890 ice crystals. Sublimation of ice crystals into water vapor occurs regardless of temperature as  
2891 long as water vapor within the ice stratus is smaller than the saturation water vapor over the  
2892 pre-existing ice crystals.

2893 A constraint is imposed such that direct deposition of water vapor into ice crystals does not  
2894 reduce grid-mean RH over ice below 1. Additional constraint is imposed such that sublimation  
2895 should not exceed the available ice crystals and not increase grid-mean RH over ice above 1.

2896 See [Gettelman et al. \[2010a\]](#) and the chapter for cloud microphysics for additional details.

2897 **Condensation within Shallow Cumulus Updraft**

2898

2899 Condensation within shallow cumulus updraft is described in [Park and Bretherton \[2009\]](#).  
2900 Shallow convective updraft rises from the PBL top but condensation occurs from the LCL.  
2901 If LCL is lower than PBL top, condensation is assumed to occur from the PBL top. During  
2902 ascent, convective updraft experiences adiabatic cooling, mixing with environmental air, and  
2903 precipitation fallout. Vertical evolutions of two conservative scalars  $q_t = q_v + q_l + q_i$ ,  $\theta_c =$   
2904  $\theta - (L_v/C_p/\pi) \cdot q_l - (L_s/C_p/\pi) \cdot q_i$  within convective updraft are explicitly computed using the  
2905 parameterized entrainment mixing and precipitation processes. From the computed  $q_t$ ,  $\theta_c$  and  
2906 saturation specific humidity  $q_s$  defined as a weighting average of the values over water  $q_{s,w}$  and  
2907 ice  $q_{s,i}$  ( the weighting factor is a function of temperature ), we compute condensate amount  
2908 within convective updraft. Since shallow convective cloud fraction  $a_{sh,cu}$  is non-zero from the  
2909 LCL ( or PBL top if LCL is below the PBL ) to the cumulus top, shallow cumulus does not  
2910 have any empty clouds.

2911 Within shallow convection scheme, condensate is partitioned into liquid and ice as a ramping  
2912 function of temperature between 248K and 268K. However, a separate re-partitioning is per-  
2913 formed for convective detrainment ( as a ramping function of temperature between 238.15K and  
2914 268.15K ) and for radiative treatment of in-cumulus condensate ( in this case, the repartitioning  
2915 function is the same as that of stratiform condensate ). When shallow convective condensate is

2916 detrain into the environment, we assume a fixed droplet radius of 8 and 25 [ $\mu \cdot m$ ] for liquid  
2917 and ice condensates, respectively.

2918 **Condensation within Deep Cumulus Updraft**

2919

2920 Condensates within deep convective updraft is computed in a similar way as shallow convec-  
2921 tive updraft. When deep convective condensate is detrain into the environment, we assume  
2922 a fixed droplet radius of 10 and 50 [ $\mu \cdot m$ ] for liquid and ice condensates, respectively. See the  
2923 chapter for deep convection for additional details.

2924 **4.8 Aerosols**

2925 Two different modal representations of the aerosol were implemented in CAM5. A 7-mode  
2926 version of the modal aerosol model (MAM-7) serves as a benchmark for the further simplification.  
2927 It includes Aitken, accumulation, primary carbon, fine dust and sea salt and coarse dust and  
2928 sea salt modes (4.3). Within a single mode, for example the accumulation mode, the mass  
2929 mixing ratios of internally-mixed sulfate, ammonium, secondary organic aerosol (SOA), primary  
2930 organic matter (POM) aged from the primary carbon mode, black carbon (BC) aged from the  
2931 primary carbon mode, sea salt, and the number mixing ratio of accumulation mode particles  
2932 are predicted. Primary carbon (OM and BC) particles are emitted to the primary carbon mode  
2933 and aged to the accumulation mode due to condensation of  $H_2SO_4$ ,  $NH_3$  and SOA (gas) and  
2934 coagulation with Aitken and accumulation mode (see section below).

2935 Aerosol particles exist in different attachment states. We mostly think of aerosol particles  
2936 that are suspended in air (either clear or cloudy air), and these are referred to as interstitial  
2937 aerosol particles. Aerosol particles can also be attached to (or contained within) different hy-  
2938 drometeors, such as cloud droplets. In CAM5, the interstitial aerosol particles and the aerosol  
2939 particles in stratiform cloud droplets<sup>1</sup> (referred to as cloud-borne aerosol particles) are both  
2940 explicitly predicted, as in [Easter et al. \[2004\]](#). The interstitial aerosol particle species are stored  
2941 in the  $q$  array of the state variable and are transported in 3 dimensions. The cloud-borne aerosol  
2942 particle species are stored in the  $qqcw$  array of the physics buffer and are not transported (ex-  
2943 cept for vertical turbulent mixing), which saves computer time but has little impact on their  
2944 predicted values [Ghan and Easter \[2006\]](#).

2945 Aerosol water mixing ratio associated with interstitial aerosol for each mode is diagnosed  
2946 following Kohler theory (see water uptake below), assuming equilibrium with the ambient rel-  
2947 ative humidity. It also is not transported in 3 dimensions, and is held in the  $qaerwat$  array of  
2948 the physics buffer.

2949 The size distributions of each mode are assumed to be log-normal, with the mode dry or  
2950 wet radius varying as number and total dry or wet volume change, and standard deviation  
2951 prescribed as given in 4.3. The total number of transported aerosol species is 31 for MAM-7.  
2952 The transported gas species are  $SO_2$ ,  $H_2O_2$ , DMS,  $H_2SO_4$ ,  $NH_3$ , and SOA (gas).

2953 For long-term (multiple century) climate simulations a 3-mode version of MAM (MAM-3) is  
2954 also developed which has only Aitken, accumulation and coarse modes (4.4). For MAM-3 the  
2955 following assumptions are made: (1) primary carbon is internally mixed with secondary aerosol  
2956 by merging the primary carbon mode with the accumulation mode; (2) the coarse dust and  
2957 sea salt modes are merged into a single coarse mode based on the assumption that the dust  
2958 and sea salt are geographically separated. This assumption will impact dust loading over the  
2959 central Atlantic transported from Sahara desert because the assumed internal mixing between  
2960 dust and sea salt there will increase dust hygroscopicity and thus wet removal; (3) the fine dust  
2961 and sea salt modes are similarly merged with the accumulation mode; and (4) sulfate is partially  
2962 neutralized by ammonium in the form of  $NH_4HSO_4$ , so ammonium is effectively prescribed and  
2963  $NH_3$  is not simulated. We note that in MAM-3 we predict the mass mixing ratio of sulfate

---

<sup>1</sup>Note that the explicitly-predicted cloud-borne aerosol particles are for stratiform clouds only, and thus are stratiform-cloud-borne aerosol particles. The convective-cloud-borne aerosol particles in deep and shallow convective clouds are not treated explicitly, and are prescribed as a fraction of the interstitial aerosol particles when calculating wet removal.

2964 aerosol in the form of  $\text{NH}_4\text{HSO}_4$  while in MAM-7 it is in the form of  $\text{SO}_4$ . The total number of  
2965 transported aerosol tracers in MAM-3 is 15.

### 2966 4.8.1 Emissions

2967 Anthropogenic (defined here as originating from industrial, domestic and agriculture activity  
2968 sectors) emissions are from the [Lamarque et al. \[2010a\]](#) IPCC AR5 emission data set. Emissions  
2969 of black carbon (BC) and organic carbon (OC) represent an update of [Bond et al. \[2007\]](#) and  
2970 [Junker and Liousse \[2008\]](#). Emissions of sulfur dioxide are an update of [Smith et al. \[2001, 2004\]](#).

2971 The IPCC AR5 emission data set includes emissions for anthropogenic aerosols and precursor  
2972 gases:  $\text{SO}_2$ , primary OM (POM), and BC. However, it does not provide injection heights and  
2973 size distributions of primary emitted particles and precursor gases for which we have followed  
2974 the AEROCOM protocols [[Dentener et al., 2006a](#)]. We assumed that 2.5% by molar of sulfur  
2975 emissions are emitted directly as primary sulfate aerosols and the rest as  $\text{SO}_2$  [[Dentener et al.,](#)  
2976 [2006a](#)]. Sulfur from agriculture, domestic, transportation, waste, and shipping sectors is emitted  
2977 at the surface while sulfur from energy and industry sectors is emitted at 100-300 m above the  
2978 surface, and sulfur from forest fire and grass fire is emitted at higher elevations (0-6 km). Sulfate  
2979 particles from agriculture, waste, and shipping (surface sources), and from energy, industry,  
2980 forest fire and grass fire (elevated sources) are put in the accumulation mode, and those from  
2981 domestic and transportation are put in the Aitken mode. POM and BC from forest fire and  
2982 grass fire are emitted at 0-6 km, while those from other sources (domestic, energy, industry,  
2983 transportation, waste, and shipping) are emitted at surface. Injection height profiles for fire  
2984 emissions are derived from the corresponding AEROCOM profiles, which vary spatially and  
2985 temporally. Mass emission fluxes for sulfate, POM and BC are converted to number emission  
2986 fluxes for Aitken and accumulation mode at surface or at higher elevations based on AEROCOM  
2987 prescribed lognormal size distributions as summarized in Table 4.1.

2988 The IPCC AR5 data set also does not provide emissions of natural aerosols and precursor  
2989 gases: volcanic sulfur, DMS,  $\text{NH}_3$ , and biogenic volatile organic compounds (VOCs). Thus AE-  
2990 ROCOM emission fluxes, injection heights and size distributions for volcanic  $\text{SO}_2$  and sulfate and  
2991 for DMS flux at surface are used. The emission flux for  $\text{NH}_3$  is prescribed from the MOZART-4  
2992 data set [[Emmons, 2010](#)]. Emission fluxes for isoprene, monoterpene, toluene, big alkenes, and  
2993 big alkanes, which are used to derive SOA (gas) emissions (see below), are prescribed from the  
2994 MOZART-2 data set [[Horowitz, 2003](#)]. These emissions represent late 1990's conditions. For  
2995 years prior to 2000, we use anthropogenic non-methane volatile organic compound (NMVOC)  
2996 emissions from IPCC AR5 data set and scale the MOZART toluene, bigene, and big alkane  
2997 emissions by the ratio of year-of-interest NMVOC emissions to year 2000 NMVOC emissions.

2998 The emission of sea salt aerosols from the ocean follows the parameterization by  
2999 [Martensson et al. \[2003\]](#) for aerosols with geometric diameter  $< 2.8 \mu\text{m}$ . The total particle  
3000 flux  $F_0$  is described by

$$\frac{dF_0}{d\log D_p} = \Phi W = (A_k T_w + B_k) W \quad (4.195)$$

3001 where  $D_p$  is the particle diameter,  $T_w$  is the water temperature and  $A_k$  and  $B_k$  are coefficients  
3002 dependent on the size interval.  $W$  is the white cap area:

$$W = 3.84 \times 10^{-4} U_{10}^{3.41} \quad (4.196)$$

3003 where  $U_{10}$  is the wind speed at 10 m. For aerosols with a geometric diameter  $> 2.8 \mu\text{m}$ , sea  
 3004 salt emissions follow the parameterization by [Monahan et al. \[1986\]](#)

$$\frac{dF_0}{d\log r} = 1.373 U_{10}^{3.41} r^{-3} (1 + 0.0057 r^{1.05}) \times 10^{1.19e^{-B^2}} \quad (4.197)$$

3005 where  $r$  is the radius of the aerosol at a relative humidity of 80% and  $B = (0.380 - \log r) / 0.650$ .  
 3006 All sea salt emissions fluxes are calculated for a size interval of  $d\log D_p = 0.1$  and then summed  
 3007 up for each modal size bin. The cut-off size range for sea salt emissions in MAM-7 is 0.02-0.08  
 3008 (Aitken), 0.08-0.3 (accumulation), 0.3-1.0 (fine sea salt), and 1.0-10  $\mu\text{m}$  (coarse sea salt); for  
 3009 MAM-3 the range is 0.02-0.08 (Aitken), 0.08-1.0 (accumulation), and 1.0-10  $\mu\text{m}$  (coarse).

3010 Dry, unvegetated soils, in regions of strong winds generate soil particles small enough to  
 3011 be entrained into the atmosphere, and these are referred to here as desert dust particles. The  
 3012 generation of desert dust particles is calculated based on the Dust Entrainment and Deposition  
 3013 Model, and the implementation in the Community Climate System Model has been described  
 3014 and compared to observations [[Mahowald et al., 2006a,b](#); [Yoshioka et al., 2007](#)]. The only change  
 3015 to the CAM5 source scheme from the previous studies is the increase in the threshold for leaf area  
 3016 index for the generation of dust from 0.1 to 0.3  $\text{m}^2/\text{m}^2$ , to be more consistent with observations  
 3017 of dust generation in more productive regions [[Okin, 2008](#)]. The cut-off size range for dust  
 3018 emissions is 0.1-2.0  $\mu\text{m}$  (fine dust) and 2.0-10  $\mu\text{m}$  (coarse dust) for MAM-7; and 0.1-1.0  $\mu\text{m}$   
 3019 (accumulation), and 1.0-10  $\mu\text{m}$  (coarse) for MAM-3.

## 3020 4.8.2 Chemistry

3021 Simple gas-phase chemistry is included for sulfate aerosol. This includes (1) DMS oxidation with  
 3022 OH and  $\text{NO}_3$  to form  $\text{SO}_2$ ; (2)  $\text{SO}_2$  oxidation with OH to form  $\text{H}_2\text{SO}_4$  (gas); (3)  $\text{H}_2\text{O}_2$  production  
 3023 ( $\text{HO}_2 + \text{HO}_2$ ); and (4)  $\text{H}_2\text{O}_2$  loss ( $\text{H}_2\text{O}_2$  photolysis and  $\text{H}_2\text{O}_2 + \text{OH}$ ). The rate coefficients for these  
 3024 reactions are provided from the MOZART model [[Emmons, 2010](#)]. Oxidant concentrations ( $\text{O}_3$ ,  
 3025 OH,  $\text{HO}_2$ , and  $\text{NO}_3$ ) are temporally interpolated from monthly averages taken from MOZART  
 3026 simulations [[Lamarque et al., 2010a](#)].

3027  $\text{SO}_2$  oxidation in bulk cloud water by  $\text{H}_2\text{O}_2$  and  $\text{O}_3$  is based on the MOZART treatment  
 3028 [[Tie et al., 2001](#)]. The pH value in the bulk cloud water is calculated from the electroneutrality  
 3029 equation between the bulk cloud-borne  $\text{SO}_4$  and  $\text{NH}_4$  ion concentrations (summation over  
 3030 modes), and ion concentrations from the dissolution and dissociation of trace gases based on the  
 3031 Henry's law equilibrium. Irreversible uptake of  $\text{H}_2\text{SO}_4$  (gas) to cloud droplets is also calculated  
 3032 [[Seinfeld and Pandis, 1998](#)]. The sulfate produced by  $\text{SO}_2$  aqueous oxidation and  $\text{H}_2\text{SO}_4$  (gas)  
 3033 uptake is partitioned to the cloud-borne sulfate mixing ratio in each mode in proportion to the  
 3034 cloud-borne aerosol number of the mode (i.e., the cloud droplet number associated with each  
 3035 aerosol mode), by assuming droplets associated with each mode have the same size. For MAM-7,  
 3036 changes to aqueous  $\text{NH}_4$  ion from dissolution of  $\text{NH}_3$  (g) are similarly partitioned among modes.  
 3037  $\text{SO}_2$  and  $\text{H}_2\text{O}_2$  mixing ratios are at the same time reduced due to aqueous phase consumption.

### 3038 4.8.3 Secondary Organic Aerosol

3039 The simplest treatment of secondary organic aerosol (SOA), which is used in many global models,  
3040 is to assume fixed mass yields for anthropogenic and biogenic precursor VOC's, then directly  
3041 emit this mass as primary aerosol particles. MAM adds one additional step of complexity  
3042 by simulating a single lumped gas-phase SOA (gas) species. Fixed mass yields for five VOC  
3043 categories of the MOZART-4 gas-phase chemical mechanism are assumed, as shown in Table  
3044 4.2. These yields have been increased by an additional 50% for the purpose of reducing aerosol  
3045 indirect forcing by increasing natural aerosols. The total yielded mass is emitted as the SOA  
3046 (gas) species. MAM then calculates condensation/evaporation of the SOA (gas) to/from several  
3047 aerosol modes. The condensation/evaporation is treated dynamically, as described later. The  
3048 equilibrium partial pressure of SOA (gas), over each aerosol mode  $m$  is expressed in terms of  
3049 Raoult's Law as:

$$P_m^* = \left( \frac{A_m^{SOA}}{A_m^{SOA} + 0.1A_m^{POA}} \right) P^0 \quad (4.198)$$

3050 where  $A_m^{SOA}$  is SOA mass concentration in mode  $m$ ,  $A_m^{POA}$  is the primary organic aerosol  
3051 (POA) mass concentration in mode  $m$  (10% of which is assumed to be oxygenated), and  $P^0$  is  
3052 the mean saturation vapor pressure of SOA whose temperature dependence is expressed as:

$$P^0(T) = P^0(298K) \times \exp\left[\frac{-\Delta H_{vap}}{R}\left(\frac{1}{T} - \frac{1}{298}\right)\right] \quad (4.199)$$

3053 where  $P^0$  (298 K) is assumed at  $1 \times 10^{-10}$  atm and the mean enthalpy of vaporization  $\Delta H_{vap}$   
3054 is assumed at 156 kJ mol<sup>-1</sup>.

3055 Treatment of the gaseous SOA and explicit condensation/evaporation provides (1) a realistic  
3056 method for calculating the distribution of SOA among different modes and (2) a minimal  
3057 treatment of the temperature dependence of the gas/aerosol partitioning.

### 3058 4.8.4 Nucleation

3059 New particle formation is calculated using parameterizations of binary H<sub>2</sub>SO<sub>4</sub>-H<sub>2</sub>O homogeneous  
3060 nucleation, ternary H<sub>2</sub>SO<sub>4</sub>-NH<sub>3</sub>-H<sub>2</sub>O homogeneous nucleation, and boundary layer nucleation.  
3061 A binary parameterization [Vehkamaki et al., 2002] is used in MAM-3, which does not predict  
3062 NH<sub>3</sub>, while a ternary parameterization [Merikanto et al., 2007] is used in MAM-7. The boundary  
3063 layer parameterization, which is used in both versions, uses the empirical 1st order nucleation  
3064 rate in H<sub>2</sub>SO<sub>4</sub> from Sihto et al. [2006], with a first order rate coefficient of  $1.0 \times 10^{-6}$  s<sup>-1</sup> as in  
3065 Wang et al. [2009]. The new particles are added to the Aitken mode, and we use the parameterization  
3066 of Kerminen and Kulmala [2002] to account for loss of the new particles by coagulation  
3067 as they grow from critical cluster size to Aitken mode size.

### 3068 4.8.5 Condensation

3069 Condensation of H<sub>2</sub>SO<sub>4</sub> vapor, NH<sub>3</sub> (MAM-7 only), and the SOA (gas) to various modes is  
3070 treated dynamically, using standard mass transfer expressions [Seinfeld and Pandis, 1998] that

3071 are integrated over the size distribution of each mode [Binkowski and Shankar, 1995]. An ac-  
3072 commodation coefficient of 0.65 is used for  $\text{H}_2\text{SO}_4$  [Poschl et al., 1998], and currently, for the  
3073 other species too.  $\text{H}_2\text{SO}_4$  and  $\text{NH}_3$  condensation are treated as irreversible.  $\text{NH}_3$  uptake stops  
3074 when the  $\text{NH}_4/\text{SO}_4$  molar ratio of a mode reaches 2. SOA (gas) condensation is reversible, with  
3075 the equilibrium vapor pressure over particles given by Eq. (4.296).

3076 In MAM-7, condensation onto the primary carbon mode produces aging of the parti-  
3077 cles in this mode. Various treatments of the aging process have been used in other models  
3078 [Cooke and Wilson, 1996; Wilson et al., 2001; Liu et al., 2005; Riemer et al., 2003]. In CAM5  
3079 a criterion of 3 mono-layers of sulfate is used to convert a fresh POM/BC particle to the aged  
3080 accumulation mode. Using this criterion, the mass of sulfate required to age all the particles  
3081 in the primary carbon mode,  $M_{\text{SO}_4,\text{age-all}}$ , is computed. If  $M_{\text{SO}_4,\text{cond}}$  condenses on the mode  
3082 during a time step, we assume that a fraction  $f_{\text{age}} = M_{\text{SO}_4,\text{cond}} / M_{\text{SO}_4,\text{age-all}}$  has been aged.  
3083 This fraction of the POM, BC, and number in the mode is transferred to the accumulation  
3084 mode, along with the condensed soluble species. SOA is included in the aging process. The  
3085 SOA that condenses in a time step is scaled by its lower hygroscopicity to give a condensed  $\text{SO}_4$   
3086 equivalent.

3087 The two continuous growth processes (condensation and aqueous chemistry) can result in  
3088 Aitken mode particles growing to a size that is nominally within the accumulation mode size  
3089 range. Most modal aerosol treatments thus transfer part of the Aitken mode number and mass  
3090 (those particles on the upper tail of the distribution) to the accumulation mode after calculating  
3091 continuous growth [Easter et al., 2004].

### 3092 4.8.6 Coagulation

3093 Coagulation of the Aitken, accumulation, and primary carbon modes is treated. Coagulation  
3094 within each of these modes reduces number but leaves mass unchanged. For coagulation of  
3095 Aitken with accumulation mode and of primary-carbon with accumulation mode, mass is trans-  
3096 ferred from Aitken or primary-carbon mode to the accumulation mode. For coagulation of  
3097 Aitken with primary-carbon mode in MAM-7, Aitken mass is first transferred to the primary-  
3098 carbon mode. This ages some of the primary-carbon particles. An aging fraction is calculated as  
3099 with condensation, then the Aitken mass and the aged fraction of the primary-carbon mass and  
3100 number are transferred to the accumulation mode. Coagulation rates are calculated using the  
3101 fast/approximate algorithms of the Community Multiscale Air Quality (CMAQ) model, version  
3102 4.6.

### 3103 4.8.7 Water Uptake

3104 Water uptake is based on the equilibrium Kohler theory [Ghan and Zaveri, 2007] using the rel-  
3105 ative humidity and the volume mean hygroscopicity for each mode to diagnose the wet volume  
3106 mean radius of the mode from the dry volume mean radius. The hygroscopicity of each com-  
3107 ponent is listed in Table 4.3. The hygroscopicities here are equivalent to the  $\kappa$  parameters of  
3108 Petters and Kreidenweis [2007]. Note that the measured solubility of dust varies widely, from  
3109 0.03 to 0.26 [Koehler et al., 2009a].

Table 4.1: Size distributions of primary emissions.

Emission Source	Geometric standard deviation, $s_g$	Number mode diameter, $D_{gn}(\mu\text{m})$	$D_{emit}$ ( $\mu\text{m}$ ) <sup>1</sup>
BC/OM			
Forest fire/grass fire	1.8	0.080	0.134
Domestic/energy/industry/ transportation/shipping/waste	See note <sup>2</sup>	See note <sup>2</sup>	0.134
SO <sub>4</sub>			
Forest fire/grass fire/waste	1.8	0.080	0.134
Energy/industry/shipping	See note <sup>3</sup>	See note <sup>3</sup>	0.261
Domestic/transportation	1.8	0.030	0.0504
Continuous volcano, 50% in Aitken mode	1.8	0.030	0.0504
Continuous volcano, 50% in accum. mode	1.8	0.080	0.134

<sup>1</sup>Demit is volume-mean diameter =  $D_{gn} \exp(1.5 \times \ln(s_g)^2)$  used in number emissions as  $E_{number} = E_{mass}/(\pi/6 \times \rho D_{emit}^3)$

<sup>2</sup>This value is intermediate between the Dentener et al. [2006a]  $D_{emit} = 0.0504\text{m}$  and Liu et al. [2005]  $D_{emit} = 0.206\text{m}$ .

<sup>3</sup>Adapted from Stier et al. [2005] where 50% of mass goes to accumulation mode with Demit = 0.207 m, and 50% goes to coarse mode with  $D_{emit} = 3.08\text{m}$ . We put all mass in accumulation mode, and  $D_{emit} = 0.261\text{m}$  gives same number emissions as Stier et al. [2005]. [Dentener et al. [2006a] put all in coarse mode with Demit = 2.06 m]

Table 4.2: Assumed SOA (gas) yields

Species	Mass yield	Reference
Big Alkanes	5%	Lim and Zieman [2005]
Big Alkenes	5%	assumed
Toluene	15%	Odum et al. [1997]
Isoprene	4%	Kroll et al. [2006]
Monoterpenes	25%	Ng et al. [2007]

Table 4.3: Hygroscopicity of aerosol components

Seasalt	sulfate	nitrate	ammonium	SOA	POM	BC	dust
1.16	0.507	0.507	0.507	0.14	0.10	$10^{-10}$	0.068

### 3110 4.8.8 Subgrid Vertical Transport and Activation/Resuspension

3111 The vertical transport of interstitial aerosols and trace gases by deep convective clouds, using  
3112 updraft and downdraft mass fluxes from the Zhang-McFarlane parameterization, is described in  
3113 [Collins et al. \[2004a\]](#). Currently this vertical transport is calculated separately from wet removal,  
3114 but a more integrated treatment is planned. Cloud-borne aerosols, which are associated with  
3115 large-scale stratiform cloud, are assumed to not interact with the convective clouds. Vertical  
3116 transport by shallow convective clouds is treated similarly, using mass fluxes from the shallow  
3117 convection parameterization. Turbulent transport of the aerosol is given a special treatment with  
3118 respect to other tracers. To strengthen the coupling between turbulent transport and aerosol  
3119 activation in stratiform clouds, the implicit time integration scheme used for turbulent transport  
3120 of heat, energy, and momentum is replaced by an explicit scheme for droplets and aerosol. A  
3121 sub-timestep is calculated for each column based on the minimum turbulent transport time in  
3122 the column. Turbulent transport is integrated over the sub-time steps using a forward time  
3123 integration scheme.

3124 Aerosol activation converts particles from the interstitial attachment state to the cloud-  
3125 borne state. In stratiform cloud, activation is treated consistently with droplet nucleation, so  
3126 that the total number of particles activated and transferred to the cloud-borne state equals to  
3127 the number of droplets nucleated. Activation is parameterized in terms of updraft velocity and  
3128 the properties of all of the aerosol modes [\[Abdul-Razzak and Ghan, 2000b\]](#), with both mass  
3129 and number transferred to the cloud-borne state. The updraft velocity is approximated by the  
3130 square root of the turbulence kinetic energy, with a minimum value of  $0.2 \text{ m s}^{-1}$ . Activation  
3131 is assumed to occur as updrafts carry air into the base of the cloud [\[Ghan et al., 1997\]](#) and as  
3132 cloud fraction increases [\[Ovtchinnikov and Ghan, 2005\]](#). In addition, activation is assumed to  
3133 occur as air is continuously cycled through clouds, assuming a cloud regeneration time scale of  
3134 one hour. Consider a model time step of 20 minutes, so that  $1/3$  of the cloud is regenerated  
3135 in a time step. We essentially dissipate then reform  $1/3$  of cloud each time step. During  
3136 dissipation, grid-cell mean cloud droplet number is reduced by  $1/3$ , and  $1/3$  of the cloud-borne  
3137 aerosols are resuspended and converted to the interstitial state. During regeneration, interstitial  
3138 aerosols are activated in the "new" cloud, and cloud droplet number is increased accordingly.  
3139 The regeneration has small impact on shallow boundary layer clouds, but it noticeably increases  
3140 droplet number in deeper free-tropospheric clouds where vertical turbulence mixing is slow.  
3141 Particles are resuspended as aerosol when droplets evaporate. This process is assumed to occur  
3142 as droplets are transferred below or above cloud and as clouds dissipate.

### 3143 4.8.9 Wet Deposition

3144 Aerosol wet removal is calculated using the CAM3.5 wet removal routine [\[Rasch et al., 2000;](#)  
3145 [Barth et al., 2000\]](#) with modifications for the consistency with cloud macro- and microphysics.  
3146 The routine treats in-cloud scavenging (the removal of cloud-borne aerosol particles) and below-  
3147 cloud scavenging (the removal of interstitial aerosol particles by precipitation particles through  
3148 impaction and Brownian diffusion).

3149 For in-cloud scavenging, the stratiform and convective cloud fraction, cloud water, and pre-  
3150 cipitation production profiles are used to calculate first-order loss rate profiles for cloud-water.  
3151 These cloud-water first-order loss rates are multiplied by "solubility factors" to obtain aerosol

3152 first-order loss rates, which are applied to the aerosol profiles. The solubility factors can be  
3153 interpreted as (the fraction of aerosols that are in cloud drops)  $\times$  (an additional tuning factor).  
3154 In CAM3.5, where the cloud-borne aerosol is not explicitly calculated, a value of 0.3 is used  
3155 for solubility factors for all aerosol types and sizes. Different values are used for the MAM.  
3156 The stratiform in-cloud scavenging only affects the stratiform-cloud-borne aerosol particles, and  
3157 these have solubility factors of 1.0. It does not affect the interstitial aerosol particles, and these  
3158 have solubility factors of 0.0.

3159 For convective in-cloud scavenging of MAM aerosols, both a solubility factor and a within-  
3160 convective-cloud activation fraction are passed to the wet removal routine. For the stratiform-  
3161 cloud-borne aerosol particles, there is no wet removal by convective clouds, and these factors are  
3162 zero. For interstitial (with respect to stratiform cloud) aerosol, the solubility factor is 0.5, and  
3163 the activation fractions are 0.0 for the primary carbon mode, 0.4 for the fine and coarse dust  
3164 modes, and 0.8 for other modes. The lower values reflect lower hygroscopicity. These factors are  
3165 applied to both number and mass species within each mode, with one exception. In MAM-3,  
3166 different activation fractions are applied to the dust and sea salt of the coarse mode (0.4 and  
3167 0.8 respectively), and a weighted average is applied to the coarse mode sulfate and number.

3168 For below-cloud scavenging, the first-order removal rate is equal to [ (solubility factor)  $\times$   
3169 (scavenging coefficient)  $\times$  (precipitation rate) ]. Again, the solubility factor can be viewed as  
3170 a tuning factor. In CAM3.5, a solubility factor of 0.3 and a scavenging coefficient of 0.1  $\text{mm}^{-1}$   
3171 are used for all aerosols. In MAM, the scavenging coefficient for interstitial aerosol is explicitly  
3172 calculated as in [Easter et al. \[2004\]](#) and thus varies strongly with particle size, with lowest values  
3173 for the accumulation mode; and the solubility factor is 0.1. For stratiform-cloud-borne aerosol,  
3174 there is no below-cloud scavenging, and the solubility factor is 0.0.

3175 Aerosol that is scavenged at one altitude can be resuspended at a lower altitude if precip-  
3176 itation evaporates. In CAM5, as in CAM3.5, this process is treated for aerosol removed by  
3177 stratiform in-cloud scavenging. A fraction of the in-cloud scavenged aerosol is resuspended, and  
3178 the resuspended fraction is equal to the fraction of precipitation that evaporates below cloud.

#### 3179 4.8.10 Dry Deposition

3180 Aerosol dry deposition velocities are calculated using the [\[Zhang et al., 2001\]](#) parameterization  
3181 with the CAM5 land-use and surface layer information. Gravitational settling velocities are  
3182 calculated at layers above the surface [\[Seinfeld and Pandis, 1998\]](#). Both velocities depend on  
3183 particle wet size and are different for mass and number and between modes. The velocities for  
3184 cloud-borne aerosols are calculated based on droplet sizes. Aerosol mixing ratio changes and  
3185 fluxes from dry deposition and sedimentation throughout a vertical column are then calculated  
3186 using the CAM5 dust deposition/sedimentation routine.

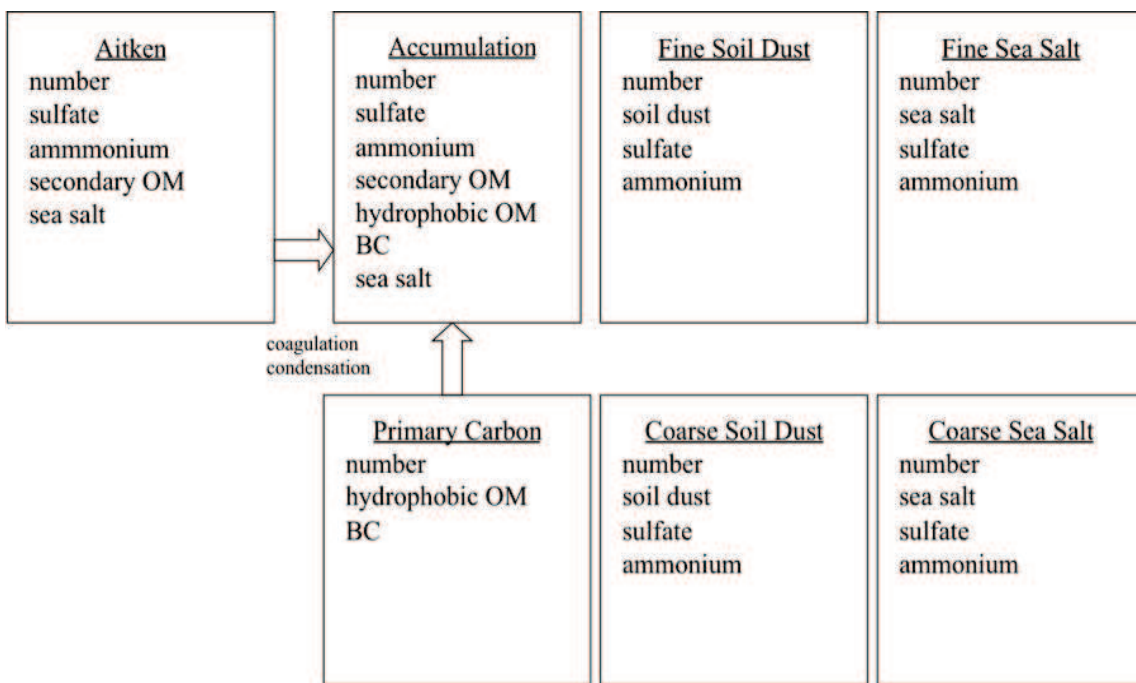


Figure 4.3: Predicted species for interstitial and cloud-borne component of each aerosol mode in MAM-7. Standard deviation for each mode is 1.6 (Aitken), 1.8 (accumulation), 1.6 (primary carbon), 1.8 (fine and coarse soil dust), and 2.0 (fine and coarse sea salt)

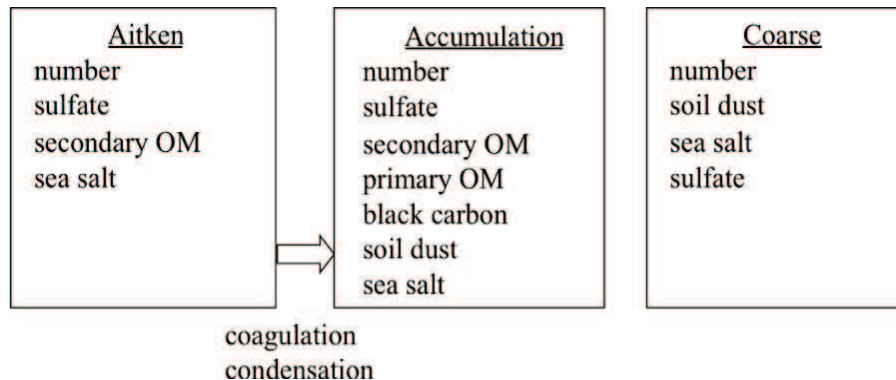


Figure 4.4: Predicted species for interstitial and cloud-borne component of each aerosol mode in MAM-3. Standard deviation for each mode is 1.6 (Aitken), 1.8 (accumulation) and 1.8 (coarse mode)

Table 4.4: Density (kg/m<sup>3</sup>) of aerosol material.

Sea salt	Sulfate	Nitrate	Ammonium	SOA	POA	BC	Dust
1900	1770	1770	1770	1000	1000	1700	2600

Table 4.5: Hygroscopicity of aerosol components.

Sea salt	Sulfate	Nitrate	Ammonium	SOA	POA	BC	Dust
1.16	0.507	0.507	0.507	0.14	1.e-10	1.e-10	0.068

## 3187 4.9 Condensed Phase Optics

3188 Condensed phase (aerosols, liquid cloud droplets, hydrometeors, and ice crystal) optics are  
 3189 provided as a mass-specific quantities in m<sup>2</sup>/kg. These optics are specified for each band of the  
 3190 shortwave and longwave radiation code. For the shortwave, unscaled extinction, single-scattering  
 3191 albedo, and asymmetry parameter are specified. For the longwave, the mass-specific absorption  
 3192 is specified. Vertical optical depths are computed by multiplying by the mass-specific quantities  
 3193 by the vertical mass path of the corresponding material.

3194 For clouds, the in-cloud values of the mixing ratios are used to compute the in-cloud values  
 3195 of cloud optical depths. The radiation does not use grid-cell average optical depths of clouds.

### 3196 4.9.1 Tropospheric Aerosol Optics

3197 While the radiation code supports a range of possible aerosol packages, the modal aerosol package  
 3198 is the default configuration, and we will discuss the optics treatment used in that package.  
 3199 Aerosol optical properties for each mode are parameterized in terms of wet refractive index  
 3200 and wet surface mode radius of the mode, as described by [Ghan and Zaveri, 2007], except  
 3201 that volume mixing rather than the Maxwell-Garnett mixing rule is used to calculate the wet  
 3202 refractive index for mixtures of insoluble and soluble particles (We found little difference between  
 3203 the volume mixing treatment and the Maxwell-Garnett mixing rule.) Refractive indices for water  
 3204 and for most aerosol components are taken from OPAC [Koepke and Schult, 1998], but for black  
 3205 carbon the value (1.95,0.79i) from [Bond and Bergstrom, 2006] is used for solar wavelengths.  
 3206 Densities for each component are listed in Table 4.4.

3207 The wet volume mean radius for each mode is calculated from the dry volume mean radius  
 3208 using equilibrium Kohler theory [Ghan and Zaveri, 2007], the relative humidity and the volume  
 3209 mean hygroscopicity. The hygroscopicity of each component is listed in Table 4.5. Note that  
 3210 the measured solubility of dust varies widely, from 0.03 to 0.26 [Koehler et al., 2009b]. The wet  
 3211 surface mode radius is calculated from the wet volume mean radius assuming a wet lognormal  
 3212 size distribution with the same geometric standard deviation as the dry size distribution. The  
 3213 geometric standard deviation is assumed to be constant for each mode.

### 3214 4.9.2 Stratospheric Volcanic Aerosol Optics

3215 CAM 5.0 specifies the volcanic aerosol as a mass mixing ratio  $q_V$  of wet volcanic aerosol to dry  
 3216 air as a function of height, latitude, longitude and time. CAM 5.0 also specifies a geometric

3217 mean radius  $r_g$  of the volcanic aerosol. The volcanic optics are stored as a lookup table as a  
 3218 function of geometric mean radius.

The size distribution is defined by a log-normal size distribution with a geometric mean radius  $r_g$  and geometric standard deviation  $\sigma_g$ . For the standard version of the optics,

$$\sigma_g = 1.8 \quad (4.200)$$

$$\mu = \ln(r_g) \quad (4.201)$$

$$\mu \in [\mu_{\min}, \mu_{\max}] \quad (4.202)$$

$$\mu_{\min} = \ln(0.01 * 10^{-6} \exp(-5/2 * (\ln \sigma_g)^2)) \quad (4.203)$$

$$\mu_{\max} = \ln(2.00 * 10^{-6} \exp(-5/2 * (\ln \sigma_g)^2)) \quad (4.204)$$

In other words,  $r_{\text{eff}}$  spans the range [0.01,2.0]  $\mu\text{m}$ . The density of the sulfuric acid / water mixture at 75% / 25% at 215K is

$$\rho = 1.75 * 10^3 \text{ kg/m}^3 \quad (4.205)$$

3219 The index of refraction is that specified by Biermann [Biermann et al., 2000] and is available  
 3220 from the HITRAN [Rothman et al., 2009] database. The index at 75%/25% weight percent  
 3221 (sulfuric acid to water) and at 215K is used.

The incomplete gamma weight,

$$L(r) = \int_0^r r^{*2} n(r^*) dr^* / \int_0^\infty r^{*2} n(r^*) dr^* \quad (4.206)$$

can be used to define the mass-specific aerosol extinction, scattering, and asymmetric scattering,

$$b_{\text{ext}} = \frac{3}{4\rho r_{\text{eff}}} \int_0^\infty q_{\text{ext}}(r) dL(r) \quad (4.207)$$

$$b_{\text{sca}} = \frac{3}{4\rho r_{\text{eff}}} \int_0^\infty q_{\text{sca}}(r) dL(r) \quad (4.208)$$

$$b_{\text{asm}} = \frac{3}{4\rho r_{\text{eff}}} \int_0^\infty q_{\text{gqsc}}(r) dL(r) \quad (4.209)$$

$$b_{\text{abs}} = \frac{3}{4\rho r_{\text{eff}}} \int_0^\infty (q_{\text{ext}}(r) - q_{\text{sca}}(r)) dL(r) \quad (4.210)$$

3222 where  $q_{\text{ext}}(r)$ ,  $q_{\text{sca}}(r)$ ,  $q_{\text{gqsc}}(r)$  are efficiencies obtained from the MIEV0 program of Wiscombe  
 3223 [Wiscombe, 1996].

3224 These mass-specific properties are averaged over each frequency band of RRTMG and pa-  
 3225 rameterized in a lookup table with  $\mu = \ln(r_g)$  as the dependent variable.

The vertical optical depths are derived as the product of vertical mass path with mass-specific aerosol properties at runtime.

$$\tau_{\text{ext}} = q_V * \frac{\Delta P_{\text{dry}}}{g} * b_{\text{ext}}(\mu) \quad (4.211)$$

3226 where  $q_V$  is the mixing ratio of volcanic aerosol. The corresponding scattering optical depth,  
 3227 asymmetric scattering optical depth, and absorption optical depth are derived similarly.

### 3228 4.9.3 Liquid Cloud Optics

For liquid clouds CAM 5.0 specifies the fraction of each grid cell occupied by liquid cloud droplets  $C_{\text{liq}}$ , the ratio of mass of condensed water to wet air in the cloud  $q_{\text{liq}}$ , and the number-size distribution in terms of the 2 parameters,  $\mu$  and  $\lambda$  of the gamma distribution,

$$n(D) = \frac{dN}{dD} = \frac{\lambda^{\mu+1}}{\Gamma(\mu+1)} D^\mu e^{-\lambda D} \quad (4.212)$$

3229 where  $D$  is the diameter of the droplets.

Both the parameters,  $\mu$  and  $\lambda$  have limited ranges:

$$2. < \mu < 15. \quad (4.213)$$

$$\frac{\mu + 1}{50 * 10^{-6}\text{m}} < \lambda < \frac{\mu + 1}{2 * 10^{-6}\text{m}} \quad (4.214)$$

3230 The liquid cloud optics are specified in terms of a lookup table in  $\mu$  and  $1/\lambda$ . These optics are  
 3231 computed as size-distribution and spectral-band averages of the quantities (e.g.,  $Q_{\text{ext}}$ ) computed  
 3232 by the MIEV0 program [Wiscombe, 1996].

The size-integrated mass-specific extinction coefficient,  $k_{\text{ext}}$ , (units  $\text{m}^2/\text{kg}$ ) is given by:

$$k_{\text{ext}}(\nu) = \frac{\frac{\pi}{4} \int_0^\infty D^2 Q_{\text{ext}}(D; \nu, m) n(D) dD}{\frac{\pi}{6} \rho_w \int_0^\infty D^3 n(D) dD} \quad (4.215)$$

3233 The corresponding quantities are used to compute mass-specific absorption in the longwave as  
 3234 well as single-scattering albedo and asymmetry parameter.

The in-cloud optical depth is then given by:

$$\tau_{\text{liq}}(\nu) = k_{\text{ext}}(\nu) q_{\text{liq}} \frac{\Delta P}{g} \quad (4.216)$$

3235 where  $q_{\text{liq}}$  is the ratio of droplet mass to dry air mass.

3236 For RRTMG, the wavenumber average values of  $\tau_{\text{liq}}$ ,  $\tau_{\text{liq}}\omega_{\text{liq}}$ ,  $\tau_{\text{liq}}\omega_{\text{liq}}g_{\text{liq}}$  on each SW band, and  
 3237 the wavenumber average value of the absorption optical depth,  $\tau_{\text{liq}}(1 - \omega_{\text{liq}})$ , on each longwave  
 3238 band.

3239 In-cloud water path variability is not treated by the optics.

### 3240 4.9.4 Ice Cloud Optics

3241 CAM 5.0 specifies an in-cloud ice water path, an ice cloud fraction, and an effective diameter  
 3242 for ice particles in the cloud. The optics for ice clouds are constructed as a lookup table as a  
 3243 function of effective diameter for each of the shortwave and longwave bands in the radiation  
 3244 code.

3245 Ice cloud optical properties have been derived using two approaches: (1) calculations of  
 3246 single ice crystal scattering properties based on electrodynamic theory, followed by their applica-  
 3247 tion to assumed ice particle size distributions (PSD) and the representation of PSD optical  
 3248 properties through the effective diameter ( $D_e$ ) of the PSD, and (2) parameterization of scatter-  
 3249 ing/absorption processes in terms of ice particle shape and size, and integrating these expressions

3250 over the PSD to produce analytical expressions of PSD optical properties in terms of ice crystal  
3251 and PSD parameters. In the latter case, the PSD extinction and absorption coefficients can be  
3252 expressed as explicit functions of the ice particle projected area- and mass-dimension power laws  
3253 and the PSD parameters of the gamma form. The modified anomalous diffraction approximation  
3254 (MADA) uses this second approach to calculate ice cloud optical properties. The development  
3255 of MADA was motivated by a desire to explicitly represent ice optical properties in terms of the  
3256 ice PSD and ice crystal shape parameters, given that the ice PSD optical properties cannot be  
3257 uniquely defined by  $D_e$  [Mitchell, 2002].

3258 MADA was developed from van de Hulst's anomalous diffraction theory or ADT  
3259 [van de Hulst, 1957] through a series of physical insights, which are:

- 3260 1. The effective photon path through a particle by which its scattering properties can be pre-  
3261 dicted is given by the ratio of particle projected area/particle volume [Bryant and Latimer,  
3262 1969; Mitchell and Arnott, 1994], where volume is defined as particle mass/bulk density  
3263 of ice (0.917 g/cm<sup>3</sup>).
- 3264 2. The processes of internal reflection and refraction can be viewed as extending the photon  
3265 path and can be parameterized using a MADA framework [Mitchell et al., 1996b].
- 3266 3. The maximum contribution of wave resonance or photon tunneling to absorption and  
3267 extinction can be estimated as a linear function of the real part of the refractive index for  
3268 ice,  $n_r$ . Photon tunneling can then be parameterized in terms of  $n_r$ , size parameter  $x$  and  
3269 the other MADA parameters described above [Mitchell, 2000].
- 3270 4. Edge effects as surface wave phenomena pertain only to extinction and can be represented  
3271 in terms of the size parameter  $x$  as described by [Wu, 1956] and modified by [Mitchell,  
3272 2000]. Based on a laboratory ice cloud study [Mitchell et al., 2001], edge effects for non-  
3273 spherical ice crystals do not appear significant.

3274 The first insight greatly simplified van de Hulst's ADT, resulting in analytic and integrable  
3275 expressions for the PSD extinction and absorption coefficients as shown in [Mitchell and Arnott,  
3276 1994]. This simplified ADT may be more accurate than the original ADT [Mitchell et al., 2006a].  
3277 This simplified ADT provided an analytical framework on which the other three insights or  
3278 processes were expressed. These processes were represented analytically for a single ice particle,  
3279 and then integrated over the PSD to produce extinction and absorption coefficients that account  
3280 for these processes. These coefficients were formulated in terms of ice particle shape (i.e. the  
3281 ice particle area- and mass-dimension power laws) and the three gamma PSD parameters. The  
3282 basic MADA equations formulated for ice clouds are given in the appendix of [Mitchell, 2002].  
3283 Details regarding their derivation and their physical basis are described in [Mitchell, 2000] and  
3284 [Mitchell et al., 1996b].

3285 The asymmetry parameter  $g$  is not treated by MADA, but was parameterized for so-  
3286 lar wavelengths as a function of wavelength and ice particle shape and size, based on ray-  
3287 tracing calculations by Andreas Macke, as described in [Mitchell et al., 1996b]. The  $g$  pa-  
3288 rameterization for quasi-spherical ice particles is based on the phase function calculations of  
3289 [Nousiainen and McFarquhar, 2004]. These parameterizations relate  $g$  for a PSD to the ice par-  
3290 ticle size that divides the PSD into equal projected areas (since scattering depends on projected

area). For terrestrial radiation, CAM 5.0  $g$  values for ice are based on the  $g$  parameterization described in [Yang et al., 2005].

### Tests of MADA

While this treatment of ice optical properties began and evolved through van de Hulst's original insights formulated in ADT, optical properties predicted by MADA closely agree with those predicted by other ice optics schemes based on electrodynamic theory. As described in [Mitchell et al., 2001, 2006a], MADA has been tested in a laboratory ice cloud experiment where the MADA extinction error was 3% on average relative to the FTIR measured extinction efficiency over the 2-14  $\mu\text{m}$  wavelength range. These same laboratory PSD were used to calculate the absorption efficiencies using MADA and T-matrix, which differed by 6% on average over the wavelength range 2-18  $\mu\text{m}$  (size parameter range 2-22). In corresponding T-matrix calculations of the single-scattering albedo, the mean MADA error was 2.5%. In another test, MADA absorption errors relative to the Finite Difference Time Domain (FDTD) method (i.e. [Yang et al., 2005] over the wavelength range 3-100  $\mu\text{m}$  were no greater than 15% for six ice particle shapes. Finally, the absorption coefficients predicted by MADA and the [Fu et al., 1998] and the [Yang et al., 2005] ice optics schemes generally agreed within 5%.

### Application to CAM 5.0

The MADA-based ice optics scheme described above is not used explicitly in CAM 5.0, but was used to generate a look-up table of optical properties as a function of effective diameter,  $D_e$ . The PSD optical properties consist of the mass-normalized extinction coefficient (volume extinction coefficient / ice water content), the single-scattering albedo and the asymmetry parameter for bands covering all solar and terrestrial wavelengths. The radiation bands coincide with those used in RRTMG. The ice refractive index values used are from [Warren and Brandt, 2008]. Since MADA is formulated to accept any ice particle shape recipe, a shape recipe corresponding to that observed for mid-latitude cirrus clouds at  $-45^\circ\text{C}$  (see [Lawson et al., 2006]) was assumed for ice particles larger than 60  $\mu\text{m}$ : 7% hexagonal columns, 50% bullet rosettes and 43% irregular ice particles. At smaller sizes, the shape recipe consists of 50% quasi-spherical, 30% irregular and 20% bullet rosette ice crystals, based on in-situ measurements in tropical cirrus [P. Lawson, 2005, personal communication].

The effective diameter is defined in a way that is universal for both ice and water clouds, which is essentially the photon path characterizing the PSD [Mitchell, 2002]:

$$D_e = \frac{3}{2} \frac{\text{IWC}}{\rho_i A} \quad (4.217)$$

where IWC is the ice water content ( $\text{g}/\text{cm}^3$ ),  $\rho_i$  is the bulk ice density ( $0.917 \text{ g}/\text{cm}^3$ ) and  $A$  is the total projected area of the PSD ( $\text{cm}^2/\text{cm}^3$ ).

#### 4.9.5 Snow Cloud Optics

CAM 5.0 specifies snow as a cloud fraction of snow, an effective diameter of snow, and an in-cloud mass mixing ratio of snow. The snow optics are identical to the optics for ice clouds.

## 3325 4.10 Radiative Transfer

3326 Radiative transfer calculations in the longwave and shortwave are provided by the radiation code  
 3327 RRTMG [Iacono et al., 2008; Mlawer et al., 1997]. This is an accelerated and modified version  
 3328 of the correlated  $k$ -distribution model, RRTM. The condensed phase radiative parameterizations  
 3329 are external to the radiation package, however the gas optics and radiative transfer solver are  
 3330 provided within RRTMG.

### 3331 4.10.1 Combination of Aerosol Radiative Properties

The number  $N_a$  of aerosol species is arbitrary; however in the standard configuration there are 3 modes. The radiative properties are combined before being passed to the radiative transfer solver. If the extinction optical depth of species  $i$  in band  $b$  is  $\tau_{ib}$  and the single-scattering albedo is  $\omega_{ib}$  and the asymmetry parameter is  $g_{ib}$  then the aerosol optics are combined as follows:

$$\tau_b = \sum_{i=1}^{N_a} \tau_{ib} \quad (4.218)$$

$$\omega_b = \sum_{i=1}^{N_a} \tau_{ib} \omega_{ib} / \tau_b \quad (4.219)$$

$$g_b = \sum_{i=1}^{N_a} \tau_{ib} \omega_{ib} g_{ib} / (\tau_b \omega_b) \quad (4.220)$$

3332 where  $\tau_b$  is the total aerosol extinction optical depth in band  $b$ ,  $\omega_b$  is the total single-scattering  
 3333 albedo in band  $b$ , and  $g_b$  is the asymmetry parameter in band  $b$ .

### 3334 4.10.2 Combination of Cloud Optics

CAM 5.0 specifies three different types of clouds: ice clouds, liquid clouds, and snow clouds. Each of these clouds has a separate cloud fraction  $C_{\text{liq}}$ ,  $C_{\text{ice}}$ ,  $C_{\text{snow}}$ , as well as an in-cloud radiative characterization in terms of optical depths  $\tau_t$ , single-scattering albedo  $\omega_t$  and asymmetry parameter  $g_t$ . The optics are smeared together into a total cloud fraction  $C$  as follows:

$$C = \max\{C_{\text{liq}}, C_{\text{ice}}, C_{\text{snow}}\} \quad (4.221)$$

$$\tau_c = \sum_{t \in \text{type}} \tau_t * C_t / C \quad (4.222)$$

$$\omega_c = \sum_{t \in \text{type}} \tau_{tb} \omega_{tb} C_t / (\tau_c C) \quad (4.223)$$

$$g_c = \sum_{t \in \text{type}} \tau_{tb} \omega_{tb} g_{tb} C_t / (\tau_c \omega_c C) \quad (4.224)$$

3335 where  $C, \tau_c, \omega_c, g_c$  are the combined cloud radiative parameters.

### 4.10.3 Radiative Fluxes and Heating Rates

Radiative fluxes and heating rates in CAM 5.0 are calculated using RRTMG [Iacono et al., 2008].

This model utilizes the correlated  $k$ -distribution technique to calculate irradiance and heating rate efficiently in broad spectral intervals, while realizing the objective of retaining a high level of accuracy relative to measurements and high-resolution line-by-line models. Sub-grid cloud characterization in RRTMG is treated in both the longwave and shortwave spectral regions with McICA, the Monte-Carlo Independent Column Approximation [Pincus and Morcrette, 2003], using the maximum-random cloud overlap assumption.

The thermodynamic state, gas concentrations, cloud fraction, condensed phase optics, and aerosol properties are specified elsewhere. The CAM 5.0 surface model provides both the surface albedo, area-averaged for each atmospheric column, and the upward longwave surface flux, which incorporates the surface emissivity, for input to the radiation. The bulk aerosol package of CAM4 continues to be supported by this radiation code as an option, however a description of this optional configuration is not provided in this document.

To provide fluxes at the top of the atmosphere, RRTMG uses with an additional layer above the CAM 5.0 model top in both the longwave and shortwave. This extra layer is specified by replicating the composition of the highest CAM 5.0 layer into a layer that extends from the top of the model to  $10^{-4}$  hPa. RRTMG does not treat non-LTE (local thermodynamic equilibrium) effects in the upper atmosphere. It provides accurate fluxes and heating rates up to about 0.1 hPa, above which non-LTE effects become more significant.

### Shortwave Radiative Transfer

RRTMG divides the solar spectrum into 14 shortwave bands that extend over the spectral range from  $0.2 \mu\text{m}$  to  $12.2 \mu\text{m}$  ( $820$  to  $50000 \text{ cm}^{-1}$ ). Modeled sources of extinction (absorption and scattering) are  $\text{H}_2\text{O}$ ,  $\text{O}_3$ ,  $\text{CO}_2$ ,  $\text{O}_2$ ,  $\text{CH}_4$ ,  $\text{N}_2$ , clouds, aerosols, and Rayleigh scattering. The model uses a two-stream  $\delta$ -Eddington approximation assuming homogeneously mixed layers, while accounting for both absorption and scattering in the calculation of reflectance and transmittance. The model distinguishes the direct solar beam from scattered (diffuse) radiation. The scattering phase function is parameterized using the Henyey-Greenstein approximation to represent the forward scattering fraction as a function of the asymmetry parameter. This delta-scaling is applied to the total irradiance as well as to the direct and diffuse components. The latter are consistent with the direct and diffuse components of the surface albedo, which are applied to the calculation of surface reflectance.

The shortwave version of RRTMG used in CAM5 is derived from RRTM\_SW [Clough et al., 2005]. It utilizes a reduced complement of 112 quadrature points (g-points) to calculate radiative transfer across the 14 spectral bands, which is half of the 224 g-points used in RRTM\_SW, to enhance computational performance with little impact on accuracy. The number of g-points needed within each band varies depending on the strength and complexity of the absorption in each spectral interval. Total fluxes are accurate to within  $1\text{-}2 \text{ W/m}^2$  relative to the standard RRTM\_SW (using DISORT with 16 streams) in clear sky and in the presence of aerosols and within  $6 \text{ W/m}^2$  in overcast sky. RRTM\_SW with DISORT is itself accurate to within  $2 \text{ W/m}^2$  of the data-validated multiple scattering model, CHARTS [Moncet and Clough, 1997]. Input absorption coefficient data for the  $k$ -distributions used by RRTMG are obtained directly from the line-by-line radiation model LBLRTM [Clough et al., 2005].

Table 4.6: RRTMG\_SW spectral band boundaries and the solar irradiance in each band.

Band Index	Band Min (μm)	Band Max (μm)	Band Min (cm <sup>-1</sup> )	Band Max (cm <sup>-1</sup> )	Solar Irradiance (W/m <sup>2</sup> )
1	3.077	3.846	2600	3250	12.11
2	2.500	3.077	3250	4000	20.36
3	2.150	2.500	4000	4650	23.73
4	1.942	2.150	4650	5150	22.43
5	1.626	1.942	5150	6150	55.63
6	1.299	1.626	6150	7700	102.93
7	1.242	1.299	7700	8050	24.29
8	0.778	1.242	8050	12850	345.74
9	0.625	0.778	12850	16000	218.19
10	0.442	0.625	16000	22650	347.20
11	0.345	0.442	22650	29000	129.49
12	0.263	0.345	29000	38000	50.15
13	0.200	0.263	38000	50000	3.08
14	3.846	12.195	820	2600	12.89

3379 RRTMG shortwave utilizes McICA, the Monte-Carlo Independent Column Approximation,  
 3380 to represent sub-grid scale cloud variability such as cloud fraction and cloud overlap. An external  
 3381 sub-column generator is used to define the stochastic cloud arrays used by the McICA technique.

3382 The Kurucz solar source function is used in the shortwave model, which assumes a total  
 3383 solar irradiance (TSI) at the top of the atmosphere of 1368.22 W/m<sup>2</sup>. However, this value is  
 3384 scaled in each spectral band through the specification of a time-varying solar spectral irradiance  
 3385 as discussed below. The TSI assumed in each RRTMG shortwave band is listed in the table  
 3386 below, along with the spectral band boundaries in μm and wavenumbers.

3387 Shortwave radiation is only calculated by RRTMG when the cosine of the zenith angle is  
 3388 larger than zero, that is, when the sun is above the horizon.

### 3389 Longwave Radiative Transfer

3390 The infrared spectrum in RRTMG is divided into 16 longwave bands that extend over the  
 3391 spectral range from 3.1 μm to 1000.0 μm (10 to 3250 cm<sup>-1</sup>). The band boundaries are listed  
 3392 in the table below. The model calculates molecular, cloud and aerosol absorption and emission.  
 3393 Scattering effects are not presently included. Molecular sources of absorption are H<sub>2</sub>O, CO<sub>2</sub>,  
 3394 O<sub>3</sub>, N<sub>2</sub>O, CH<sub>4</sub>, O<sub>2</sub>, N<sub>2</sub> and the halocarbons CFC-11 and CFC-12. CFC-11 is specified by  
 3395 CAM5 as a weighed sum of multiple CFCs (other than CFC-12). The water vapor continuum  
 3396 is treated with the CKD\_v2.4 continuum model. For completeness, band 16 includes a small  
 3397 adjustment to add the infrared contribution from the spectral interval below 3.1 μm.

3398 The longwave version of RRTMG [Iacono et al., 2008, 2003, 2000] used in CAM5 has been  
 3399 modified from RRTM\_LW [Mlawer et al., 1997] to enhance its computational efficiency with  
 3400 minimal effect on the accuracy. This includes a reduction in the total number of g-points from  
 3401 256 to 140. The number of g-points used within each band varies depending on the strength

Table 4.7: RRTMG\_LW spectral band boundaries.

Band Index	Band Min (μm)	Band Max (μm)	Band Min (cm <sup>-1</sup> )	Band Max (cm <sup>-1</sup> )
1	28.57	1000.0	10	350
2	20.00	28.57	350	500
3	15.87	20.00	500	630
4	14.29	15.87	630	700
5	12.20	14.29	700	820
6	10.20	12.20	820	980
7	9.26	10.20	980	1080
8	8.47	9.26	1080	1180
9	7.19	8.47	1180	1390
10	6.76	7.19	1390	1480
11	5.56	6.76	1480	1800
12	4.81	5.56	1800	2080
13	4.44	4.81	2080	2250
14	4.20	4.44	2250	2380
15	3.85	4.20	2380	2600
16	3.08	3.85	2600	3250

3402 and complexity of the absorption in each band. Fluxes are accurate to within 1.0 W/m<sup>2</sup> at all  
 3403 levels, and cooling rate generally agrees within 0.1 K/day in the troposphere and 0.3 K/day  
 3404 the stratosphere relative to the line-by-line radiative transfer model, LBLRTM [[Clough et al., 2005](#);  
 3405 [Clough and Iacono, 1995](#)]. Input absorption coefficient data for the  $k$ -distributions used  
 3406 by RRTMG are obtained directly from LBLRTM.

3407 This model also utilizes McICA, the Monte-Carlo Independent Column Approximation  
 3408 [[Pincus and Morcrette, 2003](#)], to represent sub-grid scale cloud variability such as cloud fraction  
 3409 and cloud overlap. An external sub-column generator is used to define the stochastic cloud  
 3410 arrays needed by the McICA technique.

3411 Within the longwave radiation model, the surface emissivity is assumed to be 1.0. However,  
 3412 the radiative surface temperature used in the longwave calculation is derived with the Stefan-  
 3413 Boltzmann relation from the upward longwave surface flux that is input from the land model.  
 3414 Therefore, this value may include some representation of surface emissivity less than 1.0 if this  
 3415 condition exists in the land model. RRTMG longwave also provides the capability of varying  
 3416 the surface emissivity within each spectral band, though this feature is not presently utilized.

3417 Longwave radiative transfer is performed over a single (diffusivity) angle (secant = 1.66) for  
 3418 one upward and one downward calculation. RRTMG includes an accuracy adjustment in profiles  
 3419 with very high water vapor that slightly varies the diffusivity angle in some bands as a function  
 3420 of total column water vapor.

#### 3421 4.10.4 Surface Radiative Properties

3422 For the shortwave, the surface albedoes are specified at every grid point at every time step. The  
3423 albedoes are partitioned for the spectral ranges  $[2.0, 0.7]\mu\text{m}$  and  $[0.7, 12.0]\mu\text{m}$ . In addition they  
3424 are partitioned between the direct and diffuse beam.

3425 In the longwave, the surface is assumed to have an emissivity of 1.0 within the radiation  
3426 model. However, the radiative surface temperature used in the longwave calculation is derived  
3427 with the Stefan-Boltzmann relation from the upward longwave surface flux that is input from  
3428 the surface models. Therefore, this value may include some representation of surface emissivity  
3429 less than 1.0, if this condition exists in surface models (e.g. the land model).

#### 3430 4.10.5 Time Sampling

3431 Both the shortwave and longwave radiation is computed at hourly intervals by default. The  
3432 heating rates and fluxes are assumed to be constant between time steps.

#### 3433 4.10.6 Diurnal Cycle and Earth Orbit

In CAM 5.0, the diurnal cycle and earth orbit is computed using the method of [Berger, 1978]. Using this formulation, the insolation can be determined for any time within  $10^6$  years of 1950 AD. The insolation at the top of the model atmosphere is given by

$$S_I = S_0 \rho^{-2} \cos \mu, \quad (4.225)$$

3434 where  $S_0$  is the solar constant,  $\mu$  is the solar zenith angle, and  $\rho^{-2}$  is the distance factor (square  
3435 of the ratio of mean to actual distance that depends on the time of year). A time series of the  
3436 solar spectral irradiance at 1 a.u. for 1870-2100 based upon [Wang et al., 2005] is included with  
3437 the standard model and is in section 4.10.7.

We represent the annual and diurnal cycle of solar insolation with a repeatable solar year of exactly 365 days and with a mean solar day of exactly 24 hours, respectively. The repeatable solar year does not allow for leap years. The expressions defining the annual and diurnal variation of solar insolation are:

$$\cos \mu = \sin \phi \sin \delta - \cos \phi \cos \delta \cos(H) \quad (4.226)$$

$$\delta = \arcsin(\sin \epsilon \sin \lambda) \quad (4.227)$$

$$\rho = \frac{1 - e^2}{1 + e \cos(\lambda - \tilde{\omega})} \quad (4.228)$$

$$\tilde{\omega} = \Pi + \psi \quad (4.229)$$

where

$$\begin{aligned}
\phi &= \text{latitude in radians} \\
\delta &= \text{solar declination in radians} \\
H &= \text{hour angle of sun during the day} \\
\epsilon &= \text{obliquity} \\
\lambda &= \text{true longitude of the earth relative to vernal equinox} \\
e &= \text{eccentricity factor} \\
\tilde{\omega} &= \text{longitude of the perihelion} + 180^\circ \\
\Pi &= \text{longitude of perihelion based on the fixed equinox} \\
\psi &= \text{general precession}
\end{aligned} \tag{4.230}$$

The hour angle  $H$  in the expression for  $\cos \mu$  depends on the calendar day  $d$  as well as model longitude:

$$H = 2\pi \left( d + \frac{\theta}{360^\circ} \right), \tag{4.231}$$

where  $\theta$  = model longitude in degrees starting from Greenwich running eastward. Note that the calendar day  $d$  varies continuously throughout the repeatable year and is updated every model time step. The values of  $d$  at 0 GMT for January 1 and December 31 are 0 and 364, respectively. This would mean, for example, that a model calendar day  $d$  having no fraction (such as 182.00) would refer to local midnight at Greenwich, and to local noon at the date line (180° longitude).

The obliquity  $\epsilon$  may be approximated by an empirical series expansion of solutions for the Earth's orbit

$$\epsilon = \epsilon^* + \sum_{j=1}^{47} A_j \cos(f_j t + \delta_j) \tag{4.232}$$

where  $A_j$ ,  $f_j$ , and  $\delta_j$  are determined by numerical fitting. The term  $\epsilon^* = 23.320556^\circ$ , and  $t$  is the time (in years) relative to 1950 AD.

Since the series expansion for the eccentricity  $e$  is slowly convergent, it is computed using

$$e = \sqrt{(e \cos \Pi)^2 + (e \sin \Pi)^2} \tag{4.233}$$

The terms on the right-hand side may also be written as empirical series expansions:

$$e \begin{Bmatrix} \cos \\ \sin \end{Bmatrix} \Pi = \sum_{j=1}^{19} M_j \begin{Bmatrix} \cos \\ \sin \end{Bmatrix} (g_j t + \beta_j) \tag{4.234}$$

where  $M_j$ ,  $g_j$ , and  $\beta_j$  are estimated from numerical fitting. Once these series have been computed, the longitude of perihelion  $\Pi$  is calculated using

$$\Pi = \arctan \left( \frac{e \sin \Pi}{e \cos \Pi} \right) \tag{4.235}$$

The general precession is given by another empirical series expansion

$$\psi = \tilde{\psi} t + \zeta + \sum_{j=1}^{78} F_j \sin(f'_j t + \delta'_j) \quad (4.236)$$

3445 where  $\tilde{\psi} = 50.439273''$ ,  $\zeta = 3.392506^\circ$ , and  $F_j$ ,  $f'_j$ , and  $\delta'_j$  are estimated from the numerical  
3446 solution for the Earth's orbit.

The calculation of  $\lambda$  requires first determining two mean longitudes for the orbit. The mean longitude  $\lambda_{m0}$  at the time of the vernal equinox is :

$$\begin{aligned} \lambda_{m0} = & 2 \left\{ \left( \frac{e}{2} + \frac{e^3}{8} \right) (1 + \beta) \sin(\tilde{\omega}) \right. \\ & - \frac{e^2}{4} \left( \frac{1}{2} + \beta \right) \sin(2\tilde{\omega}) \\ & \left. + \frac{e^3}{8} \left( \frac{1}{3} + \beta \right) \sin(3\tilde{\omega}) \right\} \end{aligned} \quad (4.237)$$

where  $\beta = \sqrt{1 - e^2}$ . The mean longitude is

$$\lambda_m = \lambda_{m0} + \frac{2\pi(d - d_{ve})}{365} \quad (4.238)$$

where  $d_{ve} = 80.5$  is the calendar day for the vernal equinox at noon on March 21. The true longitude  $\lambda$  is then given by:

$$\begin{aligned} \lambda = \lambda_m & + \left( 2e - \frac{e^3}{4} \right) \sin(\lambda_m - \tilde{\omega}) \\ & + \frac{5e^2}{4} \sin[2(\lambda_m - \tilde{\omega})] \\ & + \frac{13e^3}{12} \sin[3(\lambda_m - \tilde{\omega})] \end{aligned} \quad (4.239)$$

3447 The orbital state used to calculate the insolation is held fixed over the length of the model  
3448 integration. This state may be specified in one of two ways. The first method is to specify  
3449 a year for computing  $t$ . The value of the year is held constant for the entire length of the  
3450 integration. The year must fall within the range of  $1950 \pm 10^6$ . The second method is to specify  
3451 the eccentricity factor  $e$ , longitude of perihelion  $\tilde{\omega} - 180^\circ$ , and obliquity  $\epsilon$ . This set of values  
3452 is sufficient to specify the complete orbital state. Settings for AMIP II style integrations under  
3453 1995 AD conditions are  $\epsilon = 23.4441$ ,  $e = 0.016715$ , and  $\tilde{\omega} - 180 = 102.7$ .

#### 3454 4.10.7 Solar Spectral Irradiance

3455 The reference spectrum assumed by RRTMG is the Kurucz spectrum. CAM 5.0 specifies the  
3456 solar spectral irradiance in a file, based on the work of Lean [Wang et al., 2005]. The Kurucz  
3457 spectrum can be seen in figure 4.5. The Lean data seen in figure 4.6 is time-varying and the  
3458 graphed values are an average over one solar cycle. These two spectra postulate different values  
3459 of the total solar irradiance. A graph of the relative difference between them can be seen in  
3460 figure 4.7.

Solar Irradiance	Kurucz	Lean
Total	1368.60	1366.96
In RRTMG bands	1368.14	1366.39
> 12195 nm	0.46	0.46
[120, 200] nm	0	0.11
EUV	0	0.0047

RRTMG Band Index	$\lambda_{high}$ , nm	$\lambda_{low}$ , nm	Kurucz W/m <sup>2</sup>	Lean W/m <sup>2</sup>	Lean - Kurucz	Relative %	Lean(t) Max % Variation	Lean(t) Max $\Delta$ Flux
14	12195	3846	12.79	12.78	-0.01	-0.08	0.16	0.020
1	3846	3077	12.11	11.99	-0.12	-1.00	0.02	0.003
2	3077	2500	20.36	20.22	-0.14	-0.69	0.03	0.007
3	2500	2151	23.73	23.49	-0.24	-1.02	0.02	0.005
4	2151	1942	22.43	22.17	-0.26	-1.17	0.01	0.003
5	1942	1626	55.63	55.61	-0.02	-0.04	0.02	0.011
6	1626	1299	102.9	102.9	0.0	0.	0.02	0.019
7	1299	1242	24.29	24.79	0.50	2.06	0.04	0.011
8	1242	778	345.7	348.9	3.2	0.93	0.06	0.226
9	778	625	218.1	218.2	0.1	0.05	0.11	0.238
10	625	441	347.2	344.9	-2.3	-0.67	0.13	0.463
11	441	345	129.5	130.0	0.5	0.39	0.26	0.340
12	345	263	50.15	47.41	-2.74	-5.78	0.45	0.226
13	263	200	3.120	3.129	0.009	0.29	4.51	0.141

Table 4.8: Band-level ratio of Solar Irradiances, based on average of one solar cycle

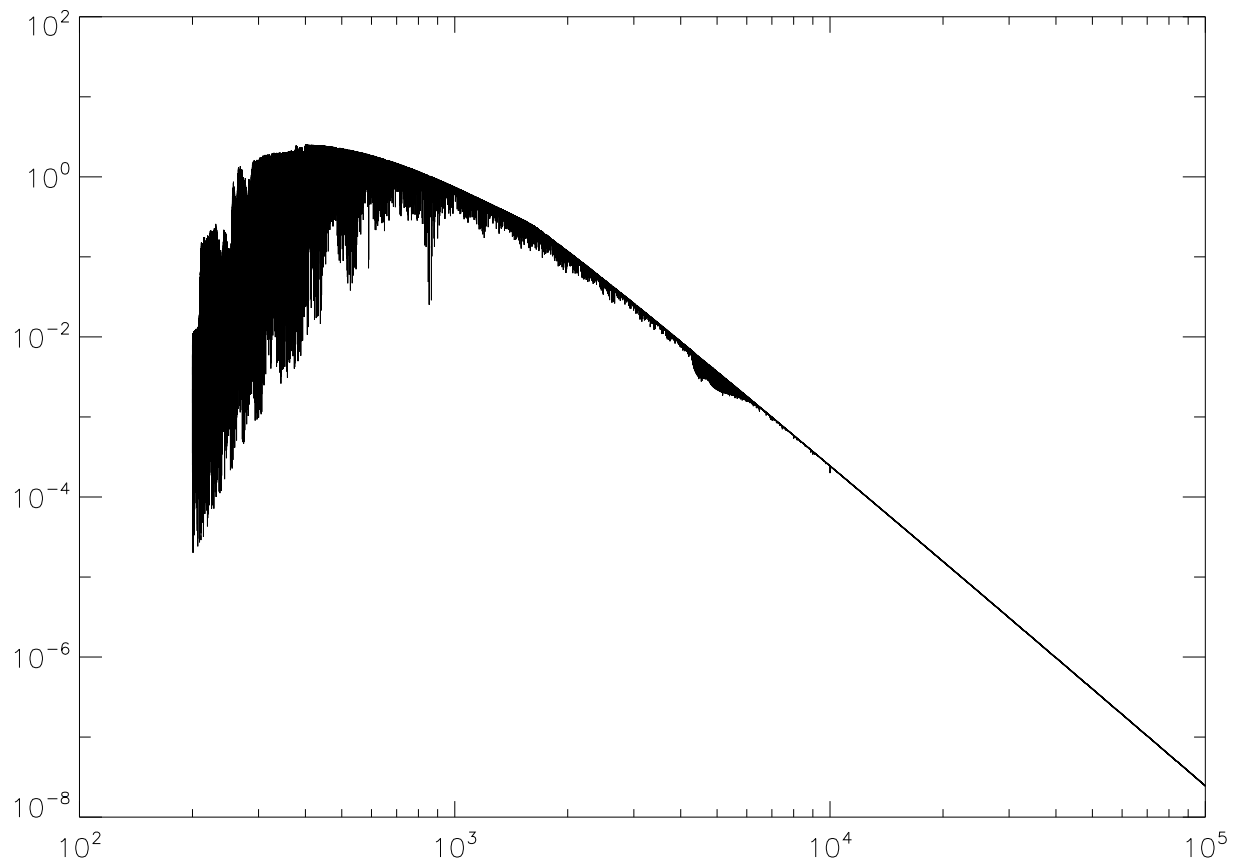


Figure 4.5: Kurucz spectrum. ssf in  $\text{W/m}^2/\text{nm}$ . Source Data: AER. Range from [20, 20000] nm.

3461 The heating in each band  $b$  is scaled by the ratio,  $\frac{\text{Lean}(t)_b}{\text{Kurucz}_b}$ , where  $\text{Kurucz}_b$  is assumed by  
 3462 RRTMG as specified in table 4.8, and  $\text{Lean}(t)_b$  is the solar irradiance specified by the time-  
 3463 dependent solar spectral irradiance file.  $\text{Lean}(t)_{14}$  includes the Lean irradiance longward of  
 3464 12195 nm to capture irradiance in the very far infrared.

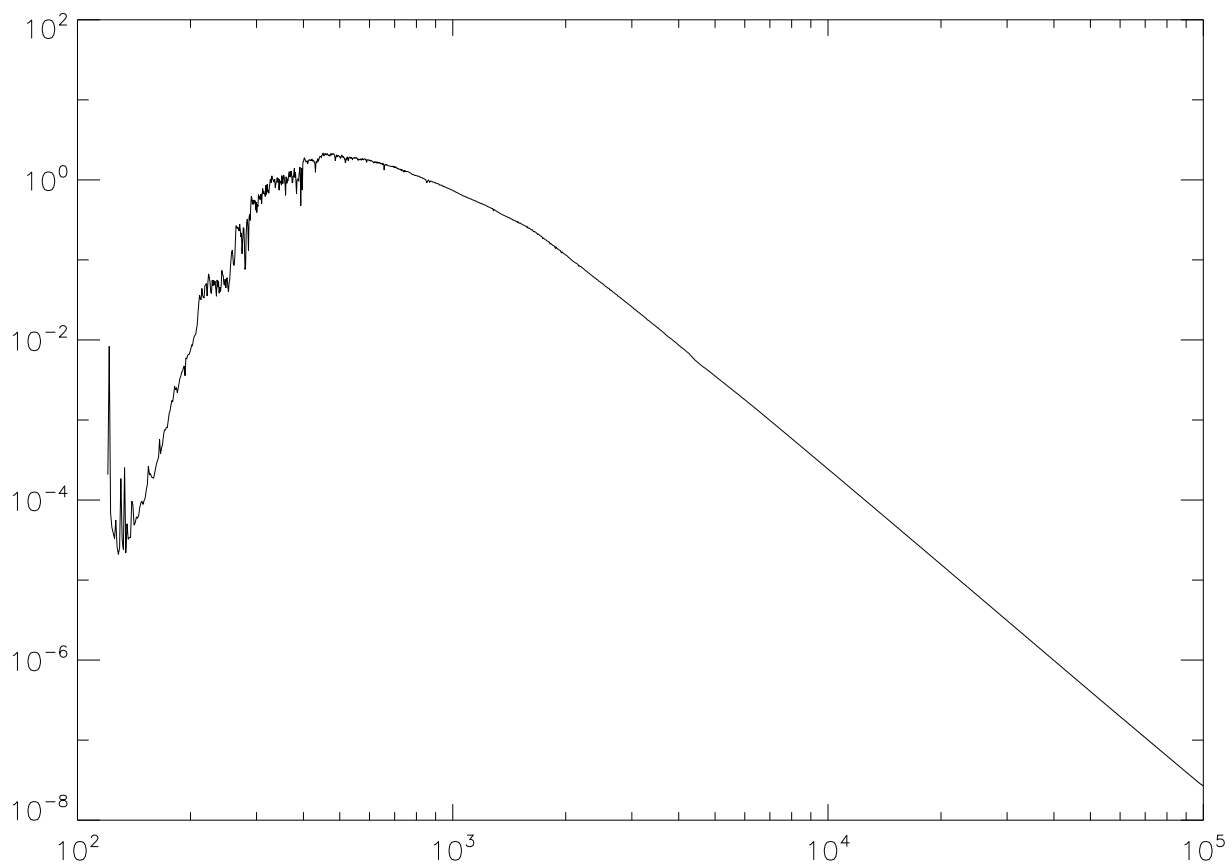


Figure 4.6: Lean spectrum. Average over 1 solar cycle, May 1, 1996 to Dec 31, 2006. Source Data: Marsh. ssf in W/m<sup>2</sup>/nm. Range from [120, 99975] nm.

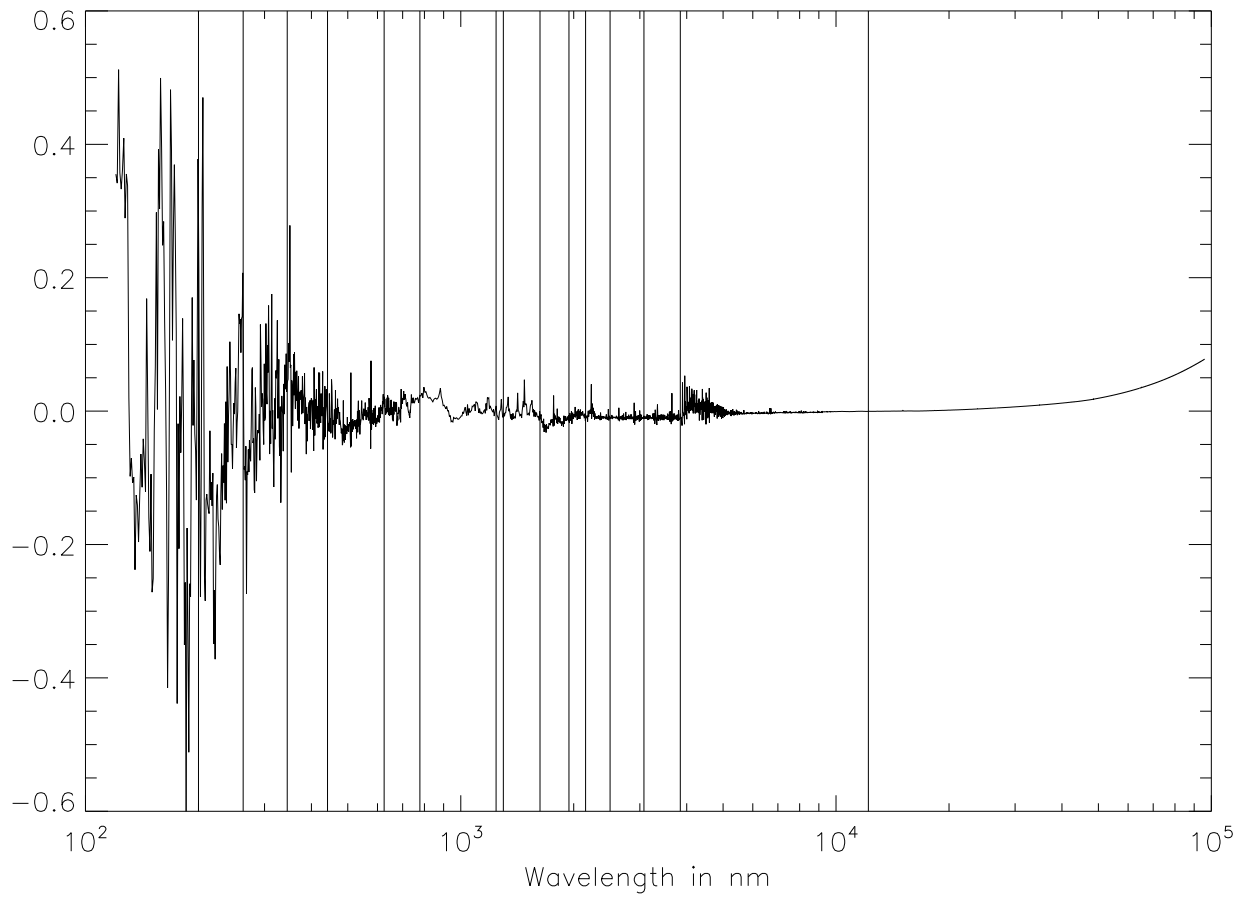


Figure 4.7: Relative difference,  $\frac{\text{Lean} - \text{Kurucz}}{.5(\text{Lean} + \text{Kurucz})}$  between spectra. RRTMG band boundaries are marked with vertical lines.

## 4.11 Surface Exchange Formulations

The surface exchange of heat, moisture and momentum between the atmosphere and land, ocean or ice surfaces are treated with a bulk exchange formulation. We present a description of each surface exchange separately. Although the functional forms of the exchange relations are identical, we present the descriptions of these components as developed and represented in the various subroutines in CAM 5.0. The differences in the exchange expressions are predominantly in the definition of roughness lengths and exchange coefficients. The description of surface exchange over ocean follows from [Bryan et al. \[1996\]](#), and the surface exchange over sea ice is discussed in the sea-ice model documentation. Over lakes, exchanges are computed by a lake model embedded in the land surface model described in the following section.

### 4.11.1 Land

In CAM 5.0, the NCAR Land Surface Model (LSM) [\[Bonan, 1996\]](#) has been replaced by the Community Land Model CLM2 [\[Bonan et al., 2002\]](#). This new model includes components treating hydrological and biogeochemical processes, dynamic vegetation, and biogeophysics. Because of the increased complexity of this new model and since a complete description is available online, users of CAM 5.0 interested in CLM should consult this documentation at <http://www.cgd.ucar.edu/tss/clm/>. A discussion is provided here only of the component of CLM which controls surface exchange processes.

Land surface fluxes of momentum, sensible heat, and latent heat are calculated from Monin-Obukhov similarity theory applied to the surface (i.e. constant flux) layer. The zonal  $\tau_x$  and meridional  $\tau_y$  momentum fluxes ( $\text{kg m}^{-1}\text{s}^{-2}$ ), sensible heat  $H$  ( $\text{W m}^{-2}$ ) and water vapor  $E$  ( $\text{kg m}^{-2}\text{s}^{-1}$ ) fluxes between the surface and the lowest model level  $z_1$  are:

$$\tau_x = -\rho_1 \overline{(u'w')} = -\rho_1 u_*^2 (u_1/V_a) = \rho_1 \frac{u_s - u_1}{r_{am}} \quad (4.240)$$

$$\tau_y = -\rho_1 \overline{(v'w')} = -\rho_1 u_*^2 (v_1/V_a) = \rho_1 \frac{v_s - v_1}{r_{am}} \quad (4.241)$$

$$H = \rho_1 c_p \overline{(w'\theta')} = -\rho_1 c_p u_* \theta_* = \rho_1 c_p \frac{\theta_s - \theta_1}{r_{ah}} \quad (4.242)$$

$$E = \rho_1 \overline{(w'q')} = -\rho_1 u_* q_* = \rho_1 \frac{q_s - q_1}{r_{aw}} \quad (4.243)$$

$$r_{am} = V_a/u_*^2 \quad (4.244)$$

$$r_{ah} = (\theta_1 - \theta_s)/u_* \theta_* \quad (4.245)$$

$$r_{aw} = (q_1 - q_s)/u_* q_* \quad (4.246)$$

where  $\rho_1$ ,  $u_1$ ,  $v_1$ ,  $\theta_1$  and  $q_1$  are the density ( $\text{kg m}^{-3}$ ), zonal wind ( $\text{m s}^{-1}$ ), meridional wind ( $\text{m s}^{-1}$ ), air potential temperature (K), and specific humidity ( $\text{kg kg}^{-1}$ ) at the lowest model level. By definition, the surface winds  $u_s$  and  $v_s$  equal zero. The symbol  $\theta_1$  represents temperature, and  $q_1$  is specific humidity at surface. The terms  $r_{am}$ ,  $r_{ah}$ , and  $r_{aw}$  are the aerodynamic resistances ( $\text{s m}^{-1}$ ) for momentum, sensible heat, and water vapor between the lowest model level at height

3488  $z_1$  and the surface at height  $z_{0m} + d$  [ $z_{0h} + d$ ]. Here  $z_{0m}$  [ $z_{0h}$ ] is the roughness length (m) for  
 3489 momentum [scalar] fluxes, and  $d$  is the displacement height (m).

3490 For the vegetated fraction of the grid,  $\theta_s = T_{af}$  and  $q_s = q_{af}$ , where  $T_{af}$  and  $q_{af}$  are the air  
 3491 temperature and specific humidity within canopy space. For the non-vegetated fraction,  $\theta_s = T_g$   
 3492 and  $q_s = q_g$ , where  $T_g$  and  $q_g$  are the air temperature and specific humidity at ground surface.  
 3493 These terms are described by [Dai et al. \[2001\]](#).

3494 **Roughness lengths and zero-plane displacement**

The aerodynamic roughness  $z_{0m}$  is used for wind, while the thermal roughness  $z_{0h}$  is used for heat and water vapor. In general,  $z_{0m}$  is different from  $z_{0h}$ , because the transfer of momentum is affected by pressure fluctuations in the turbulent waves behind the roughness elements, while for heat and water vapor transfer no such dynamical mechanism exists. Rather, heat and water vapor must ultimately be transferred by molecular diffusion across the interfacial sub-layer. Over bare soil and snow cover, the simple relation from [Zilitinkevich \[1970\]](#) can be used [[Zeng and Dickinson, 1998](#)]:

$$\ln \frac{z_{0m}}{z_{0h}} = a \left( \frac{u_* z_{0m}}{\nu} \right)^{0.45} \quad (4.247)$$

$$a = 0.13 \quad (4.248)$$

$$\nu = 1.5 \times 10^{-5} \text{ m}^2 \text{s}^{-1} \quad (4.249)$$

Over canopy, the application of energy balance

$$R_n - H - L_v E = 0 \quad (4.250)$$

3495 (where  $R_n$  is the net radiation absorbed by the canopy) is equivalent to the use of different  $z_{0m}$   
 3496 versus  $z_{0h}$  over bare soil, and hence thermal roughness is not needed over canopy [[Zeng et al.,](#)  
 3497 [1998](#)].

3498 The roughness  $z_{0m}$  is proportional to canopy height, and is also affected by fractional vegetation  
 3499 cover, leaf area index, and leaf shapes. The roughness is derived from the simple relationship  
 3500  $z_{0m} = 0.07 h_c$ , where  $h_c$  is the canopy height. Similarly, the zero-plane displacement height  $d$   
 3501 is proportional to canopy height, and is also affected by fractional vegetation cover, leaf area  
 3502 index, and leaf shapes. The simple relationship  $d/h_c = 2/3$  is used to obtain the height.

3503 **Monin-Obukhov similarity theory**

3504 **(1) Turbulence scaling parameters**

A length scale (the Monin-Obukhov length)  $L$  is defined by

$$L = \frac{\theta_v u_*^2}{kg\theta_{v*}} \quad (4.251)$$

where  $k$  is the von Kàrmán constant, and  $g$  is the gravitational acceleration.  $L > 0$  indicates stable conditions,  $L < 0$  indicates unstable conditions, and  $L = \infty$  applies to neutral conditions. The virtual potential temperature  $\theta_v$  is defined by

$$\theta_v = \theta_1 (1 + 0.61q_1) = T_a \left( \frac{p_s}{p_l} \right)^{R/c_p} (1 + 0.61q_1) \quad (4.252)$$

where  $T_1$  and  $q_1$  are the air temperature and specific humidity at height  $z_1$  respectively,  $\theta_1$  is the atmospheric potential temperature,  $p_l$  is the atmospheric pressure, and  $p_s$  is the surface pressure. The surface friction velocity  $u_*$  is defined by

$$u_*^2 = [\bar{u}'w'^2 + \bar{v}'w'^2]^{1/2} \quad (4.253)$$

The temperature scale  $\theta_*$  and  $\theta_{*v}$  and a humidity scale  $q_*$  are defined by

$$\theta_* = -\bar{w}'\bar{\theta}'/u_* \quad (4.254)$$

$$q_* = -\bar{w}'\bar{q}'/u_* \quad (4.255)$$

$$\begin{aligned} \theta_{*v} &= -\bar{w}'\bar{\theta}'_v/u_* \\ &\approx -(\bar{w}'\bar{\theta}' + 0.61\bar{\theta}\bar{w}'\bar{q}')/u_* \\ &= \theta_* + 0.61\bar{\theta}q_* \end{aligned} \quad (4.256)$$

3505 (where the mean temperature  $\bar{\theta}$  serves as a reference temperature in this linearized form of  $\theta_v$  ).

The stability parameter is defined as

$$\varsigma = \frac{z_1 - d}{L} \quad , \quad (4.257)$$

with the restriction that  $-100 \leq \varsigma \leq 2$ . The scalar wind speed is defined as

$$V_a^2 = u_1^2 + v_1^2 + U_c^2 \quad (4.258)$$

$$U_c = \begin{cases} 0.1 \text{ ms}^{-1} & , \text{ if } \varsigma \geq 0 \text{ (stable)} \\ \beta w_* = \beta \left( z_i \frac{g}{\theta_v} \theta_{*v} u_* \right)^{1/3} & , \text{ if } \varsigma < 0 \text{ (unstable)} . \end{cases} \quad (4.259)$$

3506 Here  $w_*$  is the convective velocity scale,  $z_i$  is the convective boundary layer height, and  $\beta = 1$ .

3507 The value of  $z_i$  is taken as 1000 m

## 3508 (2) Flux-gradient relations [Zeng et al., 1998]

3509 The flux-gradient relations are given by:

$$\frac{k(z_1 - d)}{\theta_*} \frac{\partial \theta}{\partial z} = \phi_h(\varsigma) \quad (4.260)$$

$$\frac{k(z_1 - d)}{q_*} \frac{\partial q}{\partial z} = \phi_q(\varsigma) \quad (4.261)$$

$$\phi_h = \phi_q \quad (4.262)$$

$$\phi_m(\varsigma) = \begin{cases} (1 - 16\varsigma)^{-1/4} & \text{for } \varsigma < 0 \\ 1 + 5\varsigma & \text{for } 0 < \varsigma < 1 \end{cases} \quad (4.263)$$

$$\phi_h(\varsigma) = \begin{cases} (1 - 16\varsigma)^{-1/2} & \text{for } \varsigma < 0 \\ 1 + 5\varsigma & \text{for } 0 < \varsigma < 1 \end{cases} \quad (4.264)$$

Under very unstable conditions, the flux-gradient relations are taken from [Kader and Yaglom \[1990\]](#):

$$\phi_m = 0.7k^{2/3}(-\varsigma)^{1/3} \quad (4.265)$$

$$\phi_h = 0.9k^{4/3}(-\varsigma)^{-1/3} \quad (4.266)$$

3510 To ensure the functions  $\phi_m(\varsigma)$  and  $\phi_h(\varsigma)$  are continuous, the simplest approach (i.e., without  
3511 considering any transition regions) is to match the above equations at  $\varsigma_m = -1.574$  for  $\phi_m(\varsigma)$   
3512 and  $\varsigma_h = -0.465$  for  $\phi_h(\varsigma)$ .

Under very stable conditions (i.e.,  $\varsigma > 1$ ), the relations are taken from [Holtslag et al. \[1990\]](#):

$$\phi_m = \phi_h = 5 + \varsigma \quad (4.267)$$

3513 **(3) Integral forms of the flux-gradient relations**

Integration of the wind profile yields:

$$V_a = \frac{u_*}{k} f_M(\varsigma) \quad (4.268)$$

$$f_M(\varsigma) = \left\{ \left[ \ln \left( \frac{\varsigma_m L}{z_{0m}} \right) - \psi_m(\varsigma_m) \right] + 1.14 [(-\varsigma)^{1/3} - (-\varsigma_m)^{1/3}] \right\}, \quad \varsigma < \varsigma_m = -1.574 \quad (4.268a)$$

$$f_M(\varsigma) = \left[ \ln \left( \frac{z_1 - d}{z_{0m}} \right) - \psi_m(\varsigma) + \psi_m \left( \frac{z_{0m}}{L} \right) \right], \quad \varsigma_m < \varsigma < 0 \quad (4.268b)$$

$$f_M(\varsigma) = \left[ \ln \left( \frac{z_1 - d}{z_{0m}} \right) + 5\varsigma \right], \quad 0 < \varsigma < 1 \quad (4.268c)$$

$$f_M(\varsigma) = \left\{ \left[ \ln \left( \frac{L}{z_{0m}} \right) + 5 \right] + [5 \ln(\varsigma) + \varsigma - 1] \right\}, \quad \varsigma > 1 \quad (4.268d)$$

Integration of the potential temperature profile yields:

$$\theta_1 - \theta_s = \frac{\theta_*}{k} f_T(\varsigma) \quad (4.269)$$

$$f_T(\varsigma) = \left\{ \left[ \ln \left( \frac{\varsigma_h L}{z_{0h}} \right) - \psi_h(\varsigma_h) \right] + 0.8 [(-\varsigma_h)^{-1/3} - (-\varsigma)^{-1/3}] \right\}, \quad \varsigma < \varsigma_h = -0.465 \quad (4.269a)$$

$$f_T(\varsigma) = \left[ \ln \left( \frac{z_1 - d}{z_{0h}} \right) - \psi_h(\varsigma) + \psi_h \left( \frac{z_{0h}}{L} \right) \right], \quad \varsigma_h < \varsigma < 0 \quad (4.269b)$$

$$f_T(\varsigma) = \left[ \ln \left( \frac{z_1 - d}{z_{0h}} \right) + 5\varsigma \right], \quad 0 < \varsigma < 1 \quad (4.269c)$$

$$f_T(\varsigma) = \left\{ \left[ \ln \left( \frac{L}{z_{0h}} \right) + 5 \right] + [5 \ln(\varsigma) + \varsigma - 1] \right\}, \quad \varsigma > 1 \quad (4.269d)$$

The expressions for the specific humidity profiles are the same as those for potential temperature except that  $(\theta_1 - \theta_s)$ ,  $\theta_*$  and  $z_{0h}$  are replaced by  $(q_1 - q_s)$ ,  $q_*$  and  $z_{0q}$  respectively. The stability functions for  $\varsigma < 0$  are

$$\psi_m = 2 \ln \left( \frac{1 + \chi}{2} \right) + \ln \left( \frac{1 + \chi^2}{2} \right) - 2 \tan^{-1} \chi + \frac{\pi}{2} \quad (4.270)$$

$$\psi_h = \psi_q = 2 \ln \left( \frac{1 + \chi^2}{2} \right) \quad (4.271)$$

where

$$\chi = (1 - 16\varsigma)^{1/4} \quad (4.272)$$

3514 Note that the CLM code contains extra terms involving  $z_{0m}/\varsigma$ ,  $z_{0h}/\varsigma$ , and  $z_{0q}/\varsigma$  for completeness. These terms are very small most of the time and hence are omitted in Eqs. 4.268 and  
 3515 4.269.

3517 In addition to the momentum, sensible heat, and latent heat fluxes, land surface albedos  
 3518 and upward longwave radiation are needed for the atmospheric radiation calculations. Surface  
 3519 albedos depend on the solar zenith angle, the amount of leaf and stem material present, their  
 3520 optical properties, and the optical properties of snow and soil. The upward longwave radiation  
 3521 is the difference between the incident and absorbed fluxes. These and other aspects of the land  
 3522 surface fluxes have been described by [Dai et al. \[2001\]](#).

### 3523 4.11.2 Ocean

The bulk formulas used to determine the turbulent fluxes of momentum (stress), water (evaporation, or latent heat), and sensible heat into the atmosphere over ocean surfaces are

$$(\boldsymbol{\tau}, E, H) = \rho_A |\Delta \mathbf{v}| (C_D \Delta \mathbf{v}, C_E \Delta q, C_p C_H \Delta \theta), \quad (4.273)$$

3524 where  $\rho_A$  is atmospheric surface density and  $C_p$  is the specific heat. Since CAM 5.0 does not  
 3525 allow for motion of the ocean surface, the velocity difference between surface and atmosphere  
 3526 is  $\Delta \mathbf{v} = \mathbf{v}_A$ , the velocity of the lowest model level. The potential temperature difference  
 3527 is  $\Delta \theta = \theta_A - T_s$ , where  $T_s$  is the surface temperature. The specific humidity difference is  
 3528  $\Delta q = q_A - q_s(T_s)$ , where  $q_s(T_s)$  is the saturation specific humidity at the sea-surface temperature.

In (4.273), the transfer coefficients between the ocean surface and the atmosphere are computed at a height  $Z_A$  and are functions of the stability,  $\zeta$ :

$$C_{(D,E,H)} = \kappa^2 \left[ \ln \left( \frac{Z_A}{Z_{0m}} \right) - \psi_m \right]^{-1} \left[ \ln \left( \frac{Z_A}{Z_{0(m,e,h)}} \right) - \psi_{(m,s,s)} \right]^{-1} \quad (4.274)$$

where  $\kappa = 0.4$  is von Kármán's constant and  $Z_{0(m,e,h)}$  is the roughness length for momentum, evaporation, or heat, respectively. The integrated flux profiles,  $\psi_m$  for momentum and  $\psi_s$  for scalars, under stable conditions ( $\zeta > 0$ ) are

$$\psi_m(\zeta) = \psi_s(\zeta) = -5\zeta. \quad (4.275)$$

For unstable conditions ( $\zeta < 0$ ), the flux profiles are

$$\begin{aligned} \psi_m(\zeta) = & 2 \ln[0.5(1 + X)] + \ln[0.5(1 + X^2)] \\ & - 2 \tan^{-1} X + 0.5\pi, \end{aligned} \quad (4.276)$$

$$\psi_s(\zeta) = 2 \ln[0.5(1 + X^2)], \quad (4.277)$$

$$X = (1 - 16\zeta)^{1/4}. \quad (4.278)$$

The stability parameter used in (4.275)–(4.278) is

$$\zeta = \frac{\kappa g Z_A}{u^{*2}} \left( \frac{\theta^*}{\theta_v} + \frac{Q^*}{(\epsilon^{-1} + q_A)} \right), \quad (4.279)$$

where the virtual potential temperature is  $\theta_v = \theta_A(1 + \epsilon q_A)$ ;  $q_A$  and  $\theta_A$  are the lowest level atmospheric humidity and potential temperature, respectively; and  $\epsilon = 0.606$ . The turbulent velocity scales in (4.279) are

$$\begin{aligned} u^* &= C_D^{1/2} |\Delta \mathbf{v}|, \\ (Q^*, \theta^*) &= C_{(E,H)} \frac{|\Delta \mathbf{v}|}{u^*} (\Delta q, \Delta \theta). \end{aligned} \quad (4.280)$$

Over oceans,  $Z_{0e} = 9.5 \times 10^{-5}$  m under all conditions and  $Z_{0h} = 2.2 \times 10^{-9}$  m for  $\zeta > 0$ ,  $Z_{0h} = 4.9 \times 10^{-5}$  m for  $\zeta \leq 0$ , which are given in [Large and Pond \[1982\]](#). The momentum roughness length depends on the wind speed evaluated at 10 m as

$$\begin{aligned} Z_{om} &= 10 \exp \left[ -\kappa \left( \frac{c_4}{U_{10}} + c_5 + c_6 U_{10} \right)^{-1} \right], \\ U_{10} &= U_A \left[ 1 + \frac{\sqrt{C_{10}^N}}{\kappa} \ln \left( \frac{Z_A}{10} - \psi_m \right) \right]^{-1}, \end{aligned} \quad (4.281)$$

3529 where  $c_4 = 0.0027$  m s<sup>-1</sup>,  $c_5 = 0.000142$ ,  $c_6 = 0.0000764$  m<sup>-1</sup> s, and the required drag coefficient  
3530 at 10-m height and neutral stability is  $C_{10}^N = c_4 U_{10}^{-1} + c_5 + c_6 U_{10}$  as given by [Large et al. \[1994\]](#).

3531 The transfer coefficients in (4.273) and (4.274) depend on the stability following (4.275)–  
3532 (4.278), which itself depends on the surface fluxes (4.279) and (4.280). The transfer coefficients  
3533 also depend on the momentum roughness, which itself varies with the surface fluxes over oceans  
3534 (4.281). The above system of equations is solved by iteration.

### 3535 4.11.3 Sea Ice

3536 The fluxes between the atmosphere and sea ice are described in detail in the sea-ice model  
3537 documentation.

3538

## 4.12 Dry Adiabatic Adjustment

If a layer is unstable with respect to the dry adiabatic lapse rate, dry adiabatic adjustment is performed. The layer is stable if

$$\frac{\partial T}{\partial p} < \frac{\kappa T}{p}. \quad (4.282)$$

In finite-difference form, this becomes

$$T_{k+1} - T_k < C1_{k+1}(T_{k+1} + T_k) + \delta, \quad (4.283)$$

where

$$C1_{k+1} = \frac{\kappa(p_{k+1} - p_k)}{2p_{k+1/2}}. \quad (4.284)$$

If there are any unstable layers in the top three model layers, the temperature is adjusted so that (4.283) is satisfied everywhere in the column. The variable  $\delta$  represents a convergence criterion. The adjustment is done so that sensible heat is conserved,

$$c_p(\hat{T}_k \Delta p_k + \hat{T}_{k+1} \Delta p_{k+1}) = c_p(T_k \Delta p_k + T_{k+1} \Delta p_{k+1}), \quad (4.285)$$

and so that the layer has neutral stability:

$$\hat{T}_{k+1} - \hat{T}_k = C1_{k+1}(\hat{T}_{k+1} + \hat{T}_k). \quad (4.286)$$

As mentioned above, the hats denote the variables after adjustment. Thus, the adjusted temperatures are given by

$$\hat{T}_{k+1} = \frac{\Delta p_k}{\Delta p_{k+1} + \Delta p_k C2_{k+1}} T_k + \frac{\Delta p_{k+1}}{\Delta p_{k+1} + \Delta p_k C2_{k+1}} T_{k+1}, \quad (4.287)$$

and

$$\hat{T}_k = C2_{k+1} \hat{T}_{k+1}, \quad (4.288)$$

where

$$C2_{k+1} = \frac{1 - C1_{k+1}}{1 + C1_{k+1}}. \quad (4.289)$$

Whenever the two layers undergo dry adjustment, the moisture is assumed to be completely mixed by the process as well. Thus, the specific humidity is changed in the two layers in a conserving manner to be the average value of the original values,

$$\hat{q}_{k+1} = \hat{q}_k = (q_{k+1} \Delta p_{k+1} + q_k \Delta p_k) / (\Delta p_{k+1} + \Delta p_k). \quad (4.290)$$

3539 The layers are adjusted iteratively. Initially,  $\delta = 0.01$  in the stability check (4.283). The column  
 3540 is passed through from  $k = 1$  to a user-specifiable lower level (set to 3 in the standard model  
 3541 configuration) up to 15 times; each time unstable layers are adjusted until the entire column is  
 3542 stable. If convergence is not reached by the 15th pass, the convergence criterion is doubled, a  
 3543 message is printed, and the entire process is repeated. If  $\delta$  exceeds 0.1 and the column is still  
 3544 not stable, the model stops.

3545 As indicated above, the dry convective adjustment is only applied to the top three levels  
 3546 of the standard model. The vertical diffusion provides the stabilizing vertical mixing at other  
 3547 levels. Thus, in practice, momentum is mixed as well as moisture and potential temperature in  
 3548 the unstable case.

## 3549 4.13 Prognostic Greenhouse Gases

3550 The principal greenhouse gases whose longwave radiative effects are included in CAM 5.0 are  
3551  $\text{H}_2\text{O}$ ,  $\text{CO}_2$ ,  $\text{O}_3$ ,  $\text{CH}_4$ ,  $\text{N}_2\text{O}$ , CFC11, and CFC12. The prediction of water vapor is described  
3552 elsewhere in this chapter, and  $\text{CO}_2$  is assumed to be well mixed. Monthly  $\text{O}_3$  fields are specified  
3553 as input, as described in chapter 6. The radiative effects of the other four greenhouse gases  
3554 ( $\text{CH}_4$ ,  $\text{N}_2\text{O}$ , CFC11, and CFC12) may be included in CAM 5.0 through specified concentration  
3555 distributions [Kiehl et al., 1998] or prognostic concentrations [Boville et al., 2001].

3556 The specified distributions are globally uniform in the troposphere. Above a latitudinally  
3557 and seasonally specified tropopause height, the distributions are zonally symmetric and decrease  
3558 upward, with a separate latitude-dependent scale height for each gas.

3559 Prognostic distributions are computed following Boville et al. [2001]. Transport equations for  
3560 the four gases are included, and losses have been parameterized by specified zonally symmetric  
3561 loss frequencies:  $\partial q/\partial t = -\alpha(y, z, t)q$ . Monthly averaged loss frequencies,  $\alpha$ , are obtained from  
3562 the two-dimensional model of Garcia and Solomon [1994].

3563 We have chosen to specify globally uniform surface concentrations of the four gases, rather  
3564 than their surface fluxes. The surface sources are imperfectly known, particularly for  $\text{CH}_4$  and  
3565  $\text{N}_2\text{O}$  in preindustrial times. Even given constant sources and reasonable initial conditions, ob-  
3566 taining equilibrium values for the loading of these gases in the atmosphere can take many years.  
3567 CAM 5.0 was designed for tropospheric simulation with relatively coarse vertical resolution in  
3568 the upper troposphere and lower stratosphere. It is likely that the rate of transport into the  
3569 stratosphere will be misrepresented, leading to erroneous loading and radiative forcing if surface  
3570 fluxes are specified. Specifying surface concentrations has the advantage that we do not need  
3571 to worry much about the atmospheric lifetime. However, we cannot examine observed features  
3572 such as the interhemispheric gradient of the trace gases. For climate change experiments, the  
3573 specified surface concentrations are varied but the stratospheric loss frequencies are not.

3574 Oxidation of  $\text{CH}_4$  is an important source of water vapor in the stratosphere, contributing  
3575 about half of the ambient mixing ratio over much of the stratosphere. Although  $\text{CH}_4$  is not  
3576 generally oxidized directly into water vapor, this is not a bad approximation, as shown by  
3577 Le Texier et al. [1988]. In CAM 5.0, it is assumed that the water vapor (volume mixing ratio)  
3578 source is twice the  $\text{CH}_4$  sink. This approach was also taken by Mote et al. [1993] for middle  
3579 atmosphere studies with an earlier version of the CCM. This part of the water budget is of  
3580 some importance in climate change studies, because the atmospheric  $\text{CH}_4$  concentrations have  
3581 increased rapidly with time and this increase is projected to continue into the next century (e.g.,  
3582 Alcamo et al. [1995]). The representation of stratospheric water vapor in CAM 5.0 is necessar-  
3583 ily crude, since there are few levels above the tropopause. However, the model is capable of  
3584 capturing the main features of the  $\text{CH}_4$  and water distributions.



3585 Chapter 5

3586 Extensions to CAM

3587 **5.1 Chemistry**

3588 **5.1.1 Introduction**

3589 In this Section, we provide a description of the neutral constituent chemical processes adopted  
3590 in CAM-chem and WACCM4.0. This section will contain a description of constituent: 1) surface  
3591 boundary conditions; 2) numerical algorithms used to solve the corresponding set of ordinary  
3592 differential equations. 3) gas-phase and heterogeneous reactions; and 4) wet and dry deposition  
3593 removal processes;

3594 **5.1.2 Emissions**

3595 Surface emissions are used in as a flux boundary condition for the diffusion equation of all  
3596 applicable tracers in the planetary boundary-layer scheme. The surface flux files used in the  
3597 released version are discussed in [Lamarque et al. \[2010b\]](#) and conservatively remapped from their  
3598 original resolution (monthly data available every decade at 0.5x0.5) to (monthly data every year  
3599 at 1.9x2.5). In addition, natural emissions from MOZART-4 were added to all relevant species.  
3600 Finally, isoprene emissions are calculated interactively (within CLM (point 2) above), leading  
3601 to approximately (emissions depend on light and temperature) 500 Tg/year.

	Anthro.	Natural	Interactive
CH <sub>2</sub> O	x	x	
CO	x	x	
DMS		x	
ISOP			x
NO	x		
SO <sub>2</sub>	x		

Table 5.1: Surface fluxes for CAM4 superfast chemistry.

3602 Additional emissions (volcanoes and aircraft) are included as three-dimension arrays,  
3603 conservatively-remapped to the CAM-chem grid. The volcanic emission are from [Dentener et al.](#)  
3604 [\[2006b\]](#) and the aircraft (NO<sub>2</sub>) emissions are from [Lamarque et al. \[2010b\]](#). In the case of vol-  
3605 canic emissions (SO<sub>2</sub> and SO<sub>2</sub>), an assumed 2% of the total sulfur mass is directly released as  
3606 SO<sub>2</sub>.

3607 **5.1.3 Lower boundary conditions**

3608 The concentration of specific long-lived chemical tracers (methane and longer lifetimes, in addi-  
3609 tion to hydrogen and methyl bromide) are fixed in the lowest model layer using the reconstructed  
3610 concentrations (CMIP5 recommended data) available from  
3611 <http://www.iiasa.ac.at/web-apps/tnt/RcpDb/dsd?Action=htmlpage&page=download>. As this  
3612 dataset only provides annual average values, a specified seasonal cycle (based on present-day  
3613 observations) is added to methane and carbon dioxide.

3614 **5.1.4 Lightning**

3615 The lightning parameterization differs slightly from that used in MOZART-2 [Horowitz et al.,  
3616 2003]. The lightning strength still depends on cloud top height, with a stronger dependence  
3617 over land than ocean [Price et al., 1997a]. The definition of ocean grid boxes has been refined  
3618 to include only boxes surrounded by ocean, so that the land parameterization is extended one  
3619 grid box beyond the continents Price and Rind [1992]. Flash frequency is determined by area,  
3620 not grid box. The vertical distribution of NO emissions has been modified from that given by  
3621 Pickering et al. [1998], to have a reduced proportion of the emissions emitted near the surface,  
3622 similar to that used by DeCaria et al. [2006]. In addition, the strength of intra-cloud (IC) light-  
3623 ning strikes is assumed to be equal to cloud-to-ground strikes, as recommended by Ridley et al.  
3624 [2005].

3625 Because the lightning NO source is very resolution-dependent, it can be scaled under non-  
3626 standard resolutions to a produce 5-7 Tg(N)/year globally.

3627 **5.1.5 Dry deposition**

3628 The list of species affected by dry deposition is subject to user selection. Dry deposition ve-  
3629 locities are computed interactively (i.e. are influenced by variations in temperature, solar in-  
3630 solation and precipitation), based on the resistance-based parameterization of Wesely [1989],  
3631 Walmsley and Wesely [1996], and Wesely and Hicks [2000]. The calculation of surface resis-  
3632 tances over land uses the vegetation distribution as defined in CLM. In addition, as the pa-  
3633 rameters in the Wesely [1989] parameterization are season-dependent (to take into account the  
3634 specific role of changes in vegetation cover), a season index is computed from the monthly-  
3635 averaged leaf-area index input file to CLM. In the case of CLM-CN or DGVM (where the LAI  
3636 is prognostic), this file is still read and seasonality is still defined accordingly. Deposition over  
3637 the ocean is computed separately in CAM (but using the same formulation), with the overall  
3638 deposition velocity computed as the weighted (by the land/ocean fraction) mean between the  
3639 land and ocean values.

3640 The deposition velocity calculation has been extended from the aforementioned references  
3641 to take into account special cases for CO, H<sub>2</sub> and PAN. In the case of CO and H<sub>2</sub>, surface  
3642 uptake is caused by the oxidation by soil bacteria or enzymes [Yonemura et al., 2000]. This has  
3643 been parameterized using the approach of Sanderson et al. [2003], which defines the deposition  
3644 velocity by a linear or quadratic function in soil moisture content (or its logarithm), depending  
3645 on the land cover type. In the case of PAN, new laboratory experiments have indicated a strong  
3646 uptake of PAN by leaves [Teklemariam and Sparks, 2004]. Using the results from that study,  
3647 we have included a leaf uptake of PAN that is vegetation-dependent, based on Sparks et al.  
3648 (2003). Results from this parameterization agreed with observations during a field experiment  
3649 [Turnipseed et al., 2006].

3650 **5.1.6 Wet removal**

3651 Wet deposition for gas-phase species is represented as a first-order loss process within the chem-  
3652 istry operator, with loss rates computed based on the large-scale and convective precip-  
3653 itation rates in CAM. Soluble species (H<sub>2</sub>O<sub>2</sub>, HNO<sub>3</sub>, CH<sub>2</sub>O, SO<sub>2</sub>) undergo wet removal by in-

3654 cloud scavenging, using the parameterization of [Giorgi and Chameides \[1985\]](#) based on their  
3655 temperature-dependent effective Henry's law constants. In addition, highly soluble species  
3656 ( $\text{HNO}_3$ ,  $\text{H}_2\text{O}_2$ ) are also removed by below-cloud washout, using the formulation described in  
3657 detail by [Brasseur et al. \[1998\]](#).

### 3658 5.1.7 Photolytic Approach (Neutral Species)

3659 The calculation of the photolysis coefficients is divided into two regions: (1) 120 nm to 200 nm  
3660 (33 wavelength intervals); (2) 200 nm to 750 nm (67 wavelength intervals). The total photolytic  
3661 rate constant ( $J$ ) for each absorbing species is derived during model execution by integrating the  
3662 product of the wavelength dependent exo-atmospheric flux ( $F_{exo}$ ); the atmospheric transmission  
3663 function (or normalized actinic flux) ( $N_A$ ), which is unity at the top of atmosphere in most wave-  
3664 length regions; the molecular absorption cross-section ( $\sigma$ ); and the quantum yield ( $\phi$ ). The exo-  
3665 atmospheric flux over these wavelength intervals can be specified from observations and varied  
3666 over the 11-year solar sunspot cycle (see section [5.3.6](#)). The wavelength-dependent transmission  
3667 function is derived as a function of the model abundance of ozone and molecular oxygen. For  
3668 wavelengths greater than 200 nm a normalized flux lookup table (LUT) approach is used, based  
3669 on the 4-stream version of the Stratosphere, Troposphere, Ultraviolet (STUV) radiative transfer  
3670 model (S. Madronich, personal communication). The transmission function is interpolated from  
3671 the LUT as a function of altitude, column ozone, surface albedo, and zenith angle. The tem-  
3672 perature and pressure dependences of the molecular cross sections and quantum yields for each  
3673 photolytic process are also represented by a LUT in this wavelength region. At wavelengths  
3674 less than 200 nm, the wavelength-dependent cross section and quantum yields for each species  
3675 are specified and the transmission function is calculated explicitly for each wavelength interval.  
3676 There are two exceptions to this approach. In the case of  $J(\text{NO})$  and  $J(\text{O}_2)$ , detailed photolysis  
3677 parameterizations are included inline. In the Schumann-Runge Band region (SRBs), the param-  
3678 eterization of NO photolysis in the  $\delta$ -bands is based on [Minschwaner and Siskind \[1993\]](#). This  
3679 parameterization includes the effect of self-absorption and subsequent attenuation of atmospheric  
3680 transmission by the model-derived NO concentration. For  $J(\text{O}_2)$ , the SRB and Lyman-alpha pa-  
3681 rameterizations are based on [Koppers and Murtagh \[1996\]](#) and [Chabriat and Kockarts \[1997\]](#),  
3682 respectively.

3683 The photolytic reactions included in WACCM4.0 are listed in Table 4. In most all cases the  
3684 photolytic rate constants are taken from JPL02-25 [\[Sander, S. P., et al., 2003\]](#). Exceptions to  
3685 this condition are described in the comment section for any given reaction.

3686 In addition, tropospheric photolysis rates can be computed interactively following [Tie et al.](#)  
3687 [\[1992\]](#). Users interested in using this capability have to contact the Chemistry-CLimate Working  
3688 Group Liaison as this is an unsupported option.

### 3689 5.1.8 Numerical Solution Approach

Chemical and photochemical processes are expressed by a system of time-dependent ordinary  
differential equations at each point in the spatial grid, of the following form:

$$\frac{d\vec{y}}{dt} = \vec{P}(\vec{y}, t) - \vec{L}(\vec{y}, t) \cdot \vec{y} \quad (5.1)$$

$$\vec{y}(t) = \{y_i(t)\} \quad i = 1, 2, \dots, N$$

where  $\vec{y}$  is the vector of all solution variables (chemical species),  $N$  is the number of variables in the system, and  $y_i$  represents the  $i^{th}$  variable.  $\vec{P}$  and  $\vec{L}$  represent the production and loss rates, which are, in general, non-linear functions of the  $y_i$ . This system of equations is solved via two algorithms: an explicit forward Euler method:

$$y_i^{n+1} = y_i^n + \Delta t \cdot f_i(t_n, y^n) \quad (5.2)$$

in the case of species with long lifetimes and weak forcing terms (e.g.,  $\text{N}_2\text{O}$ ), and a more robust implicit backward Euler method:

$$y_i^{n+1} = y_i^n + \Delta t \cdot f_i(t_{n+1}, y^{n+1}) \quad (5.3)$$

for species that comprise a “stiff system” with short lifetimes and strong forcings (e.g.,  $\text{OH}$ ). Here  $n$  represents the time step index. Each method is first order accurate in time and conservative. The overall chemistry time step,  $\Delta t = t_{n+1} - t_n$ , is fixed at 30 minutes. Preprocessing software requires the user to assign each solution variable,  $y_i$ , to one of the solution schemes. The discrete analogue for methods (5.2) and (5.3) above results in two systems of algebraic equations at each grid point. The solution to these algebraic systems for equation (5.2) is straightforward (i.e., explicit). The algebraic system from the implicit method (5.3) is quadratically non-linear. This system can be written as:

$$\vec{G}(\vec{y}^{n+1}) = \vec{y}^{n+1} - \vec{y}^n - \Delta t \cdot \vec{f}(t_{n+1}, \vec{y}^{n+1}) = 0 \quad (5.4)$$

Here  $G$  is an  $N$ -valued, non-linear vector function, where  $N$  equals the number of species solved via the implicit method. The solution to equation (5.4) is solved with a Newton- Raphson iteration approach as shown below:

$$\vec{y}_{m+1}^{n+1} = \vec{y}_m^{n+1} - \vec{J} \cdot \vec{G}(\vec{y}_m^{n+1}); \quad m = 0, 1, \dots, M \quad (5.5)$$

Where  $m$  is the iteration index and has a maximum value of ten. The elements of the Jacobian matrix  $\vec{J}$  are given by:

$$J_{ij} = \frac{\partial G_i}{\partial y_j}$$

3690 The iteration and solution of equation (5.5) is carried out with a sparse matrix solution al-  
 3691 gorithm. This process is terminated when the given solution variable changes in a relative  
 3692 measure by less than a prescribed fractional amount. This relative error criterion is set on a  
 3693 species by species basis, and is typically 0.001; however, for some species (e.g.,  $\text{O}_3$ ), where a  
 3694 tighter error criterion is desired, it is set to 0.0001. If the iteration maximum is reached (for  
 3695 any species) before the error criterion is met, the time step is cut in half and the solution to  
 3696 equation (5.5) is iterated again. The time step can be reduced five times before the solution is  
 3697 accepted. This approach is based on the work of [Sandu et al. \[1996\]](#) and [Sandu et al. \[1997\]](#); see  
 3698 also [Brasseur et al. \[1999\]](#).

3699 **5.2 Superfast Chemistry**

3700 **5.2.1 Chemical mechanism**

3701 The super-fast mechanism was developed for coupled climate model usage, and is based on  
3702 an updated version of the full non-methane hydrocarbon effects (NMHC) chemical mechanism  
3703 for the troposphere and stratosphere used in the Lawrence Livermore National Laboratory off-  
3704 line 3D global chemistry-transport model (IMPACT) [Rotman et al., 2004]. The super-fast  
3705 mechanism includes 15 photochemically active trace species ( $O_3$ , OH,  $HO_2$ ,  $H_2O_2$ , NO,  $NO_2$ ,  
3706  $HNO_3$ , CO,  $CH_2O$ ,  $CH_3O_2$ ,  $CH_3OOH$ , DMS,  $SO_2$ ,  $SO_4$ , and  $C_5H_8$ ) that allow us to calculate the  
3707 major terms by which global change operates in tropospheric ozone and sulfate photochemistry.  
3708 The families selected are Ox, HOx, NOy, the  $CH_4$  oxidation suite plus isoprene (to capture the  
3709 main NMHC effects), and a group of sulfur species to simulate natural and anthropogenic sources  
3710 leading to sulfate aerosol. Sulfate aerosols is handled following [Tie et al. \[2005\]](#). In this scheme,  
3711  $CH_4$  concentrations are read in from a file and uses CAM3.5 simulations [Lamarque et al. \[2010b\]](#).  
3712 The super-fast mechanism was validated by comparing the super-fast and full mechanisms in  
3713 side-by-side simulations.

3714 **5.2.2 LINOZ**

3715 Linoz is linearized ozone chemistry for stratospheric modeling [[McLinden et al., 2000](#)]. It cal-  
3716 culates the net production of ozone (i.e., production minus loss) as a function of only three  
3717 independent variables: local ozone concentration, temperature, and overhead column ozone).  
3718 A zonal mean climatology for these three variables as well as the other key chemical variables  
3719 such a total odd-nitrogen methane abundance is developed from satellite and other in situ ob-  
3720 servations. A relatively complete photochemical box model [Prather \[1992\]](#) is used to integrate  
3721 the radicals to a steady state balance and then compute the net production of ozone. Small  
3722 perturbations about the chemical climatology are used to calculate the coefficients of the first-  
3723 order Taylor series expansion of the net production in terms of local ozone mixing ratio ( $f$ ),  
3724 temperature ( $T$ ), and overhead column ozone ( $c$ ).

$$\begin{aligned} \frac{df}{df} &= (P - L)^o + \frac{\delta(P - L)}{\delta f} \bigg|_o (f - f^o) + \frac{\delta(P - L)}{\delta T} \bigg|_o (T - T^o) \\ &\quad + \frac{\delta(P - L)}{\delta c} \bigg|_o (c - c^o) \end{aligned} \quad (5.6)$$

3725 The photochemical tendency for the climatology is denoted by  $(P - L)_o$ , and the climatology  
3726 values for the independent variables are denoted by  $f_o$ ,  $c_o$ , and  $T_o$ , respectively. Including these  
3727 four climatology values and the three partial derivatives, Linoz is defined by seven tables. Each  
3728 table is specified by 216 atmospheric profiles: 12 months by 18 latitudes ( $85^{\circ}S$  to  $85^{\circ}N$ ). For  
3729 each profile, quantities are evaluated at every 2 km in pressure altitude from  $z^* = 10$  to 58 km  
3730 ( $z^* = 16 \text{ km } \log_{10}(1000/p)$ ). These tables (calculated for each decade, 1850-2000 to take into  
3731 account changes in  $CH_4$  and  $N_2O$ ) are automatically remapped onto the CAM-chem grid with  
3732 the mean vertical properties for each CAM-chem level calculated as the mass-weighted average

3733 of the interpolated Linoz profiles. Equation (1) is implemented for the chemical tendency of  
3734 ozone in CAM-chem.

3735 **5.2.3 PSC ozone loss**

3736 In the superfast chemistry, we incorporate the PSCs parameterization scheme of [Cariolle et al.](#)  
3737 [[1990](#)] when the temperature falls below 195 K and the sun is above the horizon at stratospheric  
3738 altitudes. The  $O_3$  loss scales as the squared stratospheric chlorine loading (normalized by the  
3739 1980 level threshold). In this formulation PSC activation invokes a rapid e-fold of  $O_3$  based  
3740 on a photochemical model, but only when the temperature stays below the PSC threshold.  
3741 The stratospheric chlorine loading (1850-2005) is input in the model using equivalent effective  
3742 stratospheric chlorine (EESC) [[Newman et al., 2007](#)] table based on observed mixing ratios at  
3743 the surface.

3744 **5.2.4 Upper boundary condition**

3745 The model top is considered a rigid lid (no flux across that boundary) for all chemical species.

## 3746 5.3 WACCM4.0 Physical Parameterizations

3747 In WACCM4.0, we extend the physical parameterizations used in CAM4 by adding constituent  
3748 separation velocities to the molecular (vertical) diffusion and modifying the gravity spectrum  
3749 parameterization. Both of these parameterizations are present, but not used, in CAM4. In  
3750 addition, we replace the CAM4 parameterizations for both solar and longwave radiation above  
3751  $\sim 65$  km, and add neutral and ion chemistry models.

### 3752 5.3.1 WACCM4.0 Domain and Resolution

WACCM4.0 has 66 vertical levels from the ground to  $5.1 \times 10^{-6}$  hPa, as in the previous WACCM  
versions. As in CAM4, the vertical coordinate is purely isobaric above 100 hPa, but is terrain  
following below that level. At any model grid point, the local pressure  $p$  is determined by

$$p(i, j, k) = A(k) p_0 + B(k) p_s(i, j) \quad (5.7)$$

3753 where  $A$  and  $B$  are functions of model level,  $k$ , only;  $p_0 = 10^3$  hPa is a reference surface pressure;  
3754 and  $p_s$  is the predicted surface pressure, which is a function of model longitude and latitude  
3755 (indexed by  $i$  and  $j$ ). The finite volume dynamical core uses locally material surfaces for its  
3756 internal vertical coordinate and remaps (conservatively interpolates) to the hybrid surfaces after  
3757 each time step.

Within the physical and chemical parameterizations, a local pressure coordinate is used, as  
described by (5.7). However, in the remainder of this note we refer to the vertical coordinate in  
terms of log-pressure altitude

$$Z = H \log \left( \frac{p_0}{p} \right). \quad (5.8)$$

3758 The value adopted for the scale height,  $H = 7$  km, is representative of the real atmosphere up to  
3759  $\sim 100$  km, above that altitude temperature increases very rapidly and the typical scale height  
3760 becomes correspondingly larger. It is important to distinguish  $Z$  from the *geopotential* height  
3761  $z$ , which is obtained from integration of the hydrostatic equation.

3762 In terms of log-pressure altitude, the model top level is found at  $Z = 140$  km ( $z \simeq 150$  km).  
3763 It should be noted that the solution in the top 15-20 km of the model is undoubtedly affected  
3764 by the presence of the top boundary. However, it should not be thought of as a *sponge layer*,  
3765 since molecular diffusion is a real process and is the primary damping on upward propagating  
3766 waves near the model top. Indeed, this was a major consideration in moving the model top  
3767 well above the turbopause. Considerable effort has been expended in formulating the upper  
3768 boundary conditions to obtain realistic solutions near the model top and all of the important  
3769 physical and chemical processes for that region have been included.

3770 The standard vertical resolution is variable; it is 3.5 km above about 65 km, 1.75 km around  
3771 the stratopause (50 km), 1.1-1.4 km in the lower stratosphere (below 30 km), and 1.1 km in  
3772 the troposphere (except near the ground where much higher vertical resolution is used in the  
3773 planetary boundary layer).

3774 Two standard horizontal resolutions are supported in WACCM4.0: the  $4 \times 5^\circ$  (latitude  $\times$   
3775 longitude) low resolution version has 72 longitude and 46 latitude points; the  $1.9 \times 2.5^\circ$  medium  
3776 resolution version has 96 longitude and 144 latitude points. A  $0.9 \times 1.25^\circ$  high resolution

3777 version of WACCM4.0 has had limited testing, and is not yet supported, due to computational  
 3778 cost constraints. The  $4 \times 5^\circ$  version has been used extensively for MLT studies, where it gives  
 3779 very similar results to the  $1.9 \times 2.5^\circ$  version. However, caution should be exercised in using  
 3780  $4 \times 5^\circ$  results below the stratopause, since the meridional resolution may not be sufficient to  
 3781 represent adequately the dynamics of either the polar vortex or synoptic and planetary waves.

3782 At all resolutions, the time step is 1800 s for the physical parameterizations. Within the finite  
 3783 volume dynamical core, this time step is subdivided as necessary for computational stability.

### 3784 5.3.2 Molecular Diffusion and Constituent Separation

3785 The vertical diffusion parameterization in CAM4 provides the interface to the turbulence pa-  
 3786 rameterization, computes the molecular diffusivities (if necessary) and finally computes the ten-  
 3787 dencies of the input variables. The diffusion equations are actually solved implicitly, so the ten-  
 3788 dencies are computed from the difference between the final and initial profiles. In WACCM4.0,  
 3789 we extend this parameterization to include the terms required for the gravitational separation  
 3790 of constituents of differing molecular weights. The formulation for molecular diffusion follows  
 3791 [Banks and Kockarts \[1973\]](#)

A general vertical diffusion parameterization can be written in terms of the divergence of diffusive fluxes:

$$\frac{\partial}{\partial t}(u, v, q) = -\frac{1}{\rho} \frac{\partial}{\partial z}(F_u, F_v, F_q) \quad (5.9)$$

$$\frac{\partial}{\partial t}s = -\frac{1}{\rho} \frac{\partial}{\partial z}F_H + D \quad (5.10)$$

where  $s = c_p T + gz$  is the dry static energy,  $z$  is the geopotential height above the local surface (does not include the surface elevation) and  $D$  is the heating rate due to the dissipation of resolved kinetic energy in the diffusion process. The diffusive fluxes are defined as:

$$F_{u,v} = -\rho K_m \frac{\partial}{\partial z}(u, v), \quad (5.11)$$

$$F_H = -\rho K_H \frac{\partial s}{\partial z} + \rho K_H^t \gamma_H, \quad (5.12)$$

$$F_q = -\rho K_q \frac{\partial q}{\partial z} + \rho K_q^t \gamma_q + \text{sep-flux.} \quad (5.13)$$

The viscosity  $K_m$  and diffusivities  $K_{q,H}$  are the sums of: turbulent components  $K_{m,q,H}^t$ , which dominate below the mesopause; and molecular components  $K_{m,q,H}^m$ , which dominate above 120 km. The non-local transport terms  $\gamma_{q,H}$  are given by the ABL parameterization and the kinetic energy dissipation is

$$D \equiv -\frac{1}{\rho} \left( F_u \frac{\partial u}{\partial z} + F_v \frac{\partial v}{\partial z} \right). \quad (5.14)$$

3792 The treatment of the turbulent diffusivities  $K_{m,q,H}^t$ , the energy dissipation  $D$  and the nonlocal  
 3793 transport terms  $\gamma_{H,q}$  is described in the CAM 5.0 Technical Description and will be omitted  
 3794 here.

3795 **Molecular viscosity and diffusivity**

The empirical formula for the molecular kinematic viscosity is

$$K_m^m = 3.55 \times 10^{-7} T^{2/3} / \rho, \quad (5.15)$$

and the molecular diffusivity for heat is

$$K_H^m = P_r K_m^m, \quad (5.16)$$

where  $P_r$  is the Prandtl number and we assume  $P_r = 1$  in WACCM4.0. The constituent diffusivities are

$$K_q^m = T^{1/2} M_w / \rho, \quad (5.17)$$

3796 where  $M_w$  is the molecular weight.

3797 **Diffusive separation velocities**

3798 As the mean free path increases, constituents of different molecular weights begin to separate  
3799 in the vertical. In WACCM4.0, this separation is represented by a separation velocity for each  
3800 constituent with respect mean air. Since WACCM4.0 extends only into the lower thermosphere,  
3801 we avoid the full complexity of the separation problem and represent mean air by the usual dry  
3802 air mixture used in the lower atmosphere ( $M_w = 28.966$ ) [Banks and Kockarts \[1973\]](#).

3803 **Discretization of the vertical diffusion equations**

In CAM4, as in previous version of the CCM, (5.9–5.12) are cast in pressure coordinates, using

$$dp = -\rho g dz, \quad (5.18)$$

and discretized in a time-split form using an Euler backward time step. Before describing the numerical solution of the diffusion equations, we define a compact notation for the discrete equations. For an arbitrary variable  $\psi$ , let a subscript denote a discrete time level, with current step  $\psi_n$  and next step  $\psi_{n+1}$ . The model has  $L$  layers in the vertical, with indexes running from top to bottom. Let  $\psi^k$  denote a layer midpoint quantity and let  $\psi^{k\pm}$  denote the value at the interface above (below)  $k$ . The relevant quantities, used below, are then:

$$\begin{aligned} \psi^{k+} &= (\psi^k + \psi^{k+1})/2, & k \in (1, 2, 3, \dots, L-1) \\ \psi^{k-} &= (\psi^{k-1} + \psi^k)/2, & k \in (2, 3, 4, \dots, L) \\ \delta^k \psi &= \psi^{k+} - \psi^{k-}, \\ \delta^{k+} \psi &= \psi^{k+1} - \psi^k, \\ \delta^{k-} \psi &= \psi^k - \psi^{k-1}, \\ \psi_{n+} &= (\psi_n + \psi_{n+1})/2, \\ \delta_n \psi &= \psi_{n+1} - \psi_n, \\ \delta t &= t_{n+1} - t_n, \\ \Delta^{k,l} &= 1, \quad k = l, \\ &= 0, \quad k \neq l. \end{aligned}$$

Like the continuous equations, the discrete equations are required to conserve momentum, total energy and constituents. Neglecting the nonlocal transport terms, the discrete forms of (5.9–5.10) are:

$$\frac{\delta_n(u, v, q)^k}{\delta t} = g \frac{\delta^k F_{u,v,q}}{\delta^k p} \quad (5.19)$$

$$\frac{\delta_n s^k}{\delta t} = g \frac{\delta^k F_H}{\delta^k p} + D^k. \quad (5.20)$$

For interior interfaces,  $1 \leq k \leq L - 1$ ,

$$F_{u,v}^{k+} = (g\rho^2 K_m)_n^{k+} \frac{\delta^{k+}(u, v)_{n+1}}{\delta^{k+} p} \quad (5.21)$$

$$F_{q,H}^{k+} = (g\rho^2 K_{q,H})_n^{k+} \frac{\delta^{k+}(u, v)_{n+1}}{\delta^{k+} p}. \quad (5.22)$$

3804 Surface fluxes  $F_{u,v,q,H}^{L+}$  are provided explicitly at time  $n$  by separate surface models for land,  
 3805 ocean, and sea ice while the top boundary fluxes are usually  $F_{u,v,q,H}^{1-} = 0$ . The turbulent  
 3806 diffusion coefficients  $K_{m,q,H}^t$  and non-local transport terms  $\gamma_{q,H}$  are calculated for time  $n$  by the  
 3807 turbulence model (identical to CAM4). The molecular diffusion coefficients, given by (5.15–5.17)  
 3808 are also evaluated at time  $n$ .

### 3809 Solution of the vertical diffusion equations

3810 Neglecting the discretization of  $K_{m,q,H}^t$ ,  $D$  and  $\gamma_{q,H}$ , a series of time-split operators is defined by  
 3811 (5.19–5.22). Once the diffusivities ( $K_{m,q,H}$ ) and the non-local transport terms ( $\gamma_{q,H}$ ) have been  
 3812 determined, the solution of (5.19–5.22), proceeds in several steps.

- 3813 1. update the bottom level values of  $u$ ,  $v$ ,  $q$  and  $s$  using the surface fluxes;  
 3814 2. invert (5.19) and (5.21) for  $u, v_{n+1}$ ;  
 3815 3. compute  $D$  and use to update the  $s$  profile;  
 3816 4. invert (5.19,5.20) and (5.22) for  $s_{n+1}$  and  $q_{n+1}$

3817 Note that since all parameterizations in CAM4 return tendencies rather modified profiles,  
 3818 the actual quantities returned by the vertical diffusion are  $\delta_n(u, v, s, q)/\delta t$ .

Equations (5.19–5.22) constitute a set of four tridiagonal systems of the form

$$-A^k \psi_{n+1}^{k+1} + B^k \psi_{n+1}^k - C^k \psi_{n+1}^{k-1} = \psi_{n'}^k, \quad (5.23)$$

where  $\psi_{n'}$  indicates  $u$ ,  $v$ ,  $q$ , or  $s$  after updating from time  $n$  values with the nonlocal and boundary fluxes. The super-diagonal ( $A^k$ ), diagonal ( $B^k$ ) and sub-diagonal ( $C^k$ ) elements of (5.23) are:

$$A^k = \frac{1}{\delta^k p} \frac{\delta t}{\delta^{k+} p} (g^2 \rho^2 K)_n^{k+}, \quad (5.24)$$

$$B^k = 1 + A^k + C^k, \quad (5.25)$$

$$C^k = \frac{1}{\delta^k p} \frac{\delta t}{\delta^{k-} p} (g^2 \rho^2 K)_n^{k-}. \quad (5.26)$$

The solution of (5.23) has the form

$$\psi_{n+1}^k = E^k \psi_{n+1}^{k-1} + F^k, \quad (5.27)$$

or,

$$\psi_{n+1}^{k+1} = E^{k+1} \psi_{n+1}^k + F^{k+1}. \quad (5.28)$$

Substituting (5.28) into (5.23),

$$\psi_{n+1}^k = \frac{C^k}{B^k - A^k E^{k+1}} \psi_{n+1}^{k-1} + \frac{\psi_{n+1}^k + A^k F^{k+1}}{B^k - A^k E^{k+1}}. \quad (5.29)$$

Comparing (5.27) and (5.29), we find

$$E^k = \frac{C^k}{B^k - A^k E^{k+1}}, \quad L > k > 1, \quad (5.30)$$

$$F^k = \frac{\psi_{n+1}^k + A^k F^{k+1}}{B^k - A^k E^{k+1}}, \quad L > k > 1. \quad (5.31)$$

The terms  $E^k$  and  $F^k$  can be determined upward from  $k = L$ , using the boundary conditions

$$E^{L+1} = F^{L+1} = A^L = 0. \quad (5.32)$$

Finally, (5.29) can be solved downward for  $\psi_{n+1}^k$ , using the boundary condition

$$C^1 = 0 \Rightarrow E^1 = 0. \quad (5.33)$$

CCM1-3 used the same solution method, but with the order of the solution reversed, which merely requires writing (5.28) for  $\psi_{n+1}^{k-1}$  instead of  $\psi_{n+1}^{k+1}$ . The order used here is particularly convenient because the turbulent diffusivities for heat and all constituents are the same but their molecular diffusivities are not. Since the terms in (5.30-5.31) are determined from the bottom upward, it is only necessary to recalculate  $A^k$ ,  $C^k$ ,  $E^k$  and  $1/(B^k - A^k E^{k+1})$  for each constituent within the region where molecular diffusion is important.

### 5.3.3 Gravity Wave Drag

Vertically propagating gravity waves can be excited in the atmosphere where stably stratified air flows over an irregular lower boundary and by internal heating and shear. These waves are capable of transporting significant quantities of horizontal momentum between their source regions and regions where they are absorbed or dissipated. Previous GCM results have shown that the large-scale momentum sinks resulting from breaking gravity waves play an important role in determining the structure of the large-scale flow. CAM4 incorporates a parameterization for a spectrum of vertically propagating internal gravity waves based on the work of [Lindzen \[1981\]](#), [Holton \[1982\]](#), [Garcia and Solomon \[1985\]](#) and [McFarlane \[1987\]](#). The parameterization solves separately for a general spectrum of monochromatic waves and for a single stationary wave generated by flow over orography, following [McFarlane \[1987\]](#). The spectrum is omitted in the standard tropospheric version of CAM4, as in previous versions of the CCM. Here we describe the modified version of the gravity wave spectrum parameterization used in WACCM4.0.

3838 **Adiabatic inviscid formulation**

Following Lindzen [1981], the continuous equations for the gravity wave parameterization are obtained from the two-dimensional hydrostatic momentum, continuity and thermodynamic equations in a vertical plane:

$$\left( \frac{\partial}{\partial t} + u \frac{\partial}{\partial x} \right) u = - \frac{\partial \Phi}{\partial x}, \quad (5.34)$$

$$\frac{\partial u}{\partial x} + \frac{\partial W}{\partial Z} = 0, \quad (5.35)$$

$$\left( \frac{\partial}{\partial t} + u \frac{\partial}{\partial x} \right) \frac{\partial \Phi}{\partial Z} + N^2 w = 0. \quad (5.36)$$

Where  $N$  is the local Brunt-Väisälä frequency, and  $W$  is the vertical velocity in log pressure height ( $Z$ ) coordinates. Eqs. (5.34)–(5.36) are linearized about a large scale background wind  $\bar{u}$ , with perturbations  $u', w'$ , and combined to obtain:

$$\left( \frac{\partial}{\partial t} + \bar{u} \frac{\partial}{\partial x} \right)^2 \frac{\partial^2 w'}{\partial Z^2} + N^2 \frac{\partial^2 w'}{\partial x^2} = 0. \quad (5.37)$$

Solutions to (5.37) are assumed to be of the form:

$$w' = \hat{w} e^{ik(x-ct)} e^{Z/2H}, \quad (5.38)$$

where  $H$  is the scale height,  $k$  is the horizontal wavenumber and  $c$  is the phase speed of the wave. Substituting (5.38) into (5.37), one obtains:

$$-k^2(\bar{u} - c)^2 \left( \frac{\partial}{\partial Z} + \frac{1}{2H} \right)^2 \hat{w} - k^2 N^2 \hat{w} = 0. \quad (5.39)$$

Neglecting  $\frac{1}{2H}$  compared to  $\frac{\partial}{\partial Z}$  in (5.39), one obtains the final form of the two dimensional wave equation:

$$\frac{d^2 \hat{w}}{dZ^2} + \lambda^2 \hat{w} = 0, \quad (5.40)$$

with the coefficient defined as:

$$\lambda = \frac{N}{(\bar{u} - c)}. \quad (5.41)$$

The WKB solution of (5.40) is:

$$\hat{w} = A \lambda^{-1/2} \exp \left( i \int_0^Z \lambda dz' \right), \quad (5.42)$$

and the full solution, from (5.38), is:

$$w'(Z, t) = A \lambda^{-1/2} \exp \left( i \int_0^Z \lambda dz' \right) e^{ik(x-ct)} e^{Z/2H}. \quad (5.43)$$

The constant  $A$  is determined from the wave amplitude at the source ( $z = 0$ ), The Reynolds stress associated with (5.43) is:

$$\tau(Z) = \tau(0) = \rho \overline{u'w'} = -\frac{2}{k} |A|^2 \rho_0 \text{sgn}(\lambda), \quad (5.44)$$

and is conserved, while the momentum flux  $\overline{u'w'} = -(m/k) \overline{w'w'}$  grows exponentially with altitude as  $\exp(Z/H)$ , per (5.43). We note that the vertical flux of wave energy is  $c_{gz} E' = (U - c) \tau$  (Andrews et al. [1987]), where  $c_{gz}$  is the vertical group velocity, so that deposition of wave momentum into the mean flow will be accompanied by a transfer of energy to the background state.

#### 3844 Saturation condition

The wave amplitude in (5.43) grows as  $e^{Z/2H}$  until the wave becomes unstable to convective overturning, Kelvin-Helmholtz instability, or other nonlinear processes. At that point, the wave amplitude is assumed to be limited to the amplitude that would trigger the instability and the wave is “saturated”. The saturation condition used in CAM4 is from McFarlane [1987], based on a maximum Froude number ( $F_c$ ), or streamline slope.

$$|\rho \overline{u'w'}| \leq \tau^* = F_c^2 \frac{k}{2} \rho \frac{|\overline{u} - c|^3}{N}, \quad (5.45)$$

where  $\tau^*$  is the saturation stress and  $F_c^2 = 0.5$ . In WACCM4.0,  $F_c^2 = 1$  and is omitted hereafter. Following Lindzen [1981], within a saturated region the momentum tendency can be determined analytically from the divergence of  $\tau^*$ :

$$\begin{aligned} \frac{\partial \overline{u}}{\partial t} &= -\frac{e}{\rho} \frac{\partial}{\partial Z} \rho \overline{u'w'}, \\ &\simeq -e \frac{k}{2} \frac{(\overline{u} - c)^3}{N} \frac{1}{\rho} \frac{\partial \rho}{\partial Z}, \\ &\simeq -e \frac{k}{2} \frac{(\overline{u} - c)^3}{NH}, \end{aligned} \quad (5.46)$$

where  $e$  is an “efficiency” factor. For a background wave spectrum,  $e$  represents the temporal and spatial intermittency in the wave sources. The analytic solution (5.46) is not used in WACCM4.0; it is shown here to illustrate how the acceleration due to breaking gravity waves depends on the intrinsic phase speed. In the model, the stress profile is computed at interfaces and differenced to get the specific force at layer midpoints.

#### 3850 Diffusive damping

In addition to breaking as a result of instability, vertically propagating waves can also be damped by molecular diffusion (both thermal and momentum) or by radiative cooling. Because the intrinsic periods of mesoscale gravity waves are short compared to IR relaxation time scales throughout the atmosphere, we ignore radiative damping. We take into account the molecular viscosity,  $K_m^m$ , such that the stress profile is given by:

$$\tau(Z) = \tau(Z_t) \exp \left( -\frac{2}{H} \int_0^Z \lambda_i dz' \right), \quad (5.47)$$

where  $Z_t$  denotes the top of the region, below  $Z$ , not affected by thermal dissipation or molecular diffusion. The imaginary part of the local vertical wavenumber,  $\lambda_i$  is then:

$$\lambda_i = \frac{N^3 K_m^m}{2k(\bar{u} - c)^4}. \quad (5.48)$$

3851 In WACCM4.0, (5.47–5.48) are only used within the domain where molecular diffusion is im-  
 3852 portant (above  $\sim 75$  km). At lower altitudes, molecular diffusion is negligible,  $\lambda_i \rightarrow 0$ , and  $\tau$  is  
 3853 conserved outside of saturation regions.

### 3854 Transport due to dissipating waves

When the wave is dissipated, either through saturation or diffusive damping, there is a transfer of wave momentum and energy to the background state. In addition, a phase shift is introduced between the wave's vertical velocity field and its temperature and constituent perturbations so that fluxes of heat and constituents are nonzero within the dissipation region. The nature of the phase shift and the resulting transport depends on the dissipation mechanism; in WACCM4.0, we assume that the dissipation can be represented by a linear damping on the potential temperature and constituent perturbations. For potential temperature,  $\theta$ , this leads to:

$$\left( \frac{\partial}{\partial t} + \bar{u} \frac{\partial}{\partial x} \right) \theta' + w' \frac{\partial \bar{\theta}}{\partial z} = -\delta \theta', \quad (5.49)$$

where  $\delta$  is the dissipation rate implied by wave breaking, which depends on the wave's group velocity,  $c_{gz}$  (see [Garcia \[2001\]](#)):

$$\delta = \frac{c_{gz}}{2H} = k \frac{(\bar{u} - c)^2}{2HN}. \quad (5.50)$$

Substitution of (5.50) into (5.49) then yields the eddy heat flux:

$$\overline{w' \theta'} = - \left[ \frac{\delta \overline{w' w'}}{k^2(\bar{u} - c)^2 + \delta^2} \right] \frac{\partial \bar{\theta}}{\partial z}. \quad (5.51)$$

3855 Similar expressions can be derived for the flux of chemical constituents, with mixing ratio sub-  
 3856 stituted in place of potential temperature in (5.51). We note that these wave fluxes are al-  
 3857 ways downgradient and that, for convenience of solution, they may be represented as vertical  
 3858 diffusion, with coefficient  $K_{zz}$  equal to the term in brackets in (5.51), but they do not repre-  
 3859 sent turbulent diffusive fluxes but rather eddy fluxes. Any additional turbulent fluxes due to  
 3860 wave breaking are ignored. To take into account the effect of localization of turbulence (e.g.,  
 3861 [Fritts and Dunkerton \[1985\]](#); [McIntyre \[1989\]](#)), (5.51) is multiplied times an inverse Prandtl  
 3862 number,  $Pr^{-1}$ ; in WACCM4.0 we use  $Pr^{-1} = 0.25$ .

### 3863 Heating due to wave dissipation

The vertical flux of wave energy density,  $E'$ , is related to the stress according to:

$$c_{gz} E' = (\bar{u} - c) \tau, \quad (5.52)$$

where  $c_{gz}$  is the vertical group velocity [Andrews et al., 1987]. Therefore, the stress divergence  $\partial\tau/\partial Z$  that accompanies wave breaking implies a loss of wave energy. The rate of dissipation of wave energy density is:

$$\frac{\partial E'}{\partial t} \simeq (\bar{u} - c) \frac{1}{c_{gz}} \frac{\partial \tau}{\partial t} = (\bar{u} - c) \frac{\partial \tau}{\partial Z} . \quad (5.53)$$

For a saturated wave, the stress divergence is given by (5.46), so that:

$$\frac{\partial E'}{\partial t} = (\bar{u} - c) \frac{\partial \tau^*}{\partial Z} = -e \cdot \rho \frac{k (U - c)^4}{2NH} . \quad (5.54)$$

This energy loss by the wave represents a heat source for the background state, as does the change in the background kinetic energy density implied by wave drag on the background flow:

$$\frac{\partial \bar{K}}{\partial t} \equiv \frac{\rho}{2} \frac{\partial \bar{u}^2}{\partial t} = \bar{u} \frac{\partial \tau^*}{\partial Z} = -e \cdot \rho \frac{k \bar{u} (\bar{u} - c)^3}{2NH} , \quad (5.55)$$

which follows directly from (5.46). The background heating rate, in K sec<sup>-1</sup>, is then:

$$Q_{gw} = -\frac{1}{\rho c_p} \left[ \frac{\partial \bar{K}}{\partial t} + \frac{\partial E'}{\partial t} \right] . \quad (5.56)$$

Using (5.54) – (5.55), this heating rate may be expressed as:

$$Q_{gw} = \frac{1}{\rho c_p} c \frac{\partial \tau^*}{\partial Z} = \frac{1}{c_p} \left[ e \cdot \frac{k c (c - \bar{u})^3}{2NH} \right] , \quad (5.57)$$

where  $c_p$  is the specific heat at constant pressure. In WACCM4.0,  $Q_{gw}$  is calculated for each component of the gravity wave spectrum using the first equality in (5.57), i.e., the product of the phase velocity times the stress divergence.

### Orographic source function

For orographically generated waves, the source is taken from [McFarlane \[1987\]](#):

$$\tau_g = |\rho \bar{u}' \bar{w}'|_0 = \frac{k}{2} h_0^2 \rho_0 N_0 \bar{u}_0 , \quad (5.58)$$

where  $h_0$  is the streamline displacement at the source level, and  $\rho_0$ ,  $N_0$ , and  $\bar{u}_0$  are also defined at the source level. For orographic waves, the subgrid-scale standard deviation of the orography  $\sigma$  is used to estimate the average mountain height, determining the typical streamline displacement. An upper bound is used on the displacement (equivalent to defining a “separation streamline”) which corresponds to requiring that the wave not be supersaturated at the source level:

$$h_0 = \min(2\sigma, \frac{\bar{u}_0}{N_0}) . \quad (5.59)$$

The source level quantities  $\rho_0$ ,  $N_0$ , and  $\bar{u}_0$  are defined by vertical averages over the source region, taken to be  $2\sigma$ , the depth to which the average mountain penetrates into the domain:

$$\psi_0 = \int_0^{2\sigma} \psi \rho dz, \quad \psi \in \{\rho, N, u, v\} . \quad (5.60)$$

The source level wind vector  $(u_0, v_0)$  determines the orientation of the coordinate system in (5.34)–(5.36) and the magnitude of the source wind  $\bar{u}_0$ .

3870 **Non-orographic source functions**

3871 The source spectrum for non-orographic gravity waves is no longer assumed to be a specified  
 3872 function of location and season, as was the case with the earlier version of the model described  
 3873 by [Garcia et al. \[2007\]](#). Instead, gravity waves are launched according to trigger functions that  
 3874 depend on the atmospheric state computed in WACCM4 at any given time and location, as  
 3875 discussed by [Richter et al. \[2010\]](#). Two trigger functions are used: convective heat release (which  
 3876 is a calculated model field) and a “frontogenesis function”, [Hoskins \[1982\]](#), which diagnoses  
 3877 regions of strong wind field deformation and temperature gradient using the horizontal wind  
 3878 components and potential temperature field calculated by the model.

3879 In the case of convective excitation, the method of [Beres et al. \[2005\]](#) is used to determine a  
 3880 phase speed spectrum based upon the properties of the convective heating field. A spectrum is  
 3881 launched whenever the deep convection parameterization in WACCM4 is active, and the vertical  
 3882 profile of the convective heating, together with the mean wind field in the heating region, are  
 3883 used to determine the phase speed spectrum of the momentum flux. Convectively generated  
 3884 waves are launched at the top of the convective region (which varies according to the depth of  
 3885 the convective heating calculated in the model).

Waves excited by frontal systems are launched whenever the frontogenesis trigger function exceeds a critical value (see [Richter et al. \[2010\]](#)). The waves are launched from a constant source level, which is specified to be 600 mb. The momentum flux phase speed spectrum is given by a Gaussian function in phase speed:

$$\tau_s(c) = \tau_b \exp \left[ - \left( \frac{c - V_s}{c_w} \right)^2 \right], \quad (5.61)$$

centered on the source wind,  $V_s = |\mathbf{V}_s|$ , with width  $c_w = 30$  m/s. A range of phase speeds with specified width and resolution is used:

$$c \in V_s + [\pm d_c, \pm 2d_c, \dots \pm c_{max}], \quad (5.62)$$

3886 with  $d_c = 2.5$  m s<sup>-1</sup> and  $c_{max} = 80$  m s<sup>-1</sup>, giving 64 phase speeds. Note that  $c = V_s$  is retained  
 3887 in the code for simplicity, but has a critical level at the source and, therefore,  $\tau_s(c = V_s) = 0$ .  
 3888 Note also that  $\tau_b$  is a tunable parameter; in practice this is set such that the height of the polar  
 3889 mesopause, which is very sensitive to gravity wave driving, is consistent with observations. In  
 3890 WACCM4,  $\tau_b = 1.5 \times 10^{-3}$  Pa.

Above the source region, the saturation condition is enforced separately for each phase speed,  $c_i$ , in the momentum flux spectrum:

$$\tau(c_i) \leq \tau_i^* = F_c^2 \frac{k}{2} \rho \frac{|\bar{u} - c_i|^3}{N}. \quad (5.63)$$

3891 **Numerical approximations**

The gravity wave drag parameterization is applied immediately after the nonlinear vertical diffusion. The interface Brunt-Väisällä frequency is

$$(N^{k+})^2 = \frac{g^2}{T^{k+}} \left( \frac{1}{c_p} - \rho^{k+} \frac{\delta^{k+} T}{\delta^{k+} p} \right), \quad (5.64)$$

Where the interface density is:

$$\rho^{k+} = \frac{RT^{k+}}{p^{k+}}. \quad (5.65)$$

3892 The midpoint Brunt-Väisällä frequencies are  $N^k = (N^{k+} + N^{k-})/2$ .

3893 The level for the orographic source is an interface determined from an estimate of the vertical  
 3894 penetration of the subgrid mountains within the grid box. The subgrid scale standard deviation  
 3895 of the orography,  $\sigma_h$ , gives the variation of the mountains about the mean elevation, which  
 3896 defines the Earth's surface in the model. Therefore the source level is defined as the interface,  
 3897  $k_s - 1/2$ , for which  $z^{k_s+} < 2\sigma_h < z^{k_s-}$ , where the interface heights are defined from the midpoint  
 3898 heights by  $z^{k+} = \sqrt{(z^k z^{k+1})}$ .

The source level wind vector, density and Brunt-Väisällä frequency are determined by vertical integration over the region from the surface to interface  $k_s + 1/2$ :

$$\psi_0 = \sum_{k=k_s}^K \psi^k \delta^k p, \quad \psi \in \{\rho, N, u, v\}. \quad (5.66)$$

The source level background wind is  $\bar{u}_0 = \sqrt{(u_0^2 + v_0^2)}$ , the unit vector for the source wind is

$$(x_0, y_0) = (u_0, v_0)/\bar{u}_0, \quad (5.67)$$

and the projection of the midpoint winds onto the source wind is

$$\bar{u}^k = u^k x_0 + v^k y_0. \quad (5.68)$$

3900 Assuming that  $\bar{u}_0 > 2 \text{ m s}^{-1}$  and  $2\sigma_h > 10 \text{ m}$ , then the orographic source term,  $\tau_g$  is given  
 3901 by (5.58) and (5.59), with  $F_c^2 = 1$  and  $k = 2\pi/10^5 \text{ m}^{-1}$ . Although the code contains a provision  
 3902 for a linear stress profile within a “low level deposition region”, this part of the code is not used  
 3903 in the standard model.

3904 The stress profiles are determined by scanning up from the bottom of the model to the top.  
 3905 The stress at the source level is determined by (5.58). The saturation stress,  $\tau_\ell^*$  at each interface  
 3906 is determined by (5.63), and  $\tau_\ell^* = 0$  if a critical level is passed. A critical level is contained  
 3907 within a layer if  $(\bar{u}^{k+} - c_\ell)/(\bar{u}^{k-} - c_\ell) < 0$ .

Within the molecular diffusion domain, the imaginary part of the vertical wavenumber is given by (5.48). The interface stress is then determined from the stress on the interface below by:

$$\tau^{k-} = \min \left[ (\tau^*)^{k-}, \tau^{k+} \exp \left( -2\lambda_i \frac{R}{g} T^k \delta^k \ln p \right) \right]. \quad (5.69)$$

3907 Below the molecular diffusion domain, the exponential term in (5.69) is omitted.

Once the complete stress profile has been obtained, the forcing of the background wind is determined by differentiating the profile during a downward scan:

$$\frac{\partial \bar{u}_\ell^k}{\partial t} = g \frac{\delta^k \tau_\ell}{\delta^k p} < \left( \frac{\partial \bar{u}_\ell^k}{\partial t} \right)^{\max}. \quad (5.70)$$

$$\left( \frac{\partial \bar{u}_\ell^k}{\partial t} \right)^{\max} = \min \left[ \frac{|c_\ell - \bar{u}_\ell^k|}{2\delta t}, 500 \text{ m s}^{-1} \text{ day}^{-1} \right]. \quad (5.71)$$

3908 The first bound on the forcing comes from requiring that the forcing not be large enough to  
 3909 push the wind more than half way towards a critical level within a time step and takes the place  
 3910 of an implicit solution. This bound is present for numerical stability, it comes into play when  
 3911 the time step is too large for the forcing. It is not feasible to change the time step, or to write  
 3912 an implicit solver, so an *a priori* bound is used instead. The second bound is used to constrain  
 3913 the forcing to lie within a physically plausible range (although the value used is extremely large)  
 3914 and is rarely invoked.

When any of the bounds in (5.70) are invoked, conservation of stress is violated. In this case, stress conservation is ensured by decreasing the stress on the lower interface to match the actual stress divergence in the layer:

$$\tau_{\ell}^{k+} = \tau_{\ell}^{k-} + \frac{\partial \bar{u}^k}{\partial t} \frac{\delta^k p}{g}. \quad (5.72)$$

3915 This has the effect of pushing some of the stress divergence into the layer below, a reasonable  
 3916 choice since the waves are propagating up from below.

Finally, the vector momentum forcing by the gravity waves is determined by projecting the background wind forcing with the unit vectors of the source wind:

$$\frac{\partial \mathbf{V}^k}{\partial t} = (x_0, y_0) \times E \sum_{\ell} \frac{\partial \bar{u}_{\ell}^k}{\partial t}. \quad (5.73)$$

3917 In addition, the frictional heating implied by the momentum tendencies,  $\frac{1}{c_p} \mathbf{V}^k \cdot \partial \mathbf{V}^k / \partial t$ , is  
 3918 added to the thermodynamic equation. This is the correct heating for orographic ( $c_{\ell} = 0$ )  
 3919 waves, but not for waves with  $c_{\ell} \neq 0$ , since it does not account for the wave energy flux. This  
 3920 flux is accounted for in some middle and upper atmosphere versions of CAM4, but also requires  
 3921 accounting for the energy flux at the source.

### 3922 5.3.4 Turbulent Mountain Stress

3923 An important difference between WACCM4 and earlier versions is the addition of surface stress  
 3924 due to unresolved orography. A numerical model can compute explicitly only surface stresses  
 3925 due to resolved orography. At the standard  $1.9^{\circ} \times 2.5^{\circ}$  (longitude x latitude) resolution used  
 3926 by WACCM4 only the gross outlines of major mountain ranges are resolved. To address this  
 3927 problem, unresolved orography is parameterized as turbulent surface drag, using the concept  
 3928 of effective roughness length developed by [Fiedler and Panofsky \[1972\]](#). Fiedler and Panofsky  
 3929 defined the roughness length for heterogeneous terrain as the roughness length that homogenous  
 3930 terrain would have to give the correct surface stress over a given area. The concept of effective  
 3931 roughness has been used in several Numerical Weather Prediction models (e.g., [Wilson \[2002\]](#);  
 3932 [Webster et al. \[2003\]](#)).

In WACCM4 the effective roughness stress is expressed as:

$$\tau = \rho C_d |\mathbf{V}| \mathbf{V}, \quad (5.74)$$

where  $\rho$  is the density and  $C_d$  is a turbulent drag coefficient,

$$C_d = \frac{f(R_i) k^2}{\ln^2 \left[ \frac{z+z_0}{z_0} \right]}, \quad (5.75)$$

3933  $k$  is von Kármán's constant;  $z$  is the height above the surface;  $z_0$  is an effective roughness length,  
3934 defined in terms of the standard deviation of unresolved orography; and  $f(R_i)$  is a function of  
3935 the Richardson number (see Richter et al. [2010] for details).

3936 The stress calculated by (5.74) is used the model's nonlocal PBL scheme to evaluate the  
3937 PBL height and nonlocal transport, per Eqs. (3.10)(3.12) of Holstlag and Boville [1993]. This  
3938 calculation is carried out only over land, and only in grid cells where the height of topography  
3939 above sea level,  $z$ , is nonzero.

### 3940 5.3.5 QBO Forcing

3941 WACCM4 has several options for forcing a quasi-biennial oscillation (QBO) by applying a  
3942 momentum forcing in the tropical stratosphere. The parameterization relaxes the simulated  
3943 winds to a specified wind field that is either fixed or varies with time. The parameterization can  
3944 also be turned off completely. The namelist variables and input files can be selected to choose  
3945 one of the following options:

- 3946 • Idealized QBO East winds, used for perpetual fixed-phase of the QBO, as described by  
3947 Matthes et al. [2010].
- 3948 • Idealized QBO West winds, as above but for the west phase.
- 3949 • Repeating idealized 28-month QBO, also described by Matthes et al. [2010].
- 3950 • QBO for the years 1953-2004 based on the climatology of Giorgetta [see:  
3951 [http://www.pa.op.dlr.de/CCMVal/Forcings/qbo\\_data\\_ccmval/u\\_profile\\_195301-200412.html](http://www.pa.op.dlr.de/CCMVal/Forcings/qbo_data_ccmval/u_profile_195301-200412.html),  
3952 2004].
- 3953 • QBO with a 51-year repetition, based on the 1953-2004 climatology of Giorgetta, which  
3954 can be used for any calendar year, past or future.

3955 The relaxation of the zonal wind is based on Balachandran and Rind [1995] and is described  
3956 in Matthes et al. [2010]. The input winds are specified at the equator and the parameterization  
3957 extends latitudinally from 22°N to 22°S, as a Gaussian function with a half width of 10° centered  
3958 at the equator. Full vertical relaxation extends from 86 to 4 hPa with a time constant of 10  
3959 days. One model level below and above this altitude range, the relaxation is half as strong and is  
3960 zero for all other levels. This procedure constrains the equatorial winds to more realistic values  
3961 while allowing resolved and parameterized waves to continue to propagate.

3962 The fixed or idealized QBO winds (first 3 options) can be applied for any calendar period.  
3963 The observed input (Giorgetta climatology) can be used only for the model years 1953-2004.  
3964 The winds in the final option were determined from the Giorgetta climatology for 1954-2004 via  
3965 filtered spectral decomposition of that climatology. This gives a set of Fourier coefficients that  
3966 can be expanded for any day and year. The expanded wind fields match the climatology during  
3967 the years 1954-2004.

### 3968 5.3.6 Radiation

3969 The radiation parameterizations in CAM4 are quite accurate up to  $\sim 65$  km, but deteriorate  
 3970 rapidly above that altitude. Because 65 km is near a local minimum in both shortwave heating  
 3971 and longwave cooling, it is a particularly convenient height to merge the heating rates from  
 3972 parameterizations for the lower and upper atmosphere. Therefore, we retain the CAM4 param-  
 3973 eterizations below  $\sim 65$  km and use new parameterizations above.

The merged shortwave and longwave radiative heatings are determined from

$$Q = w_1 Q_{CAM3} + w_2 Q_{MLT}, \quad (5.76)$$

where  $w_1(z^* < z_b^*) = 1$ ,  $w_2(z^* > z_t^*) = 1$  and  $z^* = \log(10^5/p)$  is the pressure scale height. The CAM4 radiation parameterizations are used below  $z_b^*$  and the MLT parameterizations are used above  $z_t^*$ . For  $z_b^* < z < z_t^*$ ,  $w_2 = 1 - w_1$  and

$$w_1 = 1 - \tanh\left(\frac{z^* - z_b^*}{z_w*}\right), \quad (5.77)$$

3974 where  $z_w*$  is the transition width.

3975 The merging was developed and tested separately for shortwave and longwave radiation and  
 3976 the constants are slightly different. For longwave radiation, the constants are  $z_b^* = 8.57$ ,  $z_t^* = 10$   
 3977 and  $z_w^* = 0.71$ . For shortwave radiation, the constants are  $z_b^* = 9$ ,  $z_t^* = 10$  and  $z_w^* = 0.75$ . These  
 3978 constants give smooth heating profiles. Note that a typical atmospheric scale height of  $H = 7$   
 3979 km places the transition zones between 60 and 70 km.

### 3980 Longwave radiation

3981 WACCM4.0 retains the longwave (LW) formulation used in CAM4 [Kiehl and Briegleb, 1991].  
 3982 However, in the MLT longwave radiation uses the parameterization of Fomichev et al. [1998]  
 3983 for CO<sub>2</sub> and O<sub>3</sub> cooling and the parameterization of Kockarts [1980] for NO cooling at 5.3  $\mu\text{m}$ .  
 3984 As noted above, the LW heating/cooling rates produced by these parameterizations are merged  
 3985 smoothly at 65 km with those produced by the standard CAM4 LW code, as recently revised  
 3986 by Collins et al. [2002]. In the interactive chemistry case all of the gases (O, O<sub>2</sub>, O<sub>3</sub>, N<sub>2</sub>, NO,  
 3987 and CO<sub>2</sub>) that are required by these parameterizations, are predicted within WACCM4.0.

### 3988 Shortwave radiation

3989 WACCM4.0 uses a combination of solar parameterizations to specify spectral irradiances over  
 3990 two spectral intervals. The first spectral interval covers soft x-ray and extreme ultraviolet  
 3991 irradiances (wavelengths between 0.05 nm to Lyman- $\alpha$  (121.6 nm)) and is calculated using the  
 3992 parameterization of Solomon and Qiang [2005]. The parameterizations take as input the 10.7  
 3993 cm solar radio flux ( $f10.7$ ) and its 81-day average ( $f10.7a$ ). Daily values of  $f10.7$  are obtained  
 3994 from NOAA's Space Environment Center ([www.sec.noaa.gov](http://www.sec.noaa.gov)).

The irradiance of the  $j$ th spectral interval is:

$$F_j = F_j^0 * \left\{ 1 + R_j * \left[ \frac{(f10.7 + f10.7a)}{2} - F_{min} \right] \right\} \quad (5.78)$$

3995 where  $F_{min} = 80$ .  $F_j^0$  and  $R_j$  are taken from Table A1 of [Solomon and Qiang \[2005\]](#).

3996 Fluxes for the second interval between Lyman- $\alpha$  (121.6 nm) and 100  $\mu$ m. are specified using  
 3997 an empirical model of the wavelength-dependent sunspot and facular influences [[Lean, 2000](#);  
 3998 [Wang et al., 2005](#)]. Spectral resolution is 1 nm between 121.6 nm and 750nm, 5 nm between  
 3999 750nm and 5  $\mu$ m, 10 nm between 5  $\mu$ m and 10  $\mu$ m, and 50 nm between 10  $\mu$ m and 100  $\mu$ m.

In the troposphere, stratosphere and lower mesosphere ( $z < 65$ km) WACCM4.0 retains the CAM4 shortwave heating (200 nm to 4.55  $\mu$ m) which is calculated from the net shortwave spectral flux into each layer [Collins et al. \[2004b\]](#). The solar spectrum for the CAM4 heating calculation is divided into 19 intervals [\[Collins, 1998\]](#). The heating in these intervals must be adjusted to match the irradiances calculated for the upper part of the model, and those used in the photolysis calculations. This is achieved by applying a scaling ( $S_j$ ) to the solar heating in the  $j$ th CAM4 spectral interval using the spectrum from [Lean \[2000\]](#) and [Wang et al. \[2005\]](#):

$$S_j = \frac{F_j}{F_j^{ref}}, \quad (5.79)$$

4000 where  $F_j$  is the spectral irradiance ( $\text{W/m}^2/\text{nm}$ ) integrated over the  $j$ th band, and  $F_j^{ref}$  is the  
 4001 same integral taken over a reference spectrum calculated from annual mean fluxes over a 3-solar-  
 4002 cycle period from XX to YY.

4003 In the MLT region, shortwave heating is the sum of the heating due to absorption of photons  
 4004 and subsequent exothermic chemical reactions that are initiated by photolysis. The majority  
 4005 of energy deposited by an absorbed photon goes into breaking molecular bonds, rather than  
 4006 into translational energy of the absorbing molecule (heat). Chemical heating results when con-  
 4007 stituents react to form products of lower total chemical potential energy. This heating can take  
 4008 place months after the original photon absorption and thousands of kilometers away. Heating  
 4009 rates range from 1 K/day near 75 km to 100-300 K/day near the top of the model domain. It  
 4010 is clear that quenching of  $O(^1D)$  is a large source of heating throughout the MLT. Above 100  
 4011 km ion reactions and reactions involving atomic nitrogen are significant sources of heat, while  
 4012 below that level  $O_X$  ( $= O + O_3$ ) and  $HO_X$  ( $= H + OH + HO_2$ ) reactions are the dominant  
 4013 producers of chemical heating.

Heating within the MLT from the absorption of radiation that is directly thermalized is calculated over the wavelength range of 0.05 nm to 350 nm. For wavelengths less than Lyman- $\alpha$ , it is assumed that 5% of the energy of each absorbed photon is directly thermalized:

$$Q_{EUV} = (\rho c_p)^{-1} \sum_k n_k \sum_j \epsilon J_k(\lambda_j) \frac{hc}{\lambda_j}, \quad (5.80)$$

4014 where  $\epsilon = 0.05$ . Here  $\rho$  is mass density,  $c_p$  is the specific heat of dry air,  $n$  is the number density  
 4015 of the absorbing species, and  $J$  is the photolysis/photoionization rate. The total heating is the  
 4016 sum of  $k$  photolysis reactions and  $j$  wavelengths intervals. At these wavelengths absorption of  
 4017 a photon typically leads to photoionization, with the resulting photoelectron having sufficient  
 4018 energy to ionize further molecules. Calculation of  $J_{ij}$  and ionization rates from photoelectrons  
 4019 is calculated based on the parameterization of [Solomon and Qiang \[2005\]](#). In a similar manner,  
 4020 the heating rate within the aurora ( $Q_{AUR}$ ) is calculated as the product of the total ionization  
 4021 rate, 35 eV per ion pair, and the same heating efficiency of 5%.

Between Lyman- $\alpha$  and 350 nm the energy required to break molecular bonds is explicitly accounted for. The heating rate is thus defined as:

$$Q_{UV} = (\rho c_p)^{-1} \sum_k n_k \sum_j J_k(\lambda_j) \left\{ \frac{hc}{\lambda_j} - BDE_k \right\}, \quad (5.81)$$

4022 where  $BDE$  is the bond dissociation energy.

4023 In addition to these sources of heat, WACCM4.0 calculates heating by absorption in the near-  
 4024 infrared by  $\text{CO}_2$  (between 1.05 to 4.3  $\mu\text{m}$ ), which has its largest contribution near 70km and  
 4025 can exceed 1 K/day [Fomichev et al., 2004]. Heating from this process is calculated using the  
 4026 parameterization of Ogibalov and Fomichev [2003]. Finally, the heating produced by collisions  
 4027 of electrons and neutrals (Joule heating) is also calculated using the predicted ion and electron  
 4028 concentrations. This is described in section 5.3.8. Local heating rates from joule heating can be  
 4029 very large in the auroral regions, reaching over  $10^3$ K/day in the upper levels of the model.

4030 Airglow, radiation produced when excited atoms or molecules spontaneously emit, is ac-  
 4031 counted for in WACCM4.0 for emissions of  $\text{O}_2(^1\Delta)$ ,  $\text{O}_2(^1\Sigma)$ , and vibrationally excited OH.  
 4032 Airglow from the excited molecular oxygen species are handled explicitly; radiative lifetimes for  
 4033  $\text{O}_2(^1\Delta)$  and  $\text{O}_2(^1\Sigma)$  are  $2.58 \times 10^{-4}$   $\text{s}^{-1}$  and  $0.085$   $\text{s}^{-1}$  respectively. However, modeling of the  
 4034 many possible vibrational transitions of OH is impractical in a model as large as WACCM4.0.  
 4035 Energy losses from the emission of vibrationally excited OH are therefore accounted for by  
 4036 applying an efficiency factor to the exothermicity of the reaction that produces vibrationally  
 4037 excited OH; the reaction of hydrogen and ozone. In other words, the reaction  $\text{H} + \text{O}_3$  produces  
 4038 ground state OH only, but the chemical heating from the reaction has been reduced to take  
 4039 into consideration that some of the chemical potential energy has been lost in airglow. This  
 4040 approach is the same one used by Mlynczak and Solomon [1993] and we use their recommended  
 4041 efficiency factor of 60%. Any energy lost through airglow is assumed to be lost to space, and so  
 4042 represents an energy pathway that does not generate heat.

## 4043 Volcanic Heating

4044 The sulfate aerosol heating is a function of a prescribed aerosol distribution varying in space  
 4045 and time that has a size distribution similar to that seen after a volcanic eruption [Tilmes et al.,  
 4046 2009]. The  $\text{H}_2\text{SO}_4$  mass distribution is calculated from the prescribed sulfate surface area density  
 4047 (SAD) assuming a lognormal size distribution, number of particles per  $\text{cm}^{-3}$ , and distribution  
 4048 width (see section 3.6.2). The  $\text{H}_2\text{SO}_4$  mass distribution is then passed to the radiative transfer  
 4049 code (CAMRT), which in turn calculates heating and cooling rates.

### 4050 5.3.7 WACCM4.0 chemistry

#### 4051 Chemical Mechanism (Neutral Species)

4052 WACCM4.0 includes a detailed neutral chemistry model for the middle atmosphere based on  
 4053 the Model for Ozone and Related Chemical Tracers, Version 3 [Kinnison et al., 2006]. The  
 4054 mechanism represents chemical and physical processes in the troposphere through the lower  
 4055 thermosphere. The species included within this mechanism are contained within the  $\text{O}_x$ ,  $\text{NO}_x$ ,  
 4056  $\text{HO}_x$ ,  $\text{ClO}_x$ , and  $\text{BrO}_x$  chemical families, along with  $\text{CH}_4$  and its degradation products. This

4057 mechanism contains 52 neutral species, one invariant ( $N_2$ ), 127 neutral gas-phase reactions, 48  
 4058 neutral photolytic reactions, and 17 heterogeneous reactions on three aerosol types (see below).  
 4059 Lists of the chemical species are given in Table 1. The first column lists the symbolic name  
 4060 (as used in the mechanism); the second column lists the species atomic composition; the third  
 4061 column designates which numerical solution approach is used (i.e., explicit or implicit); the  
 4062 fourth column lists any deposition processes (wet or dry) for that species; and the fifth column  
 4063 indicates whether the surface (or upper) boundary condition is fixed vmr or flux, or if a species  
 4064 has an in-situ flux (from lightning or aircraft emissions).

4065 The gas-phase reactions included in the WACCM4.0 middle atmosphere chemical mechanism  
 4066 are listed in Table 2. In most all cases the chemical rate constants are taken from JPL06-2  
 4067 [Sander, S. P., et al., 2006]. Exceptions to this condition are described in the comment section  
 4068 for any given reaction.

Heterogeneous reactions on four different aerosols types are also represented in the WACCM4.0 chemical mechanism (see Table 3): 1) liquid binary sulfate (LBS); 2) Supercooled ternary solution (STS); 3) Nitric acid trihydrate (NAT); and 4) water-ice. There are 17 reactions, six reactions on liquid sulfate aerosols (LBS or STS), five reactions on solid NAT aerosols, and six reactions on solid water-ice aerosols. The rate constants for these 17 heterogeneous reactions can be divided up into two types: 1) first order; and 2) pseudo second order. For first order hydrolysis reactions (Table 3, reactions 1-3, 7-8, 11, and 12-14), the heterogeneous rate constant is derived in the following manner:

$$k = \frac{1}{4}V \cdot SAD \cdot \gamma \quad (5.82)$$

4069 Where  $V$  = mean velocity;  $SAD$  = surface area density of LBS, STS, NAT, or water-ice, and  $\gamma$   
 4070 = reaction probability for each reaction. The units for this rate constant are  $s^{-1}$ . Here the  $H_2O$   
 4071 abundance is in excess and assumed not change relative to the other reactant trace constituents.  
 4072 The mean velocity is dependent on the molecular weight of the non- $H_2O$  reactant (i.e.,  $N_2O_5$ ,  
 4073  $ClONO_2$ , or  $BrONO_2$ ). The  $SAD$  for each aerosol type is described in section 7. The reaction  
 4074 probability is dependent on both composition and temperature for sulfate aerosol (see JPL06-2).  
 4075 The reaction probability is a fixed quantity for NAT and water-ice aerosols and is listed in Table  
 4076 3. Multiplying the rate constant times the concentration gives a loss rate in units of molecules  
 4077  $cm^{-3} sec^{-1}$  for the reactants and is used in the implicit solution approach. The non-hydrolysis  
 4078 reaction (Table 3, reactions 4-6, 9-10, and 15-17) are second order reactions. Here, the first order  
 4079 rate constant (equation 6) is divided by the  $HCl$  concentration, giving it the typical bimolecular  
 4080 rate constant unit value of  $cm^3 molecule^{-1} sec^{-1}$ . This approach assumes that all the  $HCl$  is in  
 4081 the aerosol particle.

## 4082 Stratospheric Aerosols

Heterogeneous processes on liquid sulfate aerosols and solid polar stratospheric clouds (Type 1a, 1b, and 2) are included following the approach of [Considine et al. \[2000\]](#). This approach assumes that the condensed phase mass follows a lognormal size distribution taken from [Considine et al. \[2000\]](#),

$$N(r) = \frac{N_0}{r\sigma\sqrt{2\pi}} \exp\left[\frac{-\ln(r/r_0)^2}{2\sigma^2}\right] \quad (5.83)$$

4083 where  $N$  is the aerosol number density (particles  $\text{cm}^{-3}$ );  $r$  and  $r_0$  are the particle radius and  
4084 median radius respectively; and  $\sigma$  is the standard deviation of the lognormal distribution.  $N_0$   
4085 and  $r_0$  are supplied for each aerosol type. The aerosol surface area density (SAD) is the second  
4086 moment of this distribution.

4087 At model temperatures ( $T_{\text{model}}$ ) greater than 200 K, liquid binary sulfate (LBS) is the  
4088 only aerosol present. The surface area density (SAD) for LBS is derived from observa-  
4089 tions from SAGE, SAGE-II and SAMS [Thomason et al., 1997] as updated by Considine  
4090 [World Meteorological Organization, 2003]. As the model atmosphere cools, the LBS aerosol  
4091 swells, taking up both  $\text{HNO}_3$  and  $\text{H}_2\text{O}$  to give STS aerosol. The Aerosol Physical Chemistry  
4092 Model (ACPM) is used to derive STS composition Tabazadeh et al. [1994]. The STS aerosol me-  
4093 dian radius and surface area density is derived following the approach of Considine et al. [2000].  
4094 The width of the STS size distribution ( $\sigma = 1.6$ ) and number density (10 particles  $\text{cm}^{-3}$ ) are  
4095 prescribed according to measurements from Dye et al. [1992]. The STS aerosol median radius  
4096 can swell from approximately  $0.1 \mu\text{m}$  to approximately  $0.5 \mu\text{m}$ . There is no aerosol settling  
4097 assumed for this type of aerosol. The median radius is used in derivation of sulfate aerosol  
4098 reaction probability coefficients. Both the LBS and STS surface area densities are used for the  
4099 calculation of the rate constants as listed in Table 3; reactions (1)-(6).

4100 Solid nitric acid containing aerosol formation is allowed when the model temperature reaches  
4101 a prescribed super saturation ratio of  $\text{HNO}_3$  over NAT [Hansen and Mauersberger, 1988]. This  
4102 ratio is set to 10 in WACCM4.0 [Peter et al., 1991]. There are three methods available to  
4103 handle the  $\text{HNO}_3$  uptake on solid aerosol. The first method directly follows Considine et al.  
4104 [2000, 2004]. Here, after the supersaturation ratio assumption is met, the available condensed  
4105 phase  $\text{HNO}_3$  is assumed to reside in the solid NAT aerosol. The derivation of the NAT median  
4106 radius and surface area density follows the same approach as the STS aerosol, by assuming: a  
4107 lognormal size distribution, a width of a distribution ( $\sigma = 1.6$ ; Dye et al. [1992]), and a number  
4108 density (0.01 particles  $\text{cm}^{-3}$ ; Tabazadeh et al. [2000]). The NAT radius settles with a value of  
4109  $r_0$  ranging between 2 and  $5 \mu\text{m}$ ; this value depends on the model temperature and subsequent  
4110 amount of condensed phase  $\text{HNO}_3$  formed. This NAT median radius  $r_0$  is also used to derive  
4111 the terminal velocity for settling of NAT (section 8) and the eventual irreversible denitrification.  
4112 The NAT surface area density is used to calculate the rate constants for heterogeneous reactions  
4113 7-11 (Table 3). Since the available  $\text{HNO}_3$  is included inside the NAT aerosol, there is no STS  
4114 aerosol present. However, there are still heterogeneous reactions occurring on the surface of LBS  
4115 aerosols.

4116 If the calculated atmospheric temperature,  $T$ , becomes less than or equal to the saturation  
4117 temperature ( $T_{\text{sat}}$ ) for water vapor over ice (e.g., Marti and Mauersberger [1993]), water-ice  
4118 aerosols can form. In WACCM4.0 the condensed phase  $\text{H}_2\text{O}$  is derived in the prognostic water  
4119 routines of CAM and passed into the chemistry module. Using this condensed phase  $\text{H}_2\text{O}$ , the  
4120 median radius and the surface area density for water-ice are again derived following the approach  
4121 of Considine et al. [2000]. The water-ice median radius and surface area density assumes a  
4122 lognormal size distribution, a width of a distribution = 1.6 [Dye et al., 1992], and a number  
4123 density of 0.001 particles  $\text{cm}^{-3}$  [Dye et al., 1992]. The value of  $r_0$  is typically  $10 \mu\text{m}$ . The water-  
4124 ice surface area density is used for the calculation of the rate constants for reactions 12-17 (Table  
4125 3).

4126 **Sedimentation of Stratospheric Aerosols**

The sedimentation of  $\text{HNO}_3$  in stratospheric aerosols follows the approach described in [Considine et al. \[2000\]](#). The following equation is used to derive the flux ( $F$ ) of  $\text{HNO}_3$ , as NAT aerosol, across model levels in units of molecules  $\text{cm}^{-2} \text{ sec}^{-1}$ .

$$F_i = V_i \cdot C_i \exp(8 \ln^2 \sigma_i), \quad (5.84)$$

4127 where  $i = 1$  for NAT;  $V_i$  is the terminal velocity of the aerosol particles ( $\text{cm s}^{-1}$ );  $C$  is the  
4128 condensed-phase concentration of  $\text{HNO}_3$  (molecules  $\text{cm}^{-3}$ );  $\sigma$  is the width of the lognormal size  
4129 distribution for NAT (see discussion above). The terminal velocity is dependent on the given  
4130 aerosol: 1) mass density; 2) median radius; 3) shape; 4) dynamic viscosity; and 5) Cunningham  
4131 correction factor for spherical particles (see [Fuch \[1964\]](#) and [Kasten \[1968\]](#) for the theory  
4132 behind the derivation of terminal velocity). For each aerosol type the terminal velocity could  
4133 be calculated, however, in WACCM4.0 this quantity is only derived for NAT. Settling of  $\text{HNO}_3$   
4134 contain in STS is not derived based on the assumption that the median radius is too small  
4135 to cause any significant denitrification and settling of condensed phase  $\text{H}_2\text{O}$  is handled in the  
4136 CAM4 prognostic water routines.

4137 **Ion Chemistry**

4138 WACCM4.0 includes a six constituent ion chemistry model ( $\text{O}^+$ ,  $\text{O}_2^+$ ,  $\text{N}^+$ ,  $\text{N}_2^+$ ,  $\text{NO}^+$ , and elec-  
4139 trons) that represents the the E-region ionosphere. The global mean ion and electron distribu-  
4140 tions simulated by WACCM4.0 for solar minimum conditions are shown in Figure 5.1, which  
4141 clearly shows that the dominant ions in this region are  $\text{NO}^+$  and  $\text{O}_2^+$ . Ion-neutral and recombi-  
4142 nation reactions included in WACCM4.0 are listed in Table 5.3.7. The reaction rate constants  
4143 for these reactions are taken from [R.G.Roble \[1995\]](#).

4144 Ionization sources include not only the aforementioned absorption of extreme ultraviolet and  
4145 soft x-ray photons, and photoelectron impact, but also energetic particles precipitation in the  
4146 auroral regions. The latter is calculated by a parameterization based on code from the NCAR  
4147 TIME-GCM model [\[Roble and Ridley, 1987\]](#) that rapidly calculates ion-pair production rates,  
4148 including production in the polar cusp and polar cap. The parameterization takes as input  
4149 hemispheric power (HP), the estimated power in gigawatts deposited in the polar regions by  
4150 energetic particles.

Currently WACCM4.0 uses a parameterization of HP (in GW) based on an empirical relationships between HP and the  $K_p$  planetary geomagnetic index. For  $K_p \leq 7$ , WACCM4.0 uses the relationship obtained by [Zhang and Paxton \[2008\]](#) from TIMED/GUVI observations:

$$\text{HP} = 16.82 * K_p * \exp(0.32) - 4.86 \quad (5.85)$$

For  $K_p > 7$ , WACCM4.0 linearly interpolates HP, assuming HP equals to 300 when  $K_p$  is 9, based on NOAA satellite measurements:

$$\text{HP} = 153.13 + \frac{K_p - 7}{9 - 7} * (300 - 153.13) \quad (5.86)$$

4151  $K_p$  is also available from NOAA's Space Environment Center and covers the period from 1933  
4152 to the present, making it ideal for long-term retrospective simulations.

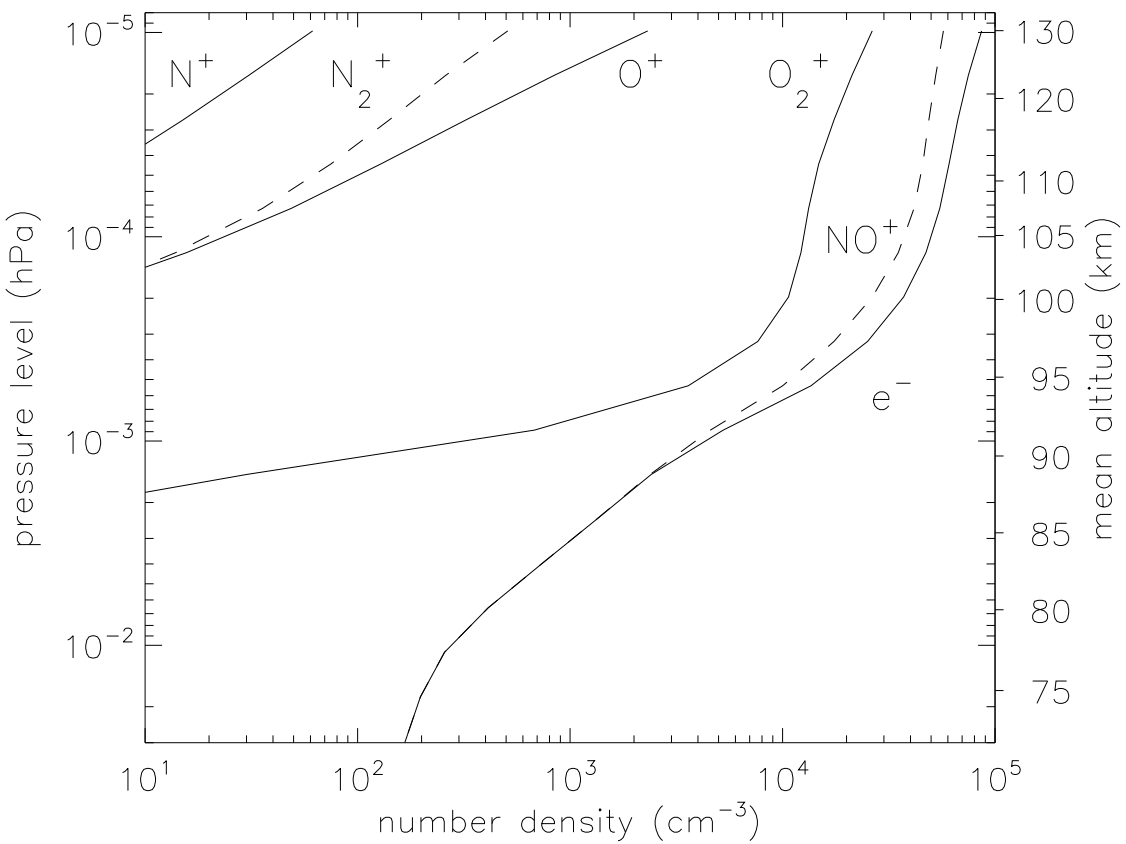


Figure 5.1: Global mean distribution of charged constituents during July solar minimum conditions.

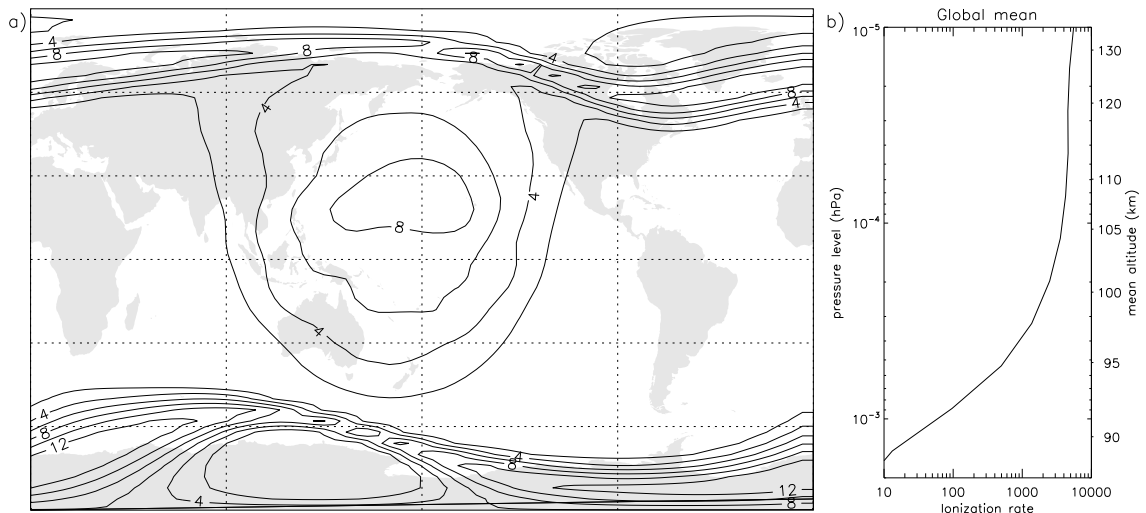
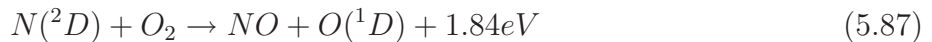


Figure 5.2: a) Global distribution of ionization rates at  $7.3 \times 10^{-5}$  hPa, July 1, UT0100 HRS. Contour interval is  $2 \times 10^3 \text{ cm}^{-3} \text{ s}^{-1}$ . b) Simultaneous global mean ionization rates ( $\text{cm}^{-3} \text{ s}^{-1}$ ) versus pressure.

4153 Total ionization rates at 110km during July for solar maximum conditions are shown in  
4154 Figure 5.2a. The broad region of ionization centered in the tropics is a result of EUV ionization,  
4155 and has a peak value of almost  $10^3$  at  $22^\circ\text{N}$ . Ionization rates from particle precipitation can  
4156 exceed this rate by 40% but are limited to the high-latitudes, as can be seen by the two bands  
4157 that are approximately aligned around the magnetic poles. The global mean ionization rate  
4158 (Figure 5.2b)

An important aspect of including ionization processes (both in the aurora and by energetic photons and photoelectrons), is that it leads to a more accurate representation of thermospheric nitric oxide. Not only does nitric oxide play an important role in the energy balance of the lower thermosphere through emission at  $5.3\text{ }\mu\text{m}$ , it might also be transported to the upper stratosphere, where it can affect ozone concentrations. Nitric oxide is produced through quenching of  $\text{N}^2\text{D}$ :



4159  $\text{N}^2\text{D}$  is produced either via recombination of  $\text{NO}^+$  (see Table 5.3.7) or directly by ionization  
4160 of molecular nitrogen. The branching ratio between  $\text{N}^2\text{D}$  and ground-state atomic nitrogen  
4161 for the photoionization process is critical in determining the effectiveness of NO production.  
4162 If ground-state atomic nitrogen is produced then it can react with NO to produce molecular  
4163 nitrogen and effectively remove members of the NOx family. In WACCM4.0 60% of the  
4164 atomic nitrogen produced is in the excited state, which implies absorption of EUV results  
4165 in a net source of NO. Also shown are maxima at high latitudes due to auroral ionization.  
4166 WACCM4.0 reproduces many of the features of the Nitric Oxide Empirical Model (NOEM)  
4167 distribution [Marsh et al., 2004], which is based on data from the Student Nitric Oxide Explorer  
4168 satellite [Barth et al., 2003]. In particular, larger NO in the winter hemisphere (a result of less  
4169 photolytic loss), and a more localized NO maximum in the Northern Hemisphere (related to the  
4170 lesser offset of geographic and magnetic poles, and so less spread when viewed as a geographic  
4171 zonal mean).

**Table 5.2: WACCM4.0 Neutral Chemical Species (51 computed species + N<sub>2</sub>)**

no.	Symbolic Name	Chemical Formula	Numerics	Deposition	Boundary Condition
1	O	O( <sup>3</sup> P)	Implicit		ubvmr
2	O1D	O( <sup>1</sup> D)	Implicit		
3	O3	O <sub>3</sub>	Implicit	dry	
4	O2	O <sub>2</sub>	Implicit		ubvmr
5	O2_1S	O <sub>2</sub> ( <sup>1</sup> Σ)	Implicit		
6	O2_1D	O <sub>2</sub> ( <sup>1</sup> Δ)	Implicit		
7	H	H	Implicit		ubvmr
8	OH	OH	Implicit		
9	HO2	HO <sub>2</sub>	Implicit		
10	H2	H <sub>2</sub>	Implicit		vmr, ubvmr
11	H2O2	H <sub>2</sub> O <sub>2</sub>	Implicit	dry, wet	
12	N	N	Implicit		ubvmr
13	N2D	N( <sup>2</sup> D)	Implicit		from TIME-GCM
14	N2	N <sub>2</sub>	Invariant		
15	NO	NO	Implicit		flux, ubvmr, lflux, airflux
16	NO2	NO <sub>2</sub>	Implicit	dry	
17	NO3	NO <sub>3</sub>	Implicit		
18	N2O5	N <sub>2</sub> O <sub>5</sub>	Implicit		
19	HNO3	HNO <sub>3</sub>	Implicit	dry, wet	
20	HO2NO2	HO <sub>2</sub> NO <sub>2</sub>	Implicit	dry, wet	
21	CL	Cl	Implicit		
22	CLO	ClO	Implicit		
23	CL2	Cl <sub>2</sub>	Implicit		
24	OCLO	OClo	Implicit		
25	CL2O2	Cl <sub>2</sub> O <sub>2</sub>	Implicit		
26	HCL	HCl	Implicit	wet	
27	HOCL	HOCl	Implicit	wet	
28	ClONO2	ClONO <sub>2</sub>	Implicit	wet	
29	BR	Br	Implicit		
30	BRO	BrO	Implicit		
31	HOBR	HOBr	Implicit	wet	
32	HBR	HBr	Implicit	wet	
33	BrONO 2	BrONO <sub>2</sub>	Implicit	wet	
34	BRCL	BrCl	Implicit		

**Table 5.1: (continued) WACCM4.0 Neutral Chemical Species (51 computed species + N<sub>2</sub>)**

no.	Symbolic Name	Chemical Formula	Numerics	Deposition	Boundary Condition
35	CH4	CH <sub>4</sub>	Implicit		vmr, airflux
36	CH3O2	CH <sub>3</sub> O <sub>2</sub>	Implicit		
37	CH3OOH	CH <sub>3</sub> OOH	Implicit	dry, wet	
38	CH2O	CH <sub>2</sub> O	Implicit	dry, wet	flux
39	CO	CO	Explicit	dry	flux, ubvmr, airflux
40	CH3CL	CH <sub>3</sub> Cl	Explicit		vmr
41	CH3BR	CH <sub>3</sub> Br	Explicit		vmr
42	CFC11	CFCl <sub>3</sub>	Explicit		vmr
43	CFC12	CF <sub>2</sub> Cl <sub>2</sub>	Explicit		vmr
44	CFC113	CCl <sub>2</sub> FCClF <sub>2</sub>	Explicit		vmr
45	HCFC22	CHClF <sub>2</sub>	Explicit		vmr
46	CCL4	CCl <sub>4</sub>	Explicit		vmr
47	CH3CCL3	CH <sub>3</sub> CCl <sub>3</sub>	Explicit		vmr
48	CF2CLBR	CBr <sub>2</sub> F <sub>2</sub> (Halon-1211)	Explicit		vmr
49	CF3BR	CBrF <sub>3</sub> (Halon-1301)	Explicit		vmr
50	H2O	H <sub>2</sub> O	Explicit		flux
51	N2O	N <sub>2</sub> O	Explicit		vmr
52	CO2	CO <sub>2</sub>	Explicit		vmr, ubvmr

**Deposition:**

wet = wet deposition included

dry = surface dry deposition included

If there is no designation in the deposition column, this species is not operated on by wet or dry deposition algorithms.

**Boundary Condition:**

flux = flux lower boundary conditions

vmr = fixed volume mixing ratio (vmr) lower boundary condition

ubvmr = fixed vmr upper boundary condition

lflux = lightning emission included for this species

airflux= aircraft emissions included for this species

If there is no designation in the Boundary Conditions column, this species has a zero flux boundary condition for the top and bottom of the model domain.

**Table 5.2: WACCM4.0 Gas-phase Reactions.**

no.	Reactions	Comments
	Oxygen Reactions	
1	$O + O_2 + M \rightarrow O_3 + M$	JPL-06
2	$O + O_3 \rightarrow 2 O_2$	JPL-06
3	$O + O + M \rightarrow O_2 + M$	Smith and Robertson (2008)
4	$O_2(^1\Sigma) + O \rightarrow O_2(^1\Delta) + O$	JPL-06
5	$O_2 1S + O_2 \rightarrow O_2(^1\Delta) + O_2$	JPL-06
6	$O_2(^1\Sigma) + N_2 \rightarrow O_2(^1\Delta) + N_2$	JPL-06
7	$O_2(^1\Sigma) + O_3 \rightarrow O_2(^1\Delta) + O_3$	JPL-06
8	$O_2(^1\Sigma) + CO_2 \rightarrow O_2(^1\Delta) + CO_2$	JPL-06
9	$O_2(^1\Sigma) \rightarrow O_2$	JPL-06
10	$O_2(^1\Delta) + O \rightarrow O_2 + O$	JPL-06
11	$O_2(^1\Delta) + O_2 \rightarrow 2 O_2$	JPL-06
12	$O_2(^1\Delta) + N_2 \rightarrow O_2 + N_2$	JPL-06
13	$O_2(^1\Delta) \rightarrow O_2$	JPL-06
14	$O(^1D) + N_2 \rightarrow O + N_2$	JPL-06
15	$O(^1D) + O_2 \rightarrow O + O_2(^1\Sigma)$	JPL-06
16	$O(^1D) + O_2 \rightarrow O + O_2$	JPL-06
17	$O(^1D) + H_2O \rightarrow 2 OH$	JPL-06
18	$O(^1D) + N_2O \rightarrow 2 NO$	JPL-06
19	$O(^1D) + N_2O \rightarrow N_2 + O_2$	JPL-06
20	$O(^1D) + O_3 \rightarrow 2 O_2$	JPL-06
21	$O(^1D) + CFC11 \rightarrow 3 Cl$	JPL-06; <a href="#">Bloomfield [1994]</a> for quenching of $O(^1D)$
22	$O(^1D) + CFC12 \rightarrow 2 Cl$	JPL-06; <a href="#">Bloomfield [1994]</a>
23	$O(^1D) + CFC113 \rightarrow 3 Cl$	JPL-06; <a href="#">Bloomfield [1994]</a>
24	$O(^1D) + HCFC22 \rightarrow Cl$	JPL-06; <a href="#">Bloomfield [1994]</a>
25	$O(^1D) + CCl_4 \rightarrow 4 Cl$	JPL-06
26	$O(^1D) + CH_3Br \rightarrow Br$	JPL-06
27	$O(^1D) + CF_2ClBr \rightarrow Cl + Br$	JPL-06
28	$O(^1D) + CF_3Br \rightarrow Br$	JPL-06
29	$O(^1D) + CH_4 \rightarrow CH_3O_2 + OH$	JPL-06
30	$O(^1D) + CH_4 \rightarrow CH_2O + H + HO_2$	JPL-06
31	$O(^1D) + CH_4 \rightarrow CH_2O + H_2$	JPL-06
32	$O(^1D) + H_2 \rightarrow H + OH$	JPL-06
33	$O(^1D) + HCl \rightarrow Cl + OH$	JPL-06
34	$O(^1D) + HBr \rightarrow Br + OH$	JPL-06

**Table 5.2: (continued) WACCM4.0 Gas-phase Reactions.**

no.	Reactions	Comments
	Nitrogen Radicals	
35	$N(^2D) + O_2 \rightarrow NO + O(^1D)$	JPL-06
36	$N(^2D) + O \rightarrow N + O$	JPL-06
37	$N + O_2 \rightarrow NO + O$	JPL-06
38	$N + NO \rightarrow N_2 + O$	JPL-06
39	$N + NO_2 \rightarrow N_2O + O$	JPL-06
40	$NO + O + M \rightarrow NO_2 + M$	JPL-06
41	$NO + HO_2 \rightarrow NO_2 + OH$	JPL-06
42	$NO + O_3 \rightarrow NO_2 + O_2$	JPL-06
43	$NO_2 + O \rightarrow NO + O_2$	JPL-06
44	$NO_2 + O + M \rightarrow NO_3 + M$	JPL-06
45	$NO_2 + O_3 \rightarrow NO_3 + O_2$	JPL-06
46	$NO_2 + NO_3 + M \rightarrow N_2O_5 + M$	JPL-06
47	$N_2O_5 + M \rightarrow NO_2 + NO_3 + M$	JPL-06
48	$NO_2 + OH + M \rightarrow HNO_3 + M$	JPL-06
49	$HNO_3 + OH \rightarrow NO_3 + H_2O$	JPL-06
50	$NO_2 + HO_2 + M \rightarrow HO_2NO_2 + M$	JPL-06
51	$NO_3 + NO \rightarrow 2 NO_2$	JPL-06
52	$NO_3 + O \rightarrow NO_2 + O_2$	JPL-06
53	$NO_3 + OH \rightarrow NO_2 + HO_2$	JPL-06
54	$NO_3 + HO_2 \rightarrow NO_2 + OH + O_2$	JPL-06
55	$HO_2NO_2 + OH \rightarrow NO_2 + H_2O + O_2$	JPL-06
56	$HO_2NO_2 + M \rightarrow HO_2 + NO_2 + M$	JPL-06

**Table 5.2: (continued) WACCM4.0 Gas-phase Reactions.**

no.	Reactions	Comments
	Hydrogen Radicals	
57	$H + O_2 + M \rightarrow HO_2 + M$	JPL-06
58	$H + O_3 + M \rightarrow OH + O_2$	JPL-06
59	$H + HO_2 \rightarrow 2 OH$	JPL-06
60	$H + HO_2 \rightarrow H_2 + O_2$	JPL-06
61	$H + HO_2 \rightarrow H_2O + O$	JPL-06
62	$OH + O \rightarrow H + O_2$	JPL-06
63	$OH + O_3 \rightarrow HO_2 + O_2$	JPL-06
64	$OH + HO_2 \rightarrow H_2O + O_2$	JPL-06
65	$OH + OH \rightarrow H_2O + O$	JPL-06
66	$OH + OH + M \rightarrow H_2O_2 + M$	JPL-06
67	$OH + H_2 \rightarrow H_2O + H$	JPL-06
68	$OH + H_2O_2 \rightarrow H_2O + HO_2$	JPL-06
69	$HO_2 + O \rightarrow OH + O_2$	JPL-06
70	$HO_2 + O_3 \rightarrow OH + 2O_2$	JPL-06
71	$HO_2 + HO_2 \rightarrow H_2O_2 + O_2$	JPL-06
72	$H_2O_2 + O \rightarrow OH + HO_2$	JPL-06
	Chlorine Radicals	
73	$Cl + O_3 \rightarrow ClO + O_2$	JPL-06
74	$Cl + H_2 \rightarrow HCl + H$	JPL-06
75	$Cl + H_2O_2 \rightarrow HCl + HO_2$	JPL-06
76	$Cl + HO_2 \rightarrow HCl + O_2$	JPL-06
77	$Cl + HO_2 \rightarrow ClO + OH$	JPL-06
78	$Cl + CH_2O \rightarrow HCl + HO_2 + CO$	JPL-06
79	$Cl + CH_4 \rightarrow CH_3O_2 + HCl$	JPL-06
80	$ClO + O \rightarrow Cl + O_2$	JPL-06
81	$ClO + OH \rightarrow Cl + HO_2$	JPL-06
82	$ClO + OH \rightarrow HCl + O_2$	JPL-06
83	$ClO + HO_2 \rightarrow HOCl + O_2$	JPL-06
84	$ClO + NO \rightarrow NO_2 + Cl$	JPL-06
85	$ClO + NO_2 + M \rightarrow ClONO_2 + M$	JPL-06

**Table 5.2: (continued) WACCM4.0 Gas-phase Reactions.**

no.	Reactions	Comments
Chlorine Radicals Continued		
86	$\text{ClO} + \text{ClO} \rightarrow 2 \text{Cl} + \text{O}_2$	JPL-06
87	$\text{ClO} + \text{ClO} \rightarrow \text{Cl}_2 + \text{O}_2$	JPL-06
88	$\text{ClO} + \text{ClO} \rightarrow \text{Cl} + \text{OCLO}$	JPL-06
89	$\text{ClO} + \text{ClO} + \text{M} \rightarrow \text{Cl}_2\text{O}_2 + \text{M}$	JPL-06
90	$\text{Cl}_2\text{O}_2 + \text{M} \rightarrow 2 \text{ClO} + \text{M}$	JPL-06
91	$\text{HCl} + \text{OH} \rightarrow \text{H}_2\text{O} + \text{Cl}$	JPL-06
92	$\text{HCl} + \text{O} \rightarrow \text{Cl} + \text{OH}$	JPL-06
93	$\text{HOCl} + \text{O} \rightarrow \text{ClO} + \text{OH}$	JPL-06
94	$\text{HOCl} + \text{Cl} \rightarrow \text{HCl} + \text{ClO}$	JPL-06
95	$\text{HOCl} + \text{OH} \rightarrow \text{ClO} + \text{H}_2\text{O}$	JPL-06
96	$\text{ClONO}_2 + \text{O} \rightarrow \text{ClO} + \text{NO}_3$	JPL-06
97	$\text{ClONO}_2 + \text{OH} \rightarrow \text{HOCl} + \text{NO}_3$	JPL-06
98	$\text{ClONO}_2 + \text{Cl} \rightarrow \text{Cl}_2 + \text{NO}_3$	JPL-06
no.	Reactions	Comments
Bromine Radicals		
99	$\text{Br} + \text{O}_3 \rightarrow \text{BrO} + \text{O}_2$	JPL-06
100	$\text{Br} + \text{HO}_2 \rightarrow \text{HBr} + \text{O}_2$	JPL-06
101	$\text{Br} + \text{CH}_2\text{O} \rightarrow \text{HBr} + \text{HO}_2 + \text{CO}$	JPL-06
102	$\text{BrO} + \text{O} \rightarrow \text{Br} + \text{O}_2$	JPL-06
103	$\text{BrO} + \text{OH} \rightarrow \text{Br} + \text{HO}_2$	JPL-06
104	$\text{BrO} + \text{HO}_2 \rightarrow \text{HOBr} + \text{O}_2$	JPL-06
105	$\text{BrO} + \text{NO} \rightarrow \text{Br} + \text{NO}_2$	JPL-06
106	$\text{BrO} + \text{NO}_2 + \text{M} \rightarrow \text{BrONO}_2 + \text{M}$	JPL-06
107	$\text{BrO} + \text{ClO} \rightarrow \text{Br} + \text{OCLO}$	JPL-06
108	$\text{BrO} + \text{ClO} \rightarrow \text{Br} + \text{Cl} + \text{O}_2$	JPL-06
109	$\text{BrO} + \text{ClO} \rightarrow \text{BrCl} + \text{O}_2$	JPL-06
110	$\text{BrO} + \text{BrO} \rightarrow 2 \text{Br} + \text{O}_2$	JPL-06
111	$\text{HBr} + \text{OH} \rightarrow \text{Br} + \text{H}_2\text{O}$	JPL-06
112	$\text{HBr} + \text{O} \rightarrow \text{Br} + \text{OH}$	JPL-06
113	$\text{HOBr} + \text{O} \rightarrow \text{BrO} + \text{OH}$	JPL-06
114	$\text{BrONO}_2 + \text{O} \rightarrow \text{BrO} + \text{NO}_3$	JPL-06

**Table 5.2: (continued) WACCM4.0 Gas-phase Reactions.**

no.	Reactions	Comments
	Halogen Radicals	
115	$\text{CH}_3\text{Cl} + \text{Cl} \rightarrow \text{HO}_2 + \text{CO} + 2\text{HCl}$	JPL-06
116	$\text{CH}_3\text{Cl} + \text{OH} \rightarrow \text{Cl} + \text{H}_2\text{O} + \text{HO}_2$	JPL-06
117	$\text{CH}_3\text{CCl}_3 + \text{OH} \rightarrow 3 \text{Cl} + \text{H}_2\text{O}$	JPL-06
118	$\text{HCFC22} + \text{OH} \rightarrow \text{Cl} + \text{H}_2\text{O} + \text{HO}_2$	JPL-06
119	$\text{CH}_3\text{Br} + \text{OH} \rightarrow \text{Br} + \text{H}_2\text{O} + \text{HO}_2$	JPL-06
	CH <sub>4</sub> and Derivatives	
120	$\text{CH}_4 + \text{OH} \rightarrow \text{CH}_3\text{O}_2 + \text{H}_2\text{O}$	JPL-06
121	$\text{CH}_3\text{O}_2 + \text{NO} \rightarrow \text{CH}_2\text{O} + \text{NO}_2 + \text{HO}_2$	JPL-06
122	$\text{CH}_3\text{O}_2 + \text{HO}_2 \rightarrow \text{CH}_3\text{OOH} + \text{O}_2$	JPL-06
123	$\text{CH}_3\text{OOH} + \text{OH} \rightarrow 0.7 \text{CH}_3\text{O}_2 + 0.3 \text{OH} + 0.3 \text{CH}_2\text{O} + \text{H}_2\text{O}$	JPL-06
124	$\text{CH}_2\text{O} + \text{NO}_3 \rightarrow \text{CO} + \text{HO}_2 + \text{HNO}_3$	JPL-06
125	$\text{CH}_2\text{O} + \text{OH} \rightarrow \text{CO} + \text{H}_2\text{O} + \text{H}$	JPL-06
126	$\text{CH}_2\text{O} + \text{O} \rightarrow \text{OH} + \text{HO}_2 + \text{CO}$	JPL-06
127	$\text{CO} + \text{OH} \rightarrow \text{H} + \text{CO}_2$	JPL-06

**Table 5.3: WACCM4.0 Heterogeneous Reactions on liquid and solid aerosols.**

no.	Reaction	Comments
	Sulfate Aerosol	
1	$\text{N}_2\text{O}_5 + \text{H}_2\text{O} \rightarrow 2 \text{HNO}_3$	JPL-06; f (sulfuric acid wt %)
2	$\text{ClONO}_2 + \text{H}_2\text{O} \rightarrow \text{HOCl} + \text{HNO}_3$	JPL-06; f (T, P, HCl, H <sub>2</sub> O, r)
3	$\text{BrONO}_2 + \text{H}_2\text{O} \rightarrow \text{HOBr} + \text{HNO}_3$	JPL-06; f (T, P, H <sub>2</sub> O, r)
4	$\text{ClONO}_2 + \text{HCl} \rightarrow \text{Cl}_2 + \text{HNO}_3$	JPL-06; f (T, P, HCl, H <sub>2</sub> O, r)
5	$\text{HOCl} + \text{HCl} \rightarrow \text{Cl}_2 + \text{H}_2\text{O}$	JPL-06; f (T, P, HCl, HCl, H <sub>2</sub> O, r)
6	$\text{HOBr} + \text{HCl} \rightarrow \text{BrCl} + \text{H}_2\text{O}$	JPL-06; f (T, P, HCl, HOBr, H <sub>2</sub> O, r)
	NAT Aerosol	
7	$\text{N}_2\text{O}_5 + \text{H}_2\text{O} \rightarrow 2 \text{HNO}_3$	JPL-06; $\gamma = 4 \times 10^{-4}$
8	$\text{ClONO}_2 + \text{H}_2\text{O} \rightarrow \text{HOCl} + \text{HNO}_3$	JPL-06; $\gamma = 4 \times 10^{-3}$
9	$\text{ClONO}_2 + \text{HCl} \rightarrow \text{Cl}_2 + \text{HNO}_3$	JPL-06; $\gamma = 0.2$
10	$\text{HCl} + \text{HCl} \rightarrow \text{Cl}_2 + \text{H}_2\text{O}$	JPL-06; $\gamma = 0.1$
11	$\text{BrONO}_2 + \text{H}_2\text{O} \rightarrow \text{HOBr} + \text{HNO}_3$	JPL-06; $\gamma = 0.3$
	Water-Ice Aerosol	
12	$\text{N}_2\text{O}_5 + \text{H}_2\text{O} \rightarrow 2 \text{HNO}_3$	JPL-06; $\gamma = 0.02$
13	$\text{ClONO}_2 + \text{H}_2\text{O} \rightarrow \text{HOCl} + \text{HNO}_3$	JPL-06; $\gamma = 0.3$
14	$\text{BrONO}_2 + \text{H}_2\text{O} \rightarrow \text{HOBr} + \text{HNO}_3$	JPL-06; $\gamma = 0.3$
15	$\text{ClONO}_2 + \text{HCl} \rightarrow \text{Cl}_2 + \text{HNO}_3$	JPL-06; $\gamma = 0.3$
16	$\text{HOCl} + \text{HCl} \rightarrow \text{Cl}_2 + \text{H}_2\text{O}$	JPL-06; $\gamma = 0.2$
17	$\text{HOBr} + \text{HCl} \rightarrow \text{BrCl} + \text{H}_2\text{O}$	JPL-06; $\gamma = 0.3$

**Table 5.4: WACCM4.0 Photolytic Reactions.**

no.	Reactants	Products	Comments
1	$O_2 + h\nu$	$O + O(^1D)$	Ly- $\alpha$ : Chabriat and Kockarts (1997, 1998) $\phi$ (Ly- $\alpha$ ): Lacoursiere et al. (1999) SRB: Koppers and Murtaugh (1996) For wavelength $\nu$ regions not Ly- $\alpha$ or SRB, $\sigma$ (120-205nm): Brasseur and Solomon (1986); $\sigma$ (205-240 nm): Yoshino et al. (1988)
2	$O_2 + h\nu$	2 O	see above
3	$O_3 + h\nu$	$O(^1D) + O_2$	$\sigma$ (120-136.5nm): Tanaka et al. (1953); $\sigma$ (136.5-175nm): Ackerman (1971); $\sigma$ (175-847nm): WMO (1985); except for $\sigma$ (185-350nm): Molina and Molina (1986) $\phi$ (<280nm): Marsh (1999) $\phi$ (>280nm): JPL-06.
4	$O_3 + h\nu$	O + O <sub>2</sub>	see above
5	$N_2O + h\nu$	$O(^1D) + N_2$	JPL-06
6	$NO + h\nu$	N + O	Minschwaner et al. (1993)
7	$NO + h\nu$	$NO^+ + e$	
8	$NO_2 + h\nu$	NO + O	JPL-06
9	$N_2O_5 + h\nu$	$NO_2 + NO_3$	JPL-06
10	$N_2O_5 + h\nu$	NO + O + NO <sub>3</sub>	JPL-06
11	$HNO_3 + h\nu$	OH + NO <sub>2</sub>	JPL-06
12	$NO_3 + h\nu$	NO <sub>2</sub> + O	JPL-06
13	$NO_3 + h\nu$	NO + O <sub>2</sub>	JPL-06
14	$HO_2NO_2 + h\nu$	OH + NO <sub>3</sub>	JPL-06
15	$HO_2NO_2 + h\nu$	NO <sub>2</sub> + HO <sub>2</sub>	JPL-06
16	$CH_3OOH + h\nu$	$CH_2O + H + OH$	JPL-06
17	$CH_2O + h\nu$	CO + 2 H	JPL-06
18	$CH_2O + h\nu$	CO + H <sub>2</sub>	JPL-06
19	$H_2O + h\nu$	H + OH	$\phi$ (Ly- $\alpha$ ): Slanger et al. (1982); $\phi$ (105-145nm): Stief et al. (1975); $\phi$ (>145): JPL-06 $\phi$ (120-182nm): Yoshino et al. (1996); $\phi$ (183-194nm): Cantrell et al. (1997)

**Table 5.4: (continued) WACCM4.0 Photolytic Reactions.**

no.	Reactants	Products	Comments
20	$\text{H}_2\text{O} + h\nu$	$\text{H}_2 + \text{O}({}^1\text{D})$	(see above)
21	$\text{H}_2\text{O} + h\nu$	$\text{H} + 2\text{O}$	(see above)
22	$\text{H}_2\text{O}_2 + h\nu$	$2\text{OH}$	JPL-06
23	$\text{Cl}_2 + h\nu$	$2\text{Cl}$	JPL-06
24	$\text{ClO} + h\nu$	$\text{Cl} + \text{O}$	JPL-06
25	$\text{OClO} + h\nu$	$\text{O} + \text{ClO}$	JPL-06
26	$\text{Cl}_2\text{O}_2 + h\nu$	$\text{Cl} + \text{ClOO}$	Burkholder et al. (1990); Stimpfle et al. (2004)
27	$\text{HOCl} + h\nu$	$\text{Cl} + \text{OH}$	JPL-06
28	$\text{HCl} + h\nu$	$\text{Cl} + \text{H}$	JPL-06
29	$\text{ClONO}_2 + h\nu$	$\text{Cl} + \text{NO}_3$	JPL-06
30	$\text{ClONO}_2 + h\nu$	$\text{ClO} + \text{NO}_2$	JPL-06
31	$\text{BrCl} + h\nu$	$\text{Br} + \text{Cl}$	JPL-06
32	$\text{BrO} + h\nu$	$\text{Br} + \text{O}$	JPL-06
33	$\text{HOBr} + h\nu$	$\text{Br} + \text{OH}$	JPL-06
34	$\text{BrONO}_2 + h\nu$	$\text{Br} + \text{NO}_3$	JPL-06
35	$\text{BrONO}_2 + h\nu$	$\text{BrO} + \text{NO}_2$	JPL-06
36	$\text{CH}_3\text{Cl} + h\nu$	$\text{Cl} + \text{CH}_3\text{O}_2$	JPL-06
37	$\text{CCl}_4 + h\nu$	$4\text{Cl}$	JPL-06
38	$\text{CH}_3\text{CCl}_3 + h\nu$	$3\text{Cl}$	JPL-06
39	$\text{CFC11} + h\nu$	$3\text{Cl}$	JPL-06
40	$\text{CFC12} + h\nu$	$2\text{Cl}$	JPL-06
41	$\text{CFC113} + h\nu$	$3\text{Cl}$	JPL-06
42	$\text{HCFC22} + h\nu$	$\text{Cl}$	JPL-06
43	$\text{CH}_3\text{Br} + h\nu$	$\text{Br} + \text{CH}_3\text{O}_2$	JPL-06
44	$\text{CF}_3\text{Br} + h\nu$	$\text{Br}$	JPL-06
45	$\text{CF}_2\text{ClBr} + h\nu$	$\text{Br} + \text{Cl}$	JPL-06
46	$\text{CO}_2 + h\nu$	$\text{CO} + \text{O}$	$\sigma$ (120-167): Nakata, et al. (1965); $\sigma$ (167-199): Huffman (1971)
47	$\text{CH}_4 + h\nu$	$\text{H} + \text{CH}_3\text{O}_2$	$\sigma$ : JPL-06; based on Brownsword et al. (1997)
48	$\text{CH}_4 + h\nu$	$\text{H}_2 + 0.18\text{CH}_2\text{O} + 0.18\text{O}$ $+ 0.44\text{CO}_2 + 0.44\text{H}_2$ $+ 0.38\text{CO} + 0.05\text{H}_2\text{O}$	see above

**Table 5.5: Ion-neutral and recombination reactions and exothermicities.**

Reaction	$\Delta H$ (kJ mol <sup>-1</sup> )
$O^+ + O_2 \rightarrow O_2^+ + O$	150.11
$O^+ + N_2 \rightarrow NO^+ + N$	105.04
$N_2^+ + O \rightarrow NO^+ + N(^2D)$	67.53
$O_2^+ + N \rightarrow NO^+ + O$	406.16
$O_2^+ + NO \rightarrow NO^+ + O_2$	271.38
$N^+ + O_2 \rightarrow O_2^+ + N$	239.84
$N^+ + O_2 \rightarrow NO^+ + O$	646.28
$N^+ + O \rightarrow O^+ + N$	95.55
$N_2^+ + O_2 \rightarrow O_2^+ + N_2$	339.59
$O_2^+ + N_2 \rightarrow NO^+ + NO$	—
$N_2^+ + O \rightarrow O^+ + N_2$	—
$NO^+ + e \rightarrow 0.2N + 0.8N(^2D) + O$	82.389
$O_2^+ + e \rightarrow 1.15O + 0.85O(^1D)$	508.95
$N_2^+ + e \rightarrow 1.1N + 0.9N(^2D)$	354.83

### 4172 5.3.8 Electric Field

4173 The global electric field is based on a composite of two empirical models for the different latitude  
 4174 regions: at high latitude the Weimer95 model [Weimer, 1995], and at low- and midlatitude the  
 4175 Scherliess model [Scherliess et al., 2002]. In the following the different models are described  
 4176 since the model is not published to date.

#### 4177 Low- and midlatitude electric potential model

The low- and mid latitude electric field model was developed by Lüdger Scherliess [Scherliess et al., 2002]. It's based on Incoherent Scatter Radar data (ISR) from Jicamarca, Arecibo, Saint Santin, Millstone Hill, and the MU radar in Shigaraki. The electric field is calculated for a given year, season, UT,  $S_a$ , local time, and with longitudinal/latitudinal variation. The empirical model is constructed from a model for low solar flux ( $S_a = 90$ ) and a high solar flux model ( $S_a = 180$ ). The global electric potential is expressed according to Richmond et al. [1980] by

$$\Phi(d, T, t, \lambda) = \sum_{k=0}^2 \sum_{l=-2}^2 \sum_{m=-n}^n \sum_{n=1}^{12} A_{klmn} P_n^m(\sin\lambda) f_m\left(\frac{2\pi t}{24}\right) f_l\left(\frac{2\pi T}{24}\right) f_{-k}\left(\frac{2\pi(d+9)}{365.24}\right) \quad (5.88)$$

**Table 5.6: Ionization reactions.**

$O + h\nu \rightarrow O^+ + e$
$O + e^* \rightarrow O^+ + e + e^*$
$N + h\nu \rightarrow N^+ + e$
$O_2 + h\nu \rightarrow O_2^+ + e$
$O_2 + e^* \rightarrow O_2^+ + e + e^*$
$O_2 + h\nu \rightarrow O + O^+ + e$
$O_2 + e^* \rightarrow O + O^+ + e + e^*$
$N_2 + h\nu \rightarrow N_2^+ + e$
$N_2 + e^* \rightarrow N_2^+ + e + e^*$
$N_2 + h\nu \rightarrow N + N^+ + e$
$N_2 + e^* \rightarrow N + N^+ + e + e^*$
$N_2 + h\nu \rightarrow N(^2D) + N^+ + e$
$N_2 + e^* \rightarrow N(^2D) + N^+ + e + e^*$

**Table 5.7: EUVAC model parameters.**

wavelength interval nm	$F_i^0$ ph cm $^{-2}$ s $^{-1}$	$R_i$
0.05 - 0.4	5.010e+01	6.240e-01
0.4 - 0.8	1.000e+04	3.710e-01
0.8 - 1.8	2.000e+06	2.000e-01
1.8 - 3.2	2.850e+07	6.247e-02
3.2 - 7.0	5.326e+08	1.343e-02
7.0 - 15.5	1.270e+09	9.182e-03
15.5 - 22.4	5.612e+09	1.433e-02
22.4 - 29.0	4.342e+09	2.575e-02
29.0 - 32.0	8.380e+09	7.059e-03
32.0 - 54.0	2.861e+09	1.458e-02
54.0 - 65.0	4.830e+09	5.857e-03
65.0 - 79.8	1.459e+09	5.719e-03
65.0 - 79.8	1.142e+09	3.680e-03
79.8 - 91.3	2.364e+09	5.310e-03
79.8 - 91.3	3.655e+09	5.261e-03
79.8 - 91.3	8.448e+08	5.437e-03
91.3 - 97.5	3.818e+08	4.915e-03
91.3 - 97.5	1.028e+09	4.955e-03
91.3 - 97.5	7.156e+08	4.422e-03
97.5 - 98.7	4.482e+09	3.950e-03
98.7 - 102.7	4.419e+09	5.021e-03
102.7 - 105.0	4.235e+09	4.825e-03
105.0 - 121.0	2.273e+10	3.383e-03

with

$$f_m(\phi) = \sqrt{2} \sin(m\phi) \quad m > 0 \quad (5.89)$$

$$f_m(\phi) = 1 \quad m = 0 \quad (5.90)$$

$$f_m(\phi) = \sqrt{2} \cos(m\phi) \quad m < 0 \quad (5.91)$$

the day of the year is denoted by  $d$ , universal time by  $T$ , magnetic local time by  $t$ , and geomagnetic latitude  $\lambda$ . The values of  $d$ ,  $T$ , and  $t$  are expressed as angles between 0 and  $2\Pi$ .  $P_n^m$  are fully normalized Legendre polynomials. Due to the assumption that the geomagnetic field lines are highly conducting, the  $n + m$  odd coefficients are set to zero to get a symmetrical electric potential about the magnetic equator. The coefficients  $A_{klmn}$  are found by a least-square fit for low and high solar flux. The solar cycle dependence is introduced by inter- and extrapolation of the sets of coefficients  $A_{klmn}^{low}$  for  $S_a = 90$  and  $A_{klmn}^{high}$  for  $S_a = 180$ .

$$A_{klmn} = A_{klmn}^{low} + S_{aM} [A_{klmn}^{high} - A_{klmn}^{low}] \quad (5.92)$$

with

$$S_{aM} = \frac{\arctan[(S_a - 65)^2/90^2] - a_{90}}{a_{180} - a_{90}} \quad (5.93)$$

$$a_{90} = \arctan[(90 - 65)^2/90^2] \quad (5.94)$$

$$a_{180} = \arctan[(180 - 65)^2/90^2] \quad (5.95)$$

4178 We are using the daily  $F_{10.7}$  number for  $S_a$ .  $S_{aM}$  levels off at high and low solar flux numbers,  
4179 and therefore the model does not predict unrealistic high or low electric potential values.

4180 The geomagnetic field is described by modified apex coordinates [Richmond, 1995] which  
already take into account the distortion of the magnetic field. Modified apex coordinates have  
a reference height associated with them, which in our case is set to 130 km. The electric field  
 $\mathbf{E}$  and the electromagnetic drift velocity  $\mathbf{v}_E$  can be expressed by quantities mapped to the  
reference height, e.g. by  $E_{d1}$ ,  $E_{d2}$  and  $v_{e1}$ ,  $v_{e2}$ . These quantities are not actual electric field or  
electromagnetic drift velocity components, but rather the representation of the electric field or  
electromagnetic drift velocities by being constant along the geomagnetic field line. The fields in  
an arbitrary direction  $\mathbf{I}$  can be expressed by

$$\mathbf{I} \cdot \mathbf{E} = \mathbf{I} \cdot \mathbf{d}_1 E_{d1} + \mathbf{I} \cdot \mathbf{d}_2 E_{d2} \quad (5.96)$$

$$\mathbf{I} \cdot \mathbf{v}_E = \mathbf{I} \cdot \mathbf{e}_1 v_{e1} + \mathbf{I} \cdot \mathbf{e}_2 v_{e2} \quad (5.97)$$

4181 The basis vector  $\mathbf{d}_1$  and  $\mathbf{e}_1$  are in more-or-less magnetic eastward direction and  $\mathbf{d}_2$  and  $\mathbf{e}_2$  in  
4182 downward/ equatorward direction. The base vectors vary with height,  $\mathbf{d}_i$  is decreasing and  $\mathbf{e}_i$   
4183 increasing with altitude. Therefore when the base vectors are applied to the mapped field at  
4184 the reference height, e.g.  $E_{d1}$ ,  $E_{d2}$  and  $v_{e1}$ ,  $v_{e2}$ , they already take into account the height and  
4185 directional variation of the corresponding quantity. Note that the modified apex coordinates  
4186 are using the International Geomagnetic Reference Field (IGRF), and in the WACCM4 code  
4187 the IGRF is only defined between the years 1900 and 2000. The description of the IGRF can  
4188 be updated every 5 years to be extended in time.

4189 **High-latitude electric potential model**

The high-latitude electric potential model from Weimer [Weimer, 1995] is used. The model is based on spherical harmonic coefficients that were derived by least square fitting of measurements from the Dynamics Explorer 2 (DE2) satellite. The variation of the spherical harmonic coefficients with the interplanetary magnetic field (IMF) clock angle, IMF strength, solar wind velocity and season can be reproduced by a combination of Fourier series and multiple linear regression formula. The final model varies with magnetic latitude, magnetic local time, season, IMF strength and direction, and solar wind velocity. For our purpose we have set the solar wind speed to a constant value of 400 km/s and only consider the effects of IMF  $B_z$  ( $B_y = 0$ ). Since the IMF conditions are not known all the time, we developed an empirical relation between  $B_z$  and the  $K_p$  index and the solar flux number  $S_a$ . Both, the  $K_p$  index and the daily solar flux number  $F_{10.7}$ , are known in the WACCM4 model.

$$B_z(K_p, F_{10.7}) = -0.085K_p^2 - 0.08104K_p + 0.4337 + 0.00794F_{10.7} - 0.00219K_pF_{10.7} \quad (5.98)$$

4190 Note that the Weimer model uses an average year of 365.24 days/year and an average month  
 4191 of 30.6001 days/month. The boundary of the Weimer model is at  $46^\circ$  magnetic latitude. The  
 4192 model was developed for an averaged northern and southern hemisphere. The  $B_y$  value and the  
 4193 season are reversed to get the values for the other hemisphere.

4194 **Combining low-/ mid-latitude with the high latitude electric potential**

After the low/mid-latitude electric potential  $\Phi_{mid}$  and the high latitude potential  $\Phi_{hgh}$  are calculated, both patterns are combined to be smooth at the boundary. The boundary between high and mid latitude  $\lambda_{bnd}$  is defined to lie where the electric field magnitude  $E$  from  $\Phi_{hgh}$  equals 15 mV/m. After finding the longitudinal variation of the high latitude boundary  $\lambda_{bnd}$ , it's shifted halfway towards  $54^\circ$  magnetic latitude. The width of the transition zone  $2\Delta\lambda_{trs}$  from high to mid latitude varies with magnetic local time. First, the high and mid latitude electric potential are adjusted by a constant factor such that the average for the high and mid latitude electric potential along the boundary  $\lambda_{bnd}$  are the same. The combined electric potential  $\Phi$  is defined by

$$\Phi = \begin{cases} \Phi_{mid} & |\lambda| < \lambda_{bnd} - \Delta\lambda_{trs} \\ \Phi_{hgh} & |\lambda| > \lambda_{bnd} + \Delta\lambda_{trs} \\ F_{int}(\Phi_{mid}, \Phi_{hgh}) & \lambda_{bnd} - \Delta\lambda_{trs} \leq |\lambda| \leq \lambda_{bnd} + \Delta\lambda_{trs} \end{cases} \quad (5.99)$$

with

$$F_{int}(\Phi_{mid}, \Phi_{hgh}) = \frac{1}{3} \frac{1}{2\Delta\lambda_{trs}} [ \{ \Phi_{mid}(\phi, \lambda_{bnd} - \Delta\lambda_{trs}) + 2\Phi_{mid}(\phi, \lambda) \} \{ \lambda_{bnd} - |\lambda| + \Delta\lambda_{trs} \} + (\Phi_{hgh}(\phi, \lambda_{bnd} + \Delta\lambda_{trs}) + 2\Phi_{hgh}(\phi, \lambda)) \{ -\lambda_{bnd} + |\lambda| + \Delta\lambda_{trs} \} ] \quad (5.100)$$

4195 **Calculation of electric field**

The electric field can be derived from the electric potential by

$$\mathbf{E} = -\nabla\Phi \quad (5.101)$$

The more-or-less magnetic eastward electric field component  $E_{d1}$  and the in general downward/equatorward  $E_{d2}$  component are calculated. These components are constant along the magnetic field line. They are calculated at a reference height  $h_r = 130$  km with  $R = R_{\text{earth}} + h_r$ . The electric field does not vary much with altitude, and therefore we assume in the code that the electric field is constant in height.

$$E_{d1} = -\frac{1}{R \cos \lambda} \frac{\partial \Phi}{\partial \phi} \quad (5.102)$$

$$E_{d2} = \frac{1}{R \sin I} \frac{\partial \Phi}{\partial \lambda} \quad (5.103)$$

4196 with  $\sin I = 2 \sin \lambda [4 - 3 \cos^2 \lambda]^{0.5}$ .

4197 **Calculation of electrodynamic drift velocity**

The electric field is calculated on a  $2^\circ \times 2^\circ$  degree geomagnetic grid with the magnetic longitude represented by the magnetic local time (MLT) from 0 MLT to 24 MLT. Therefore, the magnetic local time of the geographic longitudes of the WACCM4 grid has to be determined first to map from the geomagnetic to the geographic WACCM4 grid. The magnetic local time is calculated by using the location of the geomagnetic dipole North pole, the location of the subsolar point, and the apex longitude of the geographic WACCM4 grid point. A bilinear interpolation is used for the mapping. Note that every processor calculates the global electric field, which is computationally inexpensive. Otherwise, to calculate the electric field some communication between the different processors would be necessary to get the spatial derivatives.

The mapped electric field is rotated into the geographic direction by

$$\mathbf{E} = \mathbf{d}_1 E_{d1} + \mathbf{d}_2 E_{d2} \quad (5.104)$$

with the components of  $\mathbf{E}$  being the geographic eastward, westward and upward electric field. At high altitudes the ion-neutral collision frequency  $\nu_{in}$  is small in relation to the angular gyrofrequency of the ions  $\Omega_i$  ( $\nu_{in} \ll \Omega_i$ ), and the electron-neutral collision frequency  $\nu_{en}$  is much smaller than the angular gyrofrequency of the electrons  $\Omega_e$  ( $\nu_{en} \ll \Omega_e$ ), due to the decrease in neutral density with increasing altitude. Therefore, the ion drift  $\mathbf{v}_{i\perp}$  perpendicular to the geomagnetic field can be simplified by the electrodynamic drift velocity  $\mathbf{v}_E$

$$\mathbf{v}_{i\perp} \approx \mathbf{v}_E = \frac{\mathbf{E} \times \mathbf{B}_o}{\mathbf{B}_o^2} \quad (5.105)$$

4198 with  $\mathbf{B}_o$  the geomagnetic main field from IGRF.

4199 **Ion drag calculation**

The following is written according to the source code. Two subroutines `iondrag_calc` exist in the code, one uses the calculated ion drag coefficients if `WACCM MOZART` is used, and the other one uses look-up tables for the ion drag coefficients  $\lambda_1$  and  $\lambda_2$ .

It is assumed that the electron  $T_e$  and ion  $T_i$  temperature is equal to the neutral temperature  $T_n$ .

$$T_i = T_e = T_n \quad (5.106)$$

The dip angle  $I$  of the geomagnetic field is calculated by

$$I = \arctan \frac{B_z}{\sqrt{B_{north}^2 + B_{east}^2}} \quad (5.107)$$

with a minimum dip angle  $|I| \geq 0.17$ . The declination is

$$D = \arctan \frac{B_{east}}{B_{north}} \quad (5.108)$$

The magnetic field component  $B_z, B_{east}, B_{north}$  are determined from the International Geomagnetic Reference Field (IGRF).

The collision frequencies  $\nu$  in units of  $s^{-1}$  are determined by, e.g. [Schunk and Nagy \[2000\]](#)

$$\frac{1}{N_{O_2}} \nu_{O_2^+ - O_2} = 2.59 \times 10^{-11} \sqrt{\frac{T_i + T_e}{2}} \left[ 1 - 0.73 \log_{10} \sqrt{\frac{T_i + T_e}{2}} \right]^2 \quad (5.109)$$

$$\frac{1}{N_{O_2}} \nu_{O^+ - O_2} = 6.64 \times 10^{-10} \quad (5.110)$$

$$\frac{1}{N_{O_2}} \nu_{NO^+ - O_2} = 4.27 \times 10^{-10} \quad (5.111)$$

$$\frac{1}{N_O} \nu_{O^+ - O} = 3.67 \times 10^{-11} \sqrt{\frac{T_i + T_e}{2}} \left[ 1 - 0.064 \log_{10} \sqrt{\frac{T_i + T_e}{2}} \right]^2 f_{cor} \quad (5.112)$$

$$\frac{1}{N_O} \nu_{NO^+ - O} = 2.44 \times 10^{-10} \quad (5.113)$$

$$\frac{1}{N_O} \nu_{O_2^+ - O} = 2.31 \times 10^{-10} \quad (5.114)$$

$$\frac{1}{N_{N_2}} \nu_{O_2^+ - N_2} = 4.13 \times 10^{-10} \quad (5.115)$$

$$\frac{1}{N_{N_2}} \nu_{NO^+ - N_2} = 4.34 \times 10^{-10} \quad (5.116)$$

$$\frac{1}{N_{N_2}} \nu_{O^+ - N_2} = 6.82 \times 10^{-10} \quad (5.117)$$

with  $N_n$  the number density for the neutral n in units of  $1/cm^3$ , and the temperature in Kelvins. The collisions frequencies for  $\nu_{O_2^+ - O_2}$  and  $\nu_{O^+ - O}$  are resonant, all other are nonresonant. The

arbitrary correction factor  $f_{cor}$  multiplies the  $\nu_{O^+ - O}$  collision frequency and is set to  $f_{cor} = 1.5$  which has been found to improve agreement between calculated and observed winds and electron densities in the upper thermosphere in other models. The mean mass  $\bar{m}_{mid}$  [g/mole] at the midpoints of the height level is calculated in the Mozart module. The number densities [1/cm<sup>3</sup>] are

$$N_{O_2} = \frac{N\bar{m}_{mid}mmr_{O_2}}{m_{O_2}} \quad (5.118)$$

$$N_O = \frac{N\bar{m}_{mid}mmr_O}{m_O} \quad (5.119)$$

$$N_{N_2} = \frac{N\bar{m}_{mid}mmr_{N_2}}{m_{N_2}} \quad (5.120)$$

$$N_{O_2^+} = \frac{N\bar{m}_{mid}mmr_{O_2^+}}{m_{O_2^+}} \quad (5.121)$$

$$N_{O^+} = \frac{N\bar{m}_{mid}mmr_{O^+}}{m_{O^+}} \quad (5.122)$$

$$N_e = \frac{N\bar{m}_{mid}mmr_e}{m_e} \quad (5.123)$$

with  $mmr$  the mass mixing ratio, and  $N$  the total number density in units of 1/cm<sup>3</sup>. The pressure [dyne/cm<sup>2</sup>] and the mean mass at the midpoint  $\bar{m}_{mid}$  in units of g/mole are

$$p = 10 p_{mid} \quad (5.124)$$

$$N\bar{m}_{mid} = \frac{p \bar{m}}{k_B T_n} \quad (5.125)$$

with the factor 10 to convert from [Pa] to [dyne/cm<sup>2</sup>], and  $k_B$  the Boltzmann constant. The collision frequencies are

$$\nu_{O_2^+} = \nu_{O_2^+ - O_2} + \nu_{O_2^+ - O} + \nu_{O_2^+ - N_2} \quad (5.126)$$

$$\nu_{O^+} = \nu_{O^+ - O_2} + \nu_{O^+ - O} + \nu_{O^+ - N_2} \quad (5.127)$$

$$\nu_{NO^+} = \nu_{NO^+ - O_2} + \nu_{NO^+ - O} + \nu_{NO^+ - N_2} \quad (5.128)$$

$$\begin{aligned} \nu_{en} = & 2.33 \times 10^{-11} N_{N_2} T_e (1 - 1.21 \times 10^{-4} T_e) + \\ & 1.82 \times 10^{-10} N_{O_2} \sqrt{T_e} (1 + 3.6 \times 10^{-2} \sqrt{T_e}) + \\ & 8.9 \times 10^{-11} N_O \sqrt{T_e} (1 + 5.7 \times 10^{-4} T_e) \end{aligned} \quad (5.129)$$

The ratios  $r$  between collision frequency  $\nu$  and gyro frequency  $\Omega$  are

$$r_{O_2^+} = \frac{\nu_{O_2^+}}{\Omega_{O_2^+}} \quad (5.130)$$

$$r_{O^+} = \frac{\nu_{O^+}}{\Omega_{O^+}} \quad (5.131)$$

$$r_{NO^+} = \frac{\nu_{NO^+}}{\Omega_{NO^+}} \quad (5.132)$$

$$r_e = \frac{\nu_{en}}{\Omega_e} \quad (5.133)$$

with the gyro frequency for ions  $\Omega_i = eB/m_i$  and for electrons  $\Omega_e = eB/m_e$ . The Pedersen conductivity [ S/m] is

$$\sigma_P = \frac{e}{B} \left[ N_{O^+} \frac{r_{O^+}}{1 + r_{O^+}^2} + N_{O_2^+} \frac{r_{O_2^+}}{1 + r_{O_2^+}^2} + N_{NO^+} \frac{r_{NO^+}}{1 + r_{NO^+}^2} + N_e \frac{r_e}{1 + r_e^2} \right] \quad (5.134)$$

The Hall conductivity [S/m] is

$$\sigma_H = \frac{e}{B} \left[ -N_{O^+} \frac{1}{1 + r_{O^+}^2} - N_{O_2^+} \frac{1}{1 + r_{O_2^+}^2} - N_{NO^+} \frac{1}{1 + r_{NO^+}^2} + N_e \frac{1}{1 + r_e^2} \right] \quad (5.135)$$

The ion drag coefficients are

$$\lambda_1 = \frac{\sigma_P B^2}{\rho} \quad (5.136)$$

$$\lambda_2 = \frac{\sigma_H B^2}{\rho} \quad (5.137)$$

with  $\rho = N \frac{\bar{m}}{N_A}$ , and  $N_A$  the Avagadro number. The ion drag tensor in magnetic direction  $\underline{\lambda}^{mag}$  is

$$\underline{\lambda}^{mag} = \begin{pmatrix} \lambda_{xx}^{mag} & \lambda_{xy}^{mag} \\ \lambda_{yx}^{mag} & \lambda_{yy}^{mag} \end{pmatrix} = \begin{pmatrix} \lambda_1 & \lambda_2 \sin I \\ -\lambda_2 \sin I & \lambda_1 \sin^2 I \end{pmatrix} \quad (5.138)$$

with the x–direction in magnetic east, and y–direction magnetic north in the both hemispheres. The ion drag tensor can be rotated in geographic direction by using the rotation matrix  $\mathbf{R}$

$$\mathbf{R} = \begin{pmatrix} \cos D & \sin D \\ -\sin D & \cos D \end{pmatrix} \quad (5.139)$$

Applying the rotation to the ion drag tensor  $\mathbf{R} \underline{\lambda}^{mag} \mathbf{R}^{-1}$  leads to

$$\Lambda = \begin{pmatrix} \lambda_{xx} & \lambda_{xy} \\ \lambda_{yx} & \lambda_{yy} \end{pmatrix} = \quad (5.140)$$

$$\begin{pmatrix} \lambda_{xx}^{mag} \cos^2 D + \lambda_{yy}^{mag} \sin^2 D & \lambda_{xy}^{mag} + (\lambda_{yy}^{mag} - \lambda_{xx}^{mag}) \sin D \cos D \\ \lambda_{yx}^{mag} + (\lambda_{yy}^{mag} - \lambda_{xx}^{mag}) \sin D \cos D & \lambda_{yy}^{mag} \cos^2 D + \lambda_{xx}^{mag} \sin^2 D \end{pmatrix} \quad (5.141)$$

The ion drag acceleration  $\mathbf{a}_i$  due to the Ampère force is

$$\mathbf{a}_i = \frac{\mathbf{J} \times \mathbf{B}}{\rho} = \lambda_1 (\mathbf{v}_E - \mathbf{u}_{n\perp}) + \lambda_2 \hat{\mathbf{b}} \times (\mathbf{v}_E - \mathbf{u}_{n\perp}) \quad (5.142)$$

with  $\mathbf{u}_{n\perp}$  the neutral wind velocity perpendicular to the geomagnetic field and  $\hat{\mathbf{b}}$  the unit vector of the geomagnetic field. The tendencies on the neutral wind are calculated by

$$\frac{\partial \mathbf{v}_{En}}{\partial t} = -\Lambda \mathbf{v}_{En} \quad (5.143)$$

For stability an implicit scheme is used with

$$\frac{\mathbf{v}_{En}(t + \Delta t) - \mathbf{v}_{En}(t)}{\Delta t} = -\Lambda \mathbf{v}_{En}(t + \Delta t) \quad (5.144)$$

which leads to

$$(\frac{1}{\Delta t} I + \Lambda) \mathbf{v}_{En}(t + \Delta t) = \frac{1}{\Delta t} \mathbf{v}_{En}(t) \quad (5.145)$$

with  $I$  the unit matrix. Solving for  $\mathbf{v}_{En}(t + \Delta t)$  gives

$$\mathbf{v}_{En}(t + \Delta t) = \frac{1}{\Delta t} (\frac{1}{\Delta t} I + \Lambda)^{-1} \mathbf{v}_{En}(t) \quad (5.146)$$

The tendencies are determined by

$$\frac{\partial \mathbf{v}_{En}}{\partial t} = \frac{\mathbf{v}_{En}(t + \Delta t) - \mathbf{v}_{En}(t)}{\Delta t} = \frac{1}{\Delta t} [\frac{1}{\Delta t} (\frac{1}{\Delta t} I + \Lambda)^{-1} - 1] \mathbf{v}_{En}(t) \quad (5.147)$$

The tensor  $\frac{1}{\Delta t} I + \Lambda$  is

$$\begin{pmatrix} \lambda_{11}^* & \lambda_{12}^* \\ \lambda_{21}^* & \lambda_{22}^* \end{pmatrix} = \begin{pmatrix} \frac{1}{\Delta t} + \lambda_{xx} & \lambda_{xy} \\ \lambda_{yx} & \frac{1}{\Delta t} + \lambda_{yy} \end{pmatrix} \quad (5.148)$$

$$\frac{Det}{\Delta t} = \frac{1}{\Delta t} \frac{1}{\lambda_{11}^* \lambda_{22}^* - \lambda_{12}^* \lambda_{21}^*} \quad (5.149)$$

The tendencies applied to the neutral winds with  $\mathbf{v}_{En} = (u_E - u_n, v_E - v_n)$  gives

$$d_t u_i = \frac{1}{\Delta t} \left[ \frac{Det}{\Delta t} (\lambda_{12}^* (v_E - v_n) - \lambda_{22}^* (u_E - u_n)) + u_E - u_n \right] \quad (5.150)$$

$$d_t v_i = \frac{1}{\Delta t} \left[ \frac{Det}{\Delta t} (\lambda_{21}^* (u_E - u_n) - \lambda_{11}^* (v_E - v_n)) + v_E - v_n \right] \quad (5.151)$$

4200

4201

The electromagnetic energy transfer to the ionosphere is

$$\mathbf{J} \cdot \mathbf{E} = \mathbf{J} \cdot \mathbf{E}' + \mathbf{u}_n \cdot \mathbf{J} \times \mathbf{B} \quad (5.152)$$

The first term on the right hand side denotes the Joule heating, which is the electromagnetic energy transfer rate in the frame of reference of the neutral wind. The second term represents the generation of kinetic energy due to the Ampère force. Since the electric field is small along the magnetic field line, we consider only the perpendicular component to the magnetic field of the Joule heating  $\mathbf{J}_\perp \cdot \mathbf{E}'$ . The electric field in the frame of the neutral wind  $\mathbf{u}$  can be written as

$$\mathbf{E}' = \mathbf{E} + \mathbf{u} \times \mathbf{B} \quad (5.153)$$

The Joule heating can be expressed by

$$\mathbf{J}_\perp \cdot \mathbf{E}' = \sigma_P \mathbf{E}'^2 \quad (5.154)$$

with

$$\mathbf{E}'^2 = B^2 \left( \frac{\mathbf{E} \times \mathbf{B}}{B^2} - \mathbf{u}_\perp \right)^2 \quad (5.155)$$

and  $\frac{\mathbf{E} \times \mathbf{B}}{B^2}$  the electromagnetic drift velocity  $\mathbf{v}_E$  with the components  $u_E$  and  $v_E$ . The Joule heating  $Q_J$  is

$$Q_J = (u_E - u_n)^2 \lambda_{xx} + (u_E - u_n)(v_E - v_n)(\lambda_{xy} - \lambda_{yx}) + (v_E - v_n)^2 \lambda_{yy} \quad (5.156)$$

4202 Note, that the vertical velocity components are not taken into account here.

### 4203 5.3.9 Boundary Conditions

4204 The upper boundary conditions for momentum and for most constituents are the usual zero  
 4205 flux conditions used in CAM4. However, in the energy budget of the thermosphere, much  
 4206 of the SW radiation at wavelengths <120 nm is absorbed above 145 km (the upper bound-  
 4207 ary of the model), where LW radiation is very inefficient. This energy is transported down-  
 4208 ward by molecular diffusion to below 120 km, where it can be dissipated more efficiently by  
 4209 LW emission. Imposing a zero flux upper boundary condition on heat omits a major term  
 4210 in the heat budget and causes the lower thermosphere to be much too cold. Instead, we  
 4211 use the Mass Spectrometer-Incoherent Scatter (MSIS) model [Hedin, 1987, 1991] to specify  
 4212 the temperature at the top boundary as a function of season and phase of the solar cy-  
 4213 cle. The version of the MSIS model used in WACCM4.0 is NRLMSISE-00 [see [http://uap-](http://uap-www.nrl.navy.mil/models_web/msis/msis_home.htm)  
 4214 [www.nrl.navy.mil/models\\_web/msis/msis\\_home.htm](http://uap-www.nrl.navy.mil/models_web/msis/msis_home.htm)].

4215 For chemical constituents, surface mixing ratios of CH<sub>4</sub>, N<sub>2</sub>O, CO<sub>2</sub>, H<sub>2</sub>, CFC-11, CFC-12,  
 4216 CFC-113, HCFC-22, H-1211, H-1301, CCl<sub>4</sub>, CH<sub>3</sub>CCH<sub>3</sub>, CH<sub>3</sub>Cl, and CH<sub>3</sub>Br are specified from  
 4217 observations. The model accounts for surface emissions of NO<sub>x</sub> and CO based on the emission  
 4218 inventories described in Horowitz et al. [2003]. The NO<sub>x</sub> source from lightning is distributed  
 4219 according to the location of convective clouds based on Price et al. [1997a] and Price et al.  
 4220 [1997b], with a vertical profile following Pickering et al. [1998]. Aircraft emissions of NO<sub>x</sub> and  
 4221 CO are included in the model and based on Friedl [1997].

4222 At the upper boundary, a zero-flux upper boundary condition is used for most species whose  
 4223 mixing ratio is negligible in the lower thermosphere, while mixing ratios of other species are  
 4224 specified from a variety of sources. The MSIS model is used to specify the mixing ratios of O,  
 4225 O<sub>2</sub>, H, and N; as in the case of temperature, the MSIS model returns values of these constituents  
 4226 as functions of season and phase of the solar cycle. CO and CO<sub>2</sub> are specified at the upper  
 4227 boundary using output from the TIME-GCM [Roble and Ridley, 1994]. NO is specified using  
 4228 data from the Student Nitric Oxide Explorer (SNOE) satellite [Barth et al., 2003], which has  
 4229 been parameterized as a function of latitude, season, and phase of the solar cycle in the Nitric  
 4230 Oxide Empirical Model (NOEM) of Marsh et al. [2004]. Finally, a global-mean value (typical of  
 4231 the sunlit lower thermosphere) is specified for species such as H<sub>2</sub>O, whose abundance near the top  
 4232 of the model is very small under sunlit conditions, but which can be rapidly transported upward

<sup>4233</sup> by diffusive separation in polar night (since they are lighter than the background atmosphere).  
<sup>4234</sup> In these cases, a zero-flux boundary condition leads to unrealistically large mixing ratios at the  
<sup>4235</sup> model top in polar night.

4236

# Chapter 6

4237

## Initial and Boundary Data

4238

### 6.1 Initial Data

In this section, we describe how the time integration is started from data consistent with the spectral truncation. The land surface model requires its own initial data, as described by [Bonan \[1996\]](#). The basic initial data for the model consist of values of  $u, v, T, q, \Pi$ , and  $\Phi_s$  on the Gaussian grid at time  $t = 0$ . From these,  $U, V, T'$ , and  $\Pi$  are computed on the grid using [\(3.139\)](#), and [\(3.177\)](#). The Fourier coefficients of these variables  $U^m, V^m, T'^m, \Pi^m$ , and  $\Phi_s^m$  are determined via an FFT subroutine [\(3.277\)](#), and the spherical harmonic coefficients  $T_n^m, \Pi_n^m$ , and  $(\Phi_s)_n^m$  are determined by Gaussian quadrature [\(3.278\)](#). The relative vorticity  $\zeta$  and divergence  $\delta$  spherical harmonic coefficients are determined directly from the Fourier coefficients  $U^m$  and  $V^m$  using the relations,

$$\zeta = \frac{1}{a(1 - \mu^2)} \frac{\partial V}{\partial \lambda} - \frac{1}{a} \frac{\partial U}{\partial \mu}, \quad (6.1)$$

$$\delta = \frac{1}{a(1 - \mu^2)} \frac{\partial U}{\partial \lambda} + \frac{1}{a} \frac{\partial V}{\partial \mu}. \quad (6.2)$$

4239 The relative vorticity and divergence coefficients are obtained by Gaussian quadrature directly,  
4240 using [\(3.282\)](#) for the  $\lambda$ -derivative terms and [\(3.285\)](#) for the  $\mu$ -derivatives.

4241 Once the spectral coefficients of the prognostic variables are available, the grid-point values  
4242 of  $\zeta, \delta, T', \Pi$ , and  $\Phi_s$  may be calculated from [\(3.308\)](#), the gradient  $\nabla \Pi$  from [\(3.311\)](#) and [\(3.312\)](#),  
4243 and  $U$  and  $V$  from [\(3.317\)](#) and [\(3.318\)](#). The absolute vorticity  $\eta$  is determined from the relative  
4244 vorticity  $\zeta$  by adding the appropriate associated Legendre function for  $f$  [\(3.245\)](#). This process  
4245 gives grid-point fields for all variables, including the surface geopotential, that are consistent  
4246 with the spectral truncation even if the original grid-point data were not. These grid-point  
4247 values are then convectively adjusted (including the mass and negative moisture corrections).

4248 The first time step of the model is forward semi-implicit rather than centered semi-implicit,  
4249 so only variables at  $t = 0$  are needed. The model performs this forward step by setting the  
4250 variables at time  $t = -\Delta t$  equal to those at  $t = 0$  and by temporarily dividing  $2\Delta t$  by 2 for this  
4251 time step only. This is done so that formally the code and the centered prognostic equations of  
4252 chapter [3](#) also describe this first forward step and no additional code is needed for this special  
4253 step. The model loops through as indicated sequentially in chapter [3](#). The time step  $2\Delta t$  is set  
4254 to its original value before beginning the second time step.

## 4255 6.2 Boundary Data

4256 In addition to the initial grid-point values described in the previous section, the model also  
4257 requires lower boundary conditions. The required data are surface temperature ( $T_s$ ) at each  
4258 ocean point, the surface geopotential at each point, and a flag at each point to indicate whether  
4259 the point is land, ocean, or sea ice. The land surface model requires its own boundary data, as  
4260 described by Bonan [1996]. A surface temperature and three subsurface temperatures must also  
4261 be provided at non-ocean points.

4262 For the uncoupled configuration of the model, a seasonally varying sea-surface temperature  
4263 and sea-ice concentration dataset is used to prescribe the time evolution of these surface  
4264 quantities. This dataset prescribes analyzed monthly mid-point mean values of SST and ice  
4265 concentration for the period 1950 through 2001. The dataset is a blended product, using the  
4266 global HadISST OI dataset prior to 1981 and the Smith/Reynolds EOF dataset post-1981 (see  
4267 Hurrell, 2002). In addition to the analyzed time series, a composite of the annual cycle for the  
4268 period 1981-2001 is also available in the form of a mean “climatological” dataset. The sea-  
4269 surface temperature and sea ice concentrations are updated every time step by the model at  
4270 each grid point using linear interpolation in time. The mid-month values have been evaluated  
4271 in such a way that this linear time interpolation reproduces the mid-month values.

4272 Earlier versions of the global atmospheric model (the CCM series) included a simple land-  
4273 ocean-sea ice mask to define the underlying surface of the model. It is well known that fluxes of  
4274 fresh water, heat, and momentum between the atmosphere and underlying surface are strongly  
4275 affected by surface type. The CAM 5.0 provides a much more accurate representation of flux  
4276 exchanges from coastal boundaries, island regions, and ice edges by including a fractional spec-  
4277 ification for land, ice, and ocean. That is, the area occupied by these surface types is described  
4278 as a fractional portion of the atmospheric grid box. This fractional specification provides a  
4279 mechanism to account for flux differences due to sub-grid inhomogeneity of surface types.

4280 In CAM 5.0 each atmospheric grid box is partitioned into three surface types: land, sea ice,  
4281 and ocean. Land fraction is assigned at model initialization and is considered fixed throughout  
4282 the model run. Ice concentration data is provided by the external time varying dataset described  
4283 above, with new values determined by linear interpolation at the beginning of every time-step.  
4284 Any remaining fraction of a grid box not already partitioned into land or ice is regarded as  
4285 ocean.

Surface fluxes are then calculated separately for each surface type, weighted by the appropriate fractional area, and then summed to provide a mean value for a grid box:

$$F_{\psi T} = a_i F_{\psi i} + a_o F_{\psi o} + a_l F_{\psi l} , \quad (6.3)$$

4286 where  $F$  denotes the surface flux of the arbitrary scalar quantity  $\psi$ ,  $a$  denotes fractional area,  
4287 and the subscripts  $T, i, o$ , and  $l$  respectively denote the total, ice, ocean, and land components of  
4288 the fluxes. For each time-step the aggregated grid box fluxes are passed to the atmosphere and  
4289 all flux arrays which have been used for the accumulations are reset to zero in preparation for  
4290 the next time-step. The fractional land values for CAM 5.0 were calculated from Navy 10-Min  
4291 Global Elevation Data. An area preserving binning algorithm was used to interpolate from the  
4292 high-resolution Navy dataset to standard model resolutions.

4293 The radiation parameterization requires monthly mean ozone volume mixing ratios to be  
4294 specified as a function of the latitude grid, 23 vertical pressure levels, and time. The ozone path

4295 lengths are evaluated from the mixing-ratio data. The path lengths are interpolated to the model  
4296  $\eta$ -layer interfaces for use in the radiation calculation. As with the sea-surface temperatures, the  
4297 seasonal version assigns the monthly averages to the mid-month date and updates them every  
4298 12 hours via linear interpolation. The actual mixing ratios used in the standard version were  
4299 derived by [Chervin \[1986\]](#) from analysis of [Dütsch \[1986\]](#).

4300 The sub-grid scale standard deviation of surface orography is specified in the following man-  
4301 ner. The variance is first evaluated from the global Navy 10' topographic height data over an  
4302 intermediate grid (*e.g.*  $2^\circ \times 2^\circ$  grid for T42 and lower resolutions,  $1.67^\circ \times 1.67^\circ$  for T63, and  
4303  $1.0^\circ \times 1.0^\circ$  for T106 resolution) and is assumed to be isotropic. Once computed on the appropri-  
4304 ate grid, the standard deviations are binned to the CAM 5.0 grid (*i.e.*, all values whose latitude  
4305 and longitude centers fall within each grid box are averaged together). Finally, the standard  
4306 deviation is smoothed twice with a 1-2-1 spatial filter. Values over ocean are set to zero.



<sup>4307</sup>

# Appendix A

<sup>4308</sup>

## Physical Constants

Following the American Meteorological Society convention, the model uses the International System of Units (SI) (see August 1974 *Bulletin of the American Meteorological Society*, **Vol. 55**, No. 8, pp. 926-930).

$a$	$= 6.37122 \times 10^6$	m	Radius of earth
$g$	$= 9.80616$	$\text{m s}^{-2}$	Acceleration due to gravity
$\pi$	$= 3.14159265358979323846$		Pi
$t_s$	$= 86164.0$	s	Earth's sidereal day
$\Omega$	$= 2 * \pi / t_s$	$[\text{s}^{-1}]$	Earth's angular velocity
$\sigma_B$	$= 5.67 \times 10^{-8}$	$\text{W m}^{-2} \text{K}^{-4}$	Stefan – Boltzmann constant
$k$	$= 1.38065 \times 10^{-23}$	$\text{JK}^{-1}$	Boltzmann constant
$N$	$= 6.02214 \times 10^{26}$		Avogadro's number
$R^*$	$= k N$	$[\text{JK}^{-1}]$	Universal gas constant
$m_{air}$	$= 28.966$	kg	Molecular weight of dry air
$R$	$= R^* / m_{air}$	$[\text{J kg}^{-1} \text{K}^{-1}]$	Gas constant for dry air
$m_v$	$= 18.016$	kg	Molecular weight of water vapor
$R_v$	$= R^* / m_v$	$[\text{J kg}^{-1} \text{K}^{-1}]$	Gas constant for water vapor
$c_p$	$= 1.00464 \times 10^3$	$\text{J kg}^{-1} \text{K}^{-1}$	Specific heat of dry air at constant pressure
$\kappa$	$= 2/5$		Von Karman constant
$z_{vir}$	$= R_v / R - 1$		Ratio of gas constants for water vapor and dry air
$L_v$	$= 2.501 \times 10^6$	$\text{J kg}^{-1}$	Latent heat of vaporization
$L_i$	$= 3.337 \times 10^5$	$\text{J kg}^{-1}$	Latent heat of fusion
$\rho_{H_2O}$	$= 1.0 \times 10^3$	$\text{kg m}^{-3}$	Density of liquid water
$c_{pv}$	$= 1.81 \times 10^3$	$\text{J kg}^{-1} \text{K}^{-1}$	Specific heat of water vapor at constant pressure
$T_{melt}$	$= 273.16$	$^{\circ}\text{K}$	Melting point of ice
$p_{std}$	$= 1.01325 \times 10^5$	Pa	Standard pressure
$\rho_{air}$	$= p_{std} / (R T_{melt})$	$[\text{kg m}^{-3}]$	Density of dry air at standard pressure/temperature

<sup>4309</sup> The model code defines these constants to the stated accuracy. We do not mean to imply that

<sup>4310</sup> these constants are known to this accuracy nor that the low-order digits are significant to the

<sup>4311</sup> physical approximations employed.



<sup>4312</sup> **Appendix B**

<sup>4313</sup> **Acronyms**

<sup>4314</sup>	ABL	Atmospheric Boundary Layer
	AMIP	Atmospheric Model Intercomparison Project
	AMWG	Atmospheric Model Working Group
	BATS	Biosphere-Atmosphere Transfer Scheme
	CAM	Community Atmosphere Model
	CAPE	Convectively Available Potential Energy
	CCM	Community Climate Model
	CCN	Cloud Condensation Nucleus
	CCSM	Community Climate System Model
	CFC	Chloro-Fluoro Carbon
	CFL	Courant-Friedrichs-Levy Condition
	CGD	NCAR Climate and Global Dynamics Division
	CGS	Centimeters/grams/seconds
	CKD	Clough-Kneizys-Davies
	CLM	Community Land Model
	CMS	(NCAR) Climate Modeling Section
	CSIM	Community Sea-Ice Model
	CWP	Condensed Water Path
	DAO	(NASA Goddard) Data Assimilation Office
	DAS	Data Assimilation System
	DISORT	DIScrete-Ordinate method Radiative Transfer
	ECMWF	European Centre for Medium Range Forecasts
	EOF	Empirical Orthogonal Function
	FASCODE	FASt atmosphere Signature Code
	FFSL	Flux-Form Semi-Lagrangian Transport
	FFT	Fast Fourier Transform
	FV/fv	Finite Volume
	GCM	General Circulation Model
	GENLN	General Line-by-line Atmospheric Transmittance and Radiance Model
	GEOS	Goddard Earth Observing System
	GFDL	Geophysical Fluid Dynamics Laboratory
	GSFC	Goddard Space Flight Center
	GMT	Greenwich Mean Time

4315	HadISST	Hadley Centre for Climate Prediction and Research SST
	HITRAN	High-resolution Transmission Molecular Absorption Database
	ICA	Independent Column Approximation
	IPCC	International Panel on Climate Change
	KNMI	Royal Netherlands Meteorological Institute
	LBL	Line by line
	LCL	Lifting condensation level
	LSM	Land Surface Model
	MATCH	Model for Atmospheric Transport and Chemistry
	M/R	Maximum/Random overlap
	NASA	National Space Administration
	NCAR	National Center for Atmospheric Research
	NCEP	National Center for Environmental Prediction
	NOAA	National Oceanographic and Atmospheric Administration
	NWP	Numerical Weather Prediction
	OI	Optimal Interpolation
	OPAC	Optical Properties of Aerosols and Clouds
	PBL	Planetary Boundary Layer
	PCMDI	Program for Climate Model Diagnosis and Intercomparison
	PPM	Piece-wise Parabolic Method
	RHS	Right Hand Side
	RMS	Root-mean Square
	SCMO	Sufficient Condition for Monotonicity
	SI	International System of Units
	SOM	Slab Ocean Model
	SST	Sea-surface temperature
	TOA	Top Of Atmosphere
	TOM	Top Of Model
	UCAR	University Corporation for Atmospheric Research
	WKB	Wentzel-Kramer-Brillouin approximation

4316 **Appendix C**

4317 **Resolution and dycore-dependent  
4318 parameters**

4319 The following adjustable parameters differ between various finite volume resolutions in the CAM  
4320 5.0. Refer to the model code for parameters relevant to alternative dynamical cores.

Table C.1: Resolution-dependent parameters

Parameter	FV 1 deg	FV 2 deg	Description
$q_{ic,warm}$	2.e-4	2.e-4	threshold for autoconversion of warm ice
$q_{ic,cold}$	18.e-6	9.5e-6	threshold for autoconversion of cold ice
$k_{e,strat}$	5.e-6	5.e-6	stratiform precipitation evaporation efficiency parameter
$RH_{min}^{low}$	.92	.91	minimum RH threshold for low stable clouds
$RH_{min}^{high}$	.77	.80	minimum RH threshold for high stable clouds
$k_{1,deep}$	0.10	0.10	parameter for deep convection cloud fraction
$p_{mid}$	750.e2	750.e2	top of area defined to be mid-level cloud
$c_{0,shallow}$	1.0e-4	1.0e-4	shallow convection precip production efficiency parameter
$c_{0,deep}$	3.5E-3	3.5E-3	deep convection precipitation production efficiency parameter
$k_{e,conv}$	1.0E-6	1.0E-6	convective precipitation evaporation efficiency parameter
$v_i$	1.0	0.5	Stokes ice sedimentation fall speed (m/s)



4321 

# Bibliography

- 4322 Abdul-Razzak, H., and S. J. Ghan, A parameterization of aerosol activation 2. multiple aerosol  
4323 types, *J. Geophys. Res.*, 105 (D5), 6837–6844, 2000a.
- 4324 Abdul-Razzak, H., and S. J. Ghan, A parameterization of aerosol activation 2. multiple aerosol  
4325 types, *Journal of Geophysical Research-Atmospheres*, 105 (D5), 6837–6844, 2000b, 294KT  
4326 Times Cited:82 Cited References Count:27.
- 4327 Alcamo, J., A. Bouwman, J. Edmonds, A. Grubler, T. Morita, and A. Sugandhy, An evaluation  
4328 of the ipcc is92 emission scenarios, in *Climate Change 1994: Radiative Forcing of Climate  
4329 Change and an Evaluation of the IPCC IS92 Emission Scenarios*, edited by J. Houghton,  
4330 247–304, Cambridge University Press, 1995.
- 4331 Andrews, D. G., J. R. Holton, and C. B. Leovy, *Middle Atmosphere Dynamics*. Academic Press,  
4332 1987.
- 4333 Ansmann, A. et al., Influence of Saharan dust on cloud glaciation in southern Morocco during  
4334 the Saharan Mineral Dust Experiment, *J. Geophys. Res.*, 113 (D04210), 2008.
- 4335 Ansmann, A., M. Tesche, P. Seifert, D. Althausen, R. Engelmann, J. Furntke, U. Wandinger,  
4336 I. Mattis, and D. Müller, Evolution of the ice phase in tropical altocumulus: SAMUM lidar  
4337 observations over Cape Verde, *J. Geophys. Res.*, 114 (D17208), 2009.
- 4338 Anthes, R. A., Summary of workshop on the NCAR Community Climate/forecast Models 14–26  
4339 July 1985, Boulder, Colorado, *Bull. Am. Meteorol. Soc.*, 67, 94–198, 1986.
- 4340 Arakawa, A., and V. R. Lamb, A potential enstrophy and energy conserving scheme for the  
4341 shallow-water equations, *Mon. Wea. Rev.*, 109, 18–36, 1981.
- 4342 Asselin, R., Frequency filter for time integrations, *Mon. Wea. Rev.*, 100, 487–490, 1972.
- 4343 Baede, A. P. M., M. Jarraud, and U. Cubasch, Adiabatic formulation and organization of  
4344 ECMWF's model, Technical Report 15, ECMWF, Reading, U.K., 1979.
- 4345 Balachandran, N., and D. Rind, Modeling the effects of uv variability and the qbo on the  
4346 troposphere-stratosphere system. part i: The middle atmosphere, *J. Climate*, 8, 2058–2079,  
4347 1995.
- 4348 Banks, P. M., and G. Kockarts, *Aeronomy, Part B*. Academic Press, San Diego, Calif., 1973,  
4349 355 pp.

- 4350 Barker, H., A parameterization for computing grid-averaged solar fluxes for inhomogenous ma-  
4351 rine boundary layer clouds. part I: Methodology and homogenous biases, *J. Atmos. Sci.*, 53,  
4352 2289–2303, 1996.
- 4353 Barker, H., B. A. Weilicki, and L. Parker, A parameterization for computing grid-averaged solar  
4354 fluxes for inhomogenous marine boundary layer clouds. part II: Validation using satellite data,  
4355 *J. Atmos. Sci.*, 53, 2304–2316, 1996.
- 4356 Barth, C. A., K. D. Mankoff, S. M. Bailey, and S. Solomon, Global observations of nitric oxide  
4357 in the thermosphere, *J. Geophys. Res.*, 108, doi:10.1029/2002JA009458, 2003.
- 4358 Barth, M. C., P. J. Rasch, J. T. Kiehl, C. M. Benkovitz, and S. E. Schwartz, Sulfur chemistry  
4359 in the National Center for Atmospheric Research Community Climate Model: Description,  
4360 evaluation, features and sensitivity to aqueous chemistry, *J. Geophys. Res.*, 105, 1387–1415,  
4361 2000.
- 4362 Bates, J. R., F. H. M. Semazzi, R. W. Higgins, and S. R. Barros, Integration of the shallow  
4363 water equations on the sphere using a vector semi-Lagrangian scheme with a multigrid solver,  
4364 *Mon. Wea. Rev.*, 118, 1615–1627, 1990.
- 4365 Bath, L., J. Rosinski, and J. Olson, User's Guide to NCAR CCM2, Technical Report NCAR/TN-  
4366 379+IA, National Center for Atmospheric Research, Boulder, CO, 156 pp., 1992.
- 4367 Bath, L. M., M. A. Dias, D. L. Williamson, G. S. Williamson, and R. J. Wolski, User's Guide  
4368 to NCAR CCM1, Technical Report NCAR/TN-286+IA, National Center for Atmospheric  
4369 Research, Boulder, CO, 173 pp., 1987.
- 4370 Beheng, K. D., A parameterization of warm cloud microphysical conversion processes, *Atmos.*  
4371 *Res.*, 33, 193–206, 1994.
- 4372 Beres, J. H., R. R. Garcia, B. A. Boville, and F. Sassi, Implementation of a gravity wave source  
4373 spectrum parameterization dependent on the properties of convection in the whole atmosphere  
4374 community climate model (waccm), *J. Geophys. Res.*, 110, doi:10.1029/2004JD005504, 2005.
- 4375 Berger, A. L., Long-term variations of daily insolation and quaternary climatic changes, *J. At-*  
4376 *mos. Sci.*, 35, 2362–2367, 1978.
- 4377 Biermann, U. M., B. P. Luo, and T. Peter, Absorption spectra and optical constants of binary  
4378 and ternary solutions of h<sub>2</sub>so<sub>4</sub>, hno<sub>3</sub>, and h<sub>2</sub>o in the mid infrared at atmospheric temperatures,  
4379 *The Journal of Physical Chemistry A*, 104 (4), 783–793, 01, 2000.
- 4380 Bigg, E. K., The supercooling of water, *Proc. Phys. Soc. B*, 66, 688–694, 1953.
- 4381 Binkowski, F. S., and U. Shankar, The regional particulate matter model .1. model description  
4382 and preliminary results, *Journal of Geophysical Research-Atmospheres*, 100, 26191–26209,  
4383 1995.
- 4384 Blackadar, A. K., The vertical distribution of wind and turbulent exchange in a neutral atmo-  
4385 sphere, *J. Geophys. Res.*, 67, 3095–3102, 1962.

- 4386 Bloomfield, P., Inferred lifetimes, in *NASA Report on Concentrations, Lifetimes and Trends of*  
4387 *CFCs, Halons and Related Species*, edited by J. Kaye, S. Penkett,, and F. Osmond, NASA,  
4388 Washington, D.C., 1994.
- 4389 Bonan, G. B., A land surface model (LSM version 1.0) for ecological, hydrological, and at-  
4390 mospheric studies: Technical description and user's guide, Technical Report NCAR/TN-  
4391 417+STR, National Center for Atmospheric Research, Boulder, CO, 150 pp., 1996.
- 4392 Bonan, G. B., K. W. Oleson, M. Vertenstein, S. Levis, X. Zeng, Y. Dai, R. E. Dickinson, ,  
4393 and Z.-L. Yang, The land surface climatology of the Community Land Model coupled to the  
4394 NCAR Community Climate Model, *J. Climate*, 15, 3123–3149, 2002.
- 4395 Bond, T. C., and R. W. Bergstrom, Light absorption by carbonaceous particles: An investiga-  
4396 tive review, *Aerosol. Sci. Technol.*, 40, 27–67, 2006.
- 4397 Bond, T. C., E. Bhardwaj, R. Dong, R. Jogani, S. K. Jung, C. Roden, D. G. Streets, and  
4398 N. M. Trautmann, Historical emissions of black and organic carbon aerosol from energy-  
4399 related combustion, 1850-2000, *Global Biogeochemical Cycles*, 21 (2), –, 2007, 174KO Times  
4400 Cited:24 Cited References Count:98.
- 4401 Bourke, W., B. McAvaney, K. Puri, and R. Thurling, Global modeling of atmospheric flow by  
4402 spectral methods, in *Methods in Computational Physics*, Vol. 17, 267–324, Academic Press,  
4403 New York, 1977.
- 4404 Boville, B. A., and C. S. Bretherton, Heating and dissipation in the NCAR community atmo-  
4405 sphere model, *J. Climate*, 16, 3877–3887, 2003a.
- 4406 Boville, B. A., and C. S. Bretherton, Heating and kinetic energy dissipation in the ncac com-  
4407 munity atmosphere model, *J. Climate*, 16, 3877–3887, 2003b.
- 4408 Boville, B. A., J. T. Kiehl, P. J. Rasch, and F. O. Bryan, Improvements to the ncac csm-1 for  
4409 transient climate simulations, *J. Climate*, 14, 164–179, 2001.
- 4410 Brasseur, G. P., D. A. Hauglustaine, S. Walters, P. J. Rasch, J.-F. Muller, C. Granier, and X.-X.  
4411 Tie, Mozart: A global chemical transport model for ozone and related chemical tracers, part  
4412 1: Model description, *J. Geophys. Res.*, 103, 28,265–28,289, 1998.
- 4413 Brasseur, G. P., J. J. Orlando, and G. S. Tyndall, *Atmospheric Chemistry and Global Change*.  
4414 Oxford University Press, 1999.
- 4415 Bretherton, C. S., J. R. McCaa, and H. Grenier, A new parameterization for shallow cumulus  
4416 convection and its application to marine subtropical cloud-topped boundary layer. part i:  
4417 Description and 1d results, *Mon. Wea. Rev.*, 132, 864–882, 2004.
- 4418 Bretherton, C. S., and S. Park, A new moist turbulence parameterization in the community  
4419 atmosphere model, *J. Climate*, 22, 3422–3448, 2009a.
- 4420 Bretherton, C. S., and S. Park, A new moist turbulence parameterization in the Community  
4421 Atmosphere Model, *J. Clim.*, 22, 3422–3448, 2009b.

- 4422 Briegleb, B. P., Delta-Eddington approximation for solar radiation in the NCAR Community  
4423 Climate Model, *J. Geophys. Res.*, **97**, 7603–7612, 1992.
- 4424 Bryan, F. O., B. G. Kauffman, W. G. Large, and P. R. Gent, The NCAR CSM Flux Coupler,  
4425 Technical Report NCAR/TN-424+STR, National Center for Atmospheric Research, Boulder,  
4426 Colorado, 58 pp., 1996.
- 4427 Bryant, F. D., and P. Latimer, Optical efficiencies of large particles of arbitrary shape and  
4428 orientation, *J. Colloid Interface Sci.*, **30**, 291–304, 1969.
- 4429 Cariolle, D., A. Lasserre-Bigorry, J.-F. Royer, and J.-F. Geleyn, A general circulation model  
4430 simulation of the springtime antarctic ozone decrease and its impact on mid-latitudes., *J.*  
4431 *Geophys. Res.*, **95**, 1883–1898, 1990.
- 4432 Chabrillat, S., and G. Kockarts, Simple parameterization of the absorption of the solar lyman-  
4433 alpha line, *Geophys. Res. Lett.*, **24**, 2659–2662, 1997.
- 4434 Chervin, R. M., Interannual variability and seasonal climate predictability, *J. Atmos. Sci.*, **43**,  
4435 233–251, 1986.
- 4436 Clough, S. A., M. W. Shephard, E. H. Mlawer, J. S. Delamere, M. J. Iacono, K. Cady-Pereira,  
4437 S. Boukabara, and P. D. Brown, Atmospheric radiative transfer modeling: a summary of the  
4438 aer codes, *J. Quant. Spectrosc. Radiat. Transfer*, **91**, 233–244, 2005.
- 4439 Clough, S., and M. Iacono, Line-by-line calculation of atmospheric fluxes and cooling rates 2.  
4440 application to carbon dioxide, ozone, methane, nitrous oxide and the halocarbons., *J. Geophys.*  
4441 *Res.*, **100**, 16519–16535, 1995.
- 4442 Colella, P., and P. R. Woodward, The piecewise parabolic method (ppm) for gas-dynamical  
4443 simulations, *J. Comp. Phys.*, **54**, 174–201, 1984.
- 4444 Collins, W. D., A global signature of enhanced shortwave absorption by clouds, *J. Geophys.*  
4445 *Res.*, **103(D24)**, 31,669–31,680, 1998.
- 4446 Collins, W. D., P. J. Rasch, B. A. Boville, J. J. Hack, J. R. McCaa, D. L. Williamson, J. T.  
4447 Kiehl, B. P. Briegleb, C. Bitz, S. J. Lin, M. Zhang, and Y. Dai, Description of the ncar  
4448 community atmosphere model (cam 3.0), Technical report, National Center for Atmospheric  
4449 Research, 2004a.
- 4450 Collins, W. D., P. J. Rasch, B. A. Boville, J. J. Hack, J. R. McCaa, D. L. Williamson, J. T.  
4451 Kiehl, B. P. Briegleb, C. Bitz, S.-J. Lin, M. Zhang, and Y. Dai, *Description of the NCAR*  
4452 *Community Atmosphere Model (CAM3)*. Nat. Cent. for Atmos. Res., Boulder, Colo., 2004b.
- 4453 Collins, W., J. Hackney, and D. Edwards, A new parameterization for infrared emission and  
4454 absorption of water vapor in the national center for atmospheric research community atmo-  
4455 spheric model, *J. Geophys. Res.*, **107**, doi: 10.1029/2001JD001365, 2002.

- 4456 Considine, D. B., A. R. Douglass, D. E. Kinnison, P. S. Connell, and D. A. Rotman, A polar  
4457 stratospheric cloud parameterization for the three dimensional model of the global modeling  
4458 initiative and its response to stratospheric aircraft emissions, *J. Geophys. Res.*, 105, 3955–  
4459 3975, 2000.
- 4460 Considine, D. B., P. S. Connell, D. Bergmann, D. A. Rotman, and S. Strahan, Sensitivity of  
4461 Global Modeling Initiative CTM predictions of Antarctic ozone recovery to GCM and DAS  
4462 generated meteorological fields, *J. Geophys. Res.*, 109, doi:10.1029/20003JD004487, 2004.
- 4463 Cooke, W. F., and J. J. N. Wilson, A global black carbon aerosol model, *J. Geophys. Res.*, 101,  
4464 19395–19409, 1996.
- 4465 Côté, J., and A. Staniforth, A two-time-level semi-Lagrangian semi-implicit scheme for spectral  
4466 models, *Mon. Wea. Rev.*, 116, 2003–2012, 1988.
- 4467 Cotton, W. R., G. J. Tripoli, R. M. Rauber, and E. A. Mulvihill, Numerical simulation of the  
4468 effects of varying ice crystal nucleation rates and aggregation processes on orographic snowfall,  
4469 *J. Appl. Meteor.*, 25, 1658–1680, 1986.
- 4470 Dai, Y., X. Zeng, R. E. Dickinson, and coauthors, The Common Land Model: Documentation  
4471 and User's Guide, <http://climate.eas.gatech.edu/dai/clmdoc.pdf>, 2001.
- 4472 Daley, R., C. Girard, J. Henderson, and I. Simmonds, Short-term forecasting with a multi-level  
4473 spectral primitive equation model. Part I—model formulation, *Atmosphere*, 14, 98–116, 1976.
- 4474 DeCaria, A. J., K. E. Pickering, G. L. Stenchikov, and L. E. Ott, Lightning-generated nox  
4475 and its impact on tropospheric ozone production: A three-dimensional modeling study of a  
4476 stratosphere-troposphere experiment: Radiation, aerosols and ozone (sterao-a) thunderstorm,  
4477 *J. Geophys. Res.*, 110, D14303, 2006.
- 4478 Dennis, J., A. Fournier, W. F. Spotz, A. St.-Cyr, M. A. Taylor, S. J. Thomas, and H. Tufo,  
4479 High resolution mesh convergence properties and parallel efficiency of a spectral element  
4480 atmospheric dynamical core, *Int. J. High Perf. Comput. Appl.*, 19, 225–235, 2005.
- 4481 Dentener, F., S. Kinne, T. Bond, O. Boucher, J. Cofala, S. Generoso, P. Ginoux, S. Gong,  
4482 J. J. Hoelzemann, A. Ito, L. Marelli, J. E. Penner, J. P. Putaud, C. Textor, M. Schulz,  
4483 G. R. van derWerf, and J. Wilson, Emissions of primary aerosol and precursor gases in the  
4484 years 2000 and 1750 prescribed data-sets for aerocom, *Atmospheric Chemistry and Physics*,  
4485 6, 4321–4344, 2006a, 087YG Times Cited:81 Cited References Count:52.
- 4486 Dentener, F., D. Stevenson, K. Ellingsen et al., Global atmospheric environment for the next  
4487 generation, *Environmental Science and Technology*, 40, 3586–3594, 2006b.
- 4488 Deville, M. O., P. F. Fischer, and E. H. Mund, *High Order Methods for Incompressible Fluid  
4489 Flow*. Cambridge University Press, 1 edition, 8, 2002.
- 4490 Dickinson, R. E., A. Henderson-Sellers, P. J. Kennedy, and M. F. Wilson, Biosphere-atmosphere  
4491 transfer scheme (BATS) for the NCAR Community Climate Model, Technical Report  
4492 NCAR/TN-275+STR, National Center for Atmospheric Research, Boulder, Colorado, 69 pp.,  
4493 1987.

- 4494 Dütsch, H. U., Vertical ozone distribution on a global scale, *Pure Appl. Geophys.*, **116**, 511–529,  
4495 1986.
- 4496 Dye, J. E., D. Baumgardner, B. W. Gandrun, S. R. Kawa, K. K. Kelly, M. Loewenstein, G. V.  
4497 Ferry, K. R. Chan, and B. L. Gary, Particle size distributions in arctic polar stratospheric  
4498 clouds, growth and freezing of sulfuring acid droplets, and implications for cloud formation,  
4499 *J. Geophys. Res.*, **97**, 8015–8034, 1992.
- 4500 Easter, R. C., S. J. Ghan, Y. Zhang, R. D. Saylor, E. G. Chapman, N. S. Laulainen, H. Abdul-  
4501 Razzak, L. R. Leung, X. D. Bian, and R. A. Zaveri, Mirage: Model description and evaluation  
4502 of aerosols and trace gases, *Journal of Geophysical Research-Atmospheres*, **109** (D20), –, 2004,  
4503 867ZR Times Cited:37 Cited References Count:280.
- 4504 Eaton, B. E., User's Guide to the Community Atmosphere Model AM4.0, Technical  
4505 report, National Center for Atmospheric Research, Boulder, Colorado,  
4506 [http://www.ccsm.ucar.edu/models/ccsm4.0/cam/docs/users\\_guide/book1.html](http://www.ccsm.ucar.edu/models/ccsm4.0/cam/docs/users_guide/book1.html), 2010.
- 4507 Emmons, e. a., L. K., Description and evaluation of the model for ozone and related chemical  
4508 tracers, version 4 (mozart-4), *Geosci. Model Dev.*, **3**, 43–67, 2010.
- 4509 Ferrier, B., A double-moment multiple-phase four-class bulk ice scheme. part I: Description, *J.  
4510 Atmos. Sci.*, **51**, 249–280, 1994.
- 4511 Fiedler, F., and H. A. Panofsky, The geostrophic drag coefficient and the “effective roughness  
4512 length, *Quart. J. Roy. Meteor. Soc.*, **98**, 213–220, 1972.
- 4513 Field, P. R., O. Möhler, P. Connolly, M. Krmer, R. Cotton, A. J. Heymsfield, H. Saathoff,  
4514 and M. Schnaiter, Some ice nucleation characteristics of Asian and Saharan desert dust,  
4515 *Atmospheric Chemistry and Physics*, **6** (10), 2991–3006, 2006.
- 4516 Field, P. R., A. J. Heymsfield, and A. Bansemer, Shattering and particle inter-arrival times  
4517 measured by optical array probes in ice clouds, *J. Atmos. Oceanic Technol.*, **23**, 1357–1371,  
4518 2007.
- 4519 Fomichev, V. I., J. P. Blanchet, and D. S. Turner, Matrix parameterization of the 15  $\mu\text{m}$   $\text{CO}_2$   
4520 band cooling in the middle and upper atmosphere for variable  $\text{CO}_2$  concentration, *J. Geophys.  
4521 Res.*, **103**, 11505–11528, 1998.
- 4522 Fomichev, V. I., V. P. Ogibalov, and S. R. Beagley, Solar heating by the near-IR  $\text{CO}_2$  bands in  
4523 the mesosphere, *Geophys. Res. Lett.*, **31**, L21102, 2004.
- 4524 Fournier, A., M. A. Taylor, and J. Tribbia, The spectral element atmosphere model (SEAM):  
4525 High-resolution parallel computation and localized resolution of regional dynamics, *Mon. Wea.  
4526 Rev.*, **132**, 726–748, 2004.
- 4527 Friedl, R., editor, *Atmospheric effects of subsonic aircraft: Interim assessment report of the  
4528 advanced subsonic technology program*. 1997.

- 4529 Fritts, D. C., and T. J. Dunkerton, Fluxes of heat and constituents due to convectively unstable  
4530 gravity waves, *jas*, 42, 549–556, 1985.
- 4531 Fu, Q., P. Yang, and W. B. Sun, An accurate parameterization of the infrared radiative prop-  
4532 erties of cirrus clouds for climate models, *J. Climate*, 11, 2223–2237, 1998.
- 4533 Fuchs, N. A., *The Mechanics of Aerosols*. Pergamon, Oxford, 1964.
- 4534 Galperin, B., L. H. Kanta, S. Hassid, and A. Rosati, A quasi-equilibrium turbulent energy model  
4535 for geophysical flows, *J. Atmos. Sci.*, 45, 55–62, 1988.
- 4536 Garcia, R. R., Parameterization of planetary wave breaking in the middle atmosphere, *jas*, 2001.
- 4537 Garcia, R. R., D. R. Marsh, D. E. Kinnison, B. A. Boville, and F. Sassi, Simula-  
4538 tion of secular trends in the middle atmosphere, 1950–2003, *J. Geophys. Res.*, 112,  
4539 doi:10.1029/2006JD007485, 2007.
- 4540 Garcia, R. R., and S. Solomon, The effect of breaking gravity waves on the dynamical and  
4541 chemical composition of the mesosphere and lower thermosphere, *J. Geophys. Res.*, 90, 3850–  
4542 3868, 1985.
- 4543 Garcia, R. R., and S. Solomon, A new numerical model of the middle atmosphere. part ii: Ozone  
4544 and related species, *J. Geophys. Res.*, 99, 12937–12951, 1994.
- 4545 Gent, P. R., S. Yeager, R. B. Neale, S. Levis, and D. Bailey, Improvements in a half degree  
4546 atmopshere/land version of the CCSM., *Climate Dynamics*, 79, 25–58, 2009.
- 4547 Gettelman, A., H. Morrison, and S. J. Ghan, A new two-moment bulk stratiform cloud micro-  
4548 physics scheme in the NCAR Community Atmosphere Model (CAM3), Part II: Single-column  
4549 and global results, *J. Clim.*, 21 (15), 3660–3679, 2008.
- 4550 Gettelman, A., A. X. Liu, S. J. Ghan, H. Morrison, S. Park, A. J. Conley, S. A. Klein, J. Boyle,  
4551 D. L. Mitchell, and J. L. F. Li, Global simulations of ice nucleation and ice supersaturation  
4552 with an improved cloud scheme in the community atmosphere model, *J. Geophys. Res.*, 108,  
4553 ????–????, 2010a.
- 4554 Gettelman, A. et al., Multi-model assessment of the upper troposphere and lower stratosphere:  
4555 Tropics and trends, *in press J. Geophys. Res.*, 2010b.
- 4556 Ghan, S. J., and R. C. Easter, Computationally efficient approximations to stratiform cloud  
4557 microphysics parameterization, *Mon. Weather Rev.*, 120 (1572–1582), 1992.
- 4558 Ghan, S. J., and R. C. Easter, Impact of cloud-borne aerosol representation on aerosol direct  
4559 and indirect effects, *Atmospheric Chemistry and Physics*, 6, 4163–4174, 2006, 086FO Times  
4560 Cited:5 Cited References Count:47.
- 4561 Ghan, S. J., L. R. Leung, R. C. Easter, and K. AbdulRazzak, Prediction of cloud droplet  
4562 number in a general circulation model, *J. Geophys Res-Atmos*, 102, 21777–21794, 1997.

- 4563 Ghan, S. J., and R. A. Zaveri, Parameterization of optical properties for hydrated internally-  
4564 mixed aerosol, *J. Geophys. Res.*, 112, DOI 10.1029/2006JD007927, 2007.
- 4565 Giorgi, F., and W. Chameides, The rainout parameterization in a photochemical model, *J.  
4566 Geophys. Res.*, 90, 7872–7880, 1985.
- 4567 Giraldo, F. X., Trajectory calculations for spherical geodesic grids in cartesian space, *Mon. Wea.  
4568 Rev.*, 127, 1651–1662, 1999.
- 4569 Gregory, D., R. Kershaw, and P. M. Inness, Parameterization of momentum transport by con-  
4570 vection. ii: Tests in single column and general circulation models, *Q. J. R. Meteorol. Soc.*,  
4571 123, 1153–1184, 1997a.
- 4572 Gregory, D., R. Kershaw, and P. M. Inness, Parametrization of momentum transport by con-  
4573 vection. II: Tests in single-column and general circulation models, *Q. J. R. Meteorol. Soc.*,  
4574 123, 1153–1183, 1997b.
- 4575 Grenier, H., and C. S. Bretherton, A moist pbl parameterization for large-scale models and  
4576 its application to subtropical cloud-topped marine boundary layer, *Mon. Wea. Rev.*, 129,  
4577 357–377, 2001.
- 4578 Hack, J. J., Parameterization of moist convection in the National Center for Atmospheric Re-  
4579 search Community Climate Model (CCM2), *J. Geophys. Res.*, 99, 5551–5568, 1994a.
- 4580 Hack, J. J., Parameterization of moist convection in the national center for atmospheric research  
4581 community climate model (ccm2), *J. Geophys. Res.*, 99, 5551–5568, 1994b.
- 4582 Hack, J. J., L. M. Bath, G. W. Williamson, and B. A. Boville, Modifications and enhancements  
4583 to the NCAR Community Climate Model (CCM1), Technical Report NCAR/TN-336+STR,  
4584 National Center for Atmospheric Research, Boulder, Colorado, 97 pp., 1989.
- 4585 Hack, J. J., B. A. Boville, B. P. Briegleb, J. T. Kiehl, P. J. Rasch, and D. L. Williamson,  
4586 Description of the NCAR Community Climate Model (CCM2), Technical Report NCAR/TN-  
4587 382+STR, National Center for Atmospheric Research, 120 pp., 1993.
- 4588 Hedin, A. E., Extension of the MSIS thermosphere model into the middle and lower atmosphere,  
4589 *J. Geophys. Res.*, 96, 1159, 1991.
- 4590 Hedin, A., MSIS-86 thermospheric model, *J. Geophys. Res.*, 92, 4649, 1987.
- 4591 Heinbockel, J. H., *Introduction to Tensor Calculus and Continuum Mechanics*. Trafford Pub-  
4592 lishing, Victoria, B.C., 12, 2001.
- 4593 Held, I. M., and M. J. Suarez, A proposal for the intercomparison of the dynamical cores of  
4594 atmospheric general circulation models, *Bull. Am. Meteorol. Soc.*, 75, 1825–1830, 1994.
- 4595 Hildebrand, F. B., *Introduction to Numerical Analysis*. McGraw-Hill, New York, New York,  
4596 1956, 511 pp.

- 4597 Holtslag, A. M., and B. A. Boville, Local versus nonlocal boundary layer diffusion in a global  
4598 climate model, *J. Climate*, 6, 1825–1842, 1993.
- 4599 Holton, J. R., The role of gravity wave induced drag and diffusion in the momentum budget of  
4600 the mesosphere, *J. Atmos. Sci.*, 39, 791–799, 1982.
- 4601 Holtslag, A. A. M., and B. A. Boville, Local versus nonlocal boundary-layer diffusion in a global  
4602 climate model, *J. Climate*, 6, 1825–1842, 1993a.
- 4603 Holtslag, A. A. M., and B. A. Boville, Local versus nonlocal boundary layer diffusion in a global  
4604 model, *J. Climate*, 6, 1825–1842, 1993b.
- 4605 Holtslag, A. A. M., E. I. F. deBruijn, and H.-L. Pan, A high resolution air mass transformation  
4606 model for short-range weather forecasting, *Mon. Wea. Rev.*, 118, 1561–1575, 1990.
- 4607 Hoose, C., and J. E. Kristjansson, A classical-theory-based parameterization of heterogeneous  
4608 ice nucleation by mineral dust, soot and biological particles in a global climate model, *in  
4609 press*, *J. Atmos. Sci.*, 2010.
- 4610 Horowitz, e. a., L., A global simulation of tropospheric ozone and related tracers: Description  
4611 and evaluation of mozart, version 2, *Journal of Geophysical Research-Atmospheres*, 108, 4784,,  
4612 2003.
- 4613 Horowitz, L., S. Walters, D. Mauzerall, L. Emmons, P. Rasch, C. Granier, X. Tie, J.-F. Lamar-  
4614 que, M. Schultz, G. Tyndall, J. Orlando, and G. Brasseur, A global simulation of tropospheric  
4615 ozone and related tracers: Description and evaluation of mozart, version 2, *J. Geophys. Res.*,  
4616 108, 4784, 2003.
- 4617 Hortal, M. 1999. Aspects of the numerics of the ECMWF model. in *Proceedings of ECMWF  
4618 Seminar: Recent developments in numerical methods for atmospheric modelling*, 7–11 Septem-  
4619 ber 1998, 127–143, .
- 4620 Hoskins, B. J., The mathematical theory of frontogenesis, *Ann. Rev. Fluid Mech.*, 14, 131–151,  
4621 1982.
- 4622 Hsu, Y.-J. G., and A. Arakawa, Numerical modeling of the atmosphere with an isentropic vertical  
4623 coordinate, *Mon. Wea. Rev.*, 118, 1933–1959, 1990.
- 4624 Iacono, M., E. Mlawer, S. Clough, and J.-J. Morcrette, Impact of an improved longwave radiation  
4625 model, rrtm, on the energy budget and thermodynamic properties of the ncar community  
4626 climate model, ccm3, *J. Geophys. Res.*, 105, 14873–14890, 2000.
- 4627 Iacono, M., J. Delamere, E. Mlawer, and S. Clough, Evaluation of upper tropospheric water  
4628 vapor in the ncar community climate model (ccm3) using modeled and observed hirs radiances,  
4629 *J. Geophys. Res.*, 108(D2), 4037, 2003.
- 4630 Iacono, M., J. Delamere, E. Mlawer, M. Shephard, S. Clough, and W. Collins, Radiative forcing  
4631 by long-lived greenhouse gases: Calculations with the aer radiative transfer models, *J. Geo-  
4632 phys. Res.*, 2008.

- 4633 Ikawa, M., and K. Saito, description of the nonhydrostatic model developed at the forecast  
4634 research department of the mri, Technical Report 28, Meteorological Institute MRI, 1990.
- 4635 Jablonowski, C., and D. L. Williamson, A baroclinic instability test case for atmospheric model  
4636 dynamical cores, *Q. J. R. Meteorol. Soc.*, 132, 2943–2975, 2006.
- 4637 Junker, C., and C. Liousse, A global emission inventory of carbonaceous aerosol from historic  
4638 records of fossil fuel and biofuel consumption for the period 1860–1997, *Atmospheric Chemistry*  
4639 and *Physics*, 8 (5), 1195–1207, 2008, 273CS Times Cited:8 Cited References Count:52.
- 4640 Kader, B. A., and A. M. Yaglom, Mean fields and fluctuation moments in unstably stratified  
4641 turbulent boundary layers, *J. Fluid Mech.*, 212, 637–662, 1990.
- 4642 Kain, J. S., and J. M. Fritsch, A one-dimensional entraining/detraining plume model and its  
4643 application in convective parameterization, *J. Atmos. Sci.*, 47, 2784–2802, 1990.
- 4644 Kärcher, B., O. Möhler, P. J. DeMott, S. Pechtl, and F. Yu, Insights into the role of soot aerosols  
4645 in cirrus cloud formation, *Atmos. Chem. Phys.*, 7, 4203–4227, 2007.
- 4646 Karniadakis, G. E., and S. J. Sherwin, *Spectral/hp Element Methods for Computational Fluid*  
4647 *Dynamics (Numerical Mathematics and Scientific Computation)*. Oxford University Press,  
4648 USA, 2 edition, 8, 2005.
- 4649 Kasahara, A., Various vertical coordinate systems used for numerical weather prediction, *Mon.*  
4650 *Wea. Rev.*, 102, 509–522, 1974.
- 4651 Kasten, F., Falling speed of aerosol particles, *J. Appl. Meteorol.*, 7, 944–947, 1968.
- 4652 Kerminen, V. M., and M. Kulmala, Analytical formulae connecting the "real" and the "apparent"  
4653 nucleation rate and the nuclei number concentration for atmospheric nucleation events,  
4654 *Journal of Aerosol Science*, 33 (4), 609–622, 2002, 535VC Times Cited:67 Cited References  
4655 Count:26.
- 4656 Kershaw, R., and D. Gregory, Parametrization of momentum transport by convection. I: Theory  
4657 and cloud modelling results, *Q. J. R. Meteorol. Soc.*, 123, 1133–1151, 1997.
- 4658 Khairoutdinov, M. F., and Y. Kogan, A new cloud physics parameterization in a large-eddy  
4659 simulation model of marine stratocumulus, *Mon. Weather Rev.*, 128, 229–243, 2000.
- 4660 Kiehl, J. T., and B. P. Briegleb, A new parameterization of the absorbance due to the 15 micron  
4661 band system of carbon dioxide, *J. Geophys. Res.*, , 9013–9019, 1991.
- 4662 Kiehl, J. T., J. J. Hack, and B. P. Briegleb, The simulated Earth radiation budget of the National  
4663 Center for Atmospheric Research Community Climate Model CCM2 and comparisons with  
4664 the Earth Radiation Budget Experiment (ERBE), *J. Geophys. Res.*, 99, 20815–20827, 1994.
- 4665 Kiehl, J. T., J. Hack, G. Bonan, B. Boville, B. Briegleb, D. Williamson, and P. Rasch, De-  
4666 scription of the NCAR Community Climate Model (CCM3), Technical Report NCAR/TN-  
4667 420+STR, National Center for Atmospheric Research, Boulder, Colorado, 152 pp., 1996.

- 4668 Kiehl, J. T., J. J. Hack, G. B. Bonan, B. B. Boville, D. L. Williamson, and P. J. Rasch, The  
4669 National Center for Atmospheric Research Community Climate Model: CCM3, *J. Climate*,  
4670 11, 1131–1149, 1998.
- 4671 Kinnison, D. E., G. P. Brasseur, S. Walters, R. R. Garcia, F. Sassi, B. A. Boville, D. Marsh,  
4672 L. Harvey, C. Randall, W. Randel, J. F. Lamarque, L. K. Emmons, P. Hess, J. Orlando,  
4673 J. Tyndall, and L. Pan, Sensitivity of chemical tracers to meteorological parameters in the  
4674 mozart-3 chemical transport model, *J. Geophys. Res., in press*, 2006.
- 4675 Kockarts, G., Nitric oxide cooling in the terrestrial thermosphere, *Geophys. Res. Lett.*, 7, 137–  
4676 140, 1980.
- 4677 Koehler, K. A., S. M. Kreidenweis, P. J. DeMott, M. D. Petters, A. J. Prenni, and C. M.  
4678 Carrico, Hygroscopicity and cloud droplet activation of mineral dust aerosol, *Geophysical  
4679 Research Letters*, 36, –, 2009a, 435FB Times Cited:4 Cited References Count:25.
- 4680 Koehler, K. A., S. M. Kreidenweis, P. J. DeMott, M. D. Petters, A. J. Prenni, and C. M. Carrico,  
4681 Hygroscopicity and cloud droplet activation of mineral dust aerosol., *Geophys. Res. Lett.*, 36,  
4682 2009b.
- 4683 Koepke, M. H. P., and I. Schult, Optical properties of aerosols and clouds: The software package  
4684 opac, *Bull. Am. Meteorol. Soc.*, 79, 831–844, 1998.
- 4685 Koppers, G. A. A., and D. P. Murtagh, Model studies of the influence of O<sub>2</sub> photodissociation  
4686 parameterizations in the schumann-runge bands on ozone related photolysis in the upper  
4687 atmosphere, *Ann. Geophys.*, 14, 68–79, 1996.
- 4688 Kroll, J. H., N. L. Ng, S. M. Murphy, R. C. Flagan, and J. H. Seinfeld, Secondary organic aerosol  
4689 formation from isoprene photooxidation, *Environmental Science and Technology*, 40 (6),  
4690 1869–1877, 2006, 024RN Times Cited:121 Cited References Count:62.
- 4691 Lamarque, J. F., T. C. Bond, V. Eyring, C. Granier, A. Heil, Z. Klimont, D. Lee, C. Liousse,  
4692 A. Mieville, B. Owen, M. G. Schultz, D. Shindell, S. J. Smith, E. Stehfest, J. vanAardenne,  
4693 O. R. Cooper, M. Kainuma, N. Mahowald, J. R. McConnell, V. Naik, K. Riahi, and D. P.  
4694 van Vuuren, Historical (18502000) gridded anthropogenic and biomass burning emissions of  
4695 reactive gases and aerosols: methodology and application, *Atmospheric Chemistry and Physics  
4696 Discussion*, 10, 49635019, 2010a.
- 4697 Lamarque, J., T. C. Bond, V. Eyring, C. Granier, A. Heil, Z. Klimont, D. Lee, C. Liousse,  
4698 A. Mieville, B. Owen, M. G. Schultz, D. Shindell, S. J. Smith, E. Stehfest, J. van Aardenne,  
4699 O. R. Cooper, M. Kainuma, N. Mahowald, J. R. McConnell, V. Naik, K. Riahi, and D. P.  
4700 van Vuuren, Historical (1850-2000) gridded anthropogenic and biomass burning emissions of  
4701 reactive gases and aerosols: methodology and application, *Atmospheric Chemistry & Physics  
4702 Discussions*, 10, 4963–5019, Feb., 2010b.
- 4703 Large, W. G., J. C. McWilliams, and S. C. Doney, Oceanic vertical mixing: A review and a  
4704 model with a nonlocal boundary layer parameterization, *Rev. Geophys.*, 32, 363–403, 1994.

- 4705 Large, W. G., and S. Pond, Sensible and latent heat flux measurements over the ocean, *J. Phys.*  
4706 *Oceanogr.*, 12, 464–482, 1982.
- 4707 Lauritzen, P., C. Jablonowski, M. Taylor, and R. Nair, Rotated versions of the jablonowski  
4708 steady-state and baroclinic wave test cases: A dynamical core intercomparison, *Journal of*  
4709 *Advances in Modeling Earth Systems, In Press*, 2010.
- 4710 Lauritzen, P. H., A stability analysis of finite-volume advection schemes permitting long time  
4711 steps, *Mon. Wea. Rev.*, 135, 2658–2673, 2007.
- 4712 Lauritzen, P. H., P. A. Ullrich, and R. D. Nair, Atmospheric transport schemes: Desirable  
4713 properties and a semi-lagrangian view on finite-volume discretizations, in: P.H. Lauritzen,  
4714 R.D. nair, C. Jablonowski, M. Taylor (Eds.), Numerical techniques for global atmospheric  
4715 models, *Lecture Notes in Computational Science and Engineering*, Springer, 2010, to appear.
- 4716 Lawson, R. P., B. Barker, B. Pilson, and Q. Mo, In situ observations of the microphysical  
4717 properties of wave, cirrus and anvil clouds. Part 2: Cirrus cloud, *J. Atmos. Sci.*, 63, 3186–  
4718 3203, 2006.
- 4719 Le Texier, H., S. Solomon, and R. R. Garcia, Role of molecular hydrogen and methane oxidation  
4720 in the water vapor budget of the stratosphere, *Q. J. R. Meteorol. Soc.*, 114, 281–295, 1988.
- 4721 Lean, J., Evolution of the sun's spectral irradiance since the maunder minimum, *Geophys. Res.*  
4722 *Lett.*, 27 (16), 2425–2428, 2000.
- 4723 Lim, Y. B., and P. J. Ziemann, Products and mechanism of secondary organic aerosol formation  
4724 from reactions of n-alkanes with oh radicals in the presence of nox, *Environmental Science*  
4725 and Technology, 39 (23), 9229–9236, 2005, 989ZK Times Cited:53 Cited References Count:48.
- 4726 Lin, S.-J., W. C. Chao, Y. C. Sud, and G. K. Walker, A class of the van leer-type transport  
4727 schemes and its applications to the moisture transport in a general circulation model, *Mon.*  
4728 *Wea. Rev.*, 122, 1575–1593, 1994.
- 4729 Lin, S.-J., and R. B. Rood, Multidimensional flux form semi-lagrangian transport schemes, *Mon.*  
4730 *Wea. Rev.*, 124, 2046–2070, 1996.
- 4731 Lin, S.-J., and R. B. Rood, An explicit flux-form semi-lagrangian shallow water model on the  
4732 sphere, *Q. J. R. Meteorol. Soc.*, 123, 2531–2533, 1997.
- 4733 Lin, S.-J., A vertically lagrangian finite-volume dynamical core for global models, *Mon. Wea.*  
4734 *Rev.*, 132, 2293–2397, 2004.
- 4735 Lin, Y.-L., R. R. Farley, and H. D. Orville, Bulk parameterization of the snow field in a cloud  
4736 model, *J. Clim. Appl. Meteorol.*, 22, 1065–1092, 1983.
- 4737 Lindzen, R. S., Turbulence and stress due to gravity wave and tidal breakdown, *J. Geophys.*  
4738 *Res.*, 86, 9701–9714, 1981.
- 4739 Liu, X., J. E. Penner, S. J. Ghan, and M. Wang, Inclusion of ice microphysics in the NCAR  
4740 Community Atmosphere Model version 3 (CAM3), *J. Clim.*, 20, 4526–4547, 2007.

- 4741 Liu, X., and S. Ghan, A modal aerosol model implementation in the Community Atmosphere  
4742 Model, version 5 (CAM5), *J. Atmos. Sci.*, 2010.
- 4743 Liu, X., and J. E. Penner, Ice nucleation parameterization for global models, *Meteor. Z.*,  
4744 14 (499-514), 2005.
- 4745 Liu, X. H., J. E. Penner, and M. Herzog, Global modeling of aerosol dynamics: Model de-  
4746 scription, evaluation, and interactions between sulfate and nonsulfate aerosols, *Journal of*  
4747 *Geophysical Research-Atmospheres*, 110 (D18), –, 2005, 968RL Times Cited:39 Cited Refer-  
4748 ences Count:207.
- 4749 Lohmann, U., J. Feichter, C. C. Chuang, and J. Penner, Prediction of the number of cloud  
4750 droplets in the echam gcm, *J. Geophys. Res.*, 104 (D8), 9169–9198, 1999.
- 4751 Lord, S. J., W. C. Chao, and A. Arakawa, Interaction of a cumulus cloud ensemble with the  
4752 large-scale environment. part iv: The discrete model, *J. Atmos. Sci.*, 39, 104–113, 1982.
- 4753 Machenhauer, B., The spectral method, in *Numerical Methods Used in Atmospheric Models*,  
4754 World Meteorological Organization, Geneva, Switzerland, 1979.
- 4755 Machenhauer, B. 1998. MPI workshop on conservative transport schemes. in *Report No. 265*, .  
4756 Max-planck-Institute for Meteorology.
- 4757 Machenhauer, B., E. Kaas, and P. H. Lauritzen, Finite volume methods in meteorology, in: R.  
4758 Temam, J. Tribbia, P. Ciarlet (Eds.), Computational methods for the atmosphere and the  
4759 oceans, *Handbook of Numerical Analysis*, 14, 2009, Elsevier, 2009, pp.3-120.
- 4760 Maday, Y., and A. T. Patera, Spectral element methods for the incompressible Navier Stokes  
4761 equations, in *State of the Art Surveys on Computational Mechanics*, edited by A. K. Noor,  
4762 and J. T. Oden, 71–143, ASME, New York, 1987.
- 4763 Mahowald, N. M., D. R. Muhs, S. Levis, P. J. Rasch, M. Yoshioka, C. S. Zender, and C. Luo,  
4764 Change in atmospheric mineral aerosols in response to climate: Last glacial period, prein-  
4765 dustrial, modern, and doubled carbon dioxide climates, *Journal of Geophysical Research-  
4766 Atmospheres*, 111 (D10), –, 2006a, 050EP Times Cited:68 Cited References Count:123.
- 4767 Mahowald, N. M., M. Yoshioka, W. D. Collins, A. J. Conley, D. W. Fillmore, and D. B. Coleman,  
4768 Climate response and radiative forcing from mineral aerosols during the last glacial maximum,  
4769 pre-industrial, current and doubled-carbon dioxide climates, *Geophysical Research Letters*,  
4770 33 (20), –, 2006b, 100WD Times Cited:16 Cited References Count:21.
- 4771 Manabe, S., Climate and the ocean circulation: 1. The atmospheric circulation and the hydrology  
4772 of the earth's surface, *Mon. Wea. Rev.*, 97, 739–774, 1969.
- 4773 Marsh, D., S. Solomon, and A. Reynolds, Empirical model of nitric oxide in the lower thermo-  
4774 sphere, *J. Geophys. Res.*, 109, doi:10.1029/2003JA010199, 2004.

- 4775 Martensson, E. M., E. D. Nilsson, G. deLeeuw, L. H. Cohen, and H. C. Hansson, Laboratory  
4776 simulations and parameterization of the primary marine aerosol production, *Journal of Geo-*  
4777 *physical Research-Atmospheres*, 108 (D9), –, 2003, 682QU Times Cited:51 Cited References  
4778 Count:32.
- 4779 Marti, J., and K. Mauersberger, A survey and new measurements of ice vapor pressure at  
4780 temperatures between 170 and 250 K, *Geophys. Res. Lett.*, 20, 363–366, 1993.
- 4781 Martin, G. M., D. W. Johnson, and A. Spice, The measurement and parameterization of effective  
4782 radius of droplets in warm stratocumulus clouds, *J. Atmos. Sci.*, 51, 1823–1842, 1994.
- 4783 Matthes, K., D. R. Marsh, R. R. Garcia, D. E. Kinnison, F. Sassi, and S. Walters, The role  
4784 of the qbo in modulating the influence of the 11-year solar cycle on the atmosphere using  
4785 constant forcings, *J. Geophys. Res.*, ??, doi:10.1029/2009JD013020, 2010.
- 4786 McAvaney, B. J., W. Bourke, and K. Puri, A global spectral model for simulation of the general  
4787 circulation, *J. Atmos. Sci.*, 35, 1557–1583, 1978.
- 4788 McFarlane, N. A., The effect of orographically excited gravity wave drag on the general circula-  
4789 tion of the lower stratosphere and troposphere, *J. Atmos. Sci.*, 44, 1775–1800, 1987.
- 4790 McFarlane, R. P. S. A., and S. A. Klein, Albedo bias and the horizontal variability of clouds in  
4791 subtropical marine boundary layers: Observations from ships and satellite, *J. Geophys. Res.*,  
4792 104, 6138–6191, 1999.
- 4793 McIntyre, M. E., On dynamics and transport near the polar mesopause in summer, *J. Geophys.*  
4794 *Res.*, 94, 14,617–14,628, 1989.
- 4795 McLinden, C., S. Olsen, B. Hannegan, O. Wild, and M. Prather, Stratospheric ozone in 3-d  
4796 models: A simple chemistry and the cross-tropopause flux, *J. Geophys. Res.*, 105, 14,653–  
4797 14,665, 2000.
- 4798 Merikanto, J., I. Napari, H. Vehkamaki, T. Anttila, and M. Kulmala, New parameterization  
4799 of sulfuric acid-ammonia-water ternary nucleation rates at tropospheric conditions, *Journal*  
4800 *of Geophysical Research-Atmospheres*, 112 (D15), –, 2007, 202AA Times Cited:16 Cited  
4801 References Count:39.
- 4802 Meyers, M. P., P. J. DeMott, and W. R. Cotton, New primary ice-nucleation parameterizations  
4803 in an explicit cloud model, *J. Applied Met.*, 31, 708–721, 1992.
- 4804 Minschwaner, K., and D. E. Siskind, A new calculation of nitric oxide photolysis in the strato-  
4805 sphere, mesosphere, and lower thermosphere, *J. Geophys. Res.*, 98, 20401–20412, 1993.
- 4806 Mitchell, D. L., Parameterization of the Mie extinction and absorption coefficients for water  
4807 clouds, *J. Atmos. Sci.*, 57, 1311–1326, 2000.
- 4808 Mitchell, D. L., Effective diameter in radiation transfer: General definition, applications and  
4809 limitations, *J. Atmos. Sci.*, 59, 2330–2346, 2002.

- 4810 Mitchell, D. L., and W. P. Arnott, A model predicting the evolution of ice particle size spectra  
4811 and radiative properties of cirrus clouds. part ii: Dependence of absorption and extinction on  
4812 ice crystal morphology, *J. Atmos. Sci.*, , 817–832, 1994.
- 4813 Mitchell, D. L., A. Macke, and Y. Liu, Modeling cirrus clouds. Part II: Treatment of radiative  
4814 properties, *J. Atmos. Sci.*, 53, 2697–2988, 1996a.
- 4815 Mitchell, D. L., A. Macke, and Y. Liu, Modeling cirrus clouds. part ii: Treatment of radiative  
4816 properties, *J. Atmos. Sci.*, 53, 2967–2988, 1996b.
- 4817 Mitchell, D. L., W. P. Arnott, C. Schmitt, A. J. Baran, S. Havemann, and Q. Fu, Contributions of  
4818 photon tunneling to extinction in laboratory grown hexagonal columns, *J. Quant. Spectrosc.*  
4819 *Radiat. Transfer*, 70, 761–776, 2001.
- 4820 Mitchell, D. L., A. J. Baran, W. P. Arnott, and C. Schmitt, Testing and comparing the modified  
4821 anomalous diffraction approximation, *J. Atmos. Sci.*, 59, 2330–2346, 2006a.
- 4822 Mitchell, D. L., R. P. d'Entremont, and R. P. Lawson, Passive thermal retrievals of ice and  
4823 liquid water path, effective size and optical depth and their dependence on particle and size  
4824 distribution shape, 12th AMS Conference on Atmospheric Radiation, July, 2006b.
- 4825 Mlawer, E., S. Taubman, P. Brown, M. Iacono, and S. Clough, Radiative transfer for inhomoge-  
4826 neous atmospheres: Rrtm, a validated correlated-k model for the longwave, *J. Geophys. Res.*,  
4827 102, 16663–16682, 1997.
- 4828 Mlynczak, M. G., and S. Solomon, A detailed evaluation of the heating efficiency in the middle  
4829 atmosphere, *J. Geophys. Res.*, 98, 10,517–10,541, 1993.
- 4830 Monahan, E. C., D. E. Spiel, and K. L. Davidson, A model of marine aerosol generation via  
4831 whitecaps and wave disruption, in *Oceanic Whitecaps*, edited by E. C. Monahan, G. M.  
4832 Niocaill, and D. Reidel, Norwell, Mass., 1986.
- 4833 Moncet, J.-L., and S. Clough, Accelerated monochromatic radiative transfer for scattering at-  
4834 mospheres: Application of a new model to spectral radiance observations, *J. Geophys. Res.*,  
4835 102 (21), 853–866, 1997.
- 4836 Morrison, H., J. A. Curry, and V. I. Khvorostyanov, A new double-moment microphysics pa-  
4837 rameterization for application in cloud and climate models. part i: Description, *J. Atmos.*  
4838 *Sci.*, 62, 1665–1677, 2005.
- 4839 Morrison, H., and A. Gettelman, A new two-moment bulk stratiform cloud microphysics scheme  
4840 in the NCAR Community Atmosphere Model (CAM3), Part I: Description and numerical  
4841 tests, *J. Clim.*, 21 (15), 3642–3659, 2008.
- 4842 Morrison, H., and J. O. Pinto, Mesoscale modeling of springtime arctic mixed-phase stratiform  
4843 clouds using a new two-moment bulk microphysics scheme, *J. Atmos. Sci.*, 62, 3683–3704,  
4844 2005.

- 4845 Mote, P. W., J. R. Holton, J. M. Russell, and B. A. Boville, A comparison of observed (haloe)  
4846 and modeled (ccm2) methane and stratospheric water vapor, *grl*, **20**, 1419–1422, 1993.
- 4847 Neale, R. B., J. H. Richter, and M. Jochum, The impact of convection on ENSO: From a delayed  
4848 oscillator to a series of events, *J. Climate*, **21**, 5904–5924, 2008.
- 4849 Neale, R. B., and B. J. Hoskins, A standard test case for AGCMs including their physical  
4850 parametrizations: I: The proposal, *Atmos. Sci. Lett.*, **1**, 101–107, 2001a.
- 4851 Neale, R. B., and B. J. Hoskins, A standard test case for AGCMs including their physical  
4852 parametrizations: II: Results for the Met Office Model, *Atmos. Sci. Lett.*, **1**, 108–114, 2001b.
- 4853 Newman, P. A., J. S. Daniel, D. W. Waugh, and E. R. Nash, A new formulation of equivalent  
4854 effective stratospheric chlorine (EESC), *Atmos. Chem. Phys.*, **7** (17), 4537–4552, 2007.
- 4855 Ng, N. L., P. S. Chhabra, A. W. H. Chan, J. D. Surratt, J. H. Kroll, A. J. Kwan, D. C.  
4856 McCabe, P. O. Wennberg, A. Sorooshian, S. M. Murphy, N. F. Dalleska, R. C. Flagan, and  
4857 J. H. Seinfeld, Effect of nox level on secondary organic aerosol (soa) formation from the  
4858 photooxidation of terpenes, *Atmospheric Chemistry and Physics*, **7** (19), 5159–5174, 2007,  
4859 235MS Times Cited:42 Cited References Count:63.
- 4860 Nousiainen, T., and G. M. McFarquhar, Light scattering by quasi-spherical ice crystals, *J. At-*  
4861 *mos. Sci.*, **61**, 2229–2248, 2004.
- 4862 Odum, J. R., T. P. W. Jungkamp, R. J. Griffin, H. J. L. Forstner, R. C. Flagan, and J. H.  
4863 Seinfeld, Aromatics, reformulated gasoline, and atmospheric organic aerosol formation, *En-*  
4864 *vironmental Science and Technology*, **31** (7), 1890–1897, 1997, Xh483 Times Cited:168 Cited  
4865 References Count:29.
- 4866 Ogibalov, V. P., and V. I. Fomichev, Parameterization of solar heating by the near IR co<sub>2</sub> bands  
4867 in the mesosphere, *Adv. Space Res.*, **32**, 759–764, 2003.
- 4868 Okin, G. S., A new model of wind erosion in the presence of vegetation, *Journal of Geophysical*  
4869 *Research-Earth Surface*, **113** (F2), –, 2008, 276QS Times Cited:5 Cited References Count:41.
- 4870 Orszag, S. A., Fourier series on spheres, *Mon. Wea. Rev.*, **102**, 56–75, 1974.
- 4871 Ovtchinnikov, M., and S. J. Ghan, Parallel simulations of aerosol influence on clouds us-  
4872 ing cloud-resolving and single-column models, *Journal of Geophysical Research-Atmospheres*,  
4873 **110** (D15), –, 2005, 916EG Times Cited:9 Cited References Count:45.
- 4874 Park, S., and C. S. Bretherton, The university of washington shallow convection and moist  
4875 turbulence schemes and their impact on climate simulations with the community atmosphere  
4876 model, *J. Climate*, **22**, 3449–3469, 2009.
- 4877 Park, S., C. S. Bretherton, and P. J. Rasch, The revised cloud macrophysics in the community  
4878 atmosphere model, *J. Climate*, **000**, 0000–0000, 2010.
- 4879 Peter, T., C. Bruhl, and P. J. Crutzen, Increase in the PSC formation probability caused by  
4880 high-flying aircraft, *J. Geophys. Res.*, **18**, 1465–1468, 1991.

- 4881 Petters, M., and S. Kreidenweis, A single parameter representation of hygroscopic growth and  
4882 ccn activity, *Atmos. Chem. Phys.*, 7, 1961–1971, 2007.
- 4883 Pickering, K., Y. Wang, W.-K. Tao, C. Price, and J. Mueller, Vertical distributions of lightning  
4884 NO<sub>x</sub> for use in regional and global chemical transport models, *J. Geophys. Res.*, 103, 31,203–  
4885 31,216, 1998.
- 4886 Pincus, R. H. W. B., and J.-J. Morcrette, A fast, flexible, approximation technique for computing  
4887 radiative transfer in inhomogeneous cloud fields, *J. Geophys. Res.*, 108(D13), 4376, 2003.
- 4888 Poschl, U., M. Canagaratna, J. T. Jayne, L. T. Molina, D. R. Worsnop, C. E. Kolb, and M. J.  
4889 Molina, Mass accommodation coefficient of h<sub>2</sub>so<sub>4</sub> vapor on aqueous sulfuric acid surfaces and  
4890 gaseous diffusion coefficient of h<sub>2</sub>so<sub>4</sub> in n-2/h<sub>2</sub>o, *Journal of Physical Chemistry A*, 102 (49),  
4891 10082–10089, 1998, 146ZX Times Cited:40 Cited References Count:41.
- 4892 Prather, M., Catastrophic loss of stratospheric ozone in dense volcanic clouds, *J. Geophys. Res.*,  
4893 97, 187–10,191, 1992.
- 4894 Prenni, A. J., J. Y. Harrington, M. Tjernstrom, P. J. DeMott, A. Avramov, C. N. Long, S. M.  
4895 Kreidenweis, P. Q. Olsson, and J. Verlinde, Can ice-nucleating aerosols effect Arctic seasonal  
4896 climate?, *Bull. Am. Meteorol. Soc.*, 88, 541–550, 2007.
- 4897 Price, C., J. Penner, and M. Prather, NO<sub>x</sub> from lightning. Part 1: Global distribution based on  
4898 lightning physics, *J. Geophys. Res.*, 102, 5929–5941, 1997a.
- 4899 Price, C., J. Penner, and M. Prather, NO<sub>x</sub> from lightning. Part 2: Constraints from the global  
4900 atmospheric electric circuit, *J. Geophys. Res.*, 102, 5943–5952, 1997b.
- 4901 Price, C., and D. Rind, A simple lightning parameterization for calculating global lightning  
4902 distributions, *J. Geophys. Res.*, 97, 9919–9933, 1992.
- 4903 Pruppacher, H. R., and J. D. Klett, *Microphysics of Clouds and Precipitation*. Kluwer Academic,  
4904 1997.
- 4905 Ranić, M., R. Purser, and F. Mesinger, A global shallow-water model using an expanded  
4906 spherical cube: Gnomonic versus conformal coordinates, *Q. J. R. Meteorol. Soc.*, 122, 959–  
4907 982, 1996.
- 4908 Rasch, P. J., B. A. Boville, and G. P. Brasseur, A three-dimensional general circulation model  
4909 with coupled chemistry for the middle atmosphere, *J. Geophys. Res.*, 100, 9041–9071, 1995.
- 4910 Rasch, P. J., M. C. Barth, J. T. Kiehl, S. E. Schwartz, and C. M. Benkovitz, A description of  
4911 the global sulfur cycle and its controlling processes in the National Center for Atmospheric  
4912 Research Community Climate Model, Version 3, *J. Geophys. Res.*, 105, 1367–1385, 2000.
- 4913 Rasch, P. J., and J. E. Kristjánsson, A comparison of the CCM3 model climate using diagnosed  
4914 and predicted condensate parameterizations, *J. Climate*, 11, 1587–1614, 1998a.
- 4915 Rasch, P. J., and J. E. Kristjansson, A comparison of the ccm3 model climate using diagnosed  
4916 and predicted condensate parameterizations, *J. Climate*, 11, 1587–1614, 1998b.

- 4917 Rasch, P. J., and D. L. Williamson, On shape-preserving interpolation and semi-Lagrangian  
4918 transport, *SIAM J. Sci. Stat. Comput.*, 11, 656–687, 1990.
- 4919 Raymond, D. J., and A. M. Blyth, A stochastic mixing model for non-precipitating cumulus  
4920 clouds, *J. Atmos. Sci.*, 43, 2708–2718, 1986.
- 4921 Raymond, D. J., and A. M. Blyth, Extension of the stochastic mixing model to cumulonimbus  
4922 clouds, *J. Atmos. Sci.*, 49, 1968–1983, 1992.
- 4923 Reisner, J., R. Rasmussen, and R. T. Bruintjes, Explicit forecasting of supercooled liquid water  
4924 in winter storms using the mm5 forecast model, *Q. J. R. Meteorol. Soc.*, 124, 1071–1107,  
4925 1998.
- 4926 R.G.Roble, Energetics of the mesosphere and thermosphere, in *The upper mesosphere and lower*  
4927 *thermosphere : a review of experiment and theory*, edited by R. Johnson, and T. Killeen,  
4928 *Geophys. Monogr.*, 87, 1–21, 1995.
- 4929 Richmond, A., Ionospheric electrodynamics using magnetic apex coordinates, *J. Geomag. Geo-*  
4930 *electric.*, 47, 191, 1995.
- 4931 Richmond, A., M. Blanc, B. Emery, R. Wand, B. Fejer, R. Woodman, S. Ganguly, P. Amayenc,  
4932 R. Behnke, C. Calderon, and J. Evans, An empirical model of quiet-day ionospheric electric  
4933 fields at middle and low latitudes, *J. Geophys. Res.*, 85, 4658, 1980.
- 4934 Richter, J. H., F. Sassi, and R. R. Garcia, Towards a physically-based wave source parameteri-  
4935 zation in a general circulation model, *J. Atmos. Sci.*, 67, 136–156, 2010.
- 4936 Richter, J. H., and P. J. Rasch, Effects of convective momentum transport on the atmospheric  
4937 circulation in the community atmosphere model, version 3, *J. Climate*, 21, 1487–1499, 2008.
- 4938 Ridley, B., K. Pickering, and J. Dye, Comments on the parameterization of lightning-produced  
4939 no in global chemistry-transport models, *Atmos. Environ.*, 39, 6184–6187, 2005.
- 4940 Riemer, N., H. Vogel, B. Vogel, and F. Fiedler, Modeling aerosols on the mesoscale-gamma:  
4941 Treatment of soot aerosol and its radiative effects, *Journal of Geophysical Research-Atmospheres*, 108 (D19), –, 2003, 732EM Times Cited:17 Cited References Count:90.
- 4943 Ringler, T. D., R. P. Heikes, , and D. A. Randall, Modeling the atmospheric general circulation  
4944 using a spherical geodesic grid: A new class of dynamical cores, *Mon. Wea. Rev.*, 128, 2471–  
4945 2490, 2000.
- 4946 Ritchie, H., and M. Tanguay, A comparison of spatially averaged Eulerian and semi-Lagrangian  
4947 treatments of mountains, *Mon. Wea. Rev.*, 124, 167–181, 1996.
- 4948 Robert, A. J., The integration of a low order spectral form of the primitive meteorological  
4949 equations, *J. Meteorol. Soc. Japan*, 44, 237–245, 1966.
- 4950 Roble, R., and E. Ridley, An auroral model for the near thermospheric general circulation model  
4951 (TGCM), *Ann. Geophys.*, 87, 369, 1987.

- 4952 Roble, R., and E. Ridley, A thermosphere-ionosphere-mesosphere-electrodynamics general circu-  
4953 lation model (TIME-GCM): Equinox solar cycle minimum simulations (30-500 km), *Geophys.*  
4954 *Res. Lett.*, **21**, 417–420, 1994.
- 4955 Rothman, L. S., A. Barbe, D. C. Benner, L. R. Brown, C. Camy-Peyret, M. R. Carleer,  
4956 K. Chance, C. Clerbaux, V. Dana, V. M. Devi, A. Fayt, J.-M. Flaud, R. R. Gamache, A. Gold-  
4957 man, D. Jacquemart, K. W. Jucks, W. J. Lafferty, J.-Y. Mandin, S. T. Massie, V. Nemtchinov,  
4958 D. A. Newnham, A. Perrin, C. P. Rinsland, J. Schroeder, K. M. Smith, M. A. H. Smith,  
4959 K. Tang, R. A. Toth, J. V. Auwera, P. Varanasi, and K. Yoshino, The HITRAN molecular  
4960 spectroscopic database: Edition of 2000 including updates of 2001, *J. Quant. Spectrosc.*  
4961 *Radiat. Transfer*, **82**, 2003.
- 4962 Rothman, L., I. Gordon, A. Barbe, D. Benner, P. Bernath, M. Birk, V. Boudon, L. Brown,  
4963 A. Campargue, J.-P. Champion, K. Chance, L. Coudert, V. Dana, V. Devi, S. Fally, J.-M.  
4964 Flaud, R. Gamache, A. Goldman, D. Jacquemart, I. Kleiner, N. Lacome, W. Lafferty, J.-Y.  
4965 Mandin, S. Massie, S. Mikhailyko, C. Miller, N. Moazzen-Ahmadi, O. Naumenko, A. Nikitin,  
4966 J. Orphal, V. Perevalov, A. Perrin, A. Predoi-Cross, C. Rinsland, M. Rotger, M. Simeckov,  
4967 M. Smith, K. Sung, S. Tashkun, J. Tennyson, R. Toth, A. Vandaele, and J. V. Auwera,  
4968 The hitran 2008 molecular spectroscopic database, *Journal of Quantitative Spectroscopy and*  
4969 *Radiative Transfer*, **110 (9-10)**, 533 – 572, 2009, HITRAN.
- 4970 Rotstayn, L. D., B. F. Ryan, and J. J. Katzfey, A scheme for calculation of the liquid fraction in  
4971 mixed-phase stratiform clouds in large-scale models, *Mon. Weather Rev.*, **128 (4)**, 1070–1088,  
4972 2000.
- 4973 Sadourny, R., Conservative finite-difference approximations of the primitive equations on quasi-  
4974 uniform spherical grids, *Mon. Wea. Rev.*, **100 (2)**, 136–144, 1972.
- 4975 Sander, S. P., et al., Chemical kinetics and photochemical data for use in atmospheric stud-  
4976 ies. Evaluation number 14, Technical Report Publication 02-25, Jet Propulsion Laboratory,  
4977 Pasadena, CA, 2003.
- 4978 Sander, S. P., et al., Chemical kinetics and photochemical data for use in atmospheric stud-  
4979 ies. Evaluation number 15, Technical Report Publication 06-02, Jet Propulsion Laboratory,  
4980 Pasadena, CA, 2006.
- 4981 Sanderson, M., W. Collins, R. Derwent, and C. Johnson, Simulation of global hydrogen levels  
4982 using a lagrangian three-dimensional model, *J. Atmos. Chem.*, **46 (1)**, 15–28, SEP, 2003.
- 4983 Sandu, A., F. A. Potra, V. Damian-Iordache, and G. R. Carmichael, Efficient implementation  
4984 of fully implicit methods for atmospheric chemistry, *J. Comp. Phys.*, **129**, 101–110, 1996.
- 4985 Sandu, A., J. Verwer, M. vanLoon, G. Carmichael, F. Potra, D. Dabdub, and J. Seinfeld,  
4986 Benchmarking stiff ODE solvers for atmospheric chemistry problems I: Implicit versus explicit,  
4987 *Atmospheric Environment*, **31**, 3151–3166, 1997.
- 4988 Sangster, W. E., A meteorological coordinate system in which the Earth's surface is a coordinate  
4989 surface, Ph.D. thesis, University of Chicago, Department of Geophysical Sciences, 1960.

- 4990 Sato, R. K., L. M. Bath, D. L. Williamson, and G. S. Williamson, User's guide to NCAR  
4991 CCMOB, Technical Report NCAR/TN-211+IA, National Center for Atmospheric Research,  
4992 Boulder, Colorado, 133 pp., 1983.
- 4993 Satoh, M., *Atmospheric Circulation Dynamics and Circulation Models (Springer Praxis Books*  
4994 / *Environmental Sciences*). Springer, 1 edition, 6, 2004.
- 4995 Scherliess, L., A. Richmond, and B. Fejer. 2002. Global empirical ionospheric electric field  
4996 model. draft, Center for Atmospheric and Space Science, Utah State University, Logan.
- 4997 Schubert, W. H., J. S. Wakefield, E. J. Steiner, and S. K. Cox, Marine stratocumulus convection.  
4998 part i: Governing equations and horizontally homogeneous solutions, *J. Atmos. Sci.*, 36, 1286–  
4999 1307, 1979.
- 5000 Schunk, R., and A. Nagy, *Ionospheres: Physics, Plasma Physics, and Chemistry*. Cambridge,  
5001 University Press, 2000.
- 5002 Seinfeld, J. H., and S. N. Pandis, *Atmospheric Chemistry and Physics: From Air Pollution to*  
5003 *Climate Change*. John Wiley, Hoboken, N. J, 1998.
- 5004 Sihto, S. L., M. Kulmala, V. M. Kerminen, M. D. Maso, T. Petaja, I. Riipinen, H. Korhonen,  
5005 F. Arnold, R. Janson, M. Boy, A. Laaksonen, and K. E. J. Lehtinen, Atmospheric sulphuric  
5006 acid and aerosol formation: implications from atmospheric measurements for nucleation and  
5007 early growth mechanisms, *Atmospheric Chemistry and Physics*, 6, 4079–4091, 2006.
- 5008 Simmons, A. J., and D. M. Burridge, An energy and angular momentum conserving vertical  
5009 finite-difference scheme and hybrid vertical coordinates, *Mon. Wea. Rev.*, 109, 758–766, 1981.
- 5010 Simmons, A. J., and R. Strüfing, An energy and angular-momentum conserving finite-difference  
5011 scheme, hybrid coordinates and medium-range weather prediction, Technical Report ECMWF  
5012 Report No. 28, European Centre for Medium-Range Weather Forecasts, Reading, U.K.,  
5013 68 pp., 1981.
- 5014 Simmons, A. J., and R. Strüfing, Numerical forecasts of stratospheric warming events using a  
5015 model with hybrid vertical coordinate, *Q. J. R. Meteorol. Soc.*, 109, 81–111, 1983.
- 5016 Skamarock, W., Kinetic energy spectra and model filters, in: P.H. Lauritzen, R.D. nair, C.  
5017 Jablonowski, M. Taylor (Eds.), Numerical techniques for global atmospheric models, *Lecture*  
5018 *Notes in Computational Science and Engineering*, Springer, 2010, 2010, to appear.
- 5019 Slingo, J. M., The development and verification of a cloud prediction scheme for the ECMWF  
5020 model, *Q. J. R. Meteorol. Soc.*, 113, 899–927, 1987a.
- 5021 Slingo, J. M., The development and verification of a cloud prediction scheme for the ecmwf  
5022 model, *Q. J. R. Meteorol. Soc.*, 113, 899–927, 1987b.
- 5023 Smith, R. N. B., A scheme for predicting layer clouds and their water content in a general  
5024 circulation model, *Q. J. R. Meteorol. Soc.*, 116, 435–460, 1990.

- 5025 Smith, S. J., H. Pitcher, and T. M. L. Wigley, Global and regional anthropogenic sulfur dioxide  
5026 emissions, *Glob. Biogeochem. Cycles*, 29, 99–119, 2001.
- 5027 Smith, S. J., R. Andres, E. Conception, and J. Lurz, Historical sulfur dioxide emissions 18502000:  
5028 Methods and results, Technical report, Pacific Northwest National Laboratory, Joint Global  
5029 Change Research Institute, 2004.
- 5030 Solomon, S., and L. Qiang, Solar extreme-ultraviolet irradiance for general circulation models,  
5031 *J. Geophys. Res.*, 110, A10306, doi:10.1029/2005JA011160, 2005.
- 5032 Spiteri, R. J., and S. J. Ruuth, A new class of optimal high-order strong-stability-preserving  
5033 time discretization methods, *SIAM J. Numer. Anal.*, 40 (2), 469–491, 2002.
- 5034 Staniforth, A., N. Wood, and C. Girard, Energy and energy-like invariants for deep non-  
5035 hydrostatic atmospheres, *Q. J. R. Meteorol. Soc.*, 129, 3495–3499, 2003.
- 5036 Starr, V. P., A quasi-lagrangian system of hydrodynamical equations, *J. Meteor.*, 2, 227–237,  
5037 1945.
- 5038 Stier, P., J. Feichter, S. Kinne, S. Kloster, E. Vignati, J. Wilson, L. Ganzeveld, I. Tegen,  
5039 M. Werner, Y. Balkanski, M. Schulz, O. Boucher, A. Minikin, and A. Petzold, The aerosol-  
5040 climate model echam5-ham, *Atmospheric Chemistry and Physics*, 5, 1125–1156, 2005, 912EM  
5041 Times Cited:156 Cited References Count:125.
- 5042 Suarez, M. J., and L. L. Takacs, Documentation of the aries/geos dynamical core: Version 2,  
5043 Technical Report Technical Memorandum 104 606 Vol. 5, NASA, 1995.
- 5044 Sundqvist, H., Parameterization of condensation and associated clouds in models for weather  
5045 prediction and general circulation simulation, in *Physically-based Modeling and Simulation of*  
5046 *Climate and Climate Change*, Vol. 1, edited by M. E. Schlesinger, 433–461, Kluwer Academic,  
5047 1988.
- 5048 Tabazadeh, A., R. P. Turco, and M. Z. Jacobson, A model for studying the composition and  
5049 chemical effects of stratospheric aerosols, *J. Geophys. Res.*, 99, 12,897–12,914, 1994.
- 5050 Tabazadeh, A., M. L. Santee, M. Y. Danilin, H. C. Pumphrey, P. A. Newman, P. J. Hamill, and  
5051 J. L. Mergenthaler, Quantifying denitrification and its effect on ozone recovery, *Science*, 288,  
5052 1407–1411, 2000.
- 5053 Taylor, M. A., J. Edwards, and A. St.Cyr, Petascale atmospheric models for the community  
5054 climate system model: New developments and evaluation of scalable dynamical cores, *J.*  
5055 *Phys. Conf. Ser.*, 125 (012023), 2008.
- 5056 Taylor, M. 2010. Conservation of mass and energy for the moist atmospheric primitive equations  
5057 on unstructured grids. in *Numerical Techniques for Global Atmospheric Models, Springer*  
5058 *Lecture Notes in Computational Science and Engineering*, . Springer.
- 5059 Taylor, M., J. Tribbia, and M. Iskandarani, The spectral element method for the shallow water  
5060 equations on the sphere, *J. Comp. Phys.*, 130, 92–108, 1997.

- 5061 Taylor, M. A., A. St.Cyr, and A. Fournier. 2009. A non-oscillatory advection operator for the  
5062 compatible spectral element method. in *Computational Science ICCS 2009 Part II, Lecture*  
5063 *Notes in Computer Science* 5545, 273–282, , Berlin / Heidelberg. Springer.
- 5064 Taylor, M. A., and A. Fournier, A compatible and conservative spectral element method on  
5065 unstructured grids, *J. Comp. Phys., In Press*, –, 2010.
- 5066 Teklemariam, T., and J. Sparks, Gaseous fluxes of peroxyacetyl nitrate (PAN) into plant leaves,  
5067 *PLANT CELL AND ENVIRONMENT*, 27 (9), 1149–1158, SEP, 2004.
- 5068 Temperton, C., Treatment of the Coriolis terms in semi-Lagrangian spectral models, in *At-*  
5069 *mospheric and Ocean Modelling. The André J. Robert Memorial Volume*, edited by C. Lin,  
5070 R. Laprise,, and H. Ritchie, 293–302, Canadian Meteorological and Oceanographic Society,  
5071 Ottawa, Canada, 1997.
- 5072 Temperton, C., M. Hortal, and A. Simmons, A two-time-level semi-Lagrangian global spectral  
5073 model, *Q. J. R. Meteorol. Soc.*, 127, 111–127, 2001.
- 5074 Thomas, S., and R. Loft, Parallel semi-implicit spectral element methods for atmospheric general  
5075 circulation models, *J. Sci. Comput.*, 15, 499–518, 2000.
- 5076 Thomas, S., and R. Loft, The NCAR spectral element climate dynamical core: Semi-implicit  
5077 Eulerian formulation, *J. Sci. Comput.*, 25, 307–322, 2005.
- 5078 Thomason, L. W., L. R. Poole, and T. Deshler, A global climatology of stratospheric aerosol  
5079 surface area density measurements: 1984–1994, *J. Geophys. Res.*, 102, 8967–8976, 1997.
- 5080 Thompson, G. M., R. M. Rasmussen, and K. Manning, Explicit forecasts of winter precipitation  
5081 using and improved bulk microphysics scheme. part I: Description and sensitivity analysis,  
5082 *Mon. Weather Rev.*, 132, 519–542, 2004.
- 5083 Thompson, G., P. R. Field, R. M. Rasmussen, and W. D. Hall, Explicit forecasts of winter  
5084 precipitation using an improved bulk microphysics scheme. part ii: Implementation of a new  
5085 snow parameterization, *Monthly Weather Review*, 136 (12), 5095–5115, 2008.
- 5086 Tie, X., S. Madronich, S. Walters, D. P. Edwards, P. Ginoux, N. Mahowald, R. Zhang, C. Lou,  
5087 and G. Brasseur, Assessment of the global impact of aerosols on tropospheric oxidants, *J.*  
5088 *Geophys. Res.*, 110, D03204, 1992.
- 5089 Tie, X., G. Brasseur, L. Emmons, L. Horowitz, and D. Kinnison, Effects of aerosols on tro-  
5090 pospheric oxidants: A global model study, *Journal of Geophysical Research-Atmospheres*,  
5091 106 (D19), 22931–22964, 2001, 481UJ Times Cited:64 Cited References Count:92.
- 5092 Tie, X. X., S. Madronich, S. Walters, D. P. Edwards, P. Ginoux, N. Mahowald, R. Y. Zhang,  
5093 C. Lou, and G. Brasseur, Assessment of the global impact of aerosols on tropopshic ozidants,  
5094 *J. Geophys. Res.*, 110 (D03204), 2005.
- 5095 Tilmes, S., R. Garcia, D. Kinnisen, A. Gettelman, and P. J. Rasch, Impact of geoengineered  
5096 aerosols on the troposphere and stratosphere, *J. Geophys. Res.*, 114, 2009.

- 5097 Turnipseed, A., G. Huey, E. Nemitz, R. Stickel, J. Higgs, D. Tanner D. andSlusher, J. Sparks,  
5098 F. Flocke, and A. Guenther, Eddy covariance fluxes of peroxyacetyl nitrates (pan) and noy to  
5099 a coniferous forest, *J. Geophys. Res.*, **111**, D09304, 2006.
- 5100 van de Hulst, H. C., *Light Scattering by Small Particles*. Dover, 1957.
- 5101 Vavrus, S., and D. Waliser, An improved parameterization for simulating arctic cloud amount  
5102 in the CCSM3 climate model, *J. Climate*, **21**, 5673–5687, 2008.
- 5103 Vehkamaki, H., M. Kulmala, I. Napari, K. E. J. Lehtinen, T. T., N. Noppel, and A. Laaksonen,  
5104 an improved parameterization for sulfuric acid-water nucleation rates for tropospheric and  
5105 stratospheric conditions, *Journal of Geophysical Research-Atmospheres*, **107**, 4622, 2002.
- 5106 Walmsley, J., and M. Wesely, Modification of coded parametrizations of surface resistances to  
5107 gaseous dry deposition, *Atmos. Environ.*, **30** (7), 1181–1188, APR, 1996.
- 5108 Wang, H., J. J. Tribbia, F. Baer, A. Fournier, and M. A. Taylor, A spectral element version of  
5109 CAM2, *Mon. Wea. Rev.*, **135**, 38253840, 2007.
- 5110 Wang, M. H., J. E. Penner, and X. H. Liu, Coupled impact aerosol and NCAR CAM3 model:  
5111 Evaluation of predicted aerosol number and size distribution, *Journal of Geophysical Research-  
5112 Atmospheres*, **114**, D06302, 2009.
- 5113 Wang, Y.-M., J. Lean, and N. Sheeley, Modeling the sun's magnetic field and irradiance since  
5114 1713, *The Astrophysical Journal*, **625** (1), 2005.
- 5115 Warren, S., and R. E. Brandt, Optical constants of ice from the ultraviolet to the microwave:  
5116 A revised compilation, *J. Geophys. Res.*, **113**, 2008.
- 5117 Washington, W. M., Documentation for the Community Climate Model (CCM), Version 0,  
5118 Technical Report NTIS No. PB82 194192, National Center for Atmospheric Research, Boulder,  
5119 Colorado, 1982.
- 5120 Webster, S., A. R. Brown, D. R. Cameron, and P. Jones, Improvements to the representation of  
5121 orography in the met office unified model, *Quart. J. Roy. Meteor. Soc.*, **129**, 1989–2010, 2003.
- 5122 Weimer, D., Models of high-latitude electric potentials derived with the least error fit of spherical  
5123 harmonic coefficients, *J. Geophys. Res.*, **100**, 19,595, 1995.
- 5124 Wesely, M., Parameterization of surface resistances to gaseous dry deposition in regional-scale  
5125 numerical models, *Atmos. Environ.*, **23**, 1293–1304, 1989.
- 5126 Wesely, M., and B. Hicks, A review of the current status of knowledge on dry deposition, *Atmos.*  
5127 *Environ.*, **34** (12-14), 2261–2282, 2000.
- 5128 Wiacek, A., and T. Peter, On the availability of uncoated mineral dust ice nuclei in cold cloud  
5129 regions, *Geophys. Res. Lett.*, **36** (L17801), 2009.

- 5130 Williamson, D. L., Description of NCAR Community Climate Model (CCM0B), Technical Re-  
5131 port NCAR/TN-210+STR, National Center for Atmospheric Research, Boulder, Colorado,  
5132 NTIS No. PB83 23106888, 88 pp., 1983.
- 5133 Williamson, D. L., Time-split versus process-split coupling of parameterizations and dynamical  
5134 core, *Mon. Wea. Rev.*, 130, 2024–2041, 2002.
- 5135 Williamson, D. L., L. M. Bath, R. K. Sato, T. A. Mayer, and M. L. Kuhn, Documentation of  
5136 NCAR CCM0B program modules, Technical Report NCAR/TN-212+IA, National Center for  
5137 Atmospheric Research, Boulder, Colorado, NTIS No. PB83 263996, 198 pp., 1983.
- 5138 Williamson, D. L., J. T. Kiehl, V. Ramanathan, R. E. Dickinson, and J. J. Hack, Description  
5139 of NCAR Community Climate Model (CCM1), Technical Report NCAR/TN-285+STR,  
5140 National Center for Atmospheric Research, Boulder, Colorado, 112 pp., 1987.
- 5141 Williamson, D. L., and J. G. Olson, Climate simulations with a semi-Lagrangian version of the  
5142 NCAR Community Climate Model, *Mon. Wea. Rev.*, 122, 1594–1610, 1994a.
- 5143 Williamson, D. L., and J. G. Olson, Climate simulations with a semi-lagrangian version of the  
5144 NCAR community climate model, *Mon. Wea. Rev.*, 122, 1594–1610, 1994b.
- 5145 Williamson, D. L., and P. J. Rasch, Two-dimensional semi-Lagrangian transport with shape-  
5146 preserving interpolation, *Mon. Wea. Rev.*, 117, 102–129, 1989.
- 5147 Williamson, D. L., and J. M. Rosinski, Accuracy of reduced grid calculations, *Q. J. R. Meteorol. Soc.*, 126, 1619–1640, 2000.
- 5148 Williamson, D. L., and G. S. Williamson, Circulation statistics from January and July simula-  
5149 tions with the NCAR Community Climate Model (CCM0B), Technical Report NCAR/TN-  
5150 224+STR,, National Center for Atmospheric Research, Boulder, Colorado, NTIS No. PB85  
5151 165637/AS, 112 pp., 1984.
- 5152 Williamson, G. S., CCM2 datasets and circulation statistics, Technical Report NCAR/TN-  
5153 391+STR, National Center for Atmospheric Research, Boulder, Colorado, 85 pp., 1993.
- 5154 Williamson, G. S., and D. L. Williamson, Circulation statistics from seasonal and perpetual  
5155 January and July simulations with the NCAR Community Climate Model (CCM1): R15,  
5156 Technical Report NCAR/TN-302+STR, National Center for Atmospheric Research, Boulder,  
5157 Colorado, 199 pp., 1987.
- 5158 Wilson, J., C. Cuvelier, and F. Raes, A modeling study of global mixed aerosol fields, *Journal  
5159 of Geophysical Research-Atmospheres*, 106 (D24), 34,08134,108, 2001.
- 5160 Wilson, J. D., Representing drag on unresolved terrain as a distributed momentum sink, *J.  
5161 Atmos. Sci.*, 59, 1629–1637, 2002.
- 5162 Wiscombe, W. J., Mie scattering calculations: Advances in technique and fast, vector-speed  
5163 computer codes., Technical Report Tech. Note. NCAR/TN-140+STR, NCAR, 1996.
- 5164

- 5165 World Meteorological Organization, Scientific Assessment of Ozone Depletion: 2002 Global  
5166 Ozone Research and Monitoring Project, Report no. 47, 498 pp., Geneva, 2003.
- 5167 Wu, T. T., High frequency scattering, *Phys. Rev.*, **104**, 1201–1212, 1956.
- 5168 Yang, P., H. Wei, H. L. Huang, B. A. Baum, Y. X. Hu, G. W. Kattawar, M. I. Mishchenko, and  
5169 Q. Fu, Scattering and absorption property database for nonspherical ice particles in the near-  
5170 through far-infrared spectral region, *Appl. Opt.*, **44**, 5512–5523, 2005.
- 5171 Yonemura, S., S. Kawashima, and H. Tsuruta, Carbon monoxide, hydrogen, and methane uptake  
5172 by soils in a temperate arable field and a forest, *J. Geophys. Res.*, **105** (D11), 14,347–14,362,  
5173 JUN 16, 2000.
- 5174 Yoshioka, M., N. M. Mahowald, A. J. Conley, W. D. Collins, D. W. Fillmore, C. S. Zender,  
5175 and D. B. Coleman, Impact of desert dust radiative forcing on sahel precipitation: Relative  
5176 importance of dust compared to sea surface temperature variations, vegetation changes, and  
5177 greenhouse gas warming, *Journal of Climate*, **20** (8), 1445–1467, 2007, 157SY Times Cited:33  
5178 Cited References Count:80.
- 5179 Young, K. C., The role of contact nucleation in ice phase initiation of clouds, *J. Atmos. Sci.*,  
5180 **31**, 768–776, 1974.
- 5181 Zeng, X., and R. E. Dickinson, Effect of surface sublayer on surface skin temperature and fluxes,  
5182 *J. Climate*, **11**, 537–550, 1998.
- 5183 Zeng, X., M. Zhao, and R. E. Dickinson, Intercomparison of bulk aerodynamic algorithms for  
5184 the computation of sea surface fluxes using TOGA COARE and TAO data, *J. Climate*, **11**,  
5185 2628–2644, 1998.
- 5186 Zerroukat, M., N. Wood, and A. Staniforth, A monotonic and positive-definite filter for a  
5187 semi-lagrangian inherently conserving and efficient (slice) scheme, *Q. J. R. Meteorol. Soc.*,  
5188 **131** (611), 2923–2936, 2005.
- 5189 Zhang, G. J., and N. A. McFarlane, Sensitivity of climate simulations to the parameterization of  
5190 cumulus convection in the Canadian Climate Centre general circulation model, *Atmosphere-  
5191 Ocean*, **33**, 407–446, 1995.
- 5192 Zhang, L. M., S. L. Gong, J. Padro, and L. Barrie, A size-segregated particle dry deposition  
5193 scheme for an atmospheric aerosol module, *Atmospheric Environment*, **35** (3), 549–560, 2001,  
5194 395TK Times Cited:136 Cited References Count:49.
- 5195 Zhang, M., W. Lyn, C. S. Bretherton, J. J. Hack, and P. J. Rasch, A modified formulation  
5196 of fractional stratiform condensation rate in the ncar community atmosphere model (cam2),  
5197 *J. Geophys. Res.*, **000**, 1000–0000, 2003a.
- 5198 Zhang, M., W. Lin, C. S. Bretherton, J. J. Hack, and P. J. Rasch, A modified formulation of  
5199 fractional stratiform condensation rate in the NCAR community atmospheric model CAM2,  
5200 *J. Geophys. Res.*, **108** (D1), 2003b.

5201 Zhang, Y., and L. Paxton, An empirical kp-dependent global auroral model based on timed/guvi  
5202 fuv data, *Journal of Atmospheric and Solar-Terrestrial Physics*, 70 (8-9), 1231 – 1242, 2008.

5203 Zilitinkevich, S. S., *Dynamics of the Atmospheric Boundary Layer*. Gidrometeoizdat, Leningrad,  
5204 1970, 292 pp.